

# Structure and Properties of Energetic Materials

Symposium held November 30-December 2, 1992, Boston, Massachusetts, U.S.A.

EDITORS:

**Donald H. Liebenberg**

U.S. Office of Naval Research  
Arlington, Virginia, U.S.A.

**Ronald W. Armstrong**

University of Maryland  
College Park, Maryland, U.S.A.

**John J. Gilman**

Lawrence Berkeley Laboratory  
Berkeley, California, U.S.A.



MATERIALS RESEARCH SOCIETY  
Pittsburgh, Pennsylvania

93-13197



93 6 14 02 3

AD-A265 775

This work was supported in part by the Office of Naval Research under Grant Number N00014-93-1-0147. The United States Government has a royalty-free license throughout the world in all copyrightable material contained herein.

Single article reprints from this publication are available through University Microfilms Inc., 300 North Zeeb Road, Ann Arbor, Michigan 48106

CODEN: MRSPDH

Copyright 1993 by Materials Research Society.  
All rights reserved.

This book has been registered with Copyright Clearance Center, Inc. For further information, please contact the Copyright Clearance Center, Salem, Massachusetts.

Published by:

Materials Research Society  
9800 McKnight Road  
Pittsburgh, Pennsylvania 15237  
Telephone (412) 367-3003  
Fax (412) 367-4373

Library of Congress Cataloging in Publication Data

Structure and properties of energetic materials : symposium held November 30-

December 2, 1992, Boston, Massachusetts, U.S.A. / edited by Donald H.

Liebenberg, Donald W. Armstrong, and John J. Gilman

p. cm.—(Materials Research Society symposium proceedings.

ISSN 0272-9172 : v. 296)

Includes bibliographical references and indexes.

ISBN 1-55899-191-3

I. Explosives—Congresses. I. Liebenberg, Donald H. II. Armstrong,

Ronald W. III. Gilman, John J. (John Joseph) IV. Series: Materials Research

Society symposium proceedings, v. 296.

TP270.A1S77 1993

662'.2—dc20

93-12847

CIP

Manufactured in the United States of America

## Contents

PREFACE	ix
ACKNOWLEDGMENTS	xi
MATERIALS RESEARCH SOCIETY SYMPOSIUM PROCEEDINGS	xii

### PART I: STRUCTURE AND STABILITY

*MOLECULAR STRUCTURE AND PERFORMANCE OF HIGH EXPLOSIVES James R. Stine	3
*RECENT ADVANCES IN THE THERMAL DECOMPOSITION OF CYCLIC NITRAMINES Richard Behrens, Jr. and Suryanarayana Bulusu	13
*MOLECULAR COMPOSITION, STRUCTURE, AND SENSITIVITY OF EXPLOSIVES Carlyle B. Storm and James R. Travis	25
ENERGY TRANSFER DYNAMICS AND IMPACT SENSITIVITY Laurence E. Fried and Anthony J. Ruggiero	35
RELATIONSHIP BETWEEN RADIATION STABILITY AND MOLECULAR STRUCTURE OF NITRAMINE EXPLOSIVES James J. Pinto	41
THIN FILM INFRARED LASER PYROLYSIS STUDIES OF THERMAL DECOMPOSITION MECHANISMS IN NITRAMINE PROPELLANTS Tod R. Botcher and Charles A. Wight	47
NITROGEN RADICALS FROM THERMAL AND PHOTOCHEMICAL DECOMPOSITION OF AMMONIUM PERCHLORATE, AMMONIUM DINITRAMIDE, AND CYCLIC NITRAMINES M.D. Pace	53

### PART II: DEFORMATION, FRACTURE, AND INITIATION

*ENERGY LOCALIZATION AND THE INITIATION OF EXPLOSIVE CRYSTALS BY SHOCK OR IMPACT C.S. Coffey	63
*THE IMPORTANCE OF STERICALLY HINDERED SHEAR IN DETERMINING THE SENSITIVITY OF EXPLOSIVE CRYSTALS Jerry J. Dick	75
FRACTURE SURFACE TOPOGRAPHY OF OCTOL EXPLOSIVES M. Yvonne D. Lanzerotti, James J. Pinto, and Allan Wolfe	81
THE ELECTRON-BEAM SENSITIVITY OF BINARY METAL AZIDES Patrick J. Herley and William Jones	87
COMPARISON OF DEFORMATION AND SHOCK REACTIVITY FOR SINGLE CRYSTALS OF RDX AND AMMONIUM PERCHLORATE H.W. Sandusky, B.C. Beard, B.C. Glancy, W.L. Elban, and R.W. Armstrong	93

\*Invited Paper

OPTIC QUALITY INSPECTED 2

<div style="position: absolute; top: 5px; right: 5px;">v</div> <div style="position: absolute; bottom: 5px; left: 5px; font-size: 2em; font-weight: bold;">A-1</div>	<div style="position: absolute; top: 5px; right: 5px;">Dist</div> <div style="position: absolute; top: 5px; left: 5px;">Special</div>	<div style="position: absolute; top: 5px; right: 5px;">Codes</div> <div style="position: absolute; top: 5px; left: 5px;">and/or</div>
--	---	---

<b>MOLECULAR MODELING OF SLIP SUPPOSED TO OCCUR IN THE SHOCK INITIATION OF CRYSTALLINE PETN</b>	99
James P. Ritchie	

<b>INTERPRETING DROP-WEIGHT IMPACT RESULTS IN TERMS OF DEFORMATION DEPENDENT INITIATION CRITERIA</b>	107
P.J. Baker and A.M. Mellor	

<b>HOT SPOT HEATING FROM IMPURITIES AND VACANCIES IN A CRYSTALLINE SOLID UNDER RAPID COMPRESSION</b>	113
D.H. Tsai	

### **PART III: SHOCK PHENOMENA**

<b>*DISSOCIATIVE PHASE TRANSITIONS, SPLIT SHOCK WAVES, RAREFACTION SHOCKS, AND DETONATIONS</b>	123
C.T. White, D.H. Robertson, M.L. Elert, J.W. Mintmire, and D.W. Brenner	

<b>*FEMTOSECOND SPECTROSCOPY OF CHEMICALLY REACTIVE SOLIDS: A METHODOLOGY</b>	129
Weining Wang, Marc M. Wefers, and Keith A. Nelson	

<b>*EXPLOSION OF DROPS IMPACTING NON-WETTING RIGID SURFACES</b>	141
Clarence Zener and Dennis Prieve	

<b>AB INITIO STUDY OF ELECTRONIC STRUCTURE OF RDX MOLECULAR CRYSTAL</b>	149
Guang Gao, Ravindra Pandey, and A. Barry Kunz	

<b>MOLECULAR DYNAMICS SIMULATIONS OF SHOCKS AND DETONATIONS IN A MODEL 3D ENERGETIC CRYSTAL WITH DEFECTS</b>	155
Lee Phillips	

<b>MOLECULAR DYNAMICS SIMULATIONS OF SHOCK-DEFECT INTERACTIONS IN TWO-DIMENSIONAL NONREACTIVE CRYSTALS</b>	161
Robert S. Sinkovits, Lee Phillips, Elaine S. Oran, and Jay P. Boris	

<b>MOLECULAR LEVEL STUDY OF INSENSITIVE AND ENERGETIC LAYERED AND INTERCALATED MATERIALS</b>	167
Richard D. Bardo	

<b>OVERVIEW: HIGH SPEED DYNAMICS AND MODELLING AS IT APPLIES TO ENERGETIC SOLIDS</b>	173
J. Covino, S.A. Finnegan, O.E.R. Heimdahl, A.J. Lindfors, and J.K. Pringle	

<b>DELAYED INITIATION IN A MODEL ENERGETIC MATERIAL</b>	183
D.H. Robertson, D.W. Brenner, and C.T. White	

### **PART IV: CRYSTALS: GROWTH AND BEHAVIOR**

<b>*ELECTRONIC EXCITATIONS PRECEDING SHOCK INITIATION IN EXPLOSIVES</b>	189
J. Sharma and B.C. Beard	

<b>*PRESSURE/TEMPERATURE/REACTION PHASE DIAGRAMS FOR SEVERAL NITRAMINE COMPOUNDS</b>	199
T.P. Russell, P.J. Miller, G.J. Piermarini, and S. Block	

\*Invited Paper



<b>THE GROWTH AND PERFECTION OF SINGLE CRYSTALS OF TRINITROTOLUENE (TNT)</b>	215
Hugh G. Gallagher and John N. Sherwood	
<b>ATOMIC FORCE MICROSCOPY OF AMMONIUM PERCHLORATE</b>	221
Minsun Yoo, Seokwon Yoon, and Alex De Lozanne	
<b>ENERGETIC CRYSTAL-LATTICE-DEPENDENT RESPONSES</b>	227
R.W. Armstrong, H.L. Ammon, Z.Y. Du, W.L. Elban, and X.J. Zhang	
<b>THE MOLECULAR AND CRYSTAL STRUCTURES OF POLYCYCLIC ENERGETIC MATERIALS</b>	233
Richard Gilardi	
<b>NTO POLYMORPHS</b>	237
Kien-yin Lee and Richard Gilardi	
<b>GROWTH AND DEFECTS OF EXPLOSIVES CRYSTALS</b>	243
Howard H. Cady	
 <b>PART V: STATICS, KINEMATICS, AND DYNAMICS</b>	
<b>*SURFACE CHEMICAL CHARACTERIZATION METHODS APPLIED TO ENERGETIC MATERIALS</b>	257
B.C. Beard and J. Sharma	
<b>*SURFACE CHEMISTRY OF ENERGETIC MATERIALS AT HIGH TEMPERATURE</b>	269
Thomas B. Brill	
<b>QUANTUM DYNAMICAL STUDIES OF THE DECOMPOSITION OF ENERGETIC MATERIALS</b>	281
Herschel Rabitz and Eduardo Vilallonga	
<b>CORRELATION TIME FOR POLYMER CHAIN MOTION NEAR THE GLASS TRANSITION IN NITROCELLULOSE</b>	287
J.R.P. Jayakody, S. Bulusu, and R A Marino	
<b>HOT SPOT HISTORIES IN ENERGETIC MATERIALS</b>	293
A.M. Mellor, D.A Wiegand, and K.B. Isom	
<b>EXPERIMENTAL STUDY AND MODEL CALCULATIONS OF METAL COMBUSTION IN Al/AP UNDERWATER EXPLOSIVES</b>	299
Philip J. Miller and Raafat H. Guirguis	
<b>DETONATION STUDIES IN DISPERSED SOLID PARTICULATE EXPLOSIVES USING HIGH SPEED TIME-RESOLVED HOLOGRAPHY</b>	305
Michael J. Ehrlich, James W Wagner, Jacob Friedman, and Heinrich Eggart	
<b>REACTION KINETICS OF METALLIZED EXPLOSIVES</b>	311
Hermenzo D. Jones and Frank J. Zerilli	
 <b>PART VI: PROCESSES, PERFORMANCE, AND PROPELLANTS</b>	
<b>*COMBUSTION SYNTHESIS OF COMPOSITE MATERIALS</b>	319
J.J. Moore	
<b>*INTERRELATIONSHIP BETWEEN SOLID PROPELLANT COMBUSTION AND MATERIALS BEHAVIOR</b>	331
Kenneth K. Kuo, Thomas A. Litzinger, and Wen H Hsieh	
<b>*Invited Paper</b>	

<b>LABORATORY TESTING AND CONSTITUTIVE MODELING OF COAL INCLUDING ANISOTROPY</b>	<b>349</b>
Dar-Hao Chen, Musharraf M. Zaman, and Anant R. Kukreti	
<b>TIME LAG DIFFUSION METHOD FOR A SOLID PROPELLANT EMITTING GASES</b>	<b>355</b>
James K. Baird and Jenn-Shing Chen	
<b>ENERGETIC MATERIALS IN CERAMICS SYNTHESIS</b>	<b>361</b>
J.J. Kingsley and L.R. Pederson	
<b>INFRARED FIBER OPTIC DIAGNOSTIC FOR SOLID PROPELLANT COMBUSTION</b>	<b>367</b>
J. Wormhoudt and P.L. Kebabian	
<b>LASER-BASED SENSITIVE DETECTION OF ENERGETIC MATERIALS</b>	<b>373</b>
G.W. Lemire, J.B. Simeonsson, and R.C. Sausa	
<b>SHOCKED ENERGETIC MOLECULAR MATERIALS: CHEMICAL REACTION INITIATION AND HOT SPOT FORMATION</b>	<b>379</b>
M.D. Fayer, Andrei Tokmakoff, and Dana D. Dlott	
<b>AUTHOR INDEX</b>	<b>385</b>
<b>SUBJECT INDEX</b>	<b>387</b>

## Preface

This was the first Symposium on Energetic Materials held at a Materials Research Society Meeting. Energetic materials are substances that undergo exothermic chemical reaction in response to some stimulus and react in time scales leading to combustion, explosion, and/or detonation (millisec to femtosec). Energetic materials represent a multibillion dollar industry for both commercial and military uses. These are among the earliest of man-made classes of materials. Their historical role in the development of nations has been enormous. Land clearing, railroad and highway construction, and mining continue as important though not exclusive uses. The space program is enabled by energetic materials.

While many of the energetic materials in current use were developed in the previous century, a recent renaissance by synthetic chemists has brought forward new compounds. The response of these new materials to stimuli that cause initiation or transition from combustion to detonation and the response of energetic materials generally to a variety of new uses (such as for air bags in automobiles where the environmental conditions and longer term storage stability questions must be carefully assessed) have led to increased interest in understanding the fundamental mechanisms for initiation and decomposition and also to new methods for quality and safety assurance tests.

Understanding the sensitivity to known stimuli such as impact or heating, the routes of chemical decomposition, and the theoretical techniques that can describe these processes is a fertile field of current research addressed in this Symposium. Relations between the molecular structure and the defect structures and initiation and decomposition, properties of new materials, experimental tests and new methods for probing at the microscopic level, and theoretical progress were the main topics.

The commonality with studies of other materials using many similar experimental techniques, especially in the area of defect and the special features of the subpicosecond time scale for reactions and decomposition both in experiments and molecular dynamics simulations provides a strong bond with other materials research. The organizers hope that these proceedings will further strengthen those bonds.

Donald H. Liebenberg  
Ronald W. Armstrong  
John J. Gilman

March 1993

## **Acknowledgments**

The organizers acknowledge with thanks the efforts of Professor R. Roy and members of the Materials Research Society boards to provide a forum for the discussion of energetic materials. The support staff of MRS significantly helped this Symposium run smoothly, and encouraged the timely receipt of papers included in these proceedings. The Chairs of the Sessions are to be especially thanked for their help in the review process in addition to keeping the sessions on time and providing opportunity for stimulating discussions of the papers. These Chairs were: R. Lieb, R. Doherty, M. Berman, R. Simpson, H. Cady, W. Faust, C. Capellos, J. Oxley, J. Covino, and J. Dienes. The organizers acknowledge the support of Richard Miller and the Office of Naval Research and the response of the energetic materials community in providing an important set of papers describing current research results and future directions. We hope this Symposium has added to the breadth of materials science included in the Materials Research Society charter.

## Acknowledgments

The organizers acknowledge with thanks the efforts of Professor R. Roy and members of the Materials Research Society boards to provide a forum for the discussion of energetic materials. The support staff of MRS significantly helped this Symposium run smoothly, and encouraged the timely receipt of papers included in these proceedings. The Chairs of the Sessions are to be especially thanked for their help in the review process in addition to keeping the sessions on time and providing opportunity for stimulating discussions of the papers. These Chairs were: R. Lieb, R. Doherty, M. Berman, R. Simpson, H. Cady, W. Faust, C. Capellos, J. Oxley, J. Covino, and J. Dienes. The organizers acknowledge the support of Richard Miller and the Office of Naval Research and the response of the energetic materials community in providing an important set of papers describing current research results and future directions. We hope this Symposium has added to the breadth of materials science included in the Materials Research Society charter.

---

## MATERIALS RESEARCH SOCIETY SYMPOSIUM PROCEEDINGS

---

- Volume 258—Amorphous Silicon Technology—1992, M.J. Thompson, Y. Hamakawa, P.G. LeComber, A. Madan, E. Schiff, 1992, ISBN: 1-55899-153-0
- Volume 259—Chemical Surface Preparation, Passivation and Cleaning for Semiconductor Growth and Processing, R.J. Nemanich, C.R. Helms, M. Hirose, G.W. Rubloff, 1992, ISBN: 1-55899-154-9
- Volume 260—Advanced Metallization and Processing for Semiconductor Devices and Circuits II, A. Katz, Y.I. Nissim, S.P. Murarka, J.M.E. Harper, 1992, ISBN: 1-55899-155-7
- Volume 261—Photo-Induced Space Charge Effects in Semiconductors: Electro-optics, Photoconductivity, and the Photorefractive Effect, D.D. Nolte, N.M. Haegel, K.W. Goossen, 1992, ISBN: 1-55899-156-5
- Volume 262—Defect Engineering in Semiconductor Growth, Processing and Device Technology, S. Ashok, J. Chevallier, K. Sumino, E. Weber, 1992, ISBN: 1-55899-157-3
- Volume 263—Mechanisms of Heteroepitaxial Growth, M.F. Chisholm, B.J. Garrison, R. Hull, L.J. Schowalter, 1992, ISBN: 1-55899-158-1
- Volume 264—Electronic Packaging Materials Science VI, P.S. Ho, K.A. Jackson, C-Y. Li, G.F. Lipscomb, 1992, ISBN: 1-55899-159-X
- Volume 265—Materials Reliability in Microelectronics II, C.V. Thompson, J.R. Lloyd, 1992, ISBN: 1-55899-160-3
- Volume 266—Materials Interactions Relevant to Recycling of Wood-Based Materials. R.M. Rowell, T.L. Laufenberg, J.K. Rowell, 1992, ISBN: 1-55899-161-1
- Volume 267—Materials Issues in Art and Archaeology III, J.R. Druzik, P.B. Vandiver, G.S. Wheeler, I. Freestone, 1992, ISBN: 1-55899-162-X
- Volume 268—Materials Modification by Energetic Atoms and Ions, K.S. Grabowski, S.A. Barnett, S.M. Rossnagel, K. Wasa, 1992, ISBN: 1-55899-163-8
- Volume 269—Microwave Processing of Materials III, R.L. Beatty, W.H. Sutton, M.F. Iskander, 1992, ISBN: 1-55899-164-6
- Volume 270—Novel Forms of Carbon, C.L. Renschler, J. Pouch, D. Cox, 1992, ISBN: 1-55899-165-4
- Volume 271—Better Ceramics Through Chemistry V, M.J. Hampden-Smith, W.G. Klemperer, C.J. Brinker, 1992, ISBN: 1-55899-166-2
- Volume 272—Chemical Processes in Inorganic Materials: Metal and Semiconductor Clusters and Colloids, P.D. Persans, J.S. Bradley, R.R. Chianelli, G. Schmid, 1992, ISBN: 1-55899-167-0
- Volume 273—Intermetallic Matrix Composites II, D. Miracle, J. Graves, D. Anton, 1992, ISBN: 1-55899-168-9
- Volume 274—Submicron Multiphase Materials, R. Baney, L. Gilliom, S.-I. Hirano, H. Schmidt, 1992, ISBN: 1-55899-169-7
- Volume 275—Layered Superconductors: Fabrication, Properties and Applications, D.T. Shaw, C.C. Tsuei, T.R. Schneider, Y. Shiohara, 1992, ISBN: 1-55899-170-0
- Volume 276—Materials for Smart Devices and Micro-Electro-Mechanical Systems, A.P. Jardine, G.C. Johnson, A. Crowson, M. Allen, 1992, ISBN: 1-55899-171-9
- Volume 277—Macromolecular Host-Guest Complexes: Optical, Optoelectronic, and Photorefractive Properties and Applications, S.A. Jenekhe, 1992, ISBN: 1-55899-172-7
- Volume 278—Computational Methods in Materials Science, J.E. Mark, M.E. Glicksman, S.P. Marsh, 1992, ISBN: 1-55899-173-5

---

## MATERIALS RESEARCH SOCIETY SYMPOSIUM PROCEEDINGS

---

- Volume 279—Beam-Solid Interactions—Fundamentals and Applications, M.A. Nastasi, N. Herbots, L.R. Harriott, R.S. Averback, 1993, ISBN: 1-55899-174-3
- Volume 280—Evolution of Surface and Thin Film Microstructure, H.A. Atwater, E. Chason, M. Grabow, M. Lagally, 1993, ISBN: 1-55899-175-1
- Volume 281—Semiconductor Heterostructures for Photonic and Electronic Applications, D.C. Houghton, C.W. Tu, R.T. Tung, 1993, ISBN: 1-55899-176-X
- Volume 282—Chemical Perspectives of Microelectronic Materials III, C.R. Abernathy, C.W. Bates, D.A. Bohling, W.S. Hobson, 1993, ISBN: 1-55899-177-8
- Volume 283—Microcrystalline Semiconductors—Materials Science & Devices, Y. Aoyagi, L.T. Canham, P.M. Fauchet, I. Shimizu, C.C. Tsai, 1993, ISBN: 1-55899-178-6
- Volume 284—Amorphous Insulating Thin Films, J. Kanicki, R.A.B. Devine, W.L. Warren, M. Matsumura, 1993, ISBN: 1-55899-179-4
- Volume 285—Laser Ablation in Materials Processing—Fundamentals and Applications, B. Braren, J. Dubowski, D. Norton, 1993, ISBN: 1-55899-180-8
- Volume 286—Nanophase and Nanocomposite Materials, S. Komarneni, J.C. Parker, G.J. Thomas, 1993, ISBN: 1-55899-181-6
- Volume 287—Silicon Nitride Ceramics—Scientific and Technological Advances, I-W. Chen, P.F. Becher, M. Mitomo, G. Petzow, T-S. Yen, 1993, ISBN: 1-55899-182-4
- Volume 288—High-Temperature Ordered Intermetallic Alloys V, I. Baker, J.D. Whittenberger, R. Darolia, M.H. Yoo, 1993, ISBN: 1-55899-183-2
- Volume 289—Flow and Microstructure of Dense Suspensions, L.J. Struble, C.F. Zukoski, G. Maitland, 1993, ISBN: 1-55899-184-0
- Volume 290—Dynamics in Small Confining Systems, J.M. Drake, D.D. Awschalom, J. Klafter, R. Kopelman, 1993, ISBN: 1-55899-185-9
- Volume 291—Materials Theory and Modelling, P.D. Bristowe, J. Broughton, J.M. Newsam, 1993, ISBN: 1-55899-186-7
- Volume 292—Biomolecular Materials, S.T. Case, J.H. Waite, C. Viney, 1993, ISBN: 1-55899-187-5
- Volume 293—Solid State Ionics III, G-A. Nazri, J-M. Tarascon, M. Armand, 1993, ISBN: 1-55899-188-3
- Volume 294—Scientific Basis for Nuclear Waste Management XVI, C.G. Interrante, R.T. Pabalan, 1993, ISBN: 1-55899-189-1
- Volume 295—Atomic-Scale Imaging of Surfaces and Interfaces, D.K. Biegelson, D.S.Y. Tong, D.J. Smith, 1993, ISBN: 1-55899-190-5
- Volume 296—Structure and Properties of Energetic Materials, R.W. Armstrong, J.J. Gilman, 1993, ISBN: 1-55899-191-3

*Prior Materials Research Society Symposium Proceedings  
available by contacting Materials Research Society*

---

## PART I

---

### **Structure and Stability**



## MOLECULAR STRUCTURE AND PERFORMANCE OF HIGH EXPLOSIVES

JAMES R. STINE, Explosives Technology, Group M-1, MS C920, Los Alamos National Laboratory, Los Alamos, NM 87545.

### ABSTRACT

Empirical methods have been developed to predict density and heat of formation of proposed high explosives. These methods are parameterized in terms of molecular constituents consisting of atoms in particular bonding environments. These methods, along with the atomic composition of the molecule, are then used in an empirically based method to predict the performance of the explosive.

Together, these methods form a unified mechanism of relating molecular structure to explosive performance. Indeed, this effort, along with the synthesis effort at Los Alamos, have led to the identification of a new class of high-nitrogen molecules that may prove to be high performance explosives.

### INTRODUCTION

The goal of the high explosives synthesis effort at Los Alamos has been to synthesize an organic high explosive that has the performance of HMX (one of our best performing explosives in general use) but at the same time has the insensitivity of TATB (our most insensitive high explosive). Although numerous efforts at Los Alamos, and indeed throughout the explosives community in general, have tried to achieve this goal, few new explosives have ever made been considered for weapon systems.

If we take a glance at the synthesis history of the explosives of military interest<sup>1</sup>, we immediately see that most all of them were first synthesized in the late 1800s. The fact that synthesis efforts since this time, and particularly during the past 40 years, have not been able to realize the goal given above, was one of the reasons for the development of the methods described here.

Table I. History of the Synthesis of Explosives of Military Interest

Nitroguanidine	1877
Tetryl	1879
TNT	1880
TATB	1888
PETN	1894
RDX	1899

One common element of nearly all of the synthesis efforts during the last 40 years has been the nitration of a carbon skeleton. This has resulted in the synthesis of many polynitroaromatics, with TATB and TNT as notable examples. But, are these explosives qualitatively different from one another? To help answer this question, we developed simple empirical methods to help indicate how each molecular constituent affected an explosive's performance. In addition

to being developed as predictive tools, the primary goal of these methods is to help guide the synthesis effort by providing insight as to what constituents were beneficial to high performance and which ones were not. These methods would then complement the computer methods developed over the years in predicting properties of proposed explosives.

The empirical methods developed were concerned with density and heat of formation of the proposed explosive. Certainly, in the past, these factors have been recognized as playing an important part in the performance of an explosive. However, many synthesis efforts have had as their primary goal the synthesis of high density organic molecules instead of high performance molecules. The thought here is that the three factors of density, heat of formation, and atomic composition must all be considered when relating molecular structure to performance. Of the three factors, atomic composition has received the least emphasis.

In the sections below, we discuss the three empirical methods as related to the factors given above, and then relate them to performance.

## DENSITY

One method for predicting density was developed by Stine<sup>2</sup> in 1981. This method assumed that the volume of a molecule in the unit cell of a crystal (which in this case includes some of the void volume) is a sum of the volumes of the molecular constituents. In this case, the molecular constituent is the atom in its particular bonding environment. Thus, for example, one constituent would be a carbon atom with four single bonds, designated C(1,1,1,1), or if two of the bonds were in a ring system designated C(1,1,-1,-1). Another constituent being a carbon with a double bond and two single bonds, C(2,1,1). Table II lists all of the different constituents possible for carbon, hydrogen, nitrogen, oxygen molecules, where 1, 2, or, 3 represent a single, double, or triple bond, and -5 designates an aromatic bond. A negative value indicates that the bond is part of a ring system. Values for the constituent volumes were derived from over 2000 organic molecules with known crystal structures. A histogram of the errors between the observed and calculated densities for these 2000 compounds indicates that the calculated value is within 5-4% of the observed value. Of course only a few of the 2000 compounds were explosives, but when this method was applied to over 300 organic explosives synthesized at Los Alamos, a similar standard deviation was obtained.

Of interest here are the contributions of each constituent to the density, which are also listed in Table II. It can be seen that almost all of the carbon-containing constituents contribute a relatively low value to the density, except for C(-1,-1,-1,-1) and C(1,-1,-1,-1) whose bonds are involved in multiple ring systems. That is, to be high density, the carbons must be a part of a cage-type or spiro-type structure. However, almost all of the nitrogen and oxygen atoms contribute a high value to the density. Thus for a high density compound one would want to eliminate the carbon and hydrogen atoms in favor of nitrogen and oxygen atoms.

Table II. Constituent Volumes for the Prediction of Density

Definition	Volume $\text{\AA}^3$	Density $\text{g/cm}^3$
H(1) bonded to a Carbon	5.981	0.278
H(1) bonded to an aromatic Carbon	7.499	0.221
H(1) bonded to a Nitrogen	5.199	0.319
H(1) bonded to an Oxygen	0.366	4.536
C(1,1,1,1)	13.390	1.486
C(1,1,-1,-1)	11.709	1.702
C(1,-1,-1,-1)	9.755	2.042
C(-1,-1,-1,-1)	9.673	2.060
C(2,1,1)	14.565	1.368
C(1,-1,-2)	13.288	1.499
C(2,-1,-1)	12.654	1.575
C(-1,-1,-2)	10.410	1.914
C(1,-5,-5)	12.094	1.647
C(-1,-5,-5)	10.618	1.876
C(-5,-5,-5)	10.370	1.921
C(3,1) or C(2,2)	16.579	1.202
N(2,2,1)	10.368	2.242
N(1,1,1)	9.234	2.517
N(1,-1,-1)	9.798	2.372
N(-1,-1,-1)	8.759	2.654
N(-5,-5)	12.268	1.895
N(2,1)	14.488	1.605
N(-1,-2)	11.941	1.947
N(3)	15.599	1.490
O(1,1)	12.178	2.181
O(-1,-1)	12.172	2.183
O(2)	12.754	2.063

## HEAT OF FORMATION

A method similar to that developed for density was developed for predicting the heat of formation of a proposed explosive<sup>3</sup>. Here, however, it is important to specify the type of atom bonded to the atom of concern. Thus, for example, a carbon bonded to two other carbons, a hydrogen, and a nitrogen would be designated by C(C1, C1, H1, N1). Also of importance to the heat of formation is the contribution of ring strain. Here we only consider ring strain in rings consisting of three, four, or five atoms. Values for the constituent heats of formation were derived from measured heats of formation of over 1100 organic compounds<sup>4</sup>. As opposed to similar existing methods for estimating the heat of formation of a molecule, this method has a much smaller set of constituents, and the constituent heat of formation is based on a larger set of empirical data. A histogram of the errors between the observed and calculated values indicates a standard deviation of about 10 kcal/mole.

Here again the method indicates which molecular constituents contribute a positive amount to the overall heat of formation and which contribute a negative amount. It now becomes evident, that a particular molecular constituent might contribute in a positive way to the density, but a negative amount to the heat of formation.

## ATOMIC COMPOSITION

One aspect of performance that has not received as much consideration as density and heat of formation is the role of atomic composition. Our first consideration was to determine in what regions of atomic composition space did most existing explosives lie. We know, for example, that RDX ( $C_3H_6N_6O_6$ ) and HMX ( $C_4H_8N_8O_8$ ) have the same performance if they are pressed to the same density. Thus, the absolute number of each atom making up the molecule is not of importance, but rather their relative amounts. Hence, we can arbitrarily "normalize" the molecular formula,  $C_aH_bN_cO_d$ , to  $C_AH_BN_CO_D$  such that  $A+B+C+D=1$ . That is  $A=a/(a+b+c+d)$ , etc. Thus RDX and HMX would have the same relative formula.

Now we wish to represent the relative composition of any organic (carbon, hydrogen, nitrogen, oxygen) molecule graphically. Just as an equilateral triangle can be used to represent the fractional composition for a three component system, a tetrahedron can be used to represent the relative fractions for a four component system. That is, a tetrahedron has the property that the sum of the four distances from an internal point to each of the four sides is a constant. Thus, the relative composition of any organic molecule can be represented by a point inside a tetrahedron whose corners represent carbon, hydrogen, nitrogen, and oxygen. This tetrahedron is shown in Figure 1.

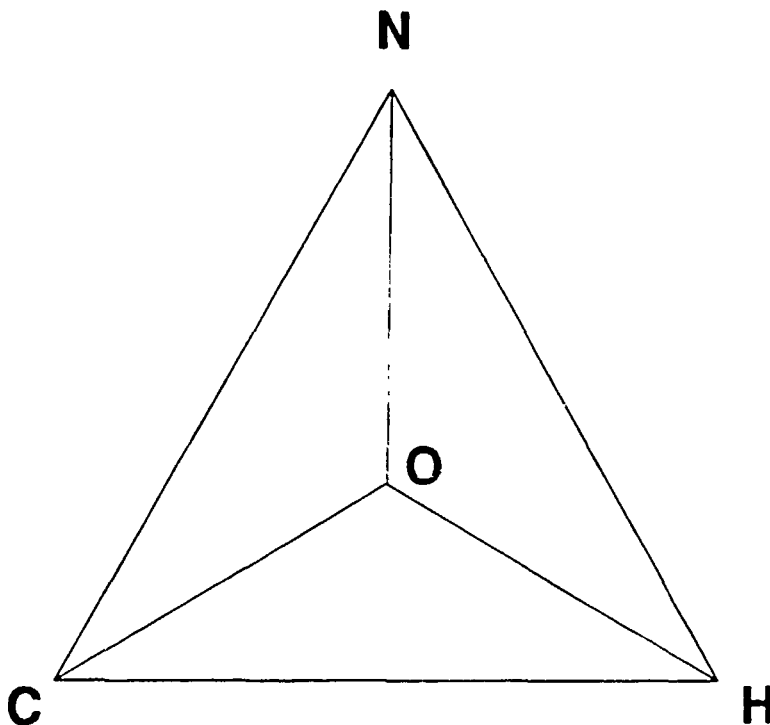


Figure 1. Composition tetrahedron for representing the relative amounts of carbon, hydrogen, nitrogen and oxygen in any organic molecule.

The ideal products in a detonation are water, carbon dioxide, and nitrogen. These molecules are represented by points on the line connecting hydrogen and oxygen, the line connecting carbon and oxygen, and the apex,

respectively. These three points then define an "oxygen balance plane," in which any point lying in this plane is said to have sufficient oxygen to convert the carbon to  $\text{CO}_2$  and the hydrogen to  $\text{H}_2\text{O}$ .

Over 300 explosives molecules were found in the literature that had been synthesized over the past 40 years. The normalized formulas for each of these explosives is plotted in Figure 2. Also seen in this figure is the oxygen balance plane. It is readily seen that most all of these explosives lie within a cluster that is characterized by high carbon - low oxygen content. Included in this cluster are explosives such as TATB, TNT, DATB, HNS, TNB, etc. These are basically low performing explosives because most of the carbon ends up as solid carbon in the form of soot. One molecule somewhat outside of this cluster is HMX, one of the best performing explosives. This indicates that perhaps molecules with as much as or greater nitrogen content might be a promising region for high performing explosives.

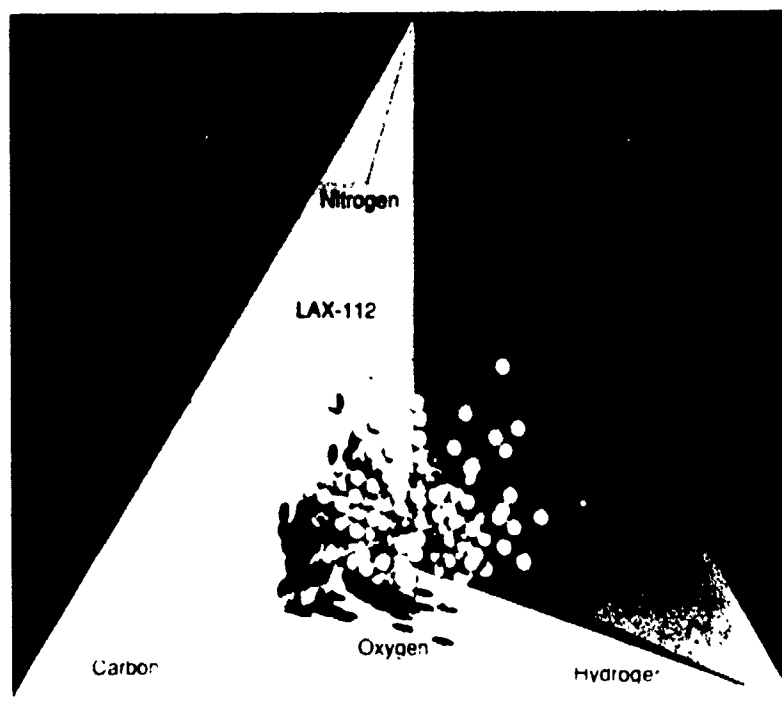


Figure 2. Composition tetrahedron showing the location of over 300 known explosives.

One molecule that consists of just nitrogen atoms is octaazacubane,  $\text{N}_8$ , (Figure 3) and is of interest to demonstrate the performance expected for a pure nitrogen molecule<sup>5</sup>. The predicted heat of formation for this molecule using *ab initio* methods is 530 kcal, and the predicted density using the above mentioned density prediction method, is  $2.65 \text{ g/cm}^3$ . These values yield a predicted detonation velocity (using the TIGER code with the BKW equation of state) of over 15 km/s and a CJ-pressure of 157.2 GPa. In fact, even if the real density differed substantially from that predicted and was found to be only  $1.90 \text{ g/cm}^3$ , and the real heat of formation found to be only 200 kcal/mole, the predicted detonation velocity would be 10.4 km/s and the CJ-pressure would be 50.1 GPa. These values are still substantially greater than those for HMX, namely 9.14 km/s and 40.5 GPa, respectively.

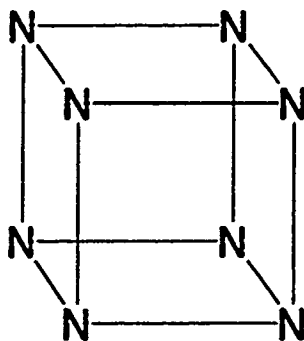


Figure 3. Molecular structure of octaazacubane.

## PERFORMANCE

The density, heat of formation, and atomic composition can now be integrated into an empirical method for predicting the performance of a proposed explosive. The approach taken here is an extension of a method first developed by Urizar<sup>6</sup> at Los Alamos in 1947. In his method, he assumed that the detonation velocity of a mixture of explosives is the sum of the detonation velocities of the constituents weighted by their respective volume fractions. He also allowed for the contribution of voids to the overall detonation velocity by assigning a "characteristic velocity" and including its contribution to the sum. Thus, for a mixture of  $n$  components we have,

$$D = \sum v_i D_i \quad i = 1, n \quad (1)$$

where  $D$  is the detonation velocity. Here we extended his method<sup>7</sup> to pure compounds by making the additional assumption that the detonation velocity of a pure compound and that of a mixture are identical if the densities, heats of formation, and atomic compositions are the same. Hence these properties of the pure compound could be simulated by an appropriate mixture of explosives with known densities, heats of formation, and molecular formulas. Thus for a pure explosive with the molecular formula  $\text{C}_a\text{H}_b\text{N}_c\text{O}_d$ , we would need a basis set of five explosives, and the addition of voids to simulate the six parameters of carbon, hydrogen, nitrogen, and oxygen content, density, and heat of formation. Equation 1 then becomes,

$$D = D_0 + \rho (\alpha a + \beta b + \gamma c + \delta d + h \Delta H_f) / M, \quad (2)$$

where  $D_0$  is the characteristic velocity of a void,  $\rho$  is the density in  $\text{g/cm}^3$ ,  $\Delta H_f$  is the heat of formation in kcal/mole, and  $M$  is the molecular weight of the pure compound.  $D_0$ ,  $\alpha$ ,  $\beta$ ,  $\gamma$ ,  $\delta$ , and  $h$  are constants whose values were obtained by a least-squares analysis to detonation velocity, density, and heat of formation data for 22 pure explosives. This analysis yielded,

$\alpha =$	-13.85	$\delta =$	68.11
$\beta =$	3.95	$h =$	0.6917
$\gamma =$	37.74	$D_0 =$	3.69

The calculated and observed values are plotted in Figure 4 for these 22 explosives.

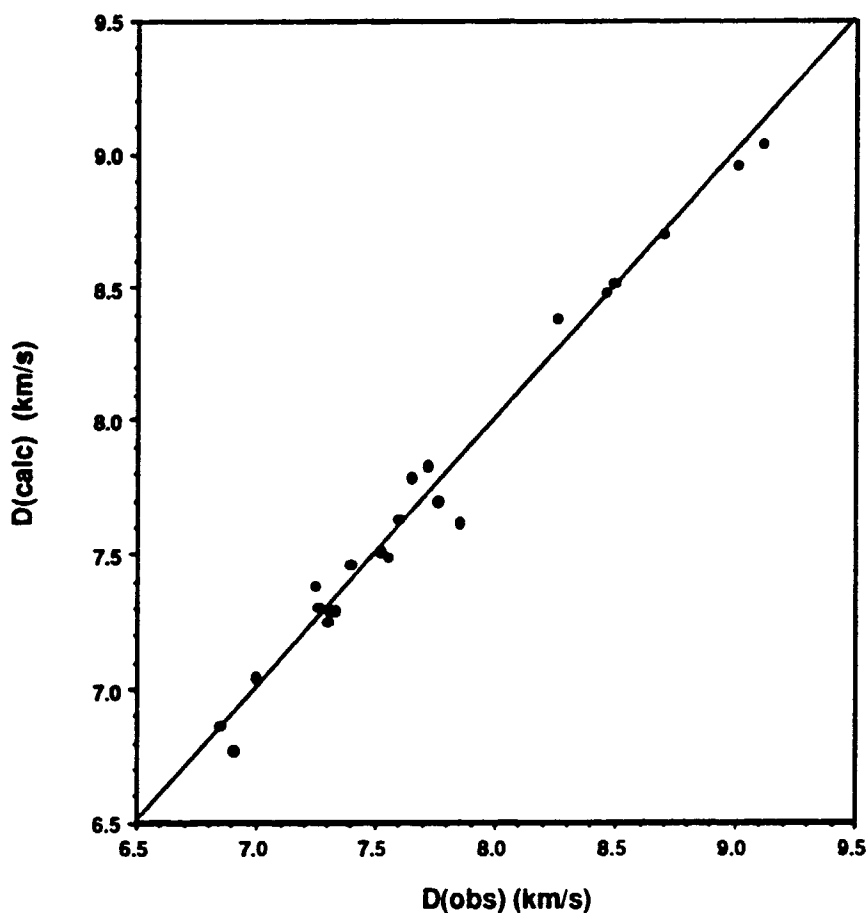


Figure 4. Plot of the detonation velocities of 22 pure explosives calculated using Equation 2 as a function of the observed detonation velocities. The straight line is the ideal case where the calculated value is equal to the observed value.

It is clear from the above values that carbon is detrimental to a high detonation velocity because  $\alpha$  is negative, but nitrogen and oxygen make a positive contribution because  $\beta$ ,  $\chi$ , and  $\delta$  are all positive. Here again, we are led to the conclusion that high nitrogen explosives should give good performance.

These data indicate that perhaps high nitrogen molecules would be high performance explosives. One compound, first synthesized at Los Alamos<sup>8</sup> in 1986, is a high nitrogen molecule that does not contain any nitro groups. The structure of this molecule is shown in Figure 5.

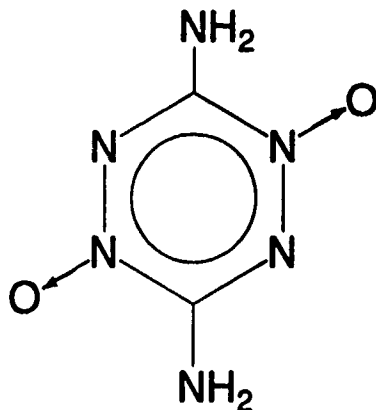


Figure 5. Molecular structure of the high nitrogen explosive, TZX

This explosive was predicted to have a detonation velocity about the same as that of HMX. Enough material was then synthesized to perform sensitivity and performance tests. It was found to have an impact sensitivity about like that of TNT, which is a relatively insensitive high explosive. Although it is not as insensitive as TATB, it is one of the few known explosives that has both a relatively good performance and good sensitivity.

## SMALL-SCALE TESTING

TZX is just one of the first high nitrogen molecule to be synthesized and its performance properties are still being tested. As was mentioned at the beginning, one must consider all factors when evaluating what molecular constituents are important contributors to performance. Although we have demonstrated that high nitrogen content is an important contributor to performance, so are density and heat of formation, and it must not be over emphasized. Indeed, these factors must be considered simultaneously when evaluating their contribution related to a particular molecule.

The results now are very encouraging that perhaps a single molecule can be both an insensitive and a high performing explosive. However, further tests must be performed on new molecules that do not lie in the cluster formed by the majority of existing explosives. This presents a problem, in that many of the standard sensitivity and performance tests require large amounts of material, usually kilograms at the very least. It is usually a Herculean task for the bench chemist to produce these quantities of material, and hence most explosives



synthesized in the past simply did not have any sensitivity of performance tests past those required for handling small quantities of material.

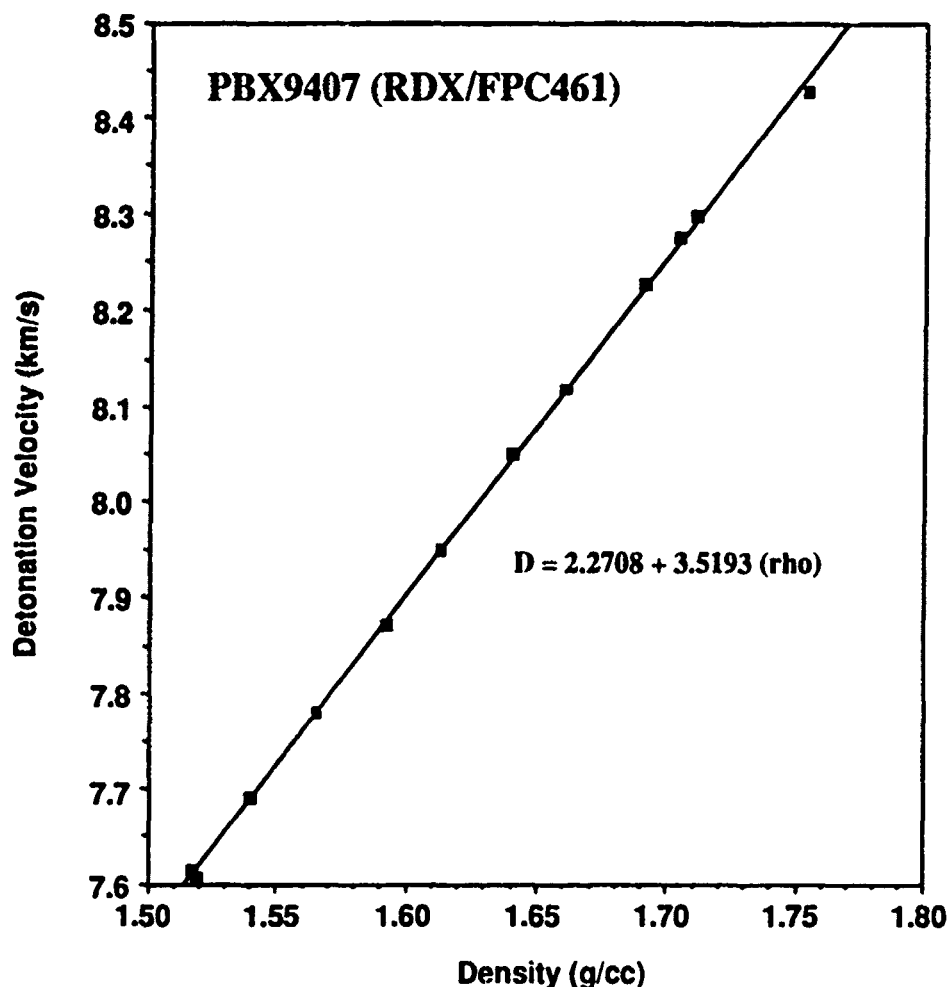


Figure 6. Detonation velocity as a function of density produced in a single PolyRho shot. The rate stick consisted of 1/2 inch diameter pellets.

To help bridge the gap between the bench chemist and the firing site engineer, various small-scale tests are being developed at Los Alamos to measure such things as detonation velocity, failure diameter, reaction zone thickness, and sensitivity to shock. These tests require a total of 50-100g of material - a quantity that is able to be synthesized in a laboratory.

One such test, requiring about 25-30g of material is the PolyRho test. This is a performance test for measuring the detonation velocity over a range of densities. Pellets, 1/2 inch in diameter and 1/2 inch in length are pressed to different densities. A rate stick is assembled from these pellets where the pellets are placed in the rate stick according to their density. The first pellet is next to the detonator and is the least dense and the last pellet is the most dense. Foil switches are placed between the pellets and an oscilloscope is used to record the arrival times of the detonation wave at each of these switches. From this data and the heights of the individual pellets one can calculate the detonation

velocity over each of the pellets and hence obtain detonation velocity as a function of density. One such plot is shown in Figure 6.

This test along with the other existing and proposed small-scale performance and sensitivity tests form a basis for obtaining valuable screening information to help aid in designing new explosives and selecting existing explosives for particular programmatic goals.

## CONCLUSIONS

Efforts related to the development of simple empirical predictive methods have interacted with the synthesis effort at Los Alamos to identify a new class of molecules that may prove useful as high-performing insensitive explosives. One member of this new class has been synthesized and tested. However, high nitrogen content is just one of the factors that influence performance and, like density and heat of formation, should not be sole consideration. Indeed, it is imperative that all of the factors be considered simultaneously because there are very few molecular constituents that contribute in a positive way to each of these factors.

The interaction between theory and synthesis has led to the realization that perhaps the elusive explosive we have been looking for may have an atomic composition and molecular structure quite different than that of most all known explosives. We now have some guidelines as to what molecular geometries to look for.

## REFERENCES

1. Encyclopedia of Explosives and Related Items, edited by B. T. Fedoroff (Picatinny Arsenal, Dover, 1960).
2. J. R. Stine, Prediction of Crystal Densities of Organic Explosives by Group Additivity, Los Alamos National Laboratory Report, LA-8920 (1981).
3. J. R. Stine and J. F. Kramer, in 26th JANNAF Combustion Meeting Proc., Vol. II, pp 53-56, CPIA Publication 529 (1989).
4. J. B. Pedley, R. D. Naylor, and S. P. Kirby, Thermochemical Data of Organic Compounds, 2nd ed. (Chapman and Hall, London, 1986).
5. R. Engelke and J. R. Stine, *J. Phys. Chem.*, **94**, 5689 (1990).
6. B. M. Dobratz and P. C. Crawford, LLNL Explosives Handbook - Properties of Chemical Explosives and Explosive Simulants, Lawrence Livermore National Laboratory UCRL-52997 (1985).
7. J. R. Stine, *J. Energetic Materials*, **8**, 41 (1990).
8. M. D. Coburn, (private communication).

## RECENT ADVANCES IN THE THERMAL DECOMPOSITION OF CYCLIC NITRAMINES

RICHARD BEHRENS, JR.\* AND SURYANARAYANA BULUSU\*\*

\*Sandia National Laboratories, Combustion Research Facility, Livermore, CA 94551

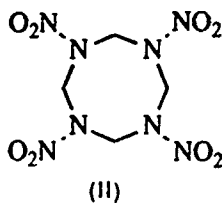
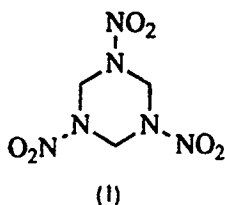
\*\* Energetic Materials Division, U.S. Army, ARDEC, Dover, NJ 07801-5001

### ABSTRACT

The effects of physical properties and molecular conformation on the thermal decomposition kinetics of several cyclic nitramines are examined and compared to the decomposition of RDX. The compounds used in the study are: octahydro-1,3,5,7-tetranitro-1,3,5,7-tetrazocine (HMX), hexahydro-1-nitroso-3,5-dinitro-s-triazine (ONDNTA), 1,3,5-trinitro-1,3,5-triazacycloheptane (TNCHP), and 2-oxo-1,3,5-trinitro-1,3,5-triazacyclohexane (K6). The decomposition pathways of HMX in the liquid phase are similar to the four parallel decomposition pathways that control the decomposition of RDX in the liquid phase. The products formed during the thermal decomposition of ONDNTA arise from multiple reaction pathways. The identities and temporal behaviors of the ONDNTA decomposition products are discussed. TNCHP is thermally stable in the liquid phase. The decomposition products from TNCHP are formed via multiple reaction pathways. One decomposition pathway for TNCHP is through its mononitroso intermediate. TNCHP does not form a stable product that is analogous to oxy-s-triazine (OST) formed in RDX or the smaller ring fragments formed in the liquid-phase decomposition of HMX. K6 is less thermally stable and the decomposition mechanism is much simpler than that of RDX, HMX and TNCHP. The thermal decomposition of K6 occurs between 150 and 180 °C. The products formed during the decomposition of K6 are mainly  $\text{CH}_2\text{O}$  and  $\text{N}_2\text{O}$  with minor amounts of  $\text{HCN}$ ,  $\text{CO}$ ,  $\text{NO}$ , and  $\text{NO}_2$ .

### INTRODUCTION

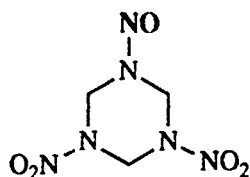
The cyclic nitramines hexahydro-1,3,5-trinitro-s-triazine RDX (I) and octahydro-1,3,5,7-tetranitro-1,3,5,7-tetrazocine HMX (II)



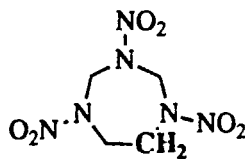
are energetic ingredients that are used in various propellants and explosives. Understanding the complex physicochemical processes that underlie the combustion of these materials can lead to methods for modifying propellant and explosive formulations in order to obtain better ignition, combustion, or sensitivity properties. The motivation for understanding the thermal decomposition processes of these materials is threefold. First, in solid-propellant combustion, thermal decomposition processes that occur in the condensed phase determine both the amount of heat released on the surface of a burning propellant and the identity and rates of production of the lower molecular weight species that are the reactants in the gas-phase flame. These processes control the burn rates of solid propellants. Second, in both propellants and explosives it is important to understand the mechanisms that control the stability of these materials when they are subjected to elevated temperatures, electrostatic discharge, impact or shock. The response of energetic materials in munitions to these stimuli determine their

degree of safety when subjected to abnormal environments such as fire. Third, an understanding of the molecular processes that control the response of energetic materials to these various stimuli will provide insight into the molecular properties that control the relative stability of these materials. This, in turn, will provide guidance for the synthesis of new, more stable, energetic materials. Thus, the goal of our work is to understand how the molecular conformation, physical properties and molecular structure affect the thermal decomposition processes in energetic materials.

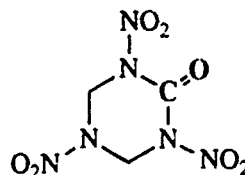
Since RDX and HMX are two cyclic nitramines used extensively in explosive and propellant formulations, our initial work<sup>1-4</sup> has focused on understanding the decomposition mechanisms of these two materials in the solid and liquid phases. To extend our knowledge of cyclic nitramine decomposition, we are currently studying the decomposition of an intermediate formed during the decomposition of RDX and several other cyclic nitramines with molecular conformations and physical properties different from RDX and HMX. In this paper we present the following: a summary of the thermal decomposition pathways for RDX in the liquid and solid phases; the results from our studies on the thermal decomposition of liquid-phase HMX, hexahydro-1-nitroso-3,5-dinitro-s-triazine (ONDNTA) (III), 1,3,5-trinitro-1,3,5-triazacycloheptane (TNCHP) (IV), and 2-oxo-1,3,5-trinitro-1,3,5-triazacyclohexane (K6) (V); a comparison of these results with those of RDX.



(III)



(IV)



(V)

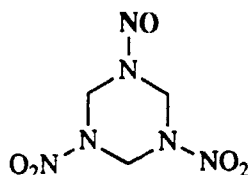
## EXPERIMENTAL

### Instrument description

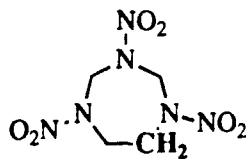
The simultaneous thermogravimetric modulated beam mass spectrometry (STMBMS) apparatus is used to conduct the thermal decomposition experiments. The apparatus and the basic data analysis procedure have been described previously.<sup>5,6</sup> This instrument allows the concentration and rate of formation of each gas phase species in a reaction cell to be measured as a function of time by correlating the ion signals at different  $m/z$  values measured with a mass spectrometer with the force measured by a microbalance at any instant. In the experimental procedure, a small sample ( $\sim 10$  mg) is placed in an alumina reaction cell that is then mounted on a thermocouple probe that is seated in a microbalance. The reaction cell is enclosed in a high vacuum environment ( $< 10^{-6}$  torr) and is radiatively heated by a bifilar-wound tungsten wire on an alumina tube. The molecules from the gaseous mixture in the reaction cell exit through a small diameter (0.0025 cm in these experiments) orifice in the cap of the reaction cell, traverse two beam-defining orifices before entering the electron-bombardment ionizer of the mass spectrometer where the ions are created by collisions of 20 eV electrons with the different molecules in the gas flow. The background pressures in the vacuum chambers are sufficiently low to eliminate significant scattering between molecules from the reaction cell and background molecules in the vacuum chambers. The different  $m/z$ -value ions are selected with a quadrupole mass filter and counted with an ion counter. The gas flow is modulated with a chopping wheel and only the modulated ion signal is recorded. The containment time of gas in the reaction cell is a function of the orifice area, the free volume within the reaction cell, and the characteristics of the flow of gas through the orifice. For the reaction cell used in the experiments, the time constant for exhausting gas from the cell is small ( $\sim 3$  sec) compared to the duration of the experiments ( $> 1000$  sec). Note that the containment time of gas within the reaction cell is short once the gas molecules are in the free volume of the cell, but it may be much longer if the gas is trapped in the condensed-phase of the material within the cell. For reactions in the liquid phase, such as those with RDX, the lighter molecular weight gases (i.e.,  $N_2O$ ) will be released from the liquid rapidly whereas for reactions that occur in the solid phase even these lower molecular weight gaseous products may be trapped for longer periods of time.

degree of safety when subjected to abnormal environments such as fire. Third, an understanding of the molecular processes that control the response of energetic materials to these various stimuli will provide insight into the molecular properties that control the relative stability of these materials. This, in turn, will provide guidance for the synthesis of new, more stable, energetic materials. Thus, the goal of our work is to understand how the molecular conformation, physical properties and molecular structure affect the thermal decomposition processes in energetic materials.

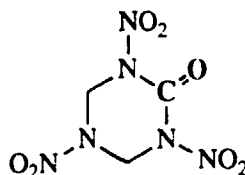
Since RDX and HMX are two cyclic nitramines used extensively in explosive and propellant formulations, our initial work<sup>1-4</sup> has focused on understanding the decomposition mechanisms of these two materials in the solid and liquid phases. To extend our knowledge of cyclic nitramine decomposition, we are currently studying the decomposition of an intermediate formed during the decomposition of RDX and several other cyclic nitramines with molecular conformations and physical properties different from RDX and HMX. In this paper we present the following: a summary of the thermal decomposition pathways for RDX in the liquid and solid phases; the results from our studies on the thermal decomposition of liquid-phase HMX, hexahydro-1-nitroso-3,5-dinitro-s-triazine (ONDNTA) (III), 1,3,5-trinitro-1,3,5-triazacycloheptane (TNCHP) (IV), and 2-oxo-1,3,5-trinitro-1,3,5-triazacyclohexane (K6) (V); a comparison of these results with those of RDX.



(III)



(IV)



(V)

## EXPERIMENTAL

### Instrument description

The simultaneous thermogravimetric modulated beam mass spectrometry (STMBMS) apparatus is used to conduct the thermal decomposition experiments. The apparatus and the basic data analysis procedure have been described previously.<sup>5,6</sup> This instrument allows the concentration and rate of formation of each gas phase species in a reaction cell to be measured as a function of time by correlating the ion signals at different  $m/z$  values measured with a mass spectrometer with the force measured by a microbalance at any instant. In the experimental procedure, a small sample (~10 mg) is placed in an alumina reaction cell that is then mounted on a thermocouple probe that is seated in a microbalance. The reaction cell is enclosed in a high vacuum environment ( $< 10^{-6}$  torr) and is radiatively heated by a bifilar-wound tungsten wire on an alumina tube. The molecules from the gaseous mixture in the reaction cell exit through a small diameter (0.0025 cm in these experiments) orifice in the cap of the reaction cell, traverse two beam-defining orifices before entering the electron-bombardment ionizer of the mass spectrometer where the ions are created by collisions of 20 eV electrons with the different molecules in the gas flow. The background pressures in the vacuum chambers are sufficiently low to eliminate significant scattering between molecules from the reaction cell and background molecules in the vacuum chambers. The different  $m/z$  value ions are selected with a quadrupole mass filter and counted with an ion counter. The gas flow is modulated with a chopping wheel and only the modulated ion signal is recorded. The containment time of gas in the reaction cell is a function of the orifice area, the free volume within the reaction cell, and the characteristics of the flow of gas through the orifice. For the reaction cell used in the experiments, the time constant for exhausting gas from the cell is small (~3.2 sec) compared to the duration of the experiments ( $> 1000$  sec). Note that the containment time of gas within the reaction cell is short once the gas molecules are in the free volume of the cell, but it may be much longer if the gas is trapped in the condensed-phase of the material within the cell. For reactions in the liquid phase, such as those with RDX, the lighter molecular weight gases (i.e.,  $N_2O$ ) will be released from the liquid rapidly whereas for reactions that occur in the solid phase even these lower molecular weight gaseous products may be trapped for longer periods of time.

### Sample preparation.

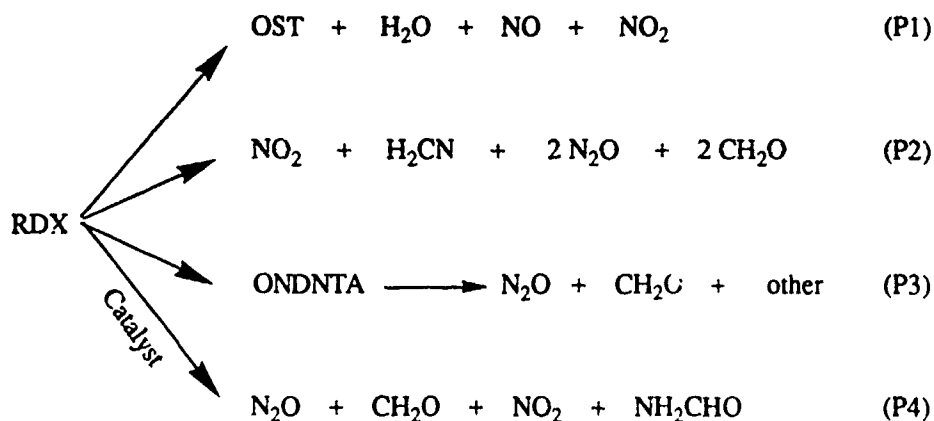
The cyclic nitramines used in the experiments were prepared according to previously published methods for ONDNTA,<sup>7</sup> TNCHP,<sup>8</sup> and K6.<sup>9</sup> The K6 sample was obtained from P. Pagoria of LLNL. The samples were characterized by NMR and IR measurements.

### Data analysis.

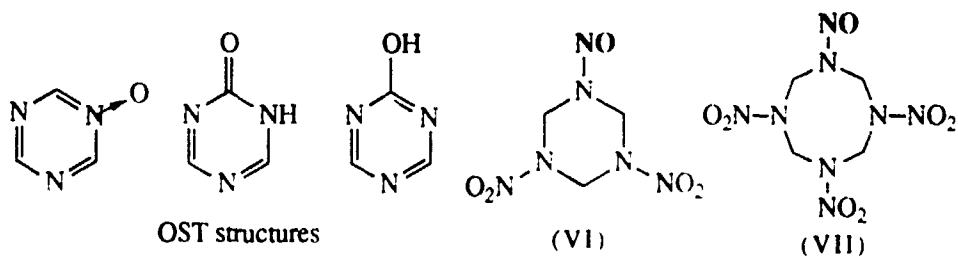
The data analysis procedures used for identifying the pyrolysis products and determining their rates of formation have been described previously.<sup>5,6,10</sup> For the qualitative comparisons of the differences in the decomposition behavior between RDX and HMX, TNCHP, and K6 only the temporal behaviors of the ion signals associated with the various decomposition products, and not the gas formation rates for each product, are presented in this paper.

## RESULTS AND DISCUSSION

Our previous work has examined the decomposition of HMX in the solid phase<sup>1,2</sup> and RDX in both the solid and liquid phases.<sup>3,4</sup> For RDX decomposition in the liquid phase, we have found that it decomposes by the following four reaction pathways:



Reaction pathway P1 is first order in RDX and accounts for approximately 30% of the total decomposition. Using <sup>2</sup>H, <sup>13</sup>C, <sup>15</sup>N, and <sup>18</sup>O isotopic analogues of RDX in isotopic scrambling and deuterium kinetic isotope experiments (DKIE), we have shown that oxy-s-triazine (OST) is formed directly from RDX and hydrogen atom transfer is involved in the rate determining step. The other products formed in this reaction path are NO, H<sub>2</sub>O, and NO<sub>2</sub>. This reaction pathway involves the elimination of HONO, leaving the RDX ring intact.



Reaction pathway P2 is also first order in RDX and accounts for approximately 10% of the total decomposition. In this pathway the C-N bonds of the RDX molecule eventually rupture, leading to the formation of N<sub>2</sub>O and CH<sub>2</sub>O. However, this does not necessarily imply that C-N bond rupture is the first step in this thermal decomposition pathway, since N-N bond rupture followed by subsequent bond breaking of the resulting radical is also consistent with our results.

Reaction pathway P3 involves the decomposition of RDX via a mononitroso-RDX (ONDNTA) intermediate (VI). Decomposition via this pathway accounts for approximately 30% of the total decomposition.  $\text{CH}_2\text{O}$  and  $\text{N}_2\text{O}$  are major products formed via the ONDNTA intermediate during the decomposition of RDX.

Reaction pathway P4 involves the autocatalytic decomposition of RDX and accounts for approximately 30% of the total RDX decomposition. The main decomposition products formed via this channel are also  $\text{CH}_2\text{O}$  and  $\text{N}_2\text{O}$ . Although the catalyst has not been identified, possible candidates for the catalyst include several amides (i.e., formamide and N-methylformamide) and the polyamide residue that forms during the decomposition of RDX. The details of reaction pathway P4 are the least well characterized of the four pathways.

### Summary of RDX Results

To compare the decomposition pathways of the other cyclic nitramines with those of RDX, we first summarize the RDX results. The decomposition pathways of RDX were determined from both the extent of isotope crossover and deuterium kinetic isotope effect (DKIE) in experiments with isotopically labeled analogues of RDX and the temporal behaviors of the gas formation rates of the decomposition products as shown in Figure 1 (additional results may be found in References 3 and 4).

For all of the decomposition products, the gas formation rates rise rapidly as the sample melts at  $200^\circ\text{C}$ . For OST, the rate of gas formation rises rapidly as the sample melts and gradually decreases as the RDX sample is depleted. This is characteristic of reaction pathway P1. For ONDNTA, the gas formation rate gradually increases as the sample is depleted. This behavior is due to the increasing vapor pressure of ONDNTA in the reaction cell which in turn is due to the increasing mole fraction of ONDNTA in the sample as the decomposition progresses. The temporal behavior of ONDNTA characterizes reaction pathway P3. For N-methylformamide (NMFA), the gas formation rate also gradually increases as the sample is depleted. This behavior is also characteristic of the other formamides formed during the

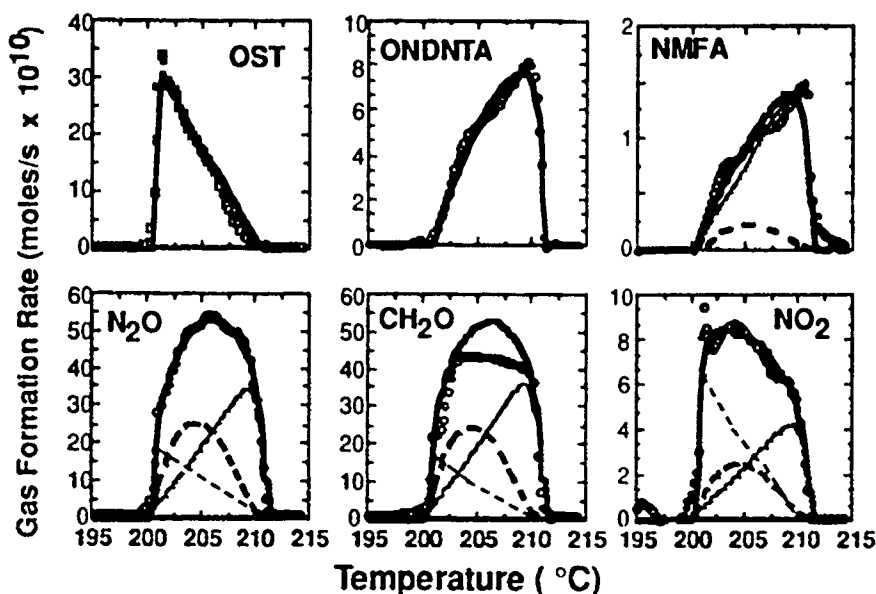


Figure 1. Contributions of the four primary decomposition pathways to the various products formed during the thermal decomposition of pure RDX. The bold line (—) in all of the graphs represents the total contribution from all of the reaction channels. The bold line (—) in OST represents the contribution by reaction pathway P1. The thin dashed (---) lines shown in  $\text{N}_2\text{O}$ ,  $\text{CH}_2\text{O}$ ,  $\text{NO}_2$ , and  $\text{NH}_2\text{CHO}$  represent the contributions from reaction pathway P2. The bold dashed lines (—) represent the contribution from the ONDNTA decomposition pathway P3. The thin solid lines (—) that peak near the highest temperature correspond to the contribution from the catalytic decomposition pathway P4. The calculated rate of formation of  $\text{CH}_2\text{O}$  is equivalent to the rate of formation of  $\text{N}_2\text{O}$ . The difference between the calculated and measured rates of formation of  $\text{CH}_2\text{O}$  is due to its reaction within the sample cell.

decomposition. The rates of gas formation shown for  $\text{N}_2\text{O}$ ,  $\text{CH}_2\text{O}$  and  $\text{NO}_2$  have temporal behaviors that are due to contributions from three of the RDX decomposition pathways. The contribution that increases rapidly as the sample melts and falls off gradually as the sample is depleted arises from reaction pathway P2. The contribution that peaks midway during the decomposition (bold dashed line in Fig. 1) arises from the decomposition of the ONDNTA intermediate in reaction pathway P3. Finally, the contribution that increases gradually during the decomposition and peaks just prior to complete depletion of the sample is characteristic of the catalytic reaction pathway P4.

#### Liquid-Phase Decomposition of HMX

Comparison of the liquid-phase decomposition of HMX to that of RDX will show whether decomposition pathways similar to RDX control the decomposition of HMX or whether the higher melting point of HMX and its decomposition in the solid phase prior to melting alter its decomposition mechanism. The liquid-phase decomposition products from HMX that are observed in our experiments include:  $\text{H}_2\text{O}$ , HCN, CO,  $\text{CH}_2\text{O}$ , NO,  $\text{N}_2\text{O}$ ,  $\text{NO}_2$ , formamide, NMFA, N,N-dimethylformamide, and ONTNTA (VII). In addition, we observe ion signals at  $m/z$  values of 70 and 97. Experiments with  $^2\text{H}$ ,  $^{13}\text{C}$ , and  $^{15}\text{N}$  isotopically labeled HMX analogues have shown that the ion signals at these two  $m/z$  values correspond to ions with formulas of  $\text{C}_2\text{N}_2\text{H}_2\text{O}$  (70) and  $\text{C}_3\text{N}_3\text{H}_3\text{O}$  (97). For RDX, the ion signals at  $m/z$  values of 70 and 97 both arise from the OST decomposition product. However, for HMX, differences in the relative intensities of these two ions, in addition to differences in their temporal behaviors in the HMX experiments, show that they arise from two different decomposition products. These ion signals clearly arise from thermal decomposition products that are similar to the OST formed during the decomposition of RDX. However, without time-of-flight (TOF) velocity-spectra measurements of these ion signals, it is not possible to determine whether the observed ion signals are molecular ions, and thus have the same formula as the thermal decomposition products, or whether they are daughter ions formed from a decomposition product with a higher molecular weight. In either case, the ion signals at  $m/z$  values of 70 and 97 are associated with fragments from the HMX ring formed in a manner similar to reaction pathway P1 for the RDX decomposition.

The results shown for the decomposition of HMX in Fig. 2 are consistent with the four decomposition pathways found for the decomposition of RDX. A reaction pathway similar to reaction pathway P1 for RDX produces the HMX-ring fragments that are characterized by the ion signals at  $m/z$  values of 70 and 97 shown in Panel b of Fig. 2. These two ion signals first appear when the HMX sample liquefies at approximately  $276^\circ\text{C}$  and their signal strength decreases as the HMX sample is depleted. This behavior is similar to that observed for OST formed in the decomposition of RDX.

The temporal behavior of the ion signals formed from the mononitroso HMX analogue, ONTNTA, (shown in Panel c of Fig. 2) is similar to the temporal behavior of ONDNTA observed in the liquid-phase RDX decomposition. Note the increase in the amount of ONTNTA associated with the vertical arrow on the right in Fig. 2. This behavior is similar to that observed for ONDNTA during the decomposition of RDX. One significant difference between the behavior of the mononitroso product in the decomposition of HMX compared with the decomposition of RDX is that a much larger amount of ONTNTA is released from the HMX sample before it liquefies. As can be seen from Fig. 2, the size of the ion signal associated with the ONTNTA product does not show a significant increase as the sample liquefies. This indicates that the decomposition of HMX to its mononitroso analogue is a major decomposition pathway in the solid-phase. This is similar to the results found for the decomposition of RDX in the solid phase except, that at the higher temperatures associated with the decomposition of HMX, the reaction rate for the formation of ONTNTA is greater and a larger fraction of the HMX sample has decomposed via a reaction pathway similar to pathway P3 prior to the liquefaction of the HMX sample.

The temporal behavior of the ion signals associated with the  $\text{CH}_2\text{O}$  and  $\text{N}_2\text{O}$  formed during the decomposition of HMX after its liquefaction have the same broad type of peaks that were observed for these products in the decomposition of RDX. Both of the ion signals associated with these products show a rapid increase as the HMX liquefies and an initial peak that is correlated with the ion signals associated with the products formed from the ring of the HMX molecule. The  $\text{CH}_2\text{O}$  and  $\text{N}_2\text{O}$  formed later in the decomposition appear to be correlated with the ONTNTA product and also display a temporal behavior that is characteristic of an autocatalytic decomposition channel similar to pathway P4 for RDX.



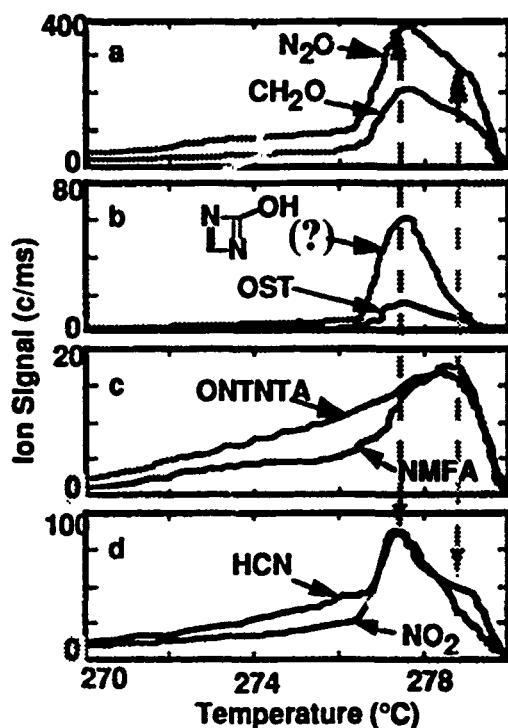


Figure 2. Ion signals associated with various thermal decomposition products formed during the decomposition of HMX as the sample melts. The sample melts at 276°C. The signal associated with thermal decomposition fragments formed from the ring (b) only appear in significant quantities as the sample melts. Other products associated with this pathway are indicated by the vertical arrow, on the left. After the sample melts a second set of products that peak later in the decomposition is observed as indicated by the arrow, on the right. These products are associated with the amides, such as the N-methylformamide. This behavior is similar to that observed for RDX decomposition in the liquid phase. However, in contrast to the decomposition of RDX, substantial amount of thermal decomposition occurs prior to melting of the sample. Note the relatively large amount of the mononitroso analogue of HMX (ONTNTA) observed prior to melting. The heating rate is 2°C/min.

The initial increase in the  $CH_2O$  and  $N_2O$  signals after the HMX sample liquefies is also similar to that observed in the decomposition of RDX and associated with decomposition via reaction pathway P2. From the relative sizes of the ion signals associated with the  $CH_2O$  and  $N_2O$  products compared to those associated with the HMX ring fragment ion signals at  $m/z$  values of 70 and 97 this would suggest that the relative amount of HMX that decomposes by a pathway similar to P2 compared to pathway P1 is greater for HMX than for RDX. In light of the fact that the decomposition of HMX occurs at a temperature about 70°C greater than RDX, the behavior of  $CH_2O$  and  $N_2O$  tends to suggest that reaction channel P2 may become more dominant than reaction pathway P1 at higher temperatures. However, it is also possible that the increase of the  $CH_2O$  and  $N_2O$  signals after the HMX sample liquefies is due to an increase in the decomposition rate of ONTNTA, formed in the solid-phase decomposition. Without further quantification of the HMX results, it is not possible at this time to determine exact relative decomposition rates of the various HMX decomposition pathways.

#### Relative Stabilities of RDX, HMX, ONDNTA, TNCHP, and K6

The relative rates of formation of the major thermal decomposition products formed from RDX, HMX, ONDNTA, TNCHP and K6 are shown as a function of temperature in Figure 3. Both RDX and HMX decompose slowly in the solid phase and exhibit a rapid increase in the decomposition rates upon melting. In comparison to RDX and HMX, both ONDNTA and TNCHP do not undergo the same rapid increase in the decomposition rate upon melting as illustrated in Fig. 3. For ONDNTA, this may be due a slower decomposition rate at the temperature associated with its lower melting point of 168°C. As ONDNTA melts there is already evidence of decomposition. The entire ONDNTA sample has decomposed below

200°C (below the melting point of RDX). TNCHP, on the other hand, is quite stable in the liquid phase. TNCHP melts at ~170°C but it does not show the first evidence of decomposition until ~205°C and only starts to decompose at more rapid rates above 240°C. Its decomposition behavior clearly differs from RDX and HMX.

The replacement of a methylene group in RDX with a keto group makes the resulting K6 compound less thermally stable as can be seen from Fig. 3. K6 starts to decompose at ~150°C and has undergone complete decomposition by 180°C. K6 appears to decompose below its nominal melting point (180°C), although such extensive decomposition below 180°C suggests that its melting point is uncertain. Consequently, we do not know at present whether K6 decomposes in the solid or liquid phase. However, it is clear that K6 is the least thermally stable cyclic nitramine of those used in the present study.

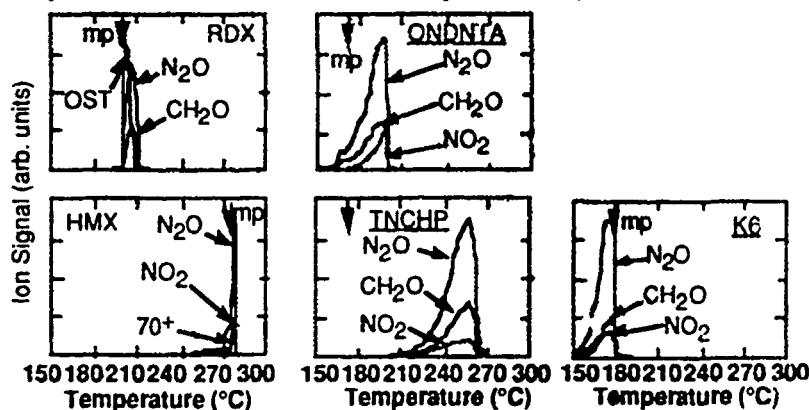


Figure 3. The ion signals associated with various decomposition products formed during the decomposition of RDX, HMX, ONDNTA, TNCHP, and K6. The heating rate for each experiment was 2°C/min. The ion signals are related to the gas formation rates of each decomposition product by an undetermined mass spectrometer sensitivity factor. Thus, the ion signals represent only the temporal behavior of each decomposition product and not their relative rates of formation.

#### Thermal Decomposition of ONDNTA

The thermal decomposition of ONDNTA is a complex process that also occurs via multiple pathways. The results presented in this paper cover our initial analysis of the thermal decomposition of ONDNTA and are used to show the qualitative behavior of the decomposition of ONDNTA. Quantification of our results requires further experiments and analysis and will appear at a later date.

The mass spectrum of ONDNTA has been presented previously.<sup>11</sup> At 20 eV, the major ion signals are  $C_2H_4N^+$  ( $m/z=42$ ) and  $C_2H_4N_2(NO)NO_2^+$  ( $m/z=132$ ). The mass spectrum of ONDNTA differs from RDX in that the ONDNTA forms most of its daughter ions by loss of fragments from the ring whereas RDX forms more of its daughter ions by loss of substituents on the ring.

The products formed during the thermal decomposition of ONDNTA are determined from STMBMS measurements that have been reported previously.<sup>11</sup> Two of the major products formed are CH<sub>2</sub>O and N<sub>2</sub>O. An ion signal measured at  $m/z=28$  also originates from a major decomposition product that may be either N<sub>2</sub>, CO, or possibly C<sub>2</sub>H<sub>6</sub>. The fourth major product observed in the decomposition forms an ion signal at  $m/z=42$  that has the formula  $C_2H_4N^+$  and is associated with a thermal decomposition product with a molecular weight less than 60 amu. Since it is less likely that the C<sub>2</sub>H<sub>4</sub>N radical is a major decomposition product, formation of C<sub>2</sub>H<sub>5</sub>N by abstraction of a hydrogen atom may be a more reasonable product. This species is consistent with the ion signals at  $m/z=43$  from ONDNTA-ul and  $m/z=48$  from ONDNTA-d<sub>6</sub> formed during the decomposition. This type of ring fragment has not been observed as a major product in the thermal decomposition of either RDX or HMX.

Other products formed during the decomposition of ONDNTA include: H<sub>2</sub>O, HCN, NO, NO<sub>2</sub>, and HO<sub>2</sub>O. Similar to the decomposition of RDX and HMX, three amides are also observed (formamide ( $m/z=45$ ), N-methylformamide ( $m/z=58,59$ ) and N,N-dimethylformamide ( $m/z=73$ )). Higher molecular weight products observed during the decomposition include two species, C<sub>3</sub>N<sub>3</sub>H<sub>3</sub> ( $m/z=81$ ) and C<sub>3</sub>N<sub>3</sub>H<sub>6</sub> ( $m/z=84$ ), in which the ONDNTA ring appears to remain intact. Two other higher molecular weight species that

appear during the decomposition are associated with the ion signals observed at  $m/z$  values of 85 and 132. Since the ONDNTA itself forms a large ion signal at  $m/z = 132$ , it has been difficult to determine the exact molecular weight of the thermal decomposition product that leads to the signal at  $m/z = 132$ . If the molecular weight of the product is 132, this would indicate that one of the decomposition pathways of ONDNTA involves elimination of methylenenitramine ( $\text{CH}_2=\text{N}-\text{NO}_2$ ). If  $\text{C}_2\text{H}_3\text{N}_3\text{O}^+$  ( $m/z=85$ ) is a molecular ion, then this thermal decomposition product may be formed by the loss of HONO from  $\text{C}_2\text{H}_4\text{N}_2(\text{NO}_2)\text{NO}$  ( $m/z=132$ ) to form a species such as  $\text{CH}_2=\text{N}-\text{CH}=\text{N}-\text{NO}$ . Further TOF velocity spectra measurements and analysis will provide more conclusive findings on these species.

The temporal behaviors of the ion signals associated with the ONDNTA thermal decomposition products are consistent with a multiple pathway decomposition mechanism. Figure 4 shows the temporal behaviors of the ion signals associated with the major products formed during an isothermal decomposition of ONDNTA-ul and ONDNTA-d6. In these experiments the sample starts to decompose as it is heated to its isothermal temperature. For a first order reaction in ONDNTA, one expects the ion signals arising from the decomposition products to decrease as the sample size decreases once the sample reaches its isothermal temperature. However, the  $\text{CH}_2\text{O}$  and  $\text{N}_2\text{O}$  signals continue to increase after the isothermal temperature is attained. This behavior is similar to that observed in the decomposition of RDX in that multiple pathways control the decomposition. This behavior is supported by the temporal behaviors of several ion signals associated with the other decomposition products. As can be seen from Figure 4, the product associated with the ion signal at  $m/z = 132$  appears to be first order in ONDNTA since the signal decreases as the sample is depleted. On the other hand the product associated with the ion signal at  $m/z = 85$  slowly increases as the sample is consumed and peaks just before the sample is depleted. Temporal behaviors similar to  $m/z = 85$  are observed for the amide products. The product associated with the ion signal at  $m/z = 132$  may originate directly from a unimolecular decomposition of ONDNTA, whereas, the amides and the products associated with the  $m/z = 85$  signal may arise through either an intermediate or an autocatalytic pathway. As shown in Figure 4a to 4c, the  $\text{CH}_2\text{O}$  and  $\text{N}_2\text{O}$  products, along with several lighter products, have temporal behaviors that increase as the sample size decreases and thus probably arise from both a first-order pathway and an intermediate or autocatalytic pathway.

The effect of hydrogen transfer in the rate limiting step of the different decomposition pathways is illustrated by the ion signals associated with the  $\text{CH}_2\text{O}$  and  $\text{N}_2\text{O}$  products shown in Figure 4a and 4d. In contrast to the temporal behaviors of the  $\text{CH}_2\text{O}$  and  $\text{N}_2\text{O}$  signals measured during the decomposition of ONDNTA-ul, the  $\text{CD}_2\text{O}$  and  $\text{N}_2\text{O}$  signals measured during the decomposition of ONDNTA-d6 show a fall off as the sample size decreases and is indicative of a first order reaction in ONDNTA. This indicates that the reaction rate of the intermediate/autocatalytic decomposition channel of ONDNTA is much slower for ONDNTA-d6 than ONDNTA-ul, and thus, the intermediate/autocatalytic channel exhibits a very strong DKIE.

One other interesting feature observed in the decomposition of ONDNTA is the evolution of  $\text{N}_2\text{O}$  and  $\text{CH}_2\text{O}$  as the sample is heated but prior to melting. These peaks occur in the  $\text{CH}_2\text{O}$  and  $\text{N}_2\text{O}$  signals between 800 and 1500 seconds in Figure 4a and 4d, and evolve over a temperature range from 120 to 170 °C. Contamination of the original sample has been eliminated as an explanation for this peak. Details of the mechanisms controlling each of the decomposition pathways of ONDNTA require a more detailed examination of the ONDNTA data, which is currently underway.

#### Thermal decomposition products from TNCHP

TNCHP is more stable in the liquid phase than either RDX or HMX. The major products formed in its decomposition are  $\text{CH}_2\text{O}$  and  $\text{N}_2\text{O}$ . Products formed to a lesser extent include:  $\text{H}_2\text{O}$ , HCN, NO, and  $\text{NO}_2$ . Ion signals, representing other decomposition products, are also observed. Further measurements utilizing deuterium labeled TNCHP and TOF velocity spectra are underway to determine the identity of the thermal decomposition products leading to these other ion signals. The temporal behaviors of the major ion signals are shown in Figure 5. These results illustrate the increased thermal stability of TNCHP in the liquid phase compared to RDX. The ion signal at  $m/z = 146$  is analogous to the ion signal at  $m/z = 132$  that arises from ONDNTA. Thus, the ion signal at  $m/z = 146$  most likely arises from the mononitroso analogue of TNCHP.

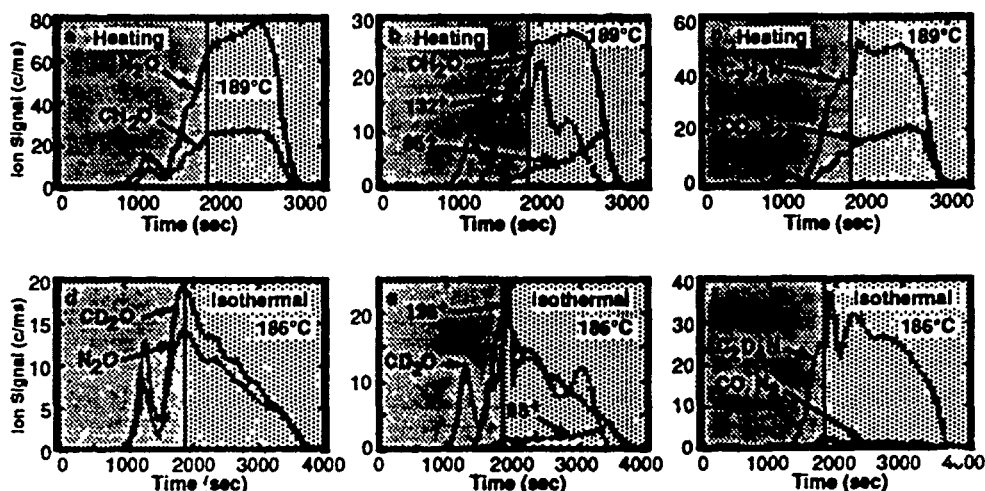


Figure 4. Ion signals associated with thermal decomposition products from ONDNTA. Signals in panels a, b and c are from unlabeled ONDNTA and signals in d, e and f are from ONDNTA-d6. The signals in the left shaded portion of the graphs were recorded during the thermal ramp of the sample and the right shaded portions were recorded at the isothermal temperature listed on each graph. The large oscillations in the ion signals at  $m/z$  values of 132 and 136 is due to the large correction factor that was used to subtract the contribution from evaporating ONDNTA at these two  $m/z$  values.

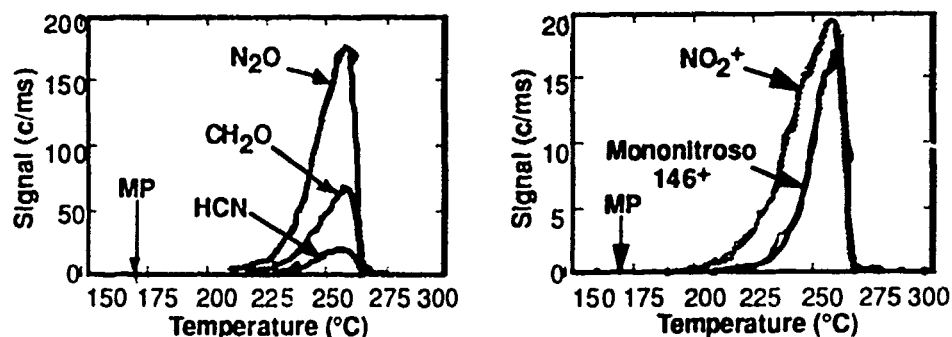


Figure 5. Ion signals associated with the products formed during the thermal decomposition of TNCHP. The heating rate is  $2\text{ }^{\circ}\text{C/min}$ .

In isothermal experiments with TNCHP, the temporal behaviors of the ion signals associated with the decomposition products from TNCHP are indicative of several parallel reaction pathways. The temporal behaviors of several of the products are illustrated in Figure 6. Ion signals associated with processes that are approximately first order in TNCHP are represented by the signals for NO and NO<sub>2</sub> in Fig. 6 and also include signals that represent HCN. Ion signals associated with intermediate products formed during the thermal decomposition are found at  $m/z$  values of 55, 84, 130, and 146. The ion signals at  $m/z$  values of 55, 84 and 130 have temporal behaviors similar to that of 146, which probably represents the mononitroso analogue of TNCHP. This suggests that the ion signals at  $m/z$  values of 55, 84 and 130 may be ion dissociation products of the TNCHP mononitroso analogue. TOF velocity spectra signals at these  $m/z$  values will resolve whether these signals are ion dissociation products formed in the mass spectrometer or whether they arise from additional thermal decomposition products.

A stable product, similar to the formation of OST in the decomposition of RDX, is not observed in the thermal decomposition of TNCHP. This inability to form a decomposition product by stabilizing the ring of the cyclic nitramine may lead to the increased thermal stability of TNCHP.

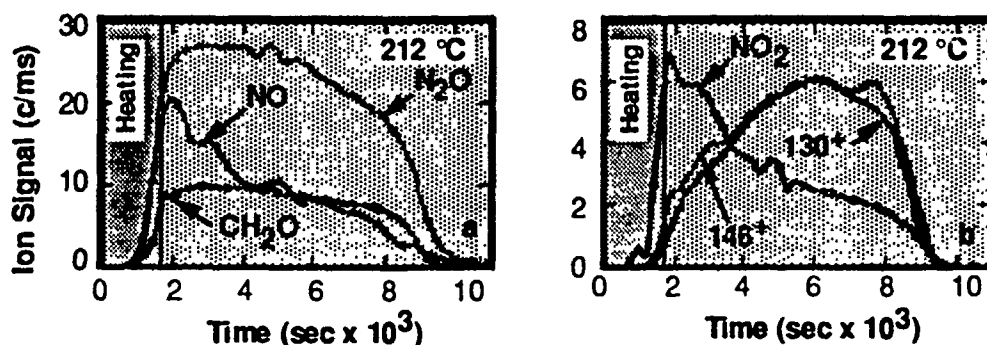


Figure 6. Ion signals associated with the thermal decomposition products from TNCHP. The region in the left shaded panel is the heating portion and the right shaded panel is the isothermal portion of the experiment. The ion signals representing NO and NO<sub>2</sub> appear to be approximately first order in liquid-phase TNCHP. The ion signals at m/z values of 130 and 146 are associated with an intermediate formed during the thermal decomposition. The ion signals associated with CH<sub>2</sub>O and N<sub>2</sub>O probably originate from pathways associated with both the first order process and the decomposition of the intermediate.

#### Thermal decomposition products from K6

The decomposition of K6 is quite different from the other cyclic nitramines used in this study. In addition to its lower thermal stability, K6 also produces fewer and simpler decomposition products. The decomposition products from K6 are mainly CH<sub>2</sub>O, N<sub>2</sub>O and CO<sub>2</sub>, with minor contributions from HCN, CO, NO and NO<sub>2</sub>. Unlike the other cyclic nitramines used in this study, K6 does not form any amides, mononitroso analogue, or residue. The temporal behaviors of the products formed during the decomposition of K6 are shown in Figure 7.

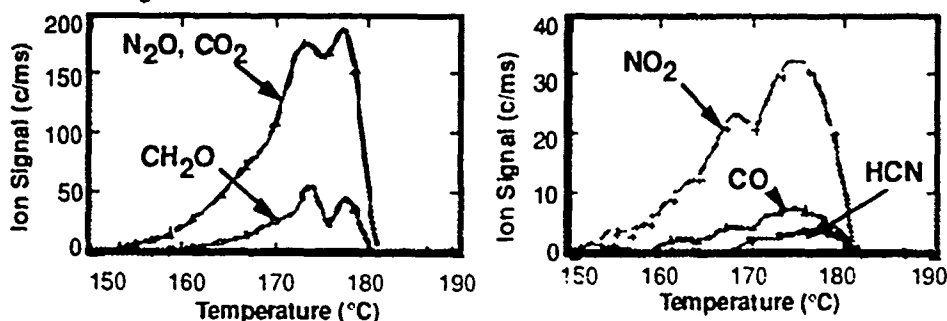


Figure 7. Ion signals formed in the mass spectrometer from products formed during the thermal decomposition of K6.

The decomposition of K6 may be initiated by attack of one of the NO<sub>2</sub> oxygen atoms on the keto group carbon atom leading to the initial elimination of CO<sub>2</sub> and followed by the rapid transformation of the remaining fragment into CH<sub>2</sub>O and N<sub>2</sub>O. The rate of decomposition of K6 through this initial four center C-N-N-O complex would appear to be competitive with N-NO<sub>2</sub> bond breaking in that no mononitroso analogue or amides are observed in the decomposition of K6.

#### SUMMARY

Through the use of measurements of the temporal behaviors of the gas formation rates of the products formed during the thermal decomposition of RDX and the analysis of results from DKIE and isotopic scrambling experiments with the <sup>2</sup>H, <sup>13</sup>C, <sup>15</sup>N, and <sup>18</sup>O labeled analogues of RDX, we have previously determined that four different primary reaction pathways control the decomposition of RDX. These pathways consist of 1) the unimolecular decomposition of RDX to form oxy-s-triazine (OST) through HONO and HNO elimination, 2) the unimolecular decomposition of RDX via the N-NO<sub>2</sub> bond breaking step with the subsequent unraveling of the RDX ring, possibly through the methylenenitramine intermediate, to form N<sub>2</sub>O and CH<sub>2</sub>O, 3) the conversion of RDX to its mononitroso analogue

ONDNTA followed by the subsequent decomposition of ONDNTA to predominantly  $N_2O$  and  $CH_2O$ , and 4) the catalytic decomposition of RDX by some catalyst formed from the RDX decomposition products. The products associated with the formation of OST exhibit a DKIE and the OST itself shows no evidence of isotopic scrambling of any of the elements in the molecule. Consequently, it appears that the formation of OST involves an intra-molecular hydrogen transfer step that controls the decomposition of RDX in this channel. Just as importantly, the  $CH_2O$  and ONDNTA products do not exhibit a DKIE and thus indicate that the products produced through the channels associated with these products do not involve transfer of hydrogen in the rate limiting step.

Through examination of the temporal behaviors of the ion signals associated with the thermal decomposition products from HMX in the liquid phase, it was found that the decomposition of HMX also occurs by multiple decomposition pathways. Ion signals associated with fragments of the HMX ring are observed for the thermal decomposition of HMX in the liquid phase. No molecular ion of an HMX decomposition product that is analogous to OST formed in the decomposition of RDX is observed. The temporal behaviors of several of the HMX decomposition products are approximately first order in HMX, indicating that pathways similar to pathways 1 and 2 observed in the decomposition of RDX are also present in the decomposition of HMX. The mononitroso analogue of HMX, ONTNTA, and its associated decomposition products are also formed during the decomposition. This behavior is similar to that of RDX. In addition, ONTNTA is formed in significant quantities in the solid phase of HMX prior to melting. However, since HMX melts at a temperature approximately 80 °C higher than RDX, more solid-phase decomposition occurs in HMX. Finally, several amides and a residue are also observed in the decomposition of HMX.

Through examination of the temporal behaviors of the ion signals associated with the thermal decomposition products from ONDNTA, the mononitroso analogue of RDX, and its deuterium labeled analogue, it was found that it also decomposes by multiple decomposition pathways. The major products formed in the decomposition of ONDNTA include  $CH_2O$ ,  $N_2O$  and a lower molecular weight product that forms  $C_2H_4N^+$  in the mass spectrometer and whose exact identity has not yet been determined. Several ion signals are associated with decomposition products that exhibit approximately first order behavior in liquid-phase ONDNTA. One higher molecular weight product that exhibits this first order behavior is associated with the ion signal at  $m/z = 132$ . One component of the ion signals associated with the  $CH_2O$  and  $N_2O$  products is associated with this first order process. Another decomposition pathway exhibits autocatalytic behavior and has a large deuterium kinetic isotope effect. The results on the thermal decomposition of ONDNTA are consistent with the behavior of the ONDNTA intermediate formed in one of the RDX decomposition pathways. The present results on the decomposition of ONDNTA show that more complicated pathways control its decomposition than assumed in its pathway for RDX. The decomposition behavior of ONDNTA formed as the intermediate in the decomposition of RDX may actually play a role in the more complicated chemistry associated with the autocatalytic pathway in RDX.

The decomposition of TNCHP and K6, two other cyclic nitramine compounds with molecular conformations similar to those of RDX, has shown the effect of different molecular conformations on the various decomposition pathways. Of the four cyclic nitramines studied, RDX, HMX, K6, and TNCHP, only TNCHP shows significant stability after melting. Our initial results on the decomposition of TNCHP show several products that exhibit a temporal behavior that is first order in liquid-phase TNCHP. However, there is no evidence of any product formed in the decomposition of TNCHP that is similar to either OST formed in the decomposition of RDX or the ring fragments formed in the decomposition of HMX. This inability to form a stable product with the ring from the cyclic nitramine intact may account for the increased stability of TNCHP in the liquid phase. There are several ion signals associated with decomposition products from TNCHP that indicate that TNCHP also forms a mononitroso intermediate that controls one of the decomposition pathways. This is similar to both RDX and HMX. The results show that the thermal stability of K6 is much less than the other two compounds. The thermal decomposition of K6 produces only  $CH_2O$ ,  $N_2O$ , and  $CO_2$  with minor amounts of HCN, CO, and  $NO_2$ . Qualitatively, the decomposition pathways of K6 appear to be less complex than those of RDX, HMX and TNCHP.

## ACKNOWLEDGMENTS

The authors thank M. G. Mitchell and K. A. Morrison for assistance in running the experiments and collecting the data and J. R. Autera for assistance in the synthesis. Research supported in part by the U. S. Army Research Office, U. S. Army ARDEC, and the U. S. Department of Energy.

- <sup>1</sup> R. Behrens, Jr., *J. Phys. Chem.*, **94**, 6706, (1990).
- <sup>2</sup> R. Behrens, Jr. and S. Bulusu, *J. Phys. Chem.*, **95**, 5838, (1991).
- <sup>3</sup> R. Behrens, Jr. and S. Bulusu, *J. Phys. Chem.*, **96**, 8877, (1992).
- <sup>4</sup> R. Behrens, Jr. and S. Bulusu, *J. Phys. Chem.*, **96**, 8891, (1992).
- <sup>5</sup> a) R. Behrens, Jr., *Rev. Sci. Instrum.*, **58**, 451, (1986); b) R. Behrens, Jr., "The Application of Simultaneous Thermogravimetric Modulated Beam Mass Spectrometry and Time-of-Flight Velocity Spectra Measurements to the Study of the Pyrolysis of Energetic Materials." In "Chemistry and Physics of Energetic Materials", Bulusu, S. N., Ed.; Proceedings of the NATO Advanced Study Institute, Vol. 309, Kluwer Academic Publishers, Netherlands, 1990, p. 327.
- <sup>6</sup> R. Behrens, Jr., *Int. J. Chem. Kinetics*, **22**, 135, (1990).
- <sup>7</sup> F. J. Brockman, D. C. Downing, and G. F. Wright, *Canadian J. of Research*, **27B**, 469, (1949).
- <sup>8</sup> G. S. Meyers and G. F. Wright, *Canadian Journal of Research*, **27B**, 489, (1949).
- <sup>9</sup> A. R. Mitchell, P. F. Pagoria, C. L. Coon, E. S. Jessop, J. F. Poco, C. M. Tarver, R.D. Breithaupt and G.L. Moody, "Synthesis, Scale-up, and Characterization of K-6", Univ. of Calif Report, UCRL-LR-109404, February, (1991).
- <sup>10</sup> R. Behrens, Jr., *Int. J. Chem. Kinetics*, **22**, 159, (1990).
- <sup>11</sup> R. Behrens, Jr. and S. Bulusu, Proceedings of the 29th JANNAF Combustion Meeting, Langley, Virginia, Chemical Propulsion Information Agency, October, 1992.

## MOLECULAR COMPOSITION, STRUCTURE, AND SENSITIVITY OF EXPLOSIVES

CARLYLE B. STORM AND JAMES R. TRAVIS

Explosives Technology and Applications Division, Los Alamos National Laboratory,  
Los Alamos, NM 87545

### ABSTRACT

High explosives, blasting agents, propellants, and pyrotechnics are all metastable relative to reaction products and are termed energetic materials. They are thermodynamically unstable but the kinetics of decomposition at ambient conditions are sufficiently slow that they can be handled safely under controlled conditions. The ease with which an energetic material can be caused to undergo a violent reaction or detonation is called its sensitivity. Sensitivity tests for energetic materials are aimed at defining the response of the material to a specific situation, usually prompt shock initiation or a delayed reaction in an accident. The observed response is always due to a combination of the physical state and the molecular structure of the material. Modeling of any initiation process must consider both factors. The physical state of the material determines how and where the energy is deposited in the material. The molecular structure in the solid state determines the mechanism of decomposition of the material and the rate of energy release. Slower inherent reaction chemistry leads to longer reaction zones in detonation and inherently safer materials. Slower chemistry also requires hot spots involved in initiation to be hotter and to survive for longer periods of time. High thermal conductivity also leads to quenching of small hot spots and makes a material more difficult to initiate. Early endothermic decomposition chemistry also delays initiation by delaying heat release to support hot spot growth. The growth to violent reaction or detonation also depends on the nature of the early reaction products. If chemical intermediates are produced that drive further accelerating autocatalytic decomposition the initiation will grow rapidly to a violent reaction.

### Introduction

The relationship between the constitution of an organic explosive and the sensitivity and performance of the material is a question of long standing interest. The subject was first reviewed in 1944.<sup>1</sup> It was demonstrated early in the systematic investigation of high explosive properties, using homogeneous mixtures of liquids of continuously varying oxygen balance, that power, detonation velocity, brisance, and sensitivity all increase as the oxygen balance moves towards a product composition of carbon dioxide and water, and then decreases as the explosive becomes overly oxygen rich.<sup>1,2</sup> In the late 1950s Kamlet and coworkers began a series of studies that related molecular composition and structure to impact sensitivity<sup>3-6</sup> in a wide variety of organic explosives. A major interest in these studies was to identify "trigger linkages" in molecular structures so as to avoid kinetically labile structural components in future synthetic efforts. A variety of other investigations have studied the effects of such parameters as bond polarities, molecular composition, electronegativity and early decomposition chemistry<sup>7-21</sup> on sensitivity.

### Sensitivity Testing

The sensitivity of an energetic material is always defined relative to a particular test. The test may be designed to give information about a particular hazard situation or to provide more general information implying how a particular energetic material will behave over a wider range of conditions. Tests are carried out to measure the explosives response to energy input from shock, impact, thermal, friction, and electrostatic discharge sources. The number of materials that have been tested under the different categories and how well the tests are characterized varies widely. Shock initiation tests are expensive and require relatively large amounts of material. The shock initiation tests tend to be well characterized but relatively few materials, either pure compounds or formulations, have been tested. Drop-weight-impact testing is



COMPOUND	Compound Number <sup>34</sup>	D <sub>Cl</sub> (mm/μs)	P <sub>CJ</sub> (GPa)	Impact <sup>21</sup> Sens.(cm)	Density (g/cm <sup>3</sup> )	ΔH <sub>f</sub> (kJ/mole)	ΔH <sub>det</sub> <sup>43,44</sup> (kJ/g)
Hexanitrobenzene	1-1	9.33 <sup>42</sup>	41.7 <sup>42</sup>	12	1.99 <sup>33</sup>	39.7 <sup>42</sup>	-6.89
Pentanitroaniline	1-4	5.12 <sup>42</sup>	35.5 <sup>42</sup>	15	1.77 <sup>33</sup>	-23.4 <sup>42</sup>	-6.25
1,2,4,5-tetranitro- benzene	1-3	8.0 <sup>26</sup>	30.1 <sup>26</sup>	27	1.82 <sup>26</sup>	-42.6 <sup>42</sup>	-6.10
Trinitrobenzene	1-5	7.27 <sup>40</sup>	22.2 <sup>41</sup>	100	1.68 <sup>40</sup>	-37.2 <sup>42</sup>	-5.85
Picr. mide	1-12	7.42 <sup>40</sup>	24.2 <sup>41</sup>	177	1.76 <sup>40</sup>	-71.1 <sup>42</sup>	-5.24
1,3-diamino-2,4,6- trinitrobenzene	1-15	7.67 <sup>40</sup>	25.9 <sup>30</sup>	320	1.84 <sup>30</sup>	-98.7 <sup>30</sup>	-4.91
1,3,5-triamino-2,4,6- trinitrobenzene	1-18	7.94 <sup>40</sup>	29.1 <sup>30</sup>	500	1.94 <sup>30</sup>	-154.2 <sup>30</sup>	-4.49
Hex. nitrobiphenyl	1-29	7.47 <sup>26</sup>	24.9 <sup>26</sup>	85	1.74 <sup>26</sup>	68.5 <sup>42</sup>	-5.93
Hexanarobiphenyl- diamine	1-33	7.49 <sup>40</sup>	26.9 <sup>26</sup>	132	1.79 <sup>30</sup>	-28.5 <sup>30</sup>	-5.42
TNT	2-3	6.96 <sup>40</sup>	21.0 <sup>30</sup>	158	1.65 <sup>30</sup>	-64.4 <sup>30</sup>	-5.43
Benzotrifuroxan	1-2	8.49 <sup>30</sup>	36.0 <sup>30</sup>	50	1.90 <sup>30</sup>	606 <sup>30</sup>	-7.07
Ammonium picrate	1-17	6.85 <sup>30</sup>	18.9 <sup>26</sup>	136	1.72 <sup>30</sup>	-393 <sup>30</sup>	-3.06
Picric acid	1-6	7.26 <sup>30</sup>	26.5 <sup>30</sup>	73	1.76 <sup>30</sup>	-214.5 <sup>30</sup>	-3.59

Table 1. Some properties of aminotrinrobenzene explosives and related compounds.

relatively simple and uses a small amount of material. However the important characteristics of the test are not understood, it exists in a bewildering variety of forms, and relies on different indicators for go/no-go responses. This test has been used to examine by far the largest variety of pure high explosive compounds and formulated materials. A summary of the LANL Type 12 impact results for 258 compounds drawn from 14 different structural classes has been published.<sup>21</sup> A compilation of Navy small scale gap test data for 52 pure materials and formulations has also been published.<sup>22</sup>

Any effort to understand structure/composition effects on sensitivity must draw upon the sensitivity testing literature for a data base. The results of any sensitivity test are affected by the physical structure of the material (macrostructure of grain size, hardness, crystal structure that can lead to topotactic reactions, etc.)<sup>23,24</sup> and the molecular structure of the material in the solid state (chemical mechanism of decomposition and rate of heat release).<sup>21,24</sup> In order to understand the role of molecular structure and composition in sensitivity one must deconvolute these different contributions to the particular test. In order to do this you will have to model the physical effects involved and the chemical kinetics of the decomposition under the conditions of the test. Success in modeling these diverse tests will move us away from a go/no-go probabilistic basis, provide insight into the dominant physical and chemical factors controlling the test result, and permit more deterministic (as opposed to probabilistic) testing methods to be developed.

#### Initiation and Propagation

The material properties of the high explosive profoundly affect the initiation and propagation of a detonation, a result of the intimate interaction of fluid mechanics and chemistry. The initiation process is driven by the localization of energy in hot spots by the shock. Hot spot formation is a complicated interaction of mechanics and chemistry. Mechanical action, such as crushing, void collapse, local shock interactions, and jet formation heat the explosive initiating decomposition. Whether the resulting reaction will build up to detonation is determined by the balance between the energy generated in the hot spot (rate of chemical decomposition), the rate of heat dissipation through thermal diffusion<sup>25</sup> (small hot spots), and the rate of quenching<sup>26</sup> by rarefactions (larger hot spots). The questions of particle size distribution and reaction rates in shocked material, including TATB, have been considered by various investigators.<sup>27</sup>

Other sensitivity tests relying on impact, electrostatic discharge, or thermal ignition sources are less well characterized than the shock initiation. The balance between energy production and energy loss in thermal initiation<sup>47</sup> was defined some time ago by Frank-Kamenetskii (FK) and remains the basis for the analysis of most initiation phenomena. If you can model the extent of localization of energy, which will give you a local temperature, the FK approach will indicate whether the local hot spot will grow or decay.

A complete mathematical description of an initiation, propagation, or detonation must have the equations of motion, the equation of state of the material and reaction products, and the heat release rate (progress variable). In principle, we must know the chemical kinetics of the reaction process to get the heat release rate. Most models now in use have a single Arrhenius rate parameter to model complex chemistry. Current research on the chemistry of energetic materials at high temperatures and pressures is providing a glimpse of the possibilities<sup>29</sup>, but this is still a demanding research area for the future. Until exact quantitative information concerning the physical and chemical factors involved in initiation and propagation can be obtained, the effects of composition and structure on sensitivity are best judged by variations in behavior in a homologous series of related compounds.

#### TATB - A Paradigm for an Insensitive High Explosive

1,3,5-Triamino-2,4,6-trinitrobenzene (TATB) was first prepared by Jackson and Wing in 1887.<sup>28</sup> In the mid-1950's the U.S. Navy investigated TATB as a potential heat-resistant explosive. They established that the material had good explosive properties, was quite heat resistant, and was extraordinarily insensitive. In the 1960's Los Alamos Scientific Laboratory

began investigations of the possibility of using TATB as an insensitive high explosive (IHE) and extensive studies of the fundamental physical properties of the material. The x-ray crystal structure determination<sup>29</sup> for TATB showed that the material had a high density and unusually strong intra- and intermolecular hydrogen bonding.

Since the intensive investigation of TATB began in the 1960s two proposals have been consistently put forward relative to its extreme insensitivity. One is that TATB is a very unusual outlier, insensitive due to a fortuitous combination of as yet unidentified properties. The implication of this approach is that equally unusual outliers may well turn up in other classes of explosives, such as nitramines or nitrate esters, if enough compounds are examined. The second proposal ascribes the insensitivity to the hydrogen bonding in TATB. The implication of this hypothesis is that one should synthesize materials with extensive hydrogen bonding in the search for other IHEs.

The question of the performance and sensitivity of TATB is best examined in the context of the properties of other substituted-nitroaromatic high explosives. In Table 1 we give a selection of physical, performance, and sensitivity properties for the nitroaromatic and aminonitroaromatic homologous series and several related compounds.

Table 2. A comparison of properties of TATB and HMX.

PROPERTY	TATB	HMX	Ref.
Density (g/cm <sup>3</sup> )	1.938	1.905	30
Thermal conductivity (cal/cm s °C)	$1 \times 10^{-3}$	$7 \times 10^{-4}$	31
Drop-weight impact (50% ht. cm.)	> 320	33	30
Small scale gap test, NSWG, (GPa @ 98% TMD)	16.5	2.0	21
Failure diameter (mm)	9	1	32
Reaction zone thickness (mm)	6	0.1	26
Detonation velocity (m/s)	7.76	9.11	30
Gurney energy (MJ/kg)	1.1	1.6	30
Heat of detonation (MJ/kg)	-5.02	-6.78	30

In Table 2 we compare the properties of TATB and cyclotetramethylenetetranitramine (HMX). HMX is the highest performance explosive in use, TATB the most insensitive high performing explosive in use. The detonation velocity of HMX is some 17% greater than that of TATB, the Gurney energy 45% greater, and the heat of detonation 35% greater. One reason that TATB performs as well as it does, given the relatively low heat of detonation, is its unusually high density. An atom additivity calculation predicts<sup>33</sup> a density of 1.80 g/cm<sup>3</sup>, well below the 1.94 g/cm<sup>3</sup> observed. This large positive density deviation is a consequence of the strong in-plane hydrogen bonding<sup>29</sup> observed in the crystal structure. Without this high density the performance of TATB would not be high enough for the material to be of any practical interest. Even with this large positive deviation in density the material is still well below HMX in all of the figures of merit for performance. However in all measures of sensitivity TATB is vastly better than HMX.

Since HMX (nitramine) and TATB (nitroaromatic) are drawn from different structural classes of organic high explosives any comparison of sensitivity to performance involves apples to oranges analogies. A comparison of TATB properties to materials drawn from a related homologous series is given in Table 1. This comparison speaks to the question of whether TATB is an unusual outlier in its sensitivity or whether it is behaving as a reasonable

began investigations of the possibility of using TATB as an insensitive high explosive (IHE) and extensive studies of the fundamental physical properties of the material. The x-ray crystal structure determination<sup>29</sup> for TATB showed that the material had a high density and unusually strong intra- and intermolecular hydrogen bonding.

Since the intensive investigation of TATB began in the 1960s two proposals have been consistently put forward relative to its extreme insensitivity. One is that TATB is a very unusual outlier, insensitive due to a fortuitous combination of as yet unidentified properties. The implication of this approach is that equally unusual outliers may well turn up in other classes of explosives, such as nitramines or nitrate esters, if enough compounds are examined. The second proposal ascribes the insensitivity to the hydrogen bonding in TATB. The implication of this hypothesis is that one should synthesize materials with extensive hydrogen bonding in the search for other IHEs.

The question of the performance and sensitivity of TATB is best examined in the context of the properties of other substituted-nitroaromatic high explosives. In Table 1 we give a selection of physical, performance, and sensitivity properties for the nitroaromatic and aminonitroaromatic homologous series and several related compounds.

Table 2. A comparison of properties of TATB and HMX.

PROPERTY	TATB	HMX	Ref.
Density (g/cm <sup>3</sup> )	1.938	1.905	30
Thermal conductivity (cal/cm s °C)	1 x 10 <sup>-3</sup>	7 x 10 <sup>-4</sup>	31
Drop-weight impact (50% ht. cm.)	> 320	33	30
Small scale gap test, NSWG, (GPa @ 98% TMD)	16.5	2.0	21
Failure diameter (mm)	9	1	32
Reaction zone thickness (mm)	6	0.1	26
Detonation velocity (m/s)	7.76	9.11	30
Gurney energy (MJ/kg)	1.1	1.6	30
Heat of detonation (MJ/kg)	-5.02	-6.78	30

In Table 2 we compare the properties of TATB and cyclotetramethylenetetranitramine (HMX). HMX is the highest performance explosive in use, TATB the most insensitive high performing explosive in use. The detonation velocity of HMX is some 17% greater than that of TATB, the Gurney energy 45% greater, and the heat of detonation 35% greater. One reason that TATB performs as well as it does, given the relatively low heat of detonation, is its unusually high density. An atom additivity calculation predicts<sup>33</sup> a density of 1.80 g/cm<sup>3</sup>, well below the 1.94 g/cm<sup>3</sup> observed. This large positive density deviation is a consequence of the strong in-plane hydrogen bonding<sup>29</sup> observed in the crystal structure. Without this high density the performance of TATB would not be high enough for the material to be of any practical interest. Even with this large positive deviation in density the material is still well below HMX in all of the figures of merit for performance. However in all measures of sensitivity TATB is vastly better than HMX.

Since HMX (nitramine) and TATB (nitroaromatic) are drawn from different structural classes of organic high explosives any comparison of sensitivity to performance involves apples to oranges analogies. A comparison of TATB properties to materials drawn from a related homologous series is given in Table 1. This comparison speaks to the question of whether TATB is an unusual outlier in its sensitivity or whether it is behaving as a reasonable

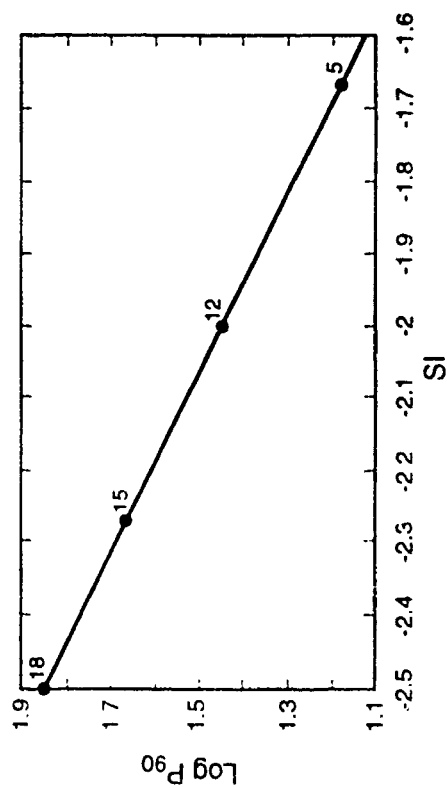


Figure 1a. A plot of the shock sensitivity at 90% TMD ( $P_{90}$ ) vs. the Sensitivity Index for trinitrobenzene (TNB) (5), picramide (MATB)(12), 1, 3-diamino-2, 4, 6-trinitrobenzene (DATB)(15), and 1, 3, 5-triamino-2, 4, 6-trinitrobenzene (TATB)(18).

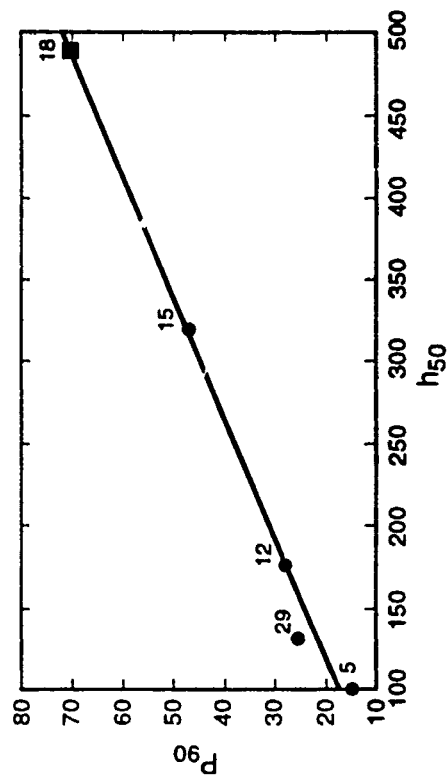


Figure 1b. A plot of the shock sensitivity at 90% TMD ( $P_{90}$ ) vs. the Type 12 impact sensitivity ( $h_{50}$ ) for (TNB) (5), hexanitrophenyldiamine (DIPAM)(33), (MATB)(12), DATB(15), and TATB(18). The impact sensitivity of TATB is estimated by the extrapolation of the line.

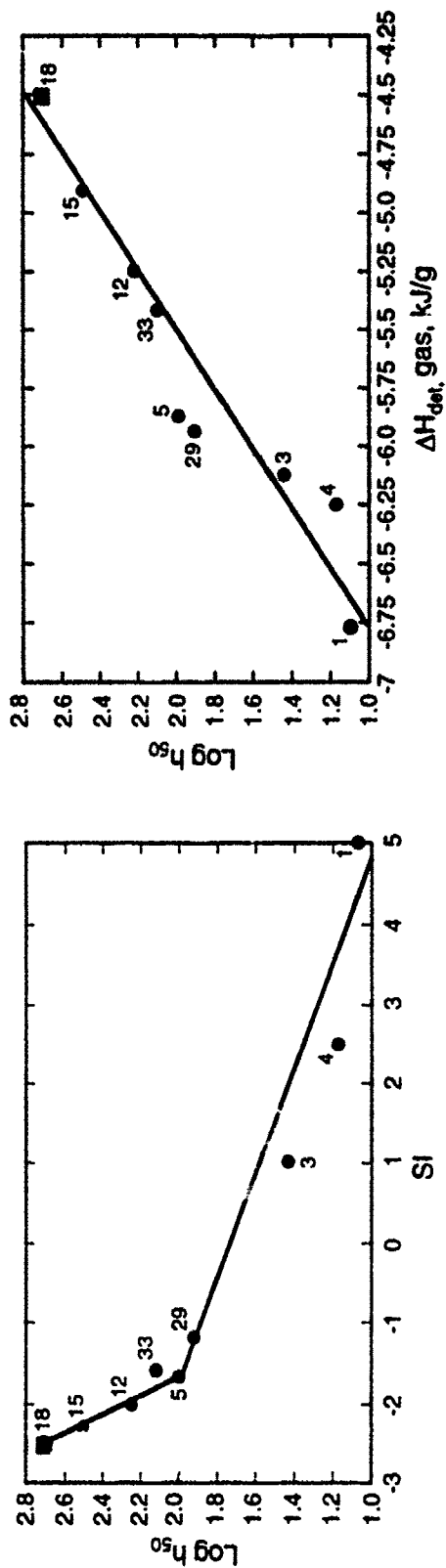


Figure 1c. A plot of the Type 12 impact sensitivity ( $h_{50}$ ) for the first nine compounds in Table 1 (1, 4, 3, 5, 12, 15, 18, 29, 33) vs. the sensitivity index (SI) for these compounds.

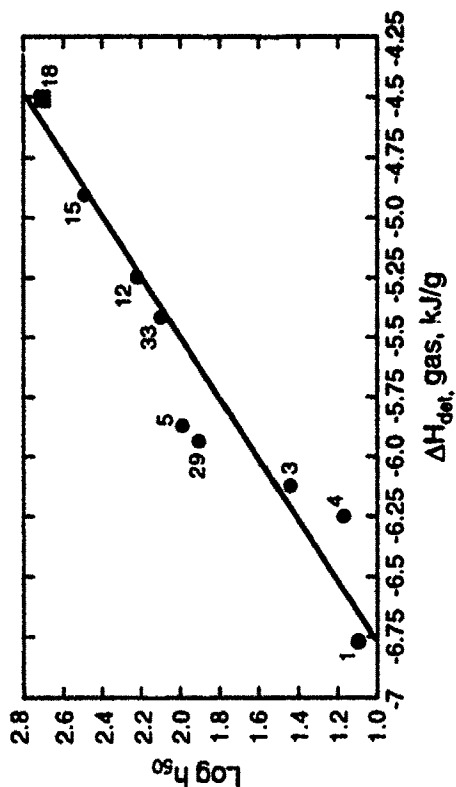


Figure 1d. A plot of the Type 12 impact sensitivity ( $h_{50}$ ) for the first nine compounds in Table 1 vs. the heat of detonation ( $\Delta H_{det}$ ) for these compounds.

member of the series of compounds it belongs to. Earlier we defined<sup>21</sup> an oxygen balance related Sensitivity Index (SI), similar to that used by Kamlet.<sup>3-6</sup> In Figure 1a we show how the shock initiation in the NSWC small scale gap test of trinitrobenzene<sup>34</sup> (TNB)(5), picramide (MATB)(12), 1,3-diamino-2,4,6-trinitrobenzene (DATB)(15) and TATB(18) vary at 90% theoretical maximum density (TMD) as a function of SI. For similar plots at 95% and 98% TMD the series takes on a regular concave upward shape. In all cases TATB sits very much where you would expect it to be based on its oxygen balance in this homologous series.

In Figure 1b we compare the drop-weight impact sensitivity of this same series (TNB, MATB, DATB) plus hexanitrobiphenyldiamine (DIPAM)(33) and extrapolate the line to the measured shock sensitivity of TATB. This estimates the drop-weight impact sensitivity of TATB at about 500 cm. The machine used in the Type 12 impact sensitivity measurement only extends to 320 cm. Thus the results are reported as >320 for any compound that gives no-go at the maximum height available on the machine. The estimate given by the comparison of the shock initiation to the impact initiation for this series is quite reasonable. That the TATB gets hot enough to react has been demonstrated by impact studies<sup>35</sup> done on heat sensitive film. Although reaction is initiated at a drop height of 320 cm it does not propagate to give a "go" on the acoustic analyzer. In a similar manner if you plot the SI of the closely related series TNB(5), MATB(12), DATB(15), TATB(18), DIPAM(33), and hexanitrobiphenyl(29) against the impact sensitivities for the series the estimated value of 500 cm for TATB fits well and is quite reasonable.

If you now extend that series to the more highly substituted polynitrobenzenes, hexanitrobenzene (1), tetranitrobenzene (3), and pentanitroaniline (4), using the SI and impact sensitivity of the first nine materials in Table 1, Figure 1c, there is a sharp break in the correlation at TNB(5). However, if you use the heat of detonation ( $\Delta H_{det}$ ) as an index for the impact sensitivity all of the related compounds fall on a single regression. This suggests that the mechanism of decomposition of this series is similar or changes gradually as you move through the series and that the ease of initiation and propagation is controlled by the rate of heat release generated in the hot spots. Insight as to the early mechanism of decomposition of TATB should provide information as to one aspect of its insensitivity.

Sharma and coworkers<sup>36-38</sup> have investigated the shock and impact induced early decomposition of TATB. They have observed several furazan and furoxan compounds resulting from the cyclization of the ortho-aminonitro functional groups, Figure 2. There are several interesting observations relative to the accumulation of these compounds. (a) The furazans and furoxans represent explosives that are known to be or are expected to be much more sensitive than TATB. For instance, the known 5,7-diamino-4,6-dinitrofuroxan observed in the shock induced decomposition has an impact sensitivity intermediate between TNT and DATB. (b) The dehydration of the ortho-aminonitro functional groups to the furazan or furoxan function is approximately thermochemically neutral. The formation of water is about 65 kcal/mole exothermic, the furazan or furoxan formation is about the same amount endothermic. (c) The chemical reaction products are chemically benign. Typically an energetic material will react by generating fuel and oxidizer by separate pathways which combine later to provide the large, prompt, release of energy. Water has no further role to play in chemical reactivity and the furazan, furoxan, or similar intermediate has to undergo further decomposition to feed the appropriate pathways. This places a very effective neutral filter in the decomposition mechanism. A mechanism of decomposition that involves a series of consecutive reactions culminating in an explosive reaction is consistent with<sup>45</sup> the observations of Catalano and Rolon on the thermal decomposition of confined TATB. They observed four separate stages to the evolution of the thermal decomposition. The culminating explosive reaction is the result of the development of either chain and/or concurrent reactions.

The early reactions proposed in the shock- and impact-induced decomposition of TATB are disfavored by pressure, as they result in the formation of multiple species. It has been suggested by Rogers<sup>46</sup>, based on solid state deuterium isotope effect studies on the thermal decomposition, that the thermal degradation of TATB involves a positive activation volume. Studies of TATB under high static pressure<sup>48</sup> in diamond anvil cells (up to 16 GPa) have shown it to be very stable to pressure effects. The vibrational frequencies show an unusual pressure dependence, ascribed to variations in the  $NH_2/NO_2$  coupling as the pressure

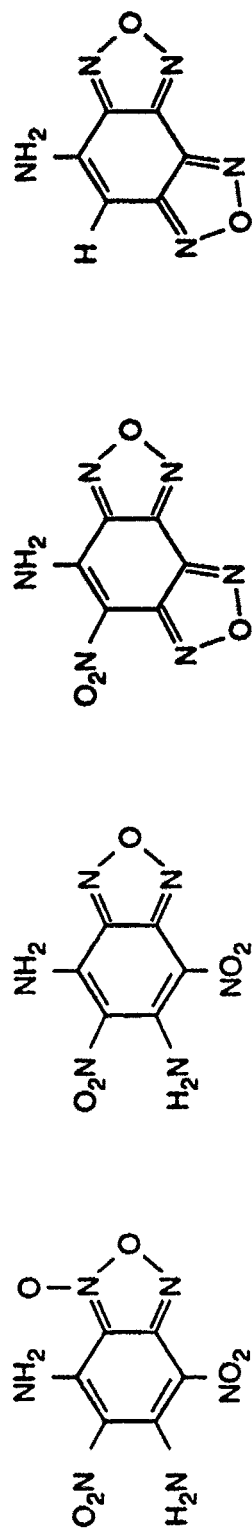


Figure 2. The structures of several of the aminonitrofurazans and furoxans isolated<sup>36-38</sup> from the impact and shock induced decomposition of TATB.



increases. A facile photolytic reaction, which gives a green product, is strongly suppressed at higher pressures.

### Summary

TATB offers a number of useful lessons regarding the origins of chemical contributions to insensitivity. It is a very insensitive material by any measure: shock, impact, or thermal initiation. If viewed in the context of the homologous series to which it belongs, TATB behaves very much as one would expect. The large decrease in sensitivity with each addition of an amino group to the nitroaromatic ring is the result of several factors working together in the same direction. The ortho-nitroamino functional arrangement favors the mechanism involving furazan and furoxan intermediates. This thermochemically neutral path requires the hot spot to "live" for a longer time before it gains energy from chemical decomposition and can grow. Also the sequential nature of the decomposition requires the build up of reactive species before chain and/or concurrent mechanisms leading to large heat release develop. The increased hydrogen bonding developed as you proceed through the homologous series from TNB to TATB also probably increases the thermal conductivity markedly. This in turn aids in quenching smaller hot spots. This increased hydrogen bonding is also responsible for the sharp increase in density, 1.68 g/cm<sup>3</sup> to 1.94 g/cm<sup>3</sup>, that takes place in the TNB to TATB series. The steady increase in performance combined with the remarkable decrease in sensitivity through the series gives an ideal trend in explosives behavior.

### Future Directions

The control of sensitivity in an energetic material lies largely in the kinetics of energy release. The release must be rapid enough for initiation, propagation, and detonation to take place, but slow enough to make the material safe to deal with under a wide range of conditions. To build into one molecular system all of the possibilities for delayed release of energy is a considerable challenge. TATB is remarkable in combining as many options as it does. Using separate components in binary or more complex systems gives better opportunities for favorable combinations. Blasting agents, combining ammonium nitrate, organic fuels, and glass micro balloons to keep hot spot temperatures competent to promote detonation offer a good example of the approach. The separation of the fuel and oxidizer into different phases makes the combination inherently slow and gives long reaction zones. A possible approach to inherently insensitive energetic materials is to use as diluents for high explosives<sup>49</sup> materials that are thermodynamically competent to be a high explosive but are not kinetically competent to detonate under any readily achievable condition. For instance, melamine (C<sub>3</sub>H<sub>6</sub>N<sub>6</sub>,  $\rho = 1.57$  g/cm<sup>3</sup>,  $\Delta H_f = -75.2$  kJ/mole) calculates to support a detonation velocity of 6 km/sec. The trihydrazine analog approaches 7 km/sec. The use of high density, high nitrogen, but not detonable, admixtures to kinetically competent high explosives should provide materials retaining high performance but having more favorable sensitivity characteristics.

### References

1. W.C. Lothrop and G.R. Handrick, *Chem. Rev.* **44**, 419 (1944).
2. J.F. Roth, *Z. ges. Schiess-u. Sprengstoffw.* **36**, 4, (1941).
3. M.J. Kamlet, *Proc. 3rd Symp. Det.* 671 (1960).
4. M.J. Kamlet, *Proc. 6th Symp. Det.* 312 (1976).
5. M.J. Kamlet and H.G. Adolph, *Prop. & Explos.* **4**, 30 (1979).
6. M.J. Kamlet and H.G. Adolph, *Proc. 7th Symp. Det.* 84 (1981).
7. A. Delpuech and J. Cherville, *Prop. & Explos.* **3**, 169 (1978).
8. A. Delpuech and J. Cherville, *Prop. & Explos.* **4**, 121 (1979).
9. A. Delpuech and J. Cherville, *Prop. & Explos.* **4**, 61 (1979).
10. A. Delpuech and J. Cherville, C. Michaud, *Proc. 7th Symp. Det.* 65 (1981).
11. S.R. Jain, K.C. Adiga, V.R. Pai Verneker, *Comb. & Flame*, **40**, 71 (1981).
12. R. Sundararajan, K.C. Adiga, S.R. Jain, *Comb. & Flame*, **41**, 243 (1981).
13. R. Sundararajan and S.R. Jain, *Comb. & Flame*, **45**, 47 (1982).
14. R. Sundararajan and S.R. Jain, *Ind. J. Tech.* **21**, 474 (1983).
15. C. Brassy, M. Roux, M. Asanneau, *Prop. Explos. & Pyrotech.* **12**, 53 (1987).
16. J. Mullay, *Prop. Explos. & Pyrotech.* **12**, 60 (1987).

17. J. Mullay, *Prop. Explos. & Pyrotech.* **12**, 121 (1987).
18. R. Engelke, D. Schiferl, C.B. Storm, W.L. Earl, *J. Phys. Chem.* **92**, 6815 (1988).
19. R. Engelke, W.L. Earl, C.B. Storm, *Prop. Explos. & Pyrotech.* **13**, 189 (1988).
20. C.B. Storm, R.R. Ryan, J.P. Ritchie, J.H. Hall, S.M. Bachrach, *J. Phys. Chem.* **93**, 1000 (1989).
21. C.B. Storm, J.R. Stine, J.F. Kramer, in Chemistry and Physics of Energetic Materials, edited by S.N. Bulusu (Kluwer Academic Publishers, Dordrecht, 1990) pp. 605-640.
22. J.N. Ayres, L.J. Montesi, R.J. Bauer, NOLTR 73-132 (1973), D. Price and T.P. Lippard, NOLTR, 66-87 (1966).
23. R.W. Armstrong, C.S. Coffey, V.F. DeVost, W.L. Elban, *J. App. Phys.* **68**, 979 (1990).
24. J.E. Field, N.K. Bourne, S.J.P. Palmer, S.M. Walley, *Philosophical Transactions of the Royal Society of London, series A*, **339**, 269 (1992), C.P. Constantinou, T. Mukukdan, M.M. Chaudhri, *ibid*, **339**, 403 (1992).
25. D.R. Kassoy, A.K. Kapila, D.S. Stewart, *Combust. Sci. and Tech.* **63**, 33, (1989).
26. C.L. Mader, Numerical Modeling of Detonations, (University of California Press, Berkely, 1979).
27. J.R. Asay, R.A. Graham, G.K. Straub, eds. Shock Waves in Condensed Matter-1983 (North-Holland, Amsterdam, 1984); S.C. Schmidt and N.C. Holmes, eds. Shockwaves in Condensed Matter-1987, (North Holland, Amsterdam, 1988).
28. C.L. Jackson and J.F. Wing, *J. Am. Chem. Soc.* **9**, 354 (1887); **10**, 287 (1888).
29. H.H. Cady and A.C. Larson, *Acta Cryst.* **23**, 601 (1967).
30. B.M. Dobratz, LLNL Explosive Handbook, (Lawrence Livermore Laboratory, Livermore, CA, 1981).
31. R.N. Rogers, *Thermochimica Acta*, **11**, 131 (1975).
32. A.W. Campbell, H.L. Flaugh, A. Popolato, J.B. Ramsay, *Proc. 7th Symp. Det.* 566 (1981), TATB as PBX 9502, 98% TMD; HMX as PBX 9501, 98% TMD.
33. J.R. Stine, Prediction of Crystal Densities of Organic Explosives by Group Additivity, (LA-8920, Los Alamos National Laboratory, 1981).
34. The numbers assigned to the compounds are taken from the Tables in ref. 21.
35. C.S. Coffey and S.J. Jacobs, *J. Appl. Phys.* **52**, 6991 (1981).
36. J. Sharma, J.C. Hoffsommer, D.J. Glover, C.S. Coffey, J.W. Forbes, T.P. Liddiard, W.L. Elban, F. Santiago, *Proc. 8th Symp. Det.* 725 (1985).
37. J. Sharma, B.C. Beard, J. Forbes, C.S. Coffee, *Proc. 9th Symp. Det.* 897 (1989).
38. J. Sharma, J.C. Hoffsommer, D.J. Glover, C.S. Coffey, F. Santiago, A. Stolovy, S. Yasuda, in Shock Waves in Condensed Matter-1983, edited by J.R. Asay, R.A. Graham, G.K. Straub, (North-Holland, Amsterdam, 1984) p. 543.
39. T.B. Brill and P.J. Brush, ref. 24, p. 377.
40. L.R. Rothstein and R. Peterson, *Prop. & Explos.* **4**, 56, (1979).
41. J. R. Stine, *J. Energetic Materials*, **8**, 41 (1990).
42. J.R. Stine, A Pure Explosive Data Base, Los Alamos National Laboratory.
43. M.J. Kamlet and S. Jacobs, *J. Chem. Phys.* **48**, 23 (1968).
44. V.I. Pepkin, M.N. Makhov, Yu.A. Lebedev, *Dok. Akademii Nauk USSR*, **232**, 852 (1977)[**232**, 155 (1977)].
45. E. Catalano and C.E. Rolon, *Thermochimica Acta*, **61**, 37 (1983).
46. R.N. Rogers, J.L. Janney, M.H. Ebinger, *Thermochimica Acta*, **59**, 287 (1982).
47. D.A. Frank-Kamenetski, Diffusion and Heat Transfer in Chemical Kinetics, (Plenum Press, New York, NY, 1969).
48. B.I. Swanson, private communication.
49. C. B. Storm, Chemical Contributions to Explosive and Propellant Sensitivity, in Workshop on Densensitization of Explosives and Propellants. TNO Prins Maurits Laboratory, The Netherlands, 1991.

## ENERGY TRANSFER DYNAMICS AND IMPACT SENSITIVITY

LAURENCE E. FRIED AND ANTHONY J. RUGGIERO

L-277, Chemistry and Materials Science Division

Lawrence Livermore National Laboratory

Livermore, CA 94550

### ABSTRACT

In this paper we focus on the relation between impact sensitivity and energy transfer rates. When a crystal receives an impact, low frequency lattice vibrations (called phonons) are excited. Typical phonon frequencies are  $0\text{--}200\text{ cm}^{-1}$ . This energy must then be converted to vibron frequencies ( $1000\text{--}2000\text{ cm}^{-1}$ ) before bond breaking can occur. We derive a simple formula for the energy transfer rate in terms of the density of vibrational states and the vibron-phonon coupling. We are able to estimate the phonon upconversion rate in widely varying energetic materials such as TATB, HMX, and Pb styphnate by examining existing inelastic neutron scattering data. We find that the estimated energy transfer rates in pure unreacted material are strongly correlated with impact sensitivity.

### INTRODUCTION

The creation of new high explosives that combine the properties of low impact sensitivity and high performance is the primary problem in energetic materials science today. Development of new materials is currently a slow and laborious process dependent largely on trial and error because the basic physical mechanisms underlying material properties are poorly understood. While many of the issues regarding the general performance of explosives and propellants can be satisfactorily dealt with via a macroscopic hydrodynamic picture, the difficult problem of impact sensitivity and molecular reactivity must be interpreted from a microscopic point of view.

In this paper we study the role that energy transfer dynamics has in impact sensitivity. Impact sensitivity is the propensity of an explosive to detonate when it receives a mechanical impact. This property is usually quantified by the drop hammer test, in which a weight is dropped from a specified height onto a small sample of explosive. The height at which the sample detonates one half of the time is a common measure of impact sensitivity.

The detonation of a crystal upon impact is a complicated process undoubtedly depending on a host of material properties. Upon impact, low frequency lattice vibrations called acoustic phonons are primarily excited. Before a detonation wave can begin, bonds must break. Therefore, the initial energy in the acoustic phonons must somehow be deposited into bond stretching modes. Acoustic phonons have frequencies less than  $100\text{ cm}^{-1}$ , whereas bond stretches have frequencies greater than  $1000\text{ cm}^{-1}$ . It is clear then, that acoustic phonon energy must be *upconverted* to higher vibrations before detonation can occur. High frequency vibrations in a molecular crystal are called *vibrons*. There has been much work on deriving theoretical expressions for phonon lifetimes in anharmonic solids[1, 2, 3]. Califano et. al. compared the theoretical expressions to the results of molecular dynamics calculations and experiments[4, 5, 6]. Holian[7] has conducted molecular dynamics simulations of vibrational energy transfer in diatomic fluids, with the aim of understanding shock induced chemistry. Dlott and Fayer[8] have studied multiphonon upconversion associated with shock induced chemistry. They derived a master equation for phonon and vibron temperatures. The master equation depends on the phonon-vibron energy transfer rate, which was estimated from experimental results on anthracene. Kim and Dlott[9, 10] have studied multiphonon up-pumping in naphthalene through molecular dynamics and the master equation approach.

In the present paper, we address the question of how the phonon-vibron energy transfer rate differs in a wide range of energetic materials. This requires a microscopic formulation of the phonon-vibron energy transfer rate. Since optical experiments probe  $k \approx 0$  states, in the past attention has been focused on the lifetimes of  $k \approx 0$  states. Impact sensitivity, however, should depend on all  $k$  values. This motivates studying the upconversion rate into an entire band. Here, we derive a simple expression for the upconversion rate into a band of a given energy.

The frequency dependence of the upconversion rate is found to be very important; in the range of 100-600  $\text{cm}^{-1}$ , the rate can vary by an order of magnitude. This means that a quantitative theory of phonon upconversion cannot be based on a single vibron-phonon rate, but rather should be based on a temperature and frequency dependent rate. We make use of the microscopic formula and existing inelastic neutron scattering data to compare the energy upconversion rate for a variety of energetic materials. We find that the predicted upconversion rate is strongly correlated with impact sensitivity. This implies that many aspects of impact sensitivity can be attributed to properties of the pure unreacted material.

## THEORY

We consider phonon upconversion rates in the limit of small anharmonicity (e.g. cubic terms in the Hamiltonian are assumed to dominate). In this case, the Hamiltonian is given by:

$$\begin{aligned} H &= H_0 + H_1 \\ H_0 &= \sum_l \hbar \omega_l (a_l^\dagger a_l + \frac{1}{2}) \\ H_1 &= \sum_{lmn} B_{lmn} A_l A_m A_n \Delta(k_l + k_m + k_n), \end{aligned} \quad (1)$$

where  $A_l \equiv a_l + a_l^\dagger$ , and  $a_l$  is defined to be the annihilation operator for phonon mode  $l$ .  $\omega_l$  is the harmonic frequency of phonon  $l$ .  $\Delta(k) = 1$  if  $k = 0$ , and is 0 otherwise.

Phonon lifetimes have been extensively studied using thermal Green functions[1], and other theoretical techniques[4]. Part of the decay rate of a phonon comes from scattering to higher frequencies; this term is called the phonon upconversion rate. In the present paper we consider a related but distinct quantity. In phonon lifetime studies the relevant rate is the collision of a pre-existing  $k = 0$  phonon of a fixed frequency with a thermal phonon of arbitrary frequency. Here, we consider the collision of two thermal phonons with a fixed energy sum but arbitrary  $k$ . This allows us to study the rate of energy transfer into a particular vibron band. Certain vibron modes are likely to lead directly to molecular dissociation, whereas others do not. The rate of energy transfer from thermal phonons into a mode that causes dissociation should be most relevant for impact initiation.

Phonon lifetimes in crystals are usually derived by calculating the imaginary part of the phonon self-energy using thermal Green functions. In the present case it suffices to use Fermi's Golden Rule, although identical results could be derived by the more sophisticated Green's function techniques. The state to state energy upconversion rate  $\gamma$  for the fusion of two phonons of frequency  $\omega_l$  and  $\omega_m$  into a phonon of frequency  $\omega_n$  is:

$$\gamma(n, l, m) = \frac{2\pi}{\hbar} \dots n_n + 1, n_m - 1, n_l - 1 | H_1 | n_n, n_m, n_l \dots \rangle^2, \quad (2)$$

where  $n_j$  is the occupation number of phonon  $j$ . Eq. (2) is easily evaluated to be

$$\gamma(n, l, m) = \frac{18\pi}{\hbar} (n_n + 1) n_l n_m |B_{lmn}|^2 \delta(\omega_n - \omega_l - \omega_m) \Delta(k_n - k_l - k_m), \quad (3)$$

Here,  $\mathbf{k}$ , is the wavevector of phonon  $j$ ,  $\omega$ , is the frequency of phonon  $j$ . For upconversion processes, it is reasonable to assume a thermal distribution of phonons  $l$  and  $m$ , with state  $n$  unpopulated[11], since low frequency phonons are primarily excited by impact, and low frequency phonons equilibrate faster (i.e. have shorter lifetimes) than high frequency phonons. This gives a thermal rate of

$$\gamma(n, l, m, T) = \frac{18\pi}{\hbar} \bar{n}_l \bar{n}_m |B_{lmn}|^2 \delta(\omega_n - \omega_l - \omega_m) \Delta(\mathbf{k}_n - \mathbf{k}_l - \mathbf{k}_m), \quad (4)$$

where  $T$  is the temperature and

$$\bar{n}_m = \bar{n}[\omega_m] \equiv [\exp(\hbar\omega_m/k_B T) - 1]^{-1}. \quad (5)$$

Next, we average over all initial states  $l$  and  $m$ . This gives

$$\begin{aligned} \gamma(c, \mathbf{k}_c, T) = & \frac{18V^2\pi}{\hbar} \sum_{a,b} \int \frac{d\mathbf{k}_a}{8\pi^3} \int \frac{d\mathbf{k}_b}{8\pi^3} \bar{n}[\omega_a(\mathbf{k}_a)] \bar{n}[\omega_b(\mathbf{k}_b)] \\ & |B(a, \mathbf{k}_a, b, \mathbf{k}_b, c, \mathbf{k}_c)|^2 \delta[\omega_c(\mathbf{k}_c) - \omega_a(\mathbf{k}_a) - \omega_b(\mathbf{k}_b)] \\ & \delta(\mathbf{k}_c - \mathbf{k}_a - \mathbf{k}_b). \end{aligned} \quad (6)$$

Here,  $a, b$  labels the bands of the initial states, while  $c$  is the band of the final state.  $V$  is the volume of the crystal. As discussed above, we are interested in the rate for upconversion into a given band averaged over all  $\mathbf{k}_c$ . Integrating over  $\mathbf{k}_c$ , we have:

$$\begin{aligned} \gamma(c, T) = & \frac{9V^2}{4\pi^2\hbar} \int \frac{d\mathbf{k}_a}{8\pi^3} \int \frac{d\mathbf{k}_b}{8\pi^3} \bar{n}[\omega_a(\mathbf{k}_a)] \bar{n}[\omega_b(\mathbf{k}_b)] \\ & |B(a, \mathbf{k}_a, b, \mathbf{k}_b, c, \mathbf{k}_a + \mathbf{k}_b)|^2 \delta[\omega_c(\mathbf{k}_a + \mathbf{k}_b) - \omega_a(\mathbf{k}_a) - \omega_b(\mathbf{k}_b)]. \end{aligned} \quad (7)$$

This equations can be substantially simplified through two approximations. Since vibrons typically have little dispersion[4] we can make Einstein approximation for the vibron band:  $\omega_c(\mathbf{k}_a + \mathbf{k}_b) = \omega$ . Also, the mode dependence of  $B$  is often weak[4]. Thus, we let  $B(a, \mathbf{k}_a, b, \mathbf{k}_b, c, \mathbf{k}_c) = B$ . Comparison with two phonon absorption lineshapes shows that this approximation is usually very good[4]. After integrating over  $\mathbf{k}_c$ , we arrive at a simple expression for the upconversion rate into a band of a given energy:

$$\gamma(\omega_c, T) = \frac{9|B|^2 V^2}{4\pi^2\hbar} \int d\omega \bar{n}(\omega) \bar{n}(\omega_c - \omega) \rho(\omega) \rho(\omega_c - \omega). \quad (8)$$

Here,  $\rho(\omega)$  is the density of states, defined by:

$$\rho(\omega) \equiv \sum_j \int \frac{d\mathbf{k}}{8\pi^3} \delta(\omega - \omega_j(\mathbf{k})) \quad (9)$$

Eq. (8) should be evaluated for discrete  $\omega_c$  corresponding to a band frequency. It is possible, however, to treat  $\omega_c$  as a continuous variable. This is motivated by the high density of vibron bands found in the large molecules considered here. The results derived in this fashion are physically meaningful as long as there exists a real vibron frequency in the neighborhood of  $\omega_c$ .

Optical probes only yield information on the density of states near  $\omega_c$ . The total density of states  $\rho(\omega)$  can be best estimated from incoherent inelastic neutron scattering. This procedure has been shown to give a good approximation to  $\rho(\omega)$ [12, 13]. The density of states derived from neutron scattering data is known only to within an arbitrary normalization factor. In order to compare energy transfer rates from different molecules, it is necessary to determine this normalization factor. The simplest alternative is to take the

integral of  $\rho(\omega)$  over all frequencies to be equal to  $3N/V$ , where  $N$  is the number of atoms in the crystal and  $V$  is the volume. Existing experimental data, however, is not available at high enough frequencies to make such a normalization feasible. Instead, we employ a simple normalization rule proposed by Dlott[14]: we normalize  $\rho(\omega)$  so that

$$\int_0^{\Omega_p} \rho(\omega) d\omega = Z(6 + Y)/V_c. \quad (10)$$

Here,  $\Omega_p$  is the maximum frequency of the phonon bands,  $Z$  is the number of molecules per unit cell, and  $Y$  is the number of molecular vibrations that have become amalgamated into the phonon band.  $V_c$  is the volume of a unit cell. (The  $V_c$  factor was added to the original normalization rule of Dlott to maintain consistency with Eq. (9).)

We have taken  $\Omega_p = 200 \text{ cm}^{-1}$ , while  $Y$  was estimated as the number of vibrational modes of the isolated molecule with frequencies less than  $\Omega_p$ . The vibrational modes were calculated with the semiempirical electronic structure program MOPAC using the PM3 Hamiltonian[15]; results are given in Table 1 along with impact sensitivity measurements[17, 19, 18].

Molecule	$Y$	$h_{50} \text{ (m)}$
$\beta$ -HMX	12	0.33 (Ref. [17])
$\gamma$ -HMX	15	0.14 (Ref. [18])
Pb styphnate	12	0.15 (Ref. [19])
Picric acid	8	0.73 (Ref. [17])
RDX	7	0.28 (Ref. [17])
Styphnic acid	8	0.73 (Ref. [19])
TATB	7	3.20 (Ref. [17])

Table 1: Number of amalgamated vibrations as calculated with MOPAC/PM3, and drop hammer test results for a 12 tool.

## RESULTS

We have used existing inelastic incoherent neutron scattering data[16, 20] to determine the density of states  $\rho(\omega)$  as described above. Using  $\rho(\omega)$ , we have evaluated the energy transfer rate in Eq. (8) by assuming that the anharmonic coupling *per molecular volume* is the same for all the compounds considered here; this is equivalent to taking  $B = V_c B_0/Z$ . We cannot evaluate  $B_0$  on the basis of existing data, although it is known that vibron lifetimes are typically a few picoseconds. In Figure 1 we show  $\gamma(\omega)$  for a variety of energetic materials at 300K. The low frequency behavior does not show a striking correlation with impact sensitivity. For instance, the energy transfer rates of TATB and  $\beta$ -HMX are very similar between 0 and  $200 \text{ cm}^{-1}$ . The energy transfer rate between 300 and  $600 \text{ cm}^{-1}$ , however, correlates well with impact sensitivity. In Figure 2, we show the energy transfer rate of the compounds considered here at  $400 \text{ cm}^{-1}$  correlated with the inverse drop hammer height. A linear fit to the data is displayed to guide the eye. It is apparent that there is a strong relation between energy transfer rates at  $400 \text{ cm}^{-1}$  and impact sensitivity. It is interesting to note that there are nitro group wagging vibrations in the neighborhood of  $400 \text{ cm}^{-1}$ , and that breaking of the nitro group from the ring is thought to be one of the first steps in detonation chemistry. The role of the nitro group in impact sensitivity, and the measurement of energy transfer rates, will be addressed by femtosecond optical experiments underway in this group.

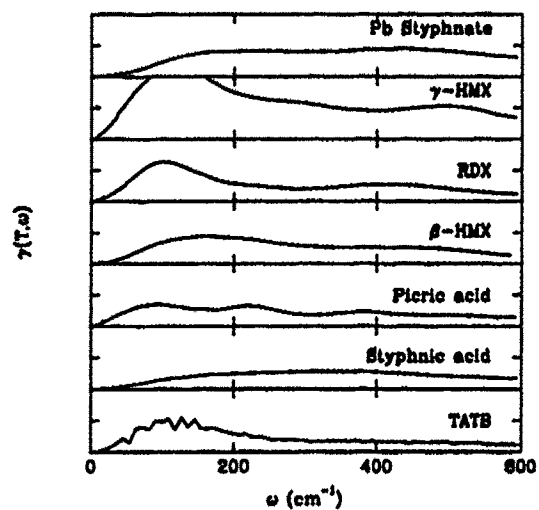


Figure 1: The energy transfer rate as a function of frequency at 300K.

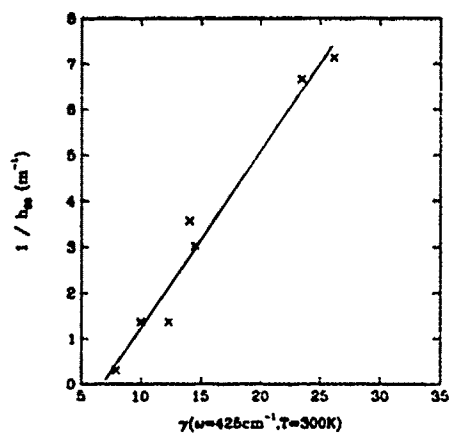


Figure 2: The correlation between impact sensitivity and energy transfer rate.

Research described in this article was performed under the auspices of the US Department of Energy by Lawrence Livermore National Laboratories under contract No. W-7405-ENG-48.

## References

- [1] A. A. Maradudin and A. E. Fein, *Phys. Rev.*, **128**, 2589(1962).
- [2] R.G. Della Valle, P. F. Fracassi, R. Righini, S. Califano, and S. H. Walmsley, *Chem. Phys.*, **44**, 189(1979).
- [3] J. Kalus, *J. Chim. Phys.*, **82**, 1985.
- [4] S. Califano, *Lattice Dynamics of Molecular Crystals*, Lecture Notes in Chemistry, Vol. 26, Springer-Verlag, Berlin, 1981.
- [5] S. Califano, *Laser Optics of Condensed Matter, Vol. 2*, E. Garmite et. al. Eds., Plenum Press, New York, 1991
- [6] P. Procacci, G. Cardini, R. Righini, and S. Califano, *Phys. Rev. B.*, **45**, 2113(1992).
- [7] B. L. Holian, *J. Chem. Phys.*, **84**, 3138(1986).
- [8] D. D. Dlott and M. D. Fayer, *J. Chem. Phys.*, **92**, 3798(1990).
- [9] H. Kim and D. D. Dlott, *J. Chem. Phys.*, **93**, 1695(1990).
- [10] H. Kim and D. D. Dlott, *J. Chem. Phys.*, **94**, 8203(1991).
- [11] F. J. Zerilli and E. D. Toton, *Phys. Rev. B*, **29**, 5891(1984).
- [12] E. L. Bokhenkov, I. Natkaniec, and E. F. Sheka, *Sov. Phys. JETP*, **43**, 536(1976).
- [13] A. V. Belushkin, E. L. Bokhenkov, A. I. Kolesnikov, I. Natkaniec, R. Righini, and E. F. Sheka, *Sov. Phys. Sol. State*, **23**, 1529(1981).
- [14] D. Dlott, *Annu. Rev. Phys. Chem.*, **37**, 157(1986).
- [15] J. J. P. Stewart, *J. Comp. Chem.*, **10**, 209 (1989); *ibid.*, p 221.
- [16] H. P. Boutin, H. J. Prask, and S. Trevino, *Picatinny Arsenal Rep.*, 1965.
- [17] B. M. Dobratz and P. C. Crawford, *LLNL Explosives Handbook*, UCRL-52997, 1985.
- [18] H. H. Cady and L. C. Smith, "Studies on the polymorphs of HMX", Los Alamos Scientific Laboratory Reports, LAMS-2652 (1962).
- [19] R. Meyer, *Explosives*, 1987, VCH, Weinheim.
- [20] V. D. Gupta and B. L. Deopura, *Mol. Phys.*, **19**, 589(1970).



## RELATIONSHIP BETWEEN RADIATION STABILITY AND MOLECULAR STRUCTURE OF NITRAMINE EXPLOSIVES

JAMES J. PINTO

U. S. Army Armament Research, Development and Engineering Center, Picatinny Arsenal, NJ 07806-5000.

### ABSTRACT

The radiation stabilities of the nitramine explosives 1,4-dinitroglycoluril (DINGU), 1,4-dimethyl-2,5-dinitroglycoluril (DMD) and hexanitrohexaazaisowurtzitane (HNIW) have been determined using XPS. Samples were exposed to x-rays for times up to eight hours while photoelectron spectra were recorded in the carbon, oxygen, and nitrogen 1s energy regions and mass spectra were recorded of gases evolved during the decomposition process. These data are compared to the previously determined stabilities for cyclotrimethylene trinitramine (RDX) and cyclotetramethylene tetranitramine (HMX). The N1s spectra of the irradiated materials show the NO<sub>2</sub> peak decreases relative to the total nitrogen signal while low binding energy peaks grow. The rate of loss of the NO<sub>2</sub> peak was fit to first order kinetics and the rate constants obtained show some correlation with the N-N bond strength as measured by the average N-N bond distance and the average NO<sub>2</sub> asymmetric stretch frequency. Despite the differences in structure of these molecules (DINGU and DMD are bicyclic rings, RDX and HMX are rings and HNIW is a cage) the radiation stability appears to be controlled by the strength of the N-N bond.

### INTRODUCTION

The relationship between molecular structure and sensitivity has been studied extensively. The stability in response to various stimuli such as thermal, shock and impact have been related to observed molecular structural parameters such as bond lengths and infrared absorption frequencies<sup>1</sup> and to calculated parameters such as mid-point potentials<sup>2</sup> and electron densities.<sup>3</sup> These studies have been carried out for nitroarene and nitramine explosives.

In recent studies x-rays and ultraviolet radiation were used to decompose explosive molecules while changes in the nitrogen chemical states of the solid residues were monitored with x-ray photoelectron spectroscopy (XPS). This technique was applied to materials such as pentaerythritoltetranitrate (PETN),<sup>4</sup> 3-nitro-1,2,4-triazole-5-one (NTO), cyclotrimethylene trinitramine (RDX) and cyclotetramethylene tetranitramine (HMX) and triaminotrinitrobenzene (TATB).<sup>5,6</sup> In this paper the radiation decomposition of a series of nitramine explosives and its relationship to molecular structure is presented. The materials studied were 1,4-dinitroglycoluril (DINGU), 1,4-dimethyl-2,5-dinitroglycoluril (DMD) and hexanitrohexaazaisowurtzitane (HNIW). For reference, the stabilities for RDX and HMX were also determined.

### EXPERIMENTAL

The DINGU used in this study was synthesized by Dr. S. Lee of LeRon Associates. The 1,4 isomer was confirmed by proton NMR and x-ray diffraction. The DMD was prepared by Dr. S. Bulusu of this laboratory. The HNIW was provided by Dr. D. Stec of GEO-Centers, Inc. X-ray diffraction showed that it was the  $\alpha$  polymorph. The HMX and RDX used for comparison were purified from commercial material.

Powdered samples were mounted on nitrogen-free double sided tape and inserted into the vacuum chamber of the spectrometer. A Kratos ES300 X-ray Photoelectron Spectrometer was used to decompose the samples and to analyze the solid residues from the decomposition process. The vacuum pressure was maintained at approximately  $10^{-7}$  mbar during the analysis and decomposition experiments. Aluminum K $\alpha$  radiation at 9 mA and 12 KV (108 Watts) was used to irradiate and analyze the materials. Samples were irradiated for times up to 9 hours and photoelectron spectra were recorded in the carbon, oxygen and nitrogen 1s energy regions approximately every hour. Each set of spectra was recorded in the time average mode over a period of approximately 15 minutes. Sample charging was accounted for by referencing to the

C1s hydrocarbon line at 285.0 eV. Smoothing and linear background subtraction were applied to the raw data and the resulting spectra were fit to Gaussians to resolve overlapping components. Integrated intensities were computed for each peak by multiplying the full width at half maximum by the peak height.

A Balzers QMG 064 residual gas analyzer (RGA) mounted to the analysis chamber of the electron spectrometer was used to record mass spectra of gases in the 0-64 amu range which evolved during the decomposition process. In these experiments, powdered samples were pressed into the roughened surface of a piece of gold foil, since the cellulose based tape evolves its own gases during x-ray exposure.

## RESULTS

The N1s photoelectron spectra of RDX, HMX and HNIW are shown in Figures 1, 2 and 3. The spectra are characterized by two peaks: the peak at 406.3 eV is from the NO<sub>2</sub> nitrogens and the peak at 401.0 eV is from the ring/cage nitrogens. The ratios of these peaks in the undecomposed samples is 1:1, reflecting the equal numbers of NO<sub>2</sub> and ring/cage nitrogens in each compound. During exposure to x-rays the N1s spectra change indicating that changes in the molecular structures are occurring. The spectra at long exposure times are also shown in Figures 1, 2 and 3. The NO<sub>2</sub> peak decreases while new peaks arise on the low and high binding energy sides of the ring/cage N peak. The rate of decay of the NO<sub>2</sub> line is calculated by plotting the following ratio versus time:

$$\left( \frac{\text{NO}_2}{\text{Total N}} \right)_t / \left( \frac{\text{NO}_2}{\text{Total N}} \right)_{t=0} \quad (1)$$

The decay of the NO<sub>2</sub> peak for the three compounds was found to follow first order kinetics with rate constants of 0.071 hr<sup>-1</sup>, 0.052 hr<sup>-1</sup> and 0.087 hr<sup>-1</sup> for RDX, HMX and HNIW, respectively. The NO<sub>2</sub> decay curves for these compounds are shown in Figure 4.

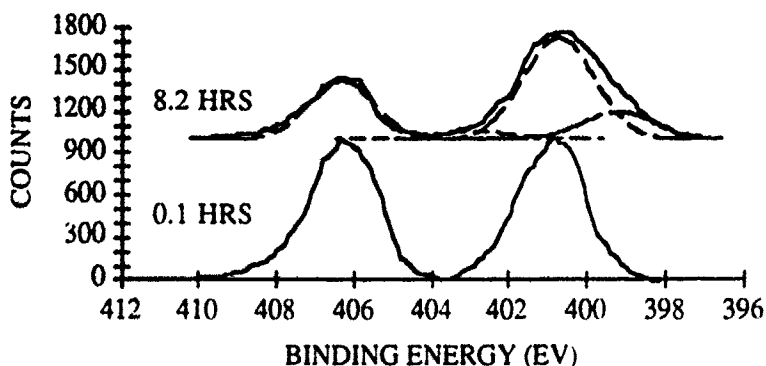


Figure 1. N1s photoelectron spectrum of RDX. Bottom curve is control material. Top curve is after 8.2 hours of x-ray exposure. Results of curve fits to Gaussian line shapes are shown.

The N1s photoelectron spectra of DMD and DINGU are shown in Figures 5 and 6. These spectra have similar features and are characterized by two peaks: the peak at 406.4 eV is from the two NO<sub>2</sub> nitrogens; the peak at 400.0 eV is from the four nitrogens in the bicyclic ring. The area ratios of the ring N to the NO<sub>2</sub> N peaks in these compounds is 2:1, reflecting the relative numbers of ring nitrogens to NO<sub>2</sub> nitrogens. The broader width of the ring nitrogen peak indicates that it is a combination of more than one line. Curve fitting shows that the ring nitrogen peak is composed of two lines 1.6 eV apart. The line at 400.8 eV is from the ring nitrogen bound to the NO<sub>2</sub> while the line at 399.2 eV is from the ring nitrogen bound to hydrogen. These assignments are based on the observation that the N1s binding energy of glycoluril is 399.0 eV. On exposure to x-rays these spectra are found to change indicating that decomposition is occurring. The NO<sub>2</sub> line is found to decrease while the low binding energy component of the ring nitrogen line increases. The spectra of these compounds at long decomposition times are also shown in Figures 5 and 6.

The decay curves for these two compounds are shown in Figure 7. They also followed first order kinetics with rate constants of  $0.12 \text{ hr}^{-1}$  and  $0.083 \text{ hr}^{-1}$  for DMD and DINGU, respectively. Mass spectra of the gaseous products from the decomposition of these materials showed that DMD liberated primarily mass 30, corresponding to NO, while DINGU liberated masses 30 and 44, corresponding to NO and  $\text{N}_2\text{O}$ .

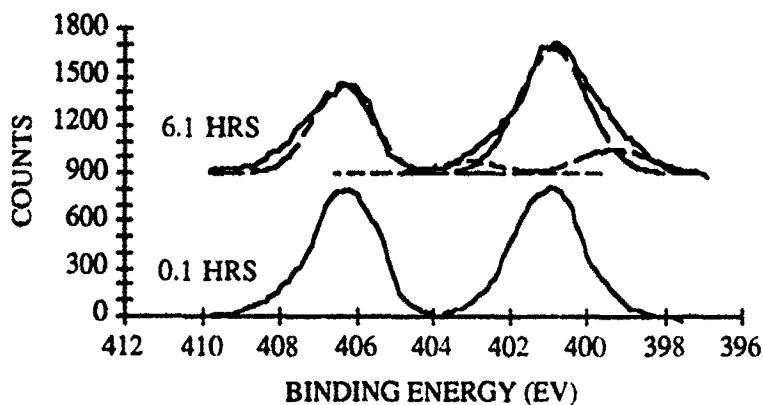


Figure 2. N1s photoelectron spectrum of HMX. Bottom curve is control material. Top curve is after 6.1 hours of x-ray exposure. Results of curve fits to Gaussian line shapes are shown.

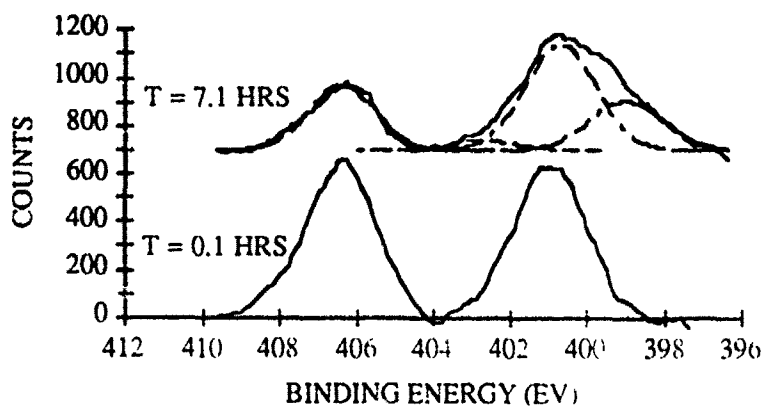


Figure 3. N1s photoelectron spectrum of HNIW. Bottom curve is control material. Top curve is after 7.1 hours of x-ray exposure. Results of curve fits to Gaussian line shapes are shown.

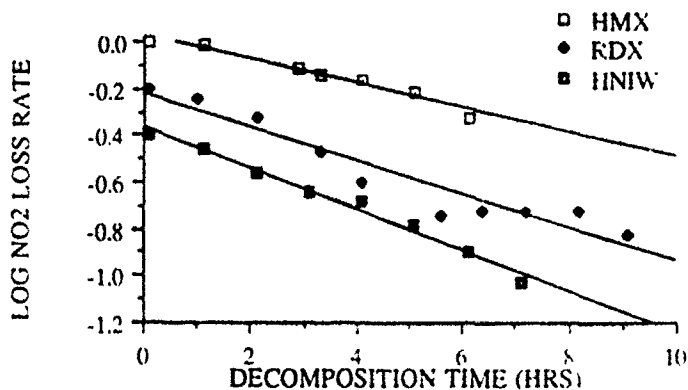


Figure 4. Log of the  $\text{NO}_2$  loss rate versus decomposition time for RDX, HMX and HNIW. Curves for RDX and HNIW have been offset for clarity.

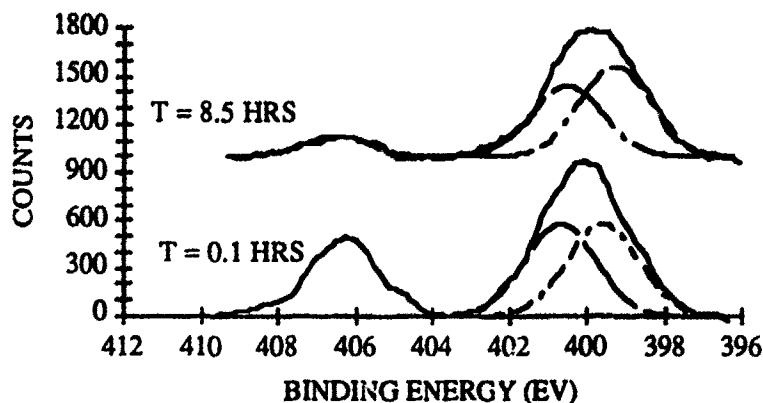


Figure 5. N1s photoelectron spectrum of DMD. Bottom curve is control material. Top curve is after 8.5 hours of x-ray exposure. Results of curve fits to Gaussian line shapes are shown.

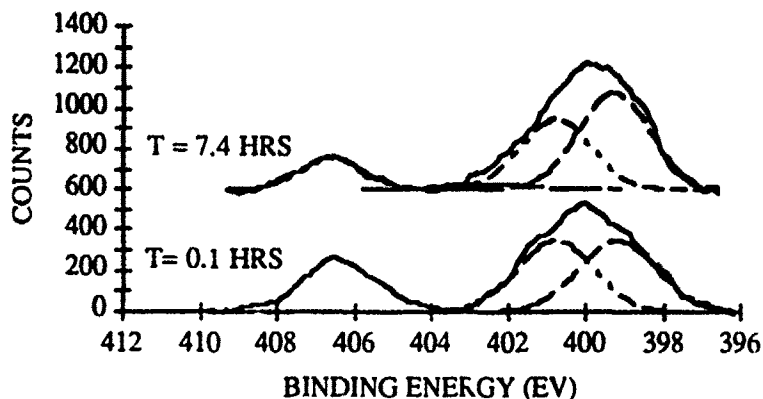


Figure 6. N1s photoelectron spectrum of DINGU. Bottom curve is control material. Top curve is after 7.4 hours of x-ray exposure. Results of curve fits to Gaussian line shapes are shown.

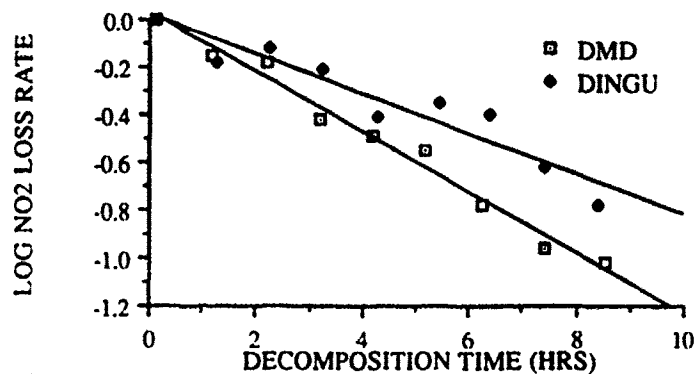


Figure 7. Log of the  $\text{NO}_2$  loss rate versus decomposition time for DMD and DINGU.

## DISCUSSION

The relative rates of radiation induced decomposition of RDX and HMX have been measured previously by Beard and Sharma<sup>5</sup> but under different instrumental conditions from those used in the present study. In their work, the x-ray operating conditions were 15 mA and 15 kV, or 225 Watts. The decomposition rates obtained for RDX and HMX were  $0.324 \text{ hr}^{-1}$  and  $0.228 \text{ hr}^{-1}$ , respectively. These differed from the values obtained in the present work by

factors of 4.56 and 4.38, respectively. The chief difference between the values obtained in each study can be attributed to the x-ray powers used, although other factors, such as age and condition of the x-ray target and window and vacuum pressure could also effect x-ray intensities at the sample and therefore measured decomposition rates.

In another study Beard<sup>6</sup> attempted to determine decomposition products from the XPS spectra of the solid residue which remained from the radiation induced decomposition of RDX. In samples decomposed at room temperature he found that as the NO<sub>2</sub> line decreased, new peaks arose on the high and low binding energy sides of the ring N peak, which he attributed to the formation of nitroso and triazine-like products. NO<sub>2</sub> loss and formation of triazine and nitroso-like products were also observed in this study during the decomposition of RDX and HMX.

HNIW is a caged analogue of RDX and HMX because of the presence of the N-NO<sub>2</sub> group. The radiation induced decomposition is found to be very similar. X-ray photoelectron spectra show that the NO<sub>2</sub> line decreases while new peaks grow on the high and low binding energy sides of the cage N peak. As in the other two nitramines, the high binding energy peak can be attributed to nitroso formation. The low binding energy peak can be attributed to the caged analogue of triazine or hexaazaisowurtzitane. As the strongly electron withdrawing NO<sub>2</sub> groups are removed from the cage structure the binding energy of the aza N decreases.

During the radiation induced decomposition of DMD and DINGU the NO<sub>2</sub> peak decreases and the low binding energy component of the ring peak increases. This is analogous to the previously discussed materials in which a triazine-like peak grows as the NO<sub>2</sub> peak decreases. In the case of the two bicyclic compounds the chemical state of the ring N bound to a proton or a methyl group differs slightly from the ring N bound to NO<sub>2</sub>. The chief effect of x-ray exposure, therefore appears to be N-N bond fission with removal of the NO<sub>2</sub> groups.

DSC and TGA experiments have shown that DMD is more thermally stable than DINGU.<sup>7</sup> This can be attributed to the stabilizing effects of the electron donating methyl group on the ring which replaces the two protons bound to the other two ring nitrogens in DINGU. However, in the present study DMD has been found to be more sensitive to radiation damage than DINGU. Mass spectral data recorded during the decomposition process shows that DINGU decomposes by N-N bond fission and by ring breakage. These competing processes have also been observed during thermal decomposition.<sup>8</sup> However, the absence of a significant N<sub>2</sub>O signal in the mass spectral data recorded during the x-ray decomposition of DMD indicates that it decomposes primarily by N-N bond fission. Breakage of this bond and loss of NO<sub>2</sub> is what is detected in these experiments.

It has been suggested that the ease with which a molecule releases NO<sub>2</sub> during thermal decomposition is related to the strength of the N-N bond.<sup>1</sup> Measures of the N-N bond strength include the bond length and the asymmetric NO<sub>2</sub> stretch frequency,  $\nu(\text{NO}_2)_{\text{as}}$ . Crystallographic data and bond lengths were available for RDX, HMX, HNIW and DINGU.<sup>9,10,11</sup>  $\nu(\text{NO}_2)_{\text{as}}$  for all five compounds was obtained from IR data. Plots of the x-ray decomposition rate versus the average N-N bond distance and  $\nu(\text{NO}_2)_{\text{as}}$  are shown in Figures 8 and 9, respectively. These plots suggest a relationship between the N-N bond strength and the radiation stability as measured by the loss of the NO<sub>2</sub> group. Studies on additional compounds are necessary in order to confirm these relations.

## SUMMARY

The stability of a series of nitramine explosives to x-ray radiation has been determined and decomposition mechanisms have been outlined. For all five compounds studied, the important step in the decomposition appears to be N-N bond scission. However, in RDX, HMX and HNIW nitroso formation has also been observed, while in DINGU ring break-up has been found to be competitive with N-N bond scission. DMD appears to be the least stable to x-ray decomposition with HNIW, DINGU, RDX and HMX increasingly more stable. While results for a small number of materials have been presented there appears to be a correlation between stability and the strength of the N-N bond as measured by the N-N bond length and  $\nu(\text{NO}_2)_{\text{as}}$ .

## ACKNOWLEDGEMENTS

I would like to thank J. Autera for his assistance in taking some of the XPS data and E. Hochberg for taking the IR spectra.

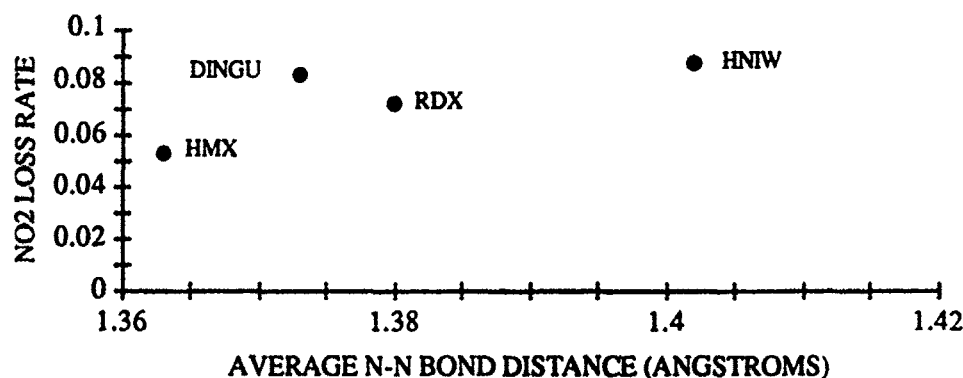


Figure 8. Log of the x-ray induced NO<sub>2</sub> loss rate versus average N-N bond distance.

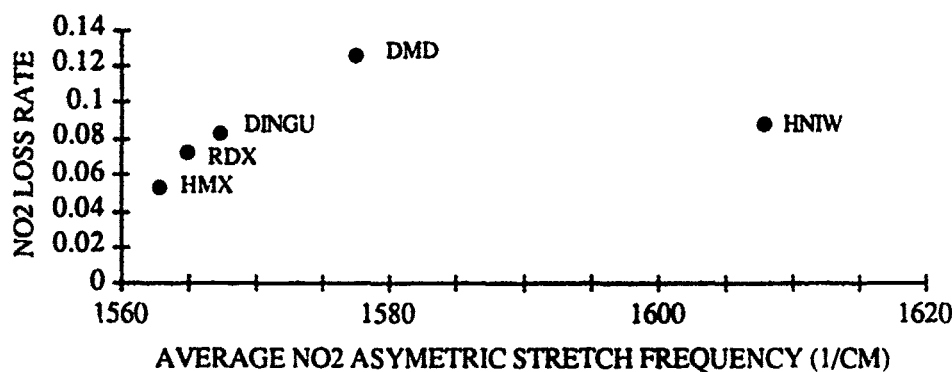


Figure 9. Log of the x-ray induced NO<sub>2</sub> loss rate versus average  $\nu(\text{NO}_2)_{\text{as}}$ .

## REFERENCES

1. T. B. Brill and Y. Oyumi, *J. Phys. Chem.*, 90 (1986) 2679.
2. F. Owens, *J. Mol. Struct. (THEOCHEM)* 121 (1985) 213.
3. J. S. Murray and P. Politzer, in *Chemistry and Physics of Energetic Materials*, edited by S. N. Bulusu (Kluwer Academic Publishers, Dordrecht, the Netherlands, 1990) 157-173, and references therein.
4. P. S. Wang and T. N. Wittberg, *J. Energet. Mat.*, 2 (1984) 167.
5. B. C. Beard and J. Sharma, *J. Energet. Mat.*, 7 (1989) 181.
6. B. C. Beard, *Propellants, Explosives and Pyrotechnics*, 16 (1991) 81.
7. J. Harris (private communication).
8. Y. Oyumi and T. B. Brill, *Propellants, Explosives and Pyrotechnics*, 13 (1988) 69.
9. C. S. Choi and E. Prince, *Acta Cryst.*, B28 (1972) 2857.
10. C. S. Choi and H. P. Boutin, *Acta Cryst.*, B26 (1970) 1235.
11. J. Boileau, E. Wimmer, R. Gilardi, M. M. Stineciphier, R. Gallo and M. Pirrot, *Acta Cryst.*, C44, (1988) 696.

## THIN FILM INFRARED LASER PYROLYSIS STUDIES OF THERMAL DECOMPOSITION MECHANISMS IN NITRAMINE PROPELLANTS

TOD R. BOTCHER AND CHARLES A. WIGHT

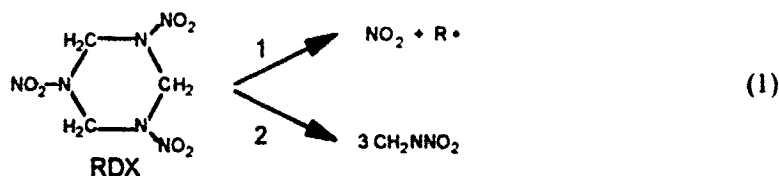
Department of Chemistry, University of Utah, Salt Lake City, UT 84112

### ABSTRACT

Thin films of RDX (1,3,5-trinitro-1,3,5-triazine) have been prepared by vapor deposition onto a 77 K substrate window and pyrolyzed with a pulsed CO<sub>2</sub> laser. Each sample is rapidly quenched after the laser pulse by heat conduction into the cold substrate, and the initial reaction products are trapped on the window for examination by transmission FTIR spectroscopy. We have detected N<sub>2</sub>O<sub>4</sub>, the dimer of nitrogen dioxide, as an initial condensed phase pyrolysis product, confirming that scission of one of the N-N bonds is the first step in the reaction mechanism. No evidence was found for formation of methylene nitramine via a proposed concerted depolymerization pathway.

### INTRODUCTION

Several recent studies have attempted to identify the *initial* step in the thermal decomposition mechanism of cyclic nitramine propellants, particularly RDX. Two proposed pathways are illustrated by the reaction



One of the obvious choices for this is scission of one of the N-N bonds. Thermodynamic studies identify this as the weakest bond in the molecule [1]. Results from thermogravimetric mass spectrometry experiments on HMX are consistent with this homolysis mechanism,[2] though there is some indication that bimolecular reaction pathways may also be important in the rate-limiting step.[3] Indirect evidence supporting the importance of the N-N bond scission mechanism can be found from thermal decomposition studies of other closely related nitramines.[4,5] Also, ultraviolet photolysis experiments on crystalline RDX have shown that N-N homolysis is a primary reaction pathway,[6] though thermal pyrolysis might not follow the same mechanism.

Zhao, *et al* have shown that when gas phase RDX molecules are heated by pulsed CO<sub>2</sub> laser irradiation, the primary decomposition pathway is concerted depolymerization that initially forms three molecules of methylenenitramine.[7] Under these conditions, the N-N bond scission channel accounts for only about one-third of the product yield. Sewell and Thompson have recently published a classical dynamics study of RDX decomposition that supports the existence of the concerted depolymerization channel.[8] Also, some of the early thermal pyrolysis work on isotopically substituted RDX supports a mechanism in which the N-N bond is preserved in the decomposition reaction.[9,10]

We have recently developed an experimental technique designed to establish the initial step in thermal decomposition of energetic materials such as RDX under conditions where the condensed phase material is rapidly heated with a pulsed CO<sub>2</sub> laser, and the initial reaction products are trapped on a cold substrate for detection by FTIR spectroscopy. The principal advantage of this new technique is that the initial products can be detected under conditions that

closely resemble those of a realistic propellant combustion environment (i.e., rapid heating in the condensed phase). By using an infrared laser to energize the sample (instead of a UV laser) we are able to detect chemistry that occurs on the ground electronic state potential surface, thereby avoiding complications due to excited state photochemical reactions. In this report, we outline some of our early findings regarding the thermal decomposition mechanism of RDX. A brief report of this work has been published elsewhere.[11]

## EXPERIMENTAL SECTION

Thin film ( $\sim 10$   $\mu\text{m}$ ) samples of RDX are prepared by vapor deposition from a Knudsen oven at  $120^\circ\text{C}$ . onto a CsI window. The window is mounted in a copper retainer at the cold tip of a liquid nitrogen reservoir, which maintains a constant temperature of 77 K. The vacuum in the sample chamber is maintained at  $10^{-5}$  torr or better. A schematic drawing of this apparatus is shown in Figure 1. The experiments performed using this apparatus can be classified into two principal categories, which we call single- and double-window configurations described below.

### Single Window Pyrolysis Experiments

In this type of experiment, a film of RDX is deposited onto the 77 K window and subsequently pyrolyzed with a pulsed  $\text{CO}_2$  laser tuned to the P(20) transition at  $944\text{ cm}^{-1}$ , which coincides with an absorption band of solid RDX. Initial products were detected by irradiating the sample with single laser pulses at gradually increasing fluence in the range  $1\text{--}5\text{ J cm}^{-2}$ . Transmission FTIR spectra are obtained after each laser pulse until product formation is detected.

In some experiments, samples are warmed to room temperature after deposition in order to form a polycrystalline film prior to laser pyrolysis. These results are compared with experiments in which the amorphous film (as initially prepared without annealing) is pyrolyzed under the same conditions (*vide infra*).

### Double Window Pyrolysis Experiments

Several experiments were conducted in which the initially prepared film was warmed to room temperature. The sample and substrate window were then removed from the vacuum chamber, covered with a second window, remounted in the chamber, and re-cooled to 77 K prior to infrared laser pyrolysis. In this arrangement, the thin film of RDX is sandwiched between two massive CsI windows so that any material that is vaporized from the original film is immediately trapped by condensation onto the other window. In this way, all of the material is conserved for spectroscopic detection.

The results from this type of experiment can be compared with analogous single-window experiments in order to assess the extent of product formation that takes place in the gas phase and in the condensed phase. It is reasonable to assume that in single-window experiments, most gas phase products escape the film and are recondensed elsewhere in the apparatus

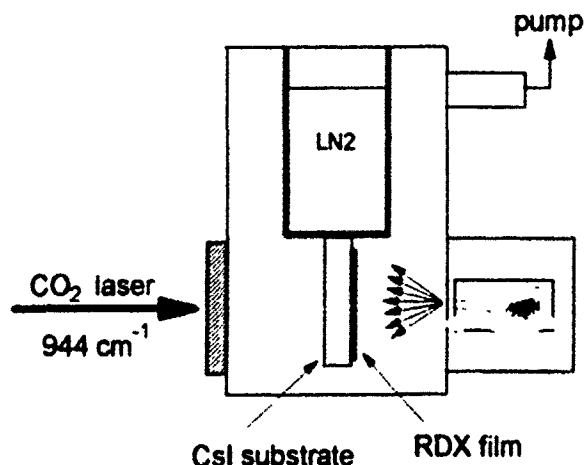


Figure 1 Schematic drawing of the experimental apparatus



Therefore, the amount by which products observed in double-window experiments exceed those formed in single window experiments provides a qualitative indication of the gas phase contribution to the thermal pyrolysis mechanism.

### Laser Pyrolysis and Product Detection

Infrared laser pyrolysis was carried out using a pulsed  $\text{CO}_2$  laser (Pulsed Systems Model LP140-G) that is tuned to an absorption band of the solid RDX at  $944\text{ cm}^{-1}$ . The nominal pulse width of this laser is  $35\text{ }\mu\text{s}$ . The beam is roughly square in shape, and the fluence of the unfocused beam is approximately  $0.5\text{ J cm}^{-2}$ . In order to pyrolyze samples at higher fluence, the beam size was reduced using a spherical concave mirror (radius of curvature =  $1\text{ m}$ ), and the beam is rastered over the thin film in a manner such that each point on the film is irradiated by only a single laser pulse at a fluence between  $1.0$  and  $4.7\text{ J cm}^{-2}$ .

During the  $35\text{ }\mu\text{s}$  laser pulse, the sample is heated from  $77\text{ K}$  to an estimated  $500\text{--}1000\text{ K}$ , depending on the laser fluence. This heat is then dissipated by thermal conduction into the massive substrate on a time scale estimated to be  $4\text{--}6\text{ ms}$ , based on the film thickness and the reported thermal conductivity of RDX.[12]

### RESULTS AND DISCUSSION

The infrared spectrum of an RDX film obtained immediately after deposition is shown in Figure 2. Many of the absorption bands exhibit inhomogeneously broadened lines due to spatial and orientational disorder that are characteristic of the amorphous state. This is a direct result of the vapor deposition process at low temperatures, which inhibits formation of the thermodynamically favored crystalline form of RDX. The same sample was then heated to room temperature and recooled to  $77\text{ K}$ . Its spectrum is shown in the lower trace of Figure 2. A significant degree of band narrowing and splitting is observed in this spectrum, showing that a transformation from the amorphous to a polycrystalline state has occurred.

Laser irradiation of amorphous samples at low fluence (less than  $1.4\text{ J cm}^{-2}$ ) did not produce any detectable product molecules. However, some narrowing and splitting of the absorption bands of RDX was noted as the heat from the laser induced a partial transition from the amorphous to the polycrystalline form. These changes in the parent band absorptions made it difficult to detect the formation of products in spectrally congested regions of the infrared spectrum. For this reason, an initial search for products was conducted on crystalline samples which had been annealed prior to laser pyrolysis.

This initial search involved subjecting a single sample to successive laser pulses at increasing fluence until product bands were first detected at  $1.4\text{ J cm}^{-2}$ . This first product absorption occurs at  $1736\text{ cm}^{-1}$  and is assigned to  $\text{N}_2\text{O}_4$ , the dimer of  $\text{NO}_2$ . The position of this band is in good agreement with previous assignments of the  $\text{N}_2\text{O}_4$  infrared spectrum by Smith and Guillory [13] and by Hisatsune.[14] In order to confirm the assignment,

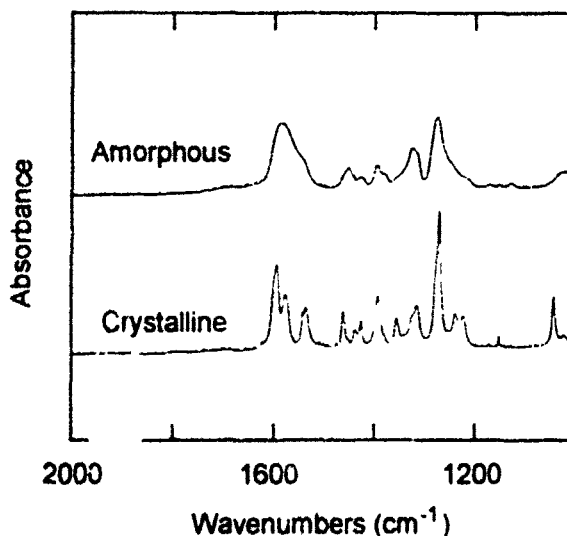


Figure 2. Infrared spectra of a thin film of vapor-deposited RDX in amorphous form (top) and in polycrystalline form after annealing to room temperature (bottom)

we prepared two thin film samples of  $\text{N}_2\text{O}_4$  in our apparatus. One was prepared by depositing an equilibrium mixture of  $\text{NO}_2/\text{N}_2\text{O}_4$  onto the substrate window. The other was prepared by co-depositing the  $\text{NO}_2/\text{N}_2\text{O}_4$  mixture with RDX from the Knudsen oven. Infrared spectra of these samples are shown in Figure 3 along with spectra of the reaction product formed from pyrolysis of an RDX sample at  $4.7 \text{ J cm}^{-2}$ .

The broad feature at  $1864 \text{ cm}^{-1}$  in Figure 3 is due to NO. This secondary product appears in RDX samples pyrolyzed at fluences higher than  $1.5 \text{ J cm}^{-2}$ . A small amount of NO is formed in one of the control experiments (trace D of Figure 3) due to thermal pyrolysis of  $\text{NO}_2$  in the Knudsen oven during vapor deposition of the RDX/ $\text{NO}_2$  mixture.

Other secondary product infrared absorption bands observed following pyrolysis at laser fluences from  $3.0$  to  $4.7 \text{ J cm}^{-2}$  include features at  $2086 \text{ cm}^{-1}$  (HCN),  $2236 \text{ cm}^{-1}$  ( $\text{N}_2\text{O}$ ), and  $2343 \text{ cm}^{-1}$  ( $\text{CO}_2$ ). These products are observed only at laser fluences significantly in excess of the threshold fluence for  $\text{N}_2\text{O}_4$  formation.

One of the significant results of our research is that there is no evidence for formation of methylene nitramine,  $\text{CH}_2\text{NNO}_2$ , under any conditions investigated in this study. Although the infrared spectrum of this molecule is not known, its vibrational frequencies have been calculated by Mowry *et al.*[15] Several of these frequencies coincide with spectrally congested regions of the RDX spectrum and might be masked by the parent absorptions. However, there are at least 4 frequencies that lie in clear regions of the spectrum where we would expect to observe the product if it were formed in the pyrolysis reaction.

Therefore, on the basis of our observation of the  $\text{NO}_2$  dimer and our failure to observe any evidence for formation of  $\text{CH}_2\text{NNO}_2$ , we conclude that *the first step in the thermal decomposition of solid RDX is scission of one of the N-N bonds.*

We were somewhat surprised to find that the initial product observed at low laser fluence is the  $\text{NO}_2$  dimer instead of the monomer. Part of the reason for this is that the strongest absorption bands of the monomer occur in a region of the spectrum that is congested by parent RDX absorption. However, it occurred to us that formation of  $\text{N}_2\text{O}_4$  could conceivably occur via a direct bimolecular reaction of neighboring RDX molecules rather than by dimerization of  $\text{NO}_2$ . To test this hypothesis, we carried out two single-window experiments under identical conditions except that one was pyrolyzed in the amorphous form after vapor deposition, whereas the other was pyrolyzed after annealing to the crystalline form. We expected that if bimolecular reaction of RDX is important in the initial reaction step, then orientational disorder present in the amorphous samples should cause the amount of  $\text{N}_2\text{O}_4$  formed to be either less than or greater than for the crystalline form, depending on whether the crystal geometry is favorable or unfavorable for reaction. The results of these experiments showed that the extent of product formation is the same for the two different structural forms (to an accuracy of about  $\pm 5\%$ ). On this basis, we conclude that *the initial reaction step is unimolecular scission of an N-N bond.*

Finally, we have compared the extent of product formation in single-window and double-window experiments. The latter type trap all of the reaction products, whereas significant losses

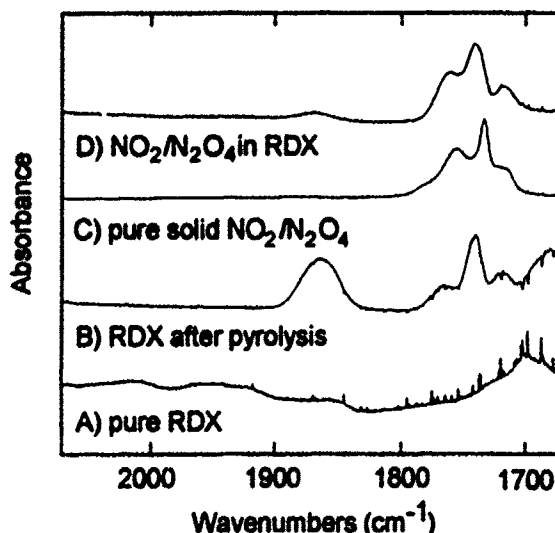


Figure 3. Infrared spectra of  $\text{N}_2\text{O}_4$  (bands near  $1735 \text{ cm}^{-1}$ ) formed as a reaction product (traces A and B) or authentic sample (C and D)

(up to 20% of the sample) may occur to the gas phase in the single-window configuration. This comparison shows that at low fluence (where sample vaporization is minimal), the amount of  $N_2O_4$  formed in the two types of experiments is essentially the same. However, at higher fluence, where secondary products are formed and the extent of sample vaporization is significant, the amounts of secondary products remaining on the window, compared with  $N_2O_4$ , is significantly higher in the double-window configuration. Our interpretation of this result is that  $N_2O_4$  is initially formed in the condensed phase propellant, whereas secondary products are formed at least partly in the gas phase.

## ACKNOWLEDGMENTS

This work is supported by the U.S. Army Research Office under Contract No. DAAL03-90-G-0043.

## REFERENCES

1. C. F. Melius, in Chemistry and Physics of Energetic Materials, edited by S. N. Bulusu, (Kluwer: London, 1990).
2. R. Behrens, Jr. and S. Bulusu, *J. Phys. Chem.* **95**, 5838 (1991).
3. S. L. Rodgers, M. B. Coolidge, W. J. Lauderdale, and S. A. Shackelford, *Thermochimica Acta* **177**, 151 (1991).
4. T. B. Brill, P. J. Brush, S. A. Kinloch, and P. Gray, *Phil. Trans. Royal Soc., Ser. A*, **339**, 337 (1992).
5. J. C. Oxley, M. Hiskey, D. Naud, and R. J. Szekeres, *J. Phys. Chem.* **96**, 2505 (1992).
6. M. D. Pace, *J. Energ. Mater.* **3**, 279 (1985).
7. X. Zhao, E. J. Hints, and Y. T. Lee, *J. Chem. Phys.* **88**, 801 (1988).
8. T. D. Sewell and D. L. Thompson, *J. Phys. Chem.* **95**, 6228 (1991).
9. B. Suryanarayana, R. J. Graybush, and J. R. Autera, *Chem. Ind.*, 2177 (1967).
10. K. Suryanarayanan and S. Bulusu, *J. Phys. Chem.* **76**, 496 (1972).
11. C. A. Wight and T. R. Botcher, *J. Am. Chem. Soc.* **114**, 8303 (1992).
12. B. T. Federoff and O. E. Sheffield, Encyclopedia of Explosives and Related Items, (Picatinny Arsenal, Dover, NJ, 1966), Rept. No. PATR-2700, Vol. III, CPIA Abstract No. 68-0238, AD 653 029, U-A.
13. G. R. Smith and W. A. Guillory, *J. Mol. Spectrosc.* **68**, 223 (1977).
14. I.C. Hisatsune, in Advances in Molecular Spectroscopy, edited by A. Mangini, (Pergamon Press; New York, 1962).
15. R. C. Mowry, M. Page, G. F. Adams, and B. H. Lengsfeld, III, *J. Chem. Phys.* **93**, 1857 (1990).

# NITROGEN RADICALS FROM THERMAL AND PHOTOCHEMICAL DECOMPOSITION OF AMMONIUM PERCHLORATE, AMMONIUM DINITRAMIDE, AND CYCLIC NITRAMINES

M. D. PACE

Code 6120, Naval Research Laboratory, Washington, D. C. 20375-5320

## ABSTRACT

Free-radical thermal and photochemical decomposition products of ammonium dinitramide (ADN), an acyclic nitramine, are compared to that of cyclic nitramines (RDX, HMX, and HNIW) and to ammonium perchlorate (AP). Photochemical formation of  $\text{NO}_2$  from uv-photolysis of ADN at 77 K is found to follow first-order kinetics; whereas, zero-order  $\text{NO}_2$  formation is observed from the cyclic nitramines under the conditions of this experiment. Mechanisms are suggested for ADN decomposition. A general trend of cyclic nitramines to thermally decompose forming nitroxide radicals is supported by  $^{15}\text{N}$ -ring-labeled HNIW results. ADN thermally decomposes at  $190^\circ\text{C}$  to form free-radical reaction products in solution with tetrahydrothiophene-1,1-dioxide.

## INTRODUCTION

In this paper the term *nitrogen radicals* refers to free-radicals having unpaired electron spin density predominantly localized at  $^{14}\text{N}$  or  $^{15}\text{N}$  nuclei. New findings for *photochemically* and *thermally* produced nitrogen radicals from ammonium dinitramide are compared to prior findings for the cyclic nitramines: cyclotrimethylenetrinitramine (RDX), and cyclotetramethylenetetranitramine (HMX); and are compared to new findings for  $^{15}\text{N}$ -labeled hexanitrohexaazaisowurtzitane (HNIW), a polycyclic nitramine; and to ammonium perchlorate (AP), an oxidizer used in propellants. The predominant nitrogen radical from *photochemical* decomposition of all materials studied is nitrogen dioxide ( $\text{NO}_2$ ). This is not surprising for the nitramines, but was not expected for AP. There now exist numerous EPR literature references supporting  $\text{NO}_2$  formation during ultraviolet photolysis of RDX, HMX, and HNIW at temperatures  $\leq 77\text{ K}$ .<sup>1,2,3</sup> In this study at 77 K the rates of production of  $\text{NO}_2$  from the cyclic nitramines under constant flux of ultraviolet (uv) light are assigned as zero-order; whereas, for ADN, a first-order rate of  $\text{NO}_2$  production is observed.  $\text{NO}_2$  is detected from uv-photolysis of AP in smaller concentration than in the nitramines and is attributed to secondary reactions or to impurities.

Thermal decomposition of RDX and HMX produces nitroxyl (or nitroxide) free-radicals.<sup>4,5</sup> A nitroxide has also been proposed from HNIW thermal decomposition.<sup>6,7</sup> In this paper, thermal decomposition of  $^{15}\text{N}$ -labeled HNIW lends further support of HNIW nitroxide radicals. In AP,  $\text{NH}_4^+$  radical ions were monitored by EPk (electron paramagnetic resonance) during heating of the AP crystals. ( $\text{NH}_4^+$  radicals were generated in AP by  $^{60}\text{Co}$   $\gamma$ -rays prior to thermolysis). Thermal decomposition of ADN produced an EPR signal at  $190^\circ\text{C}$ .

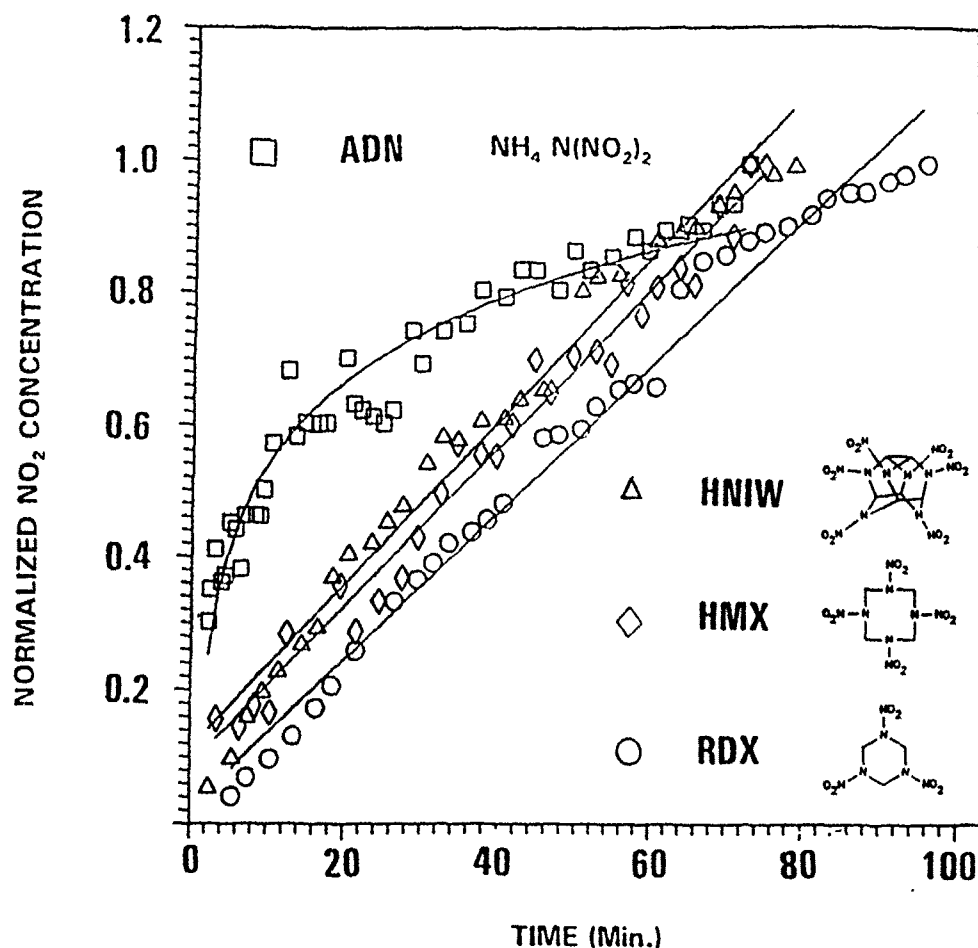


Fig. 1 Normalized NO<sub>2</sub> Concentrations From UV-Photolysis At 77 K

## EXPERIMENTAL

For uv-photolysis, powders of each material (5 - 20 mg) were placed into separate borosilica glass cells having dimensions 0.5 mm x 5 mm (sectioned into 15 cm lengths). ADN is hygroscopic and required handling under low humidity. A Hg - Xe high pressure arc lamp (Electro Powerpacs Inc., Cambridge, MA) operating at 1000 W was used for uv-photolysis experiments. The lamp was located 16 cm from the cavity and IR-filtered uv light having a 1 cm focal diameter was directed into a TM<sub>110</sub> EPR cavity containing a sample cell in liquid nitrogen at 77 K. Previous experiments have shown that nitramines absorb uv strongly from 225 nm to 235 nm.<sup>3</sup> To optimize the uv light flux, each sample was oriented so that the 0.5 cm edge of the flat cell was perpendicular to the beam direction. The exposed surface area of each sample was less than 0.5 cm<sup>2</sup> to ensure uniform irradiation. Only one side of the flat cell was irradiated. Total irradiation times were from 60 to 100 minutes. EPR spectra were recorded using a Bruker ER 200 x-band spectrometer and a Nicolet 115 computer to collect spectra. As each sample was irradiated the NO<sub>2</sub> concentration was monitored by recording EPR spectra at 2 to 4 minute intervals. Concentrations of NO<sub>2</sub> were

measured by double integration of the first-derivative EPR spectra and by comparison to a EPR standard (0.00033% pitch) with a calibrated concentration of  $3 \times 10^{13}$  spins.

Thermal decomposition experiments were similarly performed using sample cells as described above except that the nitramines were dissolved in tetrahydrothiophene-1,1-dioxide (sulfolane), having a boiling point of  $285^\circ\text{C}$ . This procedure has been used successfully in previous studies.<sup>4,5</sup> *In situ* heating in the EPR cavity was performed using  $\text{N}_2$  gas flowing through a resistive heating coil. A Varian V-4540 temperature controller was used to regulate temperature. AP samples were radiation doped with paramagnetic ions as spin probes before heating by exposing the samples to 0.5 MRad of  $^{60}\text{Co}$   $\gamma$ -rays which produces  $\text{NH}_3^+$  ions.<sup>8,9,10</sup> The  $\text{NH}_3^+$  ions were monitored by EPR during heating of AP. In all samples, temperature was monitored using a chromel-alumel thermocouple (Omega) attached directly to the sample tube within 2cm of the sample.

TABLE I  
NO<sub>2</sub> Rates and Concentrations

Nitramine	Molecules per Sample <sup>a</sup>	Rate Constants <sup>b</sup>	Spin Conc. at $t = 60 \text{ min.}^c$	% Conversion at $t = 60 \text{ min.}^d$
HNIW	$4.1 \times 10^{17}$	$1 \times 10^{13}$	$2.2 \times 10^{14}$	0.05
RDX	$2.6 \times 10^{18}$	$3 \times 10^{12}$	$1.6 \times 10^{14}$	0.005
HMX	$1.9 \times 10^{18}$	$7 \times 10^{11}$	$4.2 \times 10^{13}$	0.002
ADN	$4.0 \times 10^{19}$	0.013 (first-order) <sup>e</sup>	$4.0 \times 10^{15}$	0.01

a Estimated number of molecules exposed to uv light assuming  $10\mu\text{m}$  thick surface layer.

b For HNIW, RDX, HMX zero-order rates are given as spins/mg/min of NO<sub>2</sub> for constant uv light flux at 77 K. Rates for HNIW, RDX, HMX assume a  $10\mu\text{m}$  surface depth absorption of the uv light. For ADN see footnote e below.

c Measured spin concentration after 60 min. of uv photolysis at 77 K.

d % conversion =  $100 \times [\text{NO}_2]_{t=60 \text{ min.}} \div (\text{estimated number of molecules per sample})$   
HNIW, RDX, HMX values show good agreement with previously reported data.<sup>3</sup>

e ADN rate constant is first-order ( $\times 10^7 \text{ min}^{-1}$ ). For ADN, NO<sub>2</sub> was considered to form within the entire sample mass rather than in a  $10\mu\text{m}$  surface layer.

## RESULTS

### UV Photolysis

The formation of NO<sub>2</sub> during uv photolysis of ADN, RDX, HMX, and HNIW is compared in Fig. 1. The data in Fig. 1 are normalized to the maximum NO<sub>2</sub> concentration of each sample. At 77 K, decay of NO<sub>2</sub> radicals is negligible so that a buildup of the NO<sub>2</sub> concentration can be measured spectroscopically. For RDX, HMX, and HNIW, NO<sub>2</sub> formation follows zero-order kinetics according to:  $d[\text{NO}_2]/dt = k_0$  where time (t) is in minutes and  $[\text{NO}_2]$ , the experimentally measured concentration, is given as the number of unpaired spins per mg of sample as determined by double integrals of the EPR spectra

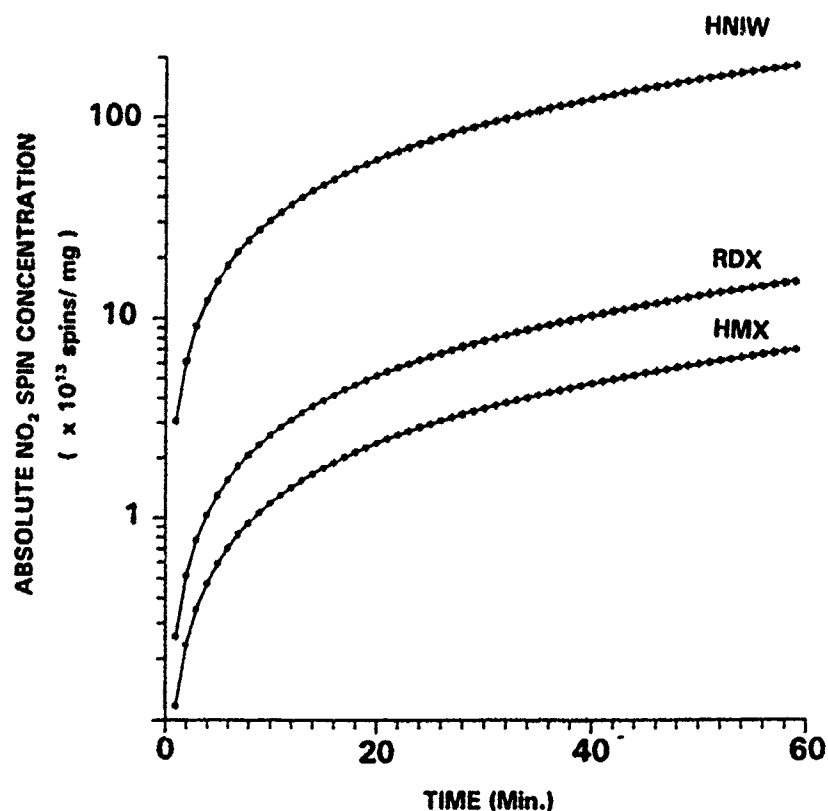


Fig. 2 Logarithmic Plots Versus Time Of Calculated  $\text{NO}_2$  Spin Concentrations Using Rates From Table I

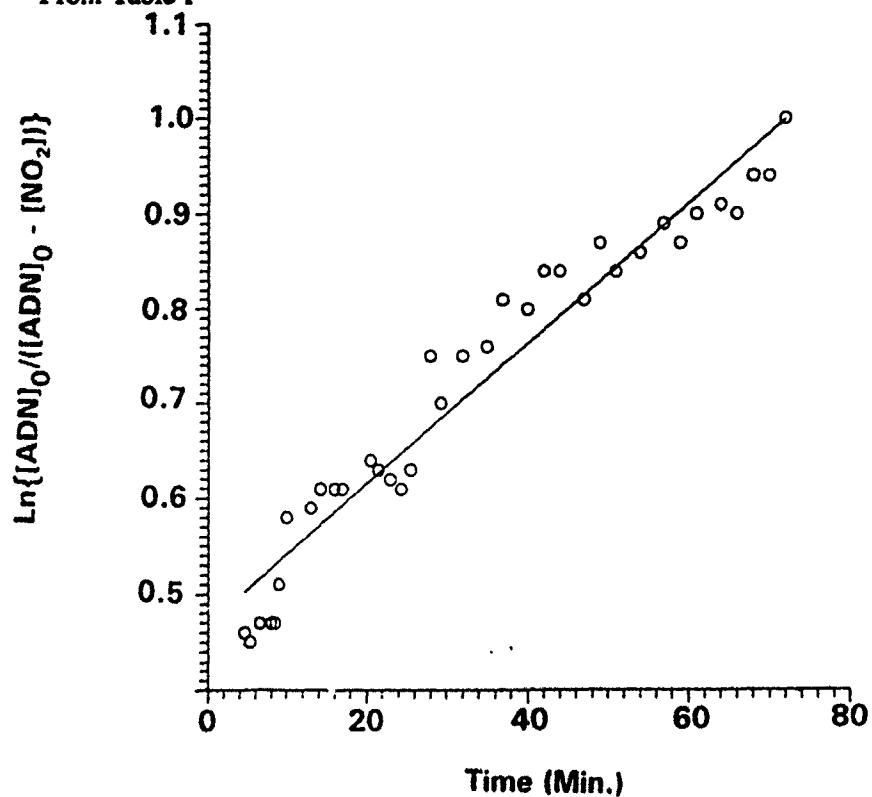
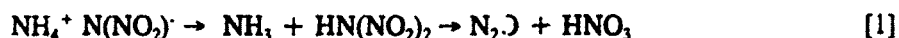


Fig. 3 Logarithmic Plot of ADN  $\text{NO}_2$  Concentrations (From Fig. 1) Versus Time

assuming one spin per  $\text{NO}_2$  radical. The cyclic nitramines HNIW, RDX, and HMX show reasonable correlation with linearity, as expected for zero-order. Near the maximum irradiation times of 60 - 100 minutes, HNIW and RDX data show nonlinear  $\text{NO}_2$  concentration buildup attributed to depletion of surface nitramine bonds exposed to uv light. The zero-order  $\text{NO}_2$  rate constants from linear fits to the data are:  $k_0 = 1 \times 10^{13}$  spins/mg/min for HNIW;  $k_0 = 3 \times 10^{12}$  spins/mg/min for RDX; and  $k_0 = 7 \times 10^{11}$  spins/mg/min for HMX. Zero-order is consistent with rate limiting conditions of the light flux. Different light intensities would give rates independent of initial concentrations of the parent nitramine, but dependent on the light flux. Therefore, lamp settings and irradiation conditions were kept constant in this study (see Experimental). Using the rate constants above, the absolute  $\text{NO}_2$  concentrations for these nitramines can be predicted under the uv-conditions of this experiment. Shown in Fig. 2 are logarithmic plots of the calculated  $\text{NO}_2$  concentrations based on these rate constants versus time. These curves are in good agreement with the experimentally measured spin concentrations. The results are consistent with previously reported uv-induced  $\text{NO}_2$  formation from HNIW, RDX, and HMX and show an order of magnitude difference in  $\text{NO}_2$  formation from HNIW relative to RDX and HMX.<sup>3</sup> Although ADN is a nitramine compound, ADN behavior in this experiment is different from the cyclic nitramines.

The normalized ADN  $\text{NO}_2$  concentration in Fig. 1, as reproduced by two separate ADN samples, shows nonlinear time dependence. A first-order rather than a zero-order rate of ADN  $\text{NO}_2$  formation is observed during uv-photolysis. As shown in Fig. 3, a plot of  $\ln\{[\text{ADN}]_0 - [\text{NO}_2]_t\}$  versus time gives a linear fit to the ADN  $\text{NO}_2$  data. The first-order rate constant determined from Fig. 3 is  $0.013 \times 10^{-7} \text{ min}^{-1}$ . The difference in rates of ADN versus the cyclic nitramines suggests that ADN does not lose  $\text{NO}_2$  by a direct nitramine bond cleavage, but as a secondary product. It is the impression of this author that the reactivity of ADN is greater than the cyclic nitramines. Darkening of ADN samples was produced by uv-photolysis and thermal decomposition. Color changes due to photolysis were not noticeable in the cyclic nitramine samples in this experiment. ADN is hygroscopic and has been suggested to decompose thermally by the following reaction:



Although this reaction does not produce  $\text{NO}_2$  directly,  $\text{NO}_2$  formation may occur following  $\text{H}^+$  transfer to form  $\text{HN}(\text{NO}_2)_2$  such as:



or by dinitramide ion decomposition according to [3] as suggested by gas phase studies:<sup>11</sup>



in which the  $\text{NO}_2$  concentration would depend on the  $\text{HN}(\text{NO}_2)_2$  or  $\text{N}(\text{NO}_2)_2^-$  concentrations. Warming photolyzed ADN from 77 K to room temperature results in gas evolution, further suggesting that reactions occur during photolysis or during sample warming. The  $\text{NO}_2$  fraction, although less than 0.1% of the total molecules of each sample, was highest in ADN and HNIW, as shown in Table I by % conversion.

In contrast to ADN no  $\text{NO}_2$  was expected from AP uv photolysis because significant decomposition of  $\text{NH}_4^+$  would be required to form  $\text{NO}_2$ . Surprisingly,  $\text{NO}_2$  was detected at a very low concentration of  $10^{13}$  spins during photolysis of AP at 77 K, but the rate of  $\text{NO}_2$



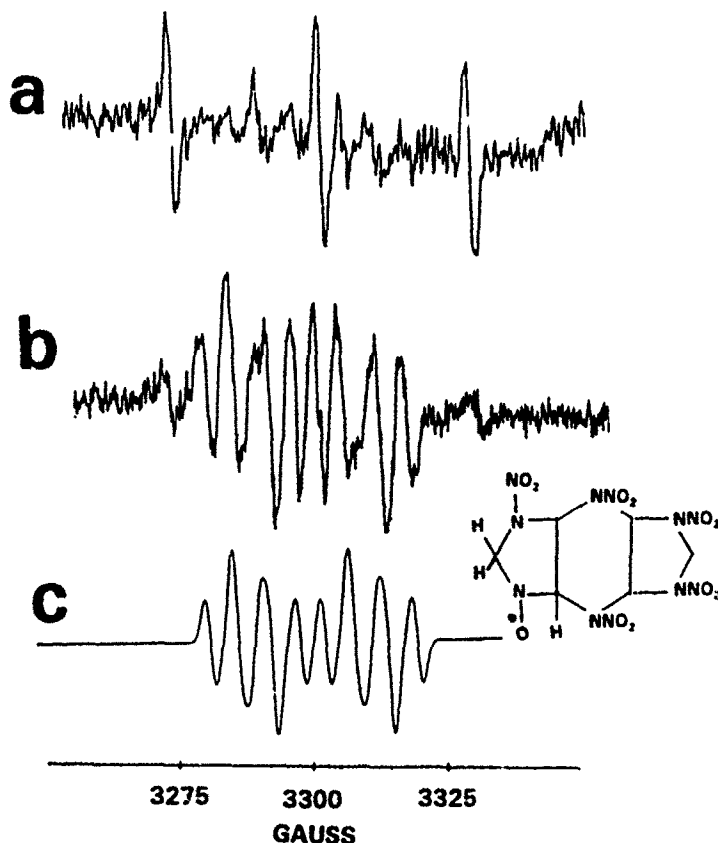


Fig. 4 (a) EPR spectrum from thermal decomposition of  $^{15}\text{N}$ -ring-labeled HNIW in sulfolane at  $120^\circ\text{C}$ . (b) EPR spectrum observed at  $140^\circ\text{C}$ . (c) Simulated EPR spectrum assuming one nitrogen hfc and three proton hfc's (values given in text). A possible decomposition radical structure is shown. Only protons which would give hfc's to the nitroxyl group are indicated by H.

growth and concentrations were not reproducible. The formation of  $\text{NO}_2$  from  $\text{NH}_4\text{ClO}_4$  requires a mechanism proposed for thermal decomposition:  $2\text{NH}_4\text{ClO}_4 \rightarrow 4\text{H}_2\text{O} + \text{Cl}_2 + \text{O}_2 + \text{NO}$  followed by  $2\text{NO} + \text{O}_2 \rightarrow 2\text{NO}_2$ .<sup>12</sup>

### Thermal Results

The second part of this paper gives qualitative slow thermal decomposition results of ADN,  $^{15}\text{N}$ -labeled HNIW, and  $\text{NH}_4\text{ClO}_4$ . Thermal experiments were carried out as slow heating experiments in which the temperature was increased at a rate  $\leq 5^\circ$  per minute. As described in the experimental section, the nitramines were dissolved in a high boiling solvent to facilitate heat transfer to the sample and to allow for low sample concentrations. To avoid reaction with the solvent, ammonium perchlorate was not dissolved in sulfolane but instead, a single crystal of ammonium perchlorate was heated in a tube open to the atmosphere. Prior studies indicate that thermally produced free radicals from the cyclic nitramines RDX, HMX and HNIW do not react with tetrahydrothiophene-1,1-dioxide.<sup>3,4,7</sup>

A free radical was detected from  $^{15}\text{N}$ -ring-labeled HNIW at  $140^\circ\text{C}$  consistent with previous results of HNIW- $d_6$  and HNIW. As shown by Fig. 4a, at  $120^\circ\text{C}$  is a spectrum of three transitions separated by 2.8 mT (10 gauss = 1 mT). At  $140^\circ\text{C}$ , this spectrum overlaps with other EPR signals which appear. The  $140^\circ\text{C}$  EPR signals are tentatively assigned to a

nitroxyl nitrogen hyperfine coupling ( $hfc[a(^{15}\text{N}) = 2.14 \text{ mT}]$  and to two symmetrically equivalent proton  $hfc[a(^{15}\text{N}) = 0.51 \text{ mT}]$  and to a third nonequivalent proton  $hfc[a(^1\text{H}) = 0.66 \text{ mT}]$ , where  $a$  is the symbol of the isotopic hyperfine coupling. Bond cleavage of the C-C bond of the parent HNIW molecule and addition of hydrogen to give a tricyclic ring as shown in Fig. 4b are required to account for three proton  $hfc$ s. However, this assignment is consistent with previously published thermal decomposition EPR spectra from HNIW- $d_6$  and HNIW in which the protons have 15% larger  $hfc$ s than in the  $^{15}\text{N}$  radicals. The radical EPR signal in Fig. 4b remained unchanged up to  $190^\circ \text{C}$ . Above  $190^\circ \text{C}$  the EPR spectrum changes to a single line which remains stable at room temperature after recooling the sample.

Thermal decomposition of ADN is accompanied by chemical reaction of decomposition products with the solvent. Reaction of decomposition products of ADN with sulfolane at  $190^\circ \text{C}$  is indicated by a color change of the sample from opaque to black accompanied by growth of a single line EPR signal (not shown) which remains stable at room temperature after recooling the sample. The radical product was not assigned but is clearly a different result from the cyclic nitramines where nitroxides are formed. Spin trapping reactions will be required to assign reaction intermediates.

For experiments with ammonium perchlorate,  $\text{NH}_4^+$  ions were first generated in AP crystals by exposure of the crystals to ionizing gamma radiation (EPR spectrum given in reference 8). As discussed by Urbanski, the  $\text{NH}_4^+$  radical defects have been reported to affect the thermal decomposition of AP.<sup>8,13</sup> For unirradiated AP crystals decomposition is reported to initiate along crystalline growth boundaries; whereas, for irradiated samples the decomposition sites occur homogeneously throughout the material. In this experiment, an AP crystal was slowly heated in order to observe any changes in EPR signal of  $\text{NH}_4^+$  ions. No changes were observed up to  $128^\circ \text{C}$  where the EPR signal decayed, consistent with previous reports. Continued heating of the sample to  $190^\circ \text{C}$  produced no new EPR signals.

## DISCUSSION

The rationale for studying this group of materials was to observe similarities and differences between the decomposition of cyclic nitramines (RDX, HMX, HNIW) and a non-cyclic nitramine (ADN) and to observe whether there are any similarities between AP and ADN in terms of the  $\text{NH}_4^+$  ion chemistry. The behavior of ADN is shown to be different from RDX, HMX, and HNIW. For example, the uv-photolysis rate data of Fig. 1 indicates that the formation of  $\text{NO}_2$  in the cyclic nitramines occurs by a similar bond cleavage mechanism, but for ADN, a non-linear  $\text{NO}_2$  formation rate during uv-photolysis suggests a different mechanism of  $\text{NO}_2$  formation. For the cyclic nitramines the uv light appears to be the rate limiting step, but for ADN there is a dependence on an unknown reaction intermediate. Logically this intermediate is related to the dinitramide anion. A possible reaction sequence is  $2\{\text{NH}_4^+ \text{N}(\text{NO}_2)_2\} \rightarrow 2\text{NH}_3 + \text{H}_2\text{N}(\text{NO}_2)_2^+$  followed by decomposition of the dinitramide acid to  $\text{H}_2\text{N} + \text{NO}_2 + \text{NO}_2^+$ . This mechanism fits into a gas phase scheme described by Melius in which  $\text{H}_2\text{N}(\text{NO}_2)_2^+$  is unstable and goes to products.<sup>14</sup> Indeed, the photolysis of ADN under these experimental conditions decomposes ADN to gas phase products which remain trapped in a frozen matrix until the sample is warmed to room temperature. ADN, unlike the cyclic nitramines which show no obvious radical reactions with sulfolane during thermal decomposition below  $200^\circ \text{C}$ , does yield radical reaction products with sulfolane further showing that ADN reactivity is higher than HMX or RDX. The similar % conversion of HNIW and ADN in Table I indicates that ADN is driven to more complete decomposition by uv light than is RDX or HMX. The implication is that ADN is chemically much more sensitive to uv light and more reactive than RDX to which it is often compared.

The thermal decomposition  $^{15}\text{N}$ -HNIW radical is consistent with RDX and HMX which thermally form nitroxides. There are only two equivalent proton hfs in a thermally formed HMX nitroxide because the eight membered ring causes two of the four HMX protons to lie coplanar with the N-O bond of the nitroxyl group. In RDX the six member ring allows boat-to-chair interconversions which average four proton hfs. If the nitroxide assignment of thermally decomposed HNIW is upheld, then a general trend of cyclic nitramines to decompose thermally forming nitroxyl radicals is supported by the HNIW results. Nitroxide radicals have recently been observed from thermal decomposition of another energetic material, 3-nitro-1,2,4-triazol-5-one.<sup>15</sup>

In AP the disappearance of  $\text{NH}_4^+$  ions at  $128^\circ\text{C}$  is consistent with the EPR AP studies of Hyde and Freeman<sup>8</sup>. The fact that no new radicals are detected up to  $190^\circ\text{C}$  suggests that AP and ADN do not share thermal decomposition pathways. However, photolysis decomposition of AP and ADN may share similar pathways assisted by the  $\text{NH}_4^+$  ion. A recent study of  $\text{AP}\cdot\text{MnO}_4$  mixed crystal uv-photolysis shows that  $\text{NH}_4^+$  is necessary for reduction of  $\text{Mn}^{7+}$  to  $\text{Mn}^{2+}$ .<sup>16</sup>

## REFERENCES

1. M. D. Pace and W. B. Moniz, *J. Magn. Reson.* **47**, 510 (1982).
2. J. M. McBride, presented at the ONR Workshop on Energetic Materials, Los Alamos, N. M., March, (1992).
3. M. D. Pace, *J. Phys. Chem.* **95**, 5858, (1991).
4. M. D. Pace, A. D. Britt, and W. B. Moniz, *J. Energ. Mater.* **1**, 127, (1983).
5. A. D. Britt, M. D. Pace, and W. B. Moniz, *J. Energ. Mater.* **1**, 367, (1983).
6. M. D. Pace, *J. Energ. Mater.* **3**, 279, (1985).
7. M. D. Pace, *Mol. Cryst. Liq. Cryst.* **219**, 139, (1992).
8. J. S. Hyde and E. S. Freeman, *J. Phys. Chem.* **65**, 1636 (1961).
9. T. Cole, *J. Chem. Phys.* **35**, 1169 (1961).
10. M. Fujimoto, and J. R. Morton, *Can. J. Chem.*, **43**, 9012, (1965).
11. R. J. Doyle, (in press).
12. L. L. Bircumshaw, and B. H. Newman, *Proc. Roy. Soc. A* **227**, 115, (1955).
13. T. Urbanski, Chemistry and Technology of Explosives, vol. II, p. 478 - 482, (Pergamon Press, New York, 1965).
14. C. Melius, work presented at the ONR Workshop on Energetic Materials, Los Alamos, N. M., March, (1992).
15. J. A. Menapace, J. E. Marlin, D. R. Bruss, and R. V. Dascher, *J. Phys. Chem.* **95**, 5509, (1991).
16. J. Yu., *J. Phys. Chem.* **96**, 5746, (1992).

## ACKNOWLEDGEMENTS

This research was sponsored by the Office of Naval Research. Dr. T. Russell of the Naval Surface Warfare Center, Silver Spring, MD and Dr. T. Nielsen of the Naval Weapons Center, China Lake, CA are acknowledged for supplying ammonium dinitramide and  $^{15}\text{N}$ -labeled HNIW. The Armed Forces Radiobiology Radiation Institute, Bethesda, MD is acknowledged for use of the  $^{60}\text{Co}$  facility.

---

## **PART II**

---

### **Deformation, Fracture, and Initiation**

## ENERGY LOCALIZATION AND THE INITIATION OF EXPLOSIVE CRYSTALS BY SHOCK OR IMPACT

C. S. COFFEY

Naval Surface Warfare Center, White Oak Laboratory  
Silver Spring, MD 20903-5000

### ABSTRACT

The initiation of chemical reaction in explosive crystals during shock or impact is shown to be a solid state, quantum mechanical, process not accessible by a classical continuum approach. The process by which dislocations move in a solid is analyzed in terms of quantum mechanical tunneling. The motion of these dislocations significantly perturbs the lattice and creates phonons which, for low dislocation velocities can cause local ignition sites and for high dislocation velocities, can have energies sufficient to directly pump the internal vibrational modes of the explosive molecules and cause rapid molecular dissociation.

### INTRODUCTION

On the microscopic level irreversible plastic deformation of a crystalline solid occurs by the creation and motion of dislocations. This is a quantum mechanical process not totally accessible by conventional classical analysis. It is suggested that the motion of dislocations occurs by quantum mechanical tunneling through the lattice potential well barriers since this is more energy efficient than the usual approach that the dislocations advance with the aid of thermal fluctuations that assist them in going over the top of the lattice potential barriers. This will be briefly developed and some results presented. The rate that energy is dissipated in the lattice due to the motion of the dislocations is developed by observing that this is a microscopic process in which the local distortion of the lattice by a passing dislocation significantly perturbs the positions of those atoms or molecules located near the path of the core of the dislocation. The energy dissipated by the moving dislocations can lead to local energy densities sufficient to cause ignition due to the shear stress induced by mild impact and in the case of high amplitude shocks, result in rapid multi-phonon molecular excitation and even dissociation typical of detonations.

#### The Motion of Dislocations

By classical theory it is impossible to move the core of a dislocation out of its initial potential well and into an adjacent well when the energy of the core is less than the depth of the potential well. Yet this process occurs during the plastic deformation that most crystalline solids undergo during shock or impact. It is possible that thermal fluctuations could enable the dislocation to occasionally overcome the potential barrier and move into an adjacent well. However, while thermal processes are important, from an energy basis it is much more likely that dislocation motion will occur by quantum mechanical tunneling. Long before the thermal energy of a dislocation has reached a level sufficient to lift it over the potential barrier and into the adjacent well the dislocation will have achieved sufficient energy to tunnel through the potential barrier and pass directly into the

adjacent well.

Tunneling easily resolves the problem of the insurmountable potential barrier posed by the classical picture. In order to describe the tunneling process consider the length of the dislocation to be composed of segments each one atom or molecule in length. Thus, an edge dislocation  $N$  atoms or molecules long will be made of  $N$  segments, each of which is bound to its adjacent core segments by the lattice potential which holds the dislocation together. We treat the dislocation core element of each segment as a quasi-particle and examine the probability that under the influence of an applied shear stress a core segment will tunnel through the potential barrier and arrive in the adjacent potential well. The lattice potential that holds the dislocation together also prevents any segment from advancing more than one atomic or molecular spacing ahead of its neighboring segments. This same assumption is implicit in the conventional view of dislocation motion due to thermal processes.

Under the influence of an applied shear stress the quasi-particles which form the core of the dislocation are forced against the potential well barrier formed by their nearest neighbors. The potential barrier,  $U$ , of importance is only that portion of the lattice potential needed to be overcome to realign the extra half plane of the edge dislocation with its nearest neighbor on the other side of the slip plane. It is unlikely that we will ever know the exact shape of the lattice potential well along the slip plane especially for complicated molecular crystals. Therefore, consider the simplest case of a lattice composed of square well potentials of depth  $U$  and barrier width  $W$ . This simple picture should be adequate for a general description of plastic deformation. It will however overestimate the tunneling probability for the lower energy dislocation segments that reside near the bottom of the potential well because in a real solid the width of the potential barrier will increase with well depth.

The probability,  $T$ , that the dislocation segment will tunnel through the barrier along the slip plane is<sup>1</sup>

$$T = \frac{1}{1 + \frac{U^2 m}{2 E \hbar^2} S(U - E)} \quad (1)$$

where

$$S(U - E) = \frac{\hbar^2}{2m(U - E)} \left\{ \chi \left( \left[ \frac{2m}{\hbar^2} (U - E) \right]^{1/2} W \right) \right\}^2, \quad (2)$$

and  $\chi() = \sinh()$  when  $E < U$ , and  $\chi() = \sin()$  when  $E > U$ .

### Plastic Strain Rate

The plastic strain rate,  $dy_p/dt$ , is

$$\frac{dy_p}{dt} = N v b, \quad (3)$$

where  $N$  is the number of moving dislocations per unit area of

surface,  $v$  is the dislocation velocity and  $b$  is the Burgers length.

The dislocation velocity is determined by observing that a dislocation residing in a potential well has both thermal and applied stress induced motions. These cause the dislocation segments to vibrate back and forth between the walls of the potential well. Occasionally the segments may tunnel through the barrier and transit into the adjacent well where they continue to oscillate between the walls of the new potential well until tunneling again occurs and the dislocation segment moves into the next potential well. If  $v$  is the number of times that a dislocation segment approaches a potential barrier, and  $T$  is the probability of tunneling through the barrier, then  $vT$  is the average number of potential barriers that the dislocation segment tunnels through per unit time. With each successful tunneling event, the dislocation moves a lattice distance  $b$ . To simplify things, it will be assumed that a sufficiently strong thermal or stress gradient exists so that mostly the dislocation segments do not tunnel back into a previously occupied well. For this case, the average velocity of a segment is approximately  $v \approx vTb/t$  where  $t$  is the time interval. It will be assumed that the time for each successful tunneling event is just the time for the lattice to rearrange itself to accommodate the new position of the dislocation. This occurs at the local sound speed,  $v_0$ , so that the time required to accomplish tunneling one lattice spacing is  $\Delta t = b/v_0$ . The appropriate time interval over which to average the dislocation velocity is just  $t = v\Delta t$  so that the average segment velocity is just  $v = Tv_0$ .

Since the dislocation is made up of a string of these core segments, each of which is linked to its two nearest neighbors by the lattice potential, the average velocity with which the dislocation moves is  $v = Tv_0$ . This form gives the correct limits for the average dislocation velocity at very low shear stress levels,  $\tau \sim 0$ , where  $T \sim 0$  and at high shear stress levels,  $\tau \gg 0$ , where  $T \sim 1$ . Since  $T \leq 1$ , the speed of the plastic wave will always be less than or equal to the local sound speed.

The number of moving dislocations can be estimated by assuming that the dislocations are created by  $N$  sources whose dislocations intercept a unit surface area of the crystal. To each of these sources is assigned a probability,  $p_s(\tau)$ , of creating a new dislocation pair at a shear stress  $\tau$  and a characteristic source size,  $l_0$ , beyond which the newly created dislocation pair must propagate before the source can create another dislocation pair. The rate at which a single source can create dislocations is

$$\frac{dn}{dt} = 2p_s(\tau) \frac{v}{l_0} \quad (4)$$

The factor of 2 accounts for the creation of a dislocation pair. If  $\tau$  does not depend strongly on time but resembles a step function,  $\tau(t) \approx \tau_0 u(t)$ , then the number of dislocations per source is

$$n(\tau, t) = \tau(t) p_s(\tau) \frac{v_0}{l_0} t \quad (5)$$

where the time  $t$  is the time from first application of the shock or impact. These dislocations are expected to be concentrated on the slip planes that contain the source and form a shear band.

Combining the above relations, the plastic strain rate from  $N_s$  dislocation sources that intercept a unit area is approximately

$$\frac{d\gamma_p}{dt} \approx 2T(\tau)^2 \frac{v_0^2 b}{l_0} p_c(\tau) N_s t \quad (6)$$

The plastic deformation rate given in equation (6) admits two time regimes of interest. These are determined by the time required for a newly created dislocation to move away from its source and encounter an obstacle which forces it to stop. Let  $L_0$  be the average distance between the dislocation source and an obstacle, then at early times after the application of a shock or impact when  $t < L_0/v$  the plastic strain rate is given by equation (6). However, at later times when  $t \geq L_0/v$ , the moving dislocations will begin to encounter obstacles and will be forced to stop. For this case the number of moving dislocations approaches a constant and the plastic strain rate is determined by substituting  $t = L_0/v$  into equation (6)

$$\frac{d\gamma_p}{dt} \approx \frac{2T(\tau) v_0 b p_c(\tau) N_s L_0}{l_0} \quad (7)$$

#### Dislocation Energy

Assume local equilibrium, so that the energy density of a dislocation in a lattice must be the same as the local energy density of the host lattice. During shock or impact the energy will have two components, one due to the shear stress of the shock or impact and the other from the shear stresses arising from the thermal background. Even for high level shocks most of the solid will behave elastically as a Hooke's law solid and most of the shear stress energy of the dislocation core will be elastic energy. The average energy with which a segment of the dislocation core approaches the potential barrier is approximately

$$E = \frac{\tau^2 V}{2G} + \frac{k\theta}{2} \quad (8)$$

where  $G$  is the shear modulus,  $\theta$  is the temperature and  $k$  is Boltzmann's constant. The thermal energy with which a dislocation segment approaches a potential barrier is just  $\frac{1}{2}k\theta$ . The effect of thermal fluctuations about the mean temperature and the non-linear contribution of the core region to the energy have been ignored.

#### Comparison with Deformation Experiments

These results can be compared with the experimental results of Campbell and Ferguson<sup>3</sup> who examined the plastic deformation rate in a mild steel for different applied shear stress levels over a wide range of temperatures. The material constants were taken as  $b = 3 \times 10^{-10} \text{ m}$ ,  $W = .5 \times 10^{-10} \text{ m}$ ,  $l_0 = 3 \times 10^{-8} \text{ m}$ ,  $v_0 = 5.5 \times 10^3 \text{ m/s}$ ,  $G = 7.5 \times 10^{11} \text{ dy/cm}^2$ ,  $\rho = 8.6 \times 10^3 \text{ kg/m}^3$ ,  $U = .5 \times 10^{13} \text{ ergs}$ . The number of dislocation sources per unit area was determined in conjunction with the distance,  $L_0$ , that a dislocation travels between its source and a blocking obstacle. It was assumed that  $N_s L_0^2 \approx 1$ .



Taking  $L_0 = 10^{-4} \text{m}$ , the approximate crystal size, then  $N_0 \approx 10^8 \text{m}^{-2}$ . The mass of a dislocation segment was taken as  $m \approx \rho b^3$ , and the volume,  $V$ , of the lattice that is perturbed by the presence of the moving dislocation was taken as a cylindrical disk centered at the dislocation core and of height  $b$  and radius  $7b$  thus  $V \approx 150b^3$ . For simplicity, it was assumed that the amplitude of the applied shear stress was large enough so that the source could readily create dislocations allowing  $p_c(\tau) \rightarrow 1$ .

Figure (1) shows the predicted behavior of the plastic deformation rate as a function of the applied shear stress for approximately the same temperatures as in the experiments of Campbell and Ferguson. Except for a less rapid increase in plastic strain rate with increased shear stress at low temperatures and lower shear stress, the predicted behavior contains all of the essential features found in the experimental data. As noted at the outset, the less rapid increase in strain rate at low shear stress levels is due mainly to the use of an idealized square well potential in which the width of the barrier is a constant. The correct solution would be to determine the width of the exact potential barrier as a function of the quasi-particle energy and solve the tunneling problem in a way that satisfies the Schrodinger equation and the boundary conditions. A somewhat more realistic potential which gives a better fit to the data is to let the width of the potential barrier be  $W = W_0(\sin(\pi E_0/2E_\tau))^3$ , where  $W_0 = .5 \times 10^{-10} \text{m}$  and  $E_0$  is the dislocation segment energy when  $\tau = 0$ .

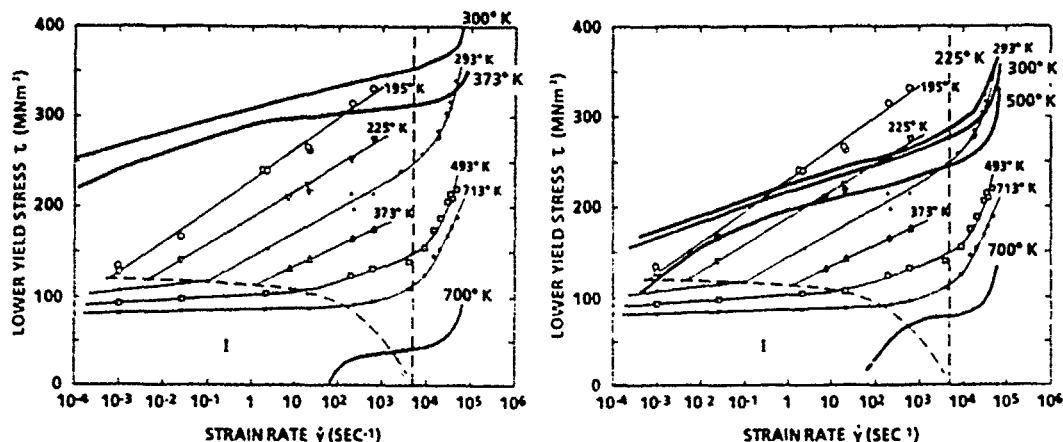


Figure (1). Plastic strain rate due to tunneling through square well potential barrier, LHS, and half sine wave barrier, RHS. Predictions are indicated by heavy lines. Also shown is the experimental data of Campbell and Ferguson.<sup>1</sup>

The predicted rapid increase in strain rate with applied shear stress that occurs at about  $\dot{\gamma} \approx 4 \times 10^3 \text{ SEC}^{-1}$  at all temperatures is due to the tunneling probability approaching unity as  $E \rightarrow U$ . This behavior is evident in the experiments of Campbell and Ferguson and has been observed in copper and  $\beta$  brass. The conventional macroscopic constitutive approach is unable to account for this rapid increase in plastic strain rate at high shear stress levels.

At low shear stress levels a nearly non-thermal behavior was observed in the experimental data. In the experiments of Campbell and Ferguson<sup>3</sup> this regime was referred to as region I. In the present analysis this behavior can be attributed to the presence of low level obstacles in the solid which impede the functioning of

the dislocation sources,  $p_c \ll 1$ , at low shear stress levels. At slightly higher shear stress levels,  $\tau > 10^2$  Mpa, these obstacles are overcome,  $p_c \approx 1$ , and dislocation motion is determined by lattice tunneling. These results can be extended to other materials. The prediction of the dislocation velocity in lithium fluoride crystals compares reasonably well with the experimental measurements of Johnson and Gilman on LiF at several temperatures.<sup>4</sup>

Finally, this analysis applies to both screw and edge dislocations since the only difference between these is the potential barrier that each type of dislocation must tunnel through. This will only alter the tunneling probability,  $T$ , and only for mid range shear stresses. The asymptotic behavior at very high and very low amplitude shear stresses will be the same in both cases as is seen in observations of dislocation velocities.<sup>4</sup>

#### High Amplitude Shock Loading

High amplitude shock loading offers a unique analytical view of plastic deformation because the energy with which the dislocations approach the potential barrier approaches the barrier height,  $E \sim U$ . The plastic strain rate at early times, equation (6), simplifies since the thermal term can be ignored. In these limits the average plastic strain rate is proportional to the fourth power of the applied shear stress. Swegle and Grady have observed that within a few tens of nanoseconds after the onset of a high amplitude shock the plastic strain rate in a number of different materials varied as the fourth power of the stress level.<sup>5</sup> Substituting representative values into equation (6) and the applied shear stress  $\tau = 2$  GPa gives  $dy/dt \approx 10^5 \text{ s}^{-1}$  at  $t = 10^{-8} \text{ s}$ , which is in the range of the experimental data.

#### Energy Dissipation During Rapid Deformation

To understand how energy is dissipated by moving dislocations, observe that the motion of a dislocation through a solid significantly displaces those atoms or molecules located near the core of the moving dislocation. These atoms/molecules can be displaced as much as  $d/10$  or more where  $d$  is the lattice constant. Dislocations moving at a speed  $v$  encounter the lattice potential at a rate of  $v/d$  times per second and in the process disturb the lattice at a frequency of  $2\pi v/d$  rad/s. The energy of this disturbance is radiated away as phonons. Since in the case of high amplitude shocks  $v$  can approach the local sound wave speed, these phonons can have frequencies in excess of  $10^{13}$  rad/s which is sufficient to pump the internal vibrational modes of most molecules of interest. We have developed this view in some detail and will briefly review it here.<sup>6,7,8</sup>

Since explosive molecules are complicated affairs having many atomic components (chiefly C, H, N, and O), it is unlikely that the stress field around the core of a dislocation in such a system will ever be well known. Nor is this necessary in order to obtain workable predictions of energy dissipation and localization in terms of shear modulus and other known physical properties of the crystal. In this spirit, we approximate the stress field of an edge dislocation in a lattice composed of explosive molecules by the classical expression for the stress field of an edge dislocation in a simple lattice composed of point atoms or molecules. The interaction Hamiltonian can be written as<sup>6</sup>

$$H_I = \frac{\Delta x}{4\pi(1-\nu)} \frac{Gb}{r} [(\sin\theta + \cos\theta) \left( \frac{\cos\theta}{d_2} - \frac{\sin\theta}{d_1} \right)] \quad (9)$$

The shear modulus  $G$  provides a measure of the coupling between the dislocation and the lattice. The quantity  $\nu$  is the Poisson ratio,  $r$  is the distance from the dislocation core,  $\theta$  is the angle between the shear stress and the strain,  $d_1$  and  $d_2$  are the lattice spacings.

The energy dissipation rate due to the motion of the core of an edge dislocation moving through a lattice at a velocity  $v$  has been determined to be<sup>7</sup>

$$\frac{dE}{dt} = N\Gamma G^2 \int (n_q + 1) dq + N \sum_j \hbar \omega_{j,j-1} \sum_{l,u} \left| \sum_{l=1} \frac{\langle lH'|l \rangle \langle lH'|u \rangle}{E_l - E_u - \hbar \sum_{j=1} \omega_{j,j-1}} \right|^2 - K \frac{dT}{dx}, \quad (10)$$

where

$$\Gamma = \frac{1}{32\pi^3 \rho} \left( \frac{Rb}{1-\nu} \right)^2 \frac{1}{v_0 d^2}.$$

$N$  is the number of moving dislocations,  $R$  is the radius of the dislocation core, and  $\rho$  is the density. The quantity  $H'$  is the interaction Hamiltonian coupling the moving dislocation with the internal molecular vibrational modes. The last term in Eqn. (10) describes the thermal conduction of energy from the shear band.

In order to obtain a closed form for the energy dissipation rate that can be numerically evaluated, the assumption was made that all of the phonons generated by the moving dislocation and located in a frequency band centered about  $\omega = 2\pi v/d$  could be approximated as being concentrated at the center frequency. The additional assumption was made that the empirical dislocation velocity-applied shear stress relation obtained by Gilman can be applied to explosive molecules,  $v = v_0 \exp(-\tau_0/\tau)$ .<sup>4</sup> The quantity  $\tau$  is the applied shear stress,  $\tau_0$  is a characteristic shear stress of the material. When these approximations are introduced into equation (10) the rate of energy dissipation per unit length of dislocation becomes<sup>8</sup>

$$\frac{dE}{dt} = \frac{4\pi\Gamma G^2 N}{d} e^{-\tau_0/\tau} + N \sum_j \hbar \omega_{j,j-1} \sum_{l,u} \left| \sum_{l=1} \frac{\langle lH'|l \rangle \langle lH'|u \rangle}{E_l - E_u - \hbar \sum_{j=1} \omega_{j,j-1}} \right|^2 - K \frac{dT}{dx}, \quad (11)$$

where  $\omega_{j,j-1} = (2\pi v_0/d) \exp(-\tau_0/\tau)$ .

The first term of (11) arises from the first order transition probability and is responsible for the dissipation due to low and low velocity dislocations. Consequently, it reflects the energy dissipation rate due to impact and low level shock. The higher order terms are mainly responsible for energy dissipation due to relatively large amplitude shocks, since for these terms to be important resonance must occur,  $\omega_{l,l-1} = (E_l - E_{l-1})/\hbar \approx 10^{13}$  rad/s. This requires that the dislocation velocity approach  $v_0$ , which

only happens when  $\tau \gg \tau_0$ . As resonance is approached, a very rapid increase in the energy dissipation rate occurs. The high number density of optical phonons, centered in a band about  $\omega = 2\pi v/d$ , produce multi-phonon resonant excitation of the internal vibrational modes of the molecules of the host lattice. At resonance the transition probability between adjacent vibrational levels approaches unity. Only for the more widely spaced lowest vibrational levels are non-resonant conditions likely to occur. Consequently, the energy dissipation-molecular excitation rate for high amplitude shocks will be determined only by the products of these few non-resonant lowest level transition probabilities. This results in an extremely fast process in which energy is transferred directly from the moving dislocations to vibrationally excite and even dissociate the molecules that lie near the path of the dislocation core.

### The Onset of Reaction

What has been developed up to this point applies to both inert and energetic crystalline materials. It is useful to examine the onset of reaction in energetic crystals in the limit where the energy density increases to a critical level,  $E_c$ , in at most a very few locations and chemical reaction starts in only a few crystals. The energy density in a shear band due to dissipation by moving dislocations can be obtained by integrating equation (11) with respect to time. Dissipation begins just as the dislocations begin to move, at the yield stress,  $\tau = \tau_y$ . Ignition will occur when this energy density exceeds the critical level,  $E_c$ , and the shear bands then become local reaction sites.

Assume an energy  $e_0$  is required to cause a molecule to dissociate. Early in the ignition, the number density of dissociated molecules,  $N_d$ , is approximately  $N_d \approx (E - E_c)/e_0$ . If each of the reacting molecules releases an amount of energy,  $u_0$ , and this initial energy release causes few if any additional molecules to react so that no reaction growth occurs, the reaction energy density is approximately  $U \approx u_0(E - E_c)/e_0$  where reaction occurs when  $U > 0$ . The initial reaction energy in a lightly confined charge is

$$U(t) = \frac{u_0}{e_0} \left( \frac{4\pi\Gamma G^2}{d} \int N e^{-\frac{\tau_0}{\tau}} dt + \hbar \int N \sum_{j=1}^j \omega_{j,j-1} \sum_{l,u} \left| \sum_l \frac{\langle \hat{H}' | l \rangle \langle l | \hat{H}' | u \rangle}{E_l - E_u - \hbar \sum_{j=1}^j \omega_{j,j-1}} \right|^2 dt - E \right) \quad (12)$$

where the thermal term has been dropped for fast processes.

The first order terms in equation (12) account for reaction during mild impact. The energy dissipation is proportional to the square of the shear modulus,  $G$ , which couples the interaction between the moving dislocations and the host lattice. Thus, all else being nearly equal, the relative sensitivity of different explosive crystals to impact should vary as the ratio of the square of their respective shear moduli. An impact insensitive crystalline explosive would have a low shear modulus, as is the case with the very insensitive explosive material TATB, which has a graphite-like structure and shear modulus. Alternatively, an intrinsically insensitive explosive molecule may release only a small amount of energy,  $u_0$ , upon dissociation or require a large

amount of energy,  $e_0$ , to cause dissociation.

At relatively high level shocks, the molecular excitation achieved by direct multi-phonon pumping of the internal molecular vibrational levels by the high energy phonons can be offset to some extent by molecular de-excitation due to decay of these excited states. Depending on the material, relaxation of the molecular vibrational level can be relatively slow, in which case molecular excitation and dissociation will occur very quickly. This is postulated to be the case with the explosives PETN, RDX and HMX which are known to have very short reaction times. The explosive TNT represents an intermediate case where the more rapid decay of the excited states would partially offset the rapid multi-phonon excitation resulting in a longer reaction time. A still more rapid vibrational decay could seriously slow or even prevent multi-phonon vibrational excitation to dissociation.

#### Extension to Multi-Crystalline Explosives

Up to this point the development has been for a single crystal for which a shear stress  $\tau$  has been applied parallel to one of its slip planes and along the slip direction. However, real explosives contain large numbers of randomly oriented crystals. To relate the single crystal results to a multi-crystalline explosive, we assumed that the slip planes of the crystals are randomly oriented in space so that, on a unit hemisphere, the probability that a slip plane lies in a plane with directions  $\theta, \phi$  is  $\sin\theta d\theta d\phi / \text{area of unit sphere}$ . The average shear stress on the slip planes of each crystal was determined to be  $\langle \tau \rangle = \tau / \pi$ . However, many crystals will have slip directions that are more closely aligned with the applied shear stress and consequently experience greater dissipation. These will cause fluctuations in the average initiation properties.

Shock and impact experiments routinely measure pressure,  $P$ , but seldom measure the shear stress. Even this pressure is an averaged quantity since the crystals in a multi-crystalline explosive charge are generally randomly sized and oriented and consequently make uneven physical contact with their neighbors. This uneven loading can introduce substantial shear forces. The maximum shear loading that could occur between crystals in uneven contact is  $\tau_A \approx P$  which produces a maximum average shear on the crystalline slip plane of  $\langle \tau \rangle_{\max} \approx P/\pi$ . The ignition threshold behavior of single crystals given in Eqn. (12) can now be extended to give the average ignition behavior of a multi-crystal explosive charge by replacing  $\tau$  with  $\langle \tau \rangle_{\max}$  as shown in Figure (2).

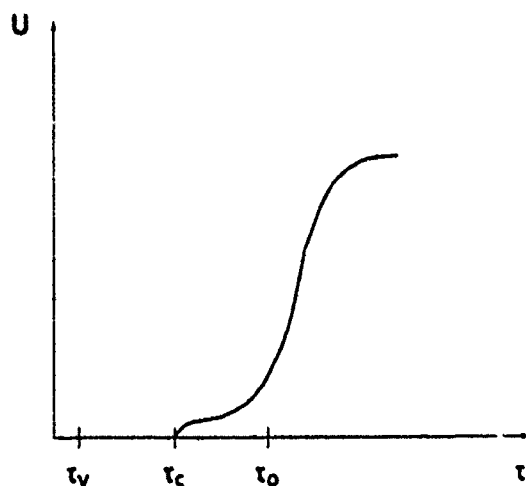


Figure (2). Predicted ignition threshold behavior for a multi-crystalline explosive charge. Transition to detonation-like multi-phonon molecular dissociation occurs at  $\tau \approx \tau_0$ .

#### Comparison with Experiment

These predictions can be compared with the experimental results on shock initiation of unconfined explosive charges obtained by Liddiard, Forbes and Price.<sup>10</sup> In these experiments a shock of known amplitude was sent down one end of an unconfined cylinder of explosive and the particle velocity due to the onset of reaction was measured at the opposite end.

To compare the predictions of Eqn. (12) for the onset of reaction in impacted or shocked multi-crystalline explosives with experimental results, let  $\tau \rightarrow \langle \tau \rangle_{\max} \approx P/\pi$  and assume that the very initial reactions are not greatly affected by reaction growth. Both theory and experiment show a similar onset of reaction at low stress levels followed at higher stress levels by a much more rapid reaction rate. In the experiments, the onset of very rapid reaction at higher shock pressure levels has been identified as the onset of detonation.<sup>10</sup> The similar onset of fast reaction in the theoretical analysis is due to the transition to fast multi-phonon driven molecular dissociation that occurs when  $\tau \approx \tau_0$ . While  $\tau_0$  remains to be determined for explosive crystals, it is unlikely that it will exceed the levels associated with the alkaline halide materials,  $.1 < \tau_0 < 1.0$  GPa. The experimental data show that for different explosive materials the average shock pressure required to cause the transition to detonation ranges from about 1.5 to in excess of 6.0 GPa.<sup>10</sup> The average shear stress at which the transition to detonation is predicted to occur in different explosives lies in the range from  $.5 < \langle \tau \rangle_{\max} < 2.0$  GPa which is similar to the range of the expected values for  $\tau_0$ .

Eliminating or severely reducing the number of moving dislocations during rapid deformation will reduce the number and intensity of shock induced hot spots within the crystal. Carefully prepared crystals of the explosives RDX, TNT, and PETN, with limited defect content and few dislocations, are nearly impossible to ignite at shock pressures often in excess of 40 GPa.<sup>11,12</sup> Similar crystals of the same materials but with high defect/dislocation content will ignite at shock pressure of 2 GPa or less.<sup>10</sup>

## SUMMARY

A quantum mechanical analysis of dislocation motion is presented which suggests that tunneling could be the means by which dislocations propagate in crystalline solids. The dissipation that occurs in a crystalline explosive during shock or impact is also a quantum mechanical process which allows molecular excitation and chemical reaction to occur at low shock or impact levels that are impossible by conventional means and accounts for the transition to a very rapid multi-phonon molecular excitation process at high amplitude shock levels.

## ACKNOWLEDGEMENTS

This work was supported by the Office of Naval Research and by the Naval Surface Warfare Center Independent Research Funds. In particular, the author wishes to thank Dr. Donald Liebenberg of the ONR and Mr. Raymond H. Riedl of NSWC for their support and encouragement.

## REFERENCES

1. A. Messiah, Quantum Mechanics, Vol. 1. (Wiley, New York, 1961). p. 77.
2. C. S. Coffey, J. Appl. Phys. 66, 1654 (1989).
3. J. D. Campbell and W. G. Ferguson, Phil. Mag. 21, 63 (1970).
4. W. G. Johnston and J. J. Gilman, J. Appl. Phys. 33, 129 (1959).
5. J. W. Swegle and D. E. Grady, J. Appl. Phys. 58, 692 (1985).
6. C. S. Coffey, Phys. Rev. B 24, 6984 (1981).
7. C. S. Coffey, Phys. Rev. B 32, 5335 (1984).
8. C. S. Coffey, J. Appl. Phys. 70 (8), 4248 (1991).
9. For the explosives PETN, TNT and TATB the shear moduli are approximately 5, 2 and  $1 \times 10^{10}$  dynes/cm<sup>2</sup> respectively. A measure of their sensitivity can be had from the drop height from which a 2.5 kg mass will cause ignition in 35 mg samples in 50 % of the impacts. For these materials  $H_{50}$  is approximately 12, 70 and  $\geq 300$  cm respectively. For other materials the agreement is not as good, but the trend is well established.
10. T. P. Liddiard, J. W. Forbes and D. Price, in Proc. of 9th Symposium on Detonation, 1989, p. 1235.
11. A. W. Campbell and J. R. Travis, in Proc. of the 8th Symposium on Detonation, 1985, p. 1057.
12. J. H. Plesch, Appl. Phys. Lett. 44, 859 (1984).

## THE IMPORTANCE OF STERICALLY HINDERED SHEAR IN DETERMINING THE SENSITIVITY OF EXPLOSIVE CRYSTALS

JERRY J. DICK

Group M-7, MS P952, Los Alamos National Laboratory, Los Alamos, NM 87545

### ABSTRACT

Sterically hindered shear in a plane shock wave in an explosive crystal is shown to be important in determining the shock sensitivity of pentaerythritol tetranitrate and nitromethane. The steric hindrance is analyzed at the intermolecular level in the unit cell, and compared to the experimental evidence.

### INTRODUCTION

A plane shock wave induces a state of uniaxial strain in a homogeneous solid. The uniaxial strain is accommodated by shear on a plane at  $45^\circ$  to the shock wave in an isotropic solid. In a crystal the shear will occur on some crystallographic plane near  $45^\circ$  to the shock and along some crystallographic direction on that plane near  $45^\circ$  to the shock direction. If the strength of the crystal is exceeded, the shear deformation will be inelastic and irreversible. In that case molecules on one side of the shear plane will be required to slide past molecules on the other side of the plane. If the molecules are sterically crowded, close approaches between atoms on molecules on opposite sides of the shear plane will occur leading to possible direct mechanical excitation and reaction. Therefore, shock directions which require shear or slip on sterically crowded slip systems will correspond to sensitive shock directions, especially at low stress levels.

### PETN ANALYSIS

Initial experimental results on pentaerythritol tetranitrate (PETN) for the crystal orientation dependence of shock sensitivity were given in Ref. 1. It was found that shock waves parallel to the  $\{110\}$  and  $\{001\}$  planes were sensitive because they could not shear on the unhindered  $\{110\}$  slip plane. The  $\{100\}$  and  $\{101\}$  shock orientations were insensitive because they could shear on the  $\{110\}$  easy slip plane. This is illustrated in Fig. 1. More complete experimental results and initial steric hindrance analysis results were provided in Ref. 2. The steric hindrance analysis considered rigid molecules and looked for intermolecular atom-atom approaches closer than  $1.7 \text{ \AA}$ . The number of close approaches was counted, and the atom-atom separations were plotted as a function of the amount of shear across the unit cell. A more sophisticated analysis using molecular mechanics is given in Ref. 3. The initial analysis in Ref. 2 correlated well with the shock sensitivity. The steric hindrance was computed for motion of the body-centered molecule across the unit cell. Since there are two molecules per unit cell, it is necessary to consider the motion of the corner molecule also for a complete analysis. The results of this are presented in Table I. The notable change is that now  $[001]$  shocks have more interactions than  $[110]$  shocks. Therefore the steric hindrance ranking in terms of total number of interactions no longer correlates completely with the shock sensitivity ranking. The  $[001]$  and  $[110]$  cases are interchanged for the two rankings. Therefore, it appears that the shock sensitivity depends in detail on the dynamical and quantum mechanical nature of the molecular interactions during the inelastic shear occurring as the molecules pass through the shock wave. More sophisticated analyses are warranted.

### ELASTIC SHOCKS IN PETN

Recently it was realized that if steric hindrance to shear flow in uniaxial strain is operative in PETN, then its effects should be manifested in the dependence of elastic shock strength on crystal orientation. The least hindered case would have the smallest elastic precursor, and the most hindered case would have the largest elastic precursor wave. Hence, a series of impact



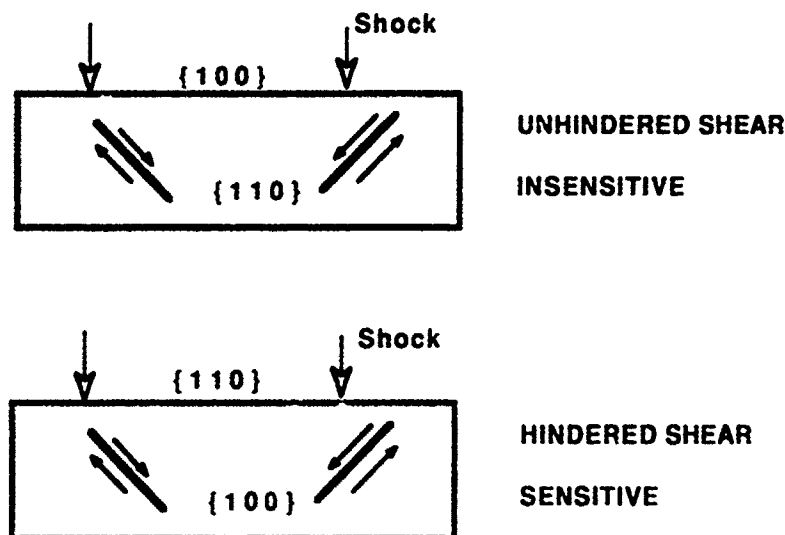


Fig. 1. Schema of the relative orientations of shock and shear planes. When the sterically unhindered  $\{110\}$  plane is available for shear, the crystal is insensitive. When the shear plane is hindered the crystal is sensitive.

experiments was performed. An aluminum projectile impacted a plus-x-cut quartz crystal 5 mm thick. The PETN crystal slab (3 to 6 mm thick) was bonded to the quartz with Sygard 184 silicone elastomer. A mirrored polymethylmethacrylate (PMMA) window was bonded to the crystal with the elastomer. The motion of the PETN/PMMA interface was monitored with a VISAR laser interferometer. Transit time through the PETN was measured using a PZT pin on the quartz crystal and the VISAR signal. Impact velocities were about 0.3 mm/ $\mu$ s. The longitudinal stress for the plastic wave was estimated to be about 1.2 GPa. Only preliminary analysis of the longitudinal stresses has been performed. In order of increasing size, the longitudinal elastic stress is about 0.37 GPa for a  $[100]$  shock, 0.58 GPa for a  $[101]$  shock, 1.0 GPa for a  $[110]$  shock, and 1.2 GPa for  $[001]$  shock. This is the same ranking as the steric hindrance from least to most hindrance (Table I) providing convincing supporting evidence for the steric hindrance model.

### STERIC HINDRANCE IN SOLID NITROMETHANE

Explosive reactions have been observed in single crystals of nitromethane when compressed rapidly in a diamond anvil cell.<sup>4</sup> The behavior was dependent on crystal orientation. The crystal deformation is neither hydrostatic nor uniaxial. Therefore the explosive behavior appears to depend on the details of the deformation process during the rapid compression process and therefore is not entirely repeatable. Nonetheless it seemed worthwhile to analyze for steric hindrance effects in nitromethane.<sup>5</sup> The analysis is not as complete as for PETN since the elastic constants, quasistatic slip systems, and dislocation structures are not known. A survey was made for hindered slip systems. Results are shown in Table II. The results show that uniaxial strain in a  $[001]$  direction will be strongly hindered. Many other directions are nearly unhindered. The results are not exhaustive, but they show that steric hindrance can play a role in solid nitromethane. If the crystal deformation is such that the maximum resolved shear stress is on a sterically hindered slip system such as  $[001]$ , then explosive reaction could occur as a result of bond breaking and subsequent reactions driven by the severe intermolecular interactions during the sterically hindered shear in the unit cell.

### SUPERCRITICAL SHEAR

Initially the inelastic or plastic shear process was modelled as due to edge dislocation motion. In this case the shear is accommodated by these line lattice imperfections sweeping through the crystal. The sterically hindered shear occurs along a line at the termination of the extra half-planes of molecules. Since PETN has two molecules per unit cell, there are

Table I. Atom-Atom Interactions for PETN.

Shock Direction	MRSS <sup>a</sup> Slip System	Atom Pair	Body-Centered Molecule		Corner Molecule	
			Number of Interactions	Closest Approach (Å)	Number of Interactions	Closest Approach (Å)
[100]	{110}<111>	O-O	3	1.05	1	1.65
[101] <sup>b</sup>	{100}<001>	O-O	4	0.78	4	0.78
[110] <sup>b</sup>	{100}<011>	O-O	9	0.54	9	0.54
		N-O	5	1.01	5	1.01
		C-O	2	0.83	2	0.83
		O-H	6	0.31	6	0.31
		N-H	4	0.80	4	0.80
		H-H	2	0.99	2	0.99
		N-N	1	1.58	1	1.58
		C-N	<u>1</u>	1.60	<u>1</u>	1.60
			30		30	
[011]	{101}<101>	O-O	3	0.86	12	0.86
		C-O	4	0.71	6	0.71
		O-H	6	0.11	10	0.11
		N-H	2	1.01	2	1.00
		C-N	1	1.52	1	1.52
		N-O	1	1.38	5	1.00
		N-N	<u>0</u>		<u>2</u>	1.58
			17		38	

<sup>a</sup>MRSS  $\equiv$  Maximum resolved shear stress.<sup>b</sup>Interactions are with the body-centered or the corner molecule but not both, for a given shear.

two adjacent half-planes. Recent analysis has shown that the critical shear stress in PETN corresponding to the measured elastic shock strengths<sup>1-3</sup> is approximately equal to estimates of the shear strength of the perfect crystal.<sup>4</sup> This is called supercritical shear, and implies simultaneous slip of one part of the crystal over the other without regard to lattice imperfections. This makes the consequences of steric hindrance even more severe. It makes it more likely that the endothermic intermolecular interactions will lead to runaway exothermic reactions and explosion or detonation.

#### DYNAMICS OF THE STERICALLY HINDERED MOLECULAR INTERACTIONS

If direct bond breaking is to occur due to the intermolecular interactions during the shear, the time scale for the interaction must be rapid. It seems worthwhile to make a rough estimate of speed of the interaction. The maximum velocity of propagation for a shear deformation is the shear wave velocity. For PETN this is about  $1.6 \text{ mm } \mu\text{s}^{-1}$  or  $1.6 \text{ nm } \text{ps}^{-1}$ . The length of the Burgers vector in PETN is about  $1 \text{ nm}$ . Therefore the shear traverses the unit cell in about 0.6 picoseconds or 600 femtoseconds. The molecular mechanics calculation done by J. Ritchie is an equilibrium calculation.<sup>3</sup> For the case of slip for a [110] shock it shows a C-O-N-O dihedral angle changing by  $60^\circ$  to  $75^\circ$  from equilibrium position in one twentieth of the Burgers vector (the resolution of the calculation). If for the sake of argument I assume that this takes place dynamically, this angle change would be forced to take place in about 30 fs. The natural

**Table II. Atom-Atom Interactions for Nitromethane.**

Shock Direction	Slip System	Shock/Slip Angle (deg)	Atom Pair	Number of Interactions	Closest Approach (Å)
[101]	{100}<001>	58.9	O-H	0	$\geq 1.70$
[101]	{001}<100>	31.1	O-H	0	$\geq 1.70$
[011]	{010}<001>	54.1	O-H	0	$\geq 1.70$
[110]	{011}<100>	50.2	O-H	2	0.97
[001]	{101}< $\bar{1}01$ >	58.9	O-H	8	1.16
			H-H	7	0.29
			C-H	4	0.36
			N-O	4	0.89
			C-C	1	1.14
			O-O	3	0.39
			N-H	2	1.15
			C-O	1	1.11
			N-N	<u>1</u>	1.53
				31	
[001]	{101}< $\bar{1}11$ >	46.7	O-H	9	0.53
			O-O	3	0.62
			N-O	5	0.58
			N-H	2	1.16
			N-N	1	1.13
			H-H	3	0.67
			C-H	2	1.23
			C-O	1	0.59
			C-N	<u>1</u>	1.21
				27	

frequency of this dihedral motion as a free rotor is  $133\text{ cm}^{-1}$  in methyl nitrate." Using an estimate of  $100\text{ cm}^{-1}$  for PETN, this corresponds to  $55\text{ fs}$  for  $60^\circ$  of rotation. The  $60^\circ$  angle change is probably much larger than the amplitude due to thermal motion in the crystal. Thus the sterically crowded intermolecular interaction happens on a time scale and with an amplitude that can force direct nonequilibrium bond breaking and reaction.

## ACKNOWLEDGMENTS

Thanks to Jim Ritchie and Robi Mulford for helpful conversations and interactions. This work was performed under the auspices of the U. S. Department of Energy and partially supported by the Office of Munitions Memo of Understanding between the Department of Energy and the Department of Defense.

## REFERENCES

1. J. J. Dick, Appl. Phys. Lett. **44**, 859 (1984).
2. J. J. Dick, R. N. Mulford, W. J. Spencer, D. R. Pettit, E. Garcia, and D. C. Shaw, J. Appl. Phys. **70**, 3572 (1991).
3. J. T. Ritchie, this symposium.
4. G. J. Piermarini, S. Block, and P. J. Miller, J. Phys. Chem. **93**, 457 (1989).
5. J. J. Dick, submitted to J. Phys. Chem.
6. J. J. Dick, to be published.
7. P. M. Halleck and Jerry Wackerle, J. Appl. Phys. **47**, 976 (1976).
8. J. J. Dick, Appl. Phys. Lett. **60**, 2494 (1992).
9. B. J. van der Vecken, G. A. Guirgis, and J. R. Durig, J. Mole. Struct. **142**, 105 (1986).

## FRACTURE SURFACE TOPOGRAPHY OF OCTOL EXPLOSIVES

M. YVONNE D. LANZEROTTI\*, JAMES J. PINTO\* AND ALLAN WOLFE\*\*

\*U. S. Army Armament Research, Development and Engineering Center, Picatinny Arsenal, NJ 07806-5000

\*\*New York City Technical College, Brooklyn, NY 11201-0000

### ABSTRACT

Energetic materials are of significant interest for scientific and practical reasons in the extraction (mining) industry, space propulsion, and ordnance. The nature of the fracture process of such materials under high acceleration is of particular interest, especially in ordnance. This paper describes new experimental and analysis techniques that allow us to characterize quantitatively and to compare the fracture surfaces of different energetic materials, and to deduce the specific fracture mechanisms. The techniques are widely applicable to other composite systems. In the materials discussed herein, topographical profiles spaced 1.0 mm apart across the fracture surfaces of two types of Octol have been obtained with a diamond stylus profilometer. Spatial power spectra (wavelengths of 1.0  $\mu\text{m}$  to 1.0 cm) have been calculated using a prolate spheroidal data window in the horizontal space domain prior to using a fast Fourier transform algorithm. The spatial power density of the fracture surface profiles is found in general to decrease with increasing spatial frequency over the region of interest,  $\approx 1 \text{ mm}^{-1}$  to  $\approx 1 \text{ cm}^{-1}$ . Quasi-periodic peaks corresponding to HMX particle sizes are observed in the Octol spatial power spectra. These peaks indicate the inhomogeneous HMX grain size distribution in the Octol fracture surfaces. Peaks in the Octol spectra indicate that intergranular fracture often occurs between the TNT and HMX grains. Fractal analysis of the Octol power spectral slopes indicates the regions of deterministic, intergranular failure and the regions of the non-deterministic, trans-granular failure through TNT or HMX grains. This non-deterministic (fractal) failure is chaotic and may indicate the origin of failure in the sample.

### INTRODUCTION

We have introduced several new fields of research to study the mechanical behavior of energetic materials during high acceleration by using an ultracentrifuge<sup>1</sup>, and to characterize the mechanical failure surfaces of energetic materials by power spectral statistical techniques<sup>2-4</sup>. This work is particularly relevant to the future development of insensitive energetic materials used in weapons with higher acceleration.

We have underway a program for studying in detail the fracture behavior of TNT, Composition B (59% cyclotrimethylene-trinitramine (RDX), 40% TNT, and 1% wax), and two types of Octol (70% cyclotetramethylene-tetranitramine (HMX) and 30% TNT;  $\approx 83\%$  HMX and  $\approx 17\%$  TNT) using an ultracentrifuge<sup>2-4</sup>. This program includes especially the study of the characteristics of the fracture surfaces of the materials. In this paper, the results and conclusions obtained from statistical studies of the fracture surface topography along several parallel scans across the fracture surfaces of two types of Octol are described.

### TECHNIQUE

The fracture surfaces of the energetic materials under study are obtained by accelerating prepared samples in a Beckman preparative model L8-80 ultracentrifuge. The sample under study can be rotated up to 60,000 rpm (500,000 g). When the tensile or shear strength of the object material is exceeded, a fracture surface is obtained. A diamond stylus profilometer<sup>5</sup> has been used to measure the topography of the surface after removal of the sample. Profiles have been obtained at several locations spaced approximately 1.0 mm apart across the surface. Spatial wavelengths along each trace of 1.0  $\mu\text{m}$  to approximately 1.0 cm have been statistically characterized. Spatial power spectra have been calculated from the data of the individual traces using a prolate spheroidal data window<sup>6,7</sup> applied in the horizontal space domain prior to using a fast Fourier transform algorithm<sup>8</sup>.

## RESULTS

The sample of melt-cast 70/30 Octol reported here was found to fracture at an acceleration of 41,000 g at 25°C. The logarithmic normal crystal size distribution of HMX as specified by military specification Class 4<sup>9</sup> is shown in Figure 1. The spatial power spectra of the fracture surface profiles across traces g and h (see inset) of 70/30 Octol are shown in Figure 2. The distribution of peaks in the spatial power density shows the inhomogeneous grain size of the HMX in 70/30 Octol. The HMX grain sizes vary discontinuously from  $\approx 0.1$  mm to  $\approx 1.0$  mm in contrast to Class 4 HMX particle size in Figure 1. Figure 2 also shows how the inhomogeneous HMX grain size distribution changes with location across the surface. In Figure 2 the spatial power spectra for 70/30 Octol falls off with increasing spatial frequency. The solid and starred lines superimposed on the spectra traces are linear fits to the sections of the spectra corresponding to the line lengths.

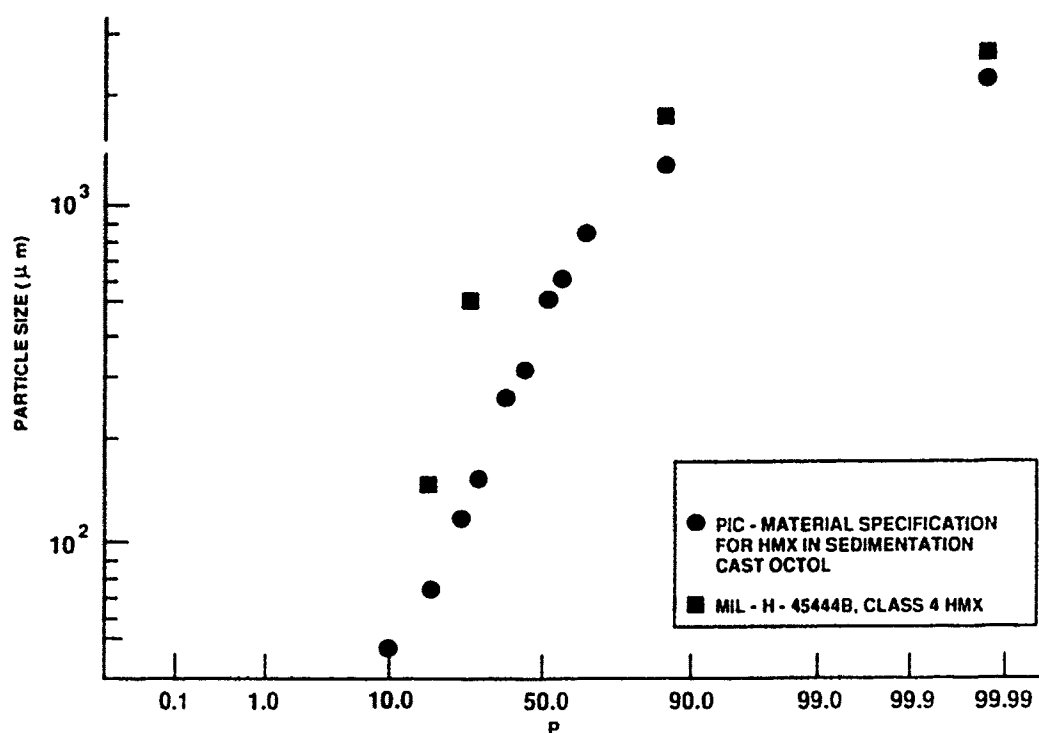


Figure 1. HMX Particle Size Distribution

The variation of the spectral slope across the surface is of considerable interest. In the frequency interval  $10^0 \text{ mm}^{-1}$  to  $10^1 \text{ mm}^{-1}$  the spectral slope of trace g is -3.9. The spectral slope of trace h is -2.7 in this frequency interval. The absolute value of the spectral slopes for profiles c through h are plotted in Figure 3 as a function of the sample trace. The spectral slopes for profiles i through m and c through g are  $\leq -3$ . The fractal dimension equals one for these profiles. Peaks, that correspond to HMX grain sizes, as well as the fractal dimensions of one indicate that, in general, intergranular failure is occurring at grain boundaries.

For spectral slopes,  $s$ , that lie in the range  $-3 < s \leq -2$ , the fractal dimension is given<sup>10-13</sup> by

$$s = -(5-2D), \quad (1)$$

where  $D$  is the fractal dimension. Equation (1) indicates that the fractal dimension for profile h is 1.1. This chaotic failure indicates that transgranular failure occurs through the grain. The chaotic region suggests that the origin of the failure is at the edge of the sample.

The sample of sedimentation-cast 83/17 Octol reported here was found to fracture at an acceleration of 60,000 g at 25°C. The logarithmic normal crystal size distribution of HMX as specified by PIC Material Specification for Sedimentation Cast Octol<sup>14</sup> is shown in Figure 4. The spatial power spectra of the fracture surface profiles across traces a and f (see inset) of 83/17 Octol are shown in Figure 5. The distribution of peaks in the spatial power spectra shows the inhomogeneous grain size of the HMX in 83/17 Octol. The HMX grain size varies discontinuously from  $\approx 0.1$  mm to  $\approx 1.0$  mm in contrast to the HMX particle size distribution used in sedimentation cast Octol as shown in Figure 4. Figure 4 also shows how the inhomogeneous HMX grain size distribution changes with location across the surface.

In the frequency interval  $10^0 \text{ mm}^{-1}$  to  $10^1 \text{ mm}^{-1}$  the spectral slope of trace f is -4.1. The spectral slope of trace a is -2.4 in this frequency interval. The absolute value of the spectral slopes for profiles a through f of 83/17 Octol is plotted in Figure 5 as a function of the sample trace. The spectral slopes of sample traces g through l and c through f are  $\leq -3$ . The fractal dimension equals one for these sample traces. Peaks that correspond to HMX grain sizes, as well as fractal dimensions of one, indicate that, in general, intergranular failure is occurring at grain boundaries.

The fractal dimension for profiles a and b are 1.3 and 1.2, respectively. This chaotic failure indicates that failure occurs through the grain: transgranular failure. The chaotic region suggests that the origin of the failure is at the edge of the sample.

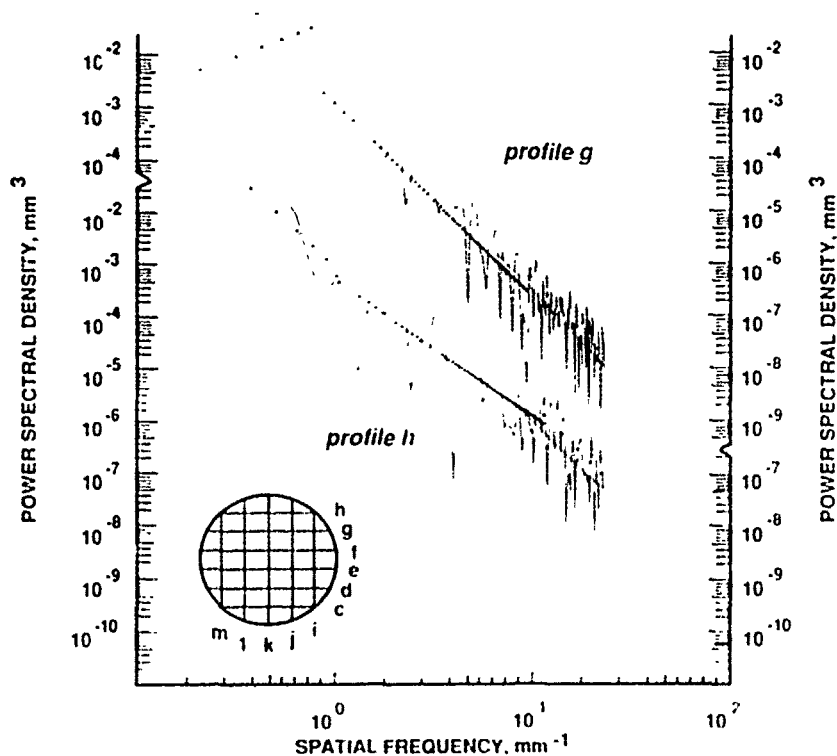


Figure 2. Spatial power spectra of the fracture surface for sample traces g and h of 70/30 Octol. The locations of the profile traces across the sample surface are shown in the inset. Diamond stylus horizontal spacing is 0.004 mm.

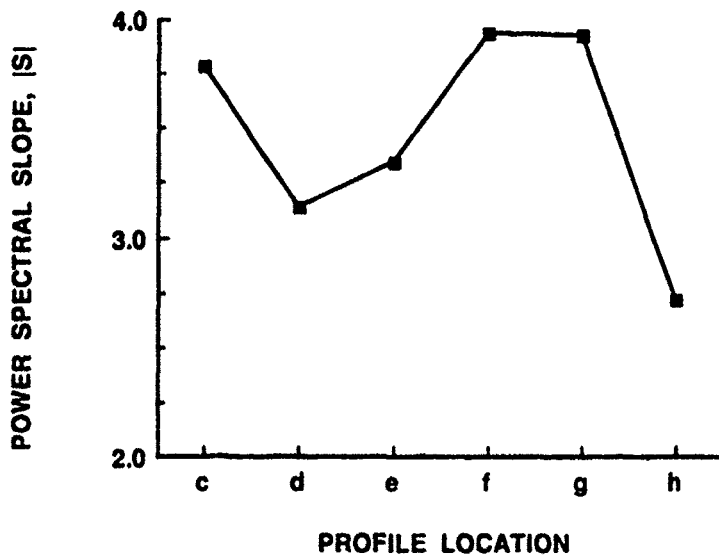


Figure 3. Spectral slopes versus profile location c through h of 70/30 Octol for spatial frequency interval  $10^0 \text{ mm}^{-1}$  to  $10^1 \text{ mm}^{-1}$ .

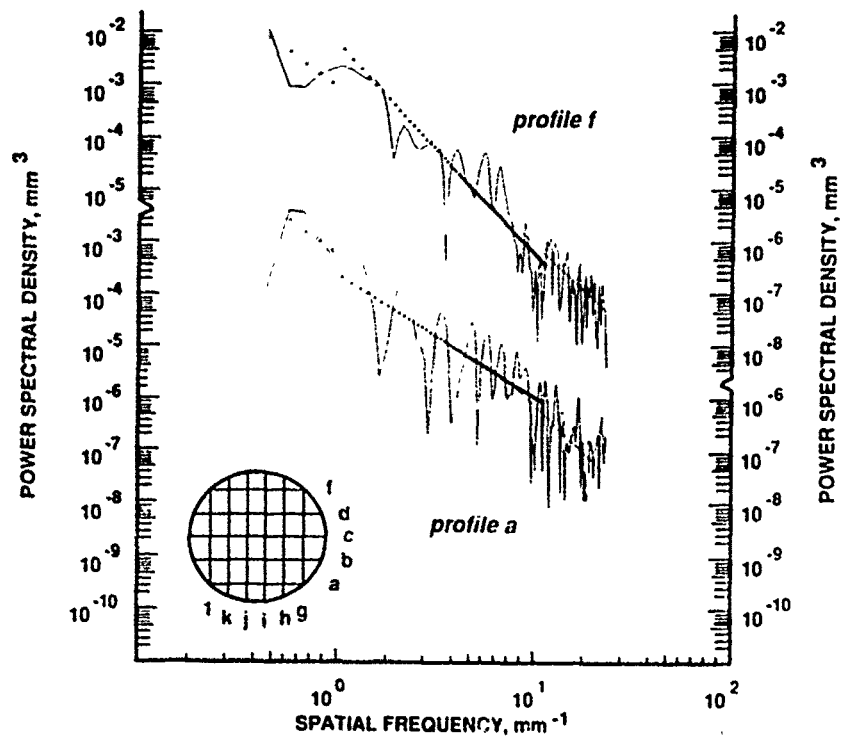


Figure 4. Spatial power spectra of the fracture surface profiles for sample traces a and f of 83/17 Octol. The locations of the profile traces across the sample surface are shown in the inset. Diamond stylus horizontal spacing is 0.004 mm.



## DISCUSSION

The results of Figures 2-3 show clearly that the fracture process under high acceleration of our 70/30 Octol sample tends to occur between the TNT and HMX grains. The results of Figure 3 show that the grain-boundary determination of the fracture is strongest at the center and at three of the four edges of the sample. A fractal dimension of 1 for these profiles is consistent with this interpretation. Figure 3 shows that transgranular failure occurs at one edge of the 70/30 Octol sample. The fractal dimension found for the other edge trace is consistent with this interpretation.

The results of Figures 4-5 show clearly that the fracture process under high acceleration of our 83/17 Octol sample tends to occur between the TNT and HMX grains. The results of Figure 4 show that the grain-boundary determination of the fracture is strongest at the center and at three of the four edges of the 83/17 Octol sample. A fractal dimension of 1 for these profiles is consistent with this interpretation. Figure 5 shows that transgranular failure occurs at the other edge of the sample. The fractal dimensions found for two traces at the same edge are consistent with this interpretation.

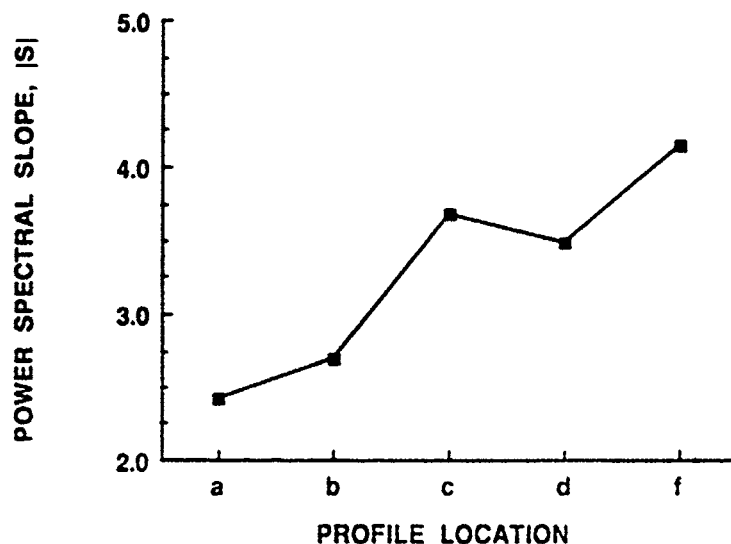


Figure 5. Spectral slopes versus profile location a through f of 83/17 Octol for spatial frequency interval  $10^0 \text{ mm}^{-1}$  to  $10^1 \text{ mm}^{-1}$ .

## CONCLUSIONS

Understanding of the fracture and rupture of energetic materials subjected to high acceleration is a key to better practical designs in several fields, including ordnance, the extraction industry, and space propulsion. In such applications the materials can often be subjected to high, fluctuating, and/or sustained accelerations. We have introduced fractal concepts and techniques to characterize the fracture surface topography of energetic materials obtained at high acceleration.

These concepts have provided new statistical ways to characterize grain sizes of explosives. Of particular importance, these experimental and analysis techniques now allow quantitative comparisons to be made between different energetic materials so that improvements and changes in cast and composition of energetic materials can be verified. These concepts have also provided unique insights into the fundamental physics of the fracture process of explosives. For example, we have demonstrated that in general intergranular fracture occurs at grain boundaries or between grains in a mixture. We have also observed chaotic transgranular fracture through the grain that may indicate the origin of the failure in the sample. We have also shown that the chaotic failure at

the sample edge appears to be similar for 70/30 Octol and 83/17 Octol. This is in contrast to chaotic failure through the sample center observed for Composition B and TNT<sup>3-4</sup>. The origin of the chaotic failure varies systematically with the percentage of TNT in the composition.<sup>3-4</sup>

This work, both in the laboratory and in the field verification, is a major breakthrough in improving the understanding of the behavior of energetic materials during the gun launch process. This work also confirms that the value of relatively inexpensive laboratory experiments conducted in an ultracentrifuge, combined with sophisticated analysis and statistical techniques, can provide important new discoveries that are relevant and important to the gun launch process. We believe the experimental and analysis techniques used here have wide applicability in future studies of energetic materials.

## ACKNOWLEDGEMENT

We would like to thank J. Rowe, R. Dunn, C. G. MacLennan, and D. J. Thomson, AT&T Bell Laboratories, Murray Hill, NJ, for helpful discussions regarding the data analysis.

## REFERENCES

1. M. Y. D. Lanzerotti and J. Sharma, App. Phys. Lett. 39 (1981) 455.
2. M. Y. D. Lanzerotti, J. Pinto and A. Wolfe, "Broad Bandwidth Study of the Topography of the Fracture Surfaces of Explosives", in The Ninth Symposium (International) on Detonation, Volume 1, pp. 355-361, 28 August - 1 September 1989, Portland OR.
3. M. Y. D. Lanzerotti, J. Pinto, and A. Wolfe, "Fracture Surface Topography of Cast TNT", in Shock Waves in Condensed Matter, 1991, eds. S.C. Schmidt, R.D. Dick, J. W. Forbes, D. G. Tasker (1992 Elsevier Science Publishers B. V., Amsterdam, The Netherlands) pp. 575-8.
4. M. Y. D. Lanzerotti, J. Pinto, A. Wolfe, and D.J. Thomson, "Power Spectral Characterization of Fracture Surfaces of TNT, Composition B, and Octol", 1992 Army Science Conference, Kissimmee, FL, 22-25 June 1992, in press.
5. F. P. Bowden and A. D. Joffe, Initiation and Growth of Explosion in Liquids and Solids (Cambridge University Press, 1952).
6. D. J. Thomson, Spectral Analysis of Short Series, Ph. D. Dissertation, Department of Electrical Engineering, Polytechnic Institute of Brooklyn, Brooklyn NY, 1971.
7. D. J. Thomson, Proc. IEEE, 70, 1055 (1982).
8. D. J. Thomson, et al, Physics of the Earth and Planetary Interiors, 12, 217 (1976).
9. HMX, MIL-H-4544B (PA), 27 February 1974.
10. S. R. Brown and C. H. Scholz, J. Geophys. Res. 90, 12,575 (1985).
11. S. E. Hough, Geophys. Res. Lett. 16, 673 (1989).
12. B. B. Mandelbrot, The Fractal Geometry of Nature (Freeman, NY, 1983).
13. B. B. Mandelbrot, Physica Scripta, 32, 257 (1985).
14. PIC Material Specification for Sedimentation Cast Octol, 1986.

## THE ELECTRON-BEAM SENSITIVITY OF BINARY METAL AZIDES

PATRICK J. HERLEY\* AND WILLIAM JONES\*\*

\*Department of Material Science and Engineering, State University of New York, Stony Brook, N.Y. 11794-2275, USA.

\*\*Department of Chemistry, University of Cambridge, Cambridge, CB2 1EW, UK.

### ABSTRACT

The metal azides (or azido complexes) of La, Ce, Ti, Fe(III), Co, Ni, Pd, Ag, Tl, Cd, Sn, Sb and Bi have been synthesised and subjected *in situ* within a high resolution transmission electron microscope, to electron-beam fluxes (ca 0.1-1.0 A/cm<sup>2</sup>) to induce rapid decomposition. The materials, which are highly energetic and some are reportedly explosively sensitive, were carefully handled during synthesis to avoid mechanical shock, and only microgram quantities were decomposed whilst on holey carbon support films. In all cases beam-induced decomposition was very rapid. The exothermicity of the reaction induced in the beam promotes vigorous melting which either precedes or is accompanied by radiolysis. The net result is a rapid evolution of nitrogen (product) gas, which causes atomisation and spallation of the metal products. These molten metal particles are hard landed on a 300-500  $\mu\text{m}^2$  area of the support film with diameters in the nanometre size range. Data is presented on the synthesis of the azides, the nature of the beam-induced process as well as representative electron micrographs of some of the pristine starting materials and the nanoparticulate products.

### INTRODUCTION

Inorganic metal azides and azido-complexes form a set of energetic materials that reportedly decompose explosively with high brisance when exposed to thermal and mechanical shock [1]. As a novel route to form clean and reactive nanoparticles *in situ* in a high resolution electron microscope (HREM) we have initiated a study of the electron-beam decomposition of a series of these azides. Decomposition was carried out under an electron flux of approximately 0.1-1.0 A/cm<sup>2</sup> within the microscope. Such experimental conditions offer exposures involving very large localised electron densities - a plasma of ionising radiation capable of simultaneously inducing radiolysis and pyrolysis. Under certain circumstances, it is possible, to subject samples *in vacuo* to deposition of the entire available energy over an area subtended by the beam (16). In these cases energy deposition is highly localised and the experiment requires only nanogram quantities of pristine material. This requirement of nanogram quantities is an important advantage of the technique given the apparent explosive nature of these materials.

Classification of the metal azides in terms of their sensitivity and energy release on explosion is difficult - for example see Chapter 1, reference 1. A simple criteria which may be used is by their bond strengths i.e. by the formal ionicity of the M--N bond. Using these criterion the azides under investigation here range between 63 and 30% ionicity (with Pd the exception at 13%). However, not all the azides, unlike the halides, are simple compounds. Different metals result in varying complex bond structures. A more definitive classification takes into account the complexity of the various types of bonding and results in a division of the metal azides into 5 distinct classes - i) normal, N; ii) mixed, M; iii) hetero, H; iv) azido complexes, C; and v) metal organo complexes, O. These abbreviations are included in the synthesis below to indicate the type of azide formed.

Although the method of synthesis of these solids has been reported [1], apart from their explosive properties, little attention has been given to studies of their physical and chemical behaviour when exposed to decomposition-inducing stimuli. For instance, data are not available on their behaviour when exposed to sufficient electron flux densities, *in vacuo*, to induce decomposition.

We report here on the synthesis, handling procedure and electron beam decomposition of these solids. We also present selected examples of the nanosized particles after atomisation.

## EXPERIMENTAL

### Synthesis

Binary metal azides of Ti, La, Fe(III), Co, Ni, Pd, Ag, Cd, Tl, Sn, Ce and Sb have been produced by the metathetical reaction of the corresponding chloride (or nitrate) with sodium azide or potassium azide in aqueous or ethanolic solutions. When necessary the pH of the solution was adjusted to prevent hydrolysis. In some instances, depending on the type of bonding, azido complex anions may be formed which precipitate as the sodium or potassium salt (for example in the cases of Sn, Ni and Ce). In other cases (e.g. Ti and Sb) a dichloride-azide complex of the type  $(N_3Cl_2)^-$  results.

We have not verified the stoichiometry of the synthesised materials; they were prepared following the procedures indicated in reference 1. After precipitation the final products were subjected to repeated washing to remove the impurity ions in solution. Each batch of crystals, however, were subjected to an *in situ* chemical analysis in the electron microscope prior to decomposition using Energy Dispersive X-ray Analysis. Abbreviated details of the synthesis of each of the azides is given below, with comments concerning stability and purity. In each case, unless otherwise noted, stoichiometric amounts of reagent grade quality reagents were used. More specific details regarding the full synthesis procedure will be found in reference 1.

**Titanium azide** Titanium chloride and sodium azide in acid (HCl) solution produced a white flocculate precipitate (M) of  $Ti(N_3)Cl_3$  which was washed several times with water. Reportedly the material is sensitive to rapid heating and mechanical shock [2]. The material decomposed in the beam, dispersing Ti metal.

**Manganese (II) azide** Manganese (II) chloride was reacted with sodium azide in ethanol to produce a white precipitate (C) of basic  $(OH)Mn(N_3)$  on standing. It reportedly explodes above 218 °C in a flame [3] but is not sensitive to mechanical shock. The material decomposed readily in the beam.

**Ferric azide** Ferric sulphate was reacted with sodium azide to form a dark red precipitate (which on evaporation yields black-brown crystals of ferric azide) (N) [4]. The precipitate was repeatedly washed until free of sulphate ions.

**Cobalt azide** A solution of cobalt nitrate  $(Co(NO_3)_2 \cdot 6H_2O)$  was reacted with a sodium azide solution to form a precipitate of cobalt azide (N). The solution was slightly acidified to reduce the likelihood of the hydrolysis of the azide to form  $(OH)Co(N_3)$ . This material reportedly explodes with high brisance when shocked thermally or mechanically and its sensitivity is the highest of all metal azides [4,5].

**Nickel azide** Nickel azide forms a complex hexa-azidonickelate(II) ion  $[Ni(N_3)_6]^{4-}$  when a nickel sulphate solution is mixed with a tenfold excess of potassium azide, and precipitated in alcohol. The white precipitate (C) (presumably the potassium salt) contained traces of potassium sulphate and was washed several times by decantation to remove traces of the sulphate ion before use. The material deflagrates but reportedly is not sensitive to mechanical shock [6].

**Palladium azide** A dense brown-black solid (M) resulted from a mixture of palladium chloride and sodium azide. The azide is very sensitive to heat, friction and impact and reportedly cannot be dried without exploding [7]. This material was found to explode when subjected to intense irradiation in the beam. No further investigations were carried out.

**Silver azide** The synthesis of silver azide (N) has been described elsewhere [8]. The material is photosensitive and explodes when heated rapidly at 300 °C. It was stored in the dark in ammoniacal solutions until use.

**Cadmium azide** A white crystalline solid (N) which tends to hydrolyse is formed when a solution of cadmium nitrate is reacted with azide ions. To minimise the formation of basic products the reaction is carried out in ethanol using potassium azide. The material is certainly an explosive but its sensitivity is questionable. Reportedly it decomposes with explosion between 190 and 330 °C. Depending upon sample amount [9], crystal size [10] and loading density [11], however, it has also been reported to explode spontaneously at room temperature [11]. The material decomposes readily in the electron microscope.

**Thallium azide** This material is very sensitive in thin layers. It explodes but with low impact sensitivity. The white, dense solid (N) was made by mixing a thallium sulphate solution with warm sodium azide [12].

**Tin azide** The sodium salt of the  $[\text{Sn}(\text{N}_3)_6]^{2-}$  complex forms a white precipitate (C) when tin chloride is mixed with excess sodium azide in aqueous solution. The precipitate is reportedly not very sensitive and deflagrates when shocked thermally, but is stable to impact [13].

**Antimony azide** When antimony chloride is mixed with potassium azide in ethanol a white flocculated precipitate (M) results. It has been reported [14,15] that the material is antimony azidochloride or chloroazide,  $\text{SbCl}_4\text{N}_3$ . The material explodes when mechanically or thermally shocked. Decomposition begins at  $107^\circ\text{C}$  followed by melting at  $131^\circ\text{C}$  and explosion. This material decomposes with melting in the electron beam.

**Bismuth azide** When bismuth nitrate is dissolved in hot HCl and then a solution of sodium azide is added to slight excess an immediate, slightly-pink, precipitate of the azide forms (M?). No details on the stability of this compound are available but it readily melts and decomposes in the electron beam.

**Cerium azide** Cerium sulphate slightly acidified with sulphuric acid to prevent hydrolysis, on reaction with sodium azide reportedly forms a basic azide complex (C) of the type  $(\text{N}_3)_2\text{CeO}(\text{N}_3)_2$  or  $(\text{OH})_2\text{CeO}(\text{N}_3)(\text{OH})$ . The material was used as synthesised and produced metallic cerium on electron beam decomposition after premelting.

**Lanthanum azide** Lanthanum chloride, slightly acidified with HCl, was added to a sodium azide solution to produce a light-brown very fine precipitate which settled on standing. Again, as for Ce above, this is most likely a basic azide (C). The material was used as synthesised.

Although among these materials are reportedly some of the most sensitive azides (e.g. Co) other more familiar explosive azides (which are known to be hazardous in small quantities e.g. copper, lead, mercury) were not examined. Now included in this later group is palladium azide which we found to explode when exposed to the electron beam in the microscope and was not, therefore, examined further.

### Technique

Since, in general, these materials are highly energetic and explosively unstable, it was felt that minimisation of mechanical shock should be of paramount importance. As a result only moist materials were handled. Only when small micron-sized samples were withdrawn for deposition on the grid for electron decomposition were the crystallites allowed to dry. The method of beam-decomposition has been reported elsewhere [16]. The microscopes used were a JEOL 2010 HREM and a Philips CM12. Both microscopes had EDAX and EELS attachments.

The quantity typically covered directly by the beam at low magnification is approximately  $10\text{ }\mu\text{m} \times 10\text{ }\mu\text{m}$  in size. It was felt that microcrystals below  $\sim 10\text{ }\mu\text{m}^2$  should be safe to produce *in situ*. We were guided in selecting this value by the previous work of Bowden *et al* [17] who reported that particles of  $\text{AgN}_3$  that had been melted in the beam and resolidified into beads did not explode below a particle size of  $\sim 40\text{ }\mu\text{m}$  when exposed to the electron beam.

## RESULTS AND DISCUSSION

The metal azides synthesised in this study are microcrystalline aggregates of varying morphologies. Figure 1 illustrates micrographs obtained. Prior to decomposition a microcluster approximately  $1\text{--}5\text{ }\mu\text{m}$  in size is selected such that the particles generated from the atomisation can be deposited unhindered onto the holey carbon.

With the exception of palladium all of the azides melted during or prior to decomposition. The molten materials did not wet the holey carbon substrate. The azides (La, Ce, Fe(III), Co, Ni, Ti, Cd, Sn, Sb and Bi) behave similar to silver azide on electron decomposition: after melting, the (exothermic) decomposition results in a rapid evolution of nitrogen gas and a spalling of fine particles radially from the central molten bead. A typical example of the process is shown in Figure 2 for thallium azide. Some azides melt and decompose readily (Ti, Sn, Co, Ag) others require a longer, more intense exposure (Ni, Sb, Ti, Ce, Mn). However, all generate metallic nanoparticles in the size range from ca  $100\text{--}1\text{ nm}$ . The results are reproducible and predictable provided stringent handling conditions are used.

Depending on the electron flux and size of the pristine cluster, either individual (i.e. separate) or overlapping particles can be generated. Their size and density vary with distance from the decomposing bead for a given azide but the overall effects are similar; the larger particles lie closest to the bead. In virtually all cases the lower size limit of the particle is less than  $10\text{ }\text{\AA}$ .

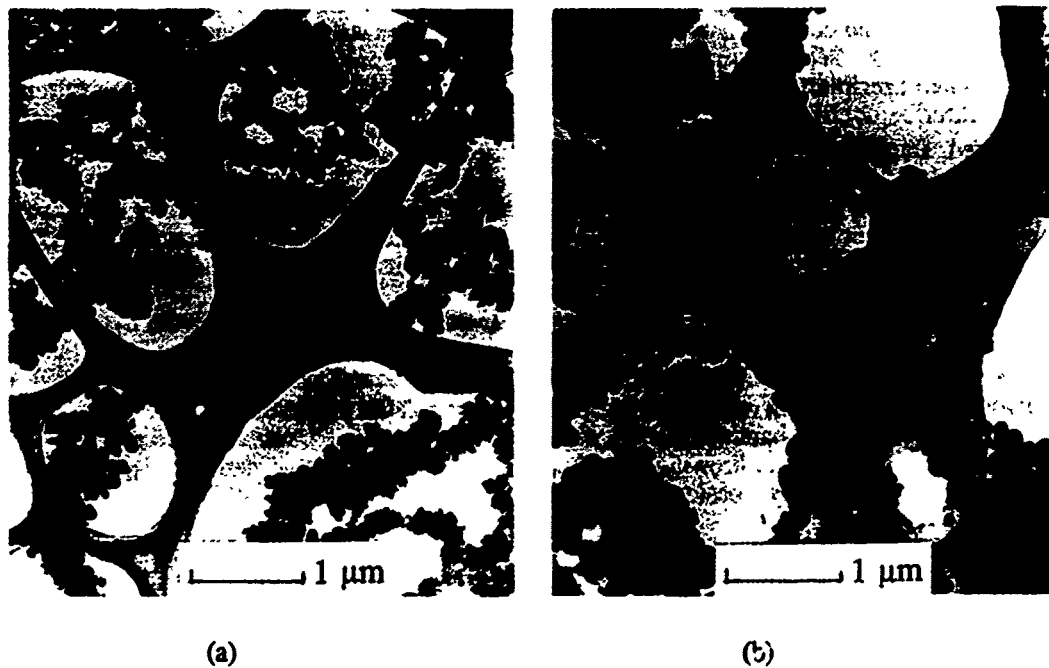


Figure 1. Electron micrographs obtained from the starting azide materials for (a) silver and (b) palladium azide.

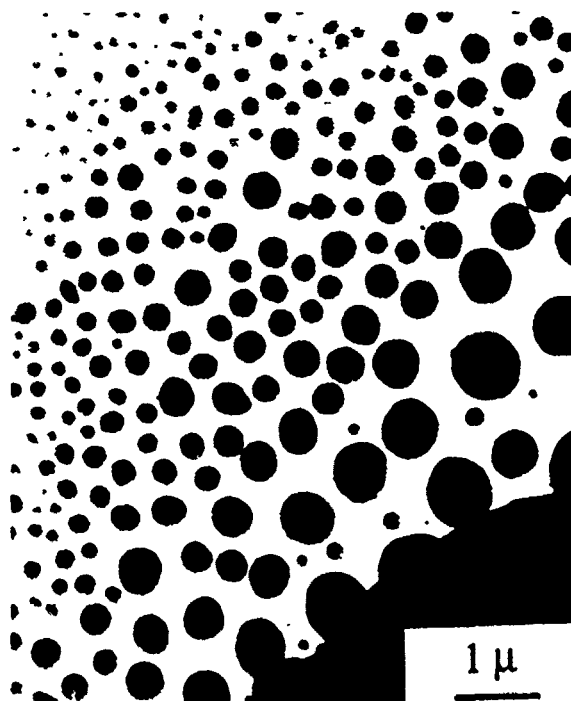


Figure 2. Transmission electron micrograph illustrating the distribution of particles from thallium azide.

Typically, the particle density (i.e. number of particles per unit area) reaches a maximum of 300 at a distance between 1.75 and 2  $\mu\text{m}$  from the source. In addition to the variation in size and density, the particle morphology also varies considerably across the size range. All the conventional shapes described by Uyeda [18] from metal smokes have been identified. Some morphologies are shown in Figure 3.

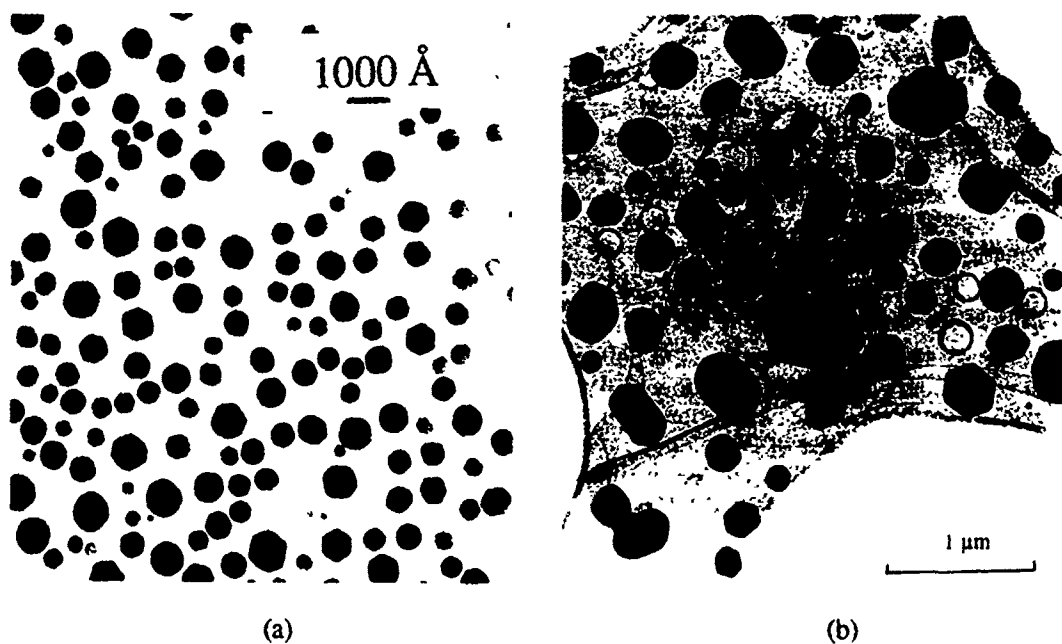


Figure 3. Particle morphology for microcrystallites resulting from (a) bismuth and (b) thallium azide.

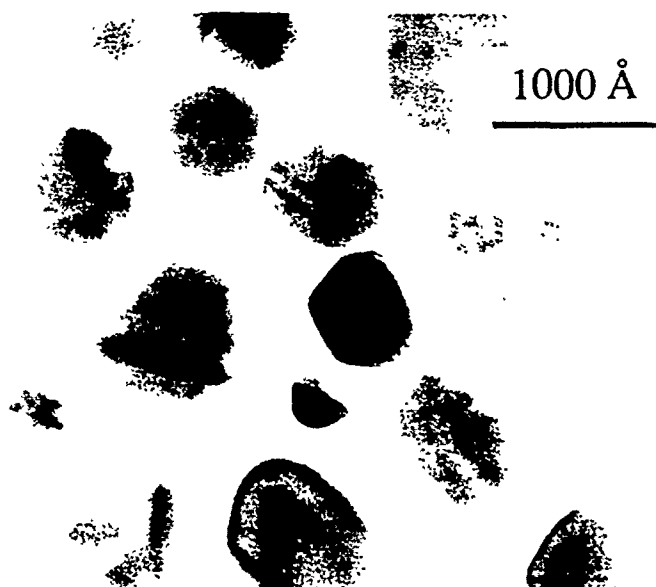


Figure 4. Defective crystallites obtained from decomposition of thallium azide.

While the majority of the nanoparticles appear to be single crystals, some contain intrinsic defects, principally stacking faults and twins (Figure 4). Multiply twinned particles are also formed. The formation of defects in these particles may be as a result of the hard landing the molten particle makes with the substrate. Also, the particles are travelling at a high velocity and can induce a high local temperature on impact. Computer simulations of a cluster travelling at 3 kilometres/sec onto a substrate surface can induce a local nano-shock phenomena of up to 106 kPa and kinetic heating to over six times room temperature ( $>3000\text{K}$ ) [19]. These impacting molten particles may thus act as initiation (nucleating) sites in surrounding material.

Notwithstanding this hard landing effect, the method is a viable technique for the generation, as required, of nanosized metal particles at specific locations on the grid *in situ* in the HRTEM repeatedly. Initially the nascent particles appear to be protected by the evolving nitrogen gas, and subsequent interaction with the vacuum gases can be monitored over a period of time. Further details of these studies will be reported elsewhere [20].

The reason for the absence of explosion/detonation in these materials of known ultra-sensitivity is most likely that suggested by Bowden previously for cadmium, lead and silver azides [17]. He exploded these azides in a 200  $\mu\text{A}$ , 75 keV electron beam but concluded that a critical size is required for the hot spot to initiate explosion. He showed that the critical size has to be ca 26-46  $\mu\text{m}$ . Our materials are polycrystalline with the actual microcrystallite size at least several orders of magnitude below this value. Indeed we have deliberately sought out ultrafine particles to prevent such explosions from occurring in the microscope.

The behaviour of Pd azide is anomalous. Admittedly it does have one of the lowest M-N bond ionicities (the lowest is Au-N[1]) and it is reportedly extremely sensitive. Notwithstanding we were able to obtain micrographs of this pristine material (Figure 1(b)) and only on exposure to an intense focused beam did the material explode. We conclude either that the hot spot is much smaller in this azide or that the dense black material aggregates or packs in such a way as to have a much higher density of material in a ca 1  $\mu\text{m}$  clusters studied.

## ACKNOWLEDGEMENTS

Financial support from NATO (award INT890275), NSF (award INT8911940) and VAL-ERO (contract DAJA45-90-C0013) is acknowledged. We appreciated the help given by Dr D A Jefferson.

## REFERENCES

1. Energetic Materials, Eds. H. Fair and R. F. Walker, Plenum Press, 1977.
2. K. Dehnicke, J. Inorg. Nucl. Chem., **27**, 809 (1965)
3. T. Curtius and A. Darapsky, J Pract Chem., **61**, 408 (1900)
4. L. Wohler and F. Martin, Ber. Dtsch. Chem. Ges., **50**, 586 (1917)
5. L. Wohler and F. Martin, Angew. Chemie, **27**, 335 (1914)
6. H. P. Fritzer and K. Torkar, Monatsh. Chem., **99**, 2333 (1968)
7. R. G. Clem and E. H. Huffman, J. Inorg. Nucl. Chem., **27**, 365 (1965)
8. P. J. Herley and W. Jones, J. Chem. Soc. Farad. Trans., **88**, 3213 (1992)
9. L. Wohler and F. Martin, Angew. Chemie, **30**, 33 (1917)
10. D. Forster and W. D. Horrocks, Inorg. Chem., **5**, 1510 (1966)
11. Y. Mizushima, Tokyo Kogyo Shikensho Hokoku, **59**, 209 (1964)
12. L. M. Dennis and M. Doan, J. Am. Chem. Soc., **18**, 970 (1896)
13. L. Wohler, Angew. Chemie, **35**, 294 (1922)
14. U. Muller and K. Dehnicke, Z. Anorg. Allg. Chem., **350**, 113 (1967)
15. N. Wiberg and K. H. Schmid, Chem. Ber., **100**, 741 (1967)
16. P. J. Herley, N. P. Fitzsimons and W. Jones, in Materials Research Society, Specimen Preparation for Transmission Electron Microscopy of Materials III, Eds. R. Anderson, T. Brayman and B. Tracy, 1992, **254**, 223.
17. F. P. Bowden and K. Singh, Proc. Roy. Soc. A, 1955, **227**, 22.
18. R. Uyeda, in Morphology of Crystals, Ed. I. Sunagawa, Terra Scientific Pub. Co. Tokyo, Part B, Chapter 6 (1987).
19. C. L. Cleveland and U. Landman, Science, **257**, 355 (1992).
20. P. J. Herley and W. Jones, to be published.



## COMPARISON OF DEFORMATION AND SHOCK REACTIVITY FOR SINGLE CRYSTALS OF RDX AND AMMONIUM PERCHLORATE

H.W. SANDUSKY\*, B.C. BEARD\*, B.C. GLANCY\*, W.L. ELBAN\*\*, AND R.W. ARMSTRONG\*\*\*

\*Naval Surface Warfare Center, 10901 New Hampshire Ave., Silver Spring, MD 20903

\*\*Loyola College, Dept. of Electrical Engineering and Engineering Science,  
4501 N. Charles Street, Baltimore, MD 21210

\*\*\*Univ. of MD, Dept. of Mechanical Engineering, College Park, MD 20742

### ABSTRACT

Deformation of cyclotrimethylenetrinitramine (RDX) and ammonium perchlorate (AP) crystals at low strain rates was studied by diamond pyramid (Vickers and Knoop) microindentation hardness testing. RDX is two to three times harder than AP and has relatively limited slip system activity. While both crystals readily crack, cracking did not reduce hardness in RDX but did in AP. Strain fields surrounding the hardness impressions in RDX were extremely localized while in AP they extended well beyond the impressions. Shock experiments were conducted on large (5-9 mm), single crystals in a fluid-filled tank designed to permit high-speed photography and sample recovery. Reaction threshold was obtained by varying the shock pressure entering the crystals. Shock-entry orientation and large hardness impressions were used to alter microstructural responses. High-speed photography showed luminous crack propagation and reaction in both materials and the same slip deformation in AP as from hardness testing. Orientation affected the microstructural response and reaction threshold for AP, and hardness impressions sensitized chemical decomposition far from the impressions. Recovered AP crystals were much more plastically deformed than RDX crystals and were often still transparent in the region opposite shock entry. Recovered RDX crystals, at even the lowest shock pressure of 8.6 kbar, were uniformly white from a high density of fine cracks. RDX reaction threshold was ~62 kbar versus 17 to 24 kbar for AP, depending on crystal orientation to the shock wave.

### INTRODUCTION

Several experimental studies have shown that material microstructure influences the shock reactivity of energetic crystals. Dick<sup>1</sup> determined that reaction was a function of crystal orientation relative to planar shocks in large single crystals of pentaerythritol-tetranitrate (PETN). In addition, Dick<sup>2</sup> found increased shock sensitivity for PETN crystals which had been microscopically damaged with gamma radiation. For two production lots of cyclotetramethylene-tetranitramine (HMX) from different manufacturers, Green and James<sup>3</sup> observed increased shock sensitivity in HMX/Viton formulations which contained crystals from the lot with the higher concentration of defects. The current work was undertaken to demonstrate that chemical decomposition from shock interaction with relatively defect-free crystals of AP and RDX occurs preferentially at sites of microstructural damage resulting from operative slip and cracking systems. It was also of interest to assess the effect that large strain centers have on the shock reactivity of these materials.

### EXPERIMENTAL APPROACH

Large (>1 cm edge dimensions), optical quality, single crystals of AP and RDX were provided, respectively, by T.L. Boggs of the Naval Air Warfare Center, China Lake, CA and H. Cady of the Los Alamos National Laboratory, Los Alamos, NM. Smaller (approaching 5 mm in size) RDX

crystals of lesser quality were grown.<sup>4</sup> The microstructural response of crystals to quasi-static loads was determined by diamond pyramid (Vickers and Knoop) microindentation hardness testing. The residual impressions were analyzed in detail to yield information about slip and cracking systems, the size and character of the cumulative dislocation strain fields surrounding the impressions, and the effect of cracking on hardness with increasing applied load. Vickers hardness testing was used in the quasi-static studies on the (001) and  $\{\bar{2}10\}$  cleavage surfaces of AP.<sup>5-7</sup> In RDX, Vickers and Knoop indenters were used in similar studies on the (120), (010), and  $\{\bar{2}10\}$  growth surfaces.<sup>4,8,9</sup> It was of interest to determine if the microstructural response of these crystals to the quasi-static loading of the hardness indenter would be similar to the high rates experienced during shock loading.

Shock loading experiments were conducted on AP and RDX samples in different orientations, with and without purposely included macroscopic strain centers, and over a range of shock pressures. Since the effect of microstructure on shock reactivity was determined primarily in post-shock analyses, the experimental arrangement was designed for "soft" recovery of the crystals. The arrangement<sup>5,6</sup> consisted of a closed chamber, mostly filled with mineral oil, that had ports for backlighting and photography. The shock pressure entering the crystal was controlled by its separation from a Reynolds RP-80 detonator containing ~200 mg of explosive. The spherically diverging shock front from the detonator is conceptually similar to hardness testing with a large ball, except that the strain rate for shock loading is orders of magnitude greater. A diverging shock, in contrast to a planar shock, permitted the desired activation of slip and cracking systems. The crystal was supported on transparent tape, for a clear field of view with the high-speed camera, above a block of oil-soaked foam. Immersion in a fluid and capture of the shocked crystal in foam permitted recovery, even for shock strengths near the reaction threshold. Unlike RDX, HMX, and PETN explosive crystals, threshold reaction in AP would likely quench, allowing recovery of the sample for post-shock analyses.

For the shock experiments, AP samples with edge dimensions of 5 to 9 mm were cleaved from larger crystals, whereas RDX samples of similar size were remotely cut using a metallurgical saw and then solvent polished with a mixture of cyclohexanone and acetone. Optical transparency of the crystals was advantageous for in-depth viewing during shock passage with an image converter camera recording at rates of 2 to 5 million frames per second. Prior to the shock loading of some crystals, localized regions of increased lattice defects and strain were created by placing Vickers indentations in exterior surfaces. A number of shocked crystals were recovered for subsequent microstructural characterization and chemical analysis. Microstructural characterization was performed using hardness testing, light microscopy, and scanning electron microscopy.<sup>5,7</sup> Bulk decomposition measurements of AP with liquid ion chromatography (LIC) were obtained to determine the reaction threshold. Another crystal with several indentations was shocked near the reaction threshold and cleaved at indentation sites for spatially specific measurements of decomposition in the crystal interior by means of x-ray photoelectron spectroscopy (XPS).<sup>7,10</sup> Chemical etch pitting on another cleaved surface was used to map dislocation densities within the shocked crystal.<sup>11</sup> XPS measurements were also obtained for shocked RDX crystals, but these had to be broken open to expose the interior.

## CRYSTAL DEFORMATION AND MICROSTRUCTURAL CHARACTERIZATION

For the  $\{\bar{2}10\}$  and (001) surfaces of AP, details of Vickers impressions and the associated slip and cracking were shown in transmitted and polarized light micrographs.<sup>6</sup> The ease of plastic deformation in AP is shown in Figure 1 with micrographs<sup>6</sup> emphasizing surface relief, viewed with transmitted light that was partially obstructed before entering the crystal. On the  $\{\bar{2}10\}$  surface, there is a (001) crack extending from the upper corner of the impression and a very shallow trough extending in the  $\pm[00\bar{1}]$  directions far from the impression. Prominent deep

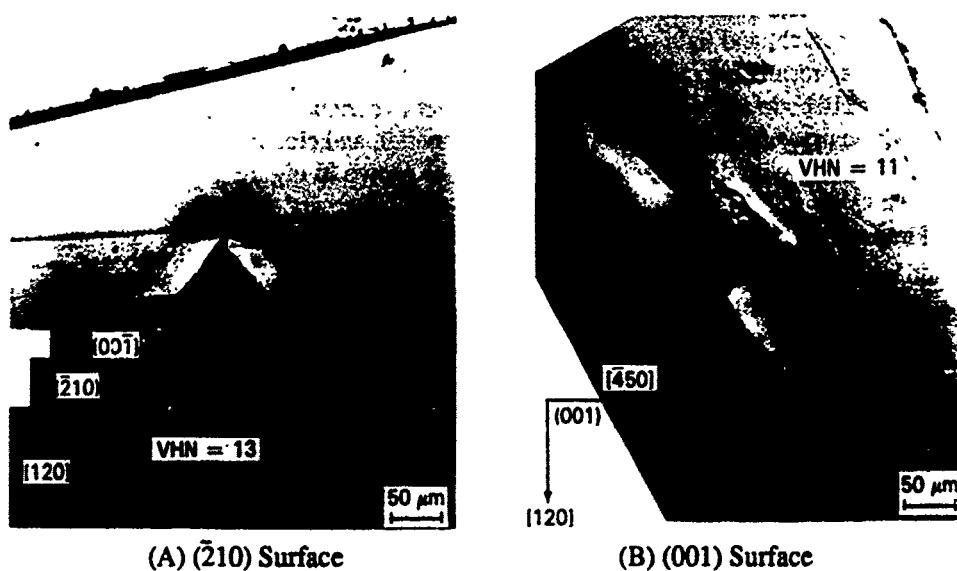


Fig. 1. Surface relief at Vickers hardness impressions in AP.

troughs were found on the (001) surface with large cracks in them. On the  $(\bar{2}10)$  surface of RDX, the micrograph of an impression in Figure 2 shows extensive cracking and extremely localized plastic deformation. A micrograph<sup>9</sup> of an impression on the (001) surface of a Holston Class D RDX crystal showed similar behavior. RDX is brittle with limited slip system activity and, therefore, readily cracks to accommodate the indenter. AP is more ductile, exhibiting a larger number of slip systems, but still readily cracks because of dislocation interactions.

For the  $(\bar{2}10)$  surface of RDX, the diagonal length of indentations when squared was proportional to the indenter force; that is, RDX had constant hardness despite the cracking.<sup>9</sup> By comparison, the hardness of the (001)<sup>5,6</sup> and the  $(\bar{2}10)$ <sup>7</sup> surfaces of AP decreased with increasing load, especially for the  $(\bar{2}10)$  surface. Also, RDX is two to three times as hard as AP. The effect of cracking in AP is to dissipate at least a portion of the strain energy in the vicinity of the impressions, whereas in RDX the strain energy is stored.

## SHOCK LOADING

AP crystals were subjected to shock entry into both the  $(\bar{2}10)$  and (001) surfaces. High-speed photographs in which the (001) surface was viewed following shock entry into the  $(\bar{2}10)$  surface were shown for shock pressures in the crystal of 16.7 kbar<sup>5</sup> and 24.4 kbar<sup>5,7</sup>. Two experiments were performed at 24.4 kbar because this shock pressure was the reaction threshold determined by LIC on the recovered crystals, as will be discussed. The high-speed photographs showed, although not in each experiment, a luminous shock front, distinct diagonal lines immediately behind the front that were attributed to the primary (100)[001] and secondary

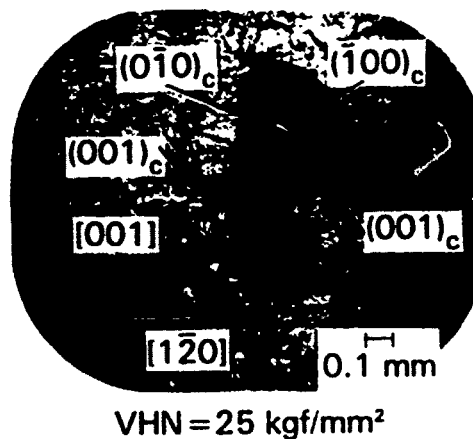


Fig. 2. Cracking at a Vickers hardness impression in RDX  $(\bar{2}10)$  growth surface.

(010)[001] slip systems observed in hardness testing, a moving luminous band that appeared to be a propagating crack, and light in the vicinity of indentations appearing  $\sim 1 \mu\text{s}$  after shock passage that was presumably due to chemical reaction. Several crystals subjected to shock entry into the  $\{2\bar{1}0\}$  surface were recovered intact after experiencing pressures as high as 38.5 kbar. These crystals had extensive plastic deformation and clouding near the shock-entry surface that lessened with distance into the crystal. As shown in Figure 3 for a crystal recovered from a shock loading of 24.4 kbar, the bottom section of the crystal (opposite shock entry) remained transparent. Near the shock-entry surface of that crystal, there was a two orders of magnitude increase<sup>11</sup> in dislocation density with a number of large, widely-spaced cracks. The damaged region seen in Figure 3 was outlined in the high-speed photographs<sup>7</sup> immediately after shock passage, thereby indicating the promptness at which the damage occurred relative to the shock loading.

High-speed photographs of shock entry into the (001) surface of AP, while viewing the  $\{2\bar{1}0\}$  surface (orthogonal to the orientation just discussed), showed no microstructural features or luminosity within the crystal during or following shock passage. After the shock exited from the bottom surface of the crystals, there was below each crystal a zone of luminosity attributed to chemical reaction. The recovered crystals were cracked apart on  $\{2\bar{1}0\}$  planes and also sometimes on (110) or (230) planes, all of which are orthogonal to the shock-entry surface.<sup>7</sup> Also, there was less cloudiness in the recovered crystals compared to those shocked in the other orientation. Thus, the microstructural response and luminous indications of reaction were dependent on crystal orientation.

RDX crystals were shock loaded, primarily through either the (100) or (010) surface while viewing the (001) growth surface, over a pressure range of 8.6 to  $>129$  kbar. There was violent reaction only for the crystal in direct contact with the detonator ( $>129$  kbar). For a shock pressure of 129 kbar there was prompt luminosity from reaction and only 9.7% of the crystal was recovered. Two crystals, each having indentations on the (100) shock-entry and (001) viewed surfaces, were shocked at 61.6 kbar and mostly recovered. There was only one small zone of luminosity near the shock-entry surface appearing in the first experiment, and in the second experiment there was light emission from the viewed edge of the (010) side. In both experiments, the luminosity appeared  $\sim 2 \mu\text{s}$  after shock passage, and there was no evidence that the late luminosity was associated with the closest impression. In addition to hardness impressions on exterior surfaces, the crystal in the first 61.6 kbar experiment had a predominantly (010) stress crack that was centrally located. This internal flaw did not emit light during shock loading. While shock pressures of 129 and 61.6 kbar are high relative to those causing light emission in shocked AP, they bracket observations<sup>12</sup> by Forbes et al. on RDX single crystals shocked at  $\sim 100$  kbar. These crystals, which were immersed in water and shocked by a 50.8 mm diameter by 50.8 mm long cylinder of 50/50 PETN/TNT, showed light emission for  $6 \mu\text{s}$  and what appeared to be reaction, but not instantaneous consumption of the crystals.

All of the recovered RDX crystals or fragments were uniformly white throughout from a high density of fine cracks, even at the lowest shock pressure of 8.6 kbar. This is illustrated in Figure 4 for a crystal that had been shocked at 16.3 kbar. Rather than the crystal being plastically deformed like AP, the only extensive deformation occurred from the  $\{2\bar{1}0\}$  system of cracks near the shock-entry surface. During the shock loading of this crystal, a luminous crack with the same orientation was observed on high-speed photographs. In all RDX experiments, transmission of backlighting through the crystals ceased immediately after shock passage, presumably due to the creation of the fine crack system observed in the recovered crystals. The opacity of these shocked crystals, in contrast to shocked AP crystals which were still somewhat transparent, allowed only surface observations with the high-speed camera. This was a disadvantage for observing luminosity due to chemical reaction which, as will be discussed, occurred primarily in the interior of the recovered AP crystals.

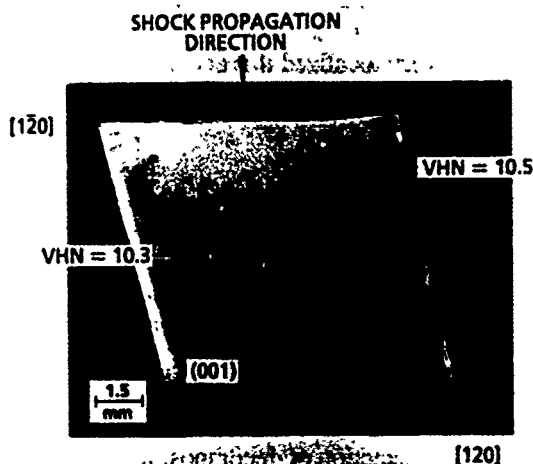


Fig. 3. Photomicrograph of AP crystal after shock loading at 24.4 kbar.

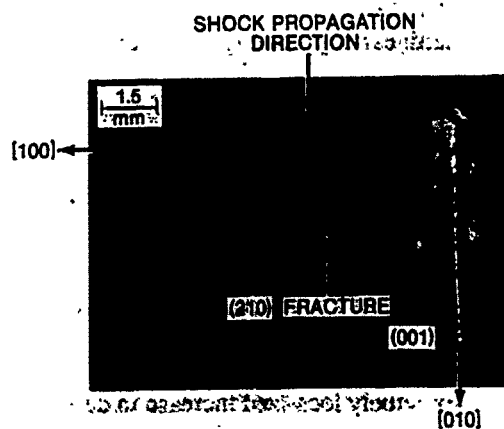


Fig. 4. Photomicrograph of RDX crystal after shock loading at 16.3 kbar.

### CHEMICAL ANALYSES OF RECOVERED CRYSTALS

For AP crystals recovered from shock loading through the  $(\bar{2}10)$  surface, LIC measurements were made for chloride, nitrite, nitrate, and chlorate. For a range of shock pressures from 1.0 to 62.5 kbar, only the chloride concentration showed a significant shift, beginning at 24.4 kbar, relative to an unshocked crystal. This reaction threshold was in agreement with the observations of luminosity from the crystals on high-speed photographs. For AP shock loaded through the (001) surface, there was significantly increased concentrations of chloride, nitrite, and nitrate (no measurements for chlorate), for shock pressures of 16.7 and 24.4 kbar. Although there were insufficient experiments to establish a reaction threshold in this orientation, it is less than that for shock entry into the  $(\bar{2}10)$  surface. This also correlates with the high-speed photographic observation of luminosity below the crystals after shock passage.

The recovered AP crystal shown in Figure 3 had large Vickers impressions placed on two surfaces prior to shock loading at 24.4 kbar, essentially the reaction threshold determined by LIC. There were two impressions on the viewed (001) surface (denoted in Figure 3) and one on the shock-entry  $(\bar{2}10)$  surface. The recovered crystal was cleaved along  $(\bar{2}10)$  planes that passed through the impression on the shock-entry surface and the left impression appearing on the viewed surface. With XPS, 1 mm x 1 mm areas were analyzed along these previously interior surfaces. The highest level of decomposition (as much as 9.5% perchlorate) was detected 2 to 3 mm below the hardness impression on the shock-entry surface. This position corresponded to the termination of the broad separation in a (001) crack that emanated from the impression. In a comparable location from the shock-entry surface on the other cleaved plane, there was less decomposition, 4.8% perchlorate, associated with shock passage through a lesser damaged region of the crystal. However, further from the shock-entry surface there was as high as 5.5% perchlorate decomposition occurring along slip planes emanating from a (001) surface impression. This is remarkable considering that the shock had significantly attenuated from 24.4 kbar after propagating through ~5 mm of crystal to reach this region. At a comparable location on the other cleaved plane there was no decomposition detected.

The first indication of reaction in RDX crystals was obtained in XPS measurements in the interior of a crystal that had been shocked to 61.6 kbar, correlating with the luminosity recorded on high-speed photographs. There was significant loss of nitro nitrogen, but the level of reaction was insufficient to observe intermediate products<sup>13</sup>, such as nitroso or triazine compounds. XPS measurements on the shock-entry surface did not reveal any reaction in the vicinity of a hardness impression placed there prior to shock loading. The fractured zone associated with the hardness

impression (similar to that in Figure 2) was not recovered but would have been easily dislodged from the shock loading as well as by any chemical reaction. In contrast to AP, any effect of hardness impressions on enhanced reactivity for RDX was very localized if it occurred at all.

## CONCLUSIONS

Zones of increased defect (dislocation) density enhanced chemical decomposition in relatively defect free, optical quality AP crystals shocked near the reaction threshold (~24 kbar) through the  $(\bar{2}\bar{1}0)$  surface. The luminosity in high-speed photographs and differences in bulk decomposition measurements using LIC for two crystal orientations indicated that shock reactivity was microstructurally based. The greatest decomposition was spatially determined, using XPS, to be near the tips of cracks and along slip planes that emanated several millimeters or more from hardness impressions placed in the crystal prior to shock loading. In RDX, the extremely localized increase in defects from hardness impressions and even a large, internal crack in one crystal did not enhance chemical reaction. The detection of decomposition by XPS measurements at 61.6 kbar correlated with observations of luminosity. The combined results, together with the nature of RDX to exhibit only localized deformation even while cracking and to retain deformation energy, suggest that much more extensive pre-shock damage is necessary in RDX for the initiation of dislocation-assisted reaction at lower shock pressures.

## REFERENCES

1. J.J. Dick, *Applied Physics Letters*, 44 (9), 859 (1984).
2. J.J. Dick, *J. of Applied Physics*, 53 (9), 6161 (1982).
3. L.G. Green and E. James, in *Fourth Symposium (International) on Detonation*, (Office of Naval Research, ACR-126, 1965) pp. 86-91.
4. W.L. Elban, J.C. Hoffsommer, and R.W. Armstrong, *J. of Materials Science*, 19, 552 (1984).
5. H.W. Sandusky, B.C. Glancy, D.W. Carlson, W.L. Elban, and R.W. Armstrong, *J. of Propulsion and Power*, 7 (4), 518 (1991).
6. W.L. Elban, P.J. Coyne, Jr., H.W. Sandusky, B.C. Glancy, D.W. Carlson, and R.W. Armstrong, *Investigation of the Origin of Hot Spots in Deformed Crystals: Studies on Ammonium Perchlorate and Reference Inert Materials* (NSWC MP 88-178, Naval Surface Warfare Center, Silver Spring, MD, 1988).
7. W.L. Elban, H.W. Sandusky, B.C. Beard, and B.C. Glancy, *Investigation of the Origin of Hot Spots in Deformed Crystals: Final Report on Ammonium Perchlorate Studies* (NSWCDD/TR-92/206, Naval Surface Warfare Center, Silver Spring, MD, to be printed).
8. W.L. Elban, R.W. Armstrong, K.C. Yoo, R.G. Rosemeier, and R.Y. Yee, *J. of Materials Science*, 24, 1273 (1989).
9. R.W. Armstrong and W.L. Elban, *Materials Science and Engineering*, A111, 35 (1989).
10. B.C. Beard, J. Sharma, H.W. Sandusky, B.C. Glancy, and W.L. Elban, *Shock Compression of Condensed Matter - 1991*, edited by S.C. Schmidt, R.D. Dick, J.W. Forbes, and D.G. Tasker (North-Holland, Amsterdam, 1992) pp. 571-574.
11. B.C. Beard, H.W. Sandusky, B.C. Glancy, and W. L. Elban, *J. of Materials Research*, to be printed.
12. J.W. Forbes, D.G. Tasker, R.H. Granholm, and P.K. Gustavson, *Shock Compression of Condensed Matter - 1990*, edited by S.C. Schmidt, J.N. Johnson, and L.W. Davison (Elsevier Science Publishers B.V., 1990) pp. 709-712.
13. B.C. Beard, *Propellants, Explosives and Pyrotechnics*, 16 (2), 81 (1991).

Acknowledgments: Work was supported by the Independent Research Program at Naval Surface Warfare Center and the Office of Naval Research

## MOLECULAR MODELING OF SLIP SUPPOSED TO OCCUR IN THE SHOCK INITIATION OF CRYSTALLINE PETN

JAMES P. RITCHIE

MS-B214, Los Alamos National Laboratory, Los Alamos, NM 87545

### ABSTRACT

Some molecular modeling of slip using both rigid and flexible molecules of PETN in perfect, but finite, lattices has been performed. Studies of rigid displacement show slip on (001)<010> to be relatively unhindered. The shock orientation with a maximum resolved shear stress in this direction would, therefore, be expected to be insensitive. Molecular mechanics calculations have also been performed. The results show that it is likely that molecular deformations occur and have an important effect in determining the shear strength of crystalline PETN.

### INTRODUCTION

Much of the thinking about the elastic and plastic properties of materials is based upon the behavior of inorganic compounds, including metals, their oxides, and ionic solids. These materials differ importantly from common explosives, many of which are organic. Polymers have been intensely studied, but these materials typically lack crystallinity due to their size and in this way also differ from many common organic explosives. We have, consequently, undertaken a study of some of the material properties of common organic explosives in order to determine how they differ from other materials.

Dick et al. have observed an orientation dependence of the shock initiation of crystalline pentaerythritol tetranitrate (PETN).<sup>1</sup> This behavior was attributed to anisotropy of plasticity. It has been proposed that this anisotropy arises from differences in steric hindrance to edge dislocation motion. A simple counting of close contacts occurring during displacement of a rigid lattice along the slip system of maximum resolved shear stress was able to distinguish between shock orientations that are insensitive and sensitive. Insensitive orientations give rise to a relatively few number of close contacts during slip, while those that are sensitive encounter more. In that analysis, atom-atom contacts of 1.05 and 0.78 Å are obtained for slip systems stimulated by shock orientations classified as relatively insensitive. The actual occurrence of such close atom contacts would result in extremely high energies for plastic deformation in the directions analyzed. It is difficult to reconcile such high energies with the observed shock-insensitivity and would make the suggested occurrence of supercritical shear in PETN<sup>2</sup> extremely difficult. This difficulty needs to be overcome to preserve the proposed mechanism. One possibility is that slip occurs rigidly along a path other than that suggested by Dick, in a fashion that avoids close contacts. Alternatively, the molecule may undergo deformation.

PETN is comprised of atoms bonded together by single bonds, except the terminal oxygens of the nitro group. Normally, rotation about single bonds can occur in the gas phase with only a small cost in energy. For example, the barrier to rotation about the O-NO<sub>2</sub> bond of methyl nitrate is estimated between 0-7 kcal/mol, from both theory and experiment.<sup>3</sup> In a molecular crystal, however, interactions with neighboring molecules can and indeed do cause the hindrance of such rotations so that the molecule is essentially frozen in a small neighborhood about a single configuration. It is therefore possible to obtain an accurate x-ray crystal structure for PETN.<sup>4</sup> During shear, the environment about the molecule changes and rotation of parts of the molecule may become possible and dramatically change the stress required to produce shear slip.

It is desirable to develop a more detailed description of Dick's experiment in particular and other crystal behavior, because of the possible insight into initiation mechanisms it affords. It is the purpose of this paper to consider the possibility of rigid slip along other paths with significant resolved shear stresses. The possibility of decreased resistance to slip resulting from molecular deformations has also been investigated.

## RIGID SLIP

Because of the complicated shape of PETN, it was desired to determine if paths that avoid close contacts other than those proposed by Dick exist on the slip planes. This was accomplished using the observed crystal and molecular structure of PETN.<sup>4a</sup> The unit cell (shown in Figure 1) was translated to form two blocks comprised of  $3 \times 3 \times 1$  unit cells each. One of the blocks was displaced in stepwise increments along each of the repeat vectors spanning the plane. This procedure gave crystal geometries in which one of the blocks differed from the initial equilibrium configuration by an amount  $a \cdot v_1 + b \cdot v_2$ , where  $v_1$  and  $v_2$  are normal lattice vectors spanning the plane of interest and  $a$  and  $b$  are fractions between zero and one. At each geometry generated in this fashion the closest atom-atom contact between different molecules was calculated and stored. The resulting mesh of values was used to produce contour plots.

Figures 2-4 show contour plots of closest contacts for slip on (110), (100), and (101).

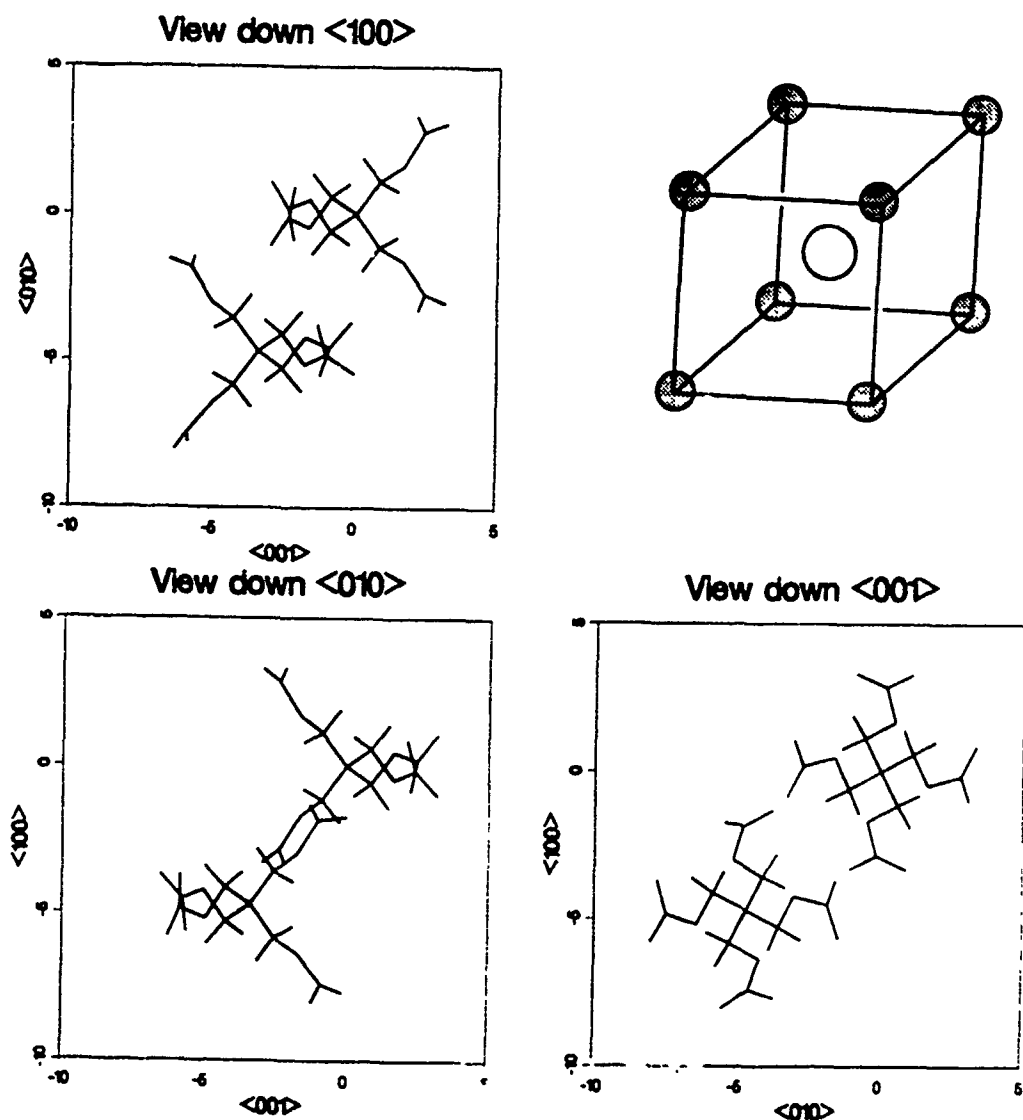


Figure 1. Three orthographic views of PETN unit cell and representation of body-centered tetragonal lattice



## Rmin on (110)

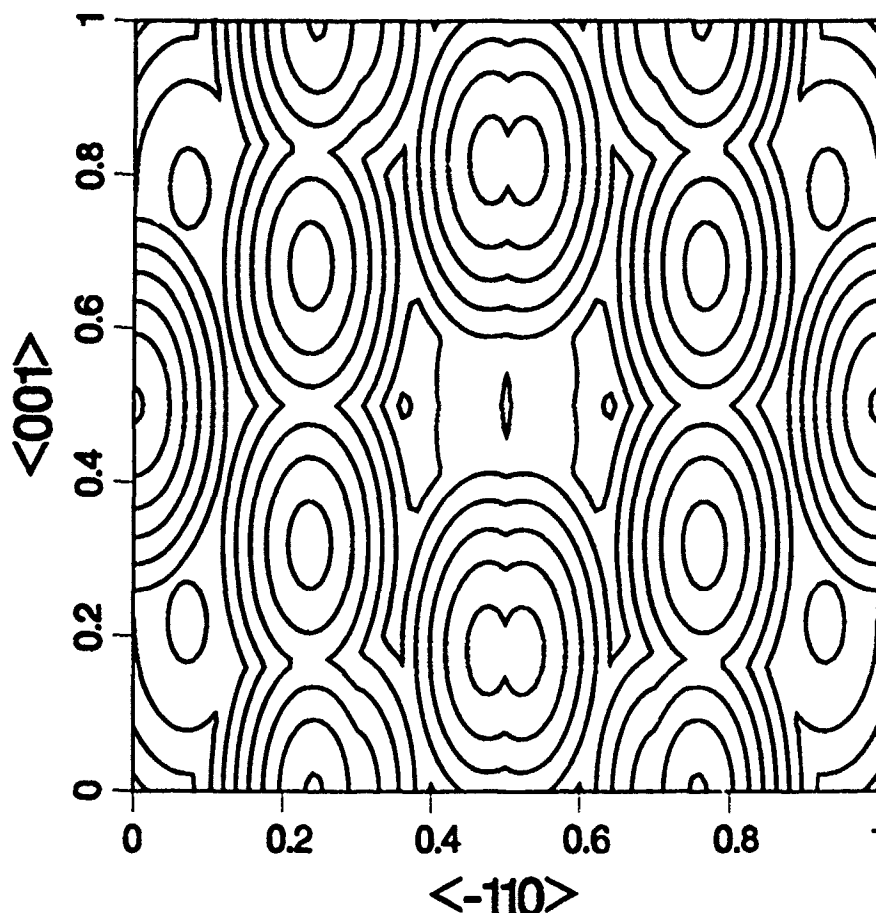


Figure 2. Contour plot of closest atom-atom contacts between PETN molecules for rigid displacement on (110). The axes represent one repeat unit in the indicated direction. The first contour encountered from any corner is 2.4 Å. Subsequent contours are 0.2 Å apart

These planes contain the maximum resolved shear stress system identified by Dick. In accord with previous analysis, inspection of Figure 2 shows slip along (110)<111> results in two close contacts between 1.0 and 1.2 Å. Interestingly, a path passing through the cols at about 0.25, 0.15 and 0.75-0.85 can be identified that differs only slightly from the proposed path, yet would lead to a considerable reduction of steric hindrance. This path results in closest contacts of between 1.4 and 1.2 Å, which is considerably longer than that for <111>, rigorously.

Figure 3 shows closest contacts on (100). Slip on <001> shows a single close contact and slip on <011> shows three, in agreement with the former slip system being insensitive and the latter sensitive. Again, it is found that a path passing through approximately 0.2, 0.5 differs only slightly from the proposed slip system and yet would lead to a significant reduction in steric hindrance. This path would result in a closest contact of between 1.0 and 1.2 Å which is significantly longer than that of about 0.8 Å otherwise. Slip on <011> is classified as sensitive and a number of close contacts in this direction are encountered, as shown in Figure 3. The distinction between this direction and <001> is clouded somewhat, however, if deviations are allowed. Slip to approximately 0.2, 0.5 followed by slip along <010> results in close contacts of between 1.0 and 1.2 Å, nearly the same as that found for a deviation of slip on <001>.

Figure 4 shows closest contacts on (101). Slip along <101> (the <101> direction shown

## Rmin on (100)

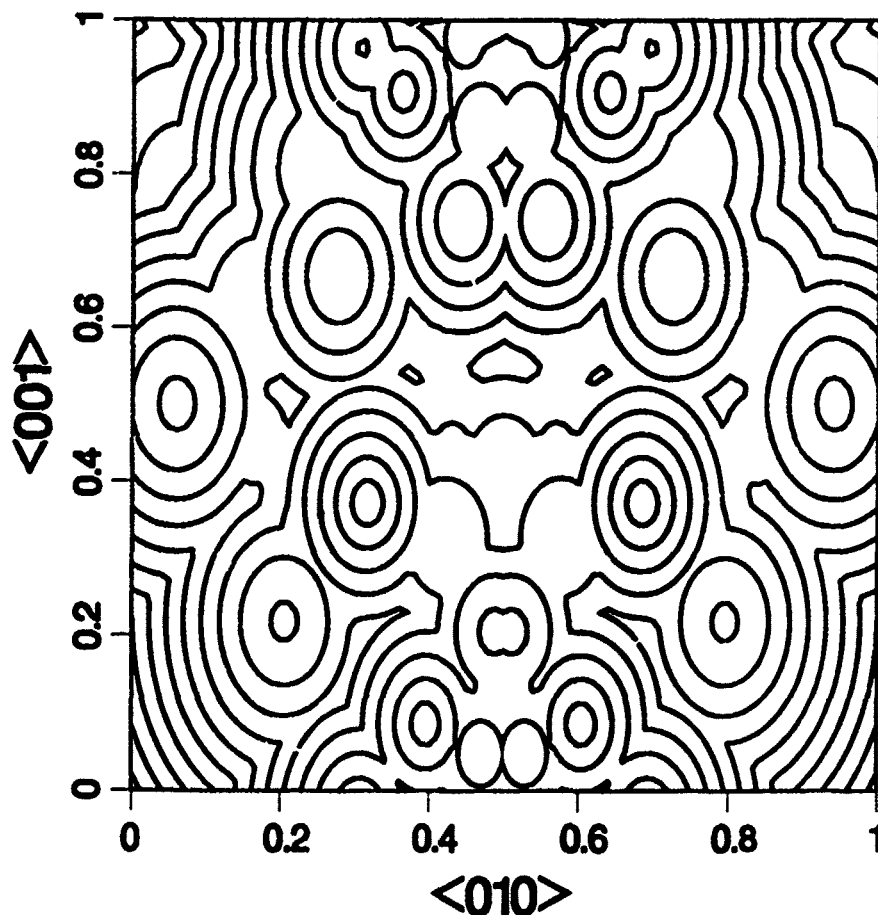


Figure 3. As in Figure 2, but for displacement on (100).

in the figure is symmetry equivalent) is classified as sensitive. Inspection of Figure 4 shows that translation in this direction always results in very close contacts. This is in agreement with previous analysis by Dick.

In performing the above calculations it was noticed that a significant spacing between molecules is observed when the crystal lattice is viewed down  $\langle 010 \rangle$ . This is shown in Figure 5. This suggests that the slip system  $(001)\langle 010 \rangle$  should NOT be sterically hindered. The contour plot of closest approaches on (001) is shown in Figure 6. It shows that rigid slip along  $\langle 010 \rangle$  results in only a single close contact of slightly less than 1.4 Å. This is longer than any of the closest contacts found for any of the other slip systems considered. Consideration of the shock orientations classified as sensitive by Dick, namely  $\langle 001 \rangle$  and  $\langle 110 \rangle$ , show there is no resolved shear stress along  $(001)\langle 010 \rangle$ . So including this slip does not alter previous arguments about the shock sensitivity. However, a resolved shear stress would result in this direction from a shock parallel to  $\langle 100 \rangle$ , for example. Such orientations have not been studied. Thus, experimental study of an orientation with a maximum resolved shear stress on  $(001)\langle 010 \rangle$  would be a new test of the steric hindrance concept.

### MOLECULAR MECHANICS

An estimate of the repulsion energy for contacts half of normal separations, such as

## Rmin on (101)

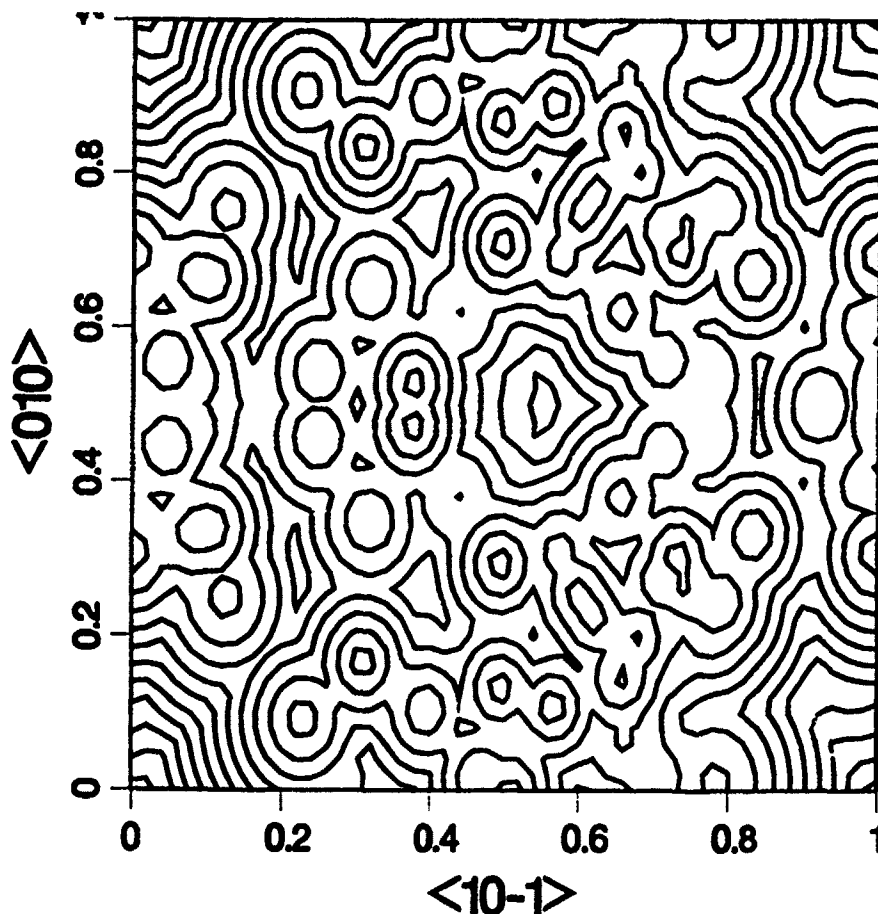


Figure 4. As in Figure 2.

are found in the rigid displacement of PETN, may be made by assuming a  $R^{-12}$  dependence. The resulting factor is about 4000. Assuming an equilibrium repulsion energy on the order of a kcal, the resulting repulsion energy at these close separations would be enormous. Another relevant fact is that the inter-planar spacing in graphite and TATB, where rigid slip is operative, is 3.35 and 3.29 Å, respectively. Consequently, the close contacts found for PETN are far too short to allow for any conception of slip on these planes occurring by rigid displacement. This has led to the consideration of the possibility of molecular deformations occurring during shear.

The calculations were performed using the program AMBER.<sup>5</sup> It has a molecular mechanics package in it that was used in this work. Briefly, the energy of molecular distortions is calculated using Eq. 1, below.

$$\begin{aligned}
 \sum_{\text{total}} = & \sum_{\text{bonds}} K_r (r - r_{eq})^2 + \sum_{\text{angles}} K_\theta (\theta - \theta_{eq})^2 + \sum_{\text{dihedrals}} \frac{V_n}{2} [1 + \cos(n\phi - \gamma)] \\
 & + \sum_{i,j} \left[ \frac{A_{ij}}{R_{ij}^{12}} - \frac{B_{ij}}{R_{ij}^6} + \frac{q_i q_j}{\epsilon R_{ij}} \right] + \sum_{H-\text{bonds}} \left[ \frac{C_{ij}}{R_{ij}^{12}} - \frac{D_{ij}}{R_{ij}^{10}} \right]
 \end{aligned} \quad (1)$$

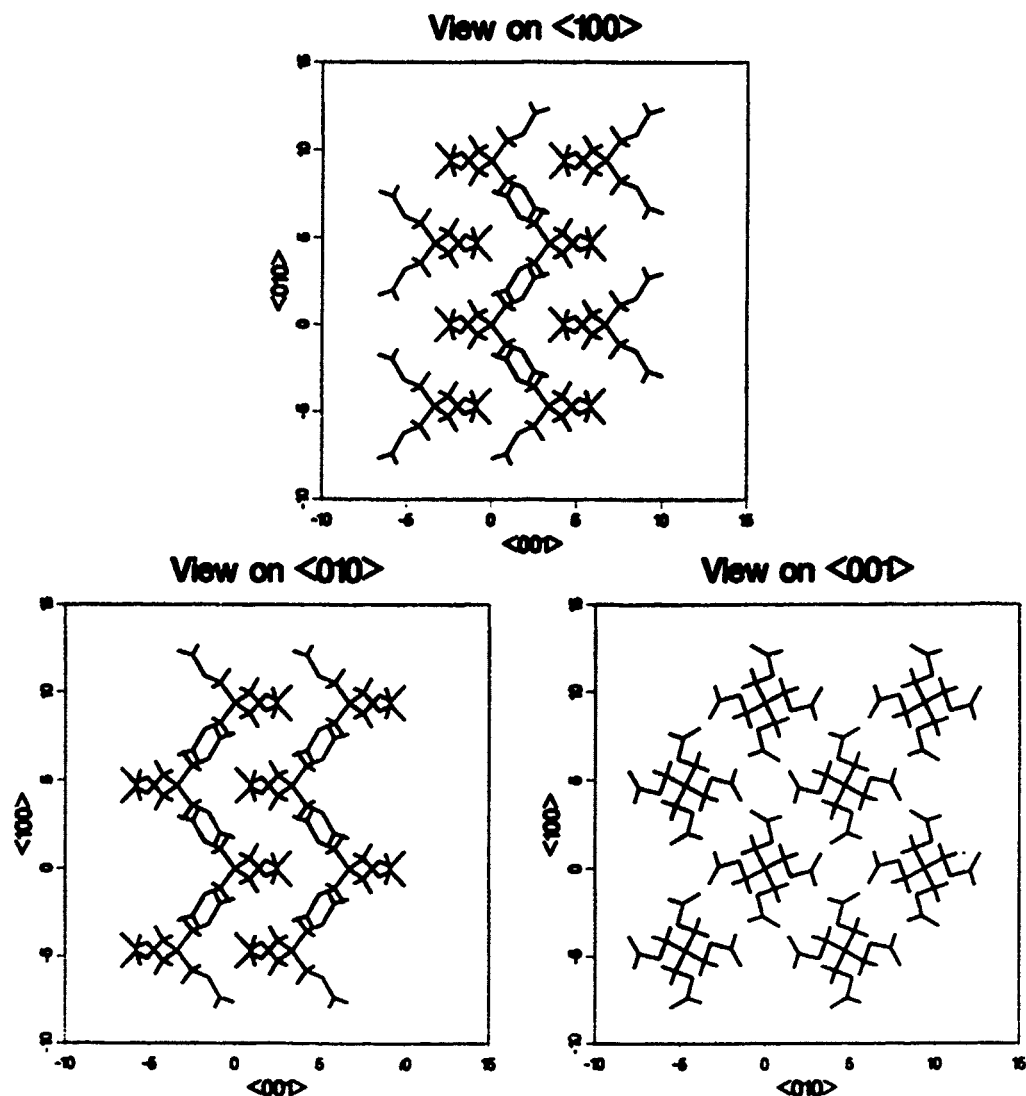


Figure 5. Orthographic projections of a lattice of PETN showing the spacings between molecules when viewed down  $\langle 010 \rangle$ .

Although this is a relatively complicated energy expression and requires a number of parameters, this type of modeling has become widely used throughout the chemical community. It also suits our present purposes quite nicely. In many cases the required parameters were available in the program. However, a number of quantum mechanical calculations were performed to obtain atom charges that were required and force constants for the nitro group rotation.

Some results obtained using this program will be discussed.

## SUMMARY AND CONCLUSION

Contour plots of closest approaches on a slip plane were examined. Some deviation from the paths previously proposed is possible leading to less steric hindrance. Slip on  $(001)\langle 010 \rangle$  was shown to result in closest approaches of slightly less than 1.4 Å. Nevertheless, these approaches are so close as to preclude rigid slip. The possibility of molecular deformation occurring during slip is being examined using a molecular mechanics program. The results show rotations about

## Rmin on (001)

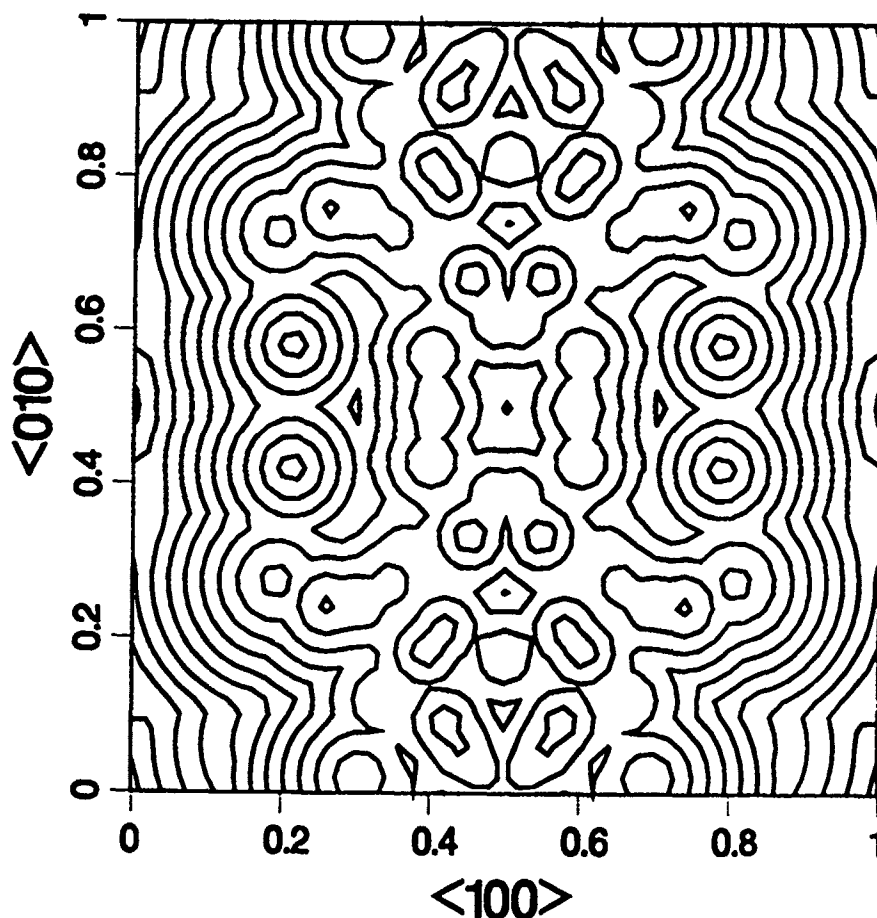


Figure 6. As in Figure 2.

single bonds in the molecule can dramatically reduce shear stress.

### ACKNOWLEDGEMENT

Helpful conversations with J. J. Dick, J. N. Johnson, E. M. Kober, and J. K. Dienes are gratefully acknowledged.

This research was supported under the Joint DOE/DOD MOU, Office of Munitions, and CX Program Element, LANL, P. Howe, Manager.

### REFERENCES

1. a) J. J. Dick, R. N. Mulford, W. J. Spencer, D. R. Pettit, E. Garcia, D. C. Shaw, J. Appl. Phys. **70**, 3572 (1991). b) J. J. Dick, Appl. Phys. Lett. **44**, 859 (1984).
2. J. J. Dick, Appl. Phys. Lett. **60**, 2494 (1992).
3. a) B. J. van der Viken, G. A. Guirgis, J. R. Durig, J. Mol. Struct. **142**, 105 (1986). b) B. J. Smith, C. J. Marsden, J. Comp. Chem. **12**, 565 (1991).

4. a) J. W. Conant, H. H. Cady, R. R. Ryan, Y. L. Yarnell, J. M. Newsam. LA-7756-MS, 1979. b) A. D. Booth, F. J. Llewellyn, J. Chem. Soc. 837 (1947). c) J. Trotter, Acta Cryst. **16**, 698 (1963).
5. S. J. Weiner, P. A. Kollman, D. A. Case, U. C. Singh, C. Ghio, G. Alagona, S. Profeta, Jr., P. Weiner, J. Am. Chem. Soc. **106**, 765 (1984).

## INTERPRETING DROP-WEIGHT IMPACT RESULTS IN TERMS OF DEFORMATION DEPENDENT INITIATION CRITERIA

P. J. BAKER AND A. M. MELLOR

Vanderbilt University, Department of Mechanical Engineering, Nashville, TN 37235

### ABSTRACT

The impact sensitivity of energetic materials is frequently measured in small-scale drop-weight tests. Plastic deformation of the sample leads to heating, the onset of chemical reaction, and eventual ignition. An analytic model provides deformation dependent estimates of the energy delivered to the sample, its stress state, and its temperature distribution. Results for hydroxy-terminated polybutadiene (HTPB/AP) propellants are interpreted in terms of two initiation criteria: critical decomposition temperature and critical thickness for shear banding. The influence of friction, impact velocity, and sample size on initiation give possible explanations of experimental results. Sample material properties variations are studied for both initiation criteria. The model includes energy localization by varying the thickness of shear layers at the sample/machine interface.

### INTRODUCTION

Understanding mechanical initiation of solid propellants is important in developing insensitive munitions. But unfortunately, the propellant community still lacks a detailed description of this process. Although it is generally accepted that plastic work leads to localized heating, initiation, and subsequent ignition, the initiation and ignition probabilities are unknown as functions of external stimulus. For low rate impacts, the instrumented small-scale drop-weight impact test quantitatively measures sensitivity<sup>1,2</sup>. By increasing impact velocity over that of 50% Go/No Go tests, the drop-weight kinetic energy dissipated prior to sample initiation can be measured and approximately equals the plastic work on the sample<sup>1</sup>. This plastic work,  $W_s$ , is called the critical energy and is a quantitative measure of work done on the sample in order to cause a reaction. Ideally critical energies could predict propellant behavior in other impact scenarios, but to do this more information about the hot-spot and initiation mechanisms is needed.

Unfortunately, the critical energy and other small-scale impact tests give little information about energy localization; therefore, modeling is required. Others have studied drop-weight impact through analytic modeling<sup>3,4</sup>. We continued in this vein in a previous paper and derived a model for drop-weight impact<sup>5</sup>; here we highlight the details of that paper. The model origin is an analysis by Avitzur of the forging process for rigid perfectly plastic disks<sup>6</sup>. When applied to drop-weight impact, plastic work and a sample temperature distribution are generated as functions of sample deformation and deformation rate. Below, the effects of friction, impact velocity, sample size, and mechanical properties are examined in terms of two initiation criteria.

### DEFORMATION MODEL

For the sample geometry shown in Fig. 1 and following Avitzur, we assume a parallel velocity field for the sample during compression (Avitzur showed that a more detailed velocity distribution should not significantly affect results<sup>7</sup>). Also retaining Avitzur's proportionality between the disk surface friction and its shear yield stress but assuming rigid body drop-weight and anvil motions, the powers required to deform the sample and to overcome friction are

$$\dot{W}_i = \pi R^2 \sigma_y (U_s - U_A) \quad ; \quad \dot{W}_f = \pi m \frac{2 \sigma_y R^2}{3 \sqrt{3} T} (U_s - U_A) \quad (1)$$

for a von Mises material, where  $m$  is the friction proportionality constant. For an energetic material, integrating  $\dot{W}_i + \dot{W}_f$  from time of impact to initiation gives the critical energy. Equating the powers in Eq. (1) with power supplied by pressure on the sample and accounting for sample rigid body motion determines the average drop-weight and anvil contact pressures as functions of instantaneous sample geometry and rate of change of thickness. The pressures determine the drop-weight and anvil accelerations. Solving the resulting simultaneous equations numerically generates time histories of sample thickness and plastic work (see Ref. [5] for more detail).

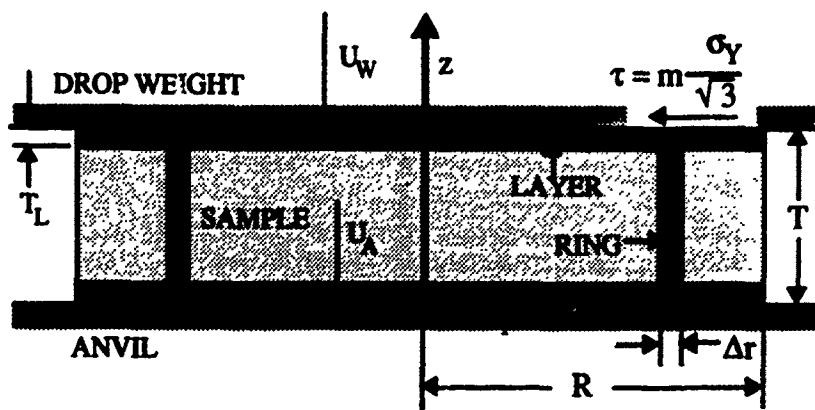


Figure 1. Geometry extending Avitzur model<sup>6</sup> to drop-weight impact. Both anvil and drop weight move. Ring of width  $\Delta r$  and layer of thickness  $T_L$  are for temperature calculations.

The plastic work heats the sample so the temperature rises. Neglecting conduction into the machine and radially in the sample during the test gives a temperature rise rate of<sup>5</sup>

$$\frac{d\theta}{dt} = \frac{\sigma_p |\dot{\epsilon}|}{\rho c T} \left( 1 + \frac{m}{\sqrt{3}} \frac{r}{T} \right) \quad (2)$$

for a cylindrical ring as shown in Fig. 1; here axial temperature gradients are neglected so heat is uniformly distributed over the ring height,  $T$  (this assumption is removed below). Integrating Eq. (2) over time at any radius gives the temperature rise, which is greatest at the sample edge since friction heating varies as  $r^2$  but ring mass only varies as  $r$ . This agrees with previous experiments showing initiation near the sample perimeter<sup>2,8</sup>.

It is reasonable to expect that the majority of friction heat is stored near the sample/machine contact surface. If one now assumes that all friction heat is deposited in two layers of thickness  $T_L$  at the interfaces, as shown in Fig. 1, the layer temperature rise rate is<sup>5</sup>

$$\frac{d\theta_L}{dt} = \frac{\sigma_p |\dot{\epsilon}|}{\rho c T} \left( 1 + \frac{m}{2\sqrt{3}} \frac{r}{T_L} \right) - (\theta_L - \theta_i) \frac{|\dot{\epsilon}|}{2T} \quad (3)$$

where  $\theta_i$  and  $\theta_L$  are instantaneous internal and layer temperatures respectively.  $\theta_i$  arises from  $W_S$  only, neglects friction, and is, thus, independent of radial location. The second term lessens the temperature rise rate since mass at the lower temperature,  $\theta_i$ , is continuously introduced to the constant thickness layer. If the available energy is sufficient, the sample thickness eventually reaches twice the layer thickness, and  $\theta_L$  returns to the uniform heating value found via Eq. (2).

Below, the time histories generated by this model help explain and predict sample behavior in drop-weight tests, with particular emphasis on  $W_S$  as it relates to two initiation criteria.

## INITIATION CRITERIA AND MODEL INPUT

One possible impact ignition mechanism for HTPB/AP propellants (the type previously tested<sup>2</sup> and presently being tested by the authors) is AP thermal decomposition, followed by reaction of the hot AP gases with the binder. According to Jacobs and Whitehead<sup>9</sup>, in thermally static tests, AP is stable at less than  $\approx 150^\circ\text{C}$ ; decomposition is self-limiting to  $\approx 30\%$  up to  $\approx 300^\circ\text{C}$ , and decomposition is rapid and complete at  $> 350^\circ\text{C}$ . Thus, critical temperature is one initiation criterion. Here critical temperature increases of 150 and  $250^\circ\text{C}$  are examined to look for possible data trends (only the highest impact velocity cases reached  $\Delta\theta = 350^\circ\text{C}$ ).

For this criterion the baseline case is perfectly plastic with a yield stress (68.9 MPa or 10,000 psi) and friction constant chosen so final computed sample radii are reasonable at impact velocities used in previous experiments<sup>2</sup> (see Table I). Baseline density and geometry, drop-weight mass, and all impact velocities also correspond to typical experiments<sup>2</sup>. The anvil is



assumed rigid (mass = 10,000 kg), and the sample specific heat is 0.34 cal/g°C (1423 J/kg°C).

A second initiation criterion is adiabatic shear banding in the propellant. Winter and Field<sup>10</sup> and Mohan et al.<sup>11</sup> both discuss the importance of localized flow in drop-weight impact. For a power law strain and strain-rate material, Staker gives the critical true strain for adiabatic shear<sup>12</sup>, which when applied to drop-weight impact is (see Nomenclature)

$$|\epsilon_c| = n_1 / \left( -\frac{1 + \frac{m}{\sqrt{3}} \frac{R}{T} \frac{\partial \sigma_y}{\partial \theta}}{\rho c} \frac{\partial \sigma_y}{\partial \theta} \bigg|_{\epsilon, \dot{\epsilon}} - \frac{n_2}{|\dot{\epsilon}|} \frac{d|\dot{\epsilon}|}{d\epsilon} \right) \quad (4)$$

This critical strain defines a critical thickness for shear band formation at the sample edge where friction causes the largest thermal softening. A simple linear thermal softening model is used here;  $\partial \sigma_y / \partial \theta$  equals the instantaneous flow stress divided by -300 °C. Below, the effects of varying  $n_1$ ,  $n_2$ , and  $K$  are studied. As before, the baseline case gives reasonable final sample radii when compared with experiment. The different cases are shown in Table II.

Thus, two critical conditions are defined for drop-weight impact initiation: a critical temperature for AP decomposition, and a critical thickness for adiabatic shear banding. Model results are discussed below; for a more detailed analysis see the authors' previous paper<sup>5</sup>.

Table I. Effects of sample thickness, impact velocity, friction, and yield stress on sensitivity of an HTPB/AP propellant sample as determined by work to reach a critical temperature increase\*.

Case Number 1 is Baseline	Initial Thickness (mm)	Impact Velocity (m/s)	Yield Stress (MPa)	Friction Constant m	Max. Temp. Increase (°C)	No Layer		0.1 mm Layer	
						WS at $\Delta\theta = 150^\circ\text{C}$ (J)	WS at $\Delta\theta = 250^\circ\text{C}$ (J)	WS at $\Delta\theta_L = 150^\circ\text{C}$ (J)	WS at $\Delta\theta_L = 250^\circ\text{C}$ (J)
1	1.16	8.4	68.9	0.4	297	6.83	10.98	6.38	10.90
2	1.00				348	5.86	9.44	5.83	9.42
3	1.32				258	7.81	12.40	6.73	12.47
4	1.16	5.54			122	N/A	N/A	N/A	N/A
5		12.95			737	6.83	10.98	6.38	10.86
6		8.4	34.5		308	6.53	10.58	6.46	10.51
7			138		283	7.18	11.54	4.18	9.13
8			68.9	1.0	305	6.58	10.72	3.14	7.68
9			68.9	0.1	287	7.22	11.44	7.21	11.41

\* The initial radius is 2.5 mm; drop-weight mass is 367 g; density is 1.83 g/cm<sup>3</sup>. For values marked N/A, the sample did not reach the temperature for that case.

Table II. Effects of varying material constants and impact velocity on shear banding of a power law strain and strain-rate hardening propellant sample.

Case 11 is Baseline	Impact Velocity (m/s)	Strength Coefficient K (MPa)	Strain Exponent $n_1$	Strain-rate Exponent $n_2$	Final Sample Radius (mm)	Thickness at Banding (mm)	Sample Work at Banding (J)
11	5.54	23	0.2	0.12	5.55	0.45	2.10
12	8.40	23			7.23	0.45	2.44
13	12.95	23			9.45	0.44	2.54
14	8.40	46			9.10	0.31	2.18
15		46			5.72	0.61	2.59
16			0.1		7.30	0.55	1.82
17			0.3		7.16	0.38	2.80
18				0.18	5.96	0.55	2.78
19				0.06	8.86	0.36	1.94

## CRITICAL TEMPERATURE RESULTS

The maximum temperature rise in Table I,  $\Delta\theta_{max}$ , neglects axial gradients and assumes all drop-weight energy has been transferred to the sample. Actual temperatures are lower since some energy is lost via elastic vibrations through the machine.  $\Delta\theta_{max}$  decreases as initial sample thickness increases (Cases 1-3) since the ratio of compression to friction work increases. Also, the work to reach critical sample or layer temperatures increases with thickness. In contrast to these results, the work per unit sample mass for 0.1 mm layer temperatures decreases with thickness. Thus, data must be analyzed carefully since the actual intrinsic drop-weight initiation probability is only indirectly a function of thickness through loading and loading rate.

Layer size affects temperature rise greatly. Figure 2 shows temperature rise histories at the baseline sample edge for 0.05 and 0.1 mm layers and no layer. For 0.1 mm the temperature returns to that of no layer when the sample thickness equals  $2T_L$ . However, for  $T_L = 0.05$  mm, the sample is always thicker than  $2T_L$ , so the layer temperature never returns to the no layer case.

The  $\Delta\theta_{max}$  variation with impact velocity (Cases 1, 4, and 5) correlates with the percent consumed results of Baker et al.<sup>2</sup>. At the three different velocities of 5.54, 8.4 and 12.95 m/s, the percent of sample reacted was on the order of 5, 50, and 100% respectively<sup>2</sup>. From Table I, at 5.54 m/s  $\Delta\theta_{max}$  is almost enough for the onset of AP decomposition; at 8.4 m/s  $\Delta\theta_{max}$  is about where rapid AP decomposition begins, and at 12.95 m/s AP would decompose vigorously<sup>9</sup>. This indicates that friction may explain impact velocity effects on the extent of reaction. The results do not change for 0.1 mm layers since the final thickness is less than  $2T_L$  so  $\Delta\theta_{max} = \Delta\theta_{L,max}$ .

For friction variations, this model predicts  $W_S$  to reach a critical temperature increases with decreasing friction constant. This agrees with critical energy measurements by Coffey et al. for a binder/AP explosive on polished and rough anvils<sup>1</sup>. As friction decreases, a larger fraction of  $W_S$  goes into compression and bulk heating, so more energy is needed to reach critical temperatures. The effect is small when friction heat is distributed uniformly over the thickness, but if focused in layers, as shown by Cases 1, 8 and 9 in Table I, friction effects are enhanced.

Equation (1) shows a large flow stress effect on deformation, and Cases 1, 6 and 7 show a localization dependent yield stress effect on critical energy. For uniform friction heat, weaker materials have smaller critical energies and are more sensitive, but the effect is reversed for friction localization. Thus, since localization is likely, increased  $\sigma_y$  increases sensitivity.

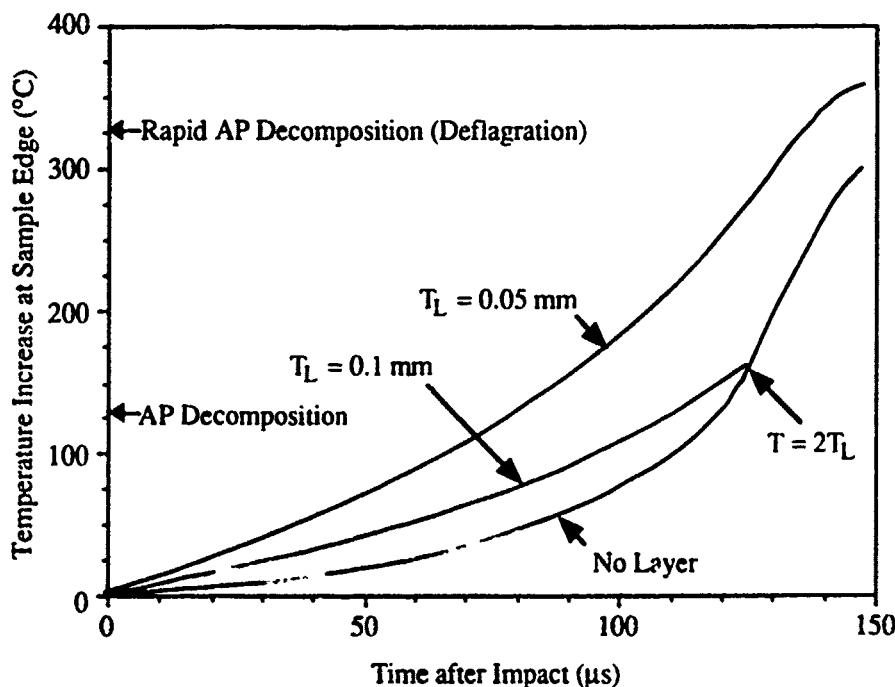


Figure 2. The effect of layer thickness on  $\Delta\theta_{max}$  for the baseline case, 1.

## SHEAR-BANDING CRITERION RESULTS

Table II shows the shear-banding initiation criterion results. Sample thickness and plastic work when flow becomes unstable are reported. Equation (4) indicates that critical strain and, hence, critical thickness,  $T_C$ , are functions of deformation. Critical thickness increases as actual thickness decreases; when the two are equal banding occurs. Baker and Mellor<sup>5</sup> discuss Eq. (4) and how changing material constants can have the competing sensitivity effects of decreasing critical strain but increasing critical energy. Here we simply highlight those results.

For the range of impact velocities chosen, the thickness at shear banding is nearly constant. On the other hand, the energy to cause banding increases with velocity since flow stress increases with strain rate. Cases 10, 13, and 14 show that increasing strength via  $K$  increases  $T_C$  by enhanced thermal softening, but also increases the work to cause banding via an increased flow stress. Similar to increasing  $K$ , increasing  $n_1$  also raises the flow stress; however, unlike  $K$ , increasing  $n_1$  decreases  $T_C$  while increasing the sample work for banding (Cases 11, 15 and 16). Thus, a highly strain-hardening material is desirable for low sensitivity based on this criterion. Cases 11, 17 and 18 show the net effect of increasing  $n_2$ . Increasing  $n_2$  is like increasing  $K$  in that it increases  $T_C$ . Thus the thermal softening effects outweigh the strain-rate effects from the second term in the denominator of Eq. (4). Also, increasing  $n_2$  increases the work required for banding by increasing the flow stress. Consequently, these results indicate that any change in the material constants which raises flow stress will reduce sensitivity based on this criterion.

## CONCLUSIONS

Results from a drop-weight impact sample deformation model were interpreted in terms of two initiation criteria. Effects of sample thickness, friction, yield stress, and impact velocity were studied for a critical temperature criterion, and varying power law material constants was studied for a shear banding criterion. Initiation at a critical specimen thickness corresponding to an AP particle size was analyzed previously<sup>5</sup> and was shown unlikely in view of experimental results<sup>1,2</sup>.

Friction results supported previous experimental data<sup>1</sup> by showing increased critical energy when friction was reduced (for a critical temperature criterion). This result was magnified when friction heating was localized. Friction is also important in explaining the percent of sample reacted observations by Baker et al.<sup>2</sup>; at low velocities the maximum temperature (at the sample edge) is less than the AP decomposition temperature, and at the highest impact velocities the temperature is above the AP deflagration point.

With localized friction heating, increasing yield stress decreases the energy required to reach the AP decomposition temperature. Therefore, for a critical temperature criterion, this model predicts a higher strength material has a lower critical energy and, consequently, is more sensitive. However, the trend is reversed when localization is ignored, and the shear banding criterion predicts that any increase in flow stress decreases sensitivity. This indicates the importance of knowing the hot-spot mechanism for a given scenario.

There is no doubt that friction affects the apparent sensitivity in a drop-weight test. The large friction effect may partially explain differing results for identical materials on otherwise identical machines. Also, the drop-weight test presents a unique loading on the propellant; strain rates in excess of  $10^4 \text{ s}^{-1}$  and strains greater than 500% exist in constrained flow of less than 1 mm thickness. Thus friction causes a large amount of heating in the flow. However, removing friction (a very smooth anvil) may allow crushing of AP in the machine to come into play; this AP constraint between two rigid surfaces would make the drop-weight test unlike any real impact scenario. Therefore, for propellant rankings useful in other scenarios a constant friction coefficient is desirable, but in order to fully understand the drop-weight test some additional basic research is needed. First, a quantitative study of friction effects on propellants with varying particle sizes can be conducted. Second, using samples of homogeneous materials with known mechanical properties similar to propellants, it should be possible with this model to estimate the friction constant of an impact machine, thus providing a means to compare impact machines and interpret data. Third, details will be added to this model to account for sample inhomogeneities and study shear banding in more detail. The improved understanding of the deformation process would facilitate relating critical energy results to other scenarios.

## ACKNOWLEDGMENTS

This work was performed under Contract DAAL03-89-K-0061 with the Army Research Office. The views, opinions, and/or findings contained in this paper are those of the authors and should not be construed as an official Department of the Army position, policy, or decision, unless so designated by other documentation. Program monitor D.M. Mann provided funding essential to this research.

## NOMENCLATURE

### English

$c$  : Mass specific heat  
 $E$  : Energy  
 $K$  : Power law strength coefficient  
 $m$  : Friction constant  
 $M$  : Mass  
 $n_1$  : Power law strain-hardening exponent  
 $n_2$  : Power law strain-rate exponent  
 $r$  : Radial coordinate  
 $R$  : Sample radius  
 $t$  : Time  
 $T$  : Sample thickness  
 $U$  : Velocity  
 $W$  : Work

### Greek

$\epsilon$  : True strain  
 $\theta$  : Temperature  
 $\rho$  : Density  
 $\sigma$  : Stress

### Subscripts

$A$  : Anvil  
 $C$  : Critical condition  
 $F$  : Friction  
 $I$  : Internal deformation  
 $L$  : Layer at the sample/machine interface  
 $W$  : Drop weight  
 $y$  : Yield

## REFERENCES

1. C.S. Coffey, DeVost, V.F. and Yergey, B.A., JANNAF Propulsion Systems Hazards Subcommittee Meeting Proceedings (CPIA Publ. 446, I, 1986).
2. P.J. Baker, Mellor, A.M. and Coffey, C.S., J. Propuls. Power. 8, 578 (1992).
3. C.S. Coffey, DeVost, V.F. and Woody, D.L., JANNAF Propulsion Systems Hazards Subcommittee Meeting Proceedings (CPIA Publ. 477, I, 1988).
4. G.T. Afanas'ev and Bobolev, V.K., Initiation of Solid Explosives by Impact, (Israel Program for Scientific Translations, Jerusalem, 1971).
5. P.J. Baker and Mellor, A.M., AIAA Paper 92-3631, 1992.
6. B. Avitzur, Metal Forming: Processes and Analysis, (McGraw-Hill Book Co., New York, 1968).
7. B. Avitzur and Kohser, R.A., J. Eng. Ind. 100, 421 (1978).
8. C.S. Coffey, Frankel, M.J., Liddiard, T.P. and Jacobs, S.J., Seventh Symposium (International) on Detonation, (NSWC MP 82-334, 1981) pp. 970-975.
9. P.W.M. Jacobs and Whitehead, H.M., Chem. Rev. 69, 551 (1969).
10. R.E. Winter and Field, J.E., Proc. R. Soc. Lond. A 343, 399 (1975).
11. V.K. Mohan, Jyothi Bhasu, V.C. and Field, J.E., Ninth Symposium (International) on Detonation, (II, OCNR 113291-7, 1989) pp. 1276-1283.
12. M.R. Staker, Acta Met. 29, 683 (1981).

## HOT SPOT HEATING FROM IMPURITIES AND VACANCIES IN A CRYSTALLINE SOLID UNDER RAPID COMPRESSION

D. H. TSAI

10400 Lloyd Road, Potomac, MD 20854

### ABSTRACT

The role of impurity atoms and vacancy defects in the heating of hot spots in a 2D, fcc, monatomic lattice, subjected to rapid, 1D compression, has been studied by means of molecular dynamics. The interaction potential of the impurity atoms, their mass, and size were allowed to differ from those of the atoms in the host lattice. Several configurations of impurity and vacancy clusters were examined. The mechanisms of heating observed here were similar to those found earlier<sup>1</sup> in a bcc lattice with vacancy defects but without impurities.

### I. INTRODUCTION

In Ref. 1 we discussed the molecular dynamics of structural relaxation around defects (vacancy clusters and slip bands) and its effect on hot spot heating in a 2D, bcc, monatomic lattice when the lattice was rapidly compressed. We found that two mechanisms were responsible for the heating of hot spots. First, since in all systems, in the gas, liquid, or solid phase, the kinetic energy distribution in equilibrium is Maxwellian, there would *always* be some regions in the system that are hotter than the average. Second, in the condensed phases, particularly the solid phase, rapid compression would often initiate structural relaxation in the system, especially if the system also contained defects. The potential energy released by the relaxation process would be converted locally to kinetic energy, creating hot spots in the relaxing region. The amount of heating was a function of the energy of defect motion. If the strain energy of the defect should be large, then a small change in the strain energy could result in a large amount of heating. The relaxation process, moreover, often would not be confined to the local defects, because the compression could create defects in other parts of the system. For example, the large shearing stresses from 1D compression could generate a system of slip planes which could propagate from their starting sites. The energy associated with the creation and the relaxation of the new defects would then cause additional heating. Thus hot spots could occur in a much larger region than the immediate neighborhood of the original defects.

We have now extended our defect model to include impurity atoms with mass and size different from those of the host atoms. We have also investigated hot spot heating in an fcc lattice which, for central forces, should be more stable than the bcc structure.

Because of space limitations, we shall discuss only one set of results here. The model is described in Sec. II. Some of the general results are discussed in Sec. III, and the conclusions are summarized in Sec. IV. A fuller account of this work, including a comparison between the fcc and bcc lattices, will be presented elsewhere.

### II. MODEL

Our model was an fcc lattice installed in Cartesian coordinates with the  $X$  and  $Y$  axes aligned in the  $[110]$  and  $[\bar{1}10]$  directions, respectively, and the  $Z$  axis in the  $[001]$  direction. In this arrangement, the ratio of the distances between lattice planes normal to the  $X$  and  $Y$  axes and between lattice planes normal to the  $Z$  axis would be  $1/\sqrt{2}$ . Our system was 40 lattice planes in the  $X$  direction, 20 in the  $Y$  direction, and 10 planes in the  $Z$  direction, and periodic boundary conditions were used in the  $X$  and  $Y$  directions. These lattice planes divided the system into contiguous cells. The position of an atom in a cell was measured from the origin of that cell, and the atom was allowed to move freely across cell boundaries. A cell without any atom in it would be a site of a vacancy. To save computation, it was assumed that all atoms had only in-plane (i.e., 2D) motion in the  $X$ - $Y$  planes, and that the motion of corresponding atoms in all  $(001)$  face planes and in all  $(001)$  body planes,

respectively, was identical. This meant that the forces in the  $Z$  direction would exactly cancel, and hence only two (001) planes of the unit cell (400 atoms) need be considered in our system. The interaction potential  $V=V_{ij}$  between atoms  $i$  and  $j$  at a distance  $R=R_{ij}$  was assumed to be a Morse potential:

$$V = A_{ab}\epsilon \{ \exp[-2a(R-R_{ab})] - 2\exp[-a(R-R_{ab})] \} + B_{ab}. \quad (1)$$

Here  $\epsilon=1.0$  is the unit of energy and  $a=\ln 2/0.1$ . The parameters  $A_{ab}$ ,  $R_{ab}$  and  $B_{ab}$  are given below for the different cases listed in Table 1. The subscripts  $a$  and  $b$  refer either to host  $h$  or impurity  $i$ :

$$\begin{array}{lll} \text{Cases 1-6:} & A_{hh} = 1.0, & R_{hh} = 1.0, & B_{hh} = 0.015564, \\ & A_{hi} = \sqrt{2}, & R_{hi} = 1.05, & B_{hi} = 0.031077, \\ & A_{ii} = 2.0, & R_{ii} = 1.1, & B_{ii} = 0.062012. \end{array} \quad (1a)$$

$$\begin{array}{lll} \text{Case 7:} & A_{hh} = 1.0, & R_{hh} = 1.0, & B_{hh} = 0.015564, \\ & A_{hi} = \sqrt{2}, & R_{hi} = 1.0, & B_{hi} = 0.022011, \\ & A_{ii} = 2.0, & R_{ii} = 1.0, & B_{ii} = 0.031128. \end{array} \quad (1b)$$

The well depth ( $A_{hi}$ ) and the atomic size ( $R_{hi}$ ) for the  $h$ - $i$  interactions were assumed to be intermediate between those of the  $h$ - $h$  and  $i$ - $i$  interactions.  $B_{ab}$  refers to the amount by which the zero axis of  $V$ , eq. (1), was lowered to make  $V=0$  at the cutoff distance  $R_c=1.7$ . For  $R \geq R_c$ , both  $V$  and its derivative were assumed to be zero. The mass of the impurity atoms,  $M_i$ , was assumed to be either unity, the same as the host atoms, or 10. With  $R_{hh}$ ,  $M_h$ , and  $\epsilon$  all set to unity, the unit of time  $t=R_{hh}\sqrt{M_h/\epsilon}$  was also unity.

In addition to impurity clusters the system also could contain other defects such as vacancy clusters. We relaxed the system to a low pressure condition by adjusting the volume. The volume was changed by multiplying the coordinates ( $X, Y, Z$ ) of the atoms in the "normalized" lattice, with lattice planes at  $(1/\sqrt{2}, 1/\sqrt{2}, 1)$  apart, by scale factors ( $X_s, Y_s, Z_s$ ), respectively. The system was then heated, equilibrated, and relaxed again. This process was repeated until an equilibrium state at near-zero temperature and pressure was reached. Each system was then heated to a range of initial temperatures, and after equilibration, these configurations were used as the starting configurations.

The system was subjected to rapid 1D compression in the  $X$  direction to different volumes by changing  $X_s$  at a rate which corresponded approximately to planar shock compression.<sup>1</sup> The energy and stress distributions in the system were recorded at discrete time intervals until a new equilibrium condition under compression was reached. These data were then examined for the development of hot spots. A hot spot was defined here as a region made up of several atoms (or molecules) whose average kinetic energy  $E_k$  was higher than the  $kT$  of the system, and moreover, the higher  $E_k$  was required to have a lifetime of a few periods of atomic oscillations, so that the region could be said to be thermalized.

Table I. Configurations of some of the cases studied. Fcc lattice, interactions as given in eq. (1), compression=0~15% in  $X$ -direction.

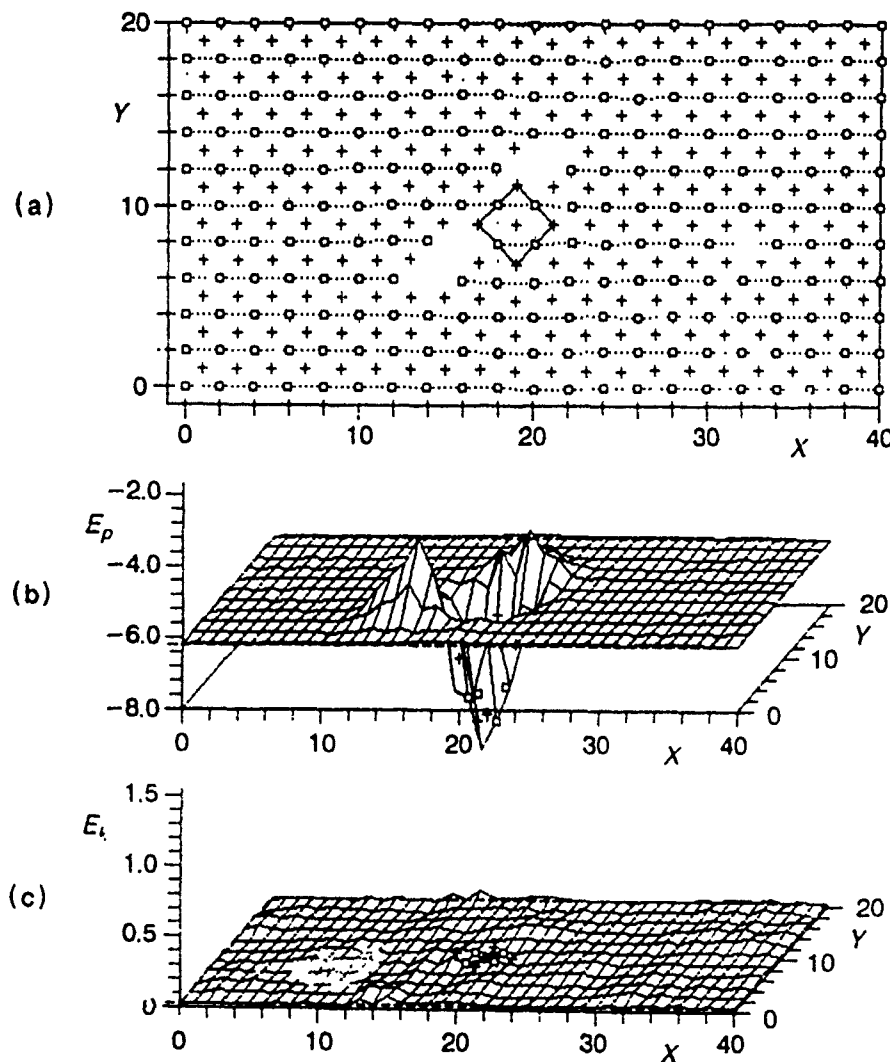
Cases	Impurities		Vacancy cluster in host lattice	Initial conditions				
	Cluster	Mass		$X_{co}$	$Y_{co}$	$Z_{co}$	$E_{ko}$	$E_{po}$
1	None		None	0.7027	0.7027	0.7041	0.0053	-6.193
2	None		1×10 atoms	0.7020	0.7025	0.7043	0.0049	-6.124
3	1×9 atoms	1	None	0.7044	0.7041	0.7090	0.0306	-6.253
4	1×9 atoms	10	None	0.7044	0.7044	0.7090	0.0515	-6.252
5	1×9 atoms	1	Fig. 1a	0.7049	0.7047	0.7082	0.0292	-6.193
6	1×9 atoms	10	Fig. 1a	0.7048	0.7047	0.7082	0.0311	-6.192
7	1×9 atoms	10	None	0.7003	0.7006	0.7071	0.0305	-6.296

### III. RESULTS

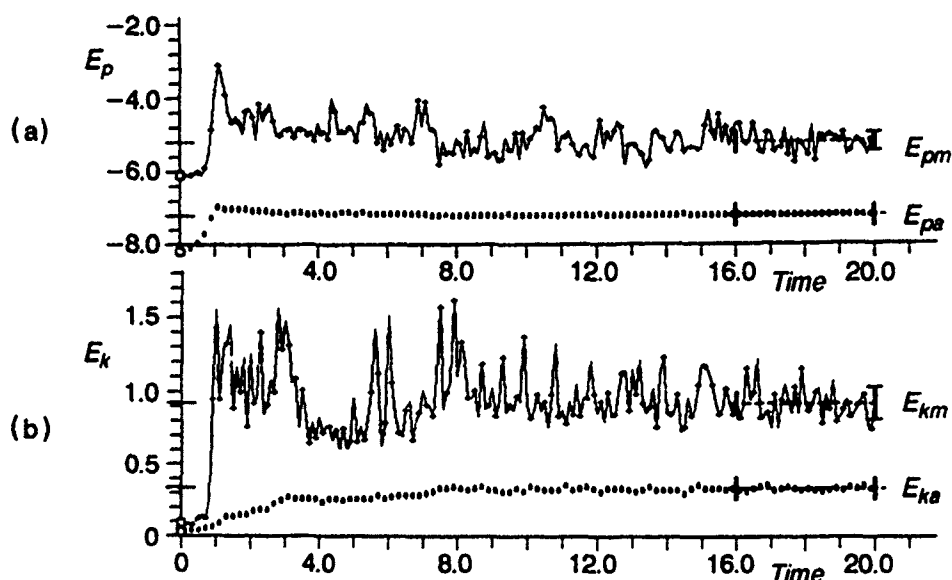
We shall discuss only one representative set of results which we select somewhat arbitrarily from Case 5 in Table 1. We shall also refer to the other cases, but without displaying the actual results. With more data available now than in Ref. 1, we shall attempt to present a more general discussion of hot spot heating from the viewpoint of molecular dynamics.

Fig. 1a shows the lattice configuration of Case 5 before compression, at  $t=0$ . The atoms in the two lattice planes of the system are shown as open squares and crosses. A cluster of nine impurity atoms were enclosed in outlines at the center. This cluster was of the size of a unit cell. It was flanked by two vacancy clusters. Fig. 1b shows the distribution of the potential energy,  $E_p$ , per atom, at each lattice site, averaged over the atom(s) at that site and those at the four nearest-neighbor sites.  $E_{pa}$  is the average of the whole system (dashed outlines), and  $E_{pm}$  is the maximum that occurred *somewhere* in the system. The depression at the center resulted from the impurity cluster. The two humps next to the depression were due to the strain energy of the vacancy clusters. Fig. 1c shows the corresponding distribution of the kinetic energy,  $E_k$ , per atom, in equilibrium.

Figs. 2a and 2b show the  $E_p$  and  $E_k$  of the lattice as a function of time  $t$  when the lattice



FIGS. 1a-1c. (a) Lattice configuration of Case 5 at  $t=0$ .  $M_h=M_l=1$ ,  $X_s=0.7049$ ,  $Y_s=0.7047$ ,  $Z_s=0.7082$ . (b) and (c)  $E_p$  and  $E_k$  distributions at  $t=0$ .  $E_{pm}=-4.124$ ,  $E_{pa}=-6.194$ ;  $E_{kn}=0.084$ ,  $E_{ka}=0.030$ .



FIGS. 2a–2b.  $E_p$  and  $E_k$  vs. time in the lattice of Fig. 1a when  $X_s$  was compressed from 0.7049 to 0.6299 in one unit of time.  $\bar{E}_{pm} = -3.205$ ,  $\bar{E}_{pa} = -5.199$ ,  $\bar{E}_{km} = 0.929$ ,  $\bar{E}_{ka} = 0.337$ .

(Fig. 1) was compressed uniaxially from  $X_s = 0.7049$  to  $X_s = 0.6299$  at a uniform rate in the first unit of time.  $\bar{E}_{pa}$  and  $\bar{E}_{pm}$  refer to the equilibrated values of  $E_{pa}$  and  $E_{pm}$  between  $t = 16$  and  $t = 20$ .  $\bar{E}_{ka}$  and  $\bar{E}_{km}$  refer to the corresponding values of  $E_{ka}$  and  $E_{km}$ .

#### Hot spots in elastic compression

During the first part of the compression, just before  $t = 0.7$  (Fig. 2), the lattice behaved elastically. We ascertained this by stopping the compression at  $t = 0.7$  and re-expanding it to its initial volume. We found that the lattice then reverted to its initial configuration.

In elastic compression, most of the work of compression is stored in the lattice as potential energy, the temperature rise is small, and the lattice configuration remains essentially unchanged. For example, Fig. 2 shows that at  $t = 0.7$ ,  $E_p$  had changed by about  $0.4\epsilon$  whereas  $E_k$  had changed only by about  $0.001\epsilon$ . The fcc structure in the present case was rather stable, and could sustain a large 1D compression without losing its elastic character, even when the structure contained defects. In all cases, we found that if the structure remained elastic, the rise in  $E_k$  due to compression would be small, whether or not the system contained defects, and whether the compression was 1D or 3D. The hot spots (averaged over eight lattice sites and over  $0.4t$ ) in these cases were not very hot, being only about 2.5 times the ambient temperature, similar to those found in Ref. 1 for the perfect bcc lattice. These hot spots clearly were the result of the Maxwellian distribution of the kinetic energy in the system, as was the case in Ref. 1.

#### Anelastic/plastic compression: Hot spots from structural relaxation

Figs. 3a–3c show the change in the lattice configuration and the energy distributions at  $t = 1.0$  at the end of compression. In Fig. 3a the lines connecting individual atoms show their displacements at the beginning and end of the time interval 0–1.0.

As Figs. 1b and 1c show, the strain energy due to the vacancy clusters was large compared with the kinetic energy of the lattice. These structural defects also tended to reduce the mechanical strength of the lattice in the neighborhood of the defects. If the compression should exceed the strength of the defect configuration, the structure could become locally unstable, at which point it would undergo deformation in an attempt to reduce its potential energy. This would allow more work to be done on the defect region than on other parts of the structure, so that the defect region would become hotter. A second and more important mechanism is that the deformation of the defect structure would lead to the conversion of

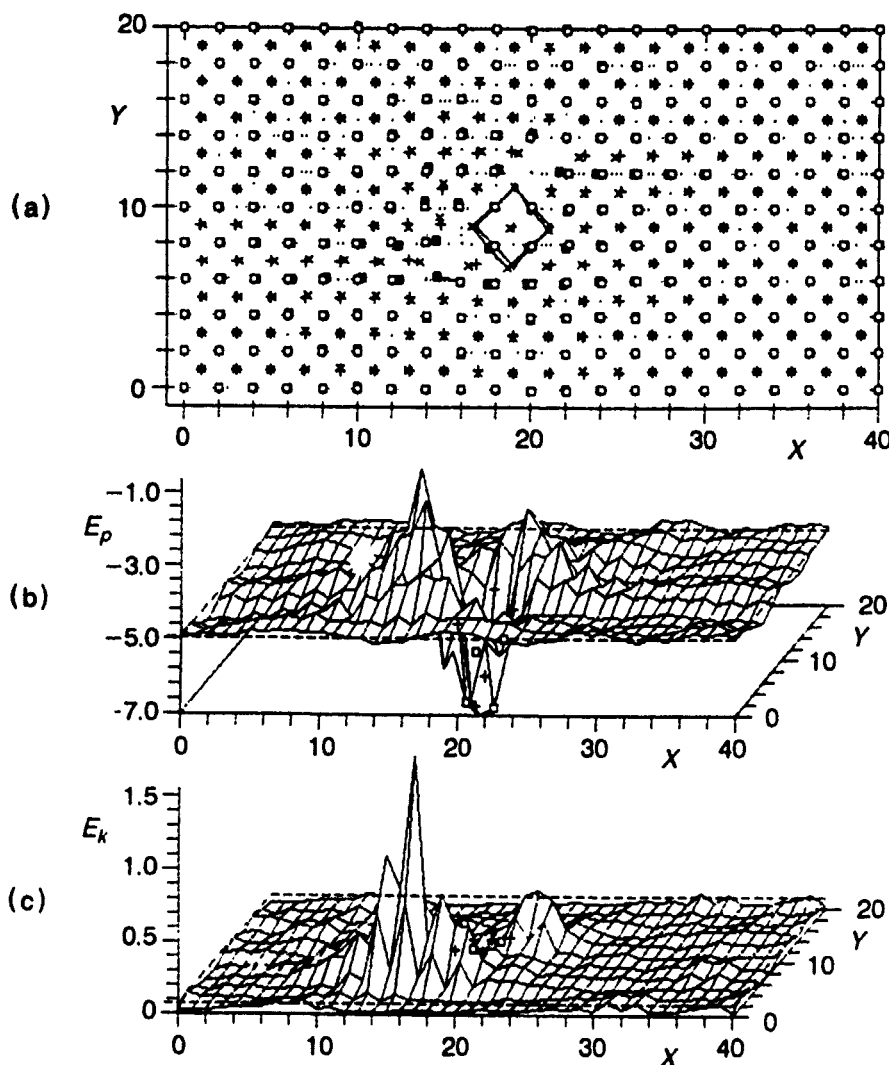


a part of the strain energy to kinetic energy which would then bring about local heating. Since the strain energy was large to begin with, a small change in the strain energy could lead to a large amount of heating.

We see an example of these two mechanisms of hot spot heating (viz., by compression and by structural relaxation) in Fig. 2. In the interval between  $t=0.7$  and  $1.0$ , both  $E_{pm}$  and  $E_{km}$  increased abruptly. These changes were accompanied by large atomic motion in the neighborhood of the defect structure in Fig. 3 at  $t=1.0$ . The displacements around the vacancy cluster to the southwest of the impurity cluster, and the accompanying rise in  $E_k$  were especially prominent. By  $t=2.0$ , the large atomic motion around the vacancy clusters had effectively filled the vacancy sites.

When we expanded this lattice to its initial volume at the end of compression, we found that the lattice would not revert to its initial configuration. The compression after  $t=0.7$  was therefore anelastic or plastic.

The two mechanisms of heating operated concurrently. To distinguish them, we could say that if the heating was accompanied by a local increase in  $E_p$ , then the hot spot would be from compression; otherwise, it would be from structural relaxation. By this criterion, we



FIGS. 3a-3c. (a) Change in the lattice configuration of Fig. 1a when  $X_1$  was compressed from 0.7049 to 0.6299 between  $t_1$  and  $t_2$  at a uniform rate.  $t_1=0$  ( $\square, +$ );  $t_2=1.0$  ( $\blacksquare, \times$ ). (b) and (c)  $E_p$  and  $E_k$  distributions at  $t_2$ .  $E_{pm}=-1.813$ ,  $E_{pa}=-4.939$ ;  $E_{km}=1.555$ ,  $E_{ka}=0.076$ .

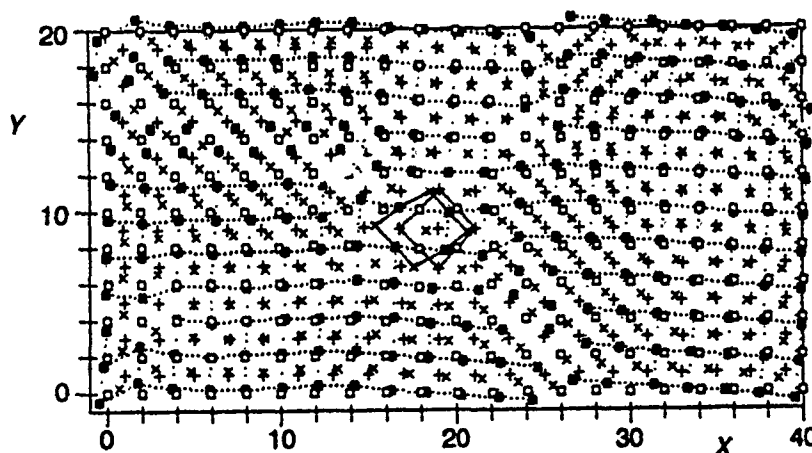


FIG. 4. Structural relaxation in the lattice of Figs. 1a and 3a in 20 units of time.  $t_1=0$  ( $\square, +$ );  $t_2=20.0$  ( $\blacksquare, \times$ ). Compression from  $X_s=0.7049$  to  $X_s=0.6299$  was applied at a uniform rate in the first unit of time, and held at  $X_s=0.6299$  between  $t=1$  and  $t=20$ .

could say that the peak  $E_{km}$  in Fig. 2b (and in Fig. 3c) at  $t=1.0$  was due to compression, and the second peak at  $t=1.4$ , which occurred to the northwest of the impurity cluster, was due to structural relaxation. By either mechanism, a part of the energy of compression was converted to heating each time a hot spot appeared. Fig. 2b shows a succession of hot spots.

These hot spots heated up the lattice as a whole ( $E_{ka}$  in Fig. 2b), until about  $t=10$ , to an average temperature ( $\bar{E}_{ka}=0.337$ ) considerably above that from elastic compression alone.

#### Propagation of defects

Structural relaxation requires time because it usually involves the coordinated movement of a number of atoms. Also, relaxation in one region would likely disturb the structure in adjoining regions, and this could create new defects which might require further relaxation. For these reasons, we expect that structural rearrangements would generally propagate to other parts of the system, and that it would usually require a long time (compared with sound propagation through the system) to obtain a fully relaxed structure. The energy conversion associated with these relaxation processes would then produce hot spots in other parts of the system. Thus the heated region could be much larger than the original defects.

Fig. 4 extends Fig. 3a and shows the aggregate changes in the lattice configuration in the interval  $t=0-20$ . Large displacements had occurred along a number of diagonal planes, reaching across the full width of the system. These complex slip systems resulted from the large shearing stresses from the uniaxial loading. The partially slipped planes tended to group themselves into bands rather than to distribute uniformly. They were observed also in a number of other cases in Table 1, and in Ref. 1 earlier. They appeared to be a common feature of the lattice rearrangement under 1D compression. The extent of the slip system was limited in our model by the periodic boundaries. But slip or partial slip should occur also in larger systems. For these reasons, it seems natural to identify these slip planes as the counterpart of the shear bands that are observed in experiments.<sup>2</sup>

In Fig. 4, the lattice at  $t=20$  also contained a number of dislocations.<sup>3,4</sup> These dislocations did not move easily after they were formed, as was also the case in Ref. 1.

In addition to the collapse of vacancy clusters and the formation of shear bands and dislocations, other modes of lattice rearrangement were also observed. For example, in the perfect fcc lattice of Case 1, the structure buckled in the  $Y$  direction when the system was compressed in the  $X$  direction to 0.893 of its initial volume. But the lattice retained its crystallinity, and the temperature rise was small ( $\bar{E}_{ka}$  changed from 0.030 to 0.043). When the buckled lattice was re-expanded to its initial volume, the system reverted to its original perfect structure. At a still higher compression, to 0.858 of its initial volume, the structure buckled to a greater extent, and there was greater amount of heating. Between  $t=4-5$  the structure underwent massive rearrangement and became disordered, indicating that local

melting had occurred. The temperature change in this case was large ( $\bar{E}_{ka}$  increased from 0.030 to 0.938). When the partially "melted" structure was re-expanded to its initial volume, the original crystalline configuration was not restored, at least not in 20 additional time units of computation.

#### Hot spots from impurities: Mass and size defects

The impurity cluster in Figs. 1 and 3 may be considered as a "molecule" embedded in the lattice, inasmuch as the interactions  $h-h$ ,  $h-i$ , and  $i-i$  were all different. Our interest in this model was in the energy transfer between the lattice and the "molecule," when the lattice was compressed.

If we denote the vibrational frequency of an atom by  $f$  and the force constant of the interatomic interactions by  $k$ , then  $f$  of the host atoms of mass  $M_h$  and that of the impurity atoms of mass  $M_i$ , each interacting with its own kind, would be in the ratio<sup>5</sup>  $f_h/f_i = (M_i k_h / M_h k_i)^{1/2}$ . We verified by separate calculations in Cases 3 and 4 that this was true to about 5% which was satisfactory. The vibrational frequency is related to the elastic properties of a lattice:<sup>5</sup> the lattice is stronger the higher its frequency and its elastic constant. Thus the impurity cluster should be mechanically stronger and less compressible than the host lattice when the mass of the impurity atoms was the same as that of the host atoms, and weaker and more compressible when the impurity mass was 10 times larger. Under the same compression, the less compressible cluster should therefore experience smaller increase in temperature. We confirmed this in Cases 3 and 4: The softer impurity cluster in Case 4 experienced larger temperature rise under compression than the stiffer cluster in Case 3, although in both cases there were hotter hot spots from defect movement and structural relaxation elsewhere.

At the interface between the impurity cluster and the host lattice, there should be some impedance mismatch which would increase the resistance to energy flow across the interface. But there should also be good thermal contact through the  $h-i$  type of interactions. The coupling, moreover, would increase under compression. Thus the impurity cluster should heat up quickly when the host lattice was heated, especially if the cluster was small. We found this to be true even in Cases 5 and 6: Here the vacancies partially separated the impurity cluster from the host lattice before compression. But good thermal contact was quickly established when the vacancies collapsed under load (Fig. 3a). The energy transfer was in fact aided by the hot spots at these sites. Thus in the various models of Table 1, the impurities clusters never appeared as "cold" spots, even when the cluster was stiff.

These results may be compared with the analysis of Dlott and Fayer.<sup>6</sup> They postulated that in a molecular solid under shock compression the increased phonon vibrations of the lattice would briefly overshoot the bulk temperature. Subsequently, molecular vibrations would be energized through anharmonic coupling between the lattice and the molecules through the "doorway" modes.

In addition to the different mass, the impurity atoms in Cases 3–6 were also larger than the host atoms ( $R_{ab}$  in eq. (1a)). The larger size had the effect of distorting the lattice structure. For example, Fig. 1a showed a slight distortion of the host lattice around the impurity cluster. But small misalignments in the lattice structure could have large effects on its strength. We found evidence of this by comparing Cases 4 and 7, in which only the size of the impurity atoms was changed, and both cases contained no vacancies. Under moderate (about 10%) compression, a number of slip planes formed in the lattice of Case 4, similar to Cases 5 and 6 in which the lattice was weakened by vacancy clusters next to the impurity cluster. In contrast, the lattice of Case 7 deformed primarily through buckling, similar to the perfect lattice of Case 1, the strongest structure by far in Table 1.

Finally, we note that in many cases the impurity cluster underwent large deformation and was grossly distorted when the compression was high. But in the range of our investigation we did not observe any break up of the cluster, even when the structure was partially melted.

#### IV. SUMMARY AND CONCLUSIONS

We have discussed some of the results of our molecular dynamical study of hot spots in an fcc lattice under rapid, uniaxial compression. Our focus has been on the role of structural

defects and the mechanisms of heating on an atomic scale. The defects included vacancy and impurity clusters of different sizes and geometries.

Under elastic compression, most of the work of compression would go into the lattice as increased potential energy, whether or not the lattice contained defects. The temperature rise would be determined principally by the *PVT* relation of the *perfect* lattice, and the rise would be small. In these cases, we found that hot spots developed from the Maxwellian distribution of the kinetic energy. They were about 2.5 times the average temperature of the lattice, and were not very hot. This was similar to the case of the perfect bcc lattice in Ref.

1. When the compression was reversed, and the lattice was allowed to expand to its initial volume, the initial configuration was restored, including the defect structure. This was so even if the compressed lattice had buckled elastically under load.

Under larger compression, if the elastic stability of the lattice should be exceeded, the structure could also undergo anelastic or plastic deformation. This kind of deformation could occur in a variety of situations. For example, if the system contained structural defects (vacancies, impurities, etc.) which generally would tend to weaken the mechanical strength of some part of the structure, the weakened part(s) would undergo structural relaxation. The relaxation would release some of the potential energy of the defect structure, and convert it to kinetic energy of the surrounding atoms and local heating. This mechanism of hot spot heating was general, and would operate as long as defects should be present. In this picture, the heating would then be a function of the energy of defect motion, which could be large compared to the temperature of the system. Moreover, structural relaxation in one part of the system could propagate to other parts, and the energy associated with such rearrangements would give rise to other hot spots. Thus the size of a hot spot could be considerably larger than the initial site of structural relaxation. Under uniaxial compression, which would generate large shearing stresses in the whole system, complex systems of slip planes often propagated far from the initial site of structural relaxation. These slip planes would group themselves into bands, which suggest that they could be identified as the shear bands commonly observed in shock wave experiments.

The hot spots also heated up the lattice as a whole. Our results showed that the amount of heating, which was large in some cases, depended on such factors as the lattice structure, the nature of the defects and their configuration, the method of compression, etc. These factors affected the response of the model through the different paths of structural relaxation, leading to different end states of partition between the potential and the kinetic energies, and hence different *PVT* relationships. In view of these results, it might be reasonable to ask whether the differences would persist, and how large they might be, in a more realistic 3D model. These questions require further investigation.

## ACKNOWLEDGMENTS

I thank R.W. Armstrong, L. Phillips, B. Rice, S. Trevino and P.K. Tsai for helpful discussions in the course of this work.

## REFERENCES

1. D.H. Tsai, *J. Chem. Phys.* **95**, 4797 (1991).
2. C.S. Coffey, W. Elban, and S. Jacobs, *Proceedings of the 16th JANAF Conference on Combustion*, Hampton, VA, 1980.
3. D.H. Tsai, in *NATO ASI Series*, edited by S.N. Bulusu (Kluwer, the Netherlands, 1990), Vol. 309, pp. 195-227.
4. F.A. Bandak, D.H. Tsai, and R.W. Armstrong, in *Shock-wave and high strain-rate phenomena in materials*, edited by M.A. Meyers, L.E. Malvern, and K.P. Staudhammer, (Dekker, New York, 1992), pp. 957-967.
5. C. Kittel, *Introduction to solid state physics*, 3rd edition, (Wiley, New York, 1967), Chap. 5.
6. D.D. Dlott and M.D. Fayer, *J. Chem. Phys.* **92**, 3798 (1990).

---

## **PART III**

---

### **Shock Phenomena**

## DISSOCIATIVE PHASE TRANSITIONS, SPLIT SHOCK WAVES, RAREFACTION SHOCKS, AND DETONATIONS

C. T. WHITE<sup>†</sup>, D. H. ROBERTSON<sup>†</sup>, M. L. ELERT<sup>‡</sup>, J. W. MINTMIRE<sup>†</sup>,  
and D. W. BRENNER<sup>†</sup>

<sup>†</sup>Theoretical Chemistry Section, Naval Research Laboratory, Washington, DC 20375

<sup>‡</sup>Chemistry Department, U. S. Naval Academy, Annapolis, MD 21402

### ABSTRACT

We present a comparative study of two different chemically-sustained shock waves. One shows behavior expected from the Zel'dovich, von Neumann, and Doering (ZND) continuum theory of planar detonations. The other exhibits the complexity of a split shock wave resulting from the presence of a polymorphic phase transition. This comparative study demonstrates the importance of carefully considering the high-pressure characteristics of the model in developing potentials for simulating detonations. This comparative study also raises the fascinating possibility of a first-order phase transition accompanying a condensed-phase detonation.

### INTRODUCTION

The shock wave accompanying a detonation typically travels through energetic materials at a velocity between five and ten kilometers per second [1]. This shock wave starts the material flowing a kilometers per second while heating it to thousands of degrees Kelvin and subjecting it to pressures of hundreds of kilobars. This rapid heating and compression of the material in turn causes the exothermic chemical reactions which ultimately sustain the detonation [1-3].

Although there have been many theoretical and experimental advances in understanding the macroscopic properties of detonations over the last forty years [1-3], much work remains to be done to clarify the atomic-scale behavior of shock-induced chemistry in energetic solids [1]. Continuum theories are not designed to treat discrete shock-induced chemistry while the extremely short time and length scales of the processes involved, together with their destructive nature, make experiment difficult and costly, if not currently impossible. In contrast, the picosecond and nanometer length scales of processes at shock fronts make them ideally suited for study using molecular dynamics (MD) simulations [4-11]. Such simulations might also clarify how discrete detonation chemistry relates to properties of planar detonations that can be understood by continuum (hydrodynamic) theories. However, any model of a detonating solid requires some form of energy release to sustain the detonation and so the Lennard-Jones potentials, which are successfully used in MD simulations of nonreactive shocks [4,5], are inadequate. Earlier MD studies have introduced exothermic chemical reactions by using a predissociative potential that incorporates all the chemical energy release into a single bond dissociation in a molecule [6]. In energetic materials, however, exothermicity typically results from the reorganization of bonding from weak to strong bonds. Therefore, predissociative potentials do not include sufficient detail to examine the atomic features of shock-induced chemistry. Studies in one dimension [9] showed the promise of employing many-body

potentials to study chemically-sustained shock waves, but the potential used in that work was ill-defined in higher dimensions.

Recently, we have introduced a new approach based on many-body potentials that not only describes bonding and chemical reaction at the atomic level with well-defined reactants, products and reaction paths but also allows for efficient computation in MD simulations involving thousands of atoms in two or three dimensions [12]. Simulations in two dimensions proved that this model can support a chemically-sustained shock wave with calculated temperature, pressure, particle flow and shock velocities, and power generation all consistent with macroscopic experimental results and the classic continuum theory of detonations [12]. These studies have also established for the first time a quantitative link between results from MD simulations that follow the individual atomic trajectories and the continuum theory of detonations based on the Navier-Stokes equations.

In this paper we present a comparative study of two qualitatively different chemically-sustained shock waves. The two models used in these studies are based on deceptively similar many-body potentials. This comparative study vividly demonstrates that it is not sufficient to focus only on reproducing physically reasonable reactants and products with realistic barriers to reaction in developing many-body potentials for simulating solid-state detonations. Rather, the high-pressure character of the model must also be carefully considered. This comparative study also illustrates the fascinating possibility of a chemically-sustained shock wave accompanied by a dissociative phase transition.

## MODEL AND METHOD

Both Model I and Model II used in this comparative study are based on the empirical bond order (EBO) potential form introduced by Tersoff [13] to describe the static properties of silicon but tailored by us in Ref. 12 to describe a simple generic model of an explosive—a model AB molecular solid that when shocked might undergo exothermic chemical reactions to form the more stable  $A_2$  and  $B_2$  molecular products. In both models formation of the  $A_2$  and  $B_2$  products releases 3 eV of energy per molecule. It is this release of energy that has the potential for sustaining the shock wave. Model I has already been introduced in Ref. 12 and shown there to yield a physically and chemically reasonable model material. The functions used to define Model II are identical to those used to describe Model I. The parameters entering these functions are also identical in the two models except for the equilibrium bond lengths of the reactant and product diatomic molecules which have been decreased from 0.12 nm in Model I to 0.1 nm in Model II. Because of the form of the EBO potential, this decrease in bond length is accomplished without changing the vibrational frequencies of the reactant and product molecules, their equilibrium molecular and crystalline binding energies, and distance of closest approach between atoms in nearest neighboring molecules in the condensed phase AB crystalline molecular solid. Reaction barriers are also similar between the two models as are their respective condensed-phase speeds of sound.

MD simulations in two dimensions using both models are initiated by impacting a flyer plate at the edge of the semi-infinite model diatomic AB molecular crystal initially at rest and at near zero temperature and pressure. This flyer plate is composed of several layers of the unreacted energetic AB molecular solid appropriate to the model. Hence, for Model I a flyer plate composed of Model I material is used, while for Model II a flyer plate composed of Model II material is used. The dynamics of the atoms in both systems are then propagated by integrating Hamiltonian's equations of motion using a Nordsieck predictor-corrector method [14]. Periodic boundary conditions are enforced

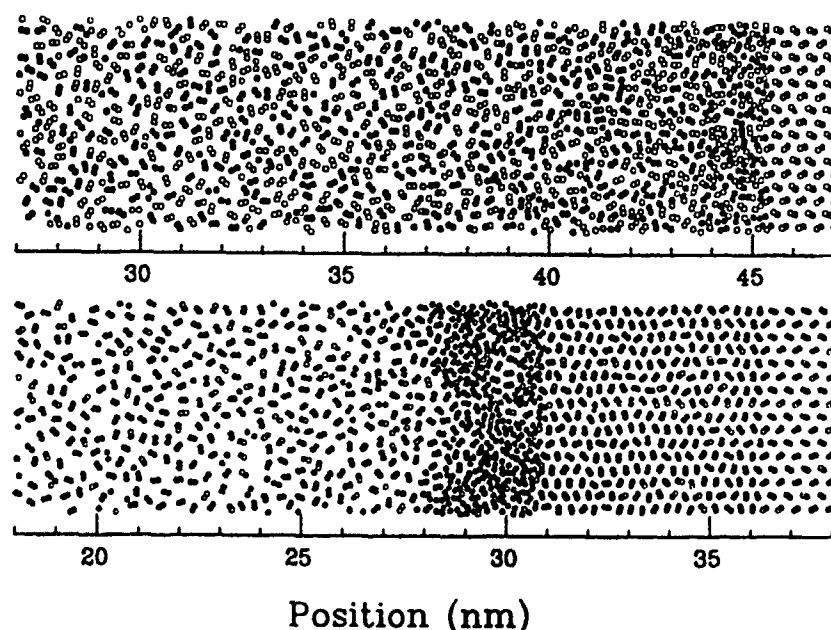


Figure 1. Snapshots of the chemically-sustained shock waves for Model I and II, top to bottom, respectively, at 5.0 ps after impact by a 4-layer flyer plate with a 6.0 km/s impact velocity.

perpendicular to the direction of shock propagation. Doubling the width of the periodic boundary has no significant effect on the results.

## RESULTS AND DISCUSSION

Figure 1 depicts typical snapshots of chemically-sustained shock waves that can result for the hypervelocity impact of a four-layer flyer plate at the edge of Model I (top) and Model II (bottom). Although only five picoseconds into the simulations, the distinctly different character of the chemically-sustained shock wave supported by Model I and Model II is already evident. Both models transform AB reactants (visible to the far right of Fig. 1) to products (visible to the far left Fig. 1) but in a qualitatively different fashion.

In Model I the shock front compresses the material to the point that chemical reactions begin. The pressure then gradually decreases leading to a lower density products region as shown in Fig. 2. By 5 ps the overall shock wave structure in Model I has already begun to develop the classic form of a von-Neumann spike followed by a developing rarefaction (Taylor) wave expected from the ZND continuum theory of planar detonations [1-3]. As we have shown elsewhere, this form becomes more distinct at longer times with the simulations rapidly approaching near-steady flow conditions close to the shock front [12].

In contrast, Model II does not exhibit the classic ZND behavior as shown in Figs. 1-2. First, in Model II there is a leading compressional wave—absent in Model I—which heats and compresses the material and starts it flowing but does not induce chemical reactions. This compressional region is then followed by a dissociative zone where the



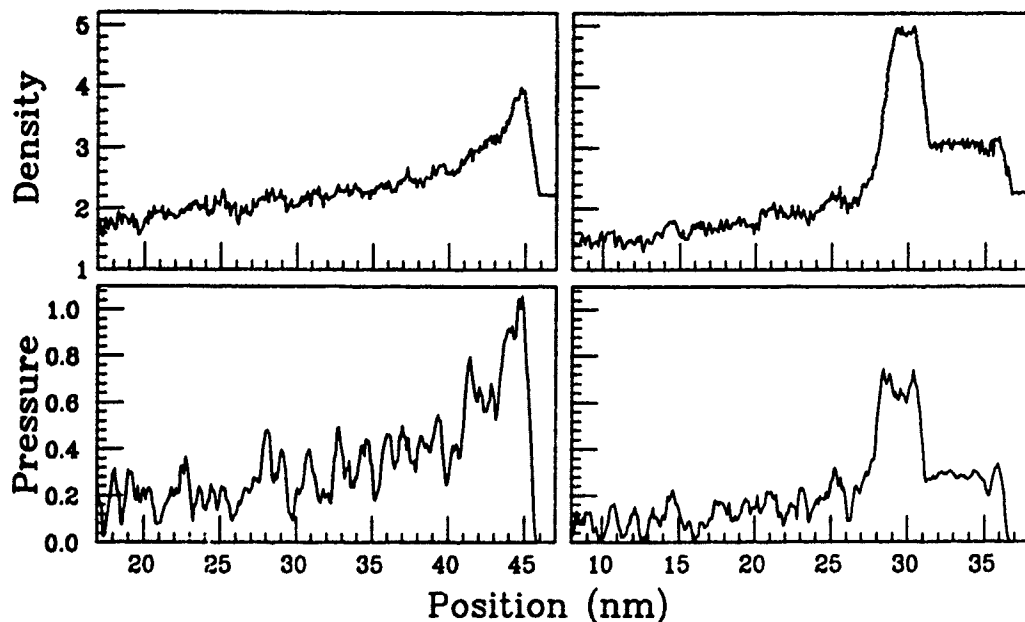


Figure 2. Plots of the pressure ( $\text{eV}\text{\AA}^{-2}$ ) and density ( $\text{amu}\text{\AA}^{-2}$ ) as a function of position for Model I (left) and Model II (right) at an elapsed time after impact of 5.0 ps.

molecules are compressed to the point that they lose their molecular identity but without the large-scale production of molecular products. Although the density is higher in this dissociative region than in the leading compressional region, the average nearest-neighbor interatomic separation has actually increased due to the greater coordination of the atoms. In addition, the dissociative region in Model II is separated from the products region at the far left of Fig. 1 by a distinct boundary across which the majority of products are abruptly produced. Furthermore, as Fig. 2 shows, Model II also exhibits a developing flat-topped shock-wave structure rather than the peak and following Taylor wave exhibited by Model I. Although the three boundaries separating the four distance regions in Model II—like the single boundary in Model I—rapidly stabilize to steady velocities, we have found that these boundaries move at velocities of 7.2, 6.4 and 5.9 km/sec [15]. Hence, the lengths of the leading compressional and dissociative regions in Model II enlarge to millimeters in microseconds.

Through longer time simulations and varying initial conditions we have verified that the qualitative differences in the chemically-sustained shock waves exhibited by Model I and Model II are not artifacts of the starting conditions but are rather intrinsic properties of these models. Thus, although Model I and Model II only essentially differ at ambient conditions in their bond lengths, these models nevertheless support altogether different chemically-sustained shock waves.

We have traced the shock-wave splitting present in Model II to a first-order polymorphic phase transition accompanied by a volume collapse [16]. This volume collapse has been made possible at the temperatures and pressures of the chemically-sustained shock wave in Model II by shortening the equilibrium bond lengths without changing

the intermolecular potential. This polymorphic phase transition is a dissociative one where the AB diatomic molecular solid transforms to a close-packed material with much higher density but larger average nearest-neighbor interatomic separations. More than 35 years ago the first shock induced polymorphic phase transition was observed [17]. An important property of these phase transitions predicted from continuum theory [17-19] and observed experimentally [17-19] is the associated compressional shock wave splitting that might occur. If split compressional shock waves are present, then continuum theory predicts [17] that the leading shock front starts the material flowing bringing it to the point of transition while the transition occurs across the second compressional shock front. This is just the behavior observed in Model II. Actually, there are not one but two polymorphic transitions visible in the snapshot of the Model II simulations. This second transition occurs at the interface between the dissociative zone and the rarefaction region as the material transforms from the dissociative close-packed phase to  $A_2$  and  $B_2$  molecular products. It is this second transition which produces the required behavior in the shock Hugoniot for a rarefaction shock wave. This product rarefaction shock front acts as a steadily moving piston producing the flat-topped shock-wave structure observed in Model II. In contrast, in Model I there is no evidence for either transition and the simulations evolve towards a classic ZND detonation.

Shock induced phase transitions accompanied by shock wave splitting are well known in energetic materials. The possibility of a dissociative phase transition induced by a chemically-sustained shock wave is fascinating because this behavior might yield a more efficient conversion of chemical energy to useful work. To our knowledge, however, a chemically-sustained shock wave accompanied by a first-order phase transition has yet to be observed. At a minimum, the results of the comparative study between Model I and Model II demonstrates the importance of carefully considering the high-pressure characteristics of the model in developing potentials for simulating condensed phase detonations.

## SUMMARY

We have presented a comparative study of two qualitatively different chemically sustained shock waves. One shows behavior expected from the ZND theory of planar detonations. The other exhibits the complexity of a split shock wave resulting from the presence of a polymorphic phase transition. The presence of this phase transition in this second model transforms the von-Neumann spike into a flat-topped profile with a preceding compaction wave which is also flat-topped. This comparative study illustrates the importance of carefully considering the high pressure characteristics of the model in developing many-body potentials for simulating chemically-sustained shock waves. This comparative study also points out the fascinating possibility of chemically-sustained shock waves accompanied by a first-order phase transition.

## ACKNOWLEDGEMENTS

This work was supported in part by the Office of Naval Research (ONR) through the Naval Research Laboratory and through the ONR Physics Division. Computational support was provided in part by a grant of computer resources from the Naval Research Laboratory and from ONR. One of us (JHR) acknowledges a NRC/NRL Postdoctoral Research Associateship. MLL was supported by the NRL-USNA Cooperative Program for Scientific Interchange.

## REFERENCES

- [1] W. C. Davis, *Sci. Am.* **256**, 106 (1987).
- [2] Ya. B. Zel'dovich and A. S. Kompaneets. *Theory of Detonation*, (Academic Press, New York, 1960) and references therein.
- [3] W. Fickett and W.C. Davis, *Detonation*, (U. Calif. Press, Berkeley, 1979); W. Fickett, *Introduction to Detonation Theory*. (*ibid.*, 1985) and references therein.
- [4] B. L. Holian, W. G. Hoover, W. Moran, and G. K. Straub, *Phys. Rev. A* **22**, 2798 (1980).
- [5] A. N. Dremin and V. Yu. Klimenko, *Prog. Astronaut. Aeronaut.* **75**, 253 (1981).
- [6] A. M. Karo, J. R. Hardy, and F. E. Walker, *Acta Astronautica* **5**, 1041 (1978).
- [7] D. H. Tsai and S. F. Trevino, *J. Chem. Phys.* **81**, 5636 (1984).
- [8] M. Peyrard, S. Odier, E. Oran, J. Boris, and J. Schnur, *Phys. Rev. B* **33**, 2350 (1986); S. G. Lambrakos, M. Peyrard, E. S. Oran, and J. P. Boris. *Phys. Rev. B* **39**, 993 (1989).
- [9] M. L. Elert, D. M. Deaven, D. W. Brenner, and C. T. White. *Phys. Rev. B* **39**, 1453 (1989).
- [10] N. C. Blais and J. R. Stine. *J. Chem. Phys.* **93**, 7914 (1990).
- [11] D. H. Robertson, D. W. Brenner, and C. T. White. *Phys. Rev. Lett.* **67**, 3132 (1991); C. T. White, D. H. Robertson, and D. W. Brenner. *Physica A* **188**, 357 (1992).
- [12] D. W. Brenner, D. H. Robertson, M. L. Elert, and C. T. White. (*submitted for publication*).
- [13] J. Tersoff, *Phys. Rev. Lett.* **56**, 632 (1986). *Phys. Rev. B* **37**, 6991 (1988).
- [14] C. W. Gear, *Numerical Initial Value Problems in Ordinary Differential Equations*, (Prentice-Hall, Englewood Cliffs, 1971).
- [15] D. H. Robertson, D. W. Brenner, M. L. Elert, and C. T. White, in *Shock Compression of Condensed Matter-1991*, S. C. Schmidt, R. D. Dick, J. W. Forbes, D. G. Tasker, Eds. (Elsevier Science Publishers B. V., Amsterdam, 1992), p. 115.
- [16] C. T. White, D. H. Robertson, D. W. Brenner, M. L. Elert, and D. W. Brenner, in *Microscopic Simulations of Complex Hydrodynamic Phenomena*, M. Mareschal and B. L. Holian, Eds. (Plenum Press, New York, 1992), p. 111.
- [17] S. Minshall, *Phys. Rev.* **98**, 271 (1955).
- [18] G. E. Duvall and R. A. Graham, *Rev. Mod. Phys.* **49**, 523 (1977).
- [19] Ya. B. Zel'dovich and Yu. P. Raizer, *Physics of Shock Waves and High-Temperature Hydrodynamic Phenomena*, Vol. 1 & 2, (Academic Press, New York, 1966, 1967).

## FEMTOSECOND SPECTROSCOPY OF CHEMICALLY REACTIVE SOLIDS: A METHODOLOGY

WEINING WANG, MARC M. WEFERS, AND KEITH A. NELSON

Department of Chemistry, Massachusetts Institute of Technology, Cambridge, MA 02139

### ABSTRACT

An experimental methodology for recording femtosecond time-resolved observations of irreversible change in solids is described. The central problem posed is that the time-dependent evolution must be observed on a single-shot (i.e. real-time) basis since the sample may be permanently altered after each excitation event. Preliminary demonstrations of real-time femtosecond spectroscopic observations are presented. In addition, one-shot data acquisition techniques open up the possibility of excitation intensities that greatly exceed optical damage thresholds of most samples. Since only one excitation pulse is used, cumulative damage mechanisms may be circumvented. Even if the sample is damaged in a single shot, in some cases the events of interest may be observed before damage occurs. The use of timed sequences of high-intensity excitation pulses to drive large-amplitude, coherent lattice vibrations is discussed. If successful, such large-amplitude lattice vibrations could assist crystalline chemical reactions or structural phase transitions.

### INTRODUCTION

#### Motivation for Real-time Femtosecond Spectroscopy

Femtosecond spectroscopy of chemical reactions in gases and liquids has been carried out since the mid-1980's [1]. In the simplest cases, optical absorption into an unstable molecular potential energy surface leads to direct photodissociation or rearrangement, and the elementary bond breakage or other chemical process takes place on subpicosecond time scales. If the reacting species is in a condensed medium, the surroundings may influence reaction dynamics considerably. Neighboring molecules may offer mechanical or dielectric resistance to the separation of photofragments, and dissipation of energy from the reactive mode into the nonreactive ("bath") modes of the molecule and its environment may prevent reaction altogether. Time-resolved spectroscopy of liquid-state chemical reactions has revealed substantial solvent effects on chemical reaction dynamics and yield [1,2].

The solid-state environment typical of most energetic materials should be expected to mediate chemical reactivity far more heavily than liquid-state surroundings. Molecular dissociation should be strongly influenced by the repulsive forces of immediate neighbors, or by the possibility of reaction between fragments and their neighbors. An ordered crystalline environment is known to be particularly influential, with reaction dynamics, yields, and branching ratios strongly dependent on the details of crystal structure and quality [3].

Chemically reactive crystals are of special interest both because of the high energy density that can be stored and because, from a fundamental point of view, the ordered environment could facilitate detailed analysis of energy flow between reactive species and their neighbors. Femtosecond spectroscopy of crystalline chemical reactions should reveal much about the sequence of events involved in energy release and about the microscopic mechanisms of reaction initiation, propagation, and termination. However, the only femtosecond spectroscopic observations of chemically reactive solids reported to date have involved reversible excimer formation reactions in which very low energies (dictated by van der Waals forces) are released [4,5].

The reason for so little solid-state femtosecond spectroscopy is simple: most solid-state samples cannot be conveniently "flowed" to remove altered material from further experimental observation. In examination of chemical reactions in the gas or liquid phase, the sample is flowed so that reaction products resulting from one excitation event (one laser "shot") are removed before the next laser shot. Data are collected not in a single shot but through many excitation-probe sequences. An excitation pulse initiates photochemical reaction at the zero of time, and a delayed probe pulse is used to monitor reaction progress at some later time. Fresh

material is then introduced into the irradiation volume, and the excitation-probe pulse sequence is repeated with a slightly different delay time. This procedure is continued until the entire process of interest is observed. Each excitation-probe repetition yields a single point on the time axis, and the data are collected point by point. Often many thousands of repetitions (with signal averaging of many repetitions at each delay time) are performed to yield a single time-dependent sweep. In this manner the time-dependent evolution of the sample following photoexcitation is recorded "point by point" along the time axis. This procedure cannot be followed with most solid samples. Only samples of excellent uniformity and optical quality and of large size may be moved after each shot to continuously expose fresh material. If this is not possible, the full time-dependent response must be recorded in a single shot. An experimental apparatus is described below in which multiple probe pulses are produced and used to monitor the sample at several different delay times following photoexcitation. Preliminary data will be shown, and current efforts to improve the apparatus will be discussed.

### Prospects for Large-amplitude Coherent Phonon Excitation

Single-shot data acquisition permits femtosecond time-resolved spectroscopy to be carried out even when a non-flowable sample is permanently altered through photoexcitation. Permanent sample change could be due to a photochemical reaction under study, as discussed above, or due to other processes. Even samples which are not ordinarily photoreactive can be optically altered ("damaged") by a sufficiently intense excitation pulse. Some optical damage mechanisms are dependent on cumulative radiation energy density over an extended time period, while others depend only on peak radiation intensity. In almost all cases the damage mechanism is unclear, with the occurrence and extent of damage dependent on not only predictable factors such as optical intensity and wavelength but also on pulse duration, repetition rate, and even the optical phase profile [6]. In general, single-shot spectroscopy should allow examination of samples which are irradiated by excitation pulses whose intensities exceed optical damage thresholds. Cumulative damage mechanisms could be avoided entirely, and even damage which results from high peak intensity may occur on a time scale longer than the one of interest. In the latter case measurements could be recorded before sample deterioration takes place.

This opens up the possibility of using intense excitation pulses to excite coherent lattice vibrations (optic phonons) of large amplitude through impulsive stimulated Raman scattering (ISRS). In ISRS, an ultrashort excitation pulse exerts a sudden ("impulsive") driving force on Raman-active vibrational modes, initiating coherent vibrational oscillations which can then be monitored. Time-dependent observations are made of the crystal lattice at various stages of collective vibrational distortion away from its equilibrium configuration. This is particularly interesting if the lattice vibrational mode plays an important role in chemical or structural rearrangement [7]. In organic excimer forming crystals, a lattice mode whose motion brings neighboring molecules toward each other along a likely reaction path was examined through ISRS [8,9]. In this case, the mode coincides well with the excited-state reaction coordinate. In ionic crystals which undergo structural phase transitions, "soft" lattice modes whose motions bring ions from their positions in one phase toward the positions they occupy in a new phase (and which therefore play the role of collective reaction coordinate) were studied [10]. In all cases to date, however, the coherent phonon amplitudes (i.e. how far molecules or ions in a crystal were driven through ISRS) were small - on the order of  $10^{-5}$ - $10^{-4}$  Å. This is much smaller than quantum or mean thermal uncertainties, and so no new chemical or structural changes were induced. Far higher coherent phonon amplitudes could be reached through the use of more intense excitation pulses with near-resonant wavelengths, but sample damage has prevented this so far. Single-shot detection methods should permit more intense ISRS excitation pulses and should allow considerably higher phonon amplitudes.

A complementary experimental approach to higher driven phonon amplitudes through ISRS is the use of multiple excitation pulses to exert a series of "impulsive" driving forces on a selected mode. This has been demonstrated on both organic and ionic crystals [9,11]. A sequence of excitation pulses is timed to match the lattice vibrational period of interest, and each pulse amplifies the coherent vibrational motion induced by pulses before it. This is closely analogous to repetitively driving a child on a swing with an appropriately timed series of pushes.

Multiple excitation pulses, each with intensity below the optical damage threshold, can result in improved phonon amplitudes and also improved mode selectivity relative to single pulses. Intense multiple excitation pulses could be used in conjunction with single-shot detection methods.

The production of femtosecond pulse sequences whose timing (and also optical phases) can be controlled is a recent achievement [12]. As described below, femtosecond "pulse shaping" originally involved the use of optical elements (spatially varying masks) which were permanently fabricated to produce a specified pulse sequence. Any pulse sequences of interest therefore needed to be specified in advance so that the corresponding masks could be manufactured. More recently, multielement liquid crystal displays (LCDs) have been used so that new pulse sequences could be produced at will. We have developed computer algorithms which permit the user to simply specify the desired pulse sequence. The necessary manipulations are then carried out on the LCD such that the pulse sequence is produced. Some illustrative results of the current capabilities will be shown, and the prospects for further development will be described.

## EXPERIMENTAL

### Single-shot Detection: Multiple Probe Pulse Apparatus

We have constructed a single-shot femtosecond spectrometer consisting of a series of partial reflectors, delay lines, and other optics such that a single probe pulse is split into sixteen pulses whose arrival times at the sample are controlled independently. The setup is illustrated in Fig. 1. The apparatus includes several sets of four reflectors whose reflectivities at the probe wavelength are 25%, 33%, 50%, and 100%. This insures reasonable equal intensities of all sixteen probe pulses. The probe pulses are overlapped spatially with the excitation pulse at the sample. The transmitted probe pulses are incident on different regions of a CCD detector and their intensities are measured. The CCD detector is equipped with software designed to locate separate "regions of interest" (i.e. separate laser spots) and to carry out simple manipulations of the intensities recorded at pixels within each region.

The laser system used to conduct preliminary multiple probe pulse experiments has been described in detail in earlier publications [13]. Briefly, an antiresonant ring dye laser is synchronously pumped by the frequency-doubled output of a cw modelocked Nd:YAG laser. The output, centered at 620 nm, is passed through a three-stage amplifier which is pumped by the frequency-doubled output of a Q-switched, modelocked, and cavity-dumped Nd:YLF laser. The Nd:YAG and Nd:YLF pump lasers are synchronized through the use of a common RF source which drives both of their modelockers. The synchronously amplified output consists of 80-fs, 10- $\mu$ J, 620-nm pulses at a 500-Hz repetition rate.

In the preliminary multiple probe pulse experiments, transient birefringence (i.e. optical Kerr effect or OKE) or transient absorption was measured. In the former case, the excitation pulse was linearly polarized at 45° from vertical (V). The probe pulses were V polarized, and a horizontal (H) polarizer was placed in front of the CCD detector. In the latter case, the excitation polarization was varied and there was no polarizer after the sample. Note that in addition to the individual delay lines for each probe pulse, there is an overall delay line which changes the timing of all the probe pulses relative to the excitation pulses but not relative to each other. Data were recorded with several choices of overall delay to check for internal consistency. In addition, data were recorded over periods of several hours to check for drift in the spatial alignment of the pulses in the sample or at the CCD detector.

### Computer Generation of Multiple Excitation Pulses

The setup for production of shaped excitation pulse sequences is illustrated in Fig. 2. The frequency components of a single femtosecond pulse are dispersed by a grating and focussed onto a spatially varying mask. This can be an amplitude mask, which blocks selected components, or a phase mask, which alters the phases of selected components. The transmitted light is incident on a second lens and grating identical to the first and with similar positions and

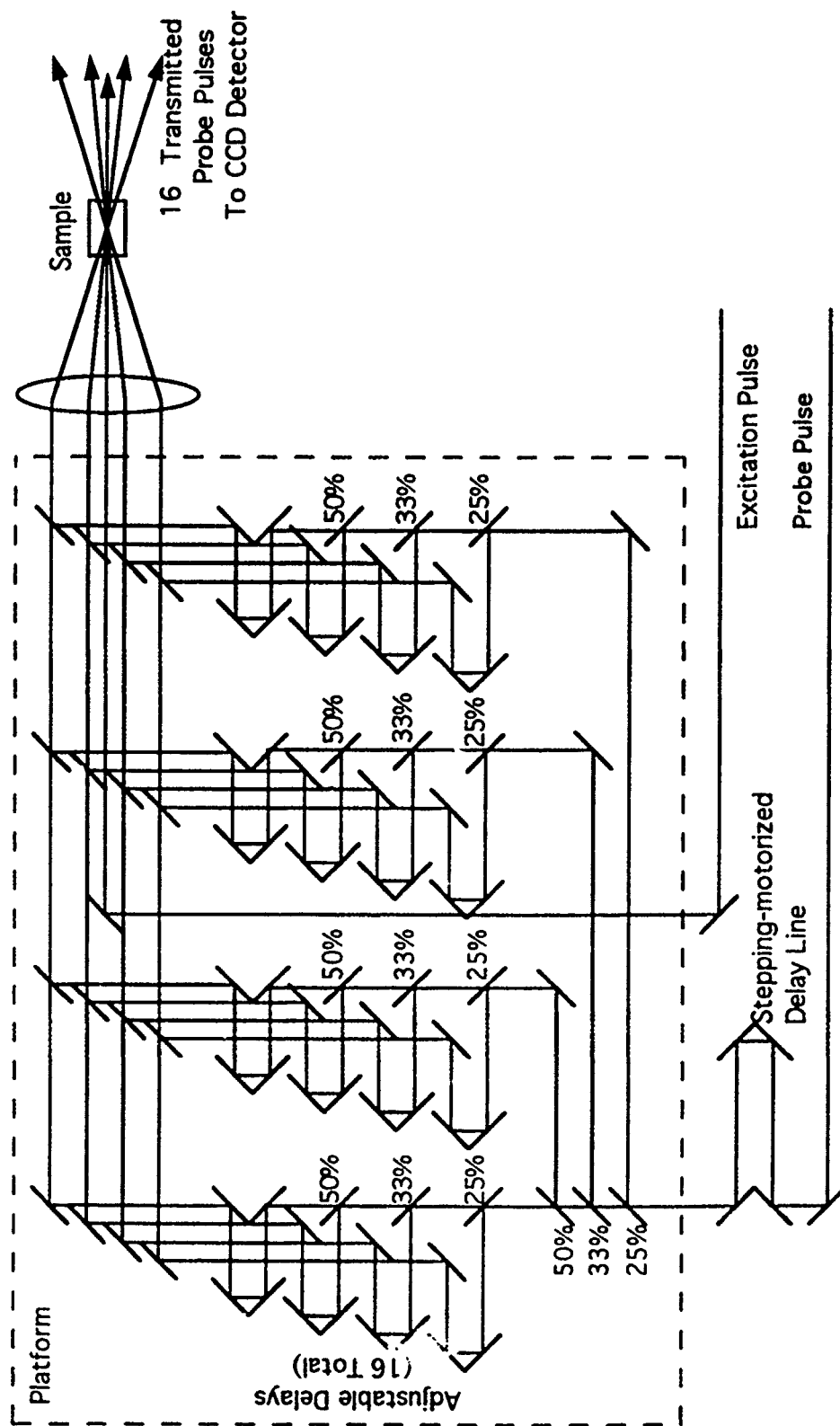
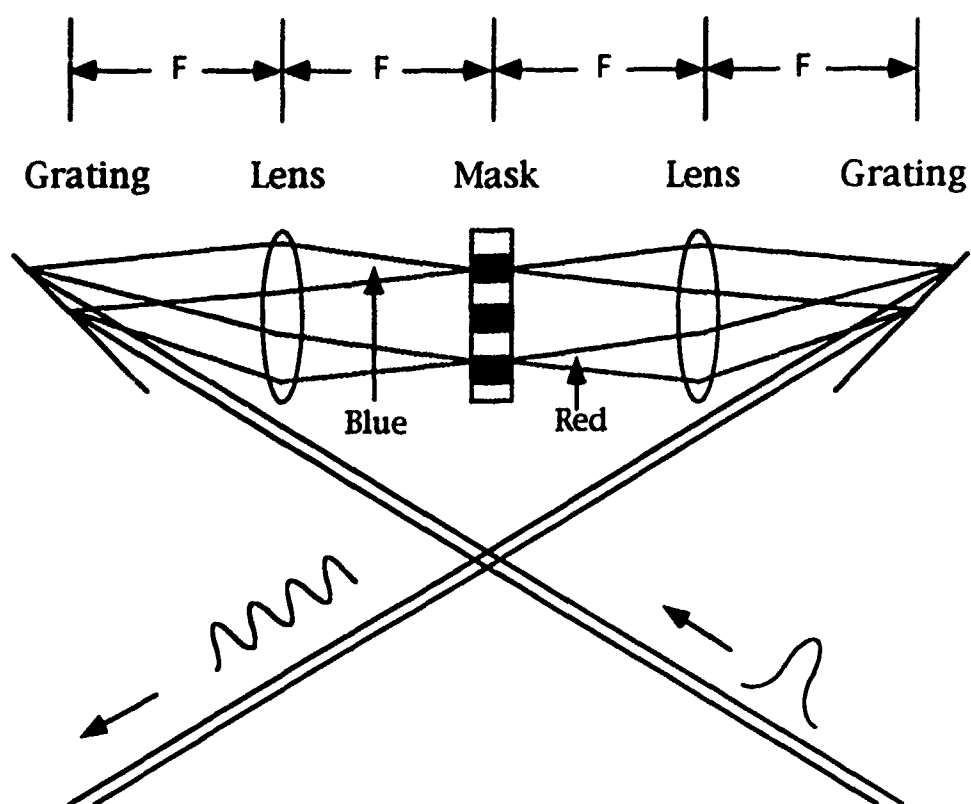


Figure 1. Schematic illustration of pump-probe experiment with 16 probe pulses.

## PULSE SHAPING APPARATUS



**Figure 2:** A schematic illustration of the pulse shaping apparatus. An ultrashort pulse is spatially dispersed and collimated by the first grating and lens. The phase and/or amplitude of differing frequency components are altered at the mask for the desired output pulse. The second grating and lens recombine the shaped pulse. Not shown are half wave plates placed between each pair of lens and grating.



orientations relative to the mask. The manipulations of the mask on the frequency profile of the pulse lead to corresponding effects on the temporal profile. With both phase and amplitude masks, the outgoing temporal profile and phase can both be controlled. The original masks were permanently etched onto glass substrates, and each mask was used to generate a single pulse sequence. In our current setup we have a multielement liquid crystal display (Meadowlark Optics) and driver (Cambridge Research and Instrumentation). The display consists of seventy pixels which are  $100\text{ }\mu\text{m}$  wide, including  $15\text{ }\mu\text{m}$  "dead" space. The computer-interfaced driver applies an ac voltage which orients the liquid crystalline material in the "live" part of each pixel. The experiments reported below were conducted with the one LCD used as a phase mask. An identical LCD is being incorporated into the system for both phase and amplitude control.

The  $15\text{-}\mu\text{m}$  dead space in between live pixel areas tends to produce a large peak at the center of the pulsetrains, since about 15% of the light is not under the control of the mask. This effect was taken into account in the algorithms which design the masks. Other limitations include the number of pixels and the spatial resolution (i.e. pixel size). These determine the total temporal range over which a pulse shaped pulse sequence can extend, and the time resolution with which a pulse sequence can be specified. With our apparatus, time resolution of about 85 fs and a total range of about 6 ps should be achievable.

The setup includes two 1800 lines/mm holographic gratings (Milton Roy) and two achromatic 15-cm focal length lenses. Also included are two half-wave plates to rotate the polarization from H to V before the mask and back to H after the mask. This is necessary because the gratings and mask require H and V polarizations respectively.

The laser system used for multiple-pulse generation is a Titanium:sapphire femtosecond laser pumped by 12 W of the output of a cw argon laser. This commercial system (Coherent), with external prisms, yields 55-fs pulses at 800 nm central wavelength with almost 1 W of power. The output is used without amplification for pulse shaping.

## RESULTS

### Multiple Probe Pulses

The first one-shot data were optical Kerr effect measurements on carbon disulphide liquid in a 2-mm thick cuvette. Typical data are shown in Fig. 3, along with data recorded in the conventional manner (many shots, with a variably delayed probe pulse). These data were recorded before the CCD detector was equipped with the software to do analysis on multiple regions of interest. The integrated intensity readings at each laser spot were recorded by hand to determine the intensity of the corresponding pulse. Differences in probe pulse intensities or in the degrees of overlap between different probe pulses and the excitation pulse were not accounted for. Thus the data show considerable scatter. Nevertheless, the overall temporal response of the sample is represented. The data were reproducible, as illustrated in Fig. 4 which shows an additional one-shot scan recorded with a slightly different "overall" delay relative to the excitation pulse but with no changes in the relative delays. The response (including scatter, which is primarily due to systematic errors described above) is the same except for the small changes in overall timing. These and other data were recorded over a period of several hours, with no apparent deterioration due to changing spatial overlap of the seventeen pulses.

Transient absorption measurements were recorded on an approximately  $10^{-3}\text{ M}$  solution of malachite green in ethanol in a 2-mm cuvette. The CCD detector was equipped with the software described earlier, and differences in probe pulse intensities were accounted for in the analysis. Differences in the extent of overlap between different probe pulses and the excitation pulse were partially accounted for by measuring the transient absorption of each probe pulse at zero delay time, and normalizing the data appropriately. Typical data are shown in Fig. 5. The data are smoother than those shown in Figs. 3 and 4, presumably because of reduced systematic errors. Remaining systematic error may be reduced with the use of a different excitation wavelength, which eliminates excitation scatter and coherent coupling of varying

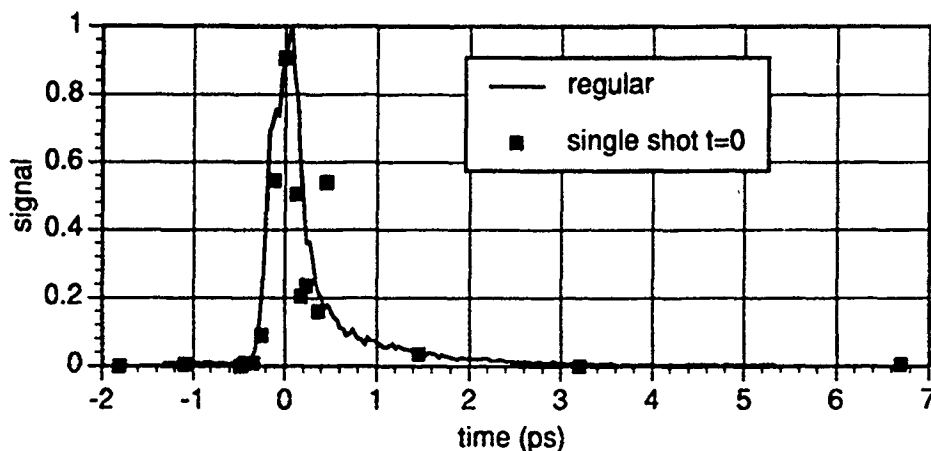


Fig.3 Femtosecond single shot experiment:  
optical Kerr effect in CS<sub>2</sub>

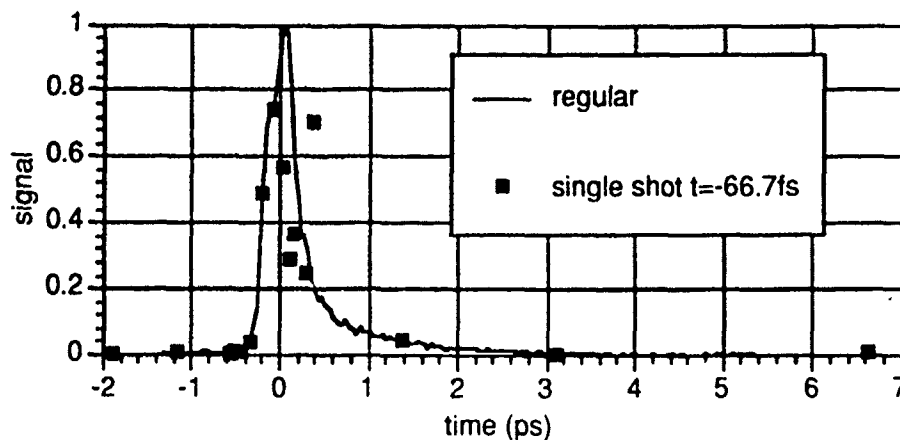


Fig.4 Optical Kerr effect in CS<sub>2</sub>. Same as Fig.3 with  
excitation pulse delayed by 67 fs

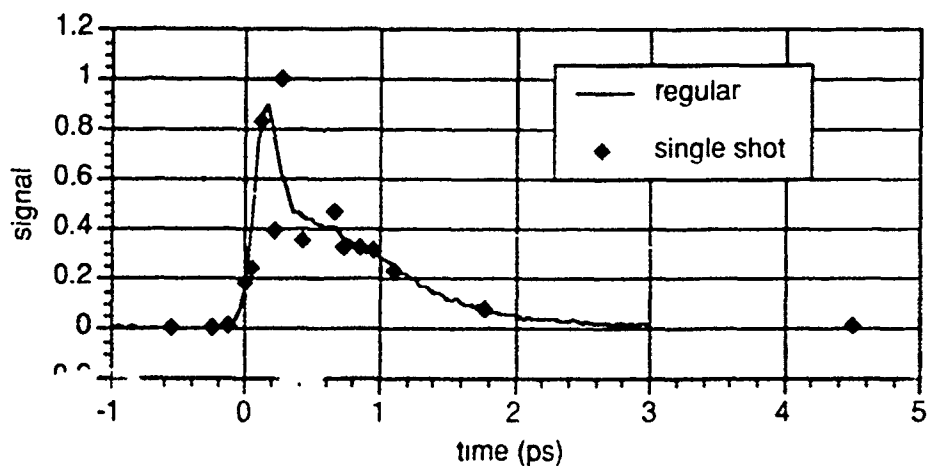


Fig.5 Femtosecond single shot pump-probe experiment  
in malachite green in methanol

amounts into the probe spots on the CCD. Additional data recorded from malachite green over periods of several hours and with different "overall" timing were consistent with that shown.

### Multiple Excitation Pulses

Autocorrelation traces of three representative pulse sequences produced by the LCD mask are shown in Fig. 6. They show distinct temporal profiles with only small amounts of distortion from the specified sequences. We emphasize that only the desired pulse shapes were specified, and the mask needed to produce the pulse shapes was determined and fabricated automatically by the computer and the LCD driver. The algorithms needed to do this will be described subsequently. Our present purpose is merely to illustrate what is currently possible.

## **DISCUSSION AND PROSPECTS**

### Real-time Femtosecond Spectroscopy

The results shown in Figs. 3-5, although preliminary, indicate that this experiment can be conducted on a routine basis even though it involves seventeen spatially overlapped beams and sixteen independently controlled delay times. Clearly the greatest limitation is the small number of points on the time axis. However this can be improved without additional large numbers of beamsplitters, delay lines, etc. The method to be adopted is illustrated in Fig. 7. A fraction of the probe pulse is split off and spectrally narrowed such that its pulse duration reaches several picoseconds. This pulse is used as the (single) probe pulse which is overlapped spatially with the excitation pulse inside the sample. The transmitted probe pulse then carries the temporal information about the sample response. If the experiment were on nanosecond or slower time scales, the transmitted probe pulse would be examined by a fast photodetector and transient digitizing analyzer and the dynamical sample response would be determined directly. In our case the "reading" of the transmitted probe pulse temporal profile must be done optically. To do this, the transmitted probe pulse is overlapped spatially inside a nonlinear optical gate (e.g. an optical Kerr cell) with the sixteen pulses produced by our multiple beamsplitting apparatus. The transmitted probe pulse temporal profile is determined through measurement (using the CCD detector) of the extent to which each of the sixteen pulses gets through the gate. This approach has several advantages over our current method. First, the probe pulse wavelength could be tuned conveniently without extensive realignment of many beams. For example, the probe pulse (after being split from the pulse which enters the sixteen-beam apparatus) could be frequency-shifted or used to generate a white-light continuum from which desired frequencies could be selected (and amplified if necessary). Second, optical quality of the sample would be somewhat less important since the CCD detector is irradiated by sixteen pulses which never go through the sample but only go through the nonlinear optical gate. Third, the multiple-pulse readout system could be readily modified to yield many more points on the time axis. This is illustrated in Fig. 7. A beamsplitter just before the nonlinear optical gate sends all the beams into another nonlinear optical gate, so the number of total readout pulses goes from 16 to 32. A small retarder (e.g. a thin piece of glass) inserted in the probe beam changes the overall timing of the pulses in the second gate, so that 32 different times are monitored. This procedure could be continued until all possible space on the CCD detector is used. In practice, at least 32 and probably considerably more spots could fit.

We note that several more "elegant" approaches to single-shot data acquisition could be tried. For example, a large angle between the excitation pulse and a single, cylindrically focussed probe beam could be used. Different, spatially separated regions of the probe beam would then overlap with the sample at different delay times, and the transmitted probe beam could be examined with an array or CCD detector. An analogous procedure could be tried with crossed excitation pulses which form a transient grating and a cylindrically focussed probe pulse whose parts are diffracted off the grating at different delay times [14]. These methods offer many more points on the time axis but their time resolution is limited by the time required for the probe pulse to traverse a distance on the order of the excitation spot size. In practice, the time resolution would almost certainly be poorer than 100 fs. Other possible methods involve introducing a linear frequency chirp in a single probe pulse, then spectrally resolving the transmitted probe pulse which should have a frequency-to-time correspondence. In this case the distinction between temporal and spectral evolution of the sample may be difficult to make.

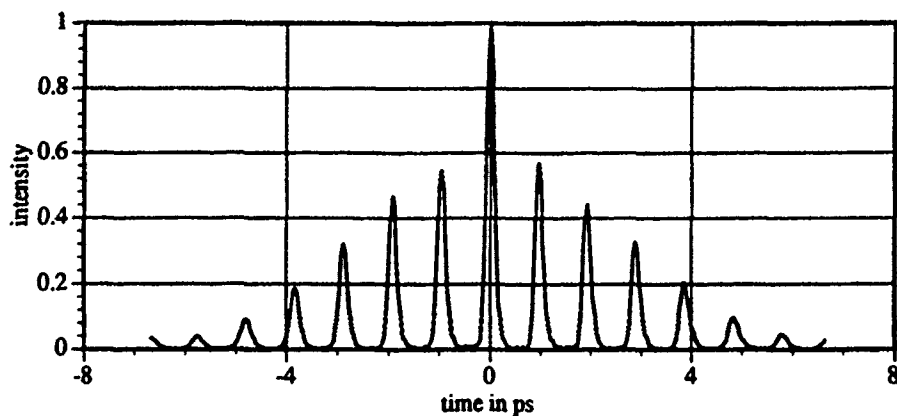


Fig. 6a: 1.05 THz pulse train generated by computer controlled LCD mask.

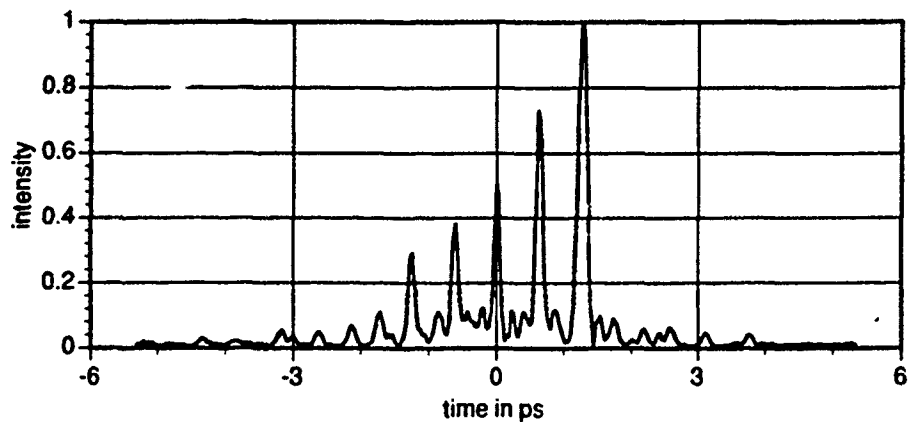


Fig. 6b: Staggered Pulse Train. The jagged base line is due to depolarization of the beam prior to pulseshaping. This has since been corrected.

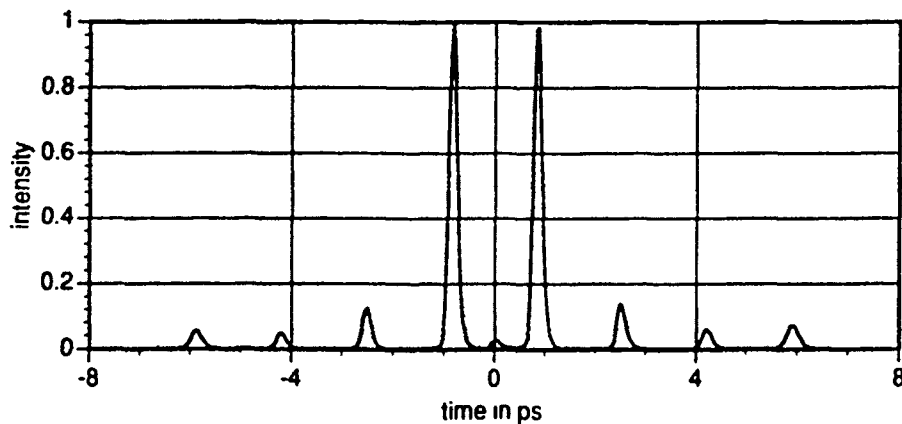


Fig. 6c: 0.60 THz Rate Train. Deliberate removal of the peak at  $t=0$  demonstrates complete compensation of the uncontrolled gap regions in the mask.

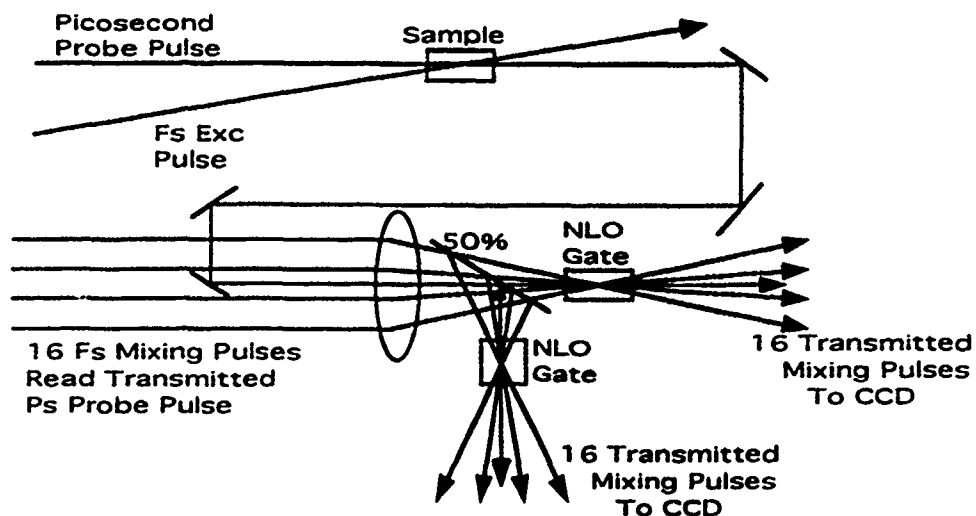


Figure 7. Illustration of single-shot detection using a single, picosecond probe pulse. The picosecond pulse can be slightly delayed before one NLO gate so that two gates yield 32 different delay times. Additional gates may be used.

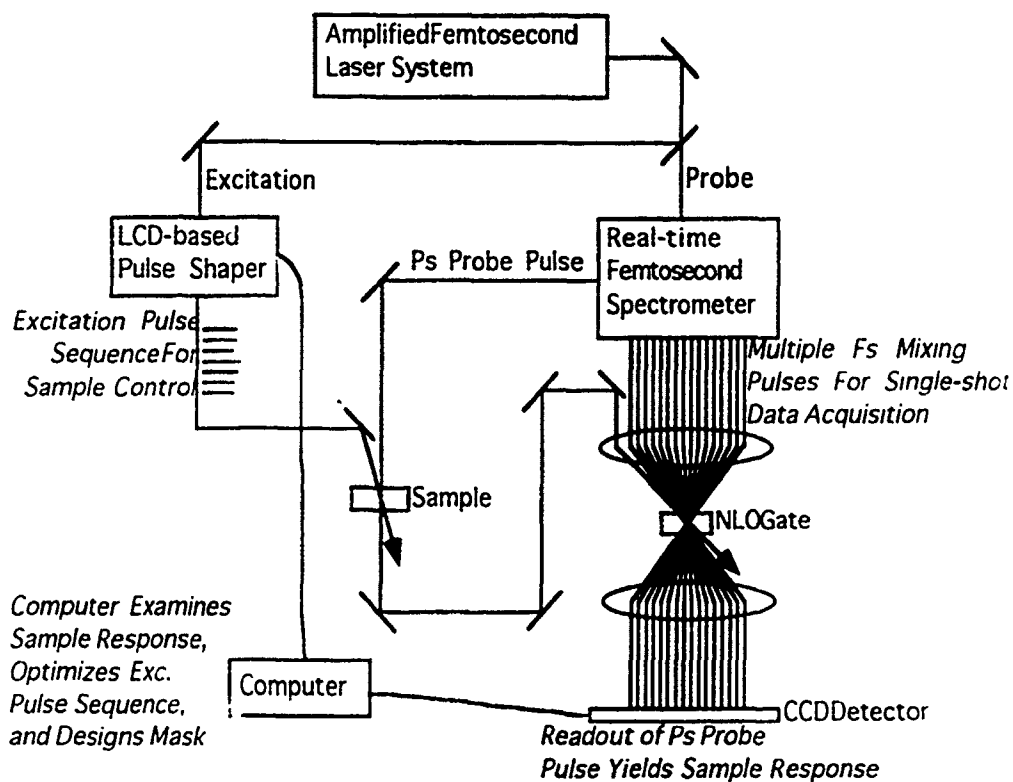


Figure 8. Schematic illustration of multiple excitation pulse, multiple probe pulse experiment under computer control.

In general, all the methods of which we are aware involve compromises of experimental difficulty, number of points, time resolution, and/or other factors. The method we have chosen is somewhat difficult and limited in the number of points, but permits very good time resolution and straightforward data analysis.

### Multiple Excitation Pulses

Our results thus far encourage us to believe that multiple-pulse femtosecond spectroscopy can soon be carried out at levels of control and convenience comparable to those typical of modern NMR spectroscopy. Improvements currently being prepared include the use of both phase and amplitude LCD masks and fabrication of improved LCD masks with more pixels and considerably smaller "dead" spaces.

### Multiple Excitation and Probe Pulses

Femtosecond time-resolved spectroscopy of solid-state photochemistry, including photochemistry in energetic solids, can be carried out with single-shot detection methods. For ISRS excitation of large-amplitude vibrational responses, it will be useful to combine multiple excitation pulse and multiple probe pulse techniques. This could permit iterative improvement of the excitation pulse sequence based on the material response observed after each shot. The procedure is illustrated schematically in Fig. 8. At the simplest level, the human experimenter analyzes the sample's response to an excitation pulse sequence, decides what pulse sequence might work more effectively, and instructs the computer to generate the improved pulse sequence. The computer does this through the present algorithms which allow it to design and execute the appropriate mask. However it may prove more effective to remove the human experimenter from the routine iteration loop. The analysis of the sample response and the optimization of the excitation pulse sequence could also be largely computerized. This appears futuristic but in fact it is already discussed widely in the context of "mode-selective chemistry" of isolated molecules in the gas phase. In fact our intentions are also to conduct a sort of mode-selective chemistry, but in the crystalline phase. We hope to use intense, near-resonant excitation pulse sequences to drive coherent phonon amplitudes of a substantial fraction of angstrom. If this proves possible, then new types of chemical or structural rearrangements might be driven and monitored in real time through single-shot detection. Optimization of the excitation waveform in the most efficient manner possible (with as little sample loss as possible along the way) will become an important part of the experimental process.

Large-amplitude phonon-induced crystalline chemical reactions, if they can be driven through ISRS excitation, would permit detailed examination of solid-state chemistry in the ground electronic state. This is most relevant to initiation of chemical change in energetic materials. In fact the large-amplitude phonon response which we hope to drive could be considered a "microshock" whose chemical initiation could resemble shock-induced initiation in energetic solids.

## **SUMMARY**

An experimental methodology for real-time femtosecond spectroscopy, in which observations are made and recorded in a single laser shot, has been described. Preliminary data have been presented which indicate that the approach is viable and can yield reproducible results. The method used will permit femtosecond time-resolved observations of photochemical reactions in energetic materials. Some substantial improvements currently being implemented have been described.

Computerized generation of femtosecond pulse sequences to be used for selective lattice vibrational excitation has been illustrated. The prospects for excitation of large-amplitude coherent lattice vibrations which could induce chemical or structural rearrangements have been discussed. These prospects depend on combination of multiple excitation pulse and single-shot detection methodologies.

## ACKNOWLEDGMENTS

This work was supported in part by ONR Grant No. N00014-90-J-4070 and by NSF grant no. CHEM-8901722. M.M.W. acknowledges support of an NSERC Predoctoral Fellowship.

## REFERENCES

1. See for example The Chemical Bond, A.H. Zewail, ed. (Academic Press, 1992).
2. Many examples are presented in G.R. Fleming, Chemical Applications of Ultrafast Spectroscopy (Oxford, 1986).
3. G. R. Desiraju, ed., Organic Solid State Chemistry, (Elsevier, 1987)..
4. L.R. Williams and K.A. Nelson, J. Chem. Phys. 87, 7346 (1987).
5. T. Tokizaki et al., Proc. of Eighth Int'l Conf. on Ultrafast Phenomena, J.L. Martin, A. Migus, G.A. Mourou, and A.H. Zewail (Springer-Verlag), in press.
6. R Kosloff, A. Dell Hammerich, and D Tannor, Phys. Rev. Lett., submitted.
7. Y.-X. Yan, E.B. Gamble, Jr., and K.A. Nelson, J. Chem. Phys. 83, 3591 (1985).
8. S. DeSilvestri, J.G. Fujimoto, E.P. Ippen, E.B. Gamble, Jr., L.R. Williams, and K.A. Nelson, Chem. Phys. Lett. 116, 146 (1985).
9. A.M. Weiner, D.E. Leaird, G.P. Wiederrecht, and K.A. Nelson, Science 247, 1317 (1990).
10. T.P. Dougherty et al., Science 258, 770 (1992).
11. G. P. Wiederrecht, T. P. Dougherty, L. Dhar, K. A. Nelson, A. M. Weiner, and D. E. Leaird, in preparation.
12. A. M. Weiner, D. E. Leaird, J. S. Patel, and J. R. Wullert, IEEE J. Quan. Elec. 28, 908 (1992).  
A. M. Weiner, J. P. Heritage, and E. M. Kirschner, J. Opt. Soc. Amer. B, 5, 1563 (1988).
13. T.P. Dougherty et al., Phys. Rev. B, submitted.
14. J.T. Fourkas, W. Wang, K.A. Nelson, and R. Trebino, in preparation.

## Explosion Of Drops Impacting Non-Wetting Rigid Surfaces

*Clarence Zener And Dennis Prieve  
Carnegie Mellon University  
Pittsburgh, PA 15213*

More than 100 years ago Worthington [1,2] reported his observations on drops exploding on impacting rigid surfaces they did not wet. Mercury was his favorite fluid, since mercury does not wet most solids. For water drops he had to especially "smoke" his surfaces to make them non-wetting. In his day high speed photography had not been developed, but he had learned to "stop" his falling drops by spark illumination. His drops had radii of typically 1 mm, fell from a height of ~10 cm and ejected always an even number of spikes, typically ~24. These spikes would shoot out from the impacted area at velocities several times higher than the impact velocity.

In this paper, we demonstrate that Worthington's reported observations follow directly from the basic physical principles governing fluid flow. As an introduction to our description of why drops explode when they impact non-wetting surfaces, we shall review the physical principles which have lead to our understanding of this explosion.

In the 17th century Newton started with the basic relation

mass  $\times$  acceleration = force

$$m\ddot{\mathbf{r}} = \mathbf{f} \quad (1)$$

During the 18th century Lagrange generalized Newton's law to describe the mechanics of a large number of interacting masses.

$$\frac{d}{dt} \frac{\partial K}{\partial \dot{q}_i} = - \frac{\partial P}{\partial q_i} \quad (2)$$

Here the  $q_i$ 's are the independent variables of the system,  $K(q_i$ 's,  $\dot{q}_i$ 's) is the total kinetic energy of the system and  $P(q_i$ 's) is the total potential energy of the system

The nineteenth century saw a great advance in understanding the mechanics of fluids. This advance came primarily through the introduction of the concept of potential flow of incompressible fluids. In such flow the velocity  $\mathbf{U}$  of every point of the fluid is given by the gradient of a harmonic function. Thus a harmonic velocity implies

$$\mathbf{U} = \nabla \phi \quad (3)$$

where  $\phi$  satisfies the differential equation:



$$\nabla^2 \phi = 0 \quad (4)$$

The two equations (3) and (4) imply that the fluid behaves as if it were incompressible,

$$\nabla \cdot \mathbf{U} = 0$$

and curl free

$$\nabla \times \mathbf{U} = 0$$

Thus harmonic flow implies both zero change in volume and zero energy loss by viscosity. Unfortunately harmonic flow cannot have stationary boundaries.

In order to emphasize the difficulty of solving this equation when one boundary is a rigid surface, we quote from Milne-Thomson [3]: "Not so many years ago the dynamics of a frictionless fluid had come to be regarded as an academic subject incapable of practical application due to the great discrepancy between calculated and observed results." He then explains how this difficulty was largely removed by the recognition of the Prandtl boundary layer which protects harmonic flow from direct contact with the rigid surface boundaries.

In 1985 Rodriguez and Mesler [4] published a paper describing what happens when water drops impact a pond of water. At low impact velocities, small drops bounce off the pond. Large drops float for a while before submerging. On reading of these experiments we suspected that an entrapped air film protected the drop from making direct contact with the water in the pond. This suspicion then led to the concept that in Worthington's experiments an entrapped air film was protecting his drops from direct contact with non-wetting solid surfaces. If correct, this entrapped air film was performing the role of the Prandtl boundary layer. The low density and low viscosity of the air film in contrast to the Prandtl boundary layer meant, however, that it would absorb a negligible amount of energy from the drop. This paper gives the results of these thoughts inspired by the observations reported by Rodriguez and Mesler.

### Analysis

With the above background we now attempt to construct the velocity potential of a drop at its instant of impacting a non-wetting rigid surface. Figure 1 presents our first attempt. Here we use symbols as well as pictures of the streamlines which these symbols represent. For the sake of clarity we represent the drop's shape as that of a truncated cylinder rather than as a sphere.  $\psi$ , representing the velocity potential at impact, is the sum of two terms. The velocity potential,  $-U_0 z$ , represents the drop just before impact. The stream lines are a set of uniformly spaced vertical lines. The second velocity potential,  $\psi^*$ , represents an initially stationary drop which has just been struck from below by an upward impulse of intensity  $U_0$ . The velocity pattern of  $\psi^*$  is that specified by the boundary conditions

$$\frac{\partial \psi^*}{\partial z} = U_0 \quad \text{at } z=0, r \leq a \quad (5)$$

$$\psi^* = 0 \quad \text{on free surface} \quad (6)$$

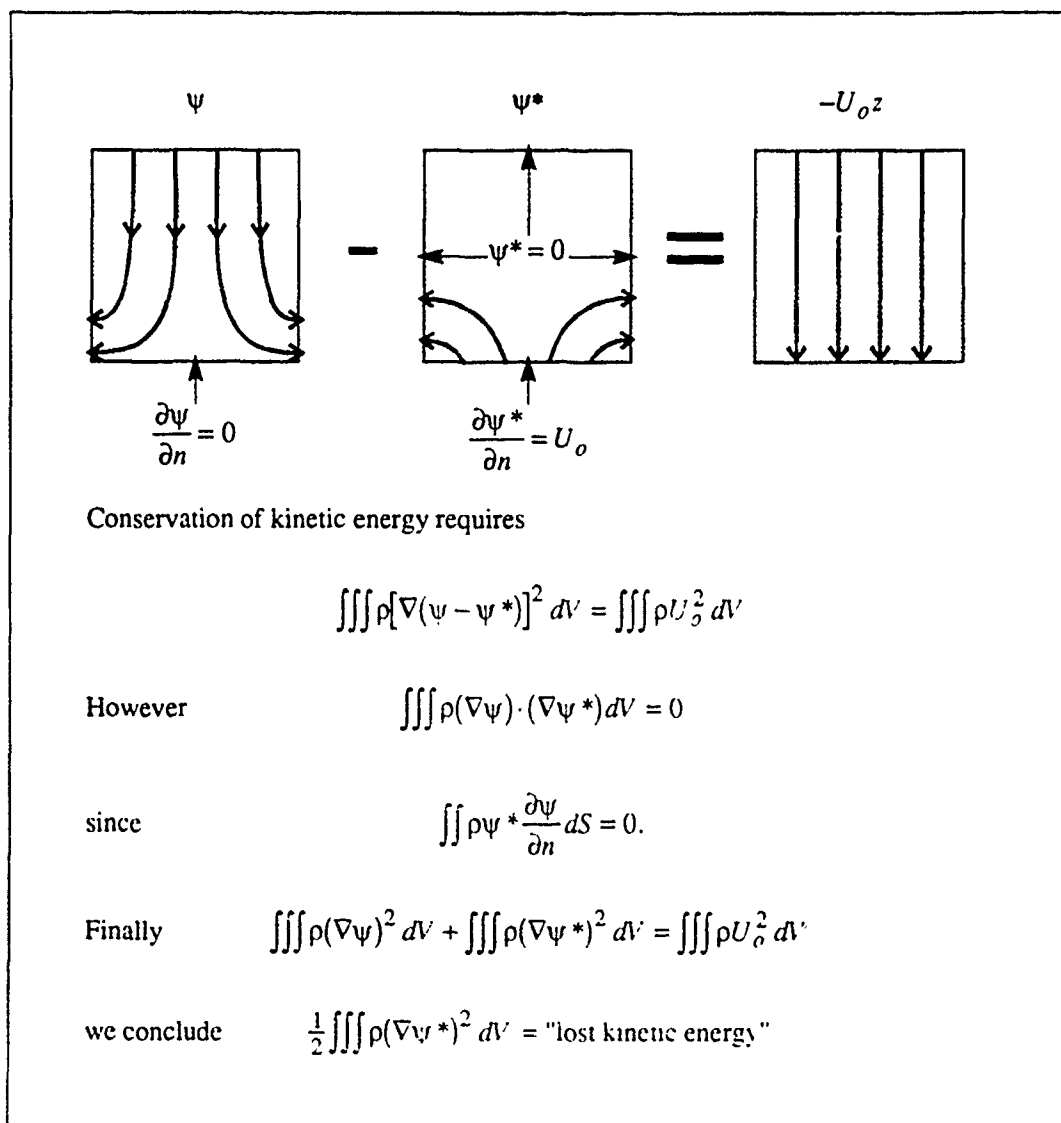


**Fig. 1.**  
Derivation of "lost kinetic energy," using Green's Theorem

Since the stream lines of  $\psi$  looked as we thought they should look, we thought they did indeed represent the real stream lines just after impact. To test this hunch, we transferred  $\psi^*$  to the left side in Fig. 1, took the gradient of both sides, then squared both sides, multiplied by the density  $\rho(r)$ , and integrated over all space, observing however, that  $\rho$  vanishes outside the drop. Making use of Green's theorem, and of the constraints (5) and (6), we find the integral of the cross-product term vanishes, leaving

$$\iiint \rho(\nabla\psi)^2 dV + \iiint \rho(\nabla\psi^*)^2 dV = \rho U_0^2 \times \text{drop volume} \quad (7)$$

Clearly a significant part of the original kinetic energy of the drop is not represented by the velocity potential  $\psi$ . According to Lord Kelvin (1849), we have only found that harmonic function of *minimum* kinetic energy which satisfies the required boundary conditions. If we wish to know what happened to the drop during impact, we must be able to describe what happened to the "lost kinetic energy",  $\frac{1}{2} \iiint \rho(\nabla\psi^*)^2 dV$ .

The dilemma we have run into has arisen because of our assumption of zero compressibility. We should have said very small compressibility rather than zero. With this change we now recognize that our "lost kinetic energy" is simply the compressive potential energy induced within the drop by its impact. We now have the most remarkable conclusion that whereas the square of the density of the stream lines of  $\psi$  gives the density of kinetic energy just after impact, the square of the density of the stream lines of  $\psi^*$  gives the density of compressive potential energy within the drop just after impact. We want to particularly emphasize that the kinetic energy and compressive potential energy are concentrated in the same regions, namely in the lower outer edges of the drop. Clearly the coexistence of a high concentration of kinetic and compressive energy in the same region encircling the drop is an ideal recipe for an explosion. We emphasize that this conclusion is independent of the drop's shape before impact.

We now describe a harmonic velocity potential which represents the essential features of a drop impacting a non-wetting surface.

$$\phi(r, \theta, z; t) = \psi(r, z) + q(t) \phi_n(r, \theta, z) \quad (8)$$

where  $r, \theta, z$  are the usual cylindrical coordinates. The velocity potential  $\psi$  has stream lines as indicated in Fig. . We have seen that it does not, however, have sufficient kinetic energy to represent our drop after impact. We shall find that the second velocity potential,

$$\phi_n = \cos(n\theta) \frac{J_n\left(\frac{\beta r}{a}\right) e^{-\beta z/a}}{\frac{\beta}{a}} \quad (9)$$

will, however, supply the missing kinetic energy provided the ratio of sound velocity of drop fluid,  $C$ , to the impact velocity  $U_0$  is sufficiently high. Towards this end we must find the coefficient  $q(t)$ .

To help visualize the remarkable explosion activated by this second velocity potential,  $\phi_n$ , we note that  $q(t)$  is the amplitude of a perturbation in the radius of the drop

$$r_B(\theta, z, t) - a = q(t) \cos(n\theta) e^{-\beta z/a} \quad (10)$$

where  $r_B$  is the radial distance from the axis to the drop's surface and

$$q(0) = 0 \quad (11)$$

The primary parameter  $n$  is an even integer representing the number of fluid rays emerging from the point of impact. The secondary parameter  $\beta$  has an upper bound limited by surface tension, and a lower bound of  $n$ . The precise value of  $\beta$  is that which gives the maximum growth rate for  $n$  modes (as in Rayleigh's analysis of long fluid jets). For water near room temperature, we find  $n = 24$  and  $\beta = 22$ .

In order to determine  $q(t)$ , we use (8) and (9) in (2) to compute the total kinetic energy  $K$ , and we use the square of the density of streamlines of  $\psi^*$  to compute one contribution to the total potential energy  $P$ . Another important contribution to  $P$  is the surface energy, which grows as the area of the drop increases. In the particular case where the fluid sound velocity  $C$  is extremely high compared to the impact velocity, i.e.,

$$C \gg U_0 \quad (12)$$

the required volume and surface integrals in (2) can be evaluated on the assumption that the drop's surface has not moved significantly before most of the "lost kinetic energy" has been transferred to the new velocity potential  $\phi_n$ . In particular, the initial velocity  $\dot{q}(0)$  is chosen to conserve energy. The differential equation thereby obtained for  $q(t)$  is

$$a\ddot{q} - b\dot{q} - cq = 0 \quad (13)$$

That solution of (13), which satisfies the boundary condition (11) and conserves kinetic energy, is

$$q(t) = q_0 \sinh\left(\frac{t}{\tau}\right) e^{bt/2a} \quad (14)$$

$$\tau^{-1} = \frac{\sqrt{b^2 + 4ac}}{2a}$$

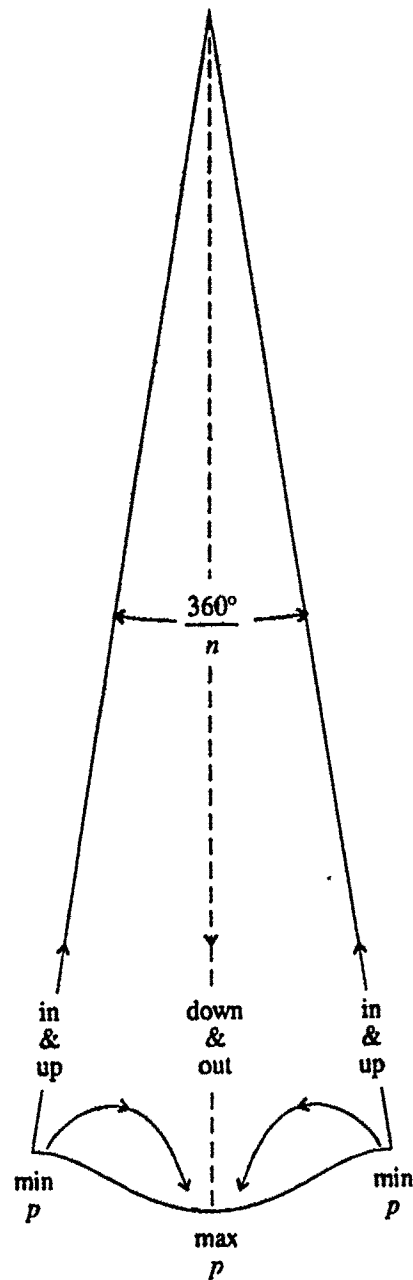


Fig. 2.

Streamlines associated with  $\phi_n$  in one of  $n$  sectors of circle of radius  $r_B$ . The streamlines of  $\phi_n$  are essentially confined to a thin surface layer. Their low inertia results in a high outward acceleration.

The analysis we have adopted leading to (14) is essentially that followed by Rayleigh [5] in his study of the stability of cylindrical columns of water under gravity-free conditions. In his case instability was driven by surface tension. In contrast, in our case instability is driven by the hammer pressure  $\rho U_o C$ , which is three orders of magnitude greater than the stagnation pressure at the base of a steady stream of fluid impacting a wetting surface at the velocity  $U_o$ .

The value of  $\tau$  which we calculate is less than one microsecond. This low value is consistent with the concept that the "lost kinetic energy" has been absorbed by the  $\phi_n$  velocity potential before the drop surface has had time to move an appreciable distance.

We now review our attempt to find the essential features of what is happening to a cylindrical drop impacting a non-wetting surface. In our analysis we make one basic assumption: the ratio of sound velocity to impact velocity,  $C/U_o$ , is so large that no observable effect would be introduced if  $C$  was increased still further. We have found that a consequence of this assumption is that a major part of the kinetic energy of the original drop, but not more than ~90%, is associated with an axially symmetric velocity potential,  $\psi$ . We have identified not only the magnitude of this "missing" kinetic energy (see last line in Fig. 1), but also its spatial distribution, namely that given by  $\frac{1}{2} \rho (\dot{q} \nabla \phi_n)^2$ .

This "missing" kinetic energy has two distinct parts, that containing the square of the vertical velocity, equal to  $\frac{1}{2} \rho U_o^2$ , and that containing the square of the radial velocity. It is evident from Fig. 1, this second component is absent in the center region near  $r = 0$ , but becomes somewhat greater than  $U_o$  near  $r = a$ . This "missing" kinetic energy density is therefore at least twice as great near the periphery as at the center. This observation is in agreement with what is found in meteorites striking the earth, namely that the maximum pressure in the impacting meteorite is much higher at the edges than at the center.[6,7]

We make one further comparison with prior impact studies. When high velocity solid cylinders impact massive plates, the front part of the cylinder deforms in much the same way as if they were, at least temporarily, liquids. This is especially the case where the cylinders are made of metals having a sharp yield stress. Such materials may respond to impact loading where at any one instant deformation is confined to narrow slip bands within which adiabatic deformation results in a local rise in temperature, and thereby a shift of impedance to local increase in deformation rate to the inertia of the material itself. This possibility has recently been explored by Holt and colleagues.[8] Towards this end, they have compared the deformation of impacted cylinders with the deformation calculated by G.I. Taylor.[9] We find the deformation represented by our  $\psi$  (see Fig. 3) is essentially the same as the Taylor deformation reported by Holt *et al.*

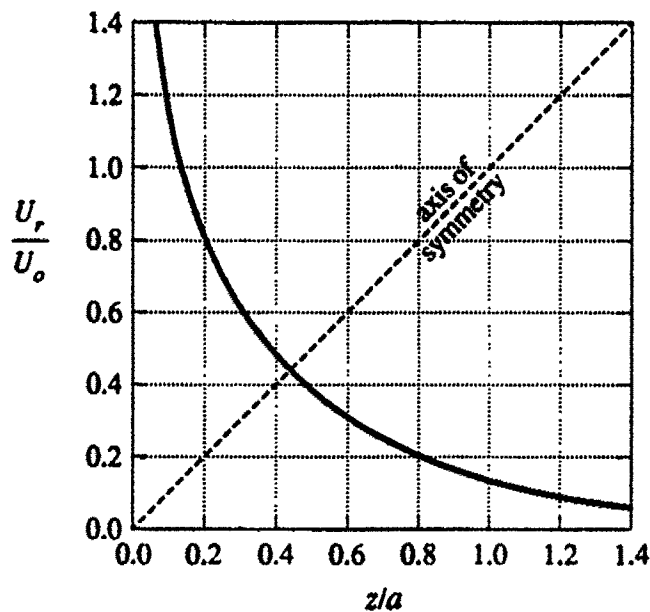


Fig. 3.

Radial impact velocity,  $U_r(a,z) = \partial\psi/\partial r$ , as a function of the distance  $z$  from impacted head.  $U_0$  is impact velocity and  $a$  is cylinder radius.

### References

1. A.M. Worthington, *Proc. Roy. Soc.* **25**, 261 and 498 (1877) and 34,217 (1882).
2. A.M. Worthington, *A Study of Splashes* (The MacMillan Co., New York, 1963).
3. L.E. Milne-Thomson, *Theoretical Hydrodynamics* (The MacMillan Company, New York, 1968) Preface.
4. F. Rodriguez and R. Mesler, *J. Colloid Interface Sci.* **106**, 347 (1985).
5. Lord Rayleigh, *Proc. Roy. Soc.* **219** 71 (1879); *Theory of Sound* (Dover Publications, New York, 1945) Vol. II, 351-365.
6. Melosh, H.J., *Impact Cratering*, Oxford University Press, 1989.
7. W. Adler, in *Treatise on Material Science and Technology*, (ed. by C.M. Preece, Academic Press, New York, 1979) Vol. 16, p157.
8. W.H. Holt *et al.* (in press).
9. G.I. Taylor, *Proc. Roy. Soc.* **A194**, 289 (1948).

## **AB INITIO STUDY OF ELECTRONIC STRUCTURE OF RDX MOLECULAR CRYSTAL**

**GUANG GAO\*, RAVINDRA PANDEY AND A. BARRY KUNZ**  
Department of Physics, Michigan Technological University, Houghton, MI 49931

\* Current address: Department of Chemical Engineering and Materials Science, University of Minnesota, Minneapolis, MN 55455

### **ABSTRACT**

An embedded molecular cluster model is used to study the electronic structure of cyclotrimethylene trinitramine (RDX) molecular crystal. In this model, a molecular cluster describing a local region of the crystal is treated in the Hartree-Fock approximation. The embedding lattice is represented by multipoles that are determined quantum-mechanically. Cluster-lattice orthogonality is achieved by transforming canonical orbitals to orbitals which are localized on individual molecular sites by means of a self-consistent localization potential. Results for the free molecule and the perfect crystal demonstrate the domination of three N-NO<sub>2</sub> groups on intermolecular properties. For the defective crystal, results show a significant distortion in the electronic structure caused by local deformations in the lattice that may account for the formation of hot spots.

### **I. INTRODUCTION**

Cyclotrimethylene trinitramine (RDX) is one of the most important representative energetic materials. A theoretical study of electronic properties of such a material can be expected to produce a fundamental understanding of its detonation behavior at the microscopic level. We note here that a direct relationship between sensitivity and electronic processes in a series of energetic materials (TATB, DATB, MATB and TNB) has been shown by Sharma and Beard [1] using X-Ray Photoelectron Spectroscopy.

One of the main problems in describing electronic properties is that these systems often contain more molecules than can be handled by using conventional quantum chemistry methods. An alternative approach is therefore to simulate the crystal by a molecular cluster that contains the local region of interest. However, in this approach the question of representation of the remaining (embedding) lattice poses the greatest difficulty. Furthermore, the nature of the cluster approach requires (cluster) molecular orbitals to be localized resulting into a very small overlap with the embedding lattice.

For ionic crystals, our group has successfully developed the ICECAP methodology that simulates the crystal by a molecular cluster embedded in a shell-model lattice.[2] In the present work, we extend this approach to study electronic properties of energetic materials that are classified as molecular crystals. We will give a brief description of the theoretical model in the next section. Results of the calculations on the RDX molecular crystal will be presented and discussed in Sec. III.

### **II. THEORETICAL MODEL**

Embedded cluster approach (ICECAP) divides a crystal into two regions: cluster (A) and environment (E). In this context, the cluster will be defined as a collection of one or more molecules. By virtue of its finite physical size, the cluster containing the local region of interest is chosen to be larger than the physical extent of the phenomena involved. The cluster Hamiltonian in the Born-Oppenheimer approximation can be written as:

$$H_A = H_{AO} + I_{AE} \quad (1)$$

where  $H_{AO}$  is the Hamiltonian for a free cluster and is  $I_{AE}$  the interaction energy between the cluster and its environment.  $H_{AO}$  and  $I_{AE}$  can be written as

$$H_{AO} = - \sum_i^A \frac{\hbar^2}{2m} \nabla_i^2 - \sum_{i,j}^{AA} \frac{Z_i e^2}{|r_i - R_j|} + \frac{1}{2} \sum_{i,j}^{AA} \frac{e^2}{|r_i - r_j|} + \frac{1}{2} \sum_{I,J}^{AA} \frac{Z_I Z_J e^2}{|R_I - R_J|} \quad (2)$$

$$I_{AE} = - \sum_{i,j}^{AE} \frac{Z_j e^2}{|r_i - R_j|} + \sum_{i,j}^{AE} \frac{e^2}{|r_i - r_j|} + \sum_{I,J}^{AE} \frac{Z_I Z_J e^2}{|R_I - R_J|} - \sum_{j,I}^{EA} \frac{Z_I e^2}{|r_j - R_I|} \quad (3)$$

where A and E represent summations within cluster and environment respectively.

We use lower case letters to represent electron properties and upper case letters to represent nuclear properties. The mass of the electron is  $m$ , its charge magnitude  $e$ , and its position  $r_i$ . If spin dependence were needed, then  $r_i$  would be position and spin coordinate. The nuclear charge at I is  $Z_I$ , and the coordinate is  $R_I$ . In the present study, we have neglected interaction energies within the environment as they are approximately constant relative to the embedded cluster.

We now introduce  $N_j$  to represent the number of electrons associated with atom J. The interaction Hamiltonian (Eq. (3)) can now be written as

$$I_{AE} = V_M + V_N + V_S \quad (4)$$

Here,  $V_M = - \sum_{i,j}^{AE} \frac{(Z_j - N_j) e^2}{|r_i - R_j|}$  the Madelung potential due to the presence of ions in the environment. However, it can be ignored for molecular crystals as  $Z_j = N_j$ . The interaction potential between the nuclei in the cluster and nuclei and electrons in the environment can be written as

$$V_N = \sum_{i,j}^{AE} \frac{Z_i Z_j e^2}{|R_i - R_j|} - \sum_{j,I}^{EA} \frac{Z_I e^2}{|r_j - R_I|} \quad (5)$$

Under the assumption of a small overlap between molecular orbitals of Cluster (A) and environment (E) region, Eq. (5) is reduces to

$$V_N = \sum_{I,J}^{AE} \frac{Z_I (Z_J - N_J) e^2}{|R_I - R_J|} \quad (6)$$

In the absence of any ions in the environment (i.e.  $Z_J = N_J$ ), we can also neglect the contribution of this term to  $I_{AE}$ . Finally,  $V_S$  is given as

$$V_S = - \sum_{i,j}^{AE} \frac{N_j e^2}{|r_i - R_j|} + \sum_{i,j}^{AE} \frac{e^2}{|r_i - r_j|} \quad (7)$$

where it is defined as the screening potential produced by electrons and nuclei in the environment.

For the case of a molecular crystal, we transform configuration coordinates of eq. (7) from nuclear-electron representation to molecule-center-nuclear electron representation as follows:

$$V_S = - \sum_{i,m}^{AEn_m} \sum_K \frac{N_K e^2}{|r_{im} - R_{Km}|} + \sum_{i,m,k}^{AEn_m} \frac{e^2}{|r_{im} - r_{km}|} \quad (8)$$



Here, the index  $m$  corresponds to a molecule;  $n_m$  is the number of atoms in the molecule  $m$ ,  $N_K$  is the number of electrons in atom  $K$  of the molecule  $m$  and  $N_m$  is the number of electrons in molecule  $m$ .

We now expand eq. (8) using Taylor's series. This expansion is based on the assumption of a small overlap between molecular orbitals of Cluster (A) and environment (E) regions, so that  $R_{Km} \ll r_{im}$  and  $r_{km} \ll r_{im}$ , and

$$V_S = -e \left( \sum_{i,m}^{\text{AE}} \frac{\mathbf{P}_{em} \cdot \mathbf{r}_{im}}{r_{im}} + \sum_{i,m}^{\text{AE}} \mathbf{Q}_{em} : \Delta \Delta \left( \frac{1}{r_{im}} \right) + \dots \right) \\ - e \left( \sum_{i,m}^{\text{AE}} \frac{\mathbf{P}_{nm} \cdot \mathbf{r}_{im}}{r_{im}} + \sum_{i,m}^{\text{AE}} \mathbf{Q}_{nm} : \Delta \Delta \left( \frac{1}{r_{im}} \right) + \dots \right) \quad (9)$$

where  $\mathbf{P}_{em} [= \sum_k^{N_m} (-e \mathbf{r}_{km})]$  and  $\mathbf{Q}_{em} [= \sum_k^{N_m} (-\frac{1}{2} e \mathbf{r}_{km} \mathbf{r}_{km})]$  are electron dipole and quadrupole moments of molecule  $m$  respectively. The terms  $\mathbf{P}_{nm} [= \sum_K^{n_m} (-e N_K \mathbf{R}_{Km})]$  and  $\mathbf{Q}_{nm} [= \sum_K^{n_m} (-\frac{1}{2} e N_K \mathbf{R}_{Km} \mathbf{R}_{Km})]$  are nuclear dipole and quadrupole moments of molecule  $m$  respectively. Eq (9) can now be rewritten as

$$V_S = -e \left( \sum_{i,m}^{\text{AE}} \frac{\mathbf{P}_{netm} \cdot \mathbf{r}_{im}}{r_{im}} + \sum_{i,m}^{\text{AE}} \mathbf{Q}_{netm} : \Delta \Delta \left( \frac{1}{r_{im}} \right) + \dots \right) \quad (10)$$

Here,  $\mathbf{P}_{netm}$  and  $\mathbf{Q}_{netm}$  are net dipole and quadrupole moments of molecule  $m$  in the environment (E).

For the environment, multipole moments are determined in a self-consistent way from Hartree-Fock calculations and are fitted to a set of point-charges. The term,  $V_S$  can then be evaluated by interaction energies between electrons (in the cluster) and multipoles fitted to point-charges (in the environment) when molecular orbitals are essentially localized.

For the transformation of canonical molecular orbitals to localized molecular orbitals, we use a formalism based on the work of Adams-Gilbert-Kunz. [3,4] Details of this formalism are given elsewhere. [5]

### III. RESULTS AND DISCUSSION

RDX molecule consists of three N-NO<sub>2</sub> groups linked to three methylene groups alternately to form a puckered, six-member C-N ring. [6] The N<sub>1</sub> - NO<sub>2</sub> group is essentially coplanar but the N<sub>2</sub> - NO<sub>2</sub> and N<sub>3</sub> - NO<sub>2</sub> groups are slightly bent. In the literature, N<sub>2</sub> - NO<sub>2</sub> and N<sub>3</sub> - NO<sub>2</sub> groups are usually referred to as axial and N<sub>1</sub> - NO<sub>2</sub> group as equatorial with respect to the triazing ring.

Gaussian type basis sets [7] were used for RDX (C<sub>3</sub>N<sub>6</sub>O<sub>6</sub>H<sub>6</sub>) in these calculations. There are totally 81 contracted basis functions associated with 114 electrons in the ground state. The calculated ground state (in the experimental configuration) comes out to be nearly singlet. Mulliken populations associated with atoms reflect similarities between the two axial N<sub>2</sub> - NO<sub>2</sub> and N<sub>3</sub> - NO<sub>2</sub> groups that is consistent with nuclear quadrupole resonance experimental results.[8]. The highest occupied molecular orbital (HOMO) is mainly associated with the (equatorial) N<sub>1</sub> - NO<sub>2</sub> group while the second highest occupied orbital is dominated by the (axial) N - NO<sub>2</sub> groups predicting their dominant role in inter-molecular bonding in the crystalline state.

In our simulation model, we use experimentally determined crystal structure [6] of RDX that crystallizes in the orthorhombic space group Pbca with eight molecules per unit cell. To begin with, our molecular cluster consists of one molecule at the origin and the environment is represented by 40 molecules that are carefully chosen to give the highest symmetry within 125 unit cells. The molecules in the environment are initially associated with multipole moments

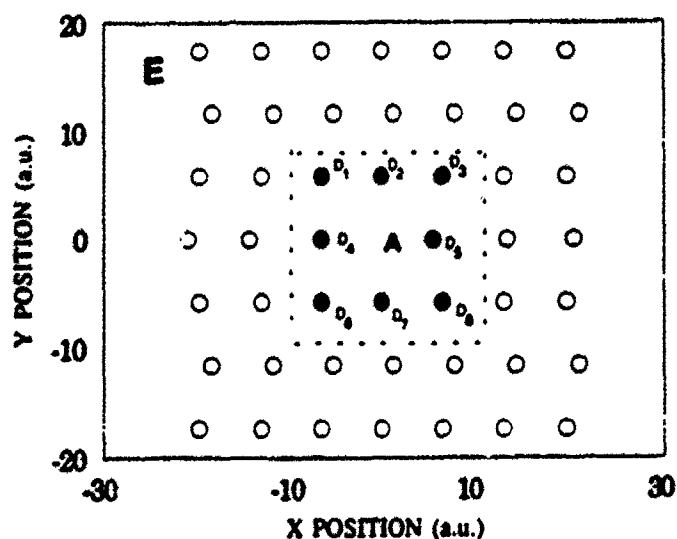


Fig. 1. Computational model of a defective RDX crystal.

TABLE I

Total energy, HOMO-LUMO gap and dipole moment of eight near-neighbor molecules (D<sub>1</sub> to D<sub>8</sub>) of a defect as shown in Fig. 1. The corresponding total energy, HOMO-LUMO gap and dipole moment of the molecule embedded in a perfect crystal are -886.6944 hartree, 15.36 eV and 1.7031 a. u. respectively.

	D <sub>1</sub>	D <sub>2</sub>	D <sub>3</sub>	D <sub>4</sub>	D <sub>5</sub>	D <sub>6</sub>	D <sub>7</sub>	D <sub>8</sub>
E(hartree)	-886.3037	-883.7130	-880.9840	-890.2072	-885.1218	-893.3103	-888.1578	-887.4688
gap (eV)	14.96	15.51	15.81	14.14	15.17	13.88	14.53	14.71
α (a. u.)	2.0137	2.0672	2.0710	2.0630	2.0488	2.1125	2.0249	2.1155

(dipole and quadrupole moments in the present case) obtained from quantum mechanical calculation of a free molecule. The Fock equation of the embedded molecule is now solved to obtain a new set of multipoles that are used to represent the environment. We iterate this cycle to obtain a self-consistency set of multipole moments representing the environment.

The calculated results show that the embedding molecule has a lower total energy (-886.6944 hartree) compared to that of a free molecule (-885.8238 hartree) due to the stabilizing interactions from its environment. Mulliken population associated with atoms of the embedding molecule show a very little difference between the axial and equatorial N-NO<sub>2</sub> groups in contrast to that of a free molecule. The calculated dipole moment comes out to be 1.7031 as compared to that of the free molecule of 1.7581 in atomic units. This decreased polarization is attributed to the environment that localizes molecular orbitals.

We now study the effect of local deformation (induced by a defect) on the electronic structure of RDX crystal. The crystal is assumed to be composed of parallel three-dimensional layers based on a structure model by Armstrong.[9] Each layer is divided into two regions. Region A is a cluster consisting of eight molecules labeled D<sub>1</sub> to D<sub>8</sub>. Region E is the environment of the cluster simulated by 40 nearest neighboring molecules. Figure 1 shows such a structure model where x and y axes are chosen to be in [100] and [010] directions respectively. The eight molecules in the cluster maintain perfect orthorhombic unit cell connections with molecules in region E. However, the intermolecular distance along [100] direction between D<sub>4</sub> and D<sub>5</sub> was chosen to be 70% larger than the perfect lattice spacing to mimic the local deformation induced by a defect.

Since the available computational resources do not permit us to represent all of the eight molecules in region A quantum-mechanically, we use the following approach. First, we solve the Fock equation for the embedding molecule D<sub>1</sub> obtaining a self-consistent set of multipole moments to represent the remaining seven molecules. This cycle is iterated sequentially to obtain a self-consistent electronic structure for all of the eight molecules in the region A. We note here that multipole moments associated with the molecules in the region E are taken to be that of the molecule embedded in a perfect crystal.

The calculated results show a significant change in the electronic properties of the molecules in the region A. For example, the local deformation caused by a defect has increased the dipole moment associated with each molecule by 20%. By examining HOMOs of the eight molecules we find that molecules around the defect show increased polarization along different directions resulting in a scenario where some of the molecules tend to attract each other while others tend to repel. Total energies of molecules around the defect appeared to confirm this view as some of the molecules in region A have higher energies than those in perfect crystal while others have lower energies (Table 1). This imbalance of intermolecular bonding leads us to one of the possible mechanism of the formation of 'hot spots' in the RDX crystal. The local deformation around a defect (which may be dislocation) polarizes its nearby molecules along different directions and produces stronger internal bonding between some of the molecules while weaker bonding to others. 'Hot spots' are then formed in those local regions where strengthening of intermolecular interaction has occurred. We note here that experimental investigations of detonation processes in this material suggest that the generation of 'hot spots' may come from the obstruction of dislocation pile-ups by strong internal obstacles which collapse suddenly to give adiabatic dissipation of the very localized interaction energy.[9]

In summary, electronic structure calculations of perfect and defective RDX crystal were performed using an embedded cluster method. The results show the domination of N-NO<sub>2</sub> groups in intermolecular bonding. In the crystalline lattice, local deformation introduced by a defect is found to induce a significant polarization in the neighboring molecules in different directions that may account for the formation of 'hot spots'.

#### ACKNOWLEDGEMENTS :

Helpful discussions with Prof. R. W. Armstrong and Prof. J. Vail are acknowledged. This work was supported in part by Office of Naval Research under contract ONR-N00014-89-J-160.

**REFERENCES :**

1. J. Sharma and B. C. Beard, This Volume.
2. J. Vail, R. Pandey and A. B. Kunz, Rev. Solid State Sciences 5, 241 (1991).
3. T. L. Gilbert, in Molecular Orbitals in Chemistry, Physics and Biology, edited by P. O. Lowdin and B. Pullman (Academic Press, New York, 1964).
4. A. B. Kunz and D. L. Klein, Phys. Rev. B17, 4614 (1978).
5. A. B. Kunz and J. M. Vail, Phys. Rev. B38, 1058 (1988); A. B. Kunz and J. M. Vail, Phys. Rev. B38, 1064 (1988).
6. C. S. Choi and E. Prince, Acta Cryst., B28, 2857(1972).
7. S. Huzinaga, Gaussian Basis Sets for Molecular Calculations (1984).
8. R. J. Karpowicz and T. B. Brill, J. Phys. Chem., 88, 348(1984).
9. R. W. Armstrong, C. S. Coffey and W. L. Elban, Acta Metall., 30, 2111(1982); R. W. Armstrong (private communication)

## MOLECULAR DYNAMICS SIMULATIONS OF SHOCKS AND DETONATIONS IN A MODEL 3D ENERGETIC CRYSTAL WITH DEFECTS

Lee Phillips

Laboratory for Computational Physics and Fluid Dynamics, Naval Research Laboratory, Washington, DC 20375

### ABSTRACT

We examine shock induced detonation in a three-dimensional model of a nitromethane crystal. The crystal may contain a defect in the form of a small void. Three regimes are identified: the shock can be weak enough that no chemical bonds are broken; the shock can be so strong that a detonation front is established in the perfect crystal; or the shock can be of intermediate strength, where chemical activity requires the existence of the defect. In all regimes, the defect increases the reaction rate and causes a hot spot to appear.

### INTRODUCTION

The purpose of the work reported in this paper is to understand some of the peculiar properties of the initiation of detonations in solid chemical explosives. In the liquid and gas phases, those properties governing the nature of the detonation process are the chemical composition of the material along with its intensive thermodynamic variables, and the details of the method used to initiate the detonation. In a solid, even when all of these quantities are held constant, there may still be significant variability in the responses of a series of samples. For example, in an experiment in which crystals are detonated by mechanical impact, the variability may take the form of a wide range of impact energies necessary for detonation in apparently identical samples. A possible source of this variable response might be some uncontrolled variation in the experimental conditions, presenting different samples with an unknown variation in initial conditions. However, a sample of solid material, unlike a fluid, is characterized not only by its chemical composition and its thermodynamic state, but also by its particular spatial arrangement of molecules. In this paper we examine the idea that minute details of the lattice structure influence the detonation process, including its initiation.

One traditional theoretical approach to understanding detonations, and the initiation of a detonation by a shock wave, involves a description in terms of thermodynamic variables that are related by an equation of state for the material.<sup>1</sup> The application of such equations of state depends on an often implicit assumption that thermodynamic equilibrium is achieved in the induction zone, and that through an equipartition process the energy in the lattice vibrations is shared with the chemical bonds. However, because of the extremely small length and time scales involved in the detonation process in a solid, the applicability of the concept of thermodynamic equilibrium, and the equation of state approach that flows from it, has been called into question.<sup>2-4</sup>

In previous work,<sup>4-6</sup> we performed molecular dynamics simulations of the passage of a shock through a two-dimensional crystal containing various types of defects. We found that the shock's encounter with certain defects led to the rapid creation of a large fluid region within the crystal, and that the collision rate in the region was so high that an equilibrium distribution of molecular speeds was achieved on a very fast timescale, when the shock was still in the neighborhood of the original defect location. This led us to speculate that in a real solid, an understanding in terms of thermal equilibrium may be relevant at all, since the thermalized fluid regions would presumably be the sites of chemical reactions, if their temperatures were high enough, and energy from detonation reactions could be available to accelerate the nearby shock. Further exploration of these ideas required more realistic simulations, upon which we report in this paper.

Table I: Parameters used in the intermolecular and intramolecular potentials.

	$V_{N-N}$	$V_{C-C}$	$V_{C-N}$	$V_a$	$V_b$
$E(\text{eV})$	0.004	0.001	0.00075	7.93467	8.93467
$S(\text{\AA}^{-1})$	2.1	1.3	1.4	1.8650	1.5749
$r_0(\text{\AA})$	5.022	5.022	4.09	1.48	1.48

## METHOD

In order to investigate the question of the effects of the details of the lattice structure on the initiation of a detonation, we have exploited as realistic a microscopic model as now seems practical for three dimensional calculations. The basic method used is computational molecular dynamics, where the forces between particles are calculated from additive classical potentials. The form of the potential between two particles depends only on the types of the particles, which determines the type of bond between them. There are two classes of potentials employed. The intermolecular interactions are governed by Morse potentials that are similar in form to the Lennard-Jones potentials used in some previous molecular dynamics calculations of solid detonations.<sup>7</sup> The intramolecular interactions, or the chemical bonds, are represented by a predissociative potential formed by the difference between two Morse potentials. This type of chemical bond model has been used successfully to model detonations in solids in several previous studies.<sup>8,3</sup> Its use has a basis in a theory that the detonation of many energetic solids depends on the population of an excited state of the molecules in the lattice, followed by the breaking of a key molecular ("predissociative") bond.<sup>9</sup> According to this theory, the molecules can be considered to act as diatoms. Whether or not these ideas are correct, the predissociative diatomic model is useful in three dimensions, where more elaborate many-body chemical models, used sometimes in one- or two-dimensional simulations,<sup>10</sup> have not yet been attempted and may be too expensive:

Our model system is a diatomic, predissociative representation of crystalline nitromethane in a simple cubic configuration.<sup>7</sup> The nitromethane molecule consists of a  $\text{CH}_3$  group, with a mass of 15 amu, bonded to an  $\text{NO}_2$  group, with a mass of 47 amu. The bond is between C and N. The diatomic model treats each group as an unbreakable molecular unit; following common practice, we refer to the  $\text{CH}_3$  group as "C" and the  $\text{NO}_2$  group as "N", and the predissociative bond between them as the "C-N bond" (the C and N groups are also often referred to as "atoms.")

The particular values of the parameters used in the potentials that we adopt here are due to the recent work of Maffre and Peyrard,<sup>11,12</sup> where the nitromethane potentials were scaled in order to produce an accurate sound speed. The intermolecular potential is given by

$$V(r - r_0) = E \left( e^{-S(r-r_0)} - 1 \right)^2 - E,$$

where the values of  $E$ ,  $S$ , and  $r_0$  depend on whether this is an N-N, N-C, or C-C interaction. The N-C intramolecular potential is given by

$$W(r - r_0) = E_a \left( e^{-S_a(r-r_0)} - 1 \right)^2 - E_a - \left( e^{-S_b(r-r_0)} - 1 \right)^2 - E_b.$$

Here  $r$  is the length of the chemical bond, and  $r_0$  is its equilibrium length. The values of all the parameters are given in Table I.

Preliminary calculations with results similar to those reported in this paper have been presented elsewhere.<sup>13</sup> The nitromethane model used was less accurate, involving arbitrary values for some of the potential parameters; this shows that the essential character of the results do not depend on the details of the potentials.

Some of the calculations reported here were performed on NRL's Cray-XMP, using a vectorized version of the Monotonic Lagrangian Grid (MLG)<sup>14</sup> algorithm. The bulk of work was performed on a Connection Machine CM-200, using one of its two 8192 processor banks on a system of 8192 particles.

The algorithms described in reference 6 for two-dimensional nonreactive molecular dynamics calculations on the Connection Machine were readily adapted to the current three-dimensional reactive calculations. The only significant changes needed were an increase in bookkeeping demanded by the multiple potentials used in the predissociative model. Also, in order to determine, in analyzing the results, when a bond is broken, each particle (N or C group) must be assigned a unique index.

## RESULTS

The reference configuration used for all of the numerical experiments described here is identical, in form, with the "type-1" stable lattice described in reference 7. It is a simple cubic lattice of N groups, to each of which is bonded a C group. The position of each C group is obtained by adding the identical displacement to the  $x$ ,  $y$ , and  $z$  coordinates of each N group; the displacements are chosen so that the length of the N-C bond is  $r_0$ , given in Table I.

Our experience in previous calculations in two dimensions<sup>5,6</sup> suggests that of all the possible crystallographic defects, the most important in a shocked crystal are small voids. We use the term "void," but these are not to be confused with the macroscopic or micron-sized voids that are known to be important in the detonation of, for, example, liquids, where the voids are actually gas bubbles that can be heated by compression by a passing shockwave. The earlier molecular dynamics calculations of Karo, Hardy, and Walker<sup>15,16</sup> also suggested, indirectly, the importance of voids in a (two-dimensional) crystal, by demonstrating that a shock's encounter with a free surface results in spalling from the surface. This is relevant because a void involves free surfaces parallel to the shock front, but, as was shown elsewhere,<sup>4-6</sup> the effect of a complete void interior to a crystal is completely different from a free surface or a gap.

The method of driving a shock into the crystal is the same in all cases. The leftmost (referring to the orientation in the figures) plane of molecules is assigned a mass of 800 amu per group, and given an initial velocity to the right. The system is then allowed to evolve freely under the action of its internal interparticle forces. Periodic boundaries are maintained transverse to the initial velocity direction, while the left and right boundaries are free surfaces. There is no computational window. This simulates the action of a piston, in that a nearly planar left free surface is maintained, with a nearly constant velocity, but avoids the continual addition of energy to the system. Shocks of different strengths are produced by varying the initial "piston" velocity.

As is well known by now,<sup>7</sup> it is possible to establish a detonation structure in a three-dimensional crystal without defects. A detonation structure is a characteristic set of moving interfaces that delineate the shock, an induction zone, and a plastic or fluid reaction zone of reaction products. Such a detonation process is illustrated in the left half of figure 1, where the piston velocity is 4.0 km/sec. and the positions of only those atoms that have become dissociated from their original molecules is plotted after 0.4 ps have elapsed. The original border of the crystal, which is a cube 75 Å on a side, is shown with a dotted outline, and the three-dimensional crystal is shown in a head-on view. This is an indication of where chemical bonds have been broken. For the purpose of producing these figures, we needed to adopt a definition of "dissociation" useful with the predissociative molecular model. An atom is considered dissociated if its current distance from the atom to which it was originally chemically bonded (bonded by the predissociative potential  $W(r - r_0)$  given above) is greater than 3.0 Å. The "breaking point" of the potential (its local maximum) is at about 2.0 Å, but the separation distance at which all the energy absorbed by the bond in stretching has been reconverted to kinetic energy is very close to 3.0 Å. A plot of dissociated atoms can then be thought of as a diagram of all of those locations where the energy originally stored in chemical bonds is being supplied to the lattice as kinetic energy. The right half of figure 1 shows the results of an identical simulation, except that a group of 32 molecules have been removed from the lattice, leaving a hole in the shape of a rectangular prism whose leading edge is at the sixth molecular plane from the left face of the crystal. The plots of dissociated atoms show that the detonation front survives the passage through the defect, and also that the defect creates a region of enhanced early bond breaking.



Figure 1: A shock through a nitromethane crystal with no defect, on the left, and a small void, on the right, showing the locations of dissociated atoms only.

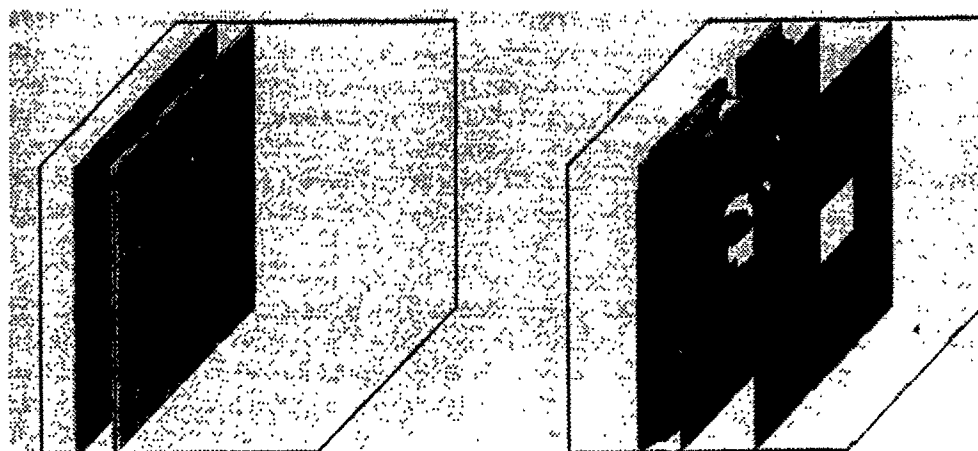


Figure 2: Speed distributions in the defective crystal.

with a localized disruption of the lattice structure. In figure 2 we have shown perspective views of the evolution of the atom speed distribution in the crystal for the same run illustrated on the right of figure 1. The features of interest have been revealed by only plotting the largest  $\approx 20\%$  of speeds; this removes the bulk of the material, which is characterized by lower particle speeds. At 0.2 ps the peaks in the speed distribution can be seen at the left face (the "piston") and at the shock front, which is propagating to the right, into the crystal. A "hot spot" can also be seen developing near the shock front, at the site of the defect. By 0.4 picoseconds (ps), a hot spot can clearly be seen at the defect site, where figure 1 shows a region of enhanced reactivity. At this point, the reacted atoms associated with the defect location have the fastest particle speeds in the system. Also here we can see the development of an energetic zone corresponding to the reaction zone that can be seen in figure 1. This shows that bond energy is being converted to kinetic energy in the reaction zone.

We have repeated this simulation down to a piston velocity of 2 km/sec, where we find that a planar reaction front is still formed, and the initiation of a detonation does not require the presence of a defect. At a piston velocity of 1 km/sec, the shock traverses the crystal without the breaking of any of the intramolecular bonds, both in the case of the perfect crystal and in a crystal containing the defect described above. When the defect is replaced by one that is slightly shorter in the direction of shock propagation and slightly longer in the other directions, involving



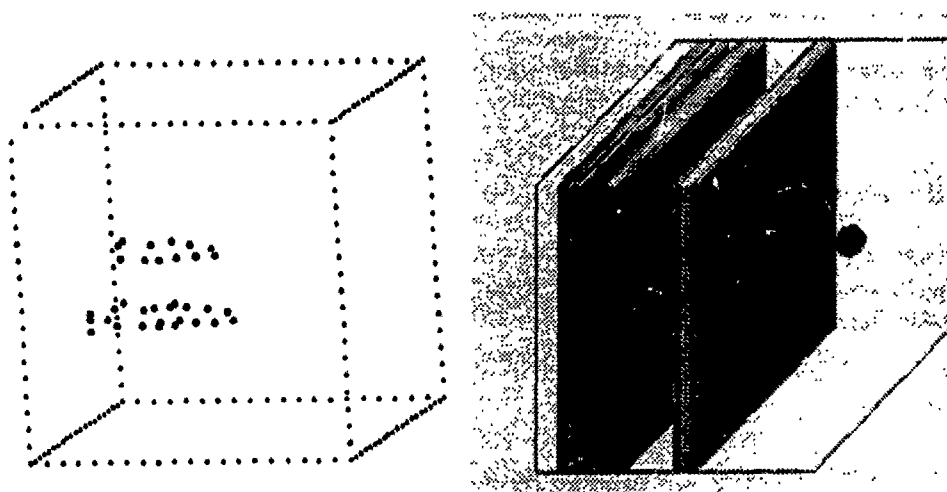


Figure 3: Locations of dissociated atoms and atom speed distribution at 0.7 ps in a nitromethane crystal with a different void shape.

the removal of 50 molecules, we seem to be in the neighborhood of an initiation threshold. As shown in the first frame of figure 3, which is a perspective view of the crystal showing the locations of dissociated atoms only, there is no planar detonation front. There is, however, a cluster of dissociated atoms at the defect site. The system under study is not long enough to determine whether the chemical-kinetic activity at the defect site will lead to the creation of an actual detonation front, as the leading shock has reached the end of the crystal before this has a chance to develop. Also in this figure is displayed the particle speed distribution at the same time, showing clusters of hot dissociated atoms near the shock front.

## CONCLUSIONS

Some intriguing experimental evidence has accumulated<sup>17</sup> that seems to show that defects must be present in order for a *single crystal* of high explosive to be detonable. The evidence involves materials with a more complex molecular structure than nitromethane and therefore less chance of being represented reasonably by a diatomic model. However, we hope that these types of molecular dynamics models capture some of the behavior of any energetic solid, where the detonation reaction always involves an endothermic phase, where the molecules absorb energy, followed by an exothermic phase, where reaction products supply kinetic energy to the crystal lattice and the shock propagating through it. Indeed, it has been shown<sup>18,7</sup> that a detonation front with the correct structure, obeying local conservation laws, can result from any of a variety of molecular dynamics models. However, if we accept the experimental evidence on the necessity of defects for detonation, there must be something crucially wrong with all of these models, including more elaborate representations involving chemical recombination.<sup>10</sup> This is because the numericist is able to cause a detonation, using a reasonable excitation energy, in a defect-free crystal. It is possible that the fault lies not in the material model itself, but rather in the way that a shockwave is created in the system. Perhaps all of the techniques used share the deficiency of involving an unrealistically efficient transfer of energy from the outside world into the vibrational modes of the crystal.

We have made no attempt to settle these issues here. However, we have shown, for the first time, that a standard molecular dynamics model may predict that a void will enhance the sensitivity of a single crystal of energetic material. Although it is still possible, with this model, to have a detonation without a defect, the defect always increases the rate of reaction in the initiation phase, and results in a hot spot. There is a regime where the shock is too weak to cause a detonation in the absence of a defect, but in this case a void can be the site of a release

of chemical energy. Whether this reaction site is powerful enough to lead to the development of a mature detonation front is beyond the scope of this study, and will have to wait for a simulations on a larger scale, carried out for longer times.

## ACKNOWLEDGMENTS

This work was supported by the Physics Division of the Office of Naval Research and by the Naval Research Laboratory. We are grateful to Jill Dahlburg and Donald Tsai for numerous valuable discussions.

## REFERENCES

1. W. Fickett and W. C. Davis, *Detonation*, U. of Cal. Press, Berkeley, 1979.
2. F. E. Walker, The initiation and detonation of explosives: an alternative concept, LLNL Report UCRL-53860, Lawrence Livermore National Laboratory, 1988.
3. D. H. Tsai and S. F. Trevino, *J. Chem. Physics* **81**, 5636 (1984).
4. L. Phillips and E. S. Oran, Molecular dynamics simulations of shocks in imperfect crystal lattices, in *Shock Compression of Condensed Matter 1991*, pages 143-146, APS, 1992.
5. L. Phillips, R. S. Sinkovits, E. S. Oran, and J. P. Boris, Molecular dynamics of shocks in crystals with defects, NRL Memorandum Report 4440-92-6998.
6. L. Phillips, R. S. Sinkovits, E. S. Oran, and J. P. Boris, The interaction of shocks and defects in lennard-jones crystals, 1992, To appear in *Journal of Physics: Condensed Matter*.
7. S. G. Lambrakos, M. Peyrard, E. S. Oran, and J. P. Boris, *Phys. Rev. B* **39**, 993 (1989).
8. M. Peyrard, S. Odier, E. Oran, J. Boris, and J. Schnur, *Phys. Rev. B* **33**, 2350 (1986).
9. S. Odier, *Journal de Physique Colloque C4*, 225 (1987).
10. M. L. Elert, D. M. Deaven, D. W. Brenner, and C. T. White, *Phys. Rev. B* **39**, 1453 (1989).
11. P. Maffre, *Modelisation de Propagation d'Onde de Detonation dans un Cristal Moleculaire Energetique*, PhD thesis, Universite de Bourgogne, 1992.
12. P. Maffre and M. Peyrard, *Phys. Rev. B* (1992), In press.
13. L. Phillips and R. S. Sinkovits, Molecular dynamics of detonation in crystals with defects, Presented at the Energetic Materials Workshop, Los Alamos, March 3-6, 1992.
14. S. G. Lambrakos and J. P. Boris, *Journal of Computational Physics* **73**, 183 (1987).
15. A. M. Karo, J. R. Hardy, and F. E. Walker, *Acta Astronautica* **5**, 1011 (1978).
16. J. R. Hardy, A. Karo, and F. E. Walker, Molecular dynamics of shock and detonation phenomena in condensed matter, in *Proc. of the 7th ICGER*, page 209, 1979.
17. A. W. Campbell and J. R. Travis, The shock desensitization of PBX-9404 and composition P 3, in *Proceedings of the Eighth Symposium (International) on Detonation*, pages 1057-106, 1986.
18. S. G. Lambrakos, M. Peyrard, and E. S. Oran, Molecular dynamics simulation of the effect of molecular dissociation and energy absorption on detonation structure in energetic solids, in *Proceedings of the Ninth Symposium (International) on Detonation*, pages 713-723, 1990.

## MOLECULAR DYNAMICS SIMULATIONS OF SHOCK-DEFECT INTERACTIONS IN TWO-DIMENSIONAL NONREACTIVE CRYSTALS

Robert S. Sinkovits\*, Lee Phillips\*, Elaine S. Oran\* and Jay P. Boris\*

\*Naval Research Laboratory, Laboratory for Computational Physics and Fluid Dynamics, Washington, DC 20375-5000

### ABSTRACT

The interactions of shocks with defects in two-dimensional square and hexagonal lattices of particles interacting through Lennard-Jones potentials are studied using molecular dynamics. In perfect lattices at zero temperature, shocks directed along one of the principal axes propagate through the crystal causing no permanent disruption. Vacancies, interstitials, and to a lesser degree, massive defects are all effective at converting directed shock motion into thermalized two-dimensional motion. Measures of lattice disruption qualitatively describe the effects of the different defects. The square lattice is unstable at nonzero temperatures, as shown by its tendency upon impact to reorganize into the lower-energy hexagonal state. This transition also occurs in the disordered region associated with the shock-defect interaction. The hexagonal lattice can be made arbitrarily stable even for shock-vacancy interactions through appropriate choice of potential parameters. In reactive crystals, these defect sites may be responsible for the onset of detonation. All calculations are performed using a program optimized for the massively parallel Connection Machine.

### INTRODUCTION

This paper investigates the propagation of strong vibrational disturbances, or shocks, through nonreactive two-dimensional lattices. The motivation is the desire to understand some of the peculiar properties of the initiation and propagation of detonations in solid chemical explosives. In particular, we wish to study the role that defects play in the initiation of detonation. In solid explosives, it is known experimentally that there can be significant variation in the response of a sample to impact. A possible source of the variability might be some unknown and uncontrolled variation in the experimental conditions, presenting different samples with significantly different initial conditions, combined with an extreme sensitivity of the system to its initial conditions. Another possibility is that the response of the energetic solid is extremely sensitive to the presence of defects in the solid. It has been suggested that minute changes in the molecular arrangement, involving the locations of just a few molecules, may have a large, even determining, effect on a macroscopic detonation.<sup>1</sup> This suggestion gains plausibility if one considers that the actual thickness of the shock front may be only a few lattice planes.<sup>2</sup> Here we examine the point of view<sup>3-6</sup> that a shock in a solid initiates detonation through the mechanical generation of scission forces on the molecules comprising the solid, breaking chemical bonds, creating a distribution of free radicals, and supplying the kinetic energy required to initiate reaction.

In this paper we use molecular dynamics to investigate the interaction of the shock front with the lattice structure with particular interest in the effects of specific types of lattice defects on the shock initiation mechanism. There are no chemical reactions in our model; the "molecules" are point particles interacting through Lennard-Jones potentials. Hence the current connection to the detonation problem is the exploration of how the conditions leading to bond scission and subsequent recombination are established. The following stage, of reaction and shock acceleration, will be treated in a subsequent paper, which will report on simulations employing a chemistry model.

## COMPUTATIONAL METHOD

Calculations were performed using 4K, 8K or 16K particles on the massively parallel Connection Machine CM-200. For systems of this size, the solution of the complete N-body problem becomes impractical. The short-range nature of the Lennard-Jones potential used in our simulations was exploited to limit the distance over which the interactions had to be computed. The particle data was distributed onto a data structure known as the monotonic Lagrangian grid (MLG),<sup>7</sup> which has the property that objects that are close in physical space have nearby indices in the data structure arrays. The search for neighboring objects is reduced from a costly search through physical space to an efficient search through index space. The MLG also has two other advantages for this type of molecular dynamics calculation. First, since the positions of the molecules themselves define the computational grid, it is not necessary to define extra space in the data arrays. Second, the performance of the MLG is not hampered by variations in the density of the system due to the passage of the shock.

The MLG is particularly well-suited for the Connection Machine architecture. The processors of the CM are configured in a two-dimensional rectangular grid to match the geometry of the problem. Molecules with adjacent MLG indices are then mapped to adjacent processors. All interparticle calculations can be performed using a series of efficient coordinated near-neighbor grid communications.

A number of different algorithms were tested for the integration of the equations of motion for the system of particles. The leapfrog method was found to be best suited for this work since interparticle forces are velocity independent.

## PHYSICAL MODEL

The particles are initially arranged in a two-dimensional square or hexagonal array with a near-neighbor particle separation of  $d$ . Free boundary conditions are used in the shock direction and periodic boundary conditions may be chosen in the y-direction. The choice between free or periodic boundary conditions was made on the basis of the propagation of disturbances across the periodic boundary and into the region of interest. The shock is induced in the lattice by impact with a flying plate of velocity  $V_p$  made of the same material as the bulk lattice.

Particle interactions are described by a Lennard-Jones potential of the form

$$V(r) = 4\epsilon[(\sigma/r)^{12} - (\sigma/r)^6]. \quad (1)$$

In our calculations, the values of our parameters in dimensionless units are:  $\epsilon = 0.0223$ ,  $\sigma = 0.891$ ,  $V_p = 2.0$ ,  $d = 1.0$  and  $m = 4.0$ . Scaling these values to the appropriate values in solid argon result in a plate velocity of 4258 m/s, an interparticle separation of 3.8 Å, and one time unit equal to  $0.88 \times 10^{-13}$  s.

## RESULTS

Simulations were performed for shock-defect interactions in square and hexagonal lattices. These defects include vacancies, interstitials, and mass defects, where by mass defects we mean that individual molecules which are replaced by molecules with a different mass than those of the host lattice. All interparticle forces are left unchanged. Figure 1 shows a sequence of molecular configurations as a plate-launched shock interacts with a pair of rectangular voids in a square lattice, producing a great deal of disorder. The same initial conditions in a system without voids lead to a shock traversing the crystal intact and causing no permanent disruption of the lattice. We see here that the voids disturb the coherence of the shock, transforming the one-dimensional directed motion into a thermalized two-dimensional motion. That these disordered regions are actually thermalized can be seen by observing the speed distributions of the molecules as shown

in Figure 2. As time advances the distribution rapidly becomes Maxwellian. Similar results are observed in the hexagonal lattice.

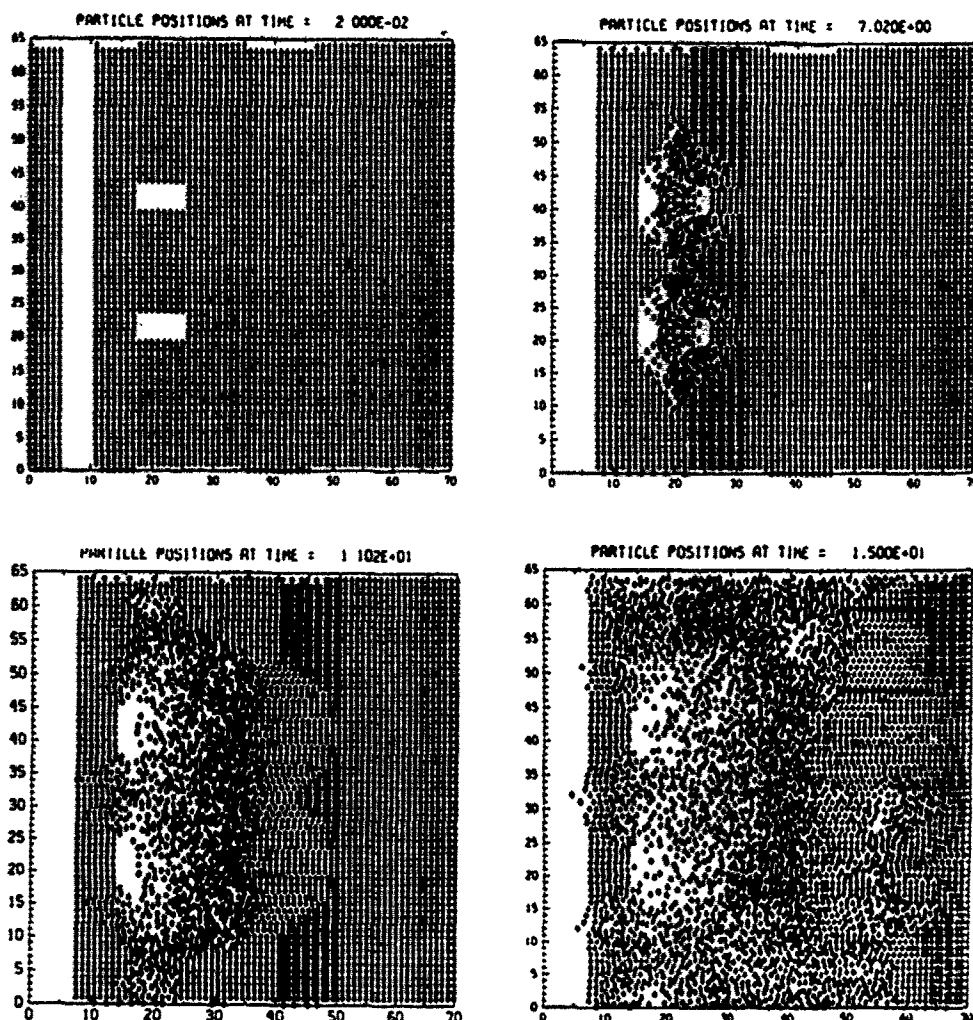


Figure 1. Particle positions for shock interacting with pair of rectangular voids in square lattice. Boxed region in last figure clearly shows the formation of the hexagonal lattice.

At elevated temperatures the difference between the square and hexagonal lattice becomes apparent. The defect-free square lattice completely dissociates upon impact by the flying plate at finite temperatures. This is to be contrasted with the behavior of the hexagonal lattice which remains stable at finite temperatures against plate impact. The effect of the various defects in the hexagonal lattice and their relative importance is not affected by temperature, but is strongly dependent on intermolecular potential well depth. For a given shock strength and defect type it is possible to increase the potential strength to the point where the lattice remains intact.

It is useful to quantify the concept of the strength of the effect of different types of lattice defects, or their efficacy in disrupting the crystal when interacting with a shock. For this purpose we have defined two "disruption factors," to be used with the two lattice symmetries. The disruption factors are defined in such a way that the elastic deformation of the lattice due to the shock itself does not make a contribution. Therefore, the disruption factors are zero for the case of a shock traversing a defect-free crystal that remains intact.

We can define disruption factors that satisfy these criteria as follows. For the square lattice the angular positions of the four nearest neighbors are found. The disruption factor,  $\chi$ , for each particle is defined as

$$\chi = \sum_{i=1}^4 |\sin \theta_i \cos \theta_i|, \quad (2)$$

where the summation is over near neighbors. For a compression or rarefaction of the lattice due to the propagation of a shock along one of the principal crystal axes, the angular positions of the near neighbors remain  $0, \pm\pi/2$ , and  $\pi$  resulting in  $\chi = 0$ .

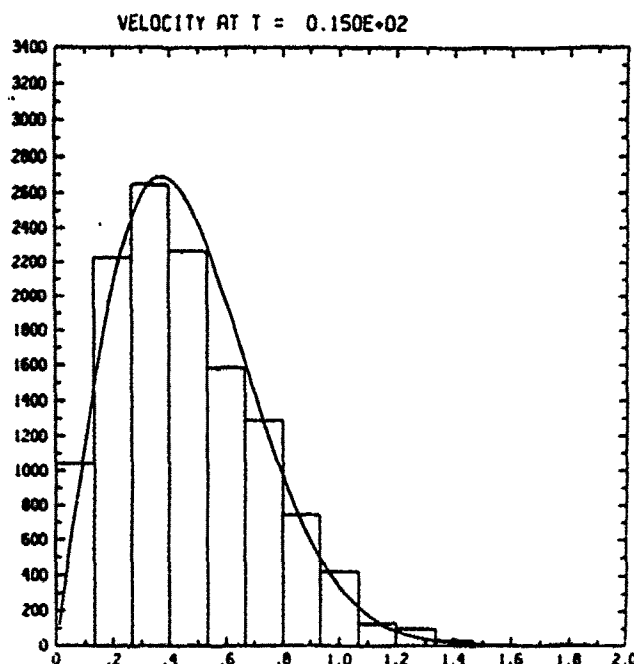


Figure 2. Velocity distribution histogram with superimposed Maxwell-Boltzmann velocity distribution corresponding to the disordered region of the last frame in Figure 1.

The hexagonal lattice disruption factor must be defined in a slightly different manner. The angular positions of the six near neighbors of each particle change as the shock propagates through the lattice. In this case the angular positions of the six near neighbors are first found. The neighbors in the lower half-plane are reflected into the upper half-plane. The near neighbors are then sorted into order of increasing angle. The disruption factor for the hexagonal lattice is defined as

$$\chi = \sin \theta_1 + \sin(\theta_3 - \theta_2) + \sin(\theta_5 - \theta_4) + \sin \theta_6. \quad (3)$$

In the case of a shock passing through a hexagonal lattice causing only a compression or rarefaction along the shock direction,  $\theta_1$  and  $\theta_6$  remain 0 and  $\pi$ , respectively. The angles  $\theta_3$  and  $\theta_2$  are equal and  $\theta_5$  and  $\theta_4$  are equal. As in the square lattice, a zero disruption is calculated.

The total disruption of the lattice is calculated by summing the per particle disruption factor over all particles. The values of the total disruption correlate well with the apparent disruption found by visual inspection of the particle positions.

Figures 3a and 3b display  $\Sigma(\chi)$  as a function of time for an assortment of crystal defects, for the hexagonal and square lattices respectively. The greater importance of voids over mass

defects is obvious, as is the unstable growth of the disordered region after the passage of the shock. Figure 3b also shows that the fastest growing disruption factor is found for an interstitial inclusion in a square lattice. The closer packed hexagonal lattice does not provide an equilibrium position for an interstitial inclusion.

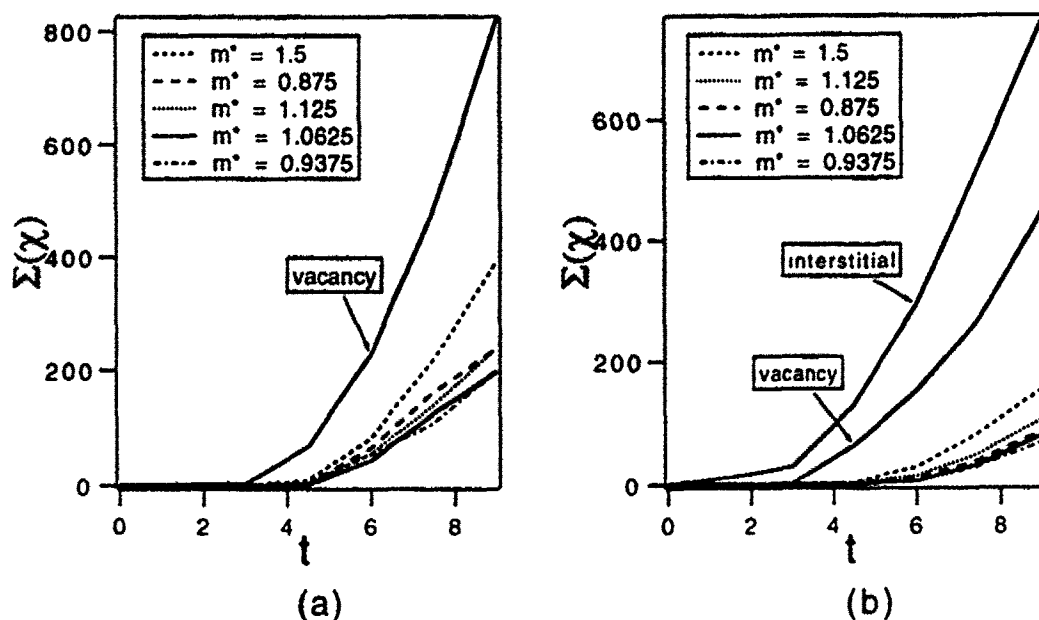


Figure 3. Disruption factor as a function of time for a variety of defects in hexagonal (a) and square (b) lattices.

## CONCLUSION

When a shock, sufficiently weak that it is able to traverse a *perfect* crystal without permanently disturbing the configuration of its lattice, encounters a void in the lattice, the void becomes the site of a rapidly growing thermalized, hot, fluid-like phase characterized by a high density and a high degree of collisionality. These characteristics should be conducive to the onset of chemical reactions, and, we suspect, it is in these regions that the reactions leading to the development of a shock-detonation structure begin. It therefore seems likely that the void distribution in the lattice is an important factor controlling the sensitivity to shock-initiation and the character of the subsequent detonation front development. A perfect crystal should be relatively insensitive. It is possible that in three dimensions, other types of defects will be seen to be equally important, but that will be treated in a subsequent paper.

In order to concentrate on the narrowly defined problem of shocks and defects in molecular crystals with as few complications as possible, we have not yet included a model of the chemical bond and simulated the behavior of moderately large systems of indivisible molecules with spherically symmetrical potentials. This approach has the advantage that our results are independent of the details of any particular model of detonation chemistry or intramolecular behavior.

Although we have been able to resolve several issues concerning the importance of defects, there are some remaining ambiguities that will not be resolved until we include polyatomic molecules in the simulations. These have their counterpart in the uncertainties in our knowledge of the bond scission process in a shocked crystal lattice. If the polyatomic bonds are broken in the shocked region due to direct energy transfer from the shock to vibrational modes of the

molecules, then the scission forces have little relevance because they occur in the disordered regions behind the shock. The importance of the defects is that the thermalization and mixing provide enhanced opportunities for the free radicals, created in the shocked region, to recombine. Of particular relevance here is the observation that thermal equilibrium is established in the disordered region close behind the shock, on a very fast timescale, implying that equilibrium equations of state may be relevant after all to the detonation process. If the chemical bonds are not broken directly by the passing shock, then the scission forces may be responsible for bond stretching and breaking in the disordered region, where conditions prevail that will enhance the subsequent reactivity. We believe that some of these questions can be addressed in the next generation of simulations that involve both defects and chemical reactions in larger polyatomic crystal lattices.

## ACKNOWLEDGEMENTS

The authors would like to thank Sam Lambrakos, Sam Trevino and Donald Tsai for their helpful discussions. This work was supported by the Naval Research Laboratory and the Office of Naval Research. One of us (RSS) would like to thank the Office of Naval Technology for support as an ONT postdoctoral fellow.

## REFERENCES

1. W. Sandusky et al., Deformation and shock loading studies on single crystals of ammonium perchlorate relating to hot spots, in *Proc. of the Ninth Symposium (International) on Detonation*, page 975, 1989.
2. A. N. Dremin and V. Y. Klimenko. *Prog. Astro. Aero.* **75**, 253 (1981).
3. F. E. Walker, The initiation and detonation of explosives: an alternative concept. LLNL Report UCRL-53860, Lawrence Livermore National Laboratory, 1988.
4. F. E. Walker and R. J. Wasley. *Propellants and Explosives* **1**, 73 (1976).
5. F. E. Walker. *Propellants, Explosives, and Pyrotechnics* **7**, 2 (1982).
6. F. E. Walker, *J. Appl. Phys.* **63**, 5548 (1988).
7. J. Boris. *J. Comput. Phys.* **66**, 1 (1986).



## MOLECULAR LEVEL STUDY OF INSENSITIVE AND ENERGETIC LAYERED AND INTERCALATED MATERIALS

RICHARD D. BARDO

Naval Surface Warfare Center, White Oak, Silver Spring, MD 20903

### ABSTRACT

An important goal in the detonation physics and chemistry community is to design explosives with high-performance capabilities, yet sufficiently low impact and shock sensitivities. The traditional ways of developing increasingly energetic explosives have led to an increase in sensitivity. It is, therefore, of practical and theoretical importance to design, from molecular level considerations, polycrystalline explosive systems which clearly exhibit directional sensitivity and initiation properties, and which approach the insensitivity of homogeneous or single-crystal explosives. Theoretical studies indicate that such systems may be constructed from special materials such as high-quality pyrolytic, layered, hexagonal boron nitride (BN) crystals. Intercalation of the crystals with various oxidizing agents can yield an explosive system with the desired properties. Under ordinary laboratory conditions and with modest pressures, the intercalate molecules readily enter the host lattice by exploiting the weak bonding between the layers, resulting in denser, metastable crystals. High energy release is achieved when products containing  $B_2O_3$  are formed.

### INTRODUCTION

New energetic compounds continue to be synthesized which give ever-improving fragment acceleration and blast pressure, but often showing a concomitant increase in sensitivity. Since the traditional "trial and error" methods used in the scale-up of the new materials from laboratory to test conditions continue to show conflicting performance and sensitivity results, it would be of practical and theoretical importance to be able to design, from the ground up, a highly-energetic explosive system which clearly exhibits the needed insensitivity and performance at all stages of development. It is, therefore, the purpose of this paper to indicate the feasibility of such a program by exploiting the current understanding of the nature of the molecular-level processes governing the behavior of energetic materials at high pressures and temperatures.

Benchmark experiments exist which show profound differences in the way homogeneous and heterogeneous explosives initiate under shock. In the case of sustained shock pulse initiation of homogeneous liquid nitromethane (NM),<sup>1</sup> which is free of discontinuities of any kind, fast reaction appears to begin close to the driver plate interface after an induction time of about  $10^{-6}$  sec. No light is emitted directly behind the initiating shock, which at 60 kbar propagates 8 mm before initiation begins at the interface. The absence of light emission indicates no appreciable excitation of electronic states with lifetimes  $\leq 10^{-6}$  sec. Similar behavior is observed in molten trinitrotoluene (TNT)<sup>1</sup> as well as in single crystals of pentaerythritol tetranitrate (PETN),<sup>1</sup> cyclotrimethylene trinitramine (RDX)<sup>2</sup> and cyclotetramethylene tetranitramine (HMX).<sup>2</sup> On the other hand, sustained shock pulse initiation of heterogeneous NM containing air and oxygen bubbles and of polycrystalline solid explosives gives rise to initiation close to the initiating shock with negligible induction times.<sup>1</sup> In all of these materials, sensitivity is a function of the defect structure and heterogeneous nature of the medium.

More recently, directional shock sensitivity has been discovered in single crystals of PETN by Dick, et al.<sup>3</sup> who showed that, in the chosen geometry, initiation is difficult to achieve along the crystal direction of greatest slip. Although existing crystals of shock-insensitive, "graphitic" triaminotrinitrobenzene (TATB) are too small to be reliably studied with the techniques used for PETN (crystal size of 1 cm), it is expected that larger specimens would show similar, but more pronounced behavior. In PETN, all three orthogonal directions have van der Waals bonding, whereas the layered structure of TATB has such bonding only in one direction and strong intralayer hydrogen bonding.<sup>4</sup> Other explosives with similarly-pronounced slip systems would be expected to show directional sensitivity properties as well. It should be emphasized that while the

above research pertains to the structure of single crystals, an understanding of the effects of polycrystalline interactions are crucial in the final analysis of shock sensitivity. Toward this goal, van der Steen, et al.<sup>5</sup> have, for example, determined that crystalline shapes significantly affect sensitivity.

The present paper introduces a program currently underway at the Naval Surface Warfare Center (NAVSWC), involving the design of high-performance explosive crystals which clearly exhibit directional shock sensitivity properties along specific crystal axes and yet which clearly approach the insensitivity of homogeneous explosives along the other axes. Such materials are being constructed from layered pyrolytic boron nitride (BN) crystals.

## INTERCALATION OF BN

Intercalation compounds are formed by insertion of a guest chemical species - an intercalate - between layers in a host material. Because of its simple structure, high-quality pyrolytic graphite is most often the preferred choice of host lattice for purposes of enhancing its electrical conductivity and chemical reactivity.<sup>6</sup> Another simple lattice is pyrolytic BN, the crystal structure of which is closely related to that of graphite and being built of hexagonal layers of the same kind, but arranged so that atoms of one layer lie vertically above those in the layers below.

Although each layer in graphite or BN is one of the most stable structures in nature, intercalation of crystals with various oxidizing agents can yield explosive systems with the desired properties. In the case of BN, highly-energetic reactions are possible with formation of  $B_2O_3$  ( $\Delta H_f = -303$  kcal/mol). Under ordinary laboratory conditions, the molecules of intercalant enter the host crystal by exploiting the weak binding energy (1.5 kcal/mol or 0.065 eV) between the layers and increasing the interlayer spacing.<sup>6</sup>

Intercalation proceeds by charge transfer from the host BN layers to the oxidizer molecules, causing bonding within the layers of intercalate. This intercalate-intercalate bonding is generally much stronger than the intercalate-host bonding, resulting in a large thermal expansion of the intercalate layer relative to that of the host layer, which exhibits almost no thermal expansion. For the oxidizer or acceptor compounds, the intercalate layer becomes negatively charged by extracting electrons predominantly from the host bounding layers. Thus, these host layers have a high concentration of holes, causing the Fermi level to fall and the corresponding cylindrical Fermi surface to shrink.

It is interesting to note here that intercalation of "graphitic" TATB would likely produce a much less stable structure, since the transfer of charge would be small and localized in the vicinity of the carbon rings. As a consequence, the intercalate-intercalate bonding would be weaker than that found in the extended structures with uniform bonding in the host layers.

While ordinary procedures of doping give random distributions of guest species, intercalation produces a highly-ordered structure. The resulting process of staging gives a mechanism for controlled variation of the physical properties of the compounds. Stage  $m$  compounds have  $m$  graphite or BN layers between successive layers of intercalate. For maximum intercalation,  $m = 1$ , and the theoretical maximum density (TMD) of the crystal falls in the range  $2.30 \leq \text{TMD} \leq 2.80$  g/cm<sup>3</sup> for the simple molecular intercalates. In this case, the host and intercalate layers alternate so that the structure is uniform and "homogeneous". In the case of planar  $NO_3$ , stacking of the BN and  $NO_3$  layers at  $\text{TMD} = 2.50$  g/cm<sup>3</sup> gives the arrangement shown in Figure 1. For higher staging (i.e. lower intercalate concentration), high resolution electron microscope (HREM) imaging shows a range of  $m$  values, as depicted in Figure 2 for the  $FeCl_3$  intercalation of graphite.<sup>7</sup>

Since slip in the layered materials must occur without breakage of the B-N bonds, basal dislocations must be present to allow deformation of the hexagons.<sup>8</sup> For stage 1 compounds, maximum slip along the glide planes of dislocations is possible, since the Burgers vectors corresponding to the active basal dislocations of the layers are parallel to the basal plane.<sup>8</sup> In this case, there is minimal slip perpendicular to the basal plane. These dislocations, which split into two partials, have associated with them shear, acoustic modes which are soft (low frequency  $\omega$ ). For stages  $m > 1$ , regions or galleries of intercalate species are formed between adjacent host layers, resulting in strain of the graphite or BN layers. These galleries are depicted in Figure 2. For graphite, the presence of a layer of intercalate causes the two adjacent host layers to undergo relative shear to bring them into eclipsed stacking. The presence of a dislocation at a boundary of a gallery has, then, a Burgers vector with basal and perpendicular components.<sup>8</sup> The presence of the

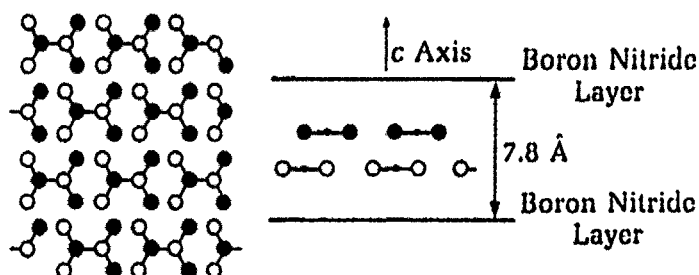


Figure 1. Possible double layer for planar  $\text{NO}_3$  intercalated between BN layers. Side view shows  $\text{NO}_3$  layers parallel to the BN layers. Eclipsed oxygen atoms are shown as closed circles in the top layer and as open circles in the bottom layer. Top view of double layer is displayed at left. Stage 1 formula is  $(\text{BN})_2\text{NO}_3$ .



Figure 2. Schematic drawing of high resolution electron microscope (HREM) image of  $\text{FeCl}_3$  - graphite, showing interpenetration of differently staged regions (Ref. 7).

latter component corresponds to an edge dislocation, allowing slip to also occur perpendicular to the basal plane.

### TIMES TO IGNITION IN SHOCKED, INTERCALATED BN

A theory<sup>9</sup> has been developed by the author which provides a formal framework and guide for the analysis of shock ignition in layered materials. This theory describes the interrelationship among bimolecular chemical reactions and processes for vibrational energy transfer between the crystal lattice and its molecules. Chemical reaction occurs only after sufficient energy is transferred for activation of the molecules. In many cases, this is the slow or rate-determining step, the characteristic time  $t_{pv}$  for which is given by

$$t_{pv} = \hbar \sqrt{\rho_a \rho_o} \quad (1)$$

where  $\hbar$ ,  $\rho_a$ , and  $\rho_o$  are, respectively, Planck's constant and the densities-of-state for the acoustic and optical lattice modes. As indicated in Reference 9,  $\rho_a$  and  $\rho_o$  may be calculated from the general expression

$$\rho = \left( \frac{\lambda}{\pi n} \right)^{1/2} \frac{(1 - 1/12n)\lambda}{h\langle \nu \rangle (1 + \eta)} \left[ \left( 1 + \frac{\eta}{2} \right) \left( 1 + \frac{2}{\eta} \right)^{n/2} \right] \quad (2a)$$

where  $n$  is the number of vibrational degrees of freedom,  $\langle \nu \rangle$  is the average of the  $n$  frequencies  $\nu_i$ , and  $\lambda$  and  $\eta$  are defined by the equations

$$\lambda^{-1} = \prod_i (\nu/\langle\nu\rangle), \quad (2b)$$

$$\eta = E/E_0. \quad (2c)$$

In Equation (2c),  $E$  is the internal energy interval and  $E_0$  is the zero-point energy. Equations (2a)-(2c) apply to both harmonic and anharmonic vibrations.

Calculation of the energy transfer times  $t_{pv}$  indicates the important role of slip in the initiation of PETN, as interpreted earlier by Dick, et al.<sup>3</sup> Since excitation of the higher-energy optical modes of the lattice is crucial to ignition,<sup>9</sup> preferential excitation of the long-wavelength acoustic modes corresponding to slip can, by Equation (1), give times  $t_{pv}$  which are too slow for the given dimensions of the explosive crystal.

The importance of  $t_{pv}$  may be seen in context with other processes occurring in the system which also have characteristic times. These processes and their corresponding rate coefficients pertain to (1) energy transfer from the host lattice into the intercalation molecules  $k_{pv} = t_{pv}^{-1}$ , (2) energy transfer from the molecules back into the host lattice  $k_{vp}$ , and (3) bimolecular reaction  $k_b$  between host and intercalate, which combine to give the total rate coefficient<sup>9</sup>

$$k_{tot} = k_{pv} k_b / (k_{vp} + k_b). \quad (3)$$

If most of the shock energy is dissipated into the low-frequency acoustic vibrations corresponding to the direction of greatest slip, little reaction is generated so that  $k_{vp} \gg k_b$  in Equation (3). If, then,  $k_{tot}^{-1} > t_r$ , where  $t_r$  is the time for arrival of rarefaction waves, any reaction is quenched and no ignition is possible, since reduction of the shock pressure  $P_s$  below a critical value inhibits the important bimolecular reactions. For the single 1 cm PETN crystals used in Reference 3, calculation shows that  $k_{tot}^{-1} \approx 10^{-5}$  sec for  $10 \leq P_s \leq 80$  kbar, and  $t_r \approx 10^{-6}$  sec for shocks along crystal direction  $\langle 100 \rangle$ . On the other hand, if  $k_{tot}^{-1} \leq t_r$  ( $t_{tot} \geq t_r$ ), ignition is possible. This is the case for orientation  $\langle 001 \rangle$  where slip is minimized and  $k_b \gg k_{vp}$ , so that  $k_{tot}^{-1} = t_{pv}$ . Here, calculation shows that  $k_{tot}^{-1} < 10^{-10}$  sec for  $10 \leq P_s \leq 80$  kbar. These results for PETN are portrayed in Figure 3.

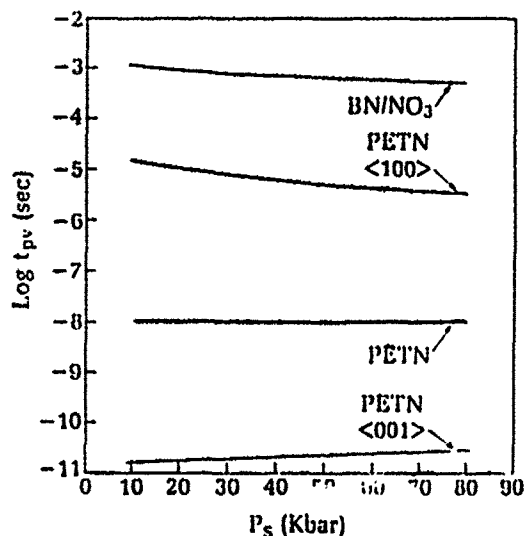


Figure 3. Comparison of shock pressure dependence of  $t_{pv}$  for acoustic and optical modes along various crystal directions in BN/NO<sub>3</sub> and PETN. The curve labelled PETN corresponds to the geometric mean of the densities-of-state, Eq. (1), for directions  $\langle 001 \rangle$  and  $\langle 100 \rangle$ . Upper two curves for BN/NO<sub>3</sub> and PETN pertain to maximum slip.

It is emphasized here that it is the slow, rate-determining step, identified with  $t_{pv}$ , which ultimately determines the ability of the explosive to ignite at certain critical pressures and temperatures.

For initiation to occur in layered crystals, planar shocks must be directed along the c-axis of the unit cell or at small angles with it. At some critical shock pressure  $P_{cs}$ , excitation of the initiating optical modes along the c-axis results in bimolecular reaction between the host and intercalate layers, and  $t_{pv} < t_r$ . For the BN/NO<sub>3</sub> system depicted in Figure 1, an estimate of  $t_{pv}$  is readily obtained from Equations (1) and (2) if the following reasonable assumptions are made: (1) initiation along the c-axis is effectively one-dimensional and (2)  $P_{cs} = 130$  kbar, which approximates the known minimal pressure required to cause significant distortion of the BN or graphite planes to form the cubic structures.<sup>10</sup> It is assumed here that the lower bound to the optical mode quantum  $h\omega$  along the c-axis of BN is about 70 cm<sup>-1</sup>, which is the value for high-quality graphite.<sup>11</sup> Also, the ratio  $\lambda \equiv 1$  in Equation (2b) and  $E = 5 \times 10^9$  ergs/g at  $P_{cs} = 130$  kbar,<sup>12</sup> so that in Equation (2c),  $\eta = 14.3$ , since  $E_0 \approx 35$  cm<sup>-1</sup>. The number of atoms per unit cell in the BN/NO<sub>3</sub> structure at stage 1 is 10, and the corresponding number of optical modes  $n$  for the one-dimensional problem is 9. Substitution of all of these values into Equation (2a) gives, then,  $\rho_0 \leq 1.2 \times 10^{24}$ /erg. Accordingly, since  $n = 1$  for the acoustic mode along the c-axis, substitution of the remaining parameters above into Equation (2a) gives  $\rho_a \leq 7.8 \times 10^{13}$ /erg. Thus, from Equation (1),  $t_{pv} \leq 10^{-8}$  sec, which is much shorter than  $t_r \approx 10^{-6}$  sec for centimeter-scale crystals.

The effects of sustained shocks of  $P_{cs} = 130$  kbar at increasing angles from the c-axis are, to good approximation, two-dimensional in the crystal, corresponding to slip of the host and intercalate planes past each other, because of the relatively weak host/intercalate interaction under shock conditions. In this case,  $n = 2$  and 18 for the acoustic and optical modes, respectively. Substitution of these values as well as the ones above for  $h\omega$ ,  $\lambda$ , and  $\eta$  into Equation (2a) gives  $\rho_a \leq 1.1 \times 10^{15}$ /erg and  $\rho_0 \leq 4.7 \times 10^{35}$ /erg, and from Equation (1),  $t_{pv} \leq 0.02$  sec. Here then,  $t_{pv} \gg t_r$ , and initiation is unlikely. For lower pressures, additional calculations indicate that  $t_{pv} \approx 10^{-3}$  sec in the range of  $10 \leq P_{cs} \leq 80$  kbar. In Figure 3, these times are seen to be longer than those for PETN, indicating the much greater insensitivity of BN/NO<sub>3</sub> crystals of comparable size.

A similar analysis of TATB, the planar molecules of which form a graphitic structure, is expected to yield times in the range  $10^{-5} \leq t_{pv} \leq 10^{-3}$ . This is a result of the rigidity ( $r$ ) of the slip planes for the shock pressures indicated, where  $r$  has the order PETN < TATB < BN/NO<sub>3</sub>.

## SUMMARY

The important criteria for optimal directional sensitivity in intercalated, layered BN materials are that (1) they must be stage 1 or close to it; (2) the interplanar activation energies for reaction between BN and the intercalate layers must be less than those for reaction within each intercalate layer; and (3) the important interlayer reactions must be bimolecular and exothermic. Criterion (1) addresses the requirement of minimal slip along the crystal axis perpendicular to the basal plane. In this case,  $t_{pv \parallel} \gg t_{pv \perp}$ , for the parallel and perpendicular directions. Criterion (2) addresses the need to eliminate or minimize reaction in the intercalate layer as a result of energy transfer from the gliding host layers caused by shocks not normal to the basal plane. This requires the careful selection of intercalate. Various oxidizing agents are currently being studied at NAVSWC. Criterion (3) guarantees that the reactions will occur in times which are short compared to arrival of rarefaction waves caused by shocks. These reactions occur with activation energies that are much lower than those in unimolecular processes. The rates of these reactions given by  $k_b$  can be sufficiently fast at the pressures and temperatures of interest in detonations,<sup>9</sup> so that "initiating" energy transfer from the BN lattice into the intercalate molecules is the slow step. Together, these criteria help to guarantee that the most likely direction of shock initiation is normal or near-normal to the basal plane.

## ACKNOWLEDGMENT

This work was funded by the Naval Surface Warfare Center's Independent Research Program. Special thanks are extended to Prof. R. Armstrong and to Dr. P. Miller for helpful discussions.

## REFERENCES

1. A. W. Campbell, W. C. Davis, and J. R. Travis, *Phys. Fluids* **4**, 498 (1961).
2. A. W. Campbell and J. R. Travis, in Proceedings of the Eighth Symposium (Int.) on Detonation, NSWC MP 86-194, 15-19 Aug 1985, p.1057.
3. J. J. Dick, R. N. Mulford, W. J. Spencer, D. R. Pettit, E. Garcia, and D. W. Shaw, *J. Appl. Phys.* **70**, 3572 (1991).
4. H. B. Cady and A. C. Larson, *Acta Cryst.* **18**, 485 (1965).
5. A. C. van der Steen, H. J. Verbeek, and J. J. Meulenbrugge, in Proceedings of the Ninth Symposium (Int.) on Detonation, Vol. 1, OCNR 113291-7, 28 Aug-1 Sep 1989, p. 83.
6. N. Bartlett and B. W. McQuillan, in Intercalation Chemistry, edited by M. S. Whittingham and A. J. Jacobson (Academic Press, New York, 1982), pp. 19-53.
7. J. M. Thomas, G. R. Millward, R. F. Schlogl, and H. P Boehm, *Mat. Res. Bull.* **15**, 671 (1980).
8. S. Amelinckx, P. Delavignette, and M. Heerschap, in Chemistry and Physics of Carbon, Vol. 1, edited by P. L. Walker (Marcel Dekker, Inc., New York, 1965), pp. 1-71.
9. R. D. Bardo, *Int. J. Quantum Chem.* **S20**, 455 (1986); R. D. Bardo, in Proceedings of the Ninth Symposium (Int.) on Detonation, Vol. 1, OCNR 113291-7, 28 Aug-1 Sep 1989, p. 235.
10. N. L. Coleburn and J. W. Forbes, *J. Chem. Phys.* **48**, 555 (1968).
11. J. F. Green, P. Bolsaitis, and I. L. Spain, *J. Phys. Chem. Solids* **34**, 1927 (1973).
12. M. H. Rice, R. G. McQueen, and J. M. Walsh, in Solid State Physics, edited by F. Seitz and D. Turnbull (Academic Press Inc., New York, 1958), pp. 1-63.

## OVERVIEW: HIGH SPEED DYNAMICS AND MODELLING AS IT APPLIES TO ENERGETIC SOLIDS

J. COVINO, S. A. FINNEGAN, O. E. R. HEIMDAHL, A. J. LINDFORS AND J. K. PRINGLE  
Research Department, Naval Air Warfare Center Weapons Division, China Lake, CA 93555-6001

### ABSTRACT

This paper discusses experimental techniques and modelling tools used to characterize energetic solids subjected to dynamic deformation and shock. Critical experiments have been designed to study shock response and impact sensitivity of energetic materials. For example, a simplified two dimensional experiment has been developed to study the critical phenomena involved in delayed detonation reactions (XDT). In addition, wedge tests are used to obtain equation-of-state data. Coupled with hydrocodes, these experiments give us an in-depth understanding of the response of energetic materials subjected to shock loading. A coupled methodology using both experimental and modelling tools is presented. Consisting of three parts, it addresses all possible responses to fragment impact. The three parts are: (1) Fragment impact modelling (hydrocodes and empirically based codes); (2) Experiments to obtain accurate data for predicting prompt detonation; and (3) Tests with planar rocket motor models to explore mechanisms related to burn reaction thresholds and degree of violence. This methodology is currently being used in weapon design and munitions hazard assessments.

### INTRODUCTION

This paper is divided into three parts and describes the work being conducted by the Naval Air War Center Weapons Division (NAWCWPNS) on the response of munitions to fragment impact. The first part describes a methodology developed to model and analyze the response of munitions to fragment impact threats. The munition response levels within the model are divided into shock-to-detonation transition (SDT), burn-to-violent reaction (BVR), and no response. The second part of this paper describes the use of the wedge test for obtaining the SDT parameters necessary to accurately model and predict prompt detonation. In BVR reactions, four basic response levels are possible. These are: (a) burn only, (b) deflagration with or without propulsion, (c) explosion and (d) delayed detonation. The third part of this paper describes a planar rocket motor model developed to explore mechanisms related to the possible thresholds in the BVR regime.

A methodology has been developed for conducting fragment impact analyses of munitions in their storage/stowage configurations. The objective of the methodology is to determine if the munition will respond adversely to any specified impact threat, and if so, how much shielding is required to prevent the adverse response. This paper presents the current status of the methodology and describes the step-by-step approach.

The methodology has been formalized in a computer code named Fragment Impact/ Munition Response Analysis for Guidance in Mitigation Assessment Program (FRAGMAP). FRAGMAP is an interactive computer program which implements the approach for assessing the likelihood of the detonation, or lesser response, of a cased munition due to fragment impact, and the effectiveness of selected mitigation measures. FRAGMAP provides a means for storing fragment threat, munition response and barrier material data. It operates on these data in a systematic manner and presents the calculated solutions in forms of tables and plots. Secondly, the program computes the probability of shock-to-detonation transition (SDT) as a function of distance for far field fragment impact situations.

To explore the shock sensitivity of propellant formulations and to determine SDT thresholds, wedge tests were conducted. These tests were conducted on propellant samples incorporating different formulation variables in an attempt to correlate shock sensitivity with specific formulation parameters.

The study of delayed reaction phenomena in rocket motors is complicated by the fact that these processes are not visible from the outside. A planar rocket motor model has been developed that allows the study of the reactions in a central bore perforated by a projectile to be viewed with high-speed photography. This experimental model will be outlined and critical mechanisms observed by the use of such model will be discussed.

### THE FRAGMENT IMPACT PROBLEM

A schematic of the fragment impact problem is depicted in Fig. 1. The actual threat that reaches a munition is degraded by the penetration process, resulting in loss of fragment mass and velocity. There are also entrained plate fragments from the various barrier perforations. It is desirable to predict how the residual threat will cause the impacted munition to respond. The critical steps involved in applying this methodology are:

- a. determine the response thresholds of the munition of concern,
- b. determine the undegraded impact threat characteristics in terms of fragment mass and velocity,
- c. determine which fragments from the specified threat will cause the unprotected munition to detonate, or cause some lesser response,

- d. determine an equivalent spaced array for all barriers intervening between the fragment source and the munition (i.e., container walls, bulkheads, etc.),
- e. determine the residual mass and velocity character of the threat fragments after perforation of the intervening barriers,
- f. determine if the residual threat will cause a detonation or some lesser response,
- g. estimate what additional shielding is required to mitigate any adverse response.

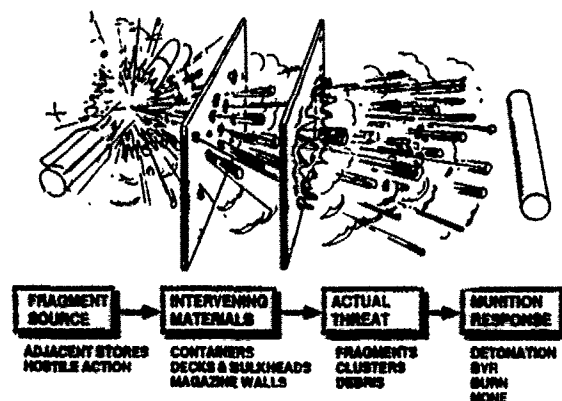


Fig. 1. The Fragment Impact Problem.

### Elements of FRAGMAP

**Response Plots.** The first response considered is prompt detonation (i.e., SDT). If prompt detonation does not occur, then lesser responses are possible. The burn-to-violent-reaction (BVR) response is dependent upon many factors. The most violent response in this regime occurs if the fragment becomes embedded, and case confinement is not relieved. A milder response occurs (burn only) when a fragment passes completely through the munition, and provides sufficient venting to release the pressure buildup of the explosive reaction. A low hazard or no response regime is defined as that which occurs when a fragment ricochets. The assumption is that any fragment having insufficient energy to penetrate the case will not cause any reaction. This assumption, however, does not hold true for all energetic materials.

The different response regimes and thresholds are indicated in Fig. 2 for a sample acceptor munition. The shock-to-detonation (SDT) threshold for the sample munition is determined using hydrocode calculations of fragment impact [1]. Reaction of the energetic material is predicted by the Forest Fire burn model [2], which is calibrated using wedge test data. The boundary for the low hazard/no response regime is the ballistic limit of the case material. We substitute the ballistic limit threshold for the ignition threshold of the energetic material due to the ease of computing ballistic limits. Between these two thresholds is the burn-to-violent reaction (BVR) zone.

**Coupling Threat and Response.** The fragment threat is generally obtained from warhead arena test characterization data. An overlay of the threat upon the response plot identifies which fragments can cause a detonation, are in the BVR region, and can not penetrate the case. Fig. 3 shows the fragment distribution of a selected donor weapon overlaid onto the response plot of Fig. 2. The size of the circles indicates the number of fragments having a given mass and velocity. The square shown represents a 250 grain, 8300 fps standard cube fragment. Only those fragments falling above the solid line will cause this specific munition to detonate. A large number of fragments fall in the BVR zone, including the 250 grain cube. The majority of fragments in this example will not cause any reaction if they individually strike the acceptor munition. It should be noted that this methodology is for single fragment impacts and a more realistic scenario includes multiple fragments. Fig. 3 serves to identify which fragments from the chosen threat have a potential to cause the acceptor munition to respond adversely. The next step is to select a barrier that will prevent the various possible responses.

**Residual Threat/Mitigation Calculations.** Two different sets of equations are used to estimate the residual threat after penetration of existing barrier materials. These are the Joint Munitions Effectiveness Manual (JMEM) penetration equations [3] and Fast Air Target Encounter (FATE) equations. Once the residual threat is defined, the munition response is estimated. Adverse response prevention requirements are then established by an iterative process. Both methods are empirically based and calculate the residual fragment threat to be slightly different. However, the calculated results do not vary significantly. Recently, the subroutines of FATEPEN-2 [4] have been adapted to FRAGMAP. These subroutines allow a greater choice of fragment material types and shapes as well as barriers materials. The accuracy is also reportedly better.



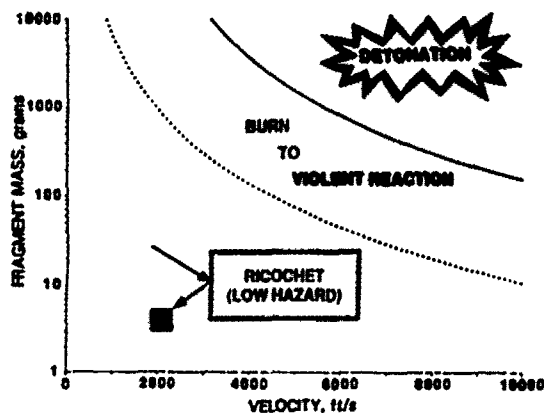


Fig. 2. Response Plot.

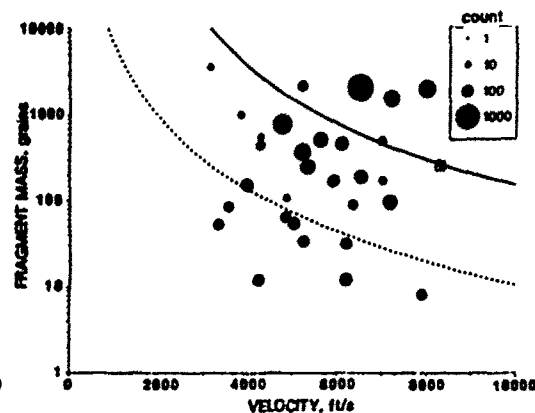


Fig. 3. Overlay of a Fragment Threat Map onto Response Plot.

### Methodology Limitations

The reactive model used to establish the SDT threshold requires wedge test data for the energetic material. Wedge tests are expensive and only work for relatively simple, sensitive explosives and propellants. Most propellants are very complex energetic materials and have more than one inherent reaction rate. A model and a calibration method is needed for handling such complex materials. The response model is currently limited to single fragment impact with axisymmetric shapes. In real situations, the munition will be struck multiply by irregular fragments. A more sophisticated response model able to account for the effects of both multiple impacts and irregular impactor shapes is therefore essential.

### Overcoming Limitations

There are ways for overcoming these limitations. However, they are generally expensive. It requires lots of test data against many different materials. Initial efforts are directed towards analytical studies. Experimental testing will be needed in the future to verify the analytical results.

To successfully model the SDT response of any energetic material, wedge test data is required for a large number of explosives. Wedge test data is specifically needed for the Forest Fire Burn Model used in our calculations. Gap tests and other sensitivity data are helpful in trying to approximate burn models based on similar materials for which there is wedge test data. For the more complex energetic materials, a model and a calibration method needs to be developed. A second limitation is modelling multiple fragment impacts. At present it can be interpolated by parametric studies.

### Potential Applications

The methodology shown can also be used in reverse for designing insensitive munitions. If the necessary data is collected, one can examine the effects of case thickness and energetic material selection on the vulnerability of a weapon. The results can also be used to select test parameters for verifying the protection provided against actual threats, for obtaining needed materials data, and for verification and validation of these models.

### WEDGE TEST FOR STUDYING SDT IN PROPELLANTS

A series of propellants with reduced shock sensitivity were developed at China Lake to replace current minimum signature propellants. Current propellants contain as much as 67% of high explosive (HMX or RDX) in nitrate ester plasticized energetic binders, which are known to be shock sensitive materials.

To explore the shock sensitivity of these new propellants, the wedge test was conducted on propellant samples incorporating different formulation variables. Variables examined included the type of high explosive (RDX or HMX) with and without high density burn rate modifiers. The sensitivity of these propellants were then compared to a conventional minimum signature propellant.

### Propellant Formulation

The basic propellant formulation consisted of RDX or HMX, AN, nitrate ester plasticized energetic binders, and other additives. All of the formulations contained 60% by weight of solids. Table I lists the specific propellants used in this study. The propellants were processed using small-particle-size solids and mixed extensively under a vacuum to minimize density discontinuities. The resulting formulations were of very good quality and 99% of theoretical maximum density.

Table 1. Propellants used in study.

PROPELLANT #	OXIDIZER*	BURN RATE MODIFIER
1	RDX-AN	PbCO <sub>3</sub>
2	HMX-AN	NONE
3	RDX-AN	NONE
4	HMX-RDX	NONE

\*RDX = Trimethylene trinitramine

AN = Ammonium nitrate

HMX = Tetramethylene tetranitramine

### Wedge Test Description

The wedge test is a method by which the shock initiation characteristics of an energetic material may be determined. A planar shock wave is introduced into the explosive to be tested. As the shock progresses through the explosive it generates hot-spots that build-up to a detonation. The objective of the wedge test is to determine the run-to-detonation point at which the detonation wave overtakes the shock wave. This point is characterized by a unique time and distance to detonation for a specific set of input conditions.

A streak camera is used to record the wedge test event. The surface of the wedge is mirrored to reflect light into the camera. When either the shock wave or detonation wave reaches the surface, the surface distorts so that the light is no longer reflected into the camera. As the detonation wave overtakes the shock wave, the slope of the reflected light trace on the film changes. Thus, the run to detonation point can be determined from the film record. Schematics of the wedge test set-up and wedge test streak camera record are shown in Fig. 4 and 5 respectively.

The results of a series of wedge tests are usually presented as plots of input pressure versus distance to detonation and time to detonation. With these plots energetic materials may be compared and their relative sensitivity can be derived. This is done by assuming that for a given distance to detonation, the energetic material that requires the lower input pressure to achieve detonation is the more sensitive.

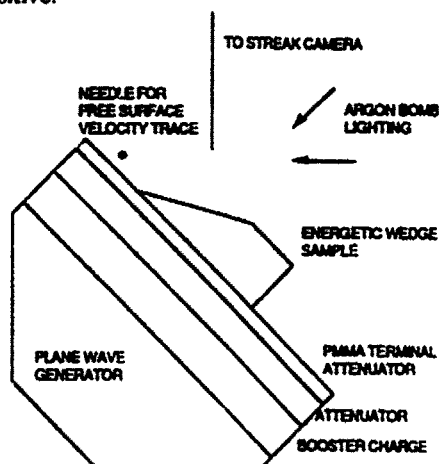


Fig. 4. Schematics of the Wedge Test Experimental Set-Up.

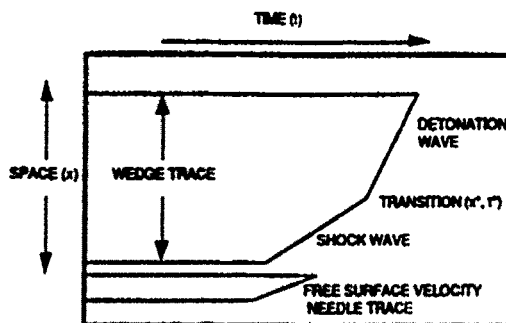


Fig. 5. Schematics of the Wedge Test Streak Camera Record.

As shown in Fig. 4 a planar shock wave is introduced into the energetic wedge sample. The input shock wave pressure is varied to achieve different run-to-detonation points.

To determine the shock Hugoniot of the energetic material only two parameters are needed. These are the shock velocity in the terminal attenuator and the shock velocity in the energetic material. To determine the shock velocity ( $U_s$ ) in the terminal attenuator one needs to know its particle velocity ( $U_p$ ) and its shock Hugoniot. The particle velocity in the (Plexiglas) terminal attenuator is found by assuming that it is one half of the free surface velocity. The shock Hugoniot for Plexiglas [5] has been well defined by:

$$U_s = 2.598 + 1.516 U_p$$

(1)

It should be noted, though, that this is just one test for sensitivity and the relative sensitivity rankings between energetic materials may vary for different tests. For example, the Naval Ordnance Laboratory Large Scale Gap Test may give markedly different sensitivity rankings for the same energetic materials, as compared to the wedge test.

### Experimental Results

From the shock velocities and the calculated particle velocities the shock Hugoniot for the four propellants are given below:

$$\text{PROPELLANT \#1} \quad U_s = 1.44 + 3.04U_p \quad (2)$$

$$\text{PROPELLANT \#2} \quad U_s = 1.77 + 2.02U_p \quad (3)$$

$$\text{PROPELLANT \#3} \quad U_s = 2.61 + 1.65U_p \quad (4)$$

$$\text{PROPELLANT \#4} \quad U_s = 2.45 + 1.61U_p \quad (5)$$

The plots in the  $U_s$ - $U_p$  plane for the same four propellants are shown in Fig. 6.

The traditional method for plotting the data from the wedge test is known as the Pop-plot after Alfonso Popolato. Popolato found that over a range of input pressures, log-log plots of run to detonation ( $x^*$ ), or time to detonation ( $t^*$ ), versus pressure ( $P$ ), are linear. The equation of the Pop-plot over the linear range, in run to detonation versus pressure form, is then:

$$\log x^* = A + B \log P \quad (6)$$

In this form  $P$  is in gigapascals,  $x^*$  is in millimeters, and  $A$  and  $B$  are determined from a least squares fit in the log-log plane. Similarly, time to detonation versus pressure takes on the same form with different constants.

For the propellants tested, Pop-plots of distance to detonation versus input pressure are shown in Fig. 7. As can be seen, at low input pressures the Pop-plot becomes non-linear and pressure approaches a vertical asymptote. This implies that a different type of mechanism is controlling the reactivity.

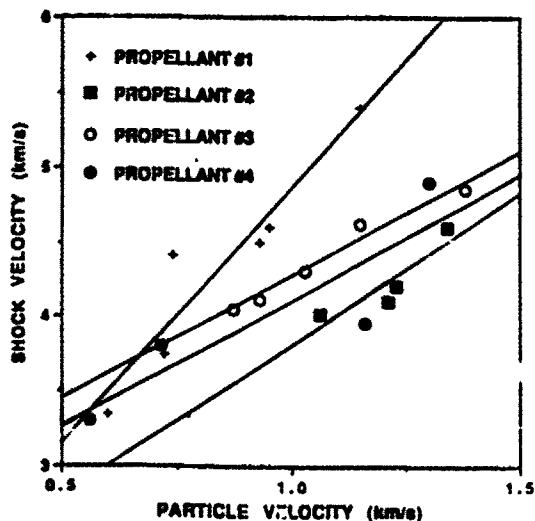


Fig. 6. Shock Hugoniot of the Propellants Tested in the  $U_s$ - $U_p$  Plane.

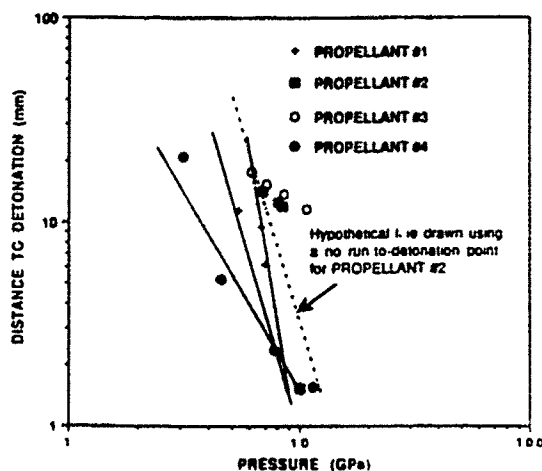


Fig. 7. Pressure Versus Run for All Four Propellants.

The interpretation of sensitivity behavior for an energetic material using these plots is done by observing the behavior of the constants  $A$  and  $B$  for the propellants tested. In Fig. 7 the intercept value,  $A$ , defines the horizontal positioning of the Pop-plot; thus it defines the shock region of interest, and  $B$  is the slope of the line. Hence, a propellant with a higher pressure intercept and steep slope would be less sensitive compared to a propellant with lower pressure intercept and shallower slope. Therefore, from Fig. 7, it can be seen that propellants #1, #2, #3 are all less sensitive than propellant #4. For two propellants with different intercepts but very similar slopes, the propellant with the higher pressure intercept is less sensitive at all pressures compared to the propellant with the lower intercept. In general, all of the propellants have steep Pop-plots. Thus, the run to detonation will occur only over a very small pressure region. From an experimental stand point this small pressure region makes it very difficult to gain a variety of run distances. For example, the pressure difference required for a 1.5 mm run and a 12 mm run is only 1.5 GPa for propellant #2. However, from a shock insensitive propellant

stand point, this type of behavior is desirable. If a propellant is going to detonate it should only occur at fairly discrete high pressures, as is the case for these propellants.

The relative low shock sensitivity of these propellants is attributed to two basic factors: a) the lower shock sensitivity of AN and b) the reduction in density discontinuities, hence the number of hot spots, through the use of small RDX or HMX particle sizes and the elimination of the high density, (6.14 gm/cc) lead carbonate burn-rate modifiers.

The reduction of AN participation in the detonation reaction can be seen from the Pop-plots. The Pop-plot for propellant #1 is well behaved and is linear until the run to detonation does not occur. In fact if one were to plot the "no go" point it would lie on the same line. However, for both propellant #2 and #3, at approximately 7.5 GPa, there is a distinct change in the Pop-plot that is quite consistent for both formulations. In the work of Stinecifer [6] on composite explosives, the partial AN reaction was attributed to intermolecular reactions in the detonation zone of only a thin layer of the AN. In this work however, it is suggested that further participation of the AN can be induced by higher shock pressures or high density discontinuities.

### Shock Sensitivity Assessments

An example of the use of the wedge test to critically examine the shock sensitivity of experimental propellants has been described. Wedge test results show that these propellants are much less shock sensitive than the conventional minimum smoke propellants. The results also indicate that the use of shock insensitive filler (AN), and fine particles of high explosive to increase the degree of homogeneity, minimizes physical discontinuities and reduces shock sensitivity. These studies also lead to some insights into the level of participation in the shock-to-detonation reaction of certain components of energetic composite materials.

### PLANAR ROCKET MOTOR TEST MODEL

Bullet or fragment impact against a solid rocket motor can cause a reaction ranging from mild burning to detonation. Prompt detonation may occur immediately on contact through the mechanism of shock-to-detonation transition (SDT). Delayed reaction (either burning or detonation) may occur at later times. Delayed reactions are believed to be associated with damage and fragmentation of propellant during penetration; however, the underlying mechanisms are not well understood. The study of delayed reaction phenomena in rocket motors is complicated by the fact that these processes occur within the motor case and are not visible from the outside. Recently, a planar rocket motor test model has been developed as an aid in visualizing these processes [7-9]. This model consists of a steel plate, a layer of propellant, an air gap, a second layer of propellant, and a second steel plate, as shown in Fig. 8. Transparent sidewalls can be added to provide a measure of confinement. The open architecture of the model allows impact and reactions within the bore (air gap) to be photographed.

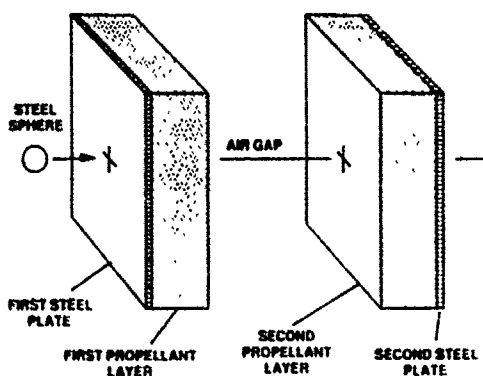


Fig. 8. Planar Rocket Motor Test Model.

Initial experiments with this model showed that a "bubble" of propellant debris forms in the air gap between energetic material layers (bore region) as a result of projectile penetration of one of the layers. Ignition of the bubble occurs upon impact with the second layer, followed by a reaction ranging from mild burning to delayed detonation, depending on the width of the air gap, properties of the energetic material, and degree of confinement [7]. Further studies showed that the most intense burn reactions and the zone of delayed detonation are both located within the air gap regime where the bubble is unbroken prior to impact [8-9].

### Debris Bubble Characterization Study.

A study of debris bubble expansion and breakup process was conducted using an Eulerian hydrocode, CSQ III, developed at Sandia National Laboratories. The study was performed to establish the basic character of the debris bubble and to establish bubble breakup trends as a function of various target and impact parameters. The output of each hydrocode run consists of a sequence of computer plots showing deformed cross-sections of the projectile and target layers at constant time intervals. An example is shown in Fig. 9. The plots indicate that the debris bubble can be regarded as an expanding

hollow shell, similar to those occurring in hypervelocity impacts [10]. An analysis of the computer runs for the various parameters studied showed that breakup elongation increases with impact velocity, propellant layer thickness, and plate density [8].

The hydrocode study also demonstrated that the debris bubble is not a spall. A spall is the result of tensile failure when a shock wave is reflected back into the material as a rarefaction at a free surface. Bubble formation in the present case is a much longer term process produced by the mechanical interaction of the projectile with the propellant layer. A comparison of initial shock pressures in the propellant (determined by impedance matching) with hydrocode-calculated breakup elongation values for various case materials also showed no correlation, indicating that the initial shock is not responsible for breakup of the bubble [8].

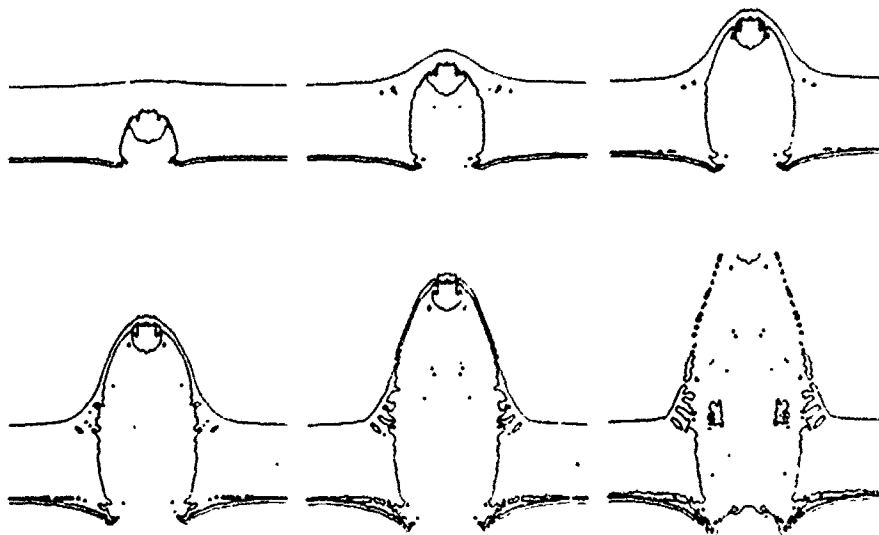


Fig. 9. Hydrocode Plots for 0.75-Inch Steel Sphere Impacting 1.5-Inch Propellant Layer with 0.06-Inch Steel Cover Plate at 3800 ft/s. (30  $\mu$ s intervals.)

### Debris Bubble Impact Studies

**Experimental Setup.** In these experiments, propellant layers and cover plates (1.5 and 0.06 in, respectively) were held constant. Hardened (370 BHN) steel was generally used for the first (impact side) cover plate, while mild (95 BHN) steel was often used for the second (exit side) plate. The air gap was varied between 0.5 and 4.5 in. in order to encompass the zone where delayed detonations, the most intense combustion reactions, and the transition region for debris bubble breakup occurred. For confinement, transparent Plexiglas sidewalls were added to the target. Energetic materials used in the various studies included conventional aluminized, reduced signature, and minimum smoke propellants along with one explosive (Composition B). The first two are considered normally shock-insensitive and nondetonable (Class 1.3), while the last two are shock sensitive, detonable materials (Class 1.1).

For comparability, a standard 0.75-in.-diameter mild steel spherical projectile, fired from a 20 mm smooth-bore powder gun, was used for most tests. Most tests were also conducted at a constant impact velocity, 3,900 ft/s, although one minimum signature propellant was tested at velocities ranging from 1,600 to 4,200 ft/s.

In-flight projectile velocities were measured using a Photec high-speed camera running at 16,000 frames/s coupled with a backlighting system consisting of an array of flash lamps and a diffusing screen. Impact processes and propellant reactions were observed using a Fastax high-speed camera running at 32,000 frames/s and a similar but separate backlighting system.

**Experimental Results.** These experiments have resulted in the identification of a number of distinct burn and delayed detonation reactions involving the debris bubble. To date, a total of six different reactions have been observed in these experiments. Four of them are burning reactions and two are delayed detonation. In the discussion that follows, a brief description of each reaction is presented. (More extensive descriptions are found in [7-9]).

Two different burn reactions, with the breakup elongation roughly serving as the boundary separating them, were identified in early tests of reduced signature, hydroxy-terminated polybutadiene/ammonium perchlorate (HTPB/AP) propellant. Both involve only bubble material that has impacted the second propellant layer and neither propagate back into bubble material that has not yet impacted the second layer. The first reaction, which occurs at air gaps less than the breakup elongation for the bubble (i.e., where the bubble is unbroken at impact), is associated with fluid-like debris that flowed out-

wards along the impact surface (Fig. 10). The second, which occurs at air gaps greater than the breakup elongation, is associated with crater debris traveling backwards through the interior of the bubble. The first reaction appeared to be the more violent of the two based on light intensity and cover-plate velocity measurements and degree-of-breakup estimates for the Plexiglas sidewalls [7-8].

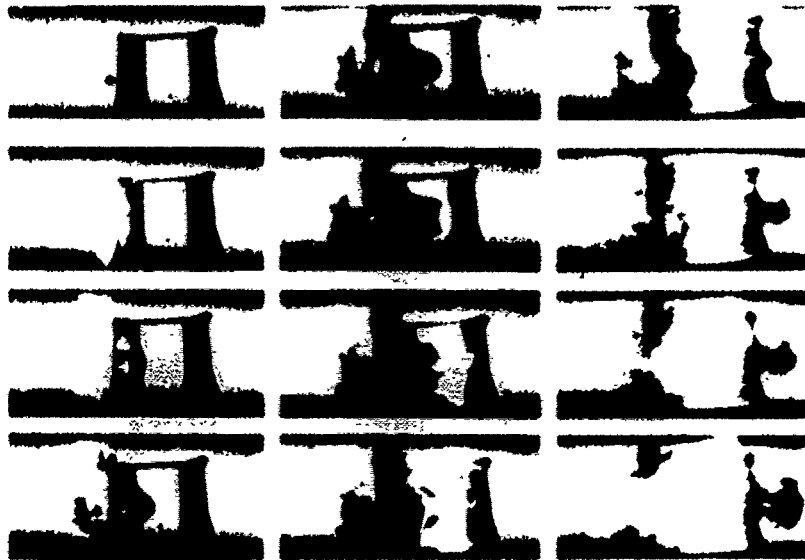


Fig. 10. Photographic Sequence Showing Impact of Unbroken Debris Bubble and Burn Reaction Involving Fluid-Like, Post-Impact Debris. (28  $\mu$ s interframe time.)

Two additional bum reaction, involving bubble material that had not yet impacted the second layer, were identified in later tests of aluminized HTPB/AP propellant [9]. One reaction, initiating after bubble impact, propagates rearwards (towards the first layer) along the outside surface of the advancing bubble. The second, observed in a nitramine-containing aluminized HTPB/AP propellant, occurs on the inner surface of the bubble (Fig. 11). Because of its location, direct visibility is only possible if the bubble broke up prior to impact.

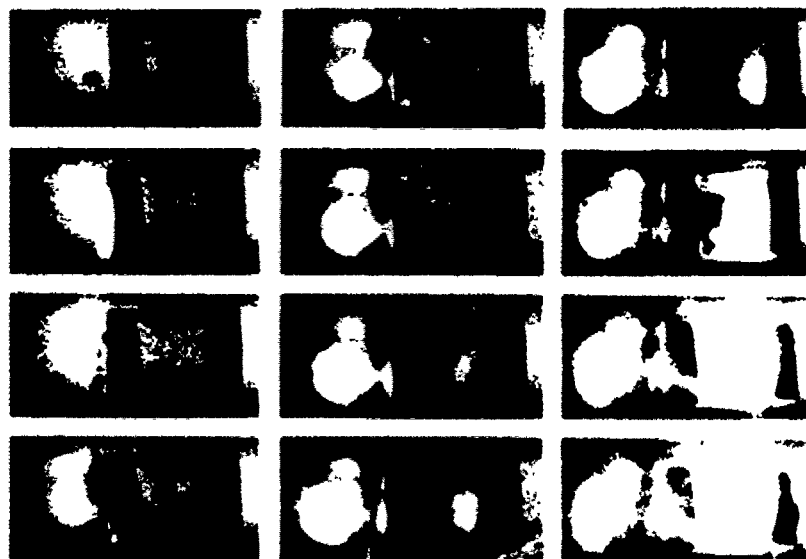


Fig. 11. Photographic Sequence Showing Breakup of Debris Bubble in Air Gap and Exposed Burn Reaction on Inner Bubble Wall. (28  $\mu$ s interframe time.)

The latter two reactions, which occur in addition to the ones involving post-impact debris (the first two), are considered to be an indication of increasing reaction sensitivity and violence. A comparison of reaction intensities for the different HTPB/AP propellants show a direct correspondence between the number of reaction paths and the degree of reaction violence.

Two different delayed detonation reactions have also been observed in tests involving minimum signature propellants. Both initiate as a result of bubble impact and occur in the air-gap regime where the bubble is unbroken at impact. One, normally found at larger air gaps ( $> 1.0$  in.), initiates almost immediately after bubble impact (within a few microseconds) and propagates rearward through the wall of the bubble towards the first layer (Fig. 12). Detonation of the upstream layer occurs first, in this situation, while the second layer detonates sympathetically after the first, rather than by reaction propagation from the bubble into that layer. Only a live first layer is required for this reaction since initiation occurs within the bubble itself. This was confirmed by experiments using inert simulant for the second layer. Confinement is also apparently not a requirement as the reaction occurs in completely open target systems. Recent experiments have shown that the bubble impact shock is responsible for reaction initiation [9]. This reaction has been observed for impact velocities as low as 1700 ft/s.

The second delayed detonation reaction, normally found at smaller air gaps ( $< 1.0$  in.), is characterized by relatively long delay times (60-180  $\mu$ s) after bubble impact. The minimum impact velocity ( $\sim 3800$  ft/s for one propellant tested) for initiation of this reaction is also considerably higher than for the other. Recent experiments show that confinement greatly enhances the probability of reaction and, (like the other), only the first layer needs to be live for reaction to occur. Although the initiation mechanism for this reaction has not been definitely established, evidence suggests that interfacial shear along the bubble-second layer contact surface, may be responsible.

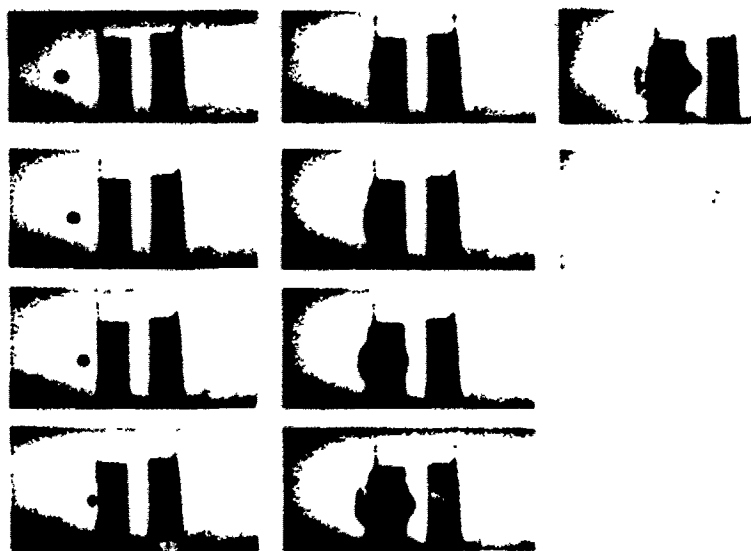


Fig. 12. Photographic Sequence Showing Initiation of Detonation Reaction in Debris Bubble Immediately After Bubble Impact. (28  $\mu$ s interframe time)

## CONCLUSION

A methodology complete with modelling tools and experimental techniques has been presented which can be used to evaluate a munition's vulnerability to fragment or bullet impact. Three parts of this methodology have been presented: I. FRAGMAP, II. Wedge testing for studying SDI in propellants and III. Planar Rocket Motor Test model. The first part of the paper outlined the FRAGMAP methodology, which couples hydrocodes and wedge test data, developed to evaluate a munition's response to fragment impact. The munition response levels within the model are divided into SDI, BVR and no response. The second section of the paper outlined the experimental approach in wedge testing to examine the shock sensitivity of propellants and explosives. The results of the experiments show that the use of shock insensitive fillers (AN), and fine particle sizes of high explosives (HMX) to increase the degree of homogeneity, minimize physical discontinuities and reduce shock sensitivity. Lastly, a planar rocket motor test model was explored to evaluate delayed reaction phenomena in rocket motors subjected to fragment and bullet impact. With the use of this model six different delayed reactions have been observed. These are: (a) two burning reactions which involve bubble material that has

not yet impacted the second layer; (b) two burn reactions which involve bubble material that has impacted the second propellant layer; and (c) two different delayed detonation reactions involving debris bubble impact.

In conclusion, this three part methodology enables the use of a coupled (experimental/modeling) approach in assessing a munition's vulnerability to bullet and fragment impact. This methodology can also be used in reverse in order to design munitions which are insensitive to projectile impacts.

#### ACKNOWLEDGEMENT

The authors would like to thank the Warhead Test Branch of the Range Department for their assistance in performing the wedge tests and the planar rocket motor impact tests. Their efforts are gratefully acknowledged.

#### REFERENCES

1. E. A. Lundstrom, Proc. 1989 JANNAF Propulsion Systems Hazards Subcommittee Meeting, CPIA Publication 477, Vol. 1, pp. 101-110, (February 1989).
2. Naval Weapons Center. *Evaluation of Forest Fire Burn Model of Reaction Kinetics of Heterogeneous Explosives*, by E. A. Lundstrom. China Lake, CA, May 1988. (NWC TP 6898).
3. Joint Technical Coordinating Group for Munitions Effectiveness. *Penetration Equations Handbook or Kinetic Energy Penetrators*. Tinker AFB, Okla., JTCG, 1977, (61 JTCG/ME-77-16).
4. FATEPEN-2: Compact Fragment Penetration Model, VOLUMES I and II, J.D. Yateau, R.H. Zernov and R.F. Recht, (publication in process).
5. Selected Hugoniot, prepared by Group GMX-6, Los Alamos Scientific Laboratory, Report LA-4167-MS, Los Alamos, NM (May 1959).
6. M. M. Stineciph, Seventh Symposium (International) on Detonation, Annapolis, Maryland, pp. 801-810. NSWC MP 82-334, June 16-19 (1981).
7. S. A. Finnegan, J. K. Pringle, J. C. Schulz, and M. D. Alexander, Proc. 1990 JANNAF Propulsion Systems Hazards Subcommittee Meeting, CPIA Pub. 538, pp. 13-24 (April 1990).
8. S. A. Finnegan, J. C. Schulz, J. K. Pringle, and A. J. Lindfors, Proc. 1991 JANNAF Propulsion Systems Hazards Subcommittee Meeting, CPIA Pub. 562, pp. 399-408 (March 1991).
9. S. A. Finnegan, J. K. Pringle, O. E. R. Heimdahl, and J. C. Schulz, Proc. 1992 JANNAF Propulsion Systems Hazards Subcommittee Meeting, CPIA Pub. 582, pp. 267-283 (April 1992).
10. H. F. Swift, D. D. Preonis and W. C. Turpin, Rev. Sci. Instr. 41, 746 (1970).



## DELAYED INITIATION IN A MODEL ENERGETIC MATERIAL

D. H. ROBERTSON, D. W. BRENNER, AND C. T. WHITE

Chemistry Division, Naval Research Laboratory, Washington, DC 20375-5320

### ABSTRACT

We present a simulation studying the initiation of a model energetic molecular solid. For low-velocity, flyer-plate impact, the model detonation initiates behind a compaction shock. The detonation front subsequently overtakes the compaction shock exhibiting a behavior qualitatively similar to that observed in experimental studies of homogeneous initiation and delayed detonation from low velocity impact.

### INTRODUCTION

Energetic materials contain potentially destructive forces in their stored energy. Once initiated they can release energy at rates that can exceed  $10^{11}$  W for a  $10\text{ cm}^2$  detonation front [1]. Unanticipated initiation of these energetic materials can result in the release of this energy with disastrous results. Modification of the sensitivity of an energetic material toward unanticipated initiation from environmental events is one of the goals of energetic materials research. A better understanding of initiation in energetic materials and the effect that molecular structure has on initiation characteristics should aid the design of safer, high-energy explosives. However, to improve the theory of the atomic-scale details of initiation, computational methods other than continuum calculations (which are not intended for atomic-scale resolution) must be employed.

Over a decade ago, molecular dynamics (MD) was shown to be an ideal tool for probing the atomic-scale details of shock waves in nonenergetic materials while also giving macroscopic properties consistent with continuum calculations [2]. Very recently, we have introduced a model energetic molecular solid that can be used in MD simulations of shock-induced chemistry [3]. Simulations using this model showed that when initiated by a flyer-plate impact of sufficient mass and velocity this model generates a chemically-sustained shock wave with a constant shock velocity and properties consistent with that expected from a detonation [3]. In that work we also reported that as the mass of the flyer-plate increases, the plate velocity required to initiate this model decreases to a limiting value of  $\approx 3.9\text{ km/s}$  consistent with the known insensitivity of crystalline explosives to high velocity impacts [4]. This paper presents a more detailed examination of the initiation characteristics in this new model energetic material for a massive (on the atomic scale) flyer plate impacting the molecular solid at an impact velocity of  $3.9\text{ km/s}$ .

### MODEL AND METHODS

The potential used to introduce chemical reactivity into these MD simulations describes the interatomic interactions in this model energetic molecular solid using the empirical-bond-order (EBO) formalism [5,6]. This EBO approach is sufficiently flexible to allow the generation of a potential energy surface with distinct reactants and products and well-defined reaction paths between them. In the current parameterization of the EBO potential, the model energetic solid is composed of AB molecules which can potentially undergo reaction to form  $A_2$  and  $B_2$  products with the release of  $3\text{ eV}$  of energy per

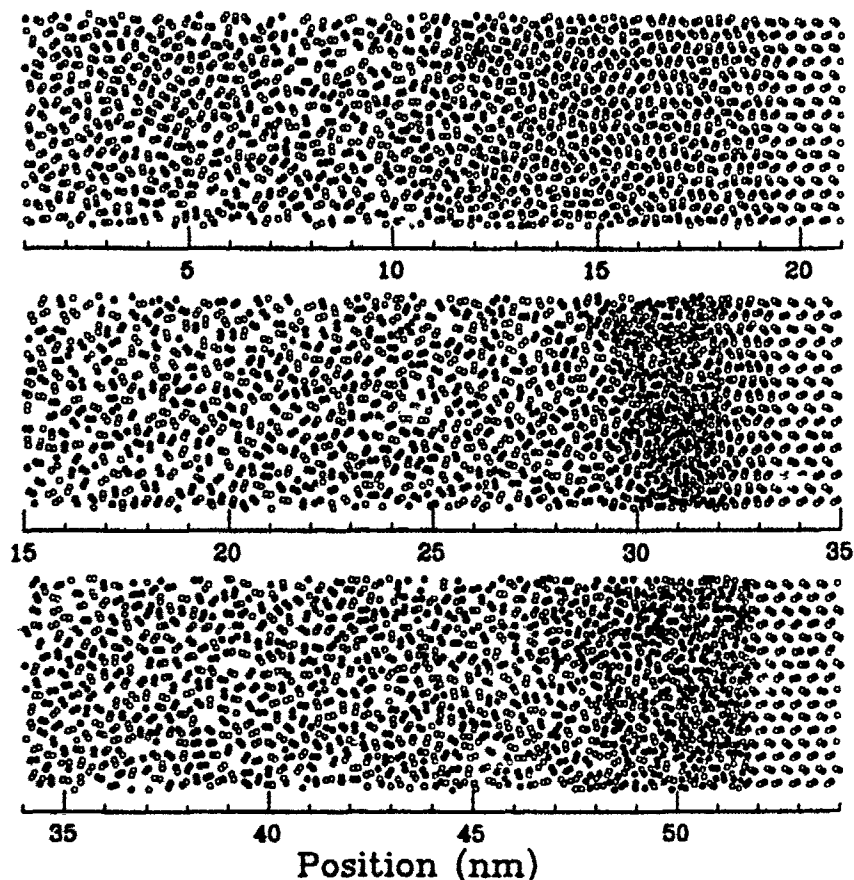


Figure 1. Snapshots of the simulation for times of 3.0, 5.0, and 7.0 ps from top to bottom, respectively. The shock waves are traveling from left to right and the type types of atoms are denoted as light and dark.

reactant molecule. This exothermic release of energy under sufficient conditions sustains the propagation of a shock wave through this model energetic molecular solid with a constant velocity. Details of the potential parameters and propagation characteristics of chemically-sustained shock waves in this AB model are detailed in a prior paper [3].

The simulation presented herein is initiated by impacting a 3.9 km/s flyer plate composed of the 20 layers of molecular solid with the edge of a 2-D semi-infinite model diatomic AB molecular crystal. The reactant crystal is initially at rest and at near zero temperature and pressure. The trajectories of the atoms using these initial conditions and EBO potential energy surface are followed by integrating Hamilton's equations of motion using a Nordsieck predictor-corrector method [7]. Periodic boundary conditions are enforced perpendicular to the direction of shock propagation.

## RESULTS

Impact from this low-velocity flyer plate does not immediately induce chemical reactions. Instead a compaction shock is generated in which the average pressure and density are below that required to initiate reactions but in which local fluctuations are sufficient to exceed the reaction barrier and initiate reactions behind the compaction shock front. This is illustrated in Figure 1 where snapshots for this simulation are shown at times

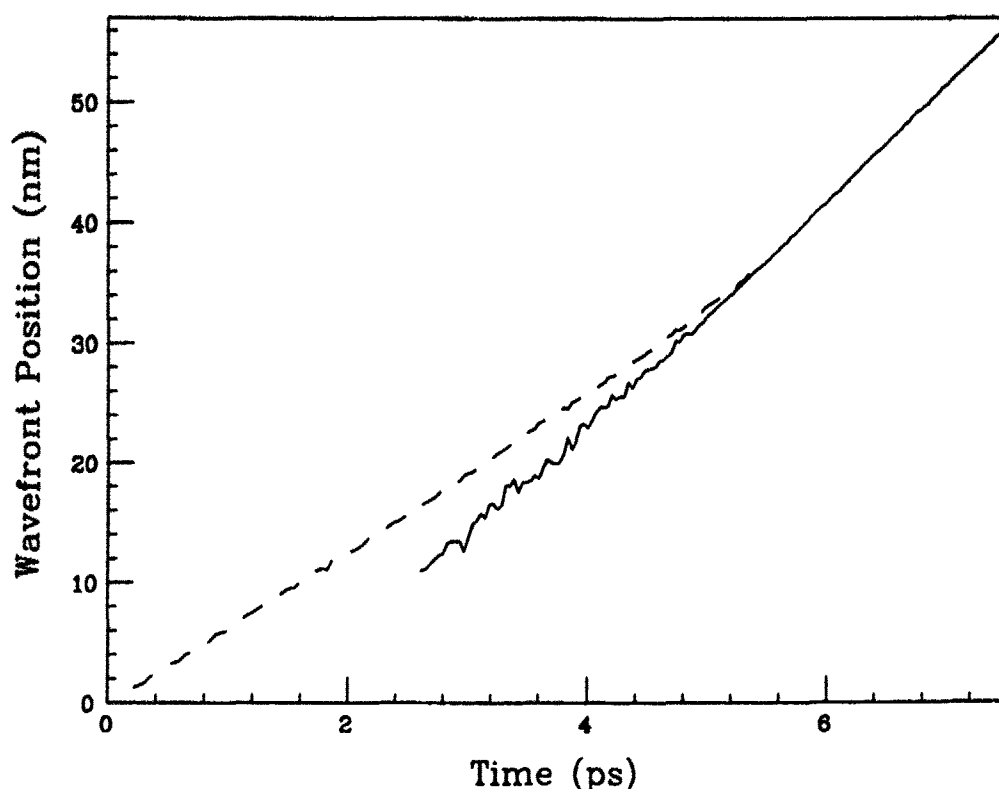


Figure 2. Positions of the compaction and detonation shock fronts plotted as a function of simulation time, drawn as dashed and solid lines, respectively.

of 3.0, 5.0, and 7.0 ps, from top to bottom, respectively. The two types of atoms, A and B, are depicted as light and dark—reactants (as seen to the right) are light/dark pairs and products are light/light and dark/dark pairs. In the 3.0 ps snapshot, products from a series of local reactions can be seen in the region of 6 to 12 nm, approximately 7 nm behind the front of the compaction shock wave (19 nm). Although reactions have been initiated in this region, there is not yet a well-defined shock front. However, by 5.0 ps more reactions have occurred generating a shock front which has propagated to approximately 32 nm by this time. The front compaction wave can still be seen at 33 nm, preceding this reaction front. Finally, as seen in the 7.0 ps snapshot, the shock front associated with the chemical reactions has overtaken the compaction shock, leaving only the chemically-sustained shock front visible in the simulation.

The formation of a detonation front associated with the onset of chemical reactions and its eventual overrun of the front compaction shock can be further clarified by Figure 2 which plots the positions of these shock fronts as a function of the simulation time. Initially, the compaction shock propagates into the material at a velocity of 6.4 km/s, shown as the dashed line in Fig. 2. Near 2 ps, chemical reactions have started occurring and by 3 ps the leading edge of this reaction zone is definable. These reactions form into a detonation front shown as the solid line in Fig. 2. This detonation front is propelled by the chemical reactions at a velocity of 9.7 km/s. Because the chemically-sustained shock front is travelling at a faster velocity than the compaction shock, the detonation front overtakes the compaction shock at  $\approx 5.3$  ps. The initial fluctuations in the position of the detonation front in Fig. 2 before this front overtakes the compaction shock is indicative

of initiation of reactions in several locations before forming into a sharper more well-defined shock front. Although the time and length scales differ, this simulation—showing the generation of a detonation front behind a compaction shock which then overtakes the front shock—predicts qualitative behavior consistent with the experimental studies of homogeneous initiation [8] and delayed detonation from low velocity impact [9].

## CONCLUSIONS

This model energetic material was used in a simulation of initiation by a flyer plate close to the critical velocity for initiation. This simulation exhibited initiation of reactions behind the leading compaction shock front resulting in the formation of a detonation wave behind the front shock. Because the chemically-sustained shock front travels faster than the compaction shock, the detonation front overtakes the compaction shock resulting in a single chemically-sustained shock front in the simulation. This simulation and the associated plot of wave front positions shows behavior qualitatively similar to experimentally observed homogeneous initiation, and delayed detonation from low velocity impact. These encouraging results suggest MD simulations of larger and more complex systems, coupled with chemically convincing potentials, can provide an increasingly important tool for clarifying the interplay between shock waves and the chemistry they can induce at the atomic scale.

This work was supported in part by the ONR through NRL, the ONR Physics Division and a grant of computer resources from NRL. DHR acknowledges a NRC-NRL Postdoctoral Research Associateship.

## REFERENCES

- [1] W. C. Davis, *Sci. Am.* **256**, 106 (1987); W. Fickett, *Introduction to Detonation Theory*, (U. Calif. Press, Berkeley, 1985).
- [2] B. L. Holian, W. G. Hoover, W. Moran, and G. K. Straub, *Phys. Rev. A* **22**, 2798 (1980); N. Dremin and V. Yu. Klimenko, *Prog. Astronaut. Aeronaut.* **75**, 253 (1981).
- [3] D. W. Brenner, D. H. Robertson, M. L. Elert, and C. T. White, (submitted for publication).
- [4] see e.g. F. P. Bowden and Y. D. Yoffe, *Initiation and Growth of Explosions in Liquids and Solids* (Cambridge U. Press, Cambridge, 1985).
- [5] J. Tersoff, *Phys. Rev. Lett.* **56**, 632 (1986); J. Tersoff, *Phys. Rev. B* **37**, 6991 (1988).
- [6] G. C. Abell, *Phys. Rev. B* **31**, 6184 (1985).
- [7] C. W. Gear, *Numerical Initial Value Problems in Ordinary Differential Equations*, (Prentice-Hall, Englewood Cliffs, 1971).
- [8] A. W. Campbell, W. C. Davis, and J. R. Travis, *Phys. Fluids* **4**, 498 (1961).
- [9] L. G. Green, E. James, E. L. Lee, E. S. Chambers, C. M. Tarver, C. Westmoreland, A. M. Weston, and B. Brown, *Proceedings of the Seventh Symposium (International) on Detonation*, (NSWC MP 82-334, Silver Spring, 1981), p. 256.

---

## **PART IV**

---

### **Crystals: Growth and Behavior**

## ELECTRONIC EXCITATIONS PRECEDING SHOCK INITIATION IN EXPLOSIVES

J. SHARMA AND B. C. BEARD

Naval Surface Warfare Center, Dahlgren Division, White Oak, Silver Spring, MD 20903-5000

### ABSTRACT

Electronic excitations which precede and can facilitate chemical reactivity of explosive molecules during shock passage will be discussed. The structurally similar family of explosives, TATB, DATB, Picramide and TNB were the focus of this work. It has been found that the energy of shake-up transitions observed in x-ray photoelectron spectra of these molecules shows a linear relation with the explosive sensitivity. To the contrary, optical absorption maxima, dependant upon dipole selection rules display a trend opposite that intuitively expected in relation to ease of initiation. The shake-up transitions are governed by monopole selection rules, so that the transitions between initial and final states of the same symmetry are allowed. The forbiddenness of the excited state may favor proton transfer, bond breakage and free radical formation relative to de-excitation by returning to the ground state. Electronic excitations of this type are believed to be important to multiphonon up pumping. The 1s core hole resulting from photoionization creates a central coulomb force that shrinks the orbitals, simulating conditions similar to those of high pressure or shock passage. These factors may be at the heart of the correlation between the shake-up promotion energy and explosive sensitivity.

### INTRODUCTION

Whether molecular deformations or electronic excitations make the first response to shock passage leading to irreversible chemical reaction is an open question. The time taken for the steady state detonation wave to traverse an explosive molecule is about 100 femtoseconds ( $10^{-13}$  seconds). In such a short time it is likely that the electronic levels, because they are so agile, will be the first to respond. Dremin[1], in his multiprocess detonation model has proposed electronic excitation as the first step. Gilman[2] has suggested that the pushing of atoms against each other during shock can cause the transfer of electrons to the Fermi level by tunneling. In this paper we are trying to identify electronic excitations that might be relevant to the start of chemistry in explosives. The relevance is based on the relationship shown between some electronic spectra and the sensitivity scale.

The sensitivity of explosives is not understood in physical terms and its prediction has been difficult and frustrating. Historically, many new explosives have been synthesized only to be rejected because they were too sensitive for handling. There was no definitive way of predicting their sensitivity, prior to their synthesis and use of the hammer. One reason behind the failure is that the processes involved in the early stage of reaction are ultrafast and could not be resolved out in time scale. Recent developments in ultrafast techniques, which can resolve events of ten femtoseconds, may be able to answer the long standing fundamental questions. For example, Schoenlein et al[3] have measured the time involved in the photoisomerization of rhodopsin in the visual system, one of the most rapid events in nature. They found it to be 200 femtoseconds. Similarly Elsaesser et al[4] have determined the time

taken for a proton transfer in an aromatic molecule (2-benzotriazole ) and found it to be 100 femtoseconds (170 femtoseconds for deuteron). It appears that a similar time scale study is needed to reveal the early action in explosives. A sustained detonation wave travels in an explosive at about ten kilometers per second. This means that the time taken to go over the dimensions of a molecule is about 100 femtoseconds(  $10^{-13}$  sec). To provide the energy required for a sustained detonation wave, some molecular process(s) must be capable of releasing energy within the molecular transit time.

A simple minded approach would be to relate sensitivity with optical absorption spectra and band gap measurements, but this does not work. As for example, TNB is transparent to shorter wavelengths and has a large band gap, but contrary to expectations it is far more sensitive than TATB. As mentioned earlier[5] and shown in Table I, the lack of correspondence indicates that these excitations, (dipole transitions from HOMO's ( $n, \pi, \sigma$ -like states) to LUMO's ( $n^*, \pi^*, \sigma^*$ -like states), although they show some photolysis, are not the transitions crucial to the initiation of chemistry. It is necessary to look for other electronic excitations and identify those which may be relevant.

TABLE I

Compilation of Optical Absorption Data on TATB Family of Compounds (D. Glover, NOLTR 62-76)

Explosive	$\lambda_{\text{max}}$ Angstrom	eV
TNB	2240	5.5
Picramide	3180	3.9
DATB	3800	3.3
TATB	4000	3.1

We have found that x-ray photoelectron shake-up spectra match sensitivity behavior of the above mentioned explosives. It has been found that the sensitivity threshold, whether measured with shock, impact or heat follows shake-up separations. The shake-up structure also agrees with the oxygen balance relation of Kamlet. The electronic excitations involved in the shake-up spectra are optically forbidden, not allowed by the dipole selection rules. The shake-up selection rules allow only transitions between initial and final states of the same total symmetry (Aberg [6]). The forbiddenness of the excited state will open up the possibility of proton transfer and non-radiative processes in competition with the direct return to the ground state.

Molecular alterations observed in sub-ignited or thermally decomposed TATB,[6] involve shift of hydrogen to produce furoxans and furazans. Furoxans are produced by the loss of two atoms of hydrogen while furazans are produced by the creation of a water molecule. The former is quite an unstable molecule and its production will facilitate further reaction[7]. Formation of water in the early stage is an important step, because it is exothermic (59 kcal/mole) and would supply energy to sustain the reaction. In view of the above, it can be imagined that shock promotes excitations of forbidden nature, providing the time required for hydrogen reactions. As mentioned above the transfer of proton takes place in roughly 100 femtoseconds. This overall picture supports the idea that the electronic excitations that are most relevant to the initiation process of explosives may be of the class

involved in the shake-up process.

As mentioned earlier, the investigation of the electronic steps should be done with the help of ultrafast laser techniques, where it may be possible to time the electronic excitations and molecular alterations that follow, as has been done by Yan et al[8] on rhodopsin. This will give time scale information on the electronic and atomic changes but of course following vertical excitations. We have used x-ray photoelectron shake-up spectra to determine the relevant electronic excitations. Although x-rays have kilovolt energies, the shake-up probes transitions of optical energy associated with valence level electron promotions. The approach is similar to that employed in the Raman effect where visible light is used to pick up vibrational and rotational level information, which have energies of the infrared region. In the shake-up process photons of 1486 eV are used to probe electronic transitions of the outer orbitals involving only a few electron volts.

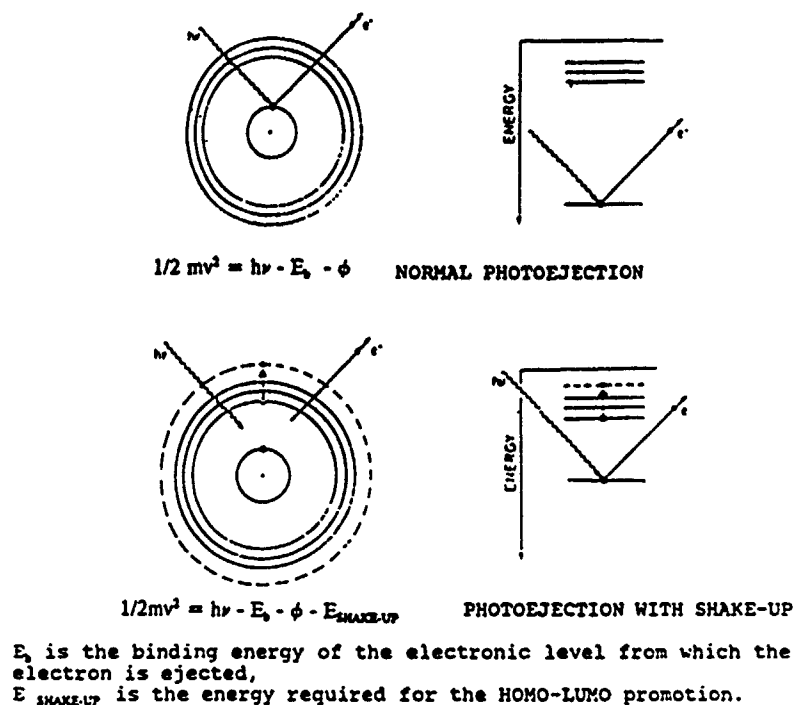


Figure 1. A comparison of normal photoejection with the shake-up process, is shown, in which the associated HOMO-LUMO promotions follow monopole selection rules  $\Delta n=1,2,3,\dots, \Delta l=0, \Delta s=0$ .

#### Normal X-ray photoelectron effect:

The conventional x-ray photoelectron effect is governed by Einstein's photoelectric equation

$$1/2mv^2 = h\nu - E_b - \phi$$

where  $E_b$  is the binding energy of the electron in an orbital from which it is ejected, and  $\phi$  is the work function of the solid.

#### Shake-up Structure in Photoelectron Spectra:

$$1/2mv^2 = h\nu - E_b - \phi - E_{\text{SHAKE-UP}}$$



The shake-up features in the photoelectron spectrum arise from energy losses by the 1s photoelectrons during emission from the atom, Figure 1. These loss events are due to promotion of outer electrons from a HOMO to a LUMO by the photoelectron resulting in a loss of kinetic energy (Svensson et al[9]). Therefore a shake-up satellites appear on the low kinetic energy side of the 1s core photoemission peak separated by the HOMO-LUMO excitation energy. The ejection of the 1s electron causes unequal shrinking of the electronic levels, charge transfer and promotions from the HOMO to LUMO states. The escaping photoelectron (K.E approx. 1000 eV, velocity greater than  $10^8$  cm/s.) leaves the vicinity of the molecule (10 Å) in less than a femtosecond. As a consequence, the shake-up brings information about the immediate response of the outer orbitals to the creation of the 1s vacancy in the nitro-nitrogen or nitro-oxygen of the molecule. Furthermore, the promotions are to forbidden states.

### Results:

Figure 2 shows the 1s spectrum of nitrogen in TATB. The line at about 406 eV is due to nitrogen in the nitro functionality and it is associated with a shake-up feature, separated by 2.7 eV to the low kinetic energy side. The structure indicates that the 1s emission is associated with charge transfer from amine-N to the nitro-N and with a HOMO-LUMO promotion [10]. This causes the nitro-nitrogen line to lose intensity. Its height should have been equal to that of the amine-nitrogen line at about 402 eV, which does not have any shake-up. The decreased height of the shake-up satellite shows that during the photo-ejection of an electron from the nitro-nitrogen, about one third of the electrons lose energy by promoting the outer most electrons. The energy involved in this promotion is 2.7 eV and represents a crucial excitation. As we go from TATB to DATB, Picramide, this separation becomes smaller (Figure 3). For TNB, the separation could not be resolved with

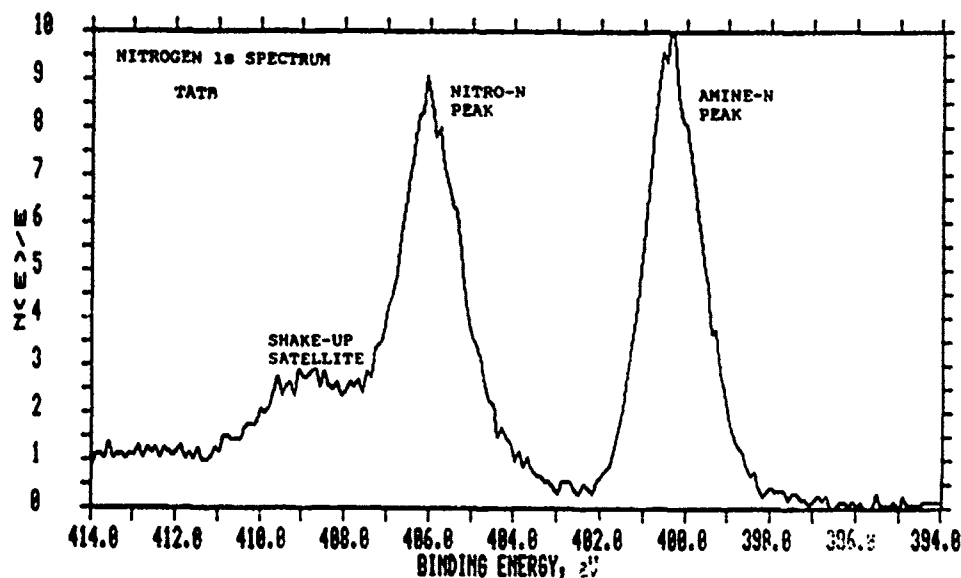


Figure 2. The XPS spectrum of nitrogen in TATB showing the shake-up structure at 2.7 eV to the left of the nitro-nitrogen peak. Note that the amine nitrogen does not show any such structure.

our instrument and is assumed to be zero. The line-width of the nitro-nitrogen in TNB is larger than that of either the amine or nitro nitrogen of TATB, indicating that there may be some structure. Figure 4 shows a relation between the shake-up separation and sensitivity of these explosives as measured by the drop test method. A good relationship over a wide range of impact sensitivity is thus exhibited. The numbers for sensitivity have been taken from the paper of Storm et al[11], in which he has refined them based on very sound arguments. A similar relationship is exhibited when the NSW small scale gap test data is considered, as shown in Figure 5, which measures the shock sensitivity. The results show that as the barrier of shake-up separation increases the threshold energy to initiate the explosives also increases.

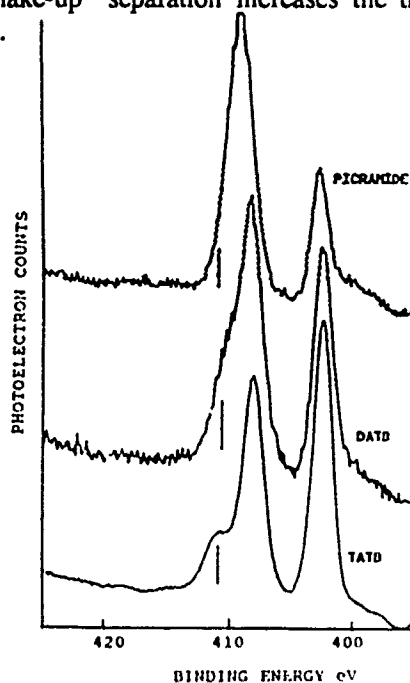
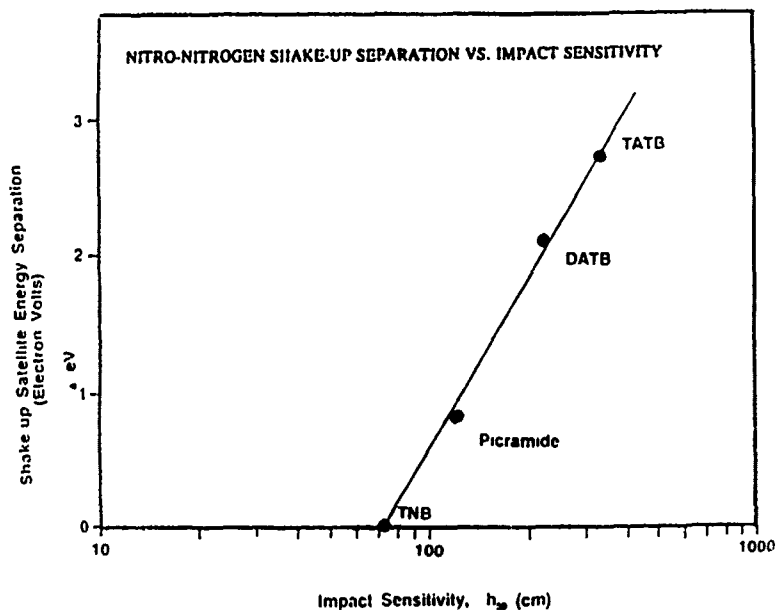


Figure 3. The shake-up structure of nitro-nitrogen shown for TATB, DATB and picramide. The structure gets closer to the main line and the height decreases. TNB showed no separable structure from the main peak, its separation has been assumed to be zero.

TABLE II

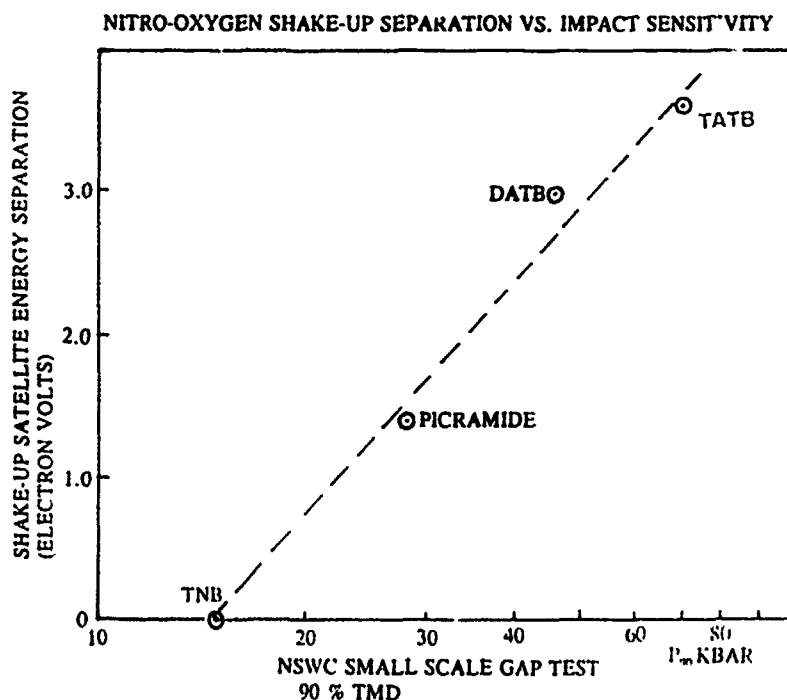
Compilation of Drop Height, Oxygen balance, Shake-up Data on the TATB Family of Explosives.

Explosive	Drop Hgt. cm.	Oxygen Balance	Shake-up $\Delta E$ N1s eV	Shake-up $\Delta E$ O1s eV
TNB	72	-1.5	0.0	0.0
Picramide	121	-1.8	0.8	1.4
DATB	215	-2.1	2.1	3.0
TATB	345	-2.3	2.7	3.6



STORM, STINE and KRAMER 1989.

Figure 4. A plot of nitro-nitrogen shake-up separation against 50% drop height, showing that impact sensitivity bears a linear relationship with shake-up.



STORM, STINE and KRAMER 1989

Figure 5. A plot of nitro-oxygen shake-up separation against shock sensitivity as measured by NSWC small gap test, showing a linear relationship.

Not only the nitrogen of the nitro group but also the oxygen atom of the nitro group shows shake-up in the compounds investigated. As in the case of nitro-nitrogen, the oxygen 1s shake-up separation in TATB, DATB, picramide and TNB decreases monotonically. The values of the nitrogen and oxygen shake-up are all given in Table II. Figure 6 shows the relation between the nitro-nitrogen shake-up and Storm's [10] comprehensive sensitive index. Jianqi et al [11] have estimated the intra-molecular charge transfer coefficient for these compounds from their results on the relative intensities of the shake-up spectra. The shake-up separation and coefficient are linearly related. Thus it can be stated that the shake-up spectra for the nitro-nitrogen and for nitro-oxygen, both show a good relation with the over all sensitivity of these explosives.

### Discussion:

The fact that certain type of electronic excitations agree with the general sensitivity scale of the above mentioned explosives is intriguing. One would not expect vertical electronic excitations of as high magnitude as two or more electron volts from multiphonon pumping from a 50 kbar shock wave, needed for initiation. However the following facts taken into consideration might throw some light on certain possibilities.

1. The shake-up spectra arise during the 1s ionized state of the nitro-nitrogen or nitro-oxygen, which causes shrinking of the outer orbitals and decrease in the HOMO-LUMO gap. This arises from the increase in the effective charge at the center of the atom from the nucleus and the ionized state from the missing 1s electron. The 1s ionized state may be simulating conditions of high pressure, which also changes orbital separation and promotes charge transfer in some compounds. (Syassen et al [12], Drickamer [13]).

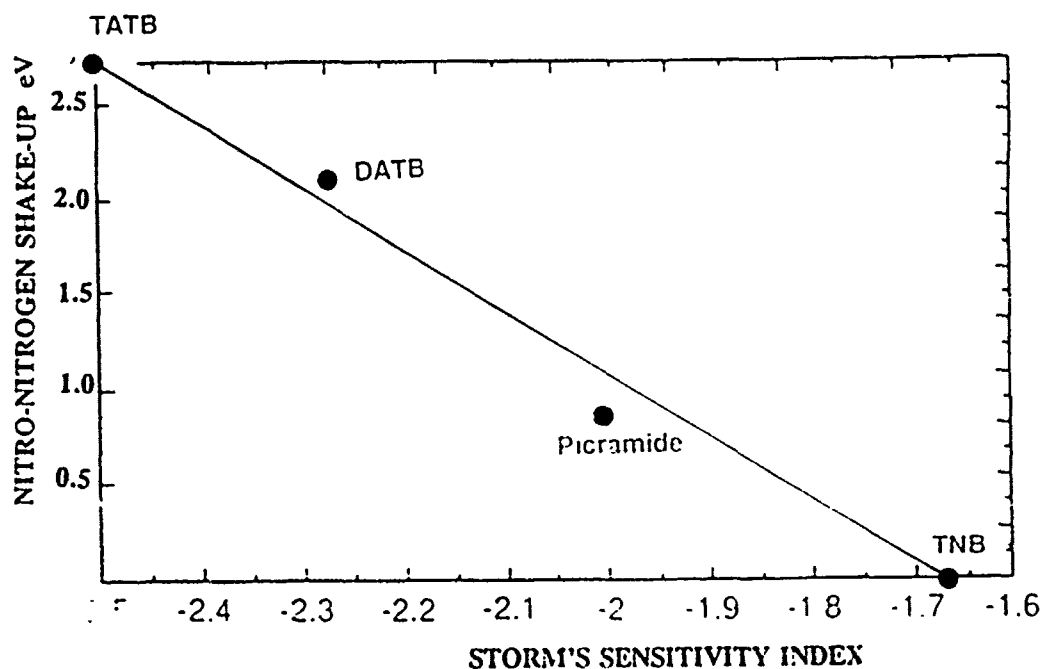


Figure 6. A plot of nitro-nitrogen shake-up against Storm's sensitivity index, which considers many factors.

2. The optically forbidden nature of these excitations can prevent immediate return of the excited electron and promote proton transfer, so that by the time the 1s vacancy is neutralized, the molecule has changed.

3. Most explosives (including those of the TATB family) exhibit strong primary kinetic deuterium isotope effect in decomposition, as shown by Shackleford[14]. This means molecular alterations arising from hydrogen movement are likely to be involved in the first chemical steps. Such transitions take about 100 femtoseconds as discussed previously. The transformation of TATB family of compounds by hydrogen transfer also agree with the calculations of Murray, Lane and Politzer[15].

4. The results of MO calculations as given by Sharma et al [16] and by Bardo[17] show that for TATB 48 molecular orbital cluster into five broad peaks in the range between 0-40 eV. These molecular orbitals have not been resolved by XPS studies. However, some of the orbitals are close to the Fermi level and are within one or fractional eV of separation amongst themselves. An examination of Von Niessen's[19] calculations on para nitroaniline leads us to believe that the  $\text{NH}_2$  HOMO orbital ( $4b_1$ ) is one of the likely orbitals that promotes electron density to the ( $5b_1$ ) orbital of the  $\text{NO}_2$  functional group. Such an event is quite likely for TATB, which is structurally and electronically like para amino nitroaniline.

Based on the points mentioned above a story can be built up that shock causes forbidden electronic excitations, from which the probability of returning to the ground state is not as usual. Then processes such as proton transfer and bond disruptions can compete. Furoxan is produced by the elimination of two hydrogen atoms. The molecule is more sensitive than TATB[7] and provides an easy path for further alterations. From TATB, furazan is produced by the elimination of a water molecule, which is an exothermic step and has the potential of giving energy to sustain the reaction. Thus a basis for chain reaction is started.

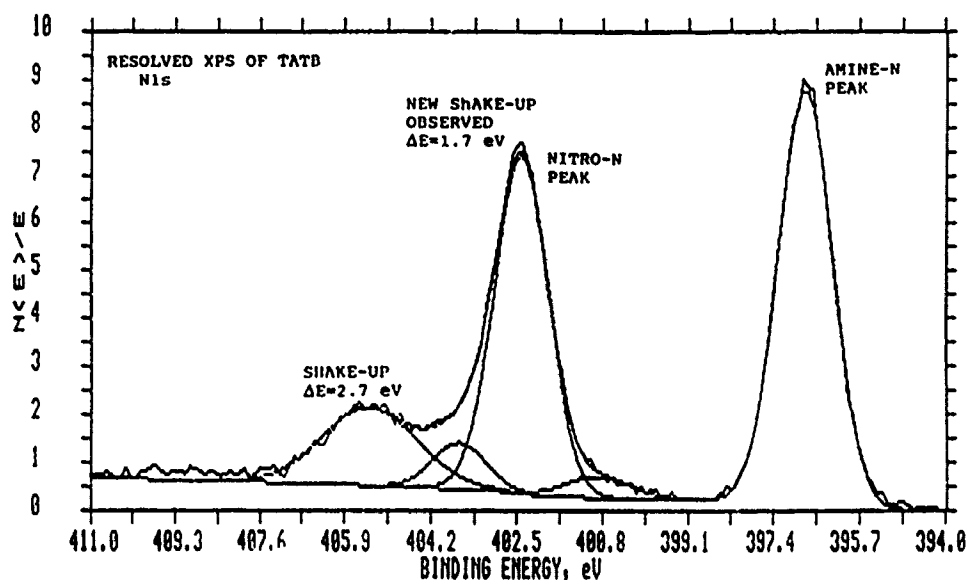


Figure 7. XPS spectrum of nitrogen in TATB obtained by using a PHI 5000 Series ESCA instrument, with an x-ray monochromator giving higher resolution. A new shake-up peak at a separation of 1.7 eV is detectable by using a curve fitting program.

There are some misgivings about the above mentioned picture. The excitation energy for these compounds as obtained from shake-up spectra are 2.7, 2.1, 0.8 eV for TATB, DATB and picramide, respectively. These are rather large vertical gaps of electronic levels to be excited by shock. According to the literature (Drickamer and Frank [14]) a pressures of 50 kbar can change electronic levels only by 0.6-0.75 eV. Even if it is assumed that thermal excitations can be half in value compared to electronic ones due to dielectric relaxation, all the same there is a large difference between threshold pressures and the electronic levels envisaged. Some explanation to bridge the gap has to be given. The role of dislocations as proposed by Coffey[20] in his model may make local transitions possible by decreasing the promotion energies. Also one can fall back on the role of incipient defects as points of minimal free energy where transitions could become possible. Another thing to remember would be that sonic oscillations in very small bubbles are known to cause light emission which involves the energy of two eV[21]. Probably shock waves can stimulate larger jumps at tiny bubbles and defects.

## CONCLUSIONS

From the present work, one can conclude that electronic levels can play a role in the initiation process, but the very levels we have measured need not be the ones that are operative. There are closer levels which have recently been observed in TATB as shown in Figures 7, resolved with a new instrument. Further work on them is in progress, which may remove the controversy. The charge transfer excitations, controlled by monopole selection rules, producing forbidden excited states may be critically important for initiation. The forbidden nature of these electronic promotions may encourage atomic reorganization and molecular disruptions rather than the immediate return of the molecule to the ground state.

This work has evolved from research supported by the Independent Research(IR) program of Naval Surface Warfare Center.

## REFERENCES:

1. A.N. Dremin, V. Yu. Klimenko, O.N. Davidova and T.A. Zoludeva, Proc. of Ninth Symposium(International) on Detonation, August 28-Sept.1, 1989, Portland, Oregon. Vol.I, OCNR 113291-7, p. 724.
2. J.J. Gilman, in Shock Compression of Condensed Matter, Edited by. Schmit, Johnson and Davison, (Elsevier Science Publishers, NY, 1990), p. 267.
3. R.W. Schoenlein, L.A. Piteanu, R.A. Mathies and C.V. Shank, Science **254**, 412, (1989).
4. T. Elsaesser, F. Laermer and W. Frey, Proc. of Int. Symp. on Ultrafast Processes in Spectroscopy, Bayreuth, (Inst. Phys. Conf. Ser. No. 126, 1991), p. 543.
5. J. Sharma, in Shock Compression of Condensed Matter 1991, edited by Schmidt, Dick, Forbes, Tasker, (Elsevier Science Publishers B.V. 1991), p. 570.
6. T. Aberg, Ann. Acad. Sci. Fennicae, Ser. A VI, 308 (1969).
7. J. Sharma, J.H. Hoffsommer, D.J. Glover, C.S. Coffey, J.W. Forbes, T.P. Liddiard, W.L. Elban and F. Santiago, Proc. Eighth Symp. (Int.) on Detonation, Naval Surface Warfare Center, USA (1985), p. 725.

8. M. Yan, D. Manor, G. Weng, H. Chao, L. Rothberg, T.M. Jedju and R.R. Alfano, Proc. Nat. Acad. Sci. U.S.A. 88, No. 21, 9809, (1991).
9. S. Svensson, B. Eriksson, N. Martensson, G. Wendin and U. Gelius, J. Electron. Spectros. rel. Phenomena, 47, 327 (1988).
10. R. Wigelow, R.J. Weagley and H.J. Freund, Chem. Phys. Lett. 82, No. 2, 305 (1981).
11. C.B. Storm, J.R. Stine and J.F. Krarner, in Chemistry and Physics of Energetic Materials, edited by S.N. Bulusu, (Kluwer Academic Publishers, Dordrecht, 1990), p. 605.
12. W. Jianqi, W. Wenhui, Z. Minxui and L. Hengyuan, J. Electron Spectros. rel. Phenom. 46, 363 (1988).
13. K. Syassen, G. Wortmann, J. Feldhaus, K.H. Frank and G. Kaind in Physics of Solids Under High Pressure, edited by Shilling and Shelton ( North-Holland, Amsterdam, 1981), p. 319.
14. H.J. Drickamer and C.W. Frank in Electronic Transitions and the High Pressure Chemistry and Physics of Solids, (Chapman and Hall, London, 1973), p. 98.
15. S.A. Shackelford in Chemistry and Physics of Energetic Materials, edited by S.N. Bulusu, (Kluwer Academic Publishers, Dordrecht, 1990), p. 433.
16. J.S. Murray, P. Lane and P. Politzer, P. R. Bolduc and R.L. Mckenney, Jr., J. Mol. Str(Theochem), 209 (1990) 349.
17. J. Sharma, W.L. Garrett, F.J. Owens and V.L. Vogel, J. Phys. Chem. 86, 1657 (1982).
18. R.D. Bardo, Proc. Seventh Symposium (Int) on Detonation, 1981, NSWC MP 82-39, p. 93.
19. W. von Niessen, J. Phys. Chem. 92, 1035 (1988).
20. C.S. Coffey, Proc. of Ninth Symposium (Int) on Detonation 1989, OCNR 113291-7, p. 58.
21. M.M. Chaudhri, Physics Today, July 1992, p. 15.

## PRESSURE/TEMPERATURE/REACTION PHASE DIAGRAMS FOR SEVERAL NITRAMINE COMPOUNDS

T. P. Russell\*, P. J. Miller\*, G. J. Piermarini\*\* and S. Block\*\*

\*Naval Surface Warfare Center Silver Spring, Maryland 20903-5000

\*\*Materials Science and Engineering Laboratory National Institute of Standards and Technology  
Gaithersburg, Maryland 20899

### ABSTRACT

Pressure/temperature/reaction phase diagrams for several nitramine compounds, including hexanitrohexaazaisowurtzitane (HNIW), 1,3,5-trinitrohexahydro-1,3,5-triazine (RDX), ammonium dinitramide (ADN), and p-nitroaniline (PNA) are presented. A diamond anvil cell was used in conjunction with optical polarizing light microscopy (OPLM), Fourier transform infrared spectroscopy (FTIR), energy dispersive X-ray diffraction (EDXD), and micro FT-Raman spectroscopy to determine these diagrams. A description is given of the diamond anvil cell and the associated techniques employed.

### INTRODUCTION

Recently, interest has been increasing in the chemistry and physics of materials under extreme conditions. Recovery as well as *insitu* experiments (shock and static) have been developed to probe extreme conditions of pressure and temperature [1]. However, to date, little is known quantitatively about material properties at both high temperatures and high pressures. In order to determine the chemical and physical properties of materials under these conditions, the pressure and temperature must be controllably produced and maintained and their effects on materials monitored in real time. One approach to studying the physical and chemical properties of materials under extreme conditions is the use of a high-pressure diamond anvil cell (DAC). In recent years, the use of the DAC as a research tool has greatly increased and new applications are being reported in the literature frequently. The DAC can be used with a variety of characterization techniques to evaluate the chemical and physical properties of materials. Use of the DAC permits the detection and measurement of phase transitions as a function of temperature and pressure, which leads to the characterization of thermodynamic stability fields of high-pressure high temperature polymorphs (phase diagrams). Also, the identification of the crystallographic structures of these polymorphs, in addition to the measurement of their compressibilities can be achieved by x-ray diffraction methods with the use of a DAC [2-4]. Chemical kinetics and reaction mechanisms can be determined by FTIR spectroscopy [4].

In this paper, we focus our discussion on the DAC and its applications to the study of energetic materials, in particular to the structural dependency of nitramines with respect to thermodynamic stability. The techniques employed to detect phase transitions, to delineate pressure/temperature stability fields, and to measure compressibility of these nitramine compounds under extreme conditions of pressure and moderate temperatures will be discussed. Finally, the determination of decomposition parameters as a function of pressure and temperature will also be presented.

### EXPERIMENTAL

All of the experimental techniques employed in the present work were reported in detail earlier [5-11]. Thus, only a brief description is given here. More detailed information can be obtained in the references cited.



## Diamond Anvil Cell

The principle for pressure application in a diamond anvil cell is relatively simple. It is based on the concept of Bridgman opposed anvils, where two miniature diamond anvils are mounted in this configuration. The first diamond anvil high-pressure cell of the opposed anvil type designed for 180° transmission use was developed in 1959 by the National Institute of Standards and Technology (NIST), formerly, the National Bureau of Standards (NBS) [12]. A second DAC design also incorporating Bridgman opposed anvils, but not with 180° transmission capability, was developed independently and was reported later in 1959 [13]. Over the years, several varying designs of the opposed diamond anvil cell have been employed [14-18]. However, the underlying principle of the design of every DAC is based on the Bridgman opposed-anvil configuration.

The pressure cell used in this work (Figure 1) is fabricated from a high-temperature, high-strength superalloy, Inconel® 718, and is designed for 180° transmission and reflection measurements with sustained static heating up to 600 °C [6].

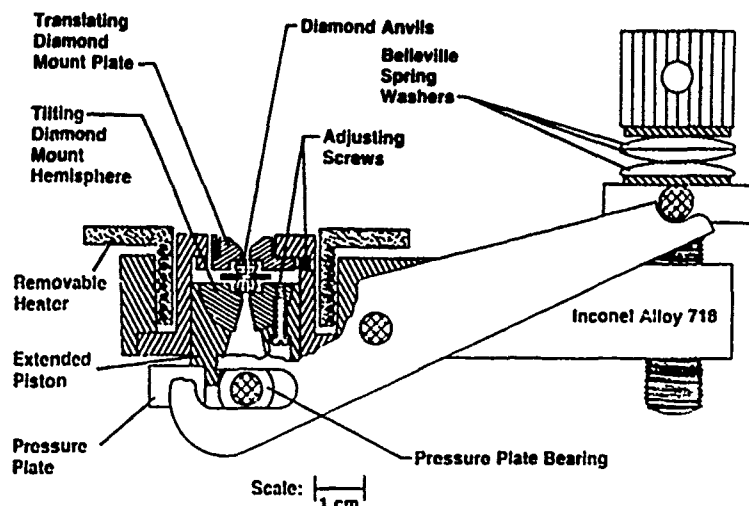


Figure 1. A cross-section diagram of the diamond anvil high pressure cell showing the diamond anvils in relation to the cell body. Force, generated by the compression of Belleville spring washers, is transmitted to the anvils via the lever-arm assembly which also multiplies the force by a factor of two.

Pressure is generated by a screw rotation which compresses Belleville spring washers that apply a continuously varying load to the moving anvil via a spring loaded lever arm assembly. Different degrees of sensitivity and load characteristics can be obtained by stacking the Belleville spring washers in series, in parallel, or in combinations of both. The applied load is transferred uniformly to the pressure plate which bears against the piston assembly. One diamond anvil is fixed in a hemisphere in the piston assembly. This anvil is driven towards a second diamond anvil which is in a fixed position in the entablature. The hemisphere can be tilted a maximum of about 5° to permit parallel alignment of the two anvil faces, while the entablature can be rotated for axial alignment of the opposing anvil faces.

A removable miniature resistance coil heater with high power output ( $\approx 70\Omega$  resistance) surrounds the diamond anvil piston-cylinder assembly and permits routine heating of the sample. The heater coil is bifilar and is sheathed in Inconel® 600 alloy packed with

The ruby fluorescence technique, originally developed at NIST in 1972, was calibrated against the compression of NaCl via the Decker equation of state in 1976 [6,7]. The pressure measurements by this method are accurate to  $\pm 0.05$  GPa when they are made in a hydrostatic environment at room temperature. The uncertainty in the pressure is greater at elevated temperatures because of line-broadening and decreasing fluorescent intensity. These effects contribute to greater uncertainty in the measurement of  $\lambda$ , the wavelength of the  $R_1$  line. Still another source of error lies in the temperature correction to  $\lambda$ , which shifts with temperature in the same direction as the pressure shift. The temperature correction has been determined from ruby fluorescence measurements made at one atmosphere in the DAC and are included in our overall uncertainty. To avoid heating effects, a 20 mW He-Cd Laser is used to excite the ruby fluorescence R lines. The focused laser beam is approximately 10  $\mu\text{m}$  in diameter, which is roughly the same size as the ruby sphere used as the pressure sensor.

#### **Fourier Transform Infrared Spectroscopy**

Infrared absorption spectra are recorded on a Nicolet<sup>®</sup> FTIR spectrometer, employing an MCT-A (narrow band) detector for improved sensitivity and a Nicolet<sup>®</sup> data acquisition system. The FTIR technique provides spectroscopic evidence for solid/solid phase transitions, formation of a new polymorphic phase (structural confirmation), and the determination of decomposition parameters. Sample thicknesses of 0.01-0.05 mm are necessary for infrared transmission experiments. It is difficult to prepare gaskets of this thickness. Furthermore, even if gaskets of this thickness were used, the ruby spheres or chips of requisite size would be pinched between the diamond anvil surfaces resulting in large errors in the pressure measurement. For these infrared absorption measurements, samples are prepared by two methods. In the first method [4], the sample is prepared in the following way. A gasket is prepared with a thickness of  $\approx 200$   $\mu\text{m}$  and a diameter of  $\approx 250$   $\mu\text{m}$ . The hole is packed with dry NaCl powder compacted to transparency by applying about 0.05 GPa with the DAC. A 0.01-0.05 mm layer of compacted NaCl is physically removed with the fine point of a needle to form a cavity in the bulk of the compacted NaCl. The sample to be investigated is in the form of a fine powder and is introduced along with a 10  $\mu\text{m}$  diameter ruby sphere into this cavity, effectively replacing the removed NaCl layer. In the second method, the gasket is not filled with NaCl, instead a thin film of sample is pressed between ungasketed diamond anvils. The thin film usually adheres to one of the anvil faces. The diameter of this film is altered to conform to the gasket hole diameter by removal of excess material. The gasket and sample film along with a 10  $\mu\text{m}$  diameter ruby sphere are assembled in the DAC and liquid nitrogen is introduced as the pressure transmitting medium (1). The use of liquid nitrogen provides a chemically inert, non-infrared active, hydrostatic pressure transmitting medium up to 30 GPa. The two methods provide both a visible and an infrared window approximately 250  $\mu\text{m}$  thick. The liquid nitrogen procedure, although much more difficult to perform, is superior in most respects to the NaCl method for FTIR measurements and is the favored technique.

#### **Micro FT-Raman Spectroscopy**

Recently, a micro FT-Raman spectroscopy technique for DAC application was developed [19]. In this method the DAC is positioned on the Raman microscope using a massive micrometer translation stage (X,Y,Z). The X,Y parameters position the sample in the DAC on the optic axis of the microscope, while the Z parameter is used for focusing the sample. A 5W CW NdYAG laser operating at 1.06  $\mu\text{m}$  is used as the excitation wavelength. The laser power is regulated by rotating a variable neutral density filter, giving laser powers from 100 mW to 5.0 W. The laser beam is directed through a 4 mm hole in a

gold coated planar mirror into the microscope. Gold coated reflecting optics are employed throughout the microscope system for improved efficiency. The laser pulse is focused onto the sample inside the DAC using a near-IR microscope objective. Scattered radiation is collected by the microscope objective and is directed through the same optical path used for the laser beam. The signal is then separated from the laser beam optical path by reflecting the sample signal into the spectrometer off the gold coated planar mirror with the 4 mm hole. Unwanted laser radiation is removed by a holographic filter placed in front of the interferometer. The sample radiation is then passed through the interferometer and is focused onto a germanium detector. The signal is processed using a Nicolet 680D computer system. The sample may be prepared as a single crystal or powder sample in a hydrostatic or non hydrostatic medium. Raman shifts are detected up to 30 GPa and between -150 °C and 300 °C. The major advantages of FT-Raman using NdYAG excitation at 1.06  $\mu\text{m}$  are: (1) reduced sample decomposition because of short exposure times, and (2) reduced fluorescence. In DAC applications, fluorescence from the diamonds and pressure transmitting medium are reduced significantly. This technique does not require Type IIA low luminescence diamond anvils.

### Energy Dispersive X-ray Diffraction

In x-ray powder diffraction experiments the sample and/or detector usually are rotated over a large angular range to bring the various crystallographic planes into the Bragg condition for diffraction. Owing to the containment requirement of the sample in a DAC for high pressure studies, this is no longer feasible. For insitu x-ray diffraction measurements using a DAC, it is best to keep the sample in a fixed position and use the energy dispersive x-ray diffraction technique [11,20-22]. The DAC can be mounted in a fixed position and white radiation can be used in conjunction with a solid state detector ( $\text{Si}_\text{Li}$ ,  $\text{Ge}_\text{Li}$ , or intrinsic Ge) and a multichannel analyzer. All data are collected simultaneously. The DAC is mounted in the x-ray beam at the center of the diffractometer by a micrometer positioning device (X, Y, Z stage). The sample is aligned by altering the x- and z-positioners and measuring the difference in absorption or by using a microscope. The y-positioner places the sample center on the diffractometer axis. Any fluorescence, characteristic tube X-ray lines or absorption edges are at a fixed energy. The observed intensities of the lines are a function of: (1) the distribution of the white radiation from the x-ray source (tube or synchrotron), (2) the absorption through the diamonds, (3) the specimen transparency, and (4) the scattering power which decreases as  $1/E^2$ . Typically, for energetic materials a limited number of diffraction lines are observed. Often these lines are a combination of multiple diffractions as represented in Figure 2. Structural change is often identified by the appearance of new diffraction lines or dramatic changes in the EDXD pattern. If the different crystallographic forms are similar, then identification of a high pressure phase may not be possible because dramatic changes in X-ray diffraction lines or appearances of new diffraction lines may not occur (Figure 2). However, if no apparent changes are observed, it may be possible to detect phase transitions by a discontinuity in the measured linear compression of diffraction peaks or calculated unit cell volume associated with the high and low pressure phases as shown in Figures 3. In addition, by measuring the linear compression of the material an estimate of the change in volume ( $\Delta V$ ) can be made by assuming that the volume decrease is proportional to the measured linear distance decrease ( $\Delta X$ ). Therefore, a first approximation of the  $\Delta V$  (volume) and  $\Delta \rho$  (density) of a material are possible during compression. If a transition has occurred this estimate in volume and density change corresponds to the compression of the original state, the  $\Delta V$  due to the transition, and the compression of the high pressure state.

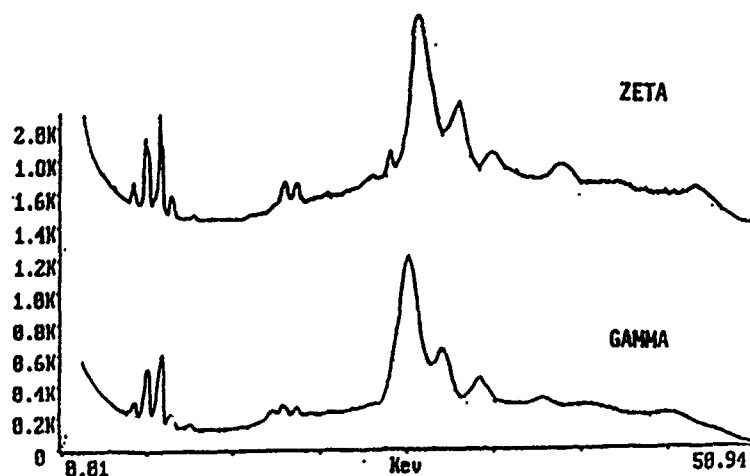


Figure 2. Comparison of the energy dispersive x-ray diffraction powder patterns for  $\gamma$  and  $\zeta$  HNIW at 1 atm and 0.9 GPa, respectively. Most peaks shown are a combination of hkl reflections which are not resolvable because of the poor resolution of the EDXD method employed.

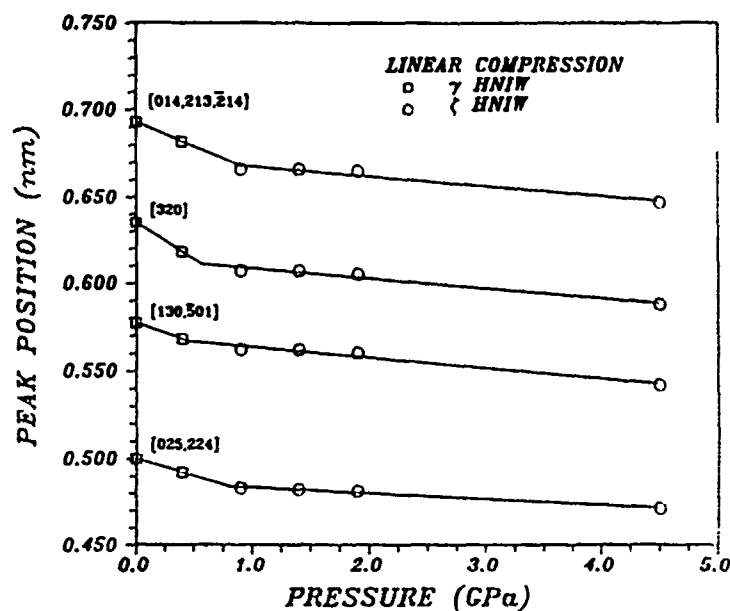


Figure 3. Pressure dependency of the position of observed diffraction peaks (in nanometers) for  $\gamma$  and  $\zeta$  HNIW polymorphs

## RESULTS AND DISCUSSION

The pressure, temperature, reaction phase diagrams for HNIW, RDX, ADN and p-nitroaniline which follow were determined earlier by one or more of the measurement techniques described above [2,9,23,24]. The details of those experiments and the associated results can be found in the references indicated. In the P,T diagrams that follow, the equilibrium phase transformation boundaries are designated by solid lines, while the nonreversible polymorphic transitions are represented by dashed lines. Although some of the transitions were found to be irreversible probably for kinetic reasons, from the overall experimental evidence, the reported stability fields indicate thermodynamic equilibrium conditions for the pure crystalline material.

### Hexanitrohexaazaisowurtzitane

Our reaction phase diagram for HNIW as a function of pressure and temperature is shown in Figures 4A and 4B. The determined polymorph stability fields are as follows: (1) the stable ambient monoclinic phase,  $\gamma$  (stable between ambient pressure and 0.7 GPa from -125 °C to decomposition), (2) the high-pressure monoclinic phase,  $\zeta$  (stable between 0.7 to 14.0 GPa from -125 °C to decomposition temperatures), (3) a high-temperature-high-pressure orthorhombic phase,  $\beta$ , (stable between 0.5-0.6 GPa and between 140-200 °C), (4) a high-temperature-high pressure monoclinic phase,  $\epsilon$ , (stable between 0.65-2.5 GPa and between 110-240 °C), and (5) the high-temperature-high-pressure orthorhombic phase,  $\alpha$ , (stable above 0.4 GPa and approximately 220 °C).

FTIR spectroscopy was used to identify high pressure and/or high temperature phase transitions and new polymorphic (structural conformation) phases. Figure 5A shows three spectra which were collected at different pressures which bracketed the  $\gamma \leftrightarrow \zeta$  transition in HNIW at 0.7 GPa identified by OPLM experiments. Spectrum A shows the initial sample,  $\gamma$  HNIW at  $0.16 \pm 0.05$  GPa. Spectrum B taken at  $0.9 \pm 0.05$  GPa, which is 0.2 GPa higher than the measured transition pressure, shows a definite change in the infrared absorption spectrum. Significant differences in absorption bands are observed between spectra A and B, in the ranges of  $3100\text{-}3000\text{ cm}^{-1}$  ( $\text{CH}_2$  symmetric/asymmetric stretching) and  $1800\text{-}700\text{ cm}^{-1}$  (finger print stretching/bending region). To confirm the formation of a new polymorph of HNIW, Spectrum B was then compared with the known infrared adsorption spectra for  $\alpha$ ,  $\beta$ , and  $\epsilon$  HNIW polymorphs at  $0.9 \pm 0.05$  GPa at room temperature (Figure 5B). No agreement between any of the known polymorphs ( $\alpha$ ,  $\beta$ , and  $\epsilon$ ) and the high pressure  $\zeta$  HNIW phase was found in the infrared spectra. Spectrum C (Figure 5A) was obtained after the sample pressure was lowered from  $0.9 \pm 0.05$  GPa to  $0.4 \pm 0.05$  GPa, and the resulting spectrum (spectrum C) agreed with that obtained for the original  $\gamma$  HNIW sample (spectrum A). This indicates that a reversible solid/solid phase transition occurred at 0.7 GPa between  $\gamma$  and  $\zeta$  HNIW polymorphs and that the  $\zeta$  HNIW phase is, indeed, a new structural conformation of HNIW.

Five solid polymorphs, identified as  $\alpha$ ,  $\beta$ ,  $\gamma$ ,  $\epsilon$ , and  $\zeta$ , were found. Each of the four HNIW polymorphs, which are all retrievable at ambient pressure and temperature, ( $\alpha$ ,  $\beta$ ,  $\gamma$ , and  $\epsilon$ ) were initially used as the starting material at the beginning of this investigation. Transitions were observed in  $\gamma$  HNIW to form all other HNIW polymorphs. However, the only transitions determined when starting with the other recovered HNIW polymorphs, corresponded to the their phase boundaries when  $\gamma$  HNIW was used as the starting material. Nine solid-solid phase transitions were observed for HNIW (Table 1). The reversibility, pressure/temperature conditions, techniques employed

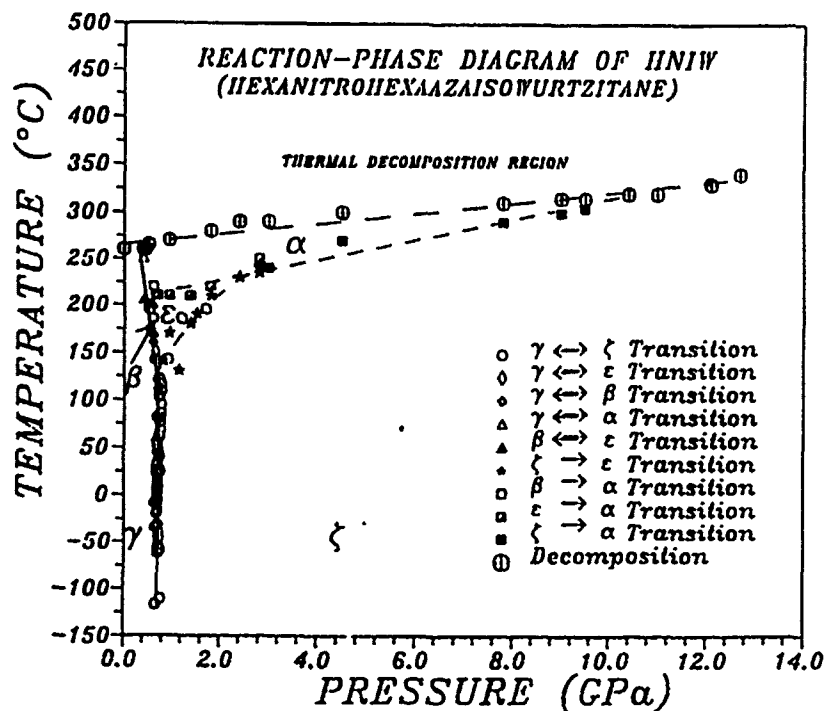
Table I. The solid/solid phase transitions among the known polymorphs of HNIW determined as a function of temperature and pressure.

Transition	Reversibility	Press. Region (GPa)	Techniques Temp. Region (°C)	Slope of Employed for Identification	Transition Boundary
$\gamma/\alpha$	REV.	0.40-0.55	>180	FTIR	NEG.
$\gamma/\beta$	REV.	0.55-0.62	160-180	FTIR	NEG.
$\gamma/\epsilon$	REV.	0.62-0.70	120-160	FTIR,OPLM	NEG.
$\gamma/\zeta$	REV.	0.70	-125-120	FTIR,OPLM,EDXD	NO
$\beta/\alpha$	NONREV.	0.4-0.55	190	FTIR	POS.
$\beta/\epsilon$	NONREV.	$\approx 0.6$	140-170	FTIR	UNDETER.
$\epsilon/\alpha$	NONREV.	0.60-2.8	190-220	FTIR	POS.
$\zeta/\epsilon$	NONREV.	0.70-2.8	130-180	FTIR	POS.
$\zeta/\alpha$	NONREV.	2.8-10	190-230	FTIR	POS.

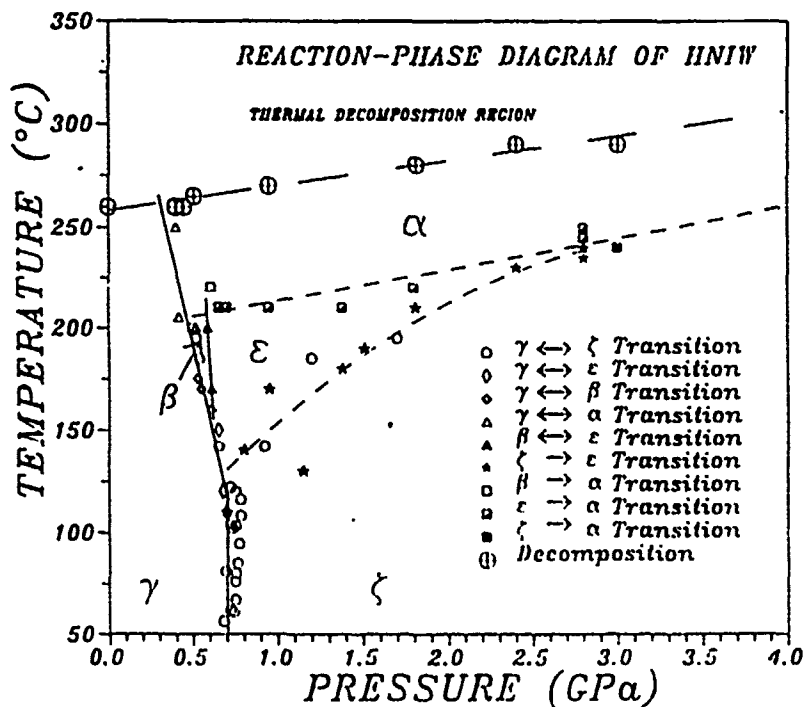
for detection, and slope of the transition boundary are listed. The reversible transitions observed included (1)  $\gamma \leftrightarrow \alpha$ , (2)  $\gamma \leftrightarrow \beta$ , (3)  $\gamma \leftrightarrow \epsilon$  and (4)  $\gamma \leftrightarrow \zeta$ . The nonreversible transitions observed included (1)  $\beta \rightarrow \alpha$ , (2)  $\beta \rightarrow \epsilon$ , (3)  $\epsilon \rightarrow \alpha$ , (4)  $\zeta \rightarrow \epsilon$  and (5)  $\zeta \rightarrow \alpha$ . The pressure and temperature thermal decomposition parameters have also been determined and reflect rapid decomposition (<1 minutes). The observed pressure/temperature decomposition parameters are provided in Table 2, which also indicates the HNIW phase and temperature/pressure conditions for decomposition at a moderate rate (1-2 min). Slow decomposition is known to occur at significantly lower temperatures at ambient pressure [25-27]. This trend is also observed at elevated pressures.

Table II. The observed temperature/pressure parameters for HNIW thermal decomposition at a moderate rate (1-2 min), indicating the decomposing HNIW phase

Polymorph	Decomposition	
	Temperature(°C)	Pressure (GPa)
$\gamma$	260	0.0-0.4
$\alpha$	260-280	0.40-10.0
$\zeta$	280-340	10.0-14.0



4A



48

Figures 4A and 4B. The reaction/phase diagram for  $\gamma$  HNIW is shown in Figures 4A and 4B. Figure 4A gives the results of the overall study for  $\gamma$  HNIW indicating the measured stability fields for the five solid phase polymorphs ( $\alpha$ ,  $\beta$ ,  $\gamma$ ,  $\epsilon$ , and  $\zeta$ ) from  $-150^{\circ}\text{C}$  to  $320^{\circ}\text{C}$  and up to 14.0 GPa. Figure 4B is an enlarged view of the region from  $50^{\circ}\text{C}$  to  $320^{\circ}\text{C}$  and up to 4.0 GPa.

MgO powder for electrical isolation. The power input to the heater is controlled by a thyristor controller and a silicon-controlled rectifier (SCR) which permits automatic control of heating with proportional, integral and derivative features for the heating rate. Other features which are available include time-proportional heating, temperature overshoot inhibition and direct temperature readout. Temperatures as low as  $-190^{\circ}\text{C}$  can be attained by replacing the removable resistance coil heater with a miniature coiled tube for passage of liquid  $\text{N}_2$ . Temperature is measured by a chromel-alumel thermocouple with its bead in contact with an Inconel<sup>®</sup> X750 alloy gasket which confines the sample under pressure. With this system, temperature can be set and automatically maintained to  $\pm 1^{\circ}\text{C}$  with an estimated accuracy of  $\pm 3^{\circ}\text{C}$  at  $300^{\circ}\text{C}$ . A fixed-point calibration method based on the melting point of several pure materials was used to determine this uncertainty [8].

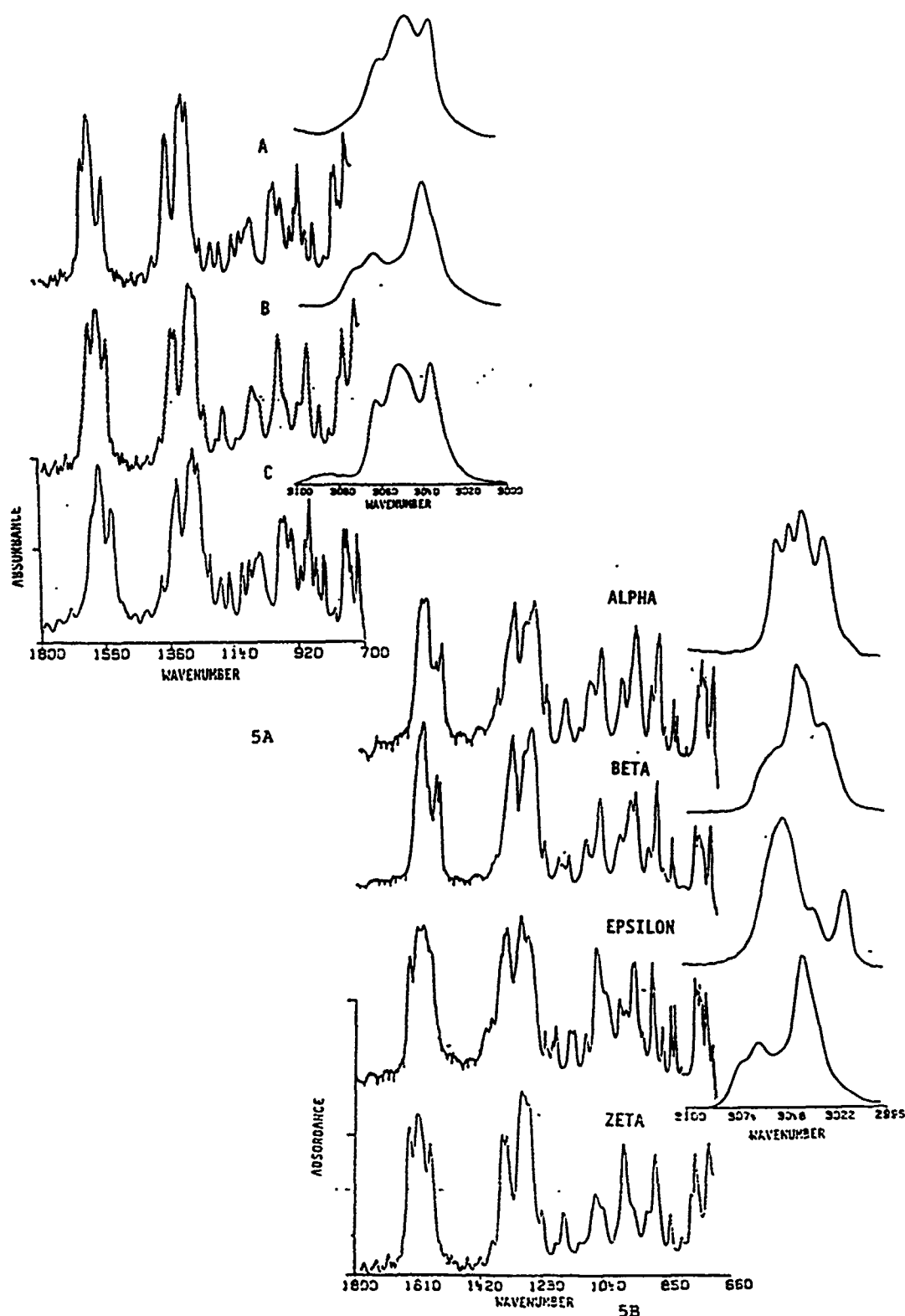
The high-pressure-high-temperature diamond anvil cell can be mounted on a micrometer positioning device for optical polarizing light microscopy, ruby fluorescence pressure measurements, Fourier transform infrared (FTIR) spectroscopy, micro FT-Raman, and energy dispersive X-ray diffraction (EDXD) measurements as described below.

### Optical Microscopy and Ruby Fluorescence Measurements

Optical polarizing light microscopy (OPLM) studies are made with an instrument also used for our ruby fluorescence pressure measurements. This system has been described earlier [5]. A massive micrometer x,y,z positioning device provides the mount for the pressure cell and permits horizontal positioning (x,y) of the sample (or ruby) in the DAC onto the optic axis of the microscope, while permitting vertical motion (z) to focus the sample (or ruby). A tungsten light source is positioned at the bottom of the microscope providing transmission illumination of the sample. This allows visual evaluation of the sample under polarizing light. Structural phase transitions are detected in samples under investigation using OPLM primarily by birefringence changes on single crystals using various pressure transmitting media, e. g., liquid  $\text{N}_2$ , n-pentane:isopentane (1:1 by volume), and Fluorinert<sup>®</sup>). The use of Fluorinert is limited to samples which are insoluble only in this liquid because its own strong birefringence does not promote sharp visual images of the crystals when viewed under polarized light. N-pentane:isopentane (1:1 by vol) and liquid  $\text{N}_2$  both permit sharp images of single crystals under polarized light with pronounced birefringence effects such as an extreme change in color moving as a wave across the crystal face when a sample undergoes a phase transformation. In some instances, by fine adjustment of the pressure, the transitions can be halted so that both phases are present simultaneously in the same specimen separated by a sharp demarcation line. The birefringence change and demarcation boundary provide distinct markers for detecting a transition as a function of pressure and temperature. Similarly, melting (freezing) as a function of pressure and temperature may be accomplished by adjusting these parameters so that both solid and liquid phases are present simultaneously.

A 20 mW CW He-Cd laser is positioned where the light source for EPI (reflection) illumination would normally be located. The He-Cd laser beam provides the excitation energy for ruby fluorescence. The light image may be transmitted to a television camera by inserting a movable mirror which contains a very small circular noncoated area. The noncoated area permits transmission of the fluorescence radiation to the monochromator. Therefore, visual observation of the sample and pressure measurement may be accomplished simultaneously. The fluorescence signal is recorded digitally by a diode array detector and is processed by an IBM<sup>®</sup> AT computer. Pressure is evaluated by a peak shift calculation or a line-shape model. Pressure measurements by this technique may be repeated routinely every 3 sec.





Figures 5A and 5B. Figure 5A shows the infrared absorption spectra of HNIW (A, B, and C) at room temperature and the following pressures: Spectrum A at 0.16 GPa; Spectrum B at 0.9 GPa; and Spectrum C after lowering the pressure from 0.9 to 0.4 GPa. Figure 5B shows the infrared absorption spectra for  $\alpha$ ,  $\beta$ ,  $\epsilon$ , and  $\zeta$  HNIW polymorphs at room temperature and 0.9 GPa showing the differences in the absorption bands among the various phases.

### 1.3.5-Trinitrohexahydro-1.3.5-triazine

Three solid polymorphs, identified as  $\alpha$ ,  $\beta$ , and  $\gamma$  were found for RDX. The equilibrium/reaction phase diagram is presented in Figure 6. The determined polymorph stability fields for the three RDX phases are as follows: (1) the stable ambient orthorhombic phase,  $\alpha$ , (2) the high pressure phase,  $\gamma$ , stable above 3.8 GPa, and (3) the high-temperature and high-pressure phase,  $\beta$ , stable above 2.7 GPa and 225 °C. Between atmospheric pressure and 2.5 GPa, no solid/solid phase transitions are observed for  $\alpha$  RDX.  $\alpha$  phase melt/decomposition is detected between 215-225 °C up to 2.5 GPa. Between 2.5 and 3.8 GPa at 225 °C, a reversible  $\alpha$ - $\beta$  solid/solid phase transition is detected.  $\alpha$  RDX is observed to change to another orthorhombic phase,  $\gamma$ , at about 3.8 GPa at room temperature. The  $\alpha$ / $\gamma$  phase boundary was found to be essentially temperature independent at 3.8 GPa to 225 °C. Above 225 °C, a unidirectional solid/solid phase transition is observed between  $\gamma$  and  $\beta$  RDX up to 7.0 GPa.  $\beta$  RDX melt/decomposition is detected between 225-275 °C and 2.5-7.0 GPa. The  $\beta$  and  $\gamma$  RDX phases may be retrieved to ambient temperature at elevated pressures above 3.8 GPa. At room temperature  $\beta$  and  $\gamma$  RDX transform to  $\alpha$  RDX when the pressure is decreased. The  $\gamma$  phase reverts to the  $\alpha$  polymorph near 3.5 GPa, while the  $\beta$  polymorph reverts to the  $\alpha$  phase as the pressure nears one atmosphere. The thermal decomposition parameters for the  $\alpha$  and  $\beta$  polymorphs are as follows: (1) below 2.5 GPa melt/decomposition of  $\alpha$  RDX is observed and (2) above 2.5 GPa  $\beta$  RDX melt/decomposition is detected. Furthermore, decomposition of  $\alpha$  and  $\beta$  phases is observed at temperatures below the melting curve. The rate of thermal decomposition of  $\alpha$  RDX increases with increasing pressure between 1.4-2.1 GPa. The  $\Delta H^\circ$  for  $\alpha$  RDX is equal to 51 Kcal/mol with an  $\Delta V^\circ$  of -5.6 cc/mol within the same pressure region [4].

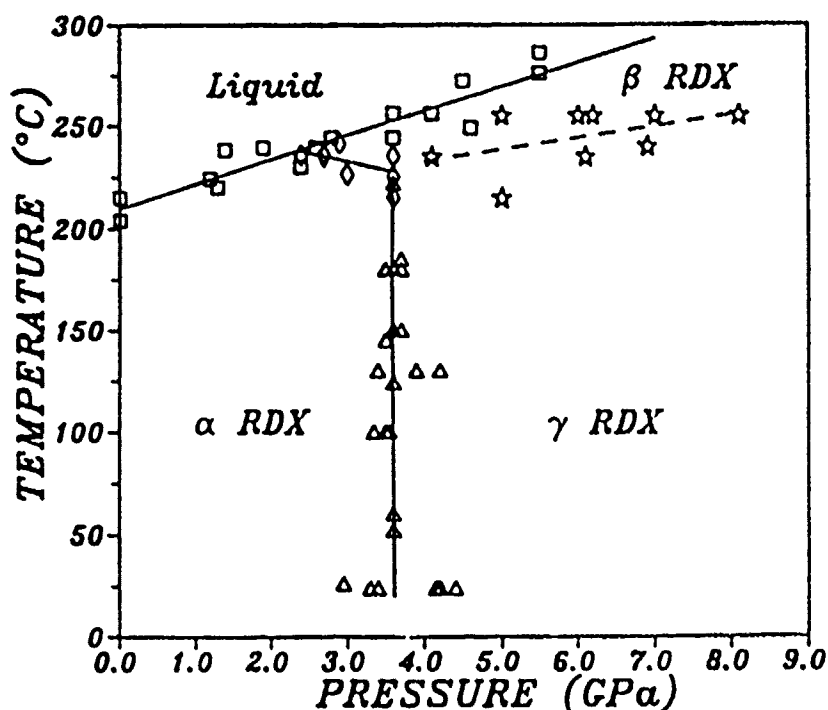


Figure 6. Equilibrium phase diagram for RDX showing the stability fields for three solid phases,  $\alpha$ ,  $\beta$  and  $\gamma$  and the liquidus or melting point.

### Ammonium Dinitramide

A preliminary equilibrium phase diagram for ADN is shown in Figure 7. Two solid ADN phases,  $\alpha$  and  $\beta$ , have been found in the pressure regime up to 10 GPa. The pressure dependence of the melting temperature has been measured. Between atmospheric pressure and 0.9 GPa, melt/decomposition is observed above 95 °C. At room temperature and approximately 2.5 GPa, a solid/solid reversible phase transition between  $\alpha$  and  $\beta$  ADN polymorphs was detected by OPLM, EDXD and Raman spectroscopy. Identification of the high pressure  $\beta$  ADN phase by FTIR spectroscopy was not possible because severe pressure broadening in the infrared absorption spectrum greatly reduced resolution. The temperature dependency of the transition has not been determined. Above 1.0 GPa and 95 °C, melt/decomposition was no longer observed. A solid phase decomposition reaction was detected by a significant change in birefringence in OPLM studies and a corresponding change in the infrared absorption spectra. The solid rearrangement observed at elevated temperatures and pressures has been identified as the conversion of ADN to ammonium nitrate (AN, phase I) and  $N_2O$ . Confirmation of the high temperature AN phase was done by OPLM studies. Upon formation of AN at high pressure and high temperature, the pressure was then decreased to atmospheric. Then, as the temperature was decreased on the sample, all the known temperature dependent phase transitions between phase I and phase IV of AN were observed at their reported transition temperatures [28]. The decomposition parameters for ADN are as follows: (1)  $\alpha$ -ADN melts/decomposes between atm and 0.9 GPa forming AN and  $N_2O$  and (2)  $\beta$ -ADN decomposes via a solid/solid rearrangement to AN (phase I) and  $N_2O$  above 0.9 GPa and 140 °C. These decomposition parameters represent a moderate decomposition rate, i.e., < 5 min. Low temperature, very slow ADN decomposition is also detected at 60 °C at atmospheric pressure [29].

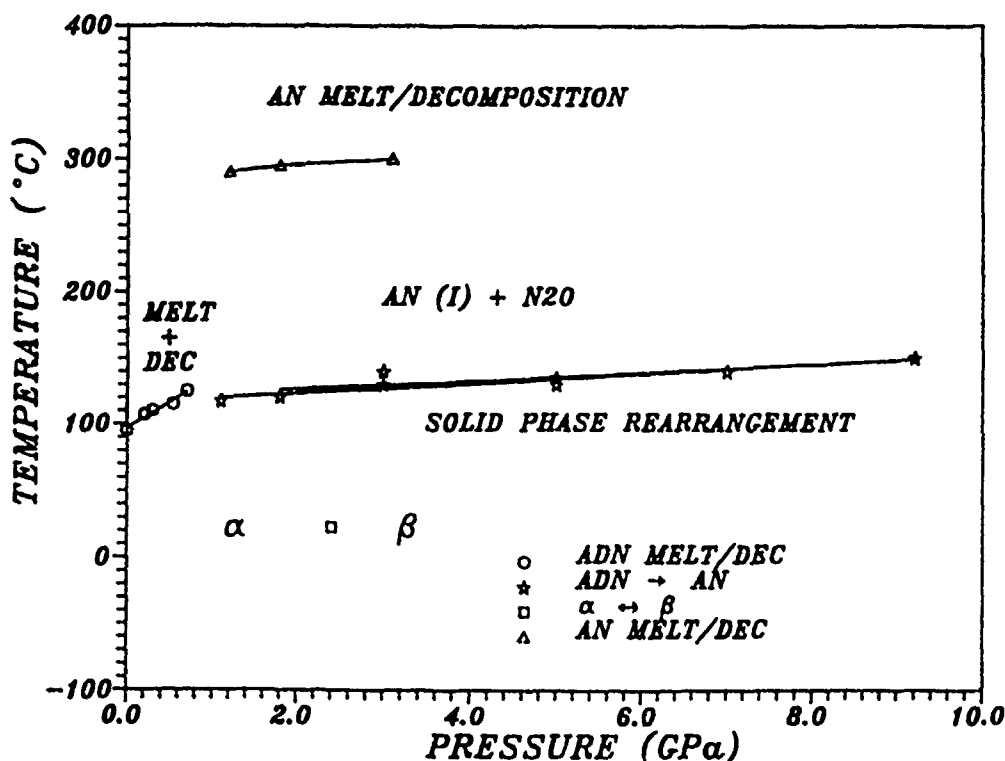


Figure 7. Preliminary Equilibrium/reaction phase diagram for ADN, indicating the reversible  $\alpha \leftrightarrow \beta$  ADN transition at room temperature, the liquidus or melting point, and the solid state conversion to AN (I) and  $N_2O$ .

### p-Nitroaniline

The equilibrium/reaction phase diagram for p-nitroaniline is shown in Figure 8. Three solid phases for PNA (I, II, and III) have been identified. The liquidus of Phase I has been measured from atmospheric pressure to 1.0 GPa and 150-240 °C. During melting the PNA undergoes a chemical reaction, becoming dark and leaving a reddish-brown residue. Between 1.0-4.0 GPa and above 140 °C, a reversible phase transition, I  $\leftrightarrow$  II, is detected. Above 245 °C, melting is not observed for phase II. Phase II decomposes above 245 °C between 1.0 and 4.0 GPa. Between 0.0-25 °C at 4.0 GPa, another reversible solid/solid phase transition, I  $\leftrightarrow$  III, has been identified. Thus, in the P, T domain studied, there appears to be three solid forms of p-nitroaniline, I, II, and III. Phases II and III, upon release of pressure revert to form I, which is the stable form at ambient conditions of pressure and temperature. The decomposition parameters for PNA are as follows: (1) below 1.0 GPa, I melts and decomposes between 140 and 245 °C, (2) between 1.0-4.0 GPa and above 245 °C, II decomposes, and (3) above 4.0 GPa and 245 °C, a black amorphous material is formed during decomposition. However, at this time it is not known whether phase II or phase III is decomposing.

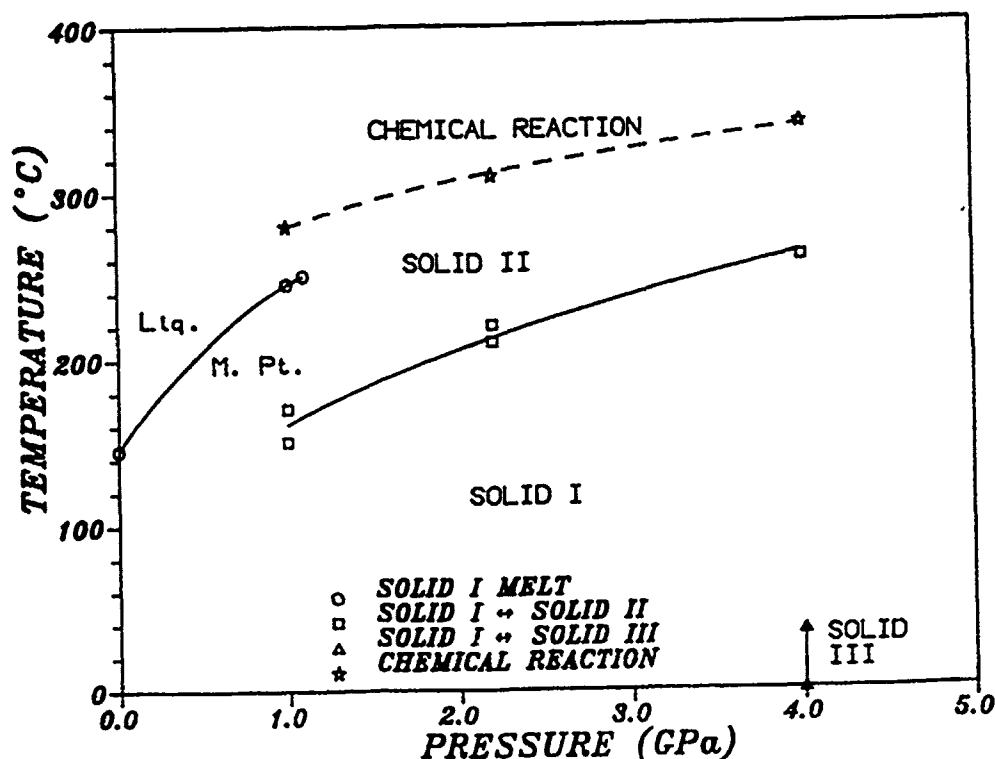


Figure 8. Equilibrium phase diagram for PNA, indicating the stability fields for the three known polymorphs (I, II, and III), the liquidus or melting point, and the solid state chemical reaction between 1.0 and 4.0 GPa above 280°C.

### ACKNOWLEDGMENTS

The authors wish to acknowledge financial support from the U.S. Army Research Office, the Office of Naval Research and the Naval Surface Warfare Center Independent Research Program.

## REFERENCES

\* Certain trade names and or products are mentioned in the text in order to adequately specify the experimental procedure and equipment used. In no case does such identification imply recommendation or endorsement by NIST nor does it imply that the product necessarily is the best available for the purpose.

1. Y. M. Gupta, Shock Compression of condensed Matter, edited by S. C. Schmidt, R. D. Dick, J. W. Forbes, and D. G. Tasker (Proceedings of the American Physical Society Topical Conference, Williamsburg, VA, 1991) pp. 15 and all included references.
2. T. P. Russell, P. J. Miller, G. J. Piermarini, S. Block, J. Phys. Chem, **96**, 5509 (1992).
3. T. P. Russell, P. J. Miller, G. J. Piermarini, S. Block, J. Phys. Chem., (in press).
4. G. J. Piermarini, S. Block, P. J. Miller, The Chemistry and Physics of Energetic Materials, ed. by S. Bulusu, (NATO Advanced Study Institute, **309**, Altavilla Milicia, Sicily, September 3-15, 1989), pp. 369-412.
5. Barnett, J. D.; Block, S.; Piermarini, G. J., Rev. Sci. Instrum., **44**, 1 (1973).
6. G. J. Piermarini, S. Block, J. D. Barnett, and R. S. Forman, J. Appl. Phys., **46**, 2774 (1975).
7. Block, S.; Piermarini, G. J., Physics Today, **29**, 44 (1976).
8. P. J. Miller, G. J. Piermarini, S. Block. Appl. Spectrosc., **38**, 680 (1984).
9. P. J. Miller, S. Block, G. J. Piermarini, Combustion and Flame, **83**, 174 (1991).
10. G. J. Piermarini, S. Block, J. D. Barnett, J. Appl. Phys., **44**, 5377 (1973).
11. F. A. Mauer, S. Block, G. J. Piermarini, American Crystallographic Association, Program and Abstracts of Summer Meeting, Boston University, Boston, MA Aug 12-17, Paper G3 (1979).
12. C. E. Weir, E. R. Lippincott, A. Van Valkenburg, and E. N. Bunting, J. Research NBS, **63A**, 55 (1959).
13. J. C. Jamieson, A. W. Lawson, N. D. Nachtrieb, Rev. Sci. Instrum., **30**, 1010 (1959).
14. G. J. Piermarini and C. E. Weir, J. Research NBS, **66A**, 325 (1962).
15. W. A. Bassett, A. T. Takahashi, and P. W. Stook, Rev. Sci. Instrum., **38**, 37 (1967).
16. H. K. Mao, and P. M. Bell, in Carnegie Institution of Washington Year Book, **77**, 904 (1978).
17. K. R. Hirsh and W. B. Holzapfel, Rev. Sci. Instrum., **52**, 52 (1974).
18. L. Merrill, and W. A. Bassett, Rev. Sci. Instrum., **45**, 209 (1974).

19. T. P. Russell and G. J. Piermarini, presented at the FT-Raman Vibrational Spectroscopy Workshop, Bethesda, MD, May 1992 (unpublished), T. P. Russell and G.J. Piermarini, (to be published).
20. B. C. Giessen and G. E. Gordon, *Science*, **159**, 973 (1968).
21. L. M. Albritton and J. L. Margrave, *High Temperatures-High Pressures* **4**, 13 (1972).
22. B. Buras, J. Staun Olsen, L. Gerward, B. Selmark, and A. Lindegaard Andersen, *Acta Cryst.*, **A31**, 327 (1975).
23. T. P. Russell, G. J. Piermarini, and S. Block, presented at ONR Workshop on ADN, Arlington, VA, Feb. 1992 (unpublished), T. P. Russell, and G. J. Piermarini, S. Block, (to be published).
24. S. Block and G. J. Piermarini, *SPIE*, **878**, 21 (1988).
25. R. Y. Yee, M. P. Nadler, A. T. Neilson, JANNAF Proceeding, CPIA publication, October 1990.
26. K. J. Kraeutle, JANNAF Proceedings, CPIA publication #498, October 1988.
27. K. J. Kraeutle, JANNAF Proceedings, CPIA publication, November 1990.
28. P. W. Bridgman, *Proc. Amer. Acad. Arts Sci.* **51**, 581 (1916).
29. T. P. Russell, A. W. Stern, W. Koppes, and C. D. Bedford, JANNAF Proceedings, CPIA Publication #593, October 1992.

## THE GROWTH AND PERFECTION OF SINGLE CRYSTALS OF TRINITROTOLUENE (TNT)

HUGH G. GALLAGHER AND JOHN N. SHERWOOD

University of Strathclyde, Department of Pure and Applied Chemistry, 295 Cathedral Street, Glasgow G1 1XL, Scotland, UK.

### ABSTRACT

A study has been made of the crystal growth behaviour and perfection of TNT. Depending on the purity and the solvent used, crystallisation from solution yields material of monoclinic, twinned monoclinic or orthorhombic forms. Of these only the monoclinic form was suitable for detailed study by X-ray topographic techniques. The crystals of the orthorhombic form were too small and imperfect for examination.

Seeded growth from ethyl acetate solution yielded lamellar twinned crystals in which the twin density was low. Under ideal conditions, relatively perfect samples could be obtained in which the dominant residual growth defects were stacking faults of Burgers vector  $b^{1/2}$  [001] and dislocations.

### INTRODUCTION

In common with other molecular solids, the physical, chemical and mechanical properties of solid explosives are influenced by lattice defects. It is hardly surprising, therefore, that crystal imperfections are believed to play a role in the initiation and subsequent decomposition of energetic materials [1]. The impact initiation of crystalline explosives is generally accepted to occur by conversion of the mechanical energy of impact into heat within small volumes of the solid known as hot spots. Several mechanisms involving dislocation slip which occurs during the plastic deformation which accompanies impact have been proposed to explain the formation of these "hot-spots" [2]. Little is known however about the nature of defects in these materials on which to base reasonable theoretical models. In order to redress this situation, a detailed study of the properties of growth and mechanically induced defects in a number of organic energetic materials has been undertaken [3,4]. The work reported here is an abbreviated description of the initial stages in the assessment of one of these materials trinitrotoluene (TNT) [5].

### CRYSTALLISATION OF TNT

TNT is known to crystallise in two basic polymorphic forms [6]

orthorhombic  $Pb2_1a$   $a = 15.005$  Å,  $b = 20.024$  Å,  $c = 6.107$  Å

monoclinic  $P2_1/c$   $a = 21.275$  Å,  $b = 6.093$  Å,  $c = 15.025$  Å,  $\beta = 110.23^\circ$

Depending on the conditions imposed, it is reported that these may crystallise separately or even simultaneously as complex mixed phase crystals. Despite intensive investigations, however, the conditions for the crystallisation of the various structural modifications have not yet been clearly defined. In order to prepare crystals suitable for examination by X-ray topography, it was necessary first of all to define the nature of polymorphism in TNT crystallised from solution.

Crystals of high optical quality were grown from a wide range of organic solvents by the slow evaporation of saturated solutions. The structural nature and perfection of these crystals were systematically determined using various x-ray diffraction techniques.

The crystals were found to exist in three basic forms: monoclinic, orthorhombic and twinned monoclinic depending on the crystallising solvent. The crystallisation results are summarised in table 1. Subsequent examination revealed that the orthorhombic polymorph is metastable under ambient conditions and transforms to the monoclinic form over a period of time. On raising the temperature the transformation is instantaneous at 344 K. The monoclinic form was found to be stable up to the melting point, 354 K.

The synchrotron radiation source proved to be extremely useful for the characterisation of the twinned and untwinned monoclinic crystals.

TABLE 1

The Influence of Crystallization Solvent on the Morphology of TNT Crystals

Solvent	Habit*	Colour	Polymorph	Twinned
Ethylacetate	L.	Faint Yellow	Monoclinic	Yes/No
Methanol	N. R. P.	Dark Amber	Monoclinic	Yes
Toluene	P.	Yellow	Monoclinic	Yes
Acetone	N. R. P.	Amber	Monoclinic	Yes
Ethanol	N. R. P.	Amber	Orthorhombic	-
Cyclohexanol	N. R. P.	Amber	Orthorhombic	-

\* L. = Lozenge; N. = Needles; R. = Rods; P. = Plates.

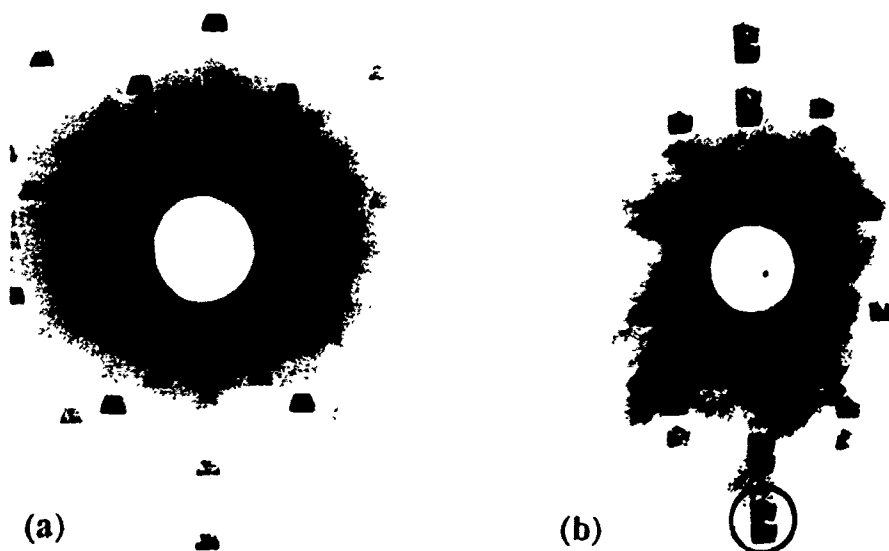
#### SYNCHROTRON X-RADIATION STUDIES OF TWINNING

The broad spectral range and low beam divergence available at the UK Synchrotron Radiation Source, Daresbury Laboratory is ideal for the study of twinned structures such as those found in TNT. Due to the large diameter of the beam (2 cm) full crystal Laue diffraction patterns can be taken in which each spot is a full topographic image of the crystal [7]. Since a twinned crystal consists of regions of identical crystallographic structure arranged in different symmetrically related orientations, then the diffraction pattern records simultaneously the diffraction pattern of each twin. Where the degree of twinning is low this enables the positions of each twin in the crystal to be identified and at the same time it allows an assessment to be made of the overall defect concentration and configuration.

The diffraction patterns of both a twinned and untwinned crystal of the monoclinic phase taken with the synchrotron beam normal to the basal (100) plane are shown in Figure 1. From the symmetry of the pattern for the twinned crystal, the twin law can be defined as  $180^\circ$  rotation about an axis normal to the (100)

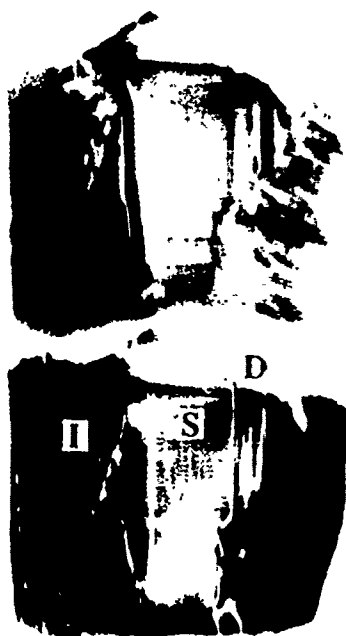


Figure 1



Full Crystal Laue Diffraction Patterns of TNT crystals  
taken using Synchrotron Radiation  
(a) Untwinned Crystal; (b) Singly twinned Crystal

Figure 2



Enlargements of the two twin images circled on Figure 1  
showing the different defect structures in the two lamellae:  
I, strain due to impurity incorporation; D, dislocations; and S, stacking fault.  
The upper surface is a fracture surface and not a habit face.

plane. To illustrate the detail in the diffraction images, an enlarged pair of twin reflections are shown in Figure 2. These clearly show the differences in the defect structure of the separate twin lamellae.

Similar diffraction patterns taken of sections of the crystals cut perpendicular to the (100) plane and with the synchrotron beam normal to the (010) plane, provide information on the distribution of the twin layers in depth and thus allow the full characterisation of the specimen. In this way, by study of the varying twin structure of crystals grown under a range of growth conditions, the conditions for the preparation of untwinned crystals can be defined.

### SINGLE CRYSTAL GROWTH AND PERFECTION

Large crystals of the stable monoclinic form of TNT were grown from ethyl acetate solutions by the slow cooling of seeded saturated solutions. Temperature lowering rates lay in the range  $0.003 - 0.01 \text{ K/hr}^{-1}$  over the temperature range 302-309 K.

X-ray transmission topography [8] of the crystals showed them to have a characteristic growth induced defect structure in which the overall perfection is determined by the incorporation of residual impurities into the lattice. Regions of high impurity concentration are strained and appear as a dark contrast on the topographs. This is well exemplified by the topographs shown in Figure 2. Several points should be noted

- the lateral growth sectors are highly strained due to the preferential incorporation of the impurities into these sectors compared with the extended growth sectors.
- the deviations in the trajectory of the boundary between the lateral and the extended growth sectors reflect changes in the relative growth rates of the faces associated with these sectors. One explanation of this is that impurities absorbed onto one of the growing faces inhibits its growth rate. The observation that these changes are frequently accompanied by growth banding in the sectors supports this view.
- linear (dislocations) and planar (stacking faults and twins) defects are generated at solvent inclusions which are trapped in the vicinity of the seed.

The dominant growth defects in high quality crystals of TNT are stacking faults, dislocations and twins. In Figure 2, the stacking fault is visible as a wedge shaped area of uniformly dark contrast bordered by well-defined lines of even greater contrast. This type of defect contrast is characteristic of stacking faults bounded by partial dislocations. Occasionally dislocations are observed but they are usually fewer in number than the other defects.

Characterisation of the topographic images using the techniques of extinction contrast [8] showed that the predominant strain vector associated with the stacking faults was  $b [001]$ .

## ACKNOWLEDGEMENTS

We gratefully acknowledge the financial support of this work by the US Office of Naval Research, Washington.

## REFERENCES

1. J.E. Field, N.K. Bonner, S.J.P. Palmer and S.M. Walley, *Phil. Trans. Roy. Soc. A329*, 269 (1992)
2. C.S. Coffey, *Phys. Rev. B24*, 6984 (1981); C.S. Coffey and S.J. Jacobs, *J. Appl. Phys.* **52** 6991 (1981); C.S. Coffey and R.W. Armstrong, Shock Waves and High Strain Rate Phenomena in Metals, edited by M.A. Myers and L.E. Murr (Plenum, NY, 1981) p. 313.
3. P.J. Halfpenny, K.J. Roberts and J.N. Sherwood, *J. Appl. Cryst.* **17**, 320 (1984); *J. Crystal Growth* **67**, 202 (1984); *J. Materials Sci.* **19**, 1629 (1984).
4. H.G. Gallagher, P.J. Halfpenny, J.C. Miller and J.N. Sherwood, *Phil. Trans. Roy. Soc. A299*, 293 (1992).
5. H.G. Gallagher and J.N. Sherwood, to be published, 1993.
6. C.R. Duke (private communication).
7. A.R. Gerson, P.J. Halfpenny, S. Pizzini, R.I. Ristic, K.J. Roberts and J.N. Sherwood, Materials Science and Technology - A Comprehensive Treatment, edited by R. Cahn and E. Lifshin (VCH, Weinheim, 1992) p. 557.
8. A.R. Lang, Diffraction and Imaging Techniques in Materials Science, edited by S. Amelinckx, R. Gevers, G. Rimaux and J. van Landuyt, N. Holland, Amsterdam, 1978) p. 623.

## ATOMIC FORCE MICROSCOPY OF AMMONIUM PERCHLORATE

MINSUN YOO, SEOKWON YOON, AND ALEX DE LOZANNE  
Department of Physics, University of Texas, Austin, TX 78712-1081, USA

### ABSTRACT

We have studied the (210) surface of ammonium perchlorate ( $\text{NH}_4\text{ClO}_4$ ) with an atomic force microscope (AFM) in air. Large scale images show monomolecular steps that are often aligned with major crystalline directions. Surface modification is clearly observed with forces as low as 30 nN, but is usually limited to the bottom and the sides of the field of view, where the tip scans for a long time and where it turns around, respectively. At the molecular scale we have observed structures with substantial order, with minimum lateral sizes of 3 Å. The identification of these features is difficult due to the large unit cell of this compound (40 atoms per unit cell), and the lack of perfect order in the images. We use the SARCH/LATUSE program developed by Van Hove and Hermann to analyze this structure. Ammonium perchlorate is hygroscopic; it is therefore possible that surface modification is enhanced by the moisture present in air. Experiments in a dry atmosphere have confirmed this explanation. We have therefore designed and built a UHV (ultra-high vacuum) AFM for these studies. The first images from this instrument are presented here.

### INTRODUCTION

Energetic crystals have been used in many applications for decades, some even have been utilized for centuries. Yet the basic mechanisms for the initiation of the exothermic reaction in these materials is not known. A large amount of empirical data exists, but a detailed understanding of what happens at the molecular level is lacking. Our long term goal is to contribute to this understanding by probing the structure of these materials down to the molecular level, and by attempting to initiate and study reactions within a microscopic volume.

Most energetic crystals are insulating; it is therefore not possible to study them with the electron-based microscopies that yield the highest resolution, namely Transmission Electron Microscopy and Scanning Tunneling Microscopy. The Atomic Force Microscope (AFM), invented by Binnig, Quate and Gerber[1], is the only instrument that can image insulators with high resolution, in some cases even atomic resolution. We have used the AFM to study crystals of ammonium perchlorate, RDX, and TATB. Thus far the most interesting results have been obtained with ammonium perchlorate, which we present here.

### CRYSTAL STRUCTURE

Ammonium perchlorate ( $\text{NH}_4\text{ClO}_4$ , denoted as AF hereafter) is an insulator with an orthorhombic unit cell of dimensions  $a=9.202\text{Å}$ ,  $b=5.816\text{Å}$ , and  $c=7.449\text{Å}$ , and Pnma space group.[2] Each unit cell contains four ammonium ions and four perchlorate ions, as illustrated in fig. 1, for a total of 40 atoms per unit cell. At room temperature the ammonium ions rotate as a single unit about their location in the unit cell.[3] We have used the SARCH/LATUSE program developed by Van Hove and Hermann[4] to analyze this crystal structure. In all our crystal diagrams the ammonium ions are drawn as the largest spheres, followed by medium spheres for the chlorine atoms and small spheres for oxygen

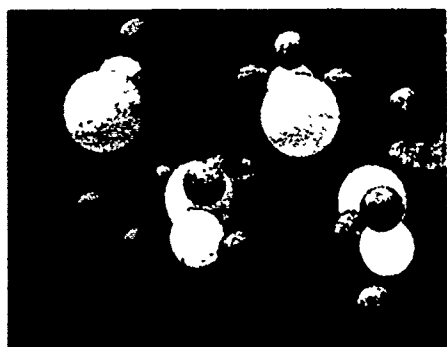


Figure 1. A perspective view of the atoms in a unit cell of  $\text{NH}_4\text{ClO}_4$ . The largest spheres represent the rotating ammonium ions, the next largest are chlorine atoms, and the smallest are oxygen atoms. The unit cell dimensions are  $a=9.202\text{Å}$  (to the right),  $b=5.816\text{Å}$  (up), and  $c=7.449\text{Å}$  (out of paper). Four  $\text{NH}_4\text{ClO}_4$  molecules are contained in the unit cell, for a total of 40 atoms. Figures 1-3 were generated with the SARCH/LATUSE program[4].

atoms. Our results for the (100), (010) and (001) projections agree with the diagrams published by Williams et al.[5]. For the sake of brevity we show only the (001) projection in figure 2, since it will be helpful in visualizing the AFM data that follows.

We have studied the (210) surface of AP, since it is a natural cleavage plane. It is not known, however, which of the many parallel (210) planes is actually exposed during cleaving. We now discuss which plane is most likely to be exposed.

The (210) planes are perpendicular to the plane of figure 2 and they intersect it along the diagonal lines shown. A crystal may cleave along these lines or along any other parallel plane. This structure has ten inequivalent (210) planes (going through the nuclei), with a  $d$  spacing of 3.608Å. It is difficult to predict which of these planes will be exposed when the crystal is cleaved. A reasonable possibility is that the cleave occurs between planes that have the largest spacing between them and the least number of molecular bonds crossing the plane. The distance between inequivalent (210) planes is, in decreasing order, 0.801Å, 0.793Å, 0.638Å, 0.328Å, 0.028Å, and 0.010Å (the last four spacings occur twice). The diagonal lines in figure 2 are midplanes between planes separated by the largest distance, 0.801Å. This is also a good choice for a cleavage plane because there are no strong bonds crossing these planes: all perchlorate ions and all ammonium ions are completely on one side or the other. This is therefore likely to be a weakly bonded plane, which would be most likely to cleave. Taking this plane to be the cleaved surface, we make a (210) projection showing only the atoms within the slab bound by the two equivalent (210) midplanes in figure 2. The thickness of this slab is 3.608Å (same as the  $d$ -spacing). This slab shows a good symmetry, which we have not observed in any other parallel slabs that we have studied. The depth of the slab is about the deepest that one would expect to see with the AFM, taking into account that the typical lateral spacing of the structure is also about 3 Å. For simplicity, a possible surface reconstruction will not be considered here.

We note that our result for the (210) projection is different from the one published in ref. 6. The main difference is that they obtained a (210) surface unit cell that is 7.42Å along the  $\langle 001 \rangle$  direction, as one would expect from the crossing of a (210) plane through a single bulk unit cell (this gives a length along  $\langle 120 \rangle$  of  $(b^2 + (a/2)^2)^{1/2} = 7.416\text{Å}$ ). A careful analysis of this geometry, however, shows that the (210) surface unit cell should cross two bulk unit cells along the  $\langle 120 \rangle$  direction, thus giving a cell length of  $2 \times 7.416\text{Å} = 14.832\text{Å}$ . The (210) surface unit cell should therefore be 14.832Å along  $\langle 120 \rangle$  by 7.449Å along  $\langle 001 \rangle$ , which agrees with the result of the SARCH/LATUS program.



Figure 2. Projection of the AP crystal along (001). Three unit cells are drawn in each direction. The  $a$ -axis ( $a=9.202\text{Å}$ ) is horizontal and the  $b$ -axis ( $b=5.816\text{Å}$ ) is vertical. The two diagonal lines indicate the intersection of two (210) planes (which are perpendicular to the paper) with the plane of the figure. The atoms contained between these two planes are projected onto the (210) surface in figure 3. The different atoms are identified as in fig. 1.

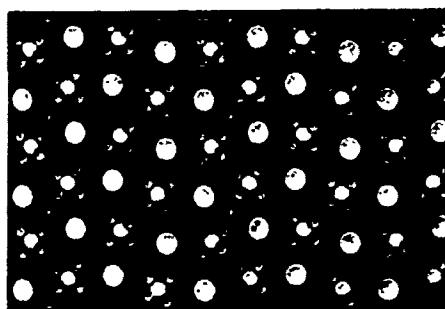


Figure 3. Projection of the AP crystal along (210). The  $\langle 120 \rangle$  axis is horizontal and the  $c$ -axis is vertical. The boxes mark two unit cells ( $14.832\text{Å} \times 7.449\text{Å}$  each). The different atoms are identified as in fig. 1.

## EXPERIMENTAL RESULTS IN AIR

The sample was cleaved to expose a fresh (210) face and was immediately imaged in air with a Park Scientific Instruments AFM (SFM-BD2) using a cantilever with dimensions  $L=100\mu\text{m}$ ,  $w=10\mu\text{m}$ , and  $t=0.6\mu\text{m}$ , and a spring constant of approximately  $0.08\text{N/m}$ . Images were obtained in the repulsive mode with a constant lever deflection of  $0.52\mu\text{m}$ , thus yielding profiles with an equal force of approximately  $42\text{nN}$ . There may be additional forces between the tip and the sample (e.g. electrostatic, or surface tension of the adsorbed water layer on the tip and the sample); we plan to measure these possible additional forces in the future. Figure 4 shows a representative image of the (210) surface on a scale of  $5\text{nm}$  on a side. The usual precautions were taken to ensure the validity of the data, namely changing the image size, the scanning frequency and scanning rotation. The interpretation of these images is complicated by the large size of the unit cell and the possibility of cleaving through various parallel planes. The image in figure 4 has a scale and symmetry similar to the (210) projection in figure 3. Unfortunately, irregularities in the data and the complexity of the surface unit cell prevent us from making a definite assignment of each feature in the image at this time.

Figure 5 shows very interesting patterns formed by the scanning tip. Trenches are dug around the side edges, where the tip turns around as it scans back and forth, or the top and bottom edges, where the tip scans repeatedly while waiting to take a new image. As larger images are taken in the same area, the trenches created by the previous image are clearly seen. The depth of the trenches is usually a multiple of the  $d$  spacing for (210) planes, namely  $N \times 3.6\text{\AA}$ . Other natural steps with similar heights are observed to run along nearly straight lines at various angles. The deviations from linearity are probably due to scanner distortion, which is common in images of this size. The angles are likely to be major crystalline directions. Indeed, a comparison with figure 4 shows that the step in the upper right corner runs exactly along one of the atomic (or molecular) rows. Another example is the straight step in the lower half (running  $20$  degrees counterclockwise from horizontal). The height of all these steps is the same. Finally, the holes in the upper right corner grew as the image was taken, while most of the other features remained unchanged, indicating that certain regions are more susceptible to mechanical damage.

An important parameter in the deformation of the surface is the pressure exerted. Taking the force estimated above ( $42\text{nN}$ ), and estimating the contact area to be the square of the width of the trenches observed ( $38\text{nm}$ ), a lower limit for the pressure is about  $29\text{MPa}$ . If the contact area is taken to be  $1\text{nm}^2$  (assuming contact over one molecule), then the upper limit is about  $40\text{GPa}$ , which is clearly an overestimate (the ultimate strength of steel is  $0.4\text{GPa}$ ).

Given that the tip modifies the surface, it is difficult to understand how an image with molecular resolution, like Fig. 4, can be obtained. We can only emphasize that such images are obtained immediately after cleaving, and that the surface modification is due to softening caused by adsorbed water, as is discussed in the next section. Furthermore, the understanding of atomic resolution in the AFM, given the large pressures exerted, is still in its infancy.



Figure 4. AFM image taken at constant force of approx.  $42\text{nN}$ , with a lateral size of approx.  $5\text{nm}$ .



Figure 5. AFM image taken at constant force of approx.  $42\text{nN}$ , with a lateral size of approx.  $2\mu\text{m}$ . Clear evidence of surface modification is observed, as well as natural steps.

## EFFECTS OF MOISTURE

Now we turn to recent measurements on the effects of ambient moisture on the surface modification of AP. Moisture was controlled by putting silica gel desiccant inside the AFM head before loading the sample. The sample was cleaved with a blade and immediately imaged using a cantilever with dimensions  $L=100\mu\text{m}$ ,  $w=10\mu\text{m}$ , and  $t=0.6\mu\text{m}$ , and a spring constant of approximately  $0.08\text{N/m}$ . Images were obtained in the repulsive mode with a constant lever deflection of  $0.52\mu\text{m}$ , thus yielding profiles with an equal force of approximately  $42\text{nN}$ . We observed no evidence of surface modification. We then removed the desiccant and continued taking data. Still, there was no surface modification: apparently it takes some time for the surface to absorb water and become soft. We increased the probing force to  $0.5\mu\text{N}$  by using a lever with  $k=.21\text{N/m}$  at a deflection of  $2.5\mu\text{m}$ . Eventually we observed surface modification, as shown in the sample image of figure 4. The modification seemed to be a function of the total time that the surface was exposed to moisture, and not related to the increase in force. To confirm this conjecture, we put the desiccant back into the AFM head. Again, no immediate change was seen, as we were still able to modify the surface. Over the period of one hour the ability to modify the surface was lost, indicating that moisture was removed.

To further study the effects of moisture we built a simple chamber for the air AFM. The chamber is pumped by a mechanical pump and backfilled with dry nitrogen. The



Figure 6. All three images are  $1.2\mu\text{m}$  on a side and were taken after scanning images of  $1/2$ ,  $1/4$ , and  $1/8$  of this size. Surface modification is observed clearly in the center image, which was taken after exposure to ambient moisture. The center of the image shows the areas scanned before this image was taken. The left image was taken with desiccant in the AFM head and a fresh cleave, while the image on the right was taken after the exposure to moisture but with desiccant again present.



Figure 7: AFM images of AP obtained in a dry nitrogen atmosphere. The image on the left, which is  $1.3\mu\text{m}$  on a side, shows very interesting steps, while the one on the right is  $13\text{ nm}$  in size and shows molecular resolution.

sample was cleaved immediately before mounting in the AFM and pumping down. The surface degradation is no longer observed in dry nitrogen, even two weeks after cleaving the sample. Clear steps are observed on this surface, as shown in Fig. 7a, while molecular resolution is not as clear as before, as shown in Fig. 7b.

We have observed other interesting effects on AP surfaces. For example, on a few images there is a popping noise that we have not observed with any other samples. An exciting possible explanation is that the tip causes local decomposition of AP, causing a localized exothermic reaction which kicks the AFM tip off the surface. Further study of these effects will be done in a more controlled environment, namely ultra high vacuum.

## ULTRA HIGH VACUUM ATOMIC FORCE MICROSCOPE

The deleterious effects of water on the surface of AP, as shown above, and the desire to study surface decomposition have motivated us to design and build a UHV AFM, since commercial instruments are not yet available. Furthermore, even if the surface of the sample is not soluble in water (like RDX and TATB), the capillary forces caused by layers of water adsorbed on the tip and sample reduce the force resolution and therefore degrade the spatial resolution of the AFM. We discuss briefly the design philosophy of our UHV AFM and demonstrate that it operates well. A full description will be published elsewhere.

The force between the tip and the sample is measured by monitoring the deflection of a microfabricated cantilever that holds the tip, a standard technique in AFM. The deflection is measured by bouncing a laser beam on the cantilever and onto a position sensitive detector. We use a He-Ne laser outside the UHV chamber, coupled to a single mode optical fiber that goes through a homemade UHV feedthrough into the chamber. The fiber ends with a sharpened cone within 20  $\mu\text{m}$  of the cantilever. We have developed an accurate and very compact positioning device to align the fiber with the cantilever. The sample is scanned in three axes with a standard piezoelectric tube scanner[7]. The coarse approach between the tip and sample is accomplished with a standard tripod of fine-threaded screws. The AFM body hangs inside the UHV chamber from soft springs. A custom window on the side of the chamber allows viewing of the tip and sample area from a distance of only 8 mm, which allows the use of an optical microscope with a high magnification of 400x.

The first test and calibration of this instrument was done in air. More recently we have demonstrated operation in vacuum. Figure 8 shows an AFM image obtained in vacuum of a test grating with a period of 1.9  $\mu\text{m}$ . In addition to the clear ripples of the grating, the image has details of imperfections on some ripples, indicating high resolution. Graphite samples will be used in the near future to test for atomic resolution.

## CONCLUSIONS

We have obtained AFM images of the (210) surface of ammonium perchlorate ( $\text{NH}_4\text{ClO}_4$ ) ranging from 5 nm to 12  $\mu\text{m}$  in size. We have observed surface features with a resolution of 3  $\text{\AA}$ , which is the first time for this material. While the size and overall structure is similar to what is expected, based on previous information about the bulk lattice, a definite assignment of features to atoms is not yet possible. Monomolecular steps are observed for the first time. Surface modification is clearly observed, which is almost certainly due to softening of the surface as it absorbs moisture from the air. Tests with desiccant and in a dry nitrogen atmosphere have confirmed this hypothesis. A novel design for a UHV AFM was implemented, built and tested. This UHV AFM should achieve higher resolution on ammonium perchlorate, TATB, RDX and CI-20.



Figure 8. AFM image obtained with a new UHV AFM operating in vacuum. The image is 12  $\mu\text{m}$  on a side; the grating has a period of 1.9  $\mu\text{m}$  and a vertical modulation of 0.5  $\mu\text{m}$ .



## ACKNOWLEDGEMENTS

We thank J. Sharma for providing AP samples as well as a wealth of basic information about this material. This work is supported by the U.S. Office of Naval Research (N00014-90-J-1858).

## REFERENCES

- [1] G. Binnig, C. F. Quate, and Ch. Gerber, *Phys. Rev. Lett.*, **56**, 930 (1986).
- [2] R.W.G. Wyckoff, *Crystal Structures*, vol. 3 (Interscience, New York, 1963) p.48
- [3] H.G. Smith and H. A. Levi, *Acta Cryst.* **15**, 1201 (1971).
- [4] SARCH/LATUSE 3.0, developed by M.A. Van Hove, Department of Chemistry, UC Berkeley, Berkeley, California 94720, USA (BITNET vanhove@LBL) and K. Hermann, Havelmatensteig 21, D-1000 Berlin 22, Fed. Rep. of Germany (BITNET: hermann@vax.hmi.dbp.de)
- [5] J.O. Williams, J.M. Thomas, Y.P. Savintsev, and V.V. Boldyrev, *J. Chem. Soc. A11 (Inorg. Phys. Theor.)*, 1757 (1971).
- [6] P.J. Herley, P.W.M. Jacobs, and P.W. Levy, *J. Chem. Soc. A11 (Inorg. Phys. Theor.)*, 434 (1971).
- [7] G. Binnig and D. P. E. Smith, *Rev. Sci. Instrum.*, **57**, 1688 (1986).

## ENERGETIC CRYSTAL-LATTICE-DEPENDENT RESPONSES

R.W. ARMSTRONG\*, H.L. AMMON+, Z.Y. DU+, W.L. Elban#, X.J. ZHANG\*  
 \*Department of Mechanical Engineering or +Department of Chemistry  
 and Biochemistry, University of Maryland, College Park, MD 20742.  
 #Dept. Engineering Science, Loyola College, Baltimore, MD 21210.

### ABSTRACT

The occurrence of [100] direction slip on the (02 $\bar{1}$ ) slip plane of orthorhombic RDX (cyclotrimethylenetrinitramine, [CH<sub>2</sub>N·NO<sub>2</sub>]<sub>3</sub>) is shown to favor the formation of 1,3-dinitroso-5-nitro-1,3,5-triazacyclohexane, as detected in drop-weight impact tests at sensitivity height levels near to those measured for initiation. Also, the reported observation of deformation twinning in the chemically-related monoclinic HMX (cyclotetramethylenetetranitramine, [CH<sub>2</sub>N·NO<sub>2</sub>]<sub>4</sub>) crystal lattice is explained on the basis of the greater flexibility of the larger HMX molecule allowing a number of bond rotations that are required to produce a relatively unusual Type II deformation twinning structure. These examples give support to the consideration that on the molecular level involved in deformation-induced decompositions there may be a direct mechanical force aspect that is additional to the established importance of "hot spot" heating, say, as described for dislocation pile-up avalanches in RDX.

### RDX HOT SPOT AND "BOND-BREAKING" DEFORMATIONS

Armstrong, Coffey, DeVost and Elban [1] have given a detailed description of the generation of hot spots in RDX at the slip band level in individual crystal particles of powder samples subjected to drop-weight impact testing. Hot spots were proposed to occur at dislocation pile-up avalanches that are produced when microslip bands break through blocking obstacles between, or possibly within, the crystals. The hottest spots occur when an avalanche is released after the microstructural stress intensity for brittle fracturing is achieved. Alternatively, RDX and related energetic crystals are observed experimentally to be relatively hard and brittle so that little plastic flow normally occurs on a macroscopic scale before considerable shattering of crystals is produced under the action of impact forces leading to the initiation of fast decomposition.

The strength properties of RDX, relative to those of a number of other materials, are illustrated in the microindentation elastic/plastic/cracking results [2] shown in Figure 1 on a continuous indentation stress/strain basis [3]. An increasing elastic stiffness for the labelled materials is indicated by the higher ordinate (hardness) stress values of the initial linear Hertzian lines shown at each value of the effective strain defined by the contact-diameter-to-ball-diameter ratio on the abscissa scale. Thus RDX is seen to be elastically more compliant than NaCl. However, the plastic hardness of RDX, shown in Figure 1 both for a number of points on a continuous indentation deformation basis or for the Vickers diamond pyramid hardness (VHN) value shown at an effective strain of 0.375 for the same range of materials, reveals that RDX is more than twice as hard as NaCl. In addition, the hardness of RDX is shown in Figure 1 to be relatively high compared to a theoretical cracking

stress that is put at the terminal points for different indenting ball diameters on the RDX and other material elastic loading lines, as evaluated on an indentation fracture mechanics basis. The comparison of properties shows that RDX, though elastically compliant is relatively hard and brittle.

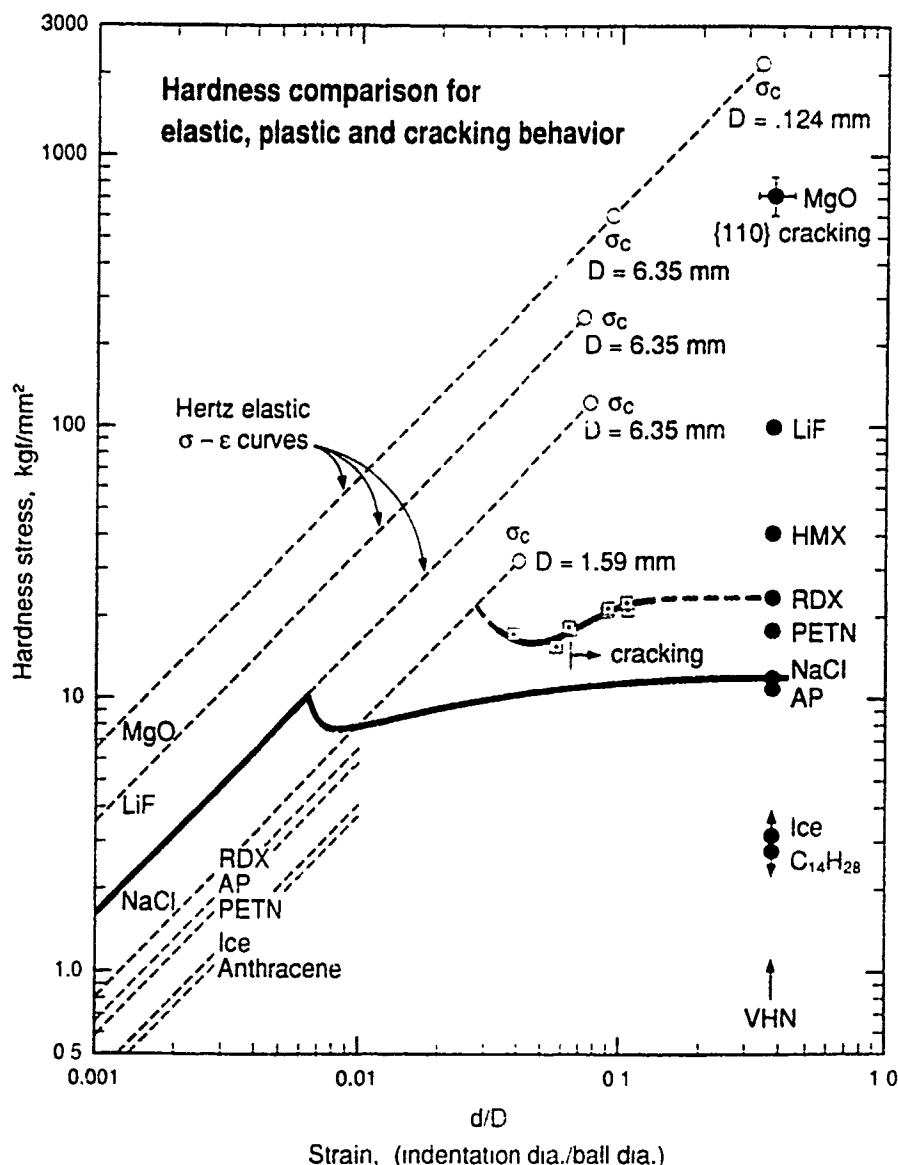


Fig. 1. Comparison for elastic/plastic/cracking behavior of RDX.

Armstrong and Elban [2,4] have proposed that the RDX deformation and fracturing properties are explained on the crystal lattice scale by the difficulty of moving individual dislocations in the molecularly configured orthorhombic Pbca structure. Figure 2 shows schematically a  $[100](040)$  edge dislocation within a half unit cell depth of the RDX lattice [4]; see the projected cell dimensions at the upper left corner of the Figure. Significant displacements of the individual molecules are necessarily shown to occur near to the dislocation core, as marked for the interchanged H4-O2 positions between adjacent

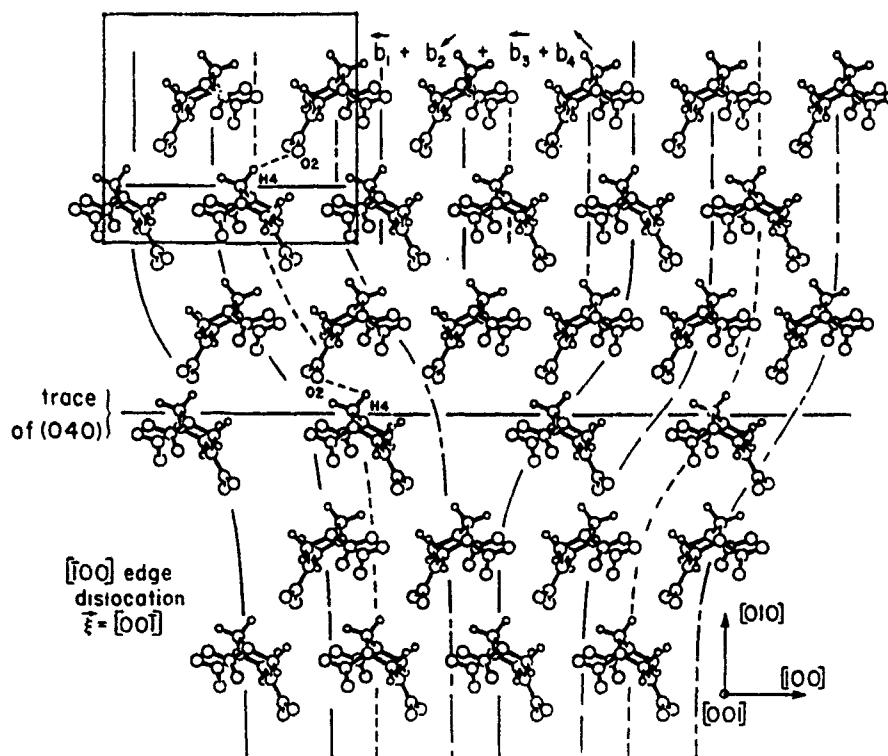


Fig. 2. Molecular displacements for an edge dislocation in RDX.

molecules both near to the dislocation and in the reference cell. The  $[100](040)$  dislocation was constructed to explain the first reported observation of  $(010)$  slip by Connick and May [5]. Slip for the smaller dislocation Burgers vector along  $[001]$  was discounted [4] on the basis of intermolecular blockages occurring in this direction across  $(0k0)$ .

Elban, Armstrong and colleagues [6-9] reported also the prominent occurrence of slip on  $(021)$  and  $(02\bar{1})$  systems at microindentations in RDX. Figure 3 indicates the intermolecular interactions occurring across the  $(02\bar{1})$  plane spanning two neighboring unit cells. As indicated, O4-O2 blockages are produced in this instance for the same favored  $[100]$  slip direction as described for the  $(040)$  slip plane. Here we note that the loss of these particular outcropping atoms will produce the specific dinitroso compound 1,3-dinitroso-5-nitro-1,3,5-triazacyclohexane (RO) that has been detected by Hoffsommer, Glover and Elban [10] in drop-weight impact tests at pre-initiation drop heights. The RO compound was found to occur in greater amounts than the trinitroso (R) compound. Hoffsommer and Glover [11] also measured the thermal decomposition of liquid RDX to nitroso compounds that were proposed to follow the sequence  $RO_3 \rightarrow RO_2 \rightarrow RO \rightarrow R$ . Behrens and Bulusu [12] have reported the formation of the nitroso  $RO_2$  compound in condensed phase pyrolysis experiments by removing an  $NO_2$  group from RDX and reacting this with pre-generated NO. It was previously suggested [4] that the  $[100](040)$  dislocation shown in Figure 2, involving single H-O interactions for the  $(010)$  slip process, could possibly relate to the formation of  $RO_2$ . This is now seen clearly to be a weaker interaction than is pointed out here for the dinitroso (RO) case possibly relating to the  $[100](02\bar{1})$  slip process.

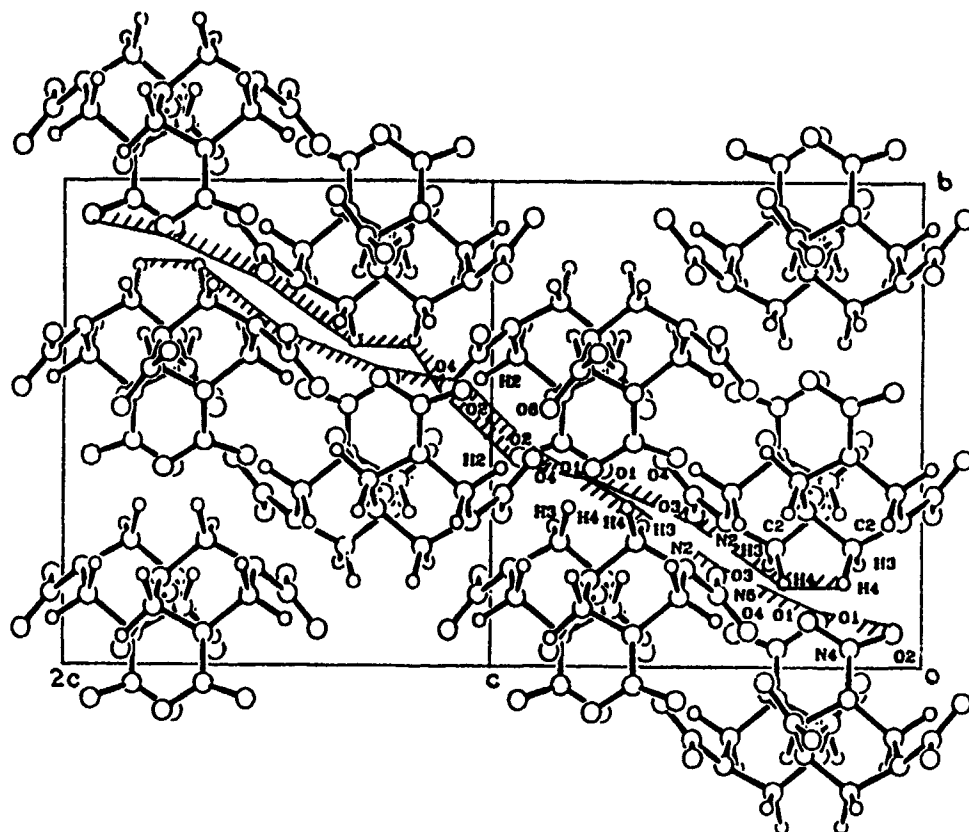
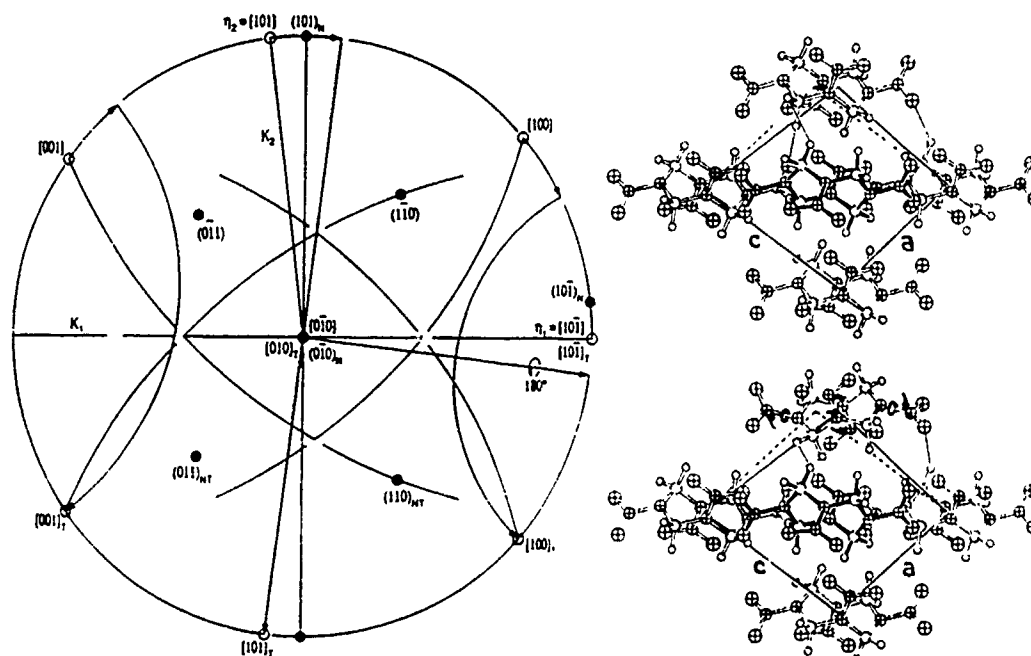


Fig. 3. Dinitroso-related interactions from  $[100](02\bar{1})$  slip.

#### MOLECULAR FLEXING FOR HMX DEFORMATION TWINS

Cady [13] has observed that the  $\beta$ -polymorph of HMX (cyclotetramethylenetetranitramine) shows growth twinning on (101) of its  $P2_1/n$  monoclinic structure and also exhibits deformation twinning on this same plane. At low stresses, the deformation twinning is reversible. The system presented itself as an interesting case for explaining on the crystal lattice scale why deformation twinning should occur for HMX as compared with slip occurring, and then only with difficulty, in the related compound RDX. Even so, Figure 1 shows that the hardness of HMX is about twice as great as that of RDX.

Figure 4 shows a stereographic projection plus intermediate and final steps for the deformation twinning process that we propose. As indicated by the twin system specification:  $K_1, \eta_1, K_2, \eta_2 = (101), [10\bar{1}], (10\bar{1}), [101]$ , respectively, the twinning has been reasoned to be of relatively unusual type II in which the twinning orientation relationship may be visualized to occur by a rotation of  $180^\circ$  about the twinning  $\eta_1$  direction, followed by a parallel translation. Such twinning has been reported recently in haematite [14]. The two-step twinning process is indicated here for the reverse sequence of first a translation parallel to  $\eta_1$ , followed by a rotation, as shown in Figure 4 so as to correspond to the physical interactions of HMX molecules traced in the sequence of modeled structures that are shown for the actual twinning mechanism.



Position Å	(T1PE*) <sub>tr</sub> Kcal/mol	Position Å	(T2PE**) <sub>tr</sub> Kcal/mol
0.000	<b>-41.97</b>	0.000	-29.95
0.265	<b>-40.91</b>	0.265	-32.43
0.530	<b>-36.79</b>	0.530	-35.91
0.790	-36.40	0.790	-37.58
1.060	-34.19	1.060	<b>-38.06<sup>‡</sup></b>

\* Type 1 Potential Energy

\*\* Type 2 Potential Energy

‡ Type 2 Potential Energy + 21° rotation of N-N bond

Fig. 4. Crystallography of Type II (101)[101] twinning in HMX.

The Table in Figure 4 gives the estimated potential energy values for the central molecule of the unit cell in the structure, in either the unrotated or 180° rotated about [101] positions, when subjected to a number of incremental translations of the upper lattice [15]. Computations were carried out with a potential function extending to 2661 surrounding molecules in accordance with an established program [16]. In the unrotated initial position before displacement, a reference value of -41.97 kcal/mole is obtained for the stable  $\beta$ -HMX structure, significantly less than the same molecule when rotated. The unrotated molecule maintains its relatively lower energy until a displacement equivalent to half of the total twinning displacement is achieved, as marked by the bold-print numbers in the Table. Further displacement is shown in the last column of the Table to occur at a lower energy for the molecule in the rotated position. Figure 4 shows in turn that the 180° rotation

for the molecule is achieved by incremental flexing of the intramolecular bonds within the molecule. Thus, the proposed explanation for twinning in HMX, albeit at a greater (hardness) strength level than for RDX is traced to the greater proposed flexibility of the larger HMX molecule.

#### REFERENCES

1. R.W. Armstrong, C.S. Coffey, V.F. DeVost, and W.L. Elban, J. Appl. Phys. 64 (3), 979-984 (1990).
2. R.W. Armstrong and W.L. Elban, presented at "The Fundamental Physics and Chemistry of the Combustion, Initiation, and Detonation of Energetic Materials", Los Alamos National Laboratory, in print as a Chemical Propulsion Information Agency Publication (1992).
3. B.L. Hammond and R.W. Armstrong, Phil. Mag. Lett. 57, 41 (1988).
4. R.W. Armstrong and W.L. Elban, in "ONR Workshop on Energetic Material Initiation Fundamentals", Chemical Propulsion Information Agency Publication 475, (The Johns Hopkins University, Applied Physics Laboratory, Laurel, MD, 1987) p. 177.
5. W. Connick and F.G.J. May, J. Cryst. Growth 5, 65 (1969).
6. W.L. Elban and R.W. Armstrong, in "Proceedings of the Seventh Symposium (International) on Detonation", (Naval Surface Weapons Center, Silver Spring, MD, 1982) NSWC MP 82-334, pp. 976-985.
7. W.L. Elban, J.C. Hoffsommer and R.W. Armstrong, J. Mater. Sci. 19, 552 (1984).
8. R.W. Armstrong and W.L. Elban, in "Microindentation Techniques in Materials Science and Engineering", edited by P.J. Blau and B.R. Lawn (American Society for Testing and Materials, Philadelphia, 1985), ASTM STP 889, p. 109.
9. W.L. Elban, R.W. Armstrong, K.C. Yoo, R.G. Rosemeier and R.Y. Yee, J. Mater. Sci. 24, 1273 (1989).
10. J.C. Hoffsommer, D.J. Glover and W.L. Elban, J. Energetic Mater. 3, 149 (1985).
11. J.C. Hoffsommer and D.J. Glover, Combust. Flame 59, 303 (1985).
12. R. Behrens and S. Bulusu, J. Phys. Chem. 96 (1992) in print.
13. H.H. Cady, private communication.
14. L.A. Bursill and P. J. Lin, Phil. Mag. Lett. 60 (10), 1-10 (1989).
15. H.L. Ammon and Z.Y. Du, private communication.
16. W.R. Busing, "WMIN, A Computer Program to Model Molecules and Crystals in Terms of Potential Functions", (Oak Ridge National Laboratory, TN, 1981) Report 5747.

## THE MOLECULAR & CRYSTAL STRUCTURES OF POLYCYCLIC ENERGETIC MATERIALS

RICHARD GILARDI

Laboratory for the Structure of Matter (6030) , The Naval Research Laboratory, Washington,  
D.C. 20375-5320 USA

### ABSTRACT

Even before the 'Buckey-ball' (or fullerene) era, organic chemists were interested in, and attracted to, the synthesis of compounds containing many rings fused together - especially the symmetric ones. By virtue of their balanced linkages, such compounds may be kinetically stable despite inclusion of massive deviations from normal bond distances and angles. These distortions, in compounds such as cubanes, tetrahedranes, dodecahedranes and prismanes, comprise a storehouse of chemical potential energy known to the chemist as 'strain energy' (unrelated to overall crystal strain discussed in many materials studies).

Besides the obvious benefit of including more potential energy in an energetic material, the arrangement of atoms in ring assemblies (rather than chains) leads to a material with a high intrinsic crystal density - a *sine qua non* for an explosive or propellant. It has long been recognized that the next generation of energetics - better in performance and/or safety - will contain many polycyclic compounds. Hundreds of model compounds were synthesized in the last decade, and their molecular structures identified or verified at the Naval Research Lab. Some of the most promising, beautiful, and unusual ones, including many energetic cubanes, will be discussed.

### ENERGY-DENSE MATERIALS

In 1990, the Department of Defense identified the production of new 'high energy density materials' as one of the 20 technologies 'most critical to our long-term defense' [1]. Better materials in this area would enable improvements in performance coupled with increased safety in the next generation of explosives and propellants. To meet these requirements, the Office of Naval Research launched a number of research initiatives which engaged the expertise of researchers from many scientific disciplines, from quantum chemistry to synthetic organic chemistry to rocket engineering.

The sudden production of hundreds of new energetic compounds and precursors to energetic compounds by this ONR program provided an opportunity to demonstrate the utility of rapid structural analysis to a synthesis program. Each new material in the program was submitted to the Naval Research Laboratory (NRL). There, X-ray analyses quickly corroborated the expected structural formula for most syntheses, but sometimes revealed completely unexpected products. The analyses also indicated the nature and quantity of solvent incorporation (if any) in solid samples, and provided accurate densities of these new materials. In the longer run, the details of the molecular structures furnished by these analyses provide a firm basis for mathematical relations between structure and properties in this class of compounds.

### DENSITY

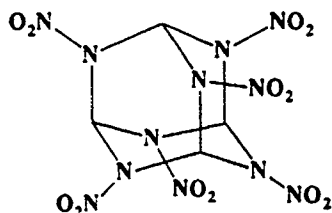
The explosive power of an explosive, as measured by its detonation pressure, and the utility of a propellant are both greatly enhanced by any increase in the mass density of the compound. Simple algorithms have been developed [2] which statistically relate the density of all the known energetic compounds to their structural formulae, and they seem to predict densities of most compounds to within about 3%. It is possible to conceive of many target molecules that are completely, or almost completely, substituted with nitro groups and then predict their density with such an algorithm. Two of the highest densities predicted so far are for the hypothetical target molecules shown in Fig. 1.

Both of these molecules are called cage compounds, because the center of the molecule is surrounded by a linked network of rings, like a spherical cage. The molecule on the left is called an adamantane, and the one on the right a cubane, after the names of the unsubstituted parent compounds. The nitro-substituted adamantane is made up of modules which resemble the successful explosive RDX. The cubane nucleus has, in addition to

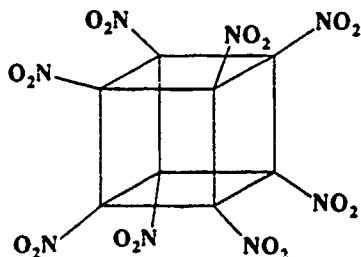


high energy through density and massive nitro substitution, a large inherent strain energy.

#### Hexanitrohexa-aza-adamantane



#### Octanitrocubane



Predicted Density = 2.0-2.2 g/cc

Predicted Density = 2.0-2.1 g/cc

Figure 1. Two examples of polycyclic target compounds that have yet to be synthesized.

### STRAIN ENERGY

What is strain energy? Molecules generally behave as if their atoms are connected by a flexible set of connections (called bonds). These bonds can be extended or compressed by external forces, but tend to assume certain values for their distances and for their inter-bond angles. However, it is impossible to connect some of the more complex ring systems found in these molecules except by forcing some of the bond angles (or, more rarely, distances) to remain at values far from their ideal. Cubanes are close to the top of the list in overall strain energy, for all the carbon bond angles are forced to remain near 90° to maintain closure of its rings, but the preferred bond angle values in this type of compound are 109.5°.

### ENERGETIC CUBANES

Three nitro-substituted cubanes, a di-, a tri-, and a tetranitrocubane, have been synthesized at the Univ. of Chicago [3]. All are quite stable. Their crystals were studied at NRL, and their densities were found to be proportional to the number of nitro substituents, namely, 1.66, 1.74 and 1.814 g/cc respectively. The tetranitrocubane is shown in Fig. 2.

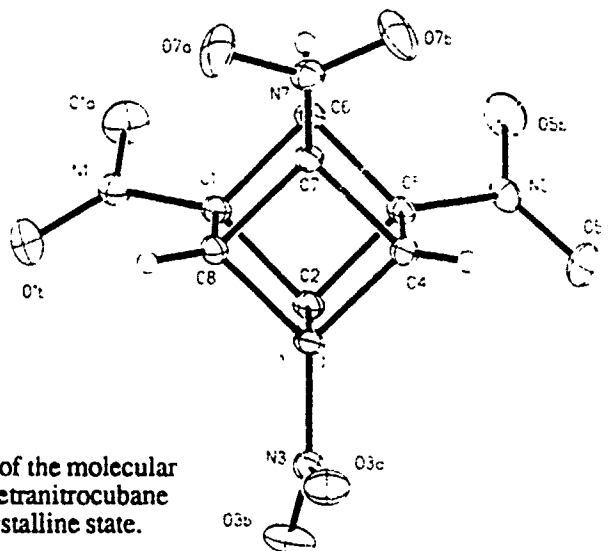


Figure 2. A drawing of the molecular structure of 1,3,5,7-tetranitrocubane as it occurs in the crystalline state.

The discovery of cubane was first reported [4] and its structure confirmed [5] in 1964. Though it attracted immediate and lasting attention, only a few new cubane compounds were made in the next 20 years. Once a cubane compound was made, it was difficult to transform it without "zipping open" the strained cage. In the 1980's, new reactions were found which could be used to add new substituents to the cubane cage without destroying it, and a large number of new compounds have since been reported. Figure 3 shows a cubanourea [6] where the cube is fused to an energetic five-membered ring. Figure 4 portrays some novel polycubane compounds analyzed at NRL [7] which may be precursors leading to future energetic materials.

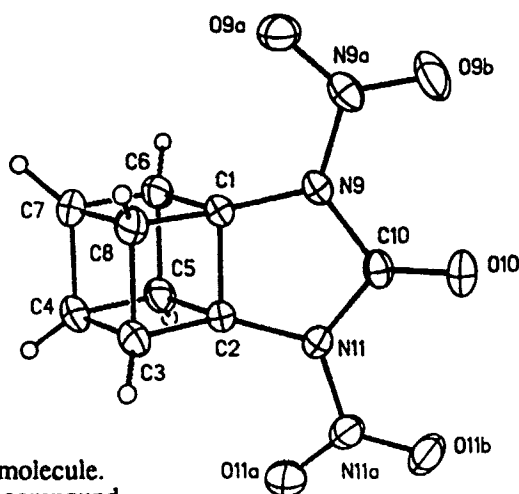


Figure 3. The N,N'-dinitrocubanourea molecule. The crystal density is 1.69 g/cc, and the compound has ample room for further energetic substitution.

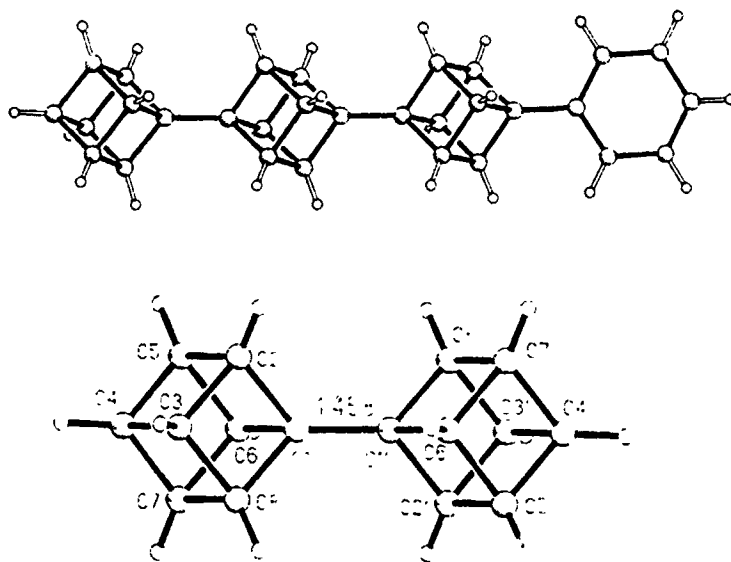


Figure 4. The structures of two polycubyl compounds: phenyltercubyl (top) and cubylcubane (bottom).

## NEW DIRECTIONS

A recent article calculated the properties of the 22 possible cubanes made up of carbon and nitrogen atoms [8]. If existing prediction schemes can be extended to this novel class of molecules, the computations indicate that substitution of four or more of the CH corners by nitrogen atoms leads to compounds denser, and more energetic, than all existing materials. One particularly promising candidate is shown in Figure 5. A search of the crystal structure literature reveals only one example where a nitrogen atom is shared by more than one four-membered (C,N) ring [9], shown in Figure 6. The fact that such a highly strained asymmetric azaprismane is stable enough to undergo an X-ray analysis indicates that the azacubane family may be a powerful source of new energetic materials.

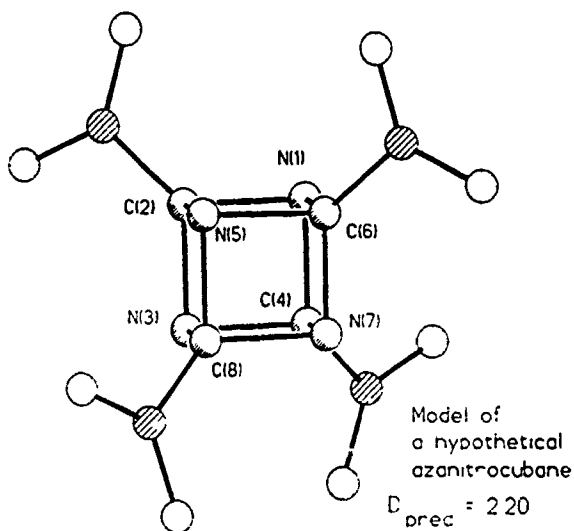


Figure 5. A drawing of a tetraazacubane, where four alternate corners of the cube are replaced by unsubstituted nitrogen atoms; the other four are nitro-substituted.

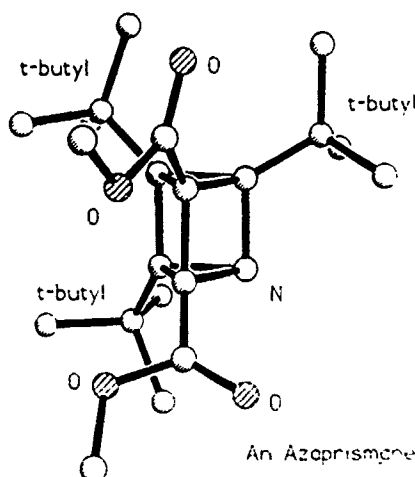


Figure 6. A prismane, a cage compound comprised of just 3- and 4-membered rings, with one azasubstituted corner.

## References

1. "Plan for Vital Defense Technologies Issued" (news article), R. Seltzer, Chemical and Engineering News, p. 5, Mar. 26, 1990.
2. J. R. Stine. Report No. LA-8920 (Los Alamos National Laboratory, Los Alamos, NM 87545, U.S.A.), 1981.
3. P. E. Eaton, Y. Xiong, and R. Gilardi; J. Org. Chem., submitted (1992).
4. P. E. Eaton and T. W. Cole Jr.; J. Am. Chem. Soc. **86**, 962 (1964).
5. E. B. Fleischer; J. Am. Chem. Soc. **86**, 3889 (1964).
6. P. E. Eaton, K. Pramod, and R. Gilardi; J. Org. Chem. **55**, 5746-5750(1990).
7. R. Gilardi, M. Maggini, and P. E. Eaton; J. Am. Chem. Soc. **110**, 7232-4 (1988).
8. R. Engelke; J. Org. Chem. **57**, 4841-6 (1992).
9. U. Hees, U. Vogelbacher, G. Michels and M. Regitz; Tetrahedron **45**, 3115(1989).

## NTO POLYMORPHS

Kien-yin Lee\* and Richard Gilardi\*\*

\* Los Alamos National Laboratory, P.O. Box 1663, Los Alamos, NM 87545

\*\* Laboratory for the Structure of Matter, Naval Research Laboratory, Washington D.C. 20375

### ABSTRACT

NTO is an explosive of current interest. It has been evaluated as an insensitive component to replace RDX in the bomb fill, and as a major ingredient for the auto air bag system. The crystal structure of the  $\beta$  form of NTO has been determined by single-crystal X-ray methods. The unit cell is monoclinic, space group  $P2_1/c$ , with  $a = 9.326$ ,  $b = 5.515$ ,  $c = 9.107$  Å,  $\beta = 100.77^\circ$ . There are four molecules in the cell, density  $1.878 \text{ g/cm}^3$ . Infinite extension of H-bonding in two-dimensional sheets occurs in the monoclinic form. Bond lengths and angles all have normal values.

Efforts have been made to determine the crystal structure of  $\alpha$ -NTO. However, a structure refined only to  $R = 17\%$  was obtained, probably due to some kind of twinning about the crystal needle axis. The unit cell is triclinic, space group  $P\bar{1}$ , with  $a = 5.12$ ,  $b = 10.30$ ,  $c = 17.9$  Å,  $\alpha = 106.7^\circ$ ,  $\beta = 97.7^\circ$ ,  $\gamma = 90.2^\circ$ . There are eight molecules in the cell, density  $1.92 \text{ g/cm}^3$ . Ribbons of NTO molecules formed by a relatively strong network of hydrogen bonds are observed. It was found that  $\alpha$ -NTO is the stable, dominating form. A variety of techniques have been chosen to identify the two polymorphs.

### BACKGROUND

5-Nitro-2,4-dihydro-3H-1,2,4-triazol-3-one, commonly known as NTO is an explosive that was developed at Los Alamos in 1983 as a result of an on-going explosives synthesis program.<sup>(1)</sup> It continues to receive attention from both defense and civilian sectors in the United States and abroad as a potential new-generation insensitive high explosive (IHE).<sup>(2)</sup> It has been studied by the Navy as an insensitive component to replace RDX in the bomb fill<sup>(3)</sup>, and as a major ingredient by Morton International, Inc. to replace sodium azide for the auto air bag system.<sup>(4)</sup> Crystals of NTO were grown to determine the crystal density for performance calculations and for structure confirmation.

### CRYSTAL STRUCTURE OF $\beta$ -NTO

#### Crystallization of $\beta$ -NTO

The crystal used to determine the structure of the  $\beta$  form of NTO was obtained by cooling a hot aqueous NTO solution. This crystalline form, while maintaining its habit and clarity, does not remain as a single crystal. A re-examination of the crystal after six months period gave no diffraction.

### Summary of Experimental Conditions:

Single-crystal X-ray diffraction analysis of 5-nitro-2,4-dihydro-3*H*-1,2,4-triazol-3-one.  $C_2H_2N_4O_3$ , F.W. = 130.1, monoclinic space group  $P2_1/c$ ,  $a = 9.326(2)$ ,  $b = 5.515(2)$ ,  $c = 9.107(2)\text{\AA}$ ,  $\beta = 100.77(2)^\circ$ ,  $V = 460.2(2)\text{\AA}^3$ ,  $Z = 4$ ,  $\rho_{\text{calc}} = 1.878\text{ g/cm}^3$ ,  $\lambda(\text{MoK}\alpha) = 0.7107\text{\AA}$ ,  $\mu = 0.174\text{ mm}^{-1}$ ,  $F(000) = 264$ ,  $T = 294^\circ\text{K}$ .

A clear colorless  $0.08 \times 0.2 \times 0.32\text{ mm}$  crystal, in the shape of a thick plate, was used for data collection on an automated Siemens R3m/V diffractometer equipped with an incident beam monochromator. Lattice parameters were determined from 25 centered reflections within  $30 \leq 2\theta \leq 37^\circ$ . The data collection range of  $hkl$  was:  $0 \leq h \leq 14$ ,  $-8 \leq k \leq 6$ ,  $-13 \leq l \leq 13$ , with  $[(\sin \theta)/\lambda]_{\text{max}} = 0.756$ . Three standards, monitored after every 97 reflections, exhibited random variations with devs. up to  $\pm 2.5\%$  during the data collection. A set of 3437 reflections was collected in the  $\theta/2\theta$  scan mode, with scan width  $[2\theta(K_{\alpha 1}) - 0.65]$  to  $[2\theta(K_{\alpha 2}) + 0.65]^\circ$  and  $\omega$  scan rate (a function of count rate) from  $3.97^\circ/\text{min.}$  to  $23.44^\circ/\text{min.}$  There were 1673 unique reflections, and 1193 were observed with  $F_o > 3\sigma(F_o)$ . The structure was solved and refined with the SHELXTL system of programs.<sup>(5)</sup> The full-matrix least-squares refinement varied 86 parameters: atom coordinates for all atoms, anisotropic thermal parameters for all non-H atoms, and isotropic thermal parameters for the hydrogen atoms. Final residuals were  $R = 0.049$  and  $wR = 0.050$  with final difference Fourier excursions of  $0.54$  and  $-0.29\text{ e}\text{\AA}^{-3}$ .

### Structure of $\beta$ -NTO

The thermal ellipsoid drawing specifying the atom numbering scheme of NTO is shown in Figure 1. The N-H protons of NTO were also confirmed to be in the 2,4 position in both the solid state and in solution by observing  $^1\text{H}$ - $^{15}\text{N}$  coupling in the nmr spectra of 5-nitro-2,4-dihydro-3*H*-1,2,4-triazol-3-one- $4$ - $^{15}\text{N}$ .<sup>(6)</sup> Infinite extension of H-bonding in two-dimensional sheets occurs in the crystal form. The H-bonding is best seen in an  $c$ -axis projection, Figure 2. The four outer molecules are at the same  $x$  level ( $\sim 0.7$ ), and the central one is slightly above ( $0.8$ ). These sheets are interleaved with inversion related sheets generated by a center at  $1/2, 1/2, 1/2$ . The bond angles and bond lengths of  $\beta$ -NTO are listed in Table I.

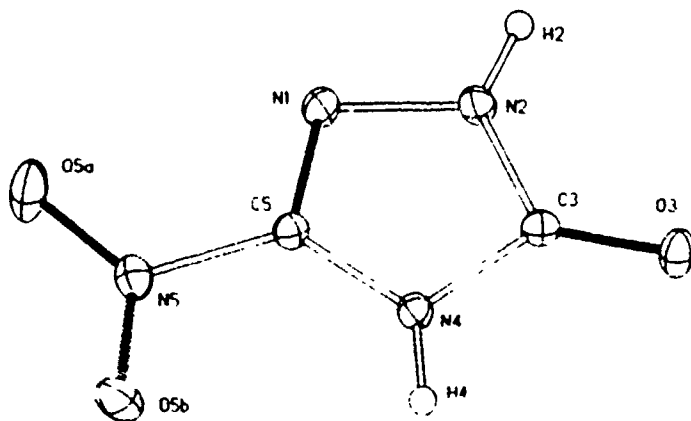


Figure 1. A Thermal ellipsoid drawing of NTO calculated from the X-ray analysis of its beta polymorph. Bonds which are formally double bonds are darkened.

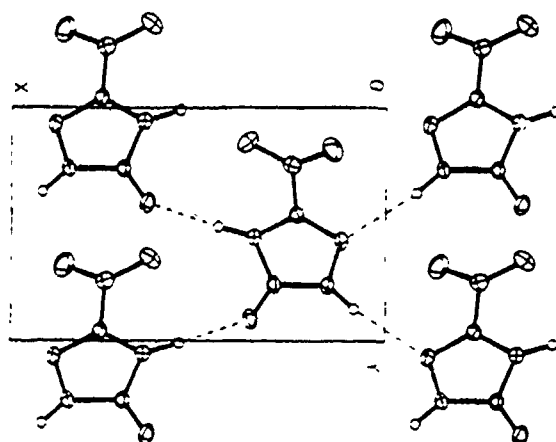


Figure 2. A view of a portion of a H-bonded sheet of  $\beta$ -NTO molecules viewed down the  $c$  axis.

Table I. Bond Angles ( $^\circ$ ) and Lengths ( $\text{\AA}$ ) of  $\beta$ -NTO

N(1)-N(2)	1.369 (2)	N(1)-C(5)	1.290 (2)
N(2)-C(3)	1.367 (2)	C(3)-O(3)	1.226 (2)
C(3)-N(4)	1.378 (2)	N(4)-C(5)	1.349 (2)
C(5)-N(5)	1.447 (2)	N(5)-O(5A)	1.217 (2)
N(5)-O(5B)	1.218 (2)		
N(2)-N(1)-C(5)	102.4(1)	N(1)-N(2)-C(3)	112.8(1)
N(2)-C(3)-O(3)	126.9(1)	N(2)-C(3)-N(4)	103.8(1)
O(3)-C(3)-N(4)	129.3(1)	C(3)-N(4)-C(5)	105.8(1)
N(1)-C(5)-N(4)	115.2(1)	N(1)-C(5)-N(5)	121.6(1)
N(4)-C(5)-N(5)	122.2(1)	C(5)-N(5)-O(5A)	117.4(1)
C(5)-N(5)-O(5B)	116.2(1)	O(5A)-N(5)-O(5B)	126.4(2)

## STRUCTURE OF $\alpha$ -NTO

### Characteristics of $\alpha$ -NTO Crystals

NTO is soluble in water (49g/l) and most organic solvents. Sizable NTO crystals suitable for X-ray crystallography can be obtained by recrystallization from water. However, if one tries to cut a needle NTO crystal perpendicular to the long axis, the crystal shatters parallel to this axis; or the ends of the crystals fray much like the end of a rope. Indeed the crystals can be permanently bent rather sharply without breaking. These properties are unusual for an organic compound except, perhaps, for crystals of polymers. The chains of NTO molecules are in a sense polymers.

### Structure of $\alpha$ -NTO

The unit cell is triclinic, space group  $P\bar{1}$ , with  $a = 5.17 \text{ \AA}$ ,  $b = 10.30 \text{ \AA}$ ,  $c = 17.90 \text{ \AA}$ ,  $\alpha = 106.7^\circ$ ,  $\beta = 97.7^\circ$ ,  $\gamma = 90.2^\circ$  and there are eight molecules in the unit cell or four molecules in the asymmetric unit. The density is  $1.92 \text{ g/cm}^3$ . The needle axis is parallel to the  $a$  axis of this triclinic cell. There is much pseudosymmetry in the diffraction pattern. A structure was found in the triclinic space group. This structure, however, refined only to  $R = 17\%$ , whereas we expect

a correct structure of a small organic molecule to refine to below  $R = 5\%$ . This poor fit could be due to the poor quality of the crystals or because of some kind of twinning about the needle axis although the agreement between equivalent reflection was normal. Nevertheless the gross features of the structure are believed to be correct. NTO molecules are joined by hydrogen bonds to form ribbons of NTO molecules. This ribbon of NTO molecules is duplicated by the center of symmetry at the origin to give a parallel ribbon. The horizontal direction is the  $a$  axis of the crystal and this repeat distance,  $5.12 \text{ \AA}$ , is the width of the molecule, Figure 3. The ribbons are joined to each other by relatively weak Van der Waal's forces.

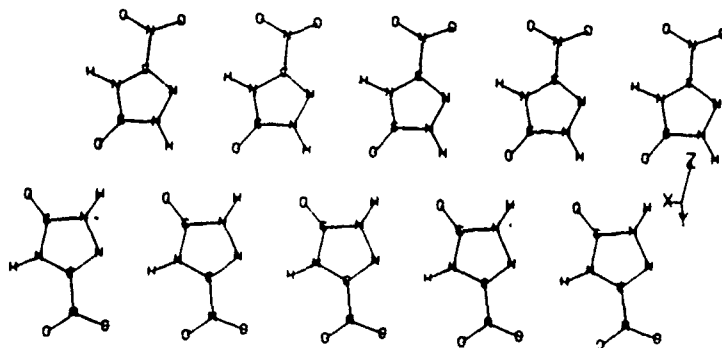


Figure 3. View of a ribbon of NTO molecules lying in the 011 plane. The X direction is horizontal.

### IDENTIFICATION OF NTO POLYMORPHS

Since the  $\beta$ -NTO is not stable, the presence of this form in the production lot of NTO could become a concern from a safety point of view. We are interested in finding techniques other than X-ray crystallography methods to identify NTO polymorphs. However, we have encountered many difficulties in obtaining a reliable solvent system that will produce enough amount of  $\beta$ -NTO for preliminary sensitivity test. Up to now,  $\beta$ -NTO has only been found in the recrystallization product of NTO from a methanol or ethanol /methylene chloride mixture.

A variety of techniques have been used to identify the two polymorphs of NTO. By using infrared spectroscopy, the two forms can be distinguished by the two different absorption spectra over the range of  $500$  to  $1800 \text{ cm}^{-1}$  (Fig. 4). Based on a calculated powder pattern of  $\beta$ -NTO, it was shown that the x-ray diffraction patterns of the two NTO forms are different (Figure 5 and 6). Furthermore, the two forms can be identified by the differences in habit of the multi-crystal agglomerates as shown by SEM photographs. Figure 7 and 8 are SEM pictures of  $\alpha$  and  $\beta$ -NTO spherulites, respectively.

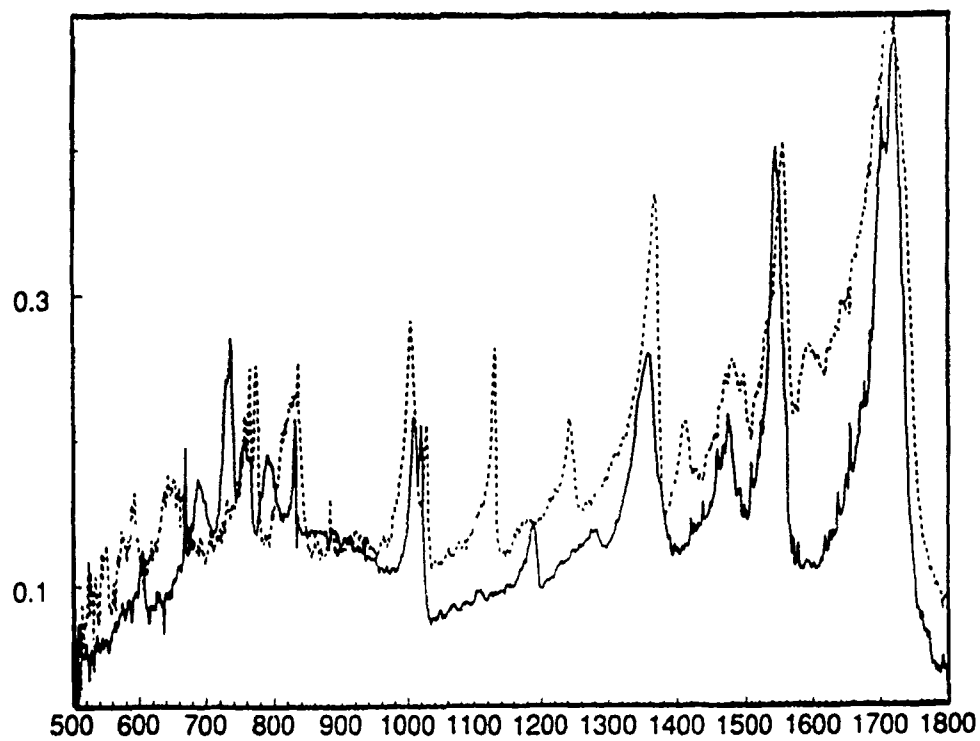


Figure 4. Infrared Absorption Spectra of  $\alpha$ - (solid) and  $\beta$ - (dash) NTO

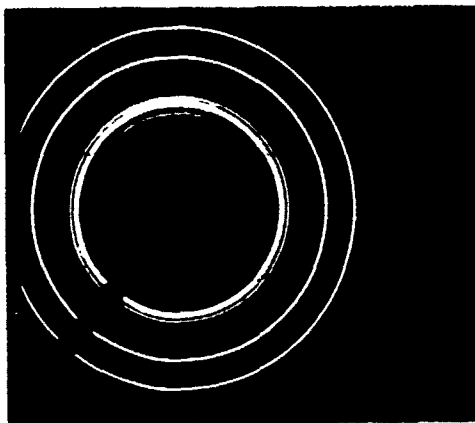


Figure 5. X-ray Diffraction Pattern of  $\alpha$ -NTO

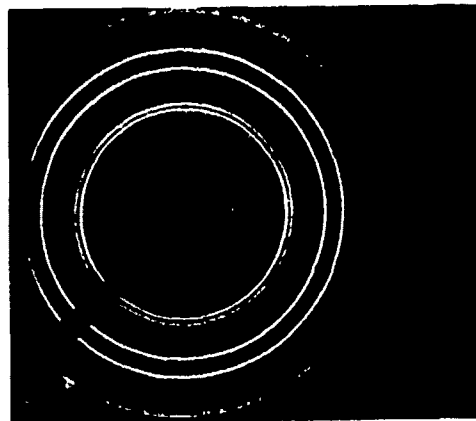


Figure 6. X-ray Diffraction Pattern of  $\beta$ -NTO





Figure 7. SEM photograph of  
 $\alpha$ -NTO Spherulite

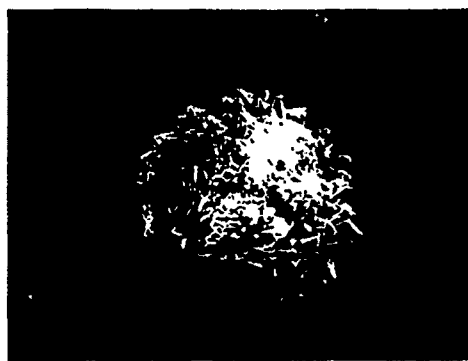


Figure 8. SEM photograph of  
 $\beta$ -NTO spherulite

### ACKNOWLEDGEMENT

The authors are grateful to Dr. Clifford George, Naval Research Laboratory for his valuable discussion; Dr. D. T. Cromer, Los Alamos National Laboratory, for  $\alpha$ -NTO structure information; Dr. H. H. Cady, Los Alamos National Laboratory, for the x-ray diffraction patterns of the two forms; Dr. S. Agnew, Los Alamos National Laboratory, for NTO infrared absorption spectra; and Dr. J. F. Weinrach, Los Alamos National Laboratory, for  $\beta$ -NTO powder pattern calculations. This work was performed under the auspices of the US Department of Energy, and was supported, in part, by the Office of Naval Research, Mechanics Division.

### REFERENCES

1. K.-Y. Lee and M.D. Coburn, US patent 4,733,610, (1988).
2. A. Becuwe and A. Delcios, 18th International Annual Conference of ICT 1987, July 1-3 (1987).
3. M. J. Stosz, S.L. Collignon, C. Gotzmer and J. F. Leahy, 38th Annual Bomb and Warhead Technical Meeting, Albuquerque, NM (1988).
4. R. B. Wardle, J. C. Hinshaw and R. M. Hajik, US patent 4,931,112 (1990).
5. G. M. Sheldrick, SHELXTL80, (1980)
6. W.L. Earl, D. G. Ott and C. B. Storm, Private Communication (1989).

## GROWTH AND DEFECTS OF EXPLOSIVES CRYSTALS

HOWARD H. CADY

Los Alamos National Laboratory, Group M-1, MS C920, Los Alamos, NM 87545

### ABSTRACT

Large single crystals of PETN, RDX, and TNT can be grown easily from evaporating ethyl acetate solutions. The crystals all share a similar type of defect that may not be commonly recognized. The defect generates conical faces, ideally mosaic crystals, and may account for the "polymorphs" of TNT and detonator grades of PETN.

TATB crystals manufactured by the amination of trichlorotrinitrobenzene in dry toluene entrain two forms of ammonium chloride. One of these forms causes "worm holes" in the TATB crystals that may be the reason for its unusually low failure diameter.

Strained HMX crystals form mechanical twins that can spontaneously revert back to the untwinned form when the straining force is removed. Large strains or temperatures above 100°C lock in the mechanical twins.

### CRYSTAL GROWING AND SINGLE CRYSTAL DEFECTS

I have recently retired. This talk is a show-and-tell on three available, unfinished materials problems that some of you might find interesting.

It has been possible to grow large transparent single crystals of nearly all explosives that are modestly soluble in ethyl acetate. The primary requirement is to keep the growing crystal and the slowly evaporating solution above it warm enough to cause ethyl acetate to reflux on the cooler portions of the apparatus thus preventing the formation of spurious seeds. I will use PETN as the example material, but TNT and RDX also exhibit the same types of crystal faces. Figure 1 shows a primitive apparatus that works satisfactorily for growing PETN crystals. A water bath heat source works better for more soluble materials.

I was requested to cut some large, transparent, apparently perfect PETN crystals to prepare slabs for measuring sound speeds in various crystallographic directions. Laue x-ray back reflection orientation techniques failed (no back reflections), so the two-circle optical goniometer and alignment laser light source shown in Figure 2 were used as an orientation tool. The returned reflected laser light beam was a surprise as it indicated a nearly flat, but conical reflecting surface. Figure 3 shows the pattern of light from a cone on the (110) face of PETN that is centered in the laser beam spot with its axis aimed at the laser source. A cone angle of  $179.8^\circ$  is determined from the geometry of the apparatus.

Cone angles come in quantum steps with  $179.8^\circ$  common,  $179.6^\circ$  occasional,  $179.4^\circ$  rare, and finally a unique most acute cone angle. This unique cone angle found on only one single crystal of PETN was  $178.5^\circ$ . This crystal cracked spontaneously as it grew and the conical surface was rough, but its cone angle was steep enough to provide for normal epi-illumination micrographs. Figure 4 shows the image obtained when one side of the cone was positioned for maximum reflection using a prismatic light source. Irregularly spaced growth spirals and a 10- $\mu$  diameter central crater were easily observed. Figure 5 shows the same crater at higher magnification. What cannot be seen in Figure 5 is a spiral stream of small bubbles that form in the bottom of the crater and lead into the interior of the crystal.

There are other useful observations concerning these defects: each crystal face has only one of these defects; the angle between the cone axes normal to (110) and the cone axes normal to (101) agrees with the x-ray unit cell *a/c* ratio, but actual face normals do not give the proper ratio.



Fig 1 Primitive apparatus for growing crystals by solvent evaporation



Fig 2 Laser source, optical goniometer with crystal, and reflected light beam target

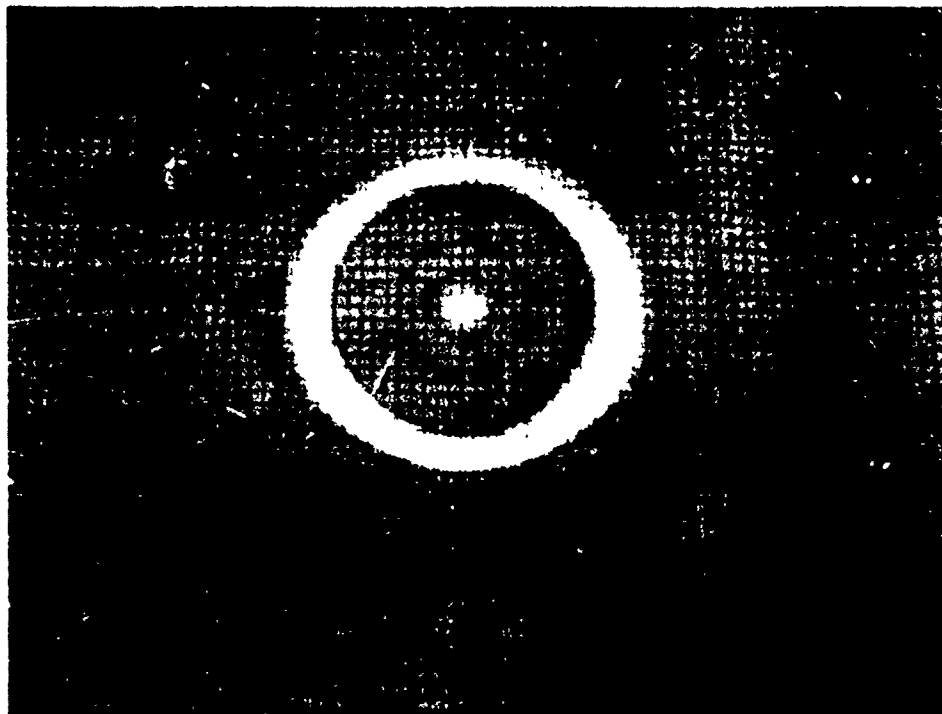


Fig 3 Light reflected by laser beam centered on cone (PETN 110 face) with axis aimed at laser



Fig 4 Photo micrograph of PETN (110) conical defect, epi-illumination, crater diam  $10\ \mu$

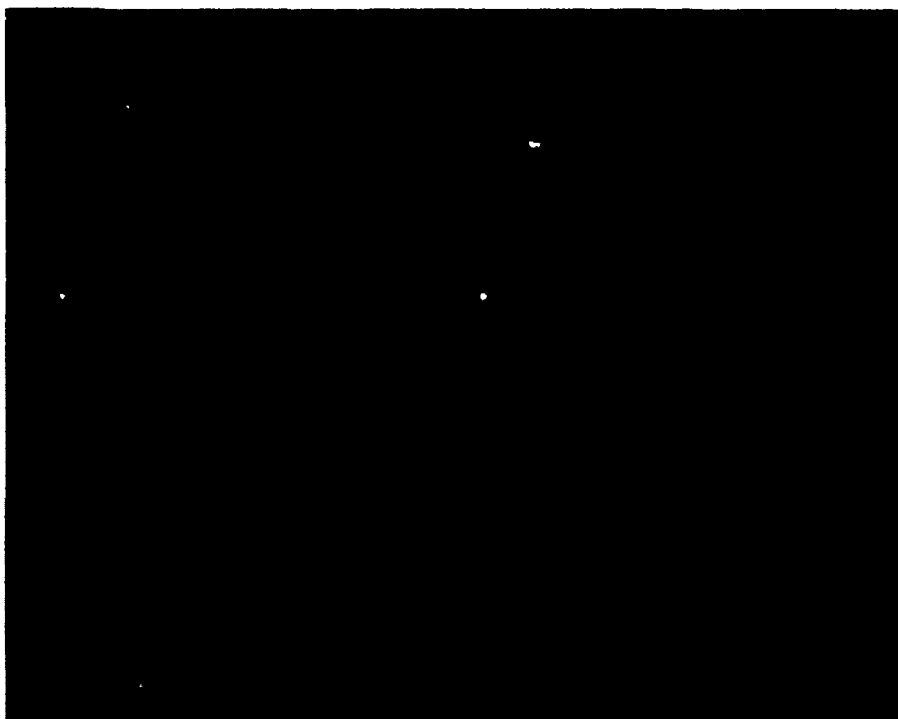


Fig 5. Same defect as Fig. 4, except at higher magnification. Long dimension of crater is  $10\ \mu$

the defects can be virtual, that is, the center of the cones can be off in space, and the spiral steps are both periodic and irregular in spacing. It follows that this defect cannot be a classical screw dislocation and that the crystal cannot be constructed using only the x-ray unit cell as a building block. The rapid growth of these PETN crystals seems to be caused by a precessing crystal axis that forms the rim of the crater and throws off a stream of repeating vertical steps that spread across the crystal face.

Figure 6 shows a series of SEM photos of detonator grade PETN where only the rim of the crater provides a region of low enough strain to grow into a crystal.

Unresolved questions: What is the defect? How does it propagate when the center of the cone is virtual? Is the defect relatively common in other materials? What other crystal defects are implied where the cone axis corresponds to the x-ray axis, but the face normal does not? Is the defect necessary for rapid growth? Does the defect imply or explain the formation of polytypic twins?

#### AMMONIUM CHLORIDE IN "DRY AMINATED" TATB

TATB, sym-triaminotrinitrobenzene, is manufactured by the amination of trichlorotrinitrobenzene in dry toluene. By-product, ammonium chloride, is removed by washing with water. Compared with its other properties, TATB has an unusually small failure diameter. The production of hot spots by the collapse of voids inside the crystals could provide the mechanism.

The SEM picture, Figure 7, shows the typical Swiss cheese appearance of dry aminated TATB. Internally these holes must be unusual because it can take helium over 40 minutes to pressure equilibrate with these TATB crystals in a gas pycnometer. In an attempt to understand the nature of the holes, an unwashed lot of TATB was requested for study.

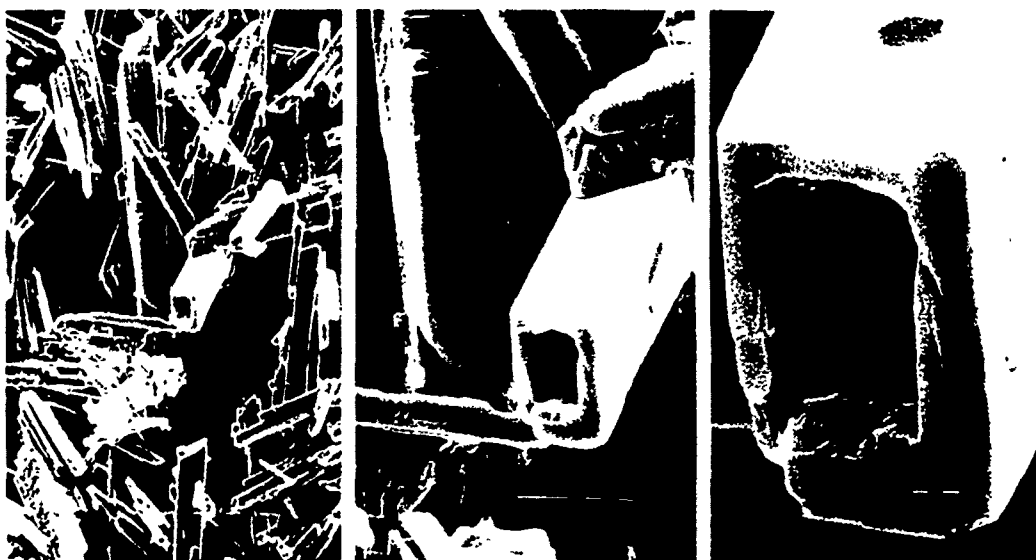


Fig 6 SEM photos of det. grade PETN at 300, 1000, and 3000x Crater hole is about  $10 \times 14 \mu$

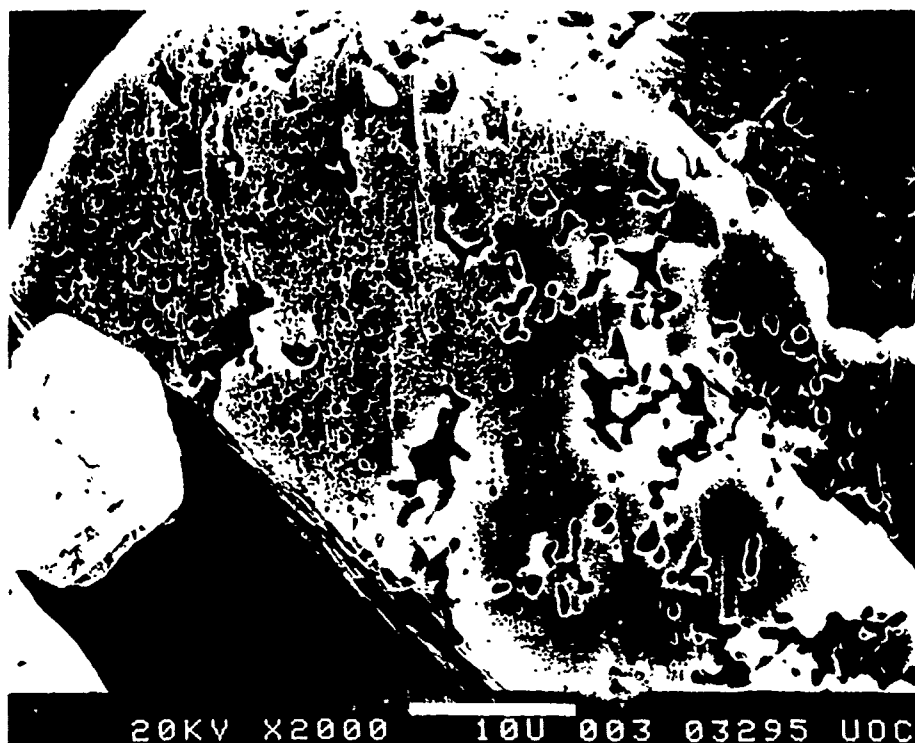


Fig 7 Dry aminated "Swiss cheese" TATB Bar length is  $10 \mu$

Figure 8 is a picture showing an unwashed TATB crystal. The rounded blobs are ammonium chloride. It is proposed that these blobs are covered with a thin aqueous solution when they form. At higher magnification, in Figure 9, it can be seen that the blobs extend from relatively large holes leading into the interior of the crystal. At this magnification there are still many smaller defects in the surface of the TATB that cannot be resolved

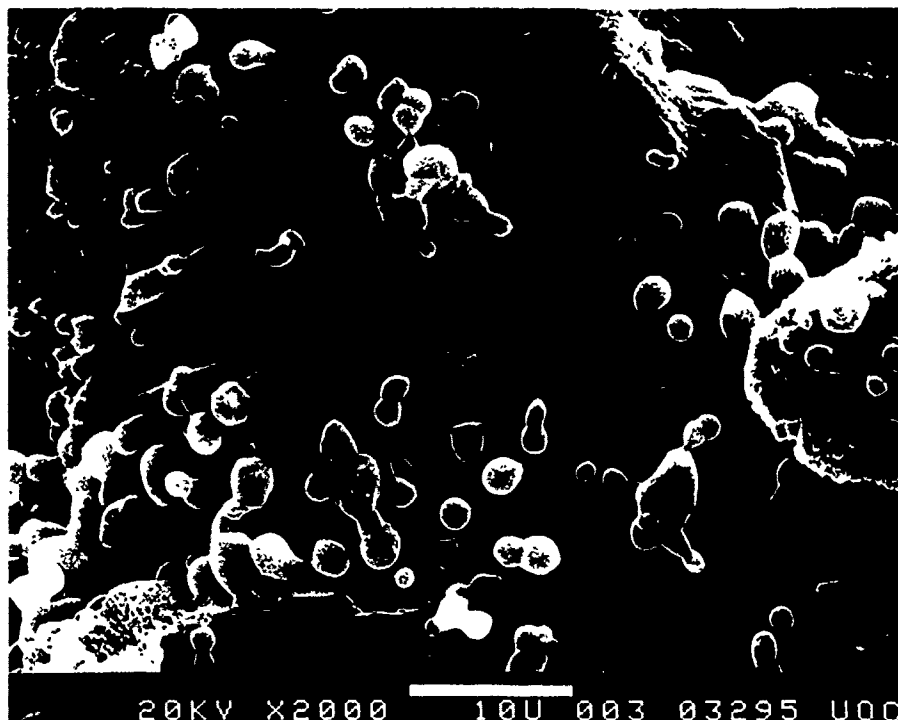


Fig 8 TATB crystal with coproduced ammonium chloride. Bar is 10  $\mu$

Another region of the crystal is shown, at the same magnification, in Figure 10. It shows that the blob shaped ammonium chloride has changed shape since the crystal was formed, and that the surface of the TATB is relatively perfect near the blobs. Square defects in the TATB surface are apparent where blobs are few in number.

At yet higher magnification, it can be seen in Figure 11 that the square holes are filled with bipyramids of ammonium chloride. Thus there are two types of ammonium chloride precipitating concurrently with TATB. It is proposed that these are a fast growing blob form that is covered with a thin film of water saturated with ammonium chloride, and a slow growing anhydrous bipyramidal habit ammonium chloride. Precipitating TATB can over grow the bipyramidal form, but the solution covered blobs grow faster than TATB and do not provide a sticky surface. The blobs grow as extended channels inside the TATB crystals. They are eventually dissolved out by wash water. Bipyramids that are overgrown will be inaccessible to wash water and will lead to an entrained ammonium chloride impurity. Figure 12 shows the interior of a cleaved TATB crystal. The ratio between the two forms of ammonium chloride is critically determined by traces of water in the initial toluene. Addition of small amounts of water to the toluene significantly reduces the final ammonium chloride impurity, but this same water also changes the internal hole structure left by the blob form. Other forms of TATB are produced with varying amounts of water added to the toluene. Water has been added up to that sufficient to dissolve all of the by-product ammonium chloride as it is produced. The hole structure in the TATB crystals changes with the amount of added water.



Fig 9 TATB with  $\text{NH}_4\text{Cl}$  Left hand part of Fig 8 at higher magnification Bar is 10  $\mu$

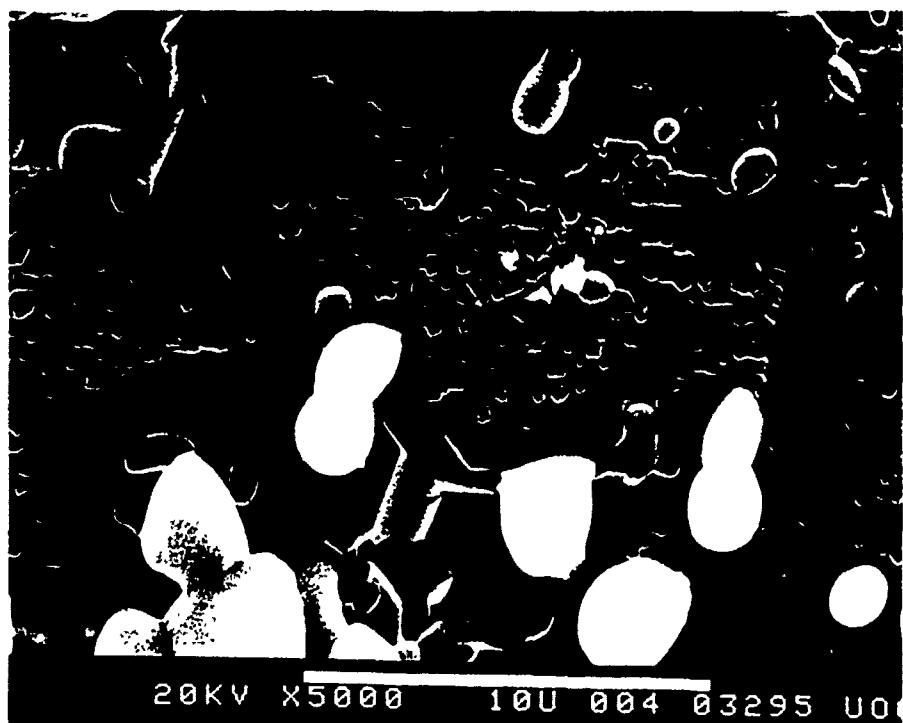


Fig 10 TATB with  $\text{NH}_4\text{Cl}$  Central part of Fig 8 at same magnification as Fig 9 Bar is 10  $\mu$





Fig 11. TATB with  $\text{NH}_4\text{Cl}$ . Center part of Fig 9 at high magnification. Bar is 1  $\mu$ .



Fig 12 Cleaved TATB crystal showing interior hole structure Bar is 10  $\mu$

Unresolved questions: Do these holes explain the unusually small failure diameter of TATB? Is there a significant lot-to-lot variation in the hole structure? Can TATB be produced without holes? What volume of the crystal is occupied by holes? Do the different types of holes in the water added TATB production also provide a similarly small failure diameter?

### MECHANICAL TWINS IN $\beta$ -HMX

HMX (cyclotetramethylenetetranitramine) often grows as crystals twinned on the 101 plane. X-ray precession photographs were used to prove that the same twin plane is the one that exhibits an elastic mode of deformation in which bands of a crystal change from one twin orientation to another and back as stress is applied and removed.

Figure 13 is a micrograph of a crystal of  $\beta$ -HMX in immersion oil between nearly crossed polars. This crystal is stressed by pressing on the cover slip with a needle, and strain is evidenced by mechanical twinning. The crystal is lying on its (0 $\bar{1}$ 1) face.

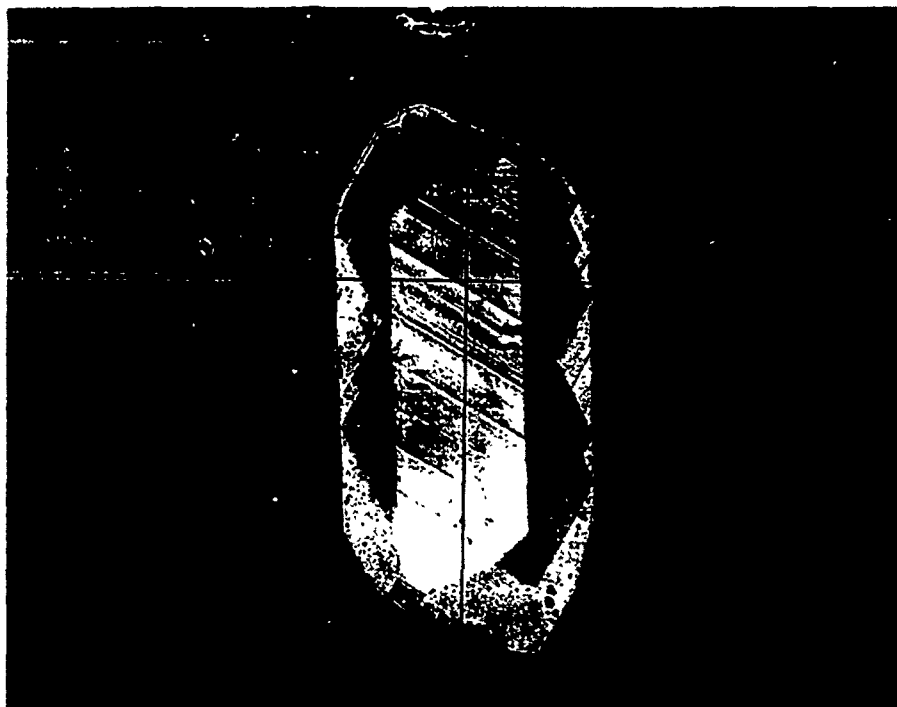


Fig 13.  $\beta$ -HMX crystal, lying on its (0 $\bar{1}$ 1) face, stressed to show mechanical twinning

Figure 14 shows the same crystal after the needle is removed from the cover slip. There is no evidence of residual mechanical twinning, and the crystal looks exactly as it did before applying any stress. Therefore, the strain shown in Fig. 13 is all elastic.

Figure 15 shows the crystal stressed to a higher level than previously. Many twin bands and other change in the polarization are apparent. At least two regions of this crystal have exceeded its first elastic limit.

Figure 16 shows the crystal after the stress is again removed. Nearly all of the mechanically twinned regions have reverted back to their original configuration, but a few twin bands remain. With high enough stress, about a quarter of the crystal can be locked into its mechanically twinned form. Such a stress is likely to fracture part of the crystal.

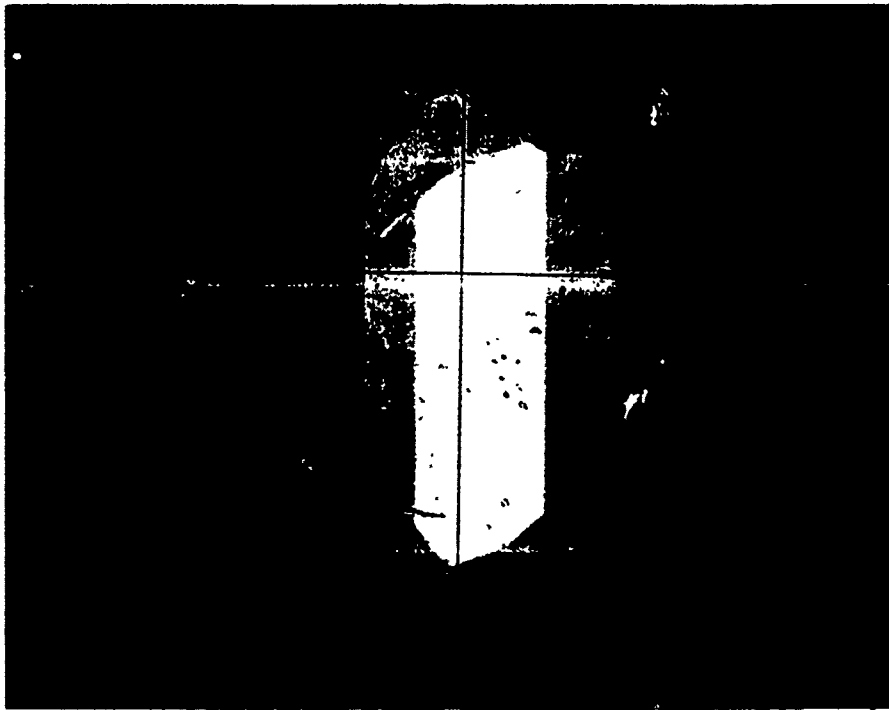


Fig 14. Same crystal after stress of Fig 13 is removed. Mechanical twinning is elastic

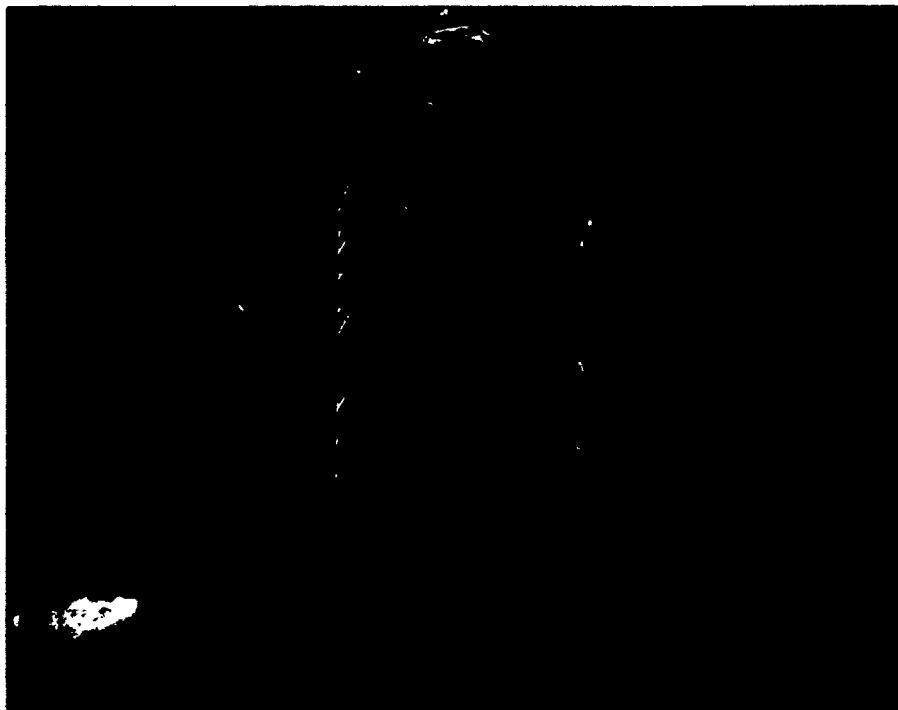


Fig 15 Same crystal, cycled to a higher stress, showing additional mechanical twinning

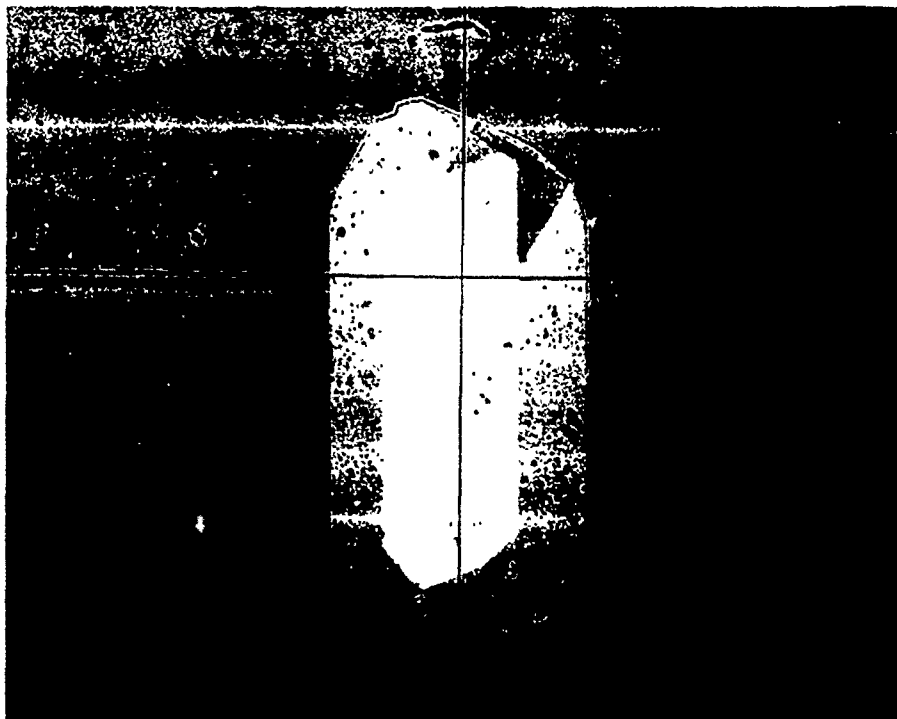


Fig 16  $\beta$ -HMX crystal of Fig 15, after stress removal showing small region of permanent mechanical twinning

Figure 17 is an SEM photo of a stress twinned HMX crystal. The permanently twinned regions are apparent, but the change in shape of the crystal where twinning has occurred is small.

Temperature affects the elastic nature of these mechanical twins. Figure 18 shows a crystal down the 2-fold monoclinic axis, and between nearly crossed polars, that was stressed when the temperature was slightly over 100°C. The twin bands are apparent, but they no longer have any elastic property. It can also be observed that they taper to a point at the leading edge.

Unresolved questions: What is the restoring force that removes the mechanical twins? What happens when the first elastic limit is exceeded? Why don't the twin bands in a heated crystal extend through the crystal?

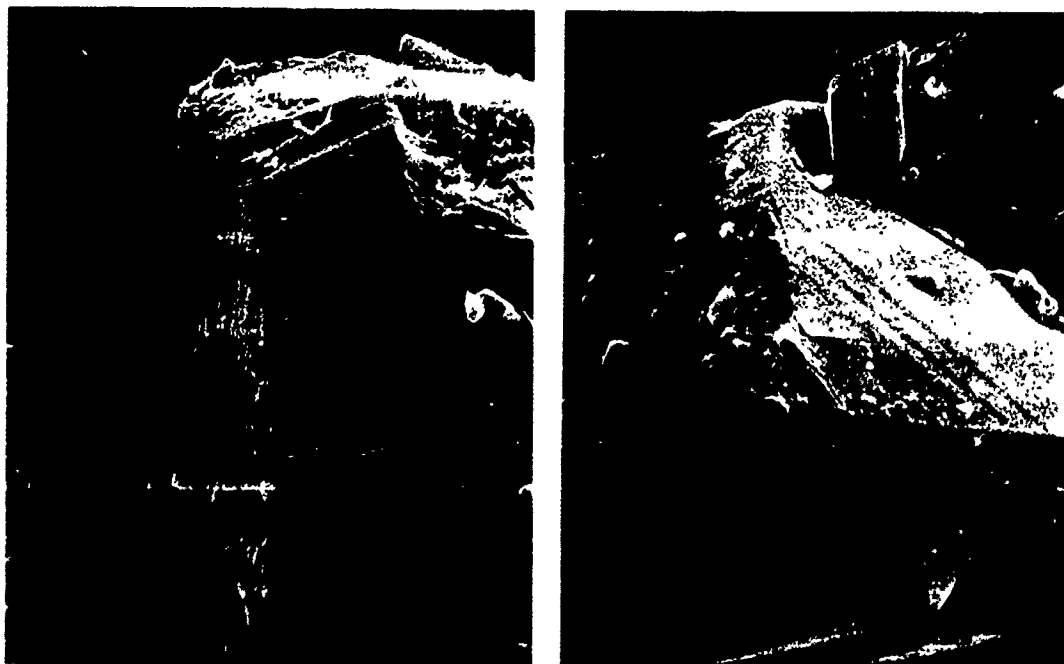


Fig 17. SEM photos of permanently stress-twinned  $\beta$ -HMX. Figure shows 80 x 65  $\mu$  fields



Fig 18  $\beta$ -HMX stressed to mechanically twin at 102°C

---

## PART V

---

### **Statics, Kinematics, and Dynamics**

## SURFACE CHEMICAL CHARACTERIZATION METHODS APPLIED TO ENERGETIC MATERIALS

B.C. BEARD AND J. SHARMA

Naval Surface Warfare Center, Dahlgren Division, White Oak, Silver Spring, MD 20903

### ABSTRACT

The reaction chemistry of energetic materials is often considered only with respect to the types and quantities of gaseous products formed. For a thorough understanding of the initial reaction steps, that largely determine the sensitivity of the material, both gaseous and solid products must be determined. In addition, it is the solid state partial decomposition intermediates remaining in a damaged material that can lead to increased sensitivity. The preference for the initial reactions to take place at the surface of particles and the low concentrations of intermediates formed demands the use of highly sensitive surface specific chemical probe techniques. State of the art surface chemical techniques will be discussed, focusing on x-ray photoelectron spectroscopy and surface mass spectrometry. Principles of operation and performance will be highlighted, comparisons will be made to bulk chemical analysis, and examples of applications will be presented.

### INTRODUCTION

The opportunity provided by this special symposium on Energetic Materials at the Materials Research Society meeting is unique by the fact that traditionally separate research communities are in direct contact. Energetic materials research has become increasingly multidisciplinary due to the complexity of the phenomena. Similarly for the materials scientist, as technology demands more and more novel materials, researchers are forced to take a broad view. The object of this paper is to bridge the gap between these communities, by discussing some of the concerns of the energetic materials community in relation to analysis techniques more familiar to the materials scientist.

The sensitivity of an energetic material is a complex issue depending upon, among others, the physical form, purity or composition of the material, and the nature of the stimulus, whether slow heating, crushing or shock. To unravel this interwoven collection of dependencies, we have undertaken the investigation of the initial reactions in pure energetic materials in response to varying level and type of stimuli.

Surface chemical characterization techniques have been employed in this effort due to the fact that as solids, energetic materials interact with any form of stimulus through their surface. Therefore, reaction leading to the formation of intermediate products will occur preferentially on the surface when the material is stimulated close to the reaction threshold level. In general the amount of reaction suffered by an explosive prior to self sustaining consumption is very small, roughly 1 part in  $10^5$ . As a result sensitivity for detecting these products in an overwhelming matrix of the parent compound is critical. Bulk analytical techniques while in terms of sheer sensitivity are better than surface analysis techniques, (i.e. HPLC - PPb, and NMR - PPb) suffer a dilution effect of at least ten orders of magnitude on going from surface monolayers ( $10^{14}$  molecules) to bulk ( $10^{26}$  molecules). As an illustration, Hoffsommer et.al.<sup>1</sup> observed concentrations of  $1-100 \times 10^{-5}\%$  nitroso derivatives of RDX formed in response to impact. Careful collection and preparation of the samples was required for these determinations.

$$E_{\text{Auger}} = E_K - E_L - E_L \quad (1)$$

The sample limitations of AES are severe owing to the utilization of the high energy electron excitation beam. Surface charging readily accumulates on insulators that cannot be compensated by means of a simple low energy electron flood source as employed in XPS. Due to the high current density within the excitation volume, sample degradation is common for organic materials. Samples are therefore limited to conducting, damage insensitive materials. The major fields of application of AES have been in semiconductor and metals related research, it is inappropriate for energetic materials.

### *X-ray Photoelectron Spectroscopy, XPS*

The photoemission process involves photon absorption into the atom followed by emission of an electron with a kinetic energy (KE) equal to that of the exciting photon ( $h\nu$ ) minus the binding energy (BE) of the electron in the atom.

$$KE = h\nu - BE \quad (2)$$

Binding energies measured from the spectrum provide rapid identification of the elemental composition of the surface. The precise energy of the detected photoelectrons is very sensitive to the chemical state and/or bonding environment of the atom. Therefore, the observed binding energy for a specific element indicate the chemical state(s) of that element present on the surface. Some elements, most notably nitrogen, show a 10-12 eV chemical shift range in their spectra on going from the most reduced to oxidized chemical state. Nitrogen has been the focus of most of the XPS studies on energetics, since the nitro or nitrate ester groupings are the source of oxygen that accommodates the energetic reactions. Early reaction of these groups is observed by the formation of new chemical states in the N(1s) spectrum. A compilation of N(1s) binding energies for a wide variety of nitrogen containing functionalities relative to the nitrate ester binding energy has been established to aid in chemical state identification.<sup>6</sup>

XPS employs characteristic x-ray lines from Mg or Al x-ray sources (1253.6 eV or 1486.6 eV respectively) for excitation of the sample. These are the sources of choice due to their intensity and narrow energy distribution (Mg K $\alpha$  width = 0.7 eV, Al K $\alpha$  width = 0.85 eV) producing sharp photoelectron peaks. Monochromatic radiation is also routinely used to produce spectra with enhanced resolution. The x-ray monochromator Bragg reflects a narrow region of the characteristic Al radiation from specially prepared quartz crystals, reducing the energy distribution (width ~0.25 eV) of the source radiation. This process provides the advantage of narrower photoelectron peaks, thereby increasing resolution and the ability to identify differing chemical states. The most recent advances in XPS resolution has been through the utilization of synchrotron radiation passed through a high performance double focusing monochromator. Photoelectron linewidths have been obtained below 0.2 eV in this work.

Since x-ray focusing is not as highly advanced as for charged particles, the current spatial resolution of XPS is on the order of tens of microns. Spatial resolution is primarily achieved by passing the photoelectrons emitted from the surface through apertures in the imaging electron lens. This approach results in decreased count rates, necessitating longer collection times, and as a result increased radiation damage to the sample.

Radiation induced damage of sensitive materials occurs in XPS but at a much slower rate than for AES. Modern XPS instruments, particularly those incorporating monochromators, have damage rates up to 100 times less than XPS instruments from a decade ago. Improvements in the efficiency of electron optics and multiple or position sensitive detectors have made it possible to collect good quality spectra before any indication of damage is observed. A N(1s) high resolution spectrum from a sample of an energetic molecule can be collected in under three



XPS analysis of pieces of the heat sensitive films, from which the impacted RDX was taken for chemical analysis, displayed up to 10% formation of nitroso derivatives.<sup>2</sup> Techniques that are highly surface specific, therefore, are at a strong advantage to chemically identify the early reaction products preferentially formed on the surface.

Surface chemical characterization techniques will be discussed with regard to theory of operation, sensitivity, specificity, information content and sample limitations. Examples of the application of these techniques will be given, focusing on x-ray photoelectron spectroscopy.

## SURFACE ANALYSIS TECHNIQUES

### Theory of Operation, Electron Spectroscopies

The essential feature of all electron spectroscopies is the creation, collection and energy analysis of characteristic electrons emitted from the sample.<sup>3,4</sup> The limited path length for transmission of low energy electrons (0-2000 eV) through the sample is the source of the surface specific nature of these electron spectroscopies. Electron mean free paths are on the order of 1 nm, limiting the analysis depth to ~5 nm. Once emitted from the sample the electrons must travel to the detector without loss of energy to maintain their analytical information. This places a severe constraint upon the design of electron spectrometers, that being the necessity for ultrahigh vacuum. All of the necessary components for the spectrometer are therefore placed within an ultrahigh vacuum chamber fabricated of stainless steel and pumped by special technology pumps to attain operating pressures of  $10^{-9}$  torr. At such vacuum levels, electron transmission proceeds through the energy analyzer to the detector without appreciable loss of intensity.<sup>5</sup>

Electron spectroscopies are sensitive to all elements but H and He. Most elements offer numerous electron energy levels for analysis and elemental identification. The sensitivity limit of these techniques is on the order of 0.1 At%, of the volume sampled. Given in terms of number of molecules, this corresponds to  $10^{14}$  molecules/monolayer  $\times$  5 monolayers analysis depth  $\times 10^3 = 5 \times 10^{11}$  molecules, or  $\sim 10^{15}$  mole. Quantification of the electron spectroscopic data to  $\pm 5\%$  can be achieved with careful attention to detail in the data analysis. Difficulties with determining accurate signal background removal, electron attenuation lengths and contamination overlayer thickness contribute to the quantitative uncertainty.

### *Auger Electron Spectroscopy, AES*

AES is an electron excited technique that possesses the advantages of focused probe techniques, with the added feature of being truly surface specific. An electron beam accelerated up to 10 keV is focused onto the sample surface defining the analysis area. State of the art instruments have beam currents that can be as low as several nanoamps with beam sizes of tens of nanometers. Imaging and surface elemental mapping on a scale of tens of nanometers can therefore be accomplished.

Auger electron emission results from a three electron process initiated by the development of a core hole (i.e. K level) produced by collision of a high energy electron with a surface atom. Relaxation of an electron from an outer orbital (i.e. L level) into the core hole produces another excited state (due to the energy difference between the core and outer orbital energy) that is compensated for by the emission of a third electron (i.e. another L level), the Auger electron. Shorthand notation for the Auger transition lists the levels involved, i.e. KLL as indicated in the preceding example. The Auger electron energy can be expressed as given in eqn. (1) using the energies of the individual electron levels involved in the process. The Auger electron energy is independent of the excitation beam energy and is characteristic of the element and in some cases the chemical state of the element.

minutes. Damage rates routinely observed on the modern instrument in this laboratory are such that greater than 30 minutes monochromatic x-ray exposure are required before damage is observed on materials such as ammonium perchlorate. Damage of organic molecules is typically manifested by the chemical reduction of highly oxidized organic functionalities (i.e. nitro groups) or the loss of a pendant group or hetero atom from the molecule (i.e. F from teflon).

Sample limitations are very modest in XPS. Insulators pose little charging problem in general, typically charging only 2-5 eV. X-ray sources produce a high background of low energy electrons that substantially reduces the surface charging. Difficulties arise when differential charging occurs, for example on the surface of a powdered insulating sample. Charge compensation by a low energy (2-10 eV) electron flood source in most cases is an adequate solution. Monochromatic sources create more severe charging problems due to the isolation of the source generated electrons by the monochromator housing. Alternative schemes can be employed in difficult charging cases to obtain useful data<sup>7</sup>.

### Theory of Operation, Ion Spectroscopies

Ion techniques determine the atomic and molecular nature of a materials surface by the mass of the fragments released from the surface in response to excitation.<sup>8</sup> The techniques, Secondary Ion Mass Spectrometry (SIMS), Secondary Neutral Mass Spectrometry (SNMS) and Surface Analysis by Laser Ionization (SALI) can be viewed as taking place in three steps, surface desorption, ionization and detection.

The first step is surface desorption, most commonly accomplished by ion sputtering with a high energy (2 - 10 KeV) ion beam directed at the surface. The desorbed fragments may be atomic or molecular, charged or uncharged. Ion sputtering employs a wide variety of ion sources, noble gas (Ar, Ne, Xe), reactive gas (O) or liquid metal (Cs, Ga) to attain the desired sputtering conditions from the surface. Sputtering rates are a critical parameter since sputtering is actually sample consumption or destruction. "Static" rates remove less than one monolayer in the time required to collect useful data to investigate the surface chemistry. "Dynamic" rates rapidly erode the upper layers of the sample to measure the depth dependence of sample composition. Removal dimensions can vary from millimeters to submicron depending greatly on the type of ion source used.

The second step in the process is ionization of the removed material prior to introduction into the mass spectrometer. At this point the three techniques listed above diverge from one another in operation. SIMS utilizes the ionized fraction of particles created during the sputtering of the surface. Due to the low ionization efficiency, <10% for most materials, and dramatic substrate ('matrix') effect upon this process, SIMS suffers from severe quantification problems. SNMS avoids the ionization probability problems associated with the sputtering process by post-ionizing the sputtered neutrals (>90% of sputtered material) by means of electron bombardment ionization. The most important advantage of SNMS is the decoupling of the ionization event from the surface, eliminating the substrate effects on quantification. SALI is a further refinement on SNMS, employing a laser as the post-ionization method. Selection of laser wavelength provides advantages for specific types of analysis.<sup>9,10</sup> A 10% ionization yield of the sputtered neutrals can be attained, enhancing the overall ionization efficiency by at least ten times. The sensitivity of SALI has been estimated in one case at the ppm level with only  $10^{10}$ g of sample utilized for the analysis,<sup>11</sup> another example estimated the amount of material needed to definitively identify a sample at  $3 \times 10^{16}$  mole<sup>12</sup>.

The final phase of surface ion spectroscopy is mass to charge analysis and detection. Three types of mass spectrometers can be employed, a magnetic sector, a quadrupole or a time-of-flight (TOF). Each type of instrument has advantages relative to the others, dynamic SIMS instruments typically employ a quadrupole analyzer, whereas, TOF is used for static analyses primarily due to its high ion transmission efficiency.

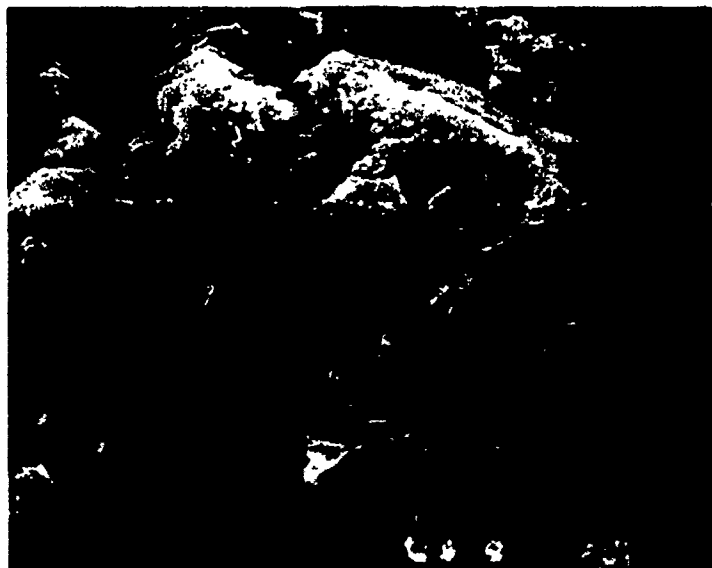


Figure 1. SEM micrograph of underwater-shocked TATB showing reaction sites as ragged holes on the edges and on the surface of TATB layers

#### Application of Surface Chemical Analysis to Energetic Materials

The majority of the data collected over the past ten years has been with XPS. Several examples of the application of XPS will be given. Studies where mass spectrometry has been greatly important to the elucidation of the molecular form of the intermediates are also included.

##### *Triamino-Trinitrobenzene*

One of the most striking results to come from the application of surface analysis techniques to energetic materials research was the first actual observation of hot spot remnants and associated chemical decomposition products in impacted or shocked TATB, Figure 1<sup>13</sup>. This work established a chemical basis of hot spot reactions and sensitization of damaged energetic materials. XPS of damaged TATB found a significant alteration in the N(1s) spectrum consistent with the formation of new nitrogen chemistries. The compounds identified were furoxan and furazan derivatives of TATB resulting from the loss of molecular hydrogen or a water molecule respectively from the parent TATB.<sup>14</sup> The identification of these intermediate products was through the use of both XPS and mass spectrometry, specifically, chemical ionization thermal desorption mass spectrometry. XPS has outstanding sensitivity for identifying the chemical state of atoms present on the surface, however, when wishing to identify a specific molecular product, mass spectrometry is far superior. In reference 14 a discussion of the analysis of TATB recovered from the verge of ignition is described in full.

Once the nature of the intermediate decomposition products of TATB were known, the relative sensitivity of these molecules to TATB could be assessed. The furoxan compounds were found to be significantly more sensitive than TATB, while the furazan compounds were equivalent to TATB<sup>15</sup>. The presence of intermediate decomposition products adjacent to the extinguished hot spot sites gave clear indication of the sensitizing effect created in damaged material.

### *Ammonium Perchlorate*

Ammonium perchlorate (AP) is a powerful oxidizer commonly found in energetic compositions. The decomposition mechanism of this material in its pure state has been the subject of many publications, particularly in the early days of solid propellant development. The studies presented here have focused on the early reactions of AP as a means of gaining insight into potential safety problems associated with AP containing compositions. This type of study is fundamental with regard to new insensitive munitions performance sought by the military. (Important to the development of insensitive compositions is the minimization of response by the material to unintentional impact, electrostatic discharge, thermal and shock stimuli.)

Powdered AP was subjected to impact by a 10 Kg weight, dropped from a range of heights. The sample was sandwiched between heat sensitive film to aid in the identification of areas that experienced exothermic reaction. Of particular interest in this case was the intermediate reaction chemistry of the perchlorate anion that supplies the oxygen for continued oxidation reactions. XPS spectra of control AP show a single chemical state for the chlorine, that is Cl(+7), with the Cl(2p,3/2) photoelectron line appearing at 208.5 eV. The Cl(2p) photoelectron spectrum is comprised of a spin split pair of peaks, separated by ~1.6 eV, and of 1:2 area ratio. Impacted material can show as many as three additional chemical states. Figure 2 is a Cl(2p) spectrum from impacted AP (10 Kg, 135 cm). The chemical states observed arise from Cl(+5), Cl(-1), and Cl(+1). The Cl(-1) state is assigned to chloride formation resulting from the liberation of two moles of O<sub>2</sub> from the original perchlorate anion. Cl(+5) is attributed to partial reduction of the perchlorate to ClO<sub>3</sub>, chlorate, a species previously observed in gas phase decomposition and radiolysis studies.<sup>16</sup> The other product is identified as Cl(+1) based on the peak position in the spectrum. The known stability of the oxy-chloride anions, however, suggests that Cl(+1) as hypochlorite would not be stable under ambient conditions.<sup>17</sup>

Impacting the sample from greater drop heights results in little change in the type of products formed. The trend observed is for ever increasing chloride concentration with an associated decrease in perchlorate concentration. A small amount of chlorate is often observed as well as the Cl(+1) species. These species are apparently true intermediates, since their concentration does not increase over a few percent regardless of the extent of conversion of perchlorate to chloride.

In some cases, nitrogen in a more oxidized state has been observed, suggesting the formation of oxidized nitrogen.

The formation of reaction products on the surface and in the solid structure of an energetic material can have dramatic effects on the stability and reaction threshold of the remaining material. Chloride has been found to strongly affect the melting point of metal perchlorates, reducing the melting point by as much as 120°C for RbClO<sub>4</sub> mixed with 30% RbCl<sup>18</sup>. Immediately at the onset of melting the material exothermically decomposes. Similar catalytic effects of chloride in AP have been observed resulting in increased favorability for reaction or auto-dissociation. Chlorates have been found to accelerate the decomposition of AP<sup>19</sup>. The identification of these two intermediate products provides clear evidence for the existence of chemical sensitization in damaged materials containing AP.

Surface mass spectrometry by SALI has been employed to aid in the identification of the molecular nature of the Cl(+1) product observed in damaged AP. In this case the damage to

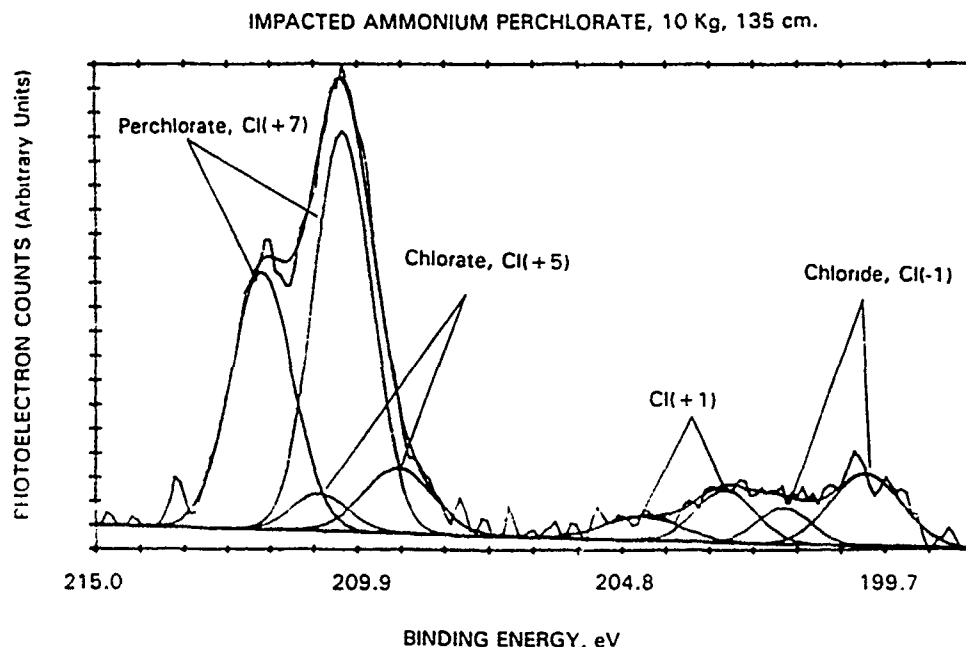


Figure 2. Cl(2p) XPS spectrum of impacted (10 Kg, 135 cm) AP.

the crystalline AP was impacted by prolonged x-ray irradiation causing photo-degradation of the surface. SALI analysis was performed at Physical Electronics Laboratories, Eden Prairie, MN on a prototype instrument. The SALI results indicated an increase relative to the control sample in the concentration of  $\text{NO}$ ,  $\text{H}_2\text{NCl}$  and  $\text{HClO}_2$  after irradiation. New species assigned to  $\text{HNCl}_2$  and  $\text{H}_2\text{ClO}_2$  were observed in the damaged sample. These new spectral features were attributed to the formation chlorate and chloramines. The observation of chloramines is consistent with earlier work where  $\text{NH}_2\text{Cl}$  was observed as a product of condensed-phase decomposition by mass spectrometry<sup>20</sup>. Significant to the stability of damaged AP is the fact that the chloramines  $\text{H}_2\text{NCl}$  or  $\text{HNCl}_2$  in either the liquid or solid state has been found to be quite unstable<sup>21</sup>. Chloramine can be chemically prepared by the action of  $\text{ClO}_2$  on  $\text{NH}_3$ , both of which are present in the decomposition of AP. Stabilization of the chloramine by or in the solid lattice may therefore be occurring to make it visible to surface analysis techniques long after creation. Analysis of impact damaged AP by SIMS has not been able to reproduce the results obtained by SALI on the irradiated sample. The difference in the results may reflect the differences in the location of the damaged material (soft x-ray irradiated samples have the majority of the decomposition occurring on the surface), the techniques themselves and the greater sensitivity of SALI. While the evidence is not overwhelming for the chloramine, the consequences of the presence of all the intermediates observed in damaged AP can significantly aggravate the sensitivity of damaged AP containing compositions.

Another aspect affecting the initial reaction chemistry of an energetic material are physical structures that concentrate or localize the stimulus energy. XPS has played a major part in an investigation that clearly demonstrated the effect of localized defect concentrations on the onset of chemical reaction<sup>22</sup>. An AP single crystal with defects induced in localized areas of the surface was subjected to sub-threshold shock. Cleaving through the crystal and recovery at the surface location of an induced defect provided a surface for investigation by XPS. Chemical decomposition was observed only in the area directly adjacent to the defect concentration, Figure 3. The exceptional surface and chemical sensitivity of XPS was able to identify the low levels of reaction products and map out their distribution across the cleaved surface. This result is a highly significant demonstration of the role of defects as energy concentrators leading to the localized onset of early reaction chemistry.

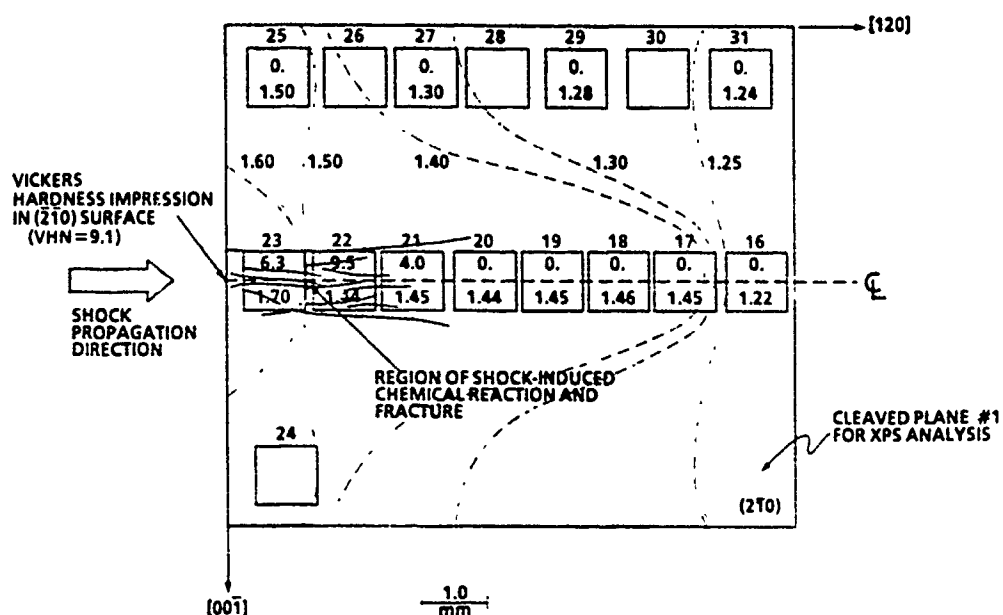


Figure 3. Diagram of cleaved surface of shocked AP single crystal. Boxes represent area of XPS analyses with the run number at the top of each box. The top number inside each box represents the amount of chlorate formed by shock induced chemistry. The lower number in each box is the linewidth of the Cl(2p,3/2) peak from the perchlorate and areas of equivalent linewidth spectra are joined by the dotted lines.

#### *Surface analysis of adhesion at the propellant-liner interface*

Surface analysis is often called upon to assist in the resolution of real world problems associated with energetic materials. One example of this type of practical application was the investigation into the failure of a new lot of small propellant units<sup>23</sup>. Upon acceptance testing of this new lot of propellant units, failures were occurring at a high rate. Studies of the recovered fragments by SEM and IR were unable to isolate the reason for the failures. XPS analysis of casing fragments from a failed test unit indicated the presence of Si as a contaminant on the interior casing surface. High resolution analysis of the Si(2p) photoelectron line found the chemical state of this silicon to be intermediate between zero valent silicon and silicon dioxide. By comparison to a series of reference samples, the chemical state was found to correspond to a silicone oil. Film thickness determinations indicated the contamination to be on the order of 1.1 nm thick, about 2 molecular layers. Control samples from various steps along the process route were supplied by the contractor resulting in the identification of the process step that introduced the contamination. With this information the process could be controlled to eliminate this problem in the future. The surface specificity, ability to identify elements and the chemical sensitivity of XPS came together in this study to provide a clear understanding of the nature and source of the failures.

#### *Nitramine Decomposition by slow radiation degradation*

One potential pit-fall that must be carefully avoided in the XPS analysis of organic materials is the chemical changes induced by extended irradiation of the sample, as previously discussed. However, by using x-rays as a controllable damage method, investigations of the early reaction chemistry in a material can be performed in a controlled manner

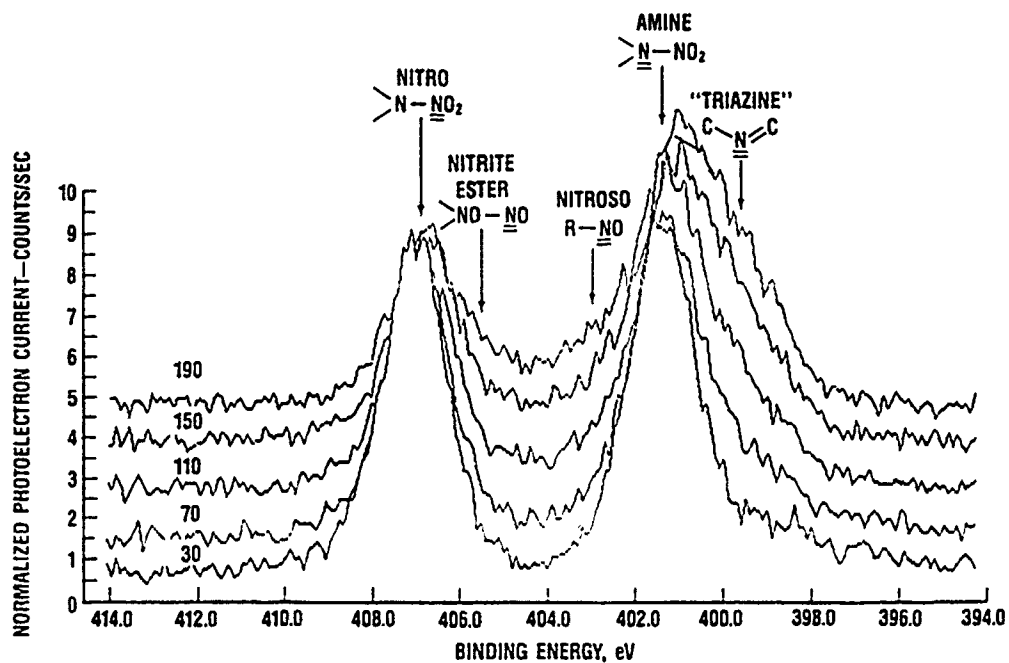


Figure 4. N(1s) spectra from RDX at -50°C as a function of x-ray time, numbers above each curve indicate the duration of continuous x-ray irradiation in minutes

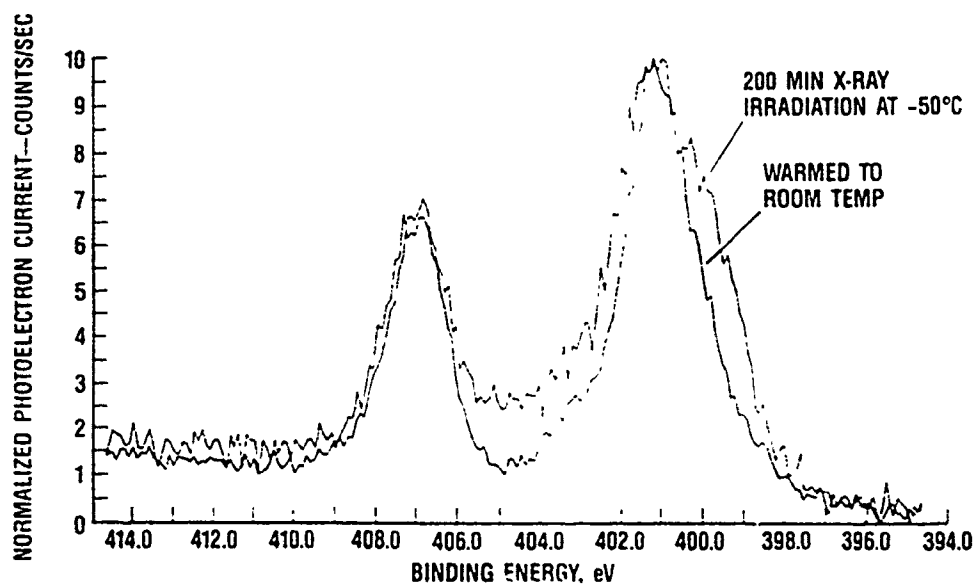


Figure 5. N(1s) XPS spectrum from RDX irradiated for 200 minutes at -50°C and following warming to room temperature.

In an interesting study of the early reaction chemistry of the nitramine RDX, x-ray damage was used to create reaction intermediates with simultaneous evaluation by XPS.<sup>24</sup> The powder sample was freshly ground, mounted on double-sided tape and cooled to -50°C. By continuously shining the x-ray beam on the sample and collecting repeated XPS spectra, the changes in the surface chemistry as a function of irradiation time were observed. Figure 4 shows the original N(1s) spectrum from RDX and the accumulation of damage products as a function of extended irradiation time. The products that developed were a nitroso derivative, a triazine product and a newly discovered unstable intermediate, nitrite ester. The nitroso and triazine products have been observed before<sup>1,2</sup> in room temperature studies of damaged RDX. At the lower temperature, however, intermediates that would otherwise spontaneously dissociate were stabilized for clear identification. Warming of the damaged material to room temperature, (figure 5) demonstrates the temperature sensitivity of the nitrite ester, as well as some of the forms of nitroso and triazine produced during the irradiation. The similarity of these results to those obtained by thermal decomposition<sup>25</sup>, suggest that the same mechanism is active for both photolysis and thermolysis. The exciting results obtained in this short term study suggest this as a general method for the elucidation of early reaction products under "pseudo-thermal decomposition" conditions. This experimental arrangement provides several advantages, access to low temperature, control of the environment and real time characterization of product formation. With the addition of a residual gas analysis mass spectrometer it would also be possible to follow the gaseous products formed both during irradiation and subsequent warming to room temperature.

## SUMMARY

This paper has focused on the basic background and application of surface analytical techniques to the study of energetic materials. X-ray photoelectron spectroscopy has been highlighted as it is particularly suited to this specific application due to the chemical state information obtained, the range of spatial analysis areas obtainable and the limited sample damage rate compared to AES or SIMS. Illustrations have been provided of a small collection of the work performed in this laboratory over the past ten years. These provide a demonstration of the capability of these powerful materials research tools when applied to the demanding field of energetic materials research.

## ACKNOWLEDGEMENT

The authors wish to acknowledge support for this work by the Independent Research Program at the Naval Surface Warfare Center, Silver Spring, MD.

## REFERENCES

1. J.C. Hoffsommer, D.J. Glover and W.L. Elban, *J. Energetic Materials*, **3** (1985) 149.
2. J. Sharma, J.C. Hoffsommer, D.J. Glover, C.S. Coffey, J.W. Forbes, T.P. Liddiard, W.L. Elban and F. Santiago, Eighth Symposium (International) on Detonation, July 15-19 1985, Albuquerque, New Mexico, NSWC MP 86-194. Naval Surface Warfare Center, Silver Spring MD. 20903-5000, pg 931.
3. D. Briggs and M.P. Seah, Practical Surface Analysis, by Auger and X-ray Photoelectron Spectroscopy, John Wiley & Sons, New York, ©1983



4. Methods and Phenomena 1 / Methods of Surface Analysis, Ed. A.W. Czanderna, Elsevier Scientific Pub. Co., Amsterdam, ©1975.
5. R.C.G. Leckey, J. Elec. Spectr. Rel. Phen., 43 (1987) 183
6. "Cellulose Nitrate as a Binding Energy Reference in N(1s) XPS Studies of Nitrogen Containing Organic Molecules", B.C. Beard, *Applied Surface Science* 45 (1990) 221.
7. A. Cros, J. Elect. Spectr. Rel. Phen., 59 (1992) 1
8. Secondary Ion Mass Spectrometry, Basic Concepts, Instrumental Aspects, Applications and Trends, A. Benninghoven, F.G. Rudenauer and H.W. Werner, Wiley-Interscience, Chemical Analysis series Volume 86, ©1987.
9. C.H. Becker and K.T. Gillen, *Anal. Chem.* 56 (1984) 1671
10. U. Schuhle, J.B. Pallix and C.H. Becker, *J. Vac. Sci. Tech.*, A6(3) (1988) 936
11. C.H. Becker and K.T. Gillen, *Anal. Chem.*, 56 (1984) 1671.
12. U. Schuhle, J.B. Pallix and C.H. Becker, *J. Am. Chem. Soc.*, 110 (1988) 2323.
13. J. Sharma, J.W. Forbes, C.S. Coffey and T.P. Liddiard, *J. Phys. Chem.*, 91 (1987) 5139
14. Comparative Study of Molecular Fragmentation in Sub-initiated TATB Caused by Impact, UV, Heat and Electron Beams, J. Sharma, J.C. Hoffsommer, D.J. Glover, C.S. Coffey, F. Santiago, in *SHOCK WAVES IN CONDENSED MATTER - 1983*, J.R. Asay, R.A. Graham and F.K. Straub (Editors), ©Elsevier Science Publishers B.V., 1984
15. R.L. Willer, Technical Report No. TP 6397, 1982 Naval Weapons Center, China Lake, CA, Technical Report No. TP 6461, 1983, Naval Weapons Center, China Lake, CA
16. Structure and Stability of Salts of Halogen Oxyacids in the Solid Phase, F. Solymosi, John Wiley & Sons, New York, ©1977, pg 259.
17. Kirk-Othmer, Encyclopedia of Chemical Technology, Third Edition, Vol. 5, ©1981, John Wiley & Sons.
18. Structure and Stability of Salts of Halogen Oxyacids in the Solid Phase, F. Solymosi, John Wiley & Sons, New York, ©1977, pg 129.
19. *ibid*, pg 259.
20. J.R. Majer and M. Smith, *Combustion and Flame*, 13 (1969) 635.
21. *Advanced Inorganic Chemistry*, F.A. Cotton and F. Wilkinson, Fifth Ed., John Wiley & Sons, New York, ©1988, Pg 332.
22. Dislocation Density Variation in Shocked Single Crystal Ammonium Perchlorate under Compression of Condensed Matter 1991, Williamsburg, VA, S.C. Schmidt, R.D. Dick, J.W. Forbes and D.G. Tasker (Editors), Pg 571, North-Holland, New York, ©1992.
23. "Correlation of Catastrophic Solid Rocket Motor Failure with Silicone Contamination at the Propellant/Liner Interface." B.C. Beard and B. Crowley, NSWC-TR-89-64, 1 March 1989

24. "X-Ray Radiation Decomposition of (RDX), Cyclo-1,3,5-trimethylene-2,4,6-trinitramine, at Low Temperature: Initial Reaction Steps", B.C. Beard, Propellants Explosives and Pyrotechnics, 16 (1991) 81.
25. J.C. Hoffsommer and D.J. Glover, Combustion and Flame, 59 (1985) 303.

## SURFACE CHEMISTRY OF ENERGETIC MATERIALS AT HIGH TEMPERATURE

THOMAS B. BRILL

University of Delaware, Department of Chemistry, Newark, DE 19716

### ABSTRACT

The chemistry at the surface of a burning propellant plays a major role in the burn-rate, the stability of the flame, and the potential for a run-away hazardous event. Chemical details can be determined experimentally by simulating the burning surface with a thin film of material heated rapidly to the surface temperature. T-Jump/FTIR spectroscopy is designed to create these conditions. The dominant, initial, heat-producing reactions in the surface zone of  $\text{NH}_4\text{ClO}_4$ ,  $\text{NH}_4\text{NO}_3$ ,  $\text{NH}_4[\text{N}(\text{NO}_2)_2]$ , HMX, RDX, and DNNC are elucidated at high temperatures representative of the burning surface.

### THE BURNING SURFACE

One of the challenges that remains in the field of propellant combustion is to obtain a sufficiently detailed description of the heterogeneous gas-condensed phase zone at the burning surface. A generalized one-dimensional picture of this zone is shown in Fig. 1. Conceptual models of combustion that include this zone have been formulated in many

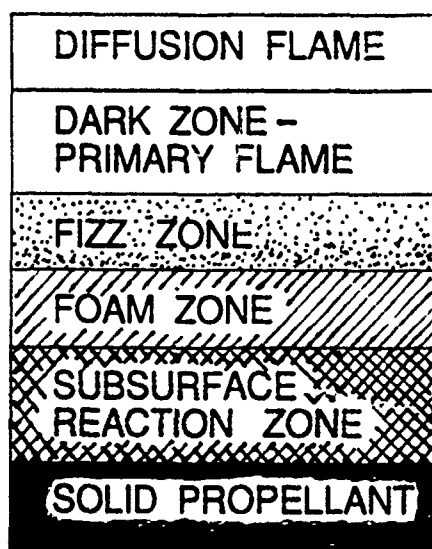


Fig. 1. Generalized Surface Reaction Zone of a Burning Propellant.

works with Rice and Ginell [1], Williams, et al. [2,3], Ben-Reuven and Caveny [4], Cohen, et al. [5], and Kubota and Sakamoto [6] being several examples. However, the description of the burning surface that is based in experiment is vitally important because entirely unanticipated pathways sometimes arise. For example, diaminofurazan and diaminoglyoxime are found to retard the burn rate of ammonium perchlorate composite propellants [7]. The mechanism was discovered in rapid thermal decomposition studies to be retardation of heat and mass transfer at the burning surface due to formation of highly thermally stable azine polymers, including melem and melon [8]. This mechanism would not have been considered without experimental evidence.

Of special interest in the surface reaction zone of propellants are the early highly exothermic reactions because they

play a disproportionately large role in the combustion characteristics. For instance, the burn-rate is strongly influenced by the amount and rate of heat released at the surface. Instability of combustion in the diffusion flame causes pressure and temperature oscillation at the surface. Highly exothermic reactions in the surface reaction zone provide the chemical connection of these oscillations to the surface. Also, controlling the early highly exothermic reactions is a central scientific issue in reducing the sensitiveness of an energetic material.

The complexity of the chemical and physical details of the burning surface is so great as to defy direct study with the flame present. The reaction zone is physically thin (1-100  $\mu\text{m}$  depending on the pressure), spatially transient, a mixture of solid, liquid and gas, and not in chemical equilibrium, all as a result of the steep temperature gradient. Based on these characteristics, a "snap shot" simulation of a burning surface would be a film of material heated at a high rate to a temperature typical of the surface during steady combustion [9]. The advantage of this simulation is that various spectroscopic diagnostics can be used to resolve chemical events in time. Therefore, the sequential chemistry of energetic materials under relevant pressure and temperature conditions can be determined for the first time.

## EXPERIMENTAL TECHNIQUES

T-Jump/FTIR spectroscopy has been described elsewhere [9]. In a typical experiment approximately 200  $\mu\text{g}$  of polycrystalline sample is spread on a Pt ribbon filament that is housed in a gas-tight IR cell having about 1.5  $\text{in}^3$  internal volume. The cell is flushed with Ar and pressurized as desired. The filament is heated by a power control unit at about 2000  $^\circ\text{C/s}$  to a constant temperature in the 240-500  $^\circ\text{C}$  range depending on the sample. Control is achieved by rapidly sensing the Pt resistance. Endothermicity and exothermicity of the sample is detected by monitoring the control voltage required to maintain constant resistance. The difference control voltage is obtained by subtracting the voltage of the filament without sample from the voltage when the sample is present. A negative excursion represents an exotherm of the sample.

Because of the small mass, the sample temperature is relatively uniform. However, the interfacial heat transfer is complex. The sample and the filament form a reaction zone that contains the gas and condensed phase in close contact with the heat source. From the point of view of the chemistry of the heterophase surface, this condition qualitatively resembles a surface during combustion. Instead of forming a flame, the decomposition products rise into and are quenched by the cool Ar atmosphere. The beam of a rapid-scan FTIR spectrometer is positioned about 3 mm above the sample surface. Collection of complete IR spectra every 100 msec gives the identity, sequence of formation, and relative concentrations of the products.

The IR absorbances for each product are converted to concentrations by multiplying the absorbance of a characteristic vibrational mode by a factor derived from the absolute absorbance [10]. In this way the rate of evolution of the product is ascertained. IR inactive products are not detected.  $\text{H}_2\text{O}$  is detected but was not quantified.

The SMATCH/FTIR technique and data reduction methods have been described elsewhere [11-14]. Briefly, a film of sample of known mass is coated onto the stainless steel end-tip of the quartz vibration element. The rate of weight loss during heating at 250  $^\circ\text{C/s}$  is determined by the change of the vibrational frequency of the tube. A thermocouple spot-welded to the metal end-tip provides a real-time temperature measurement. The initial 50% of weight loss is fit by the polynomial equation (E1).

$$1 - \alpha = \sum_{i=0}^3 a_i t^i \quad (\text{E1})$$

This polynomial and its first derivative yield  $1-\alpha$ , and  $d\alpha/dt$ , respectively, for use in E2 where  $\alpha$  is the fraction of the sample decomposed [12-14]. E2 was found to be linear by the appropriate choice of  $n$ . The resulting activation energy and prefactor apply only at

$$\ln \left[ \frac{d\alpha}{dt} \frac{1}{(1-\alpha)^n} \right] = \ln A - \frac{E_a}{RT} \quad (\text{E2})$$

the pressure and temperature conditions of the experiment. The regression rate of the film,  $\dot{r}$ , is calculated by a modified version of the pyrolysis law, E3, where  $h$  is the film

$$\dot{r} = A h e^{-E_a/RT} \quad (\text{E3})$$

thickness. E3 is valid if  $h$  is approximately the thickness of the surface reaction zone during combustion at 1 atm.

### REGRESSION RATE OF A BULK MATERIAL VS. A THIN FILM

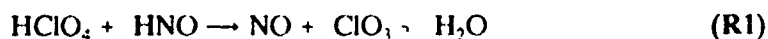
The burn rate of bulk monopropellants and oxidizers extrapolate reasonably well to the regression rate computed from the Arrhenius data determined by SMATCH/FTIR

Table 1. Burn rate comparisons		
Compound	$\dot{r}$ , mm/sec (1 atm)	
	SMATCH	Strand burner
AP	0.16	0.25
HMX	0.37	0.5
RDX	0.38	0.38
DNNC	0.27	0.27
13%N NC	0.3	0.4
GAP	1.35	1.7

spectroscopy [12-16]. Table 1 shows selected data that are evidence of the connection. The good correlation gives confidence in the use of decomposition data obtained from rapidly heated thin films to characterize the dominant chemistry at a burning surface. The identity of dominant exothermic reactions of important energetic materials emerges from T-jump/FTIR studies. Selected studies are given below on compounds of practical use as explosives and propellants.

### THE $\text{HClO}_4$ - $\text{HNO}$ REACTION OF $\text{NH}_4\text{ClO}_4$

In excess of 1000 reactions may be involved in the decomposition and combustion of ammonium perchlorate (AP),  $\text{NH}_4\text{ClO}_4$ , [17] because of the presence of four elements and the full range of oxidation states utilized by nitrogen and chlorine. A limited chain reaction scheme of 10 reactions employed by Guirao and Williams [2] to model AP combustion was expanded to 80 reactions by Ermolin, et al., [17] to simulate the gas products in the flame zone measured by microprobe-mass spectrometry [18]. Of the many reactions, Guirao and Williams and Ermolin, et al., both emphasize the important role that R1 plays in controlling the rate of the gas phase reaction.



T-Jump/FTIR spectroscopy [9] has the potential to provide evidence of R1 as well as other aspects of the rapid decomposition mechanism of AP. For example, during the rapid decomposition of bulk AP, a drop in the  $\text{HClO}_{4(g)}$  production accompanied by a sharp rise in the  $\text{NO}$  and  $\text{H}_2\text{O}$  concentrations during the stage of rapid heat release would be good evidence for R1 in the heterogeneous gas-condensed phase.

Figure 2 shows the change of concentration of the gas products from AP measured from the absorbances by rapid-scan FTIR spectroscopy, along with the heat balance sensed by the Pt control voltage [16]. Before the exotherm IR active gas products are first detected at about 5 s and consist of  $\text{HNO}_3$ ,  $\text{NO}_2$ ,  $\text{N}_2\text{O}$ ,  $\text{H}_2\text{O}$ ,  $\text{HClO}_4$ , and  $\text{HClO}_{4(aq)}$ . The rise in gas product concentrations over the next few seconds indicates that the amount of sample decomposing gradually increases. The overall process is exothermic because the control voltage acquires a slight negative slope during this time.

The initial decomposition reaction of AP is widely regarded to be dissociative evaporation R2. Evidence of this reaction exists below 3 atm where recombination



of  $\text{NH}_{3(g)}$  and  $\text{HClO}_{4(g)}$  to form  $\text{NH}_4\text{ClO}_{4(\text{aerosol})}$  is observed in the IR spectrum. Below 13 atm Ar, no  $\text{NH}_4\text{ClO}_{4(\text{aerosol})}$  and  $\text{NH}_3$  are detected, but  $\text{HClO}_4$  is present, mostly in the hydrated form. The fact that some  $\text{HClO}_4$  survives to reach the cool atmosphere, whereas  $\text{NH}_3$  does not, may simply result from the fact that AP is over oxidized. Not all of the  $\text{HClO}_4$  is needed to oxidize  $\text{NH}_3$ . Hydrated  $\text{HClO}_4$  from AP was confirmed by the match of the  $\text{ClO}_4^-$  asymmetric stretching mode with that of the gas phase above a rapidly heated 70%  $\text{HClO}_4$  solution [16].

The  $\text{NH}_3$  from R2 is oxidized very rapidly in the heterogeneous gas-condensed phase zone by  $\text{HClO}_4$ . No  $\text{NH}_3$  survives to reach the IR beam because the inversion doublet at 968 and 932  $\text{cm}^{-1}$  is absent. The reduction product of  $\text{HClO}_4$  is  $\text{Cl}_2$  because no  $\text{HCl}_{(g)}$ , hydrated  $\text{HCl}$ , or  $\text{NH}_4\text{Cl}_{(\text{aerosol})}$  are observed in this stage of decomposition.  $\text{NO}_2$ ,  $\text{N}_2\text{O}$ ,  $\text{HNO}_3$  and  $\text{H}_2\text{O}$  are products of ammonia oxidation.  $\text{HNO}_3$  may simply result from hydrolysis of  $\text{NO}_2$  and, as such, would not be an important product were a flame present.  $\text{N}_2\text{O}$  can form by R3. Preventing the build-up of  $\text{HNO}$  (*vide infra*) by R3 would be one of the chemical ways that AP is able to decompose slowly at lower temperature without developing a runaway release of heat.



The development and growth of the exotherm of AP in Fig. 2 is a sharp event. The gas product concentrations during the exotherm are unusual in the occurrence of the large pulse of  $\text{NO}$ ,  $\text{HCl}$  and  $\text{H}_2\text{O}$ . The  $\text{HClO}_4$  concentration remains at or below the pre-exotherm level. The behavior of  $\text{HClO}_4$ ,  $\text{NO}$  and  $\text{H}_2\text{O}$  are fully consistent with a major role of R1 in the acceleratory exothermic phase of AP decomposition. R1 increases in importance and ultimately controls the overall rate because  $\text{HNO}$  accumulates with time [17]. At the time when R1 dominates the rate, R3 is largely

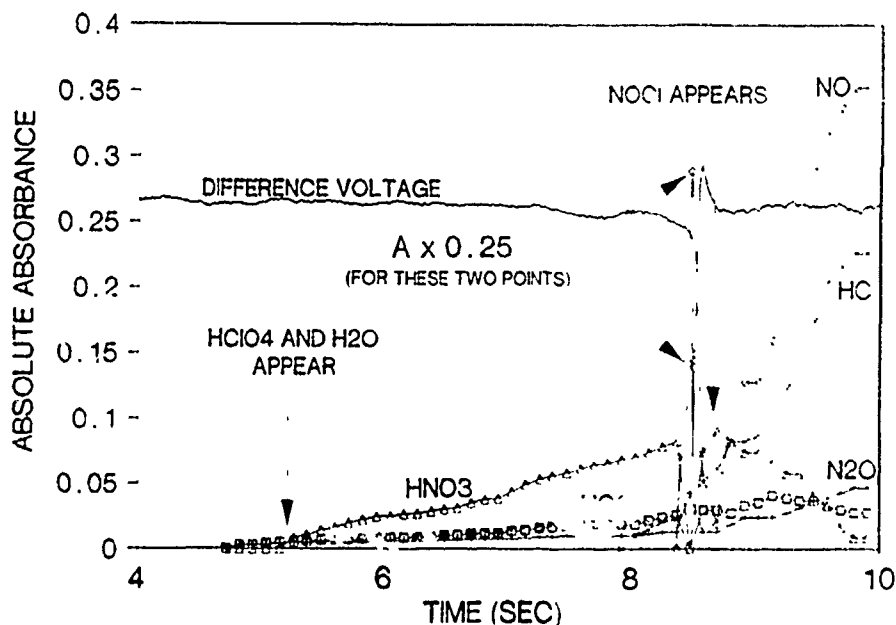


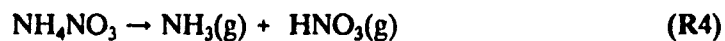
Fig. 2. Gas Products and the Heat Change of  $\text{NH}_4\text{ClO}_4$  at 440°C under 13 atm Ar.

shunted as evidenced by the fact that the final concentration of  $N_2O$  is only approximately double the pre-exotherm value. Because of their reactivity and short-life time at the temperature of the experiment, HNO and  $ClO_2$  are not detected. In fact, for the same reason, no chlorine oxides or HClO are observed, but they are by mass spectrometry [17,18]. HNO has also been detected by mass spectrometry in the decomposition of AP in other work [19].

The importance of Cl-O homolysis of  $HClO_4$  in initiating and perhaps controlling rapid decomposition of AP has been repeatedly emphasized in many studies. It is highly likely that a fundamental role exists for HNO in the sense that products of both the early stage and exothermic stage are consistent with reactions of involving HNO. It plays a major role in the regression rate of AP.

### THE $NH_3$ - $NO_2$ REACTION IN AMMONIUM NITRATE-LIKE SALTS

Interest is growing in oxidizers that might replace ammonium perchlorate (AP) in solid propellants. Upon combustion, AP liberates HCl and  $H_2O$  that form an environmentally undesirable plume of  $HCl_{(aq)}$ . Nucleation of  $H_2O$  into droplets by HCl contributes to a prominently visible signature. These detracting features have rekindled interest in ammonium nitrate (AN). Unfortunately, AN has a low surface temperature and a low burn rate. The decomposition chemistry of AN is largely responsible for the low energy release. For example, two major decomposition reactions of AN, R4 and R5, are endothermic and mildly exothermic, respectively.



The decomposition of AN is compared to that of ammonium dinitramide (ADN),  $NH_4[N(NO_2)_2]$  [20]. Unlike AN, ADN decomposes very rapidly. Part of the additional energy release is attributable to the higher heat of formation of ADN (-35 kcal/mol [21]) compared to AN (-78 kcal/mol). Beyond this difference, the chemical reactions that cause ADN to decompose very exothermically are not obvious because the gas products from rapid thermolysis of ADN are similar to those of AN. Both compounds liberate  $HNO_3$ ,  $NH_3$ ,  $N_2O$ ,  $NO_2$ , NO,  $H_2O$  and  $N_2$ , although the mole fractions differ somewhat. By T-jump/FTIR spectroscopy it seems likely that the reaction of  $NH_3$  and  $NO_2$  near the surface plays a major role in driving the regression of the surface [20].

Although pure AN will not burn at 1 atm, a sample can be driven by the T-jump method to a temperature that is at or above the measured surface temperature of AN burning at 25 atm or above (300-350°C [22]). Figure 3 shows the gas products and thermal response of a 200  $\mu$ g film of AN heated at 2000°C, to 383°C and held at 383°C. The concentration data in this plot are based on the scaled growth of the IR absorbance values for each product. The superposition of several stoichiometric reactions is indicated. Of course, many elementary steps are imbedded in each of these stoichiometric reactions, but they are not determinable by T-jump/FTIR spectroscopy.

The first event is rapid endothermic melting of AN as indicated by the upward deflection in the difference control voltage trace. The control voltage decreases upon completion of melting from 0.5 - 1 s. The process turns markedly endothermic again at about 1 s. This second endothermic event corresponds to the appearance and growth of AN aerosol. The aerosol forms from the endothermic dissociation of AN and desorption to  $HNO_3(g) + NH_3(g)$ , followed by recombination of  $NH_3$  and  $HNO_3$  in the gas phase (Scheme I, reaction A). Only the endothermic first step of reaction A is included in  $\Delta H$  given for reaction A because the second step occurs in the cooler region of the cell away from the filament. Hence, the exothermic second step is not sensed by the filament. However, a white smoke of AN aerosol is visually observed.

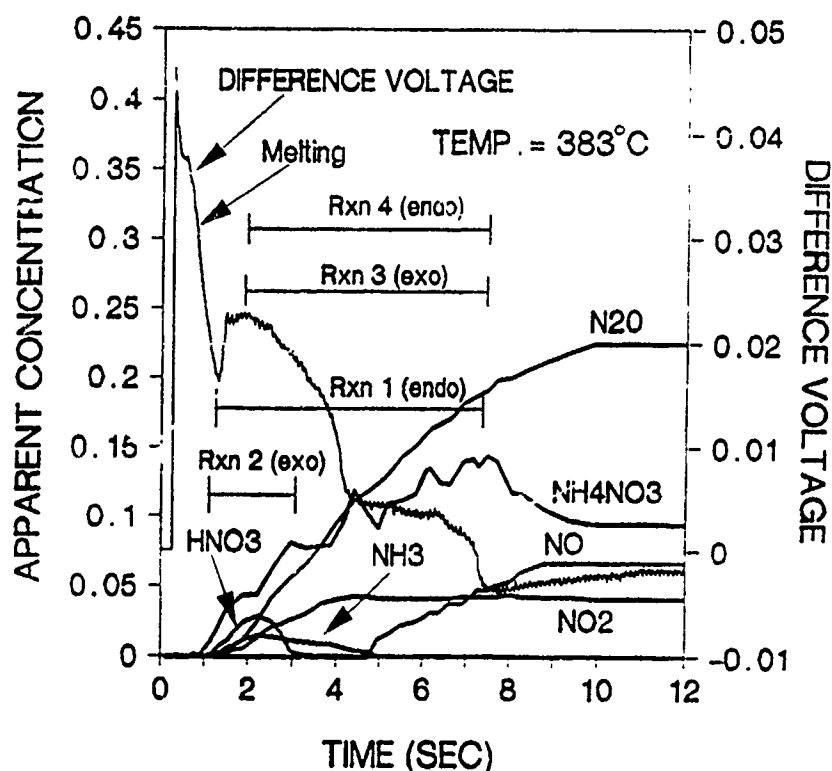


Fig. 3. Gas Products and the Heat Changes of  $\text{NH}_4\text{NO}_3$  at  $383^\circ\text{C}$  under 1 atm Ar. The Reactions are shown in Scheme 1.

**SCHEME 1. PROPOSED REACTIONS THAT ACCOUNT FOR THE PRODUCTS OF HIGH TEMPERATURE DECOMPOSITION OF AN (see Figure 3).**

	Approx $\Delta H$ , kcal
A. $4[\text{NH}_4\text{NO}_3(\text{l}) \rightarrow \text{HNO}_3(\text{g}) + \text{NH}_3(\text{g}) \rightarrow \text{NH}_4\text{NO}_3(\text{solid aerosol})]$	4(44) <sup>1</sup>
B. $3[5\text{NH}_4\text{NO}_3(\text{l}) \rightarrow 2\text{HNO}_3 + 4\text{N}_2 + 9\text{H}_2\text{O}]$	3(-35)
C. $5[\text{NH}_4\text{NO}_3(\text{l}) \rightarrow \text{N}_2\text{O} + 2\text{H}_2\text{O}]$	5(-13)
D. $4\text{NH}_4\text{NO}_3(\text{l}) \rightarrow 2\text{NH}_3 + 3\text{NO}_2 + \text{NO} + \text{N}_2 + 5\text{H}_2\text{O}$	81
A-D <sup>2</sup> . $28\text{NH}_4\text{NO}_3(\text{l}) \rightarrow 6\text{HNO}_3 + 3\text{NO}_2 + \text{NO} + 2\text{NH}_3 + 5\text{N}_2\text{O} + 13\text{N}_2 + 42\text{H}_2\text{O} + 4\text{NH}_4\text{NO}_3(\text{aerosol})$	87

<sup>1</sup>  $\Delta H$  for the desorption step only (see text).

<sup>2</sup> Gives the approximate IR active gas product ratios at 2 s for AN at  $383^\circ\text{C}$  (Fig. 3).

Despite the continuation of reaction A throughout the decomposition process as evidenced by the growth of the AN aerosol concentration, the decomposition process becomes less endothermic again at about 2 s.  $\text{H}_2\text{O}$  (not quantified) and excess  $\text{HNO}_3$  form at this time which is consistent with the occurrence reaction B. This reaction is known and its enthalpy has been deduced [23]. It is exothermic and would reduce the overall endothermicity of the decomposition process, as is found.

The process becomes still less endothermic from 2-4 s as the amount of  $\text{HNO}_3$  diminishes. However,  $\text{N}_2\text{O}$  grows rapidly in concentration through this time suggesting that the exothermic reaction C plays an increasingly important role. However, there is evidence of yet another reaction that occurs in parallel as indicated by the appearance of  $\text{NO}_2$  and the eventual decrease in exothermicity again between 4-6 s. Also,  $\text{NO}$ , whose IR absorbance is very small, probably forms earlier than is indicated in Fig. 3. Reaction D [24] accounts for these observations. Its endothermicity is superimposed on

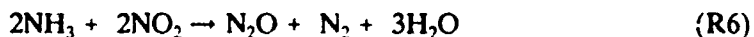


the exothermicity of reaction C and results in a leveling of the control voltage trace (heat flow is balanced) at 4-7 s. Reaction D is also a source of  $\text{NH}_3$ , which appears as a product for a much longer time than  $\text{HNO}_3$ .

The multiplicative factors of the reactions in Scheme I were determined by the need to match the approximate relative concentrations of the gas products at a time when all of the reactions contribute. The concentrations at 2 s were chosen. The stoichiometry of the net reaction in Scheme I approximates that found at 2 s in Fig. 3. Although the enthalpy of the net reaction is slightly exothermic as written, the relative contribution of reaction A need only be increased somewhat to produce a net endothermic process.

The formation of  $\text{NH}_3$  and  $\text{NO}_2$  by reaction D raises the possibility that the process could become exothermic when confined by pressure. The reaction of  $\text{NH}_3$  and  $\text{NO}_2$  becomes rapid and exothermic in the 330-530°C range [25,26]. However, significant generation of heat requires confinement to enhance the concentration of  $\text{NH}_3$  and  $\text{NO}_2$  in the hot zone around the condensed phase.

Figure 4 shows the decomposition process of a 200  $\mu\text{g}$  film of AN heated at 2000°C/s to 415°C under 33 atm of Ar. The concentrations are shown as relative percents throughout so that the behavior early in the decomposition process can be clearly seen. The melting endotherm initially dominates. The heat of reactions A-D leading to the formation of AN aerosol,  $\text{N}_2\text{O}$ ,  $\text{HNO}_3$ ,  $\text{NH}_3$ , and  $\text{NO}_2$  are overall endothermic until 1.5 s. At this time the concentrations of  $\text{NH}_3$  and  $\text{NO}_2$  formed by reaction D drop markedly and are accompanied by an exotherm which suggests that R6 occurs.  $\Delta H$  is about -148 kcal for this reaction as written. Under pressure, this nominally gas phase reaction could



occur in the heterogeneous gas-condensed phase (eg. bubbles and voids) and contribute to the condensed phase heat balance under combustion conditions.

The thermal decomposition behavior of bulk ADN is very different from that of AN despite the fact that similar gas products are formed upon rapid decomposition. Figure 5 shows T-jump/FTIR data for a 200  $\mu\text{g}$  film of ADN heated at 2000°C/s to 260°C. This temperature compares with a preliminary surface temperature measurement of burning

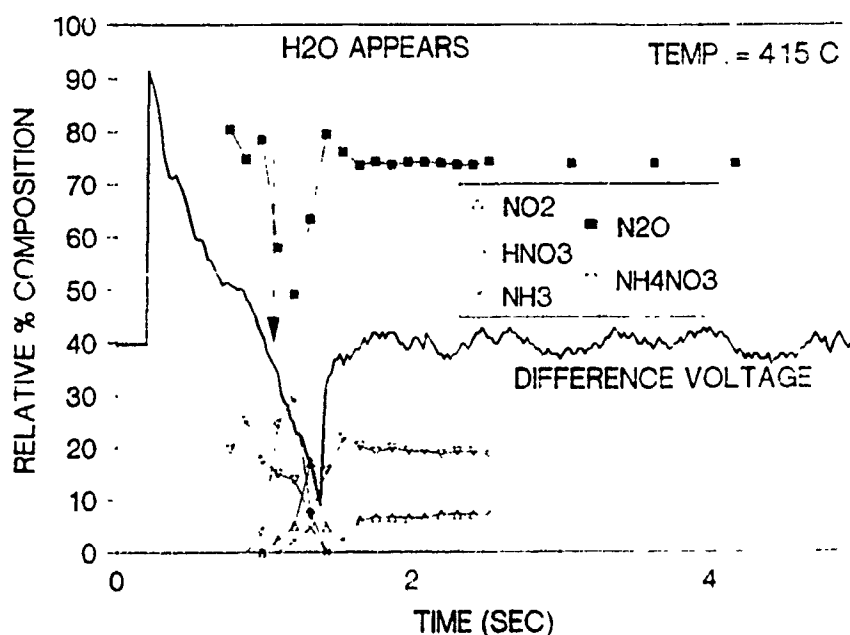


Fig. 4. Gas Products and the Heat Changes of  $\text{NH}_4\text{NO}_3$  at 415°C under 33 atm of Ar.

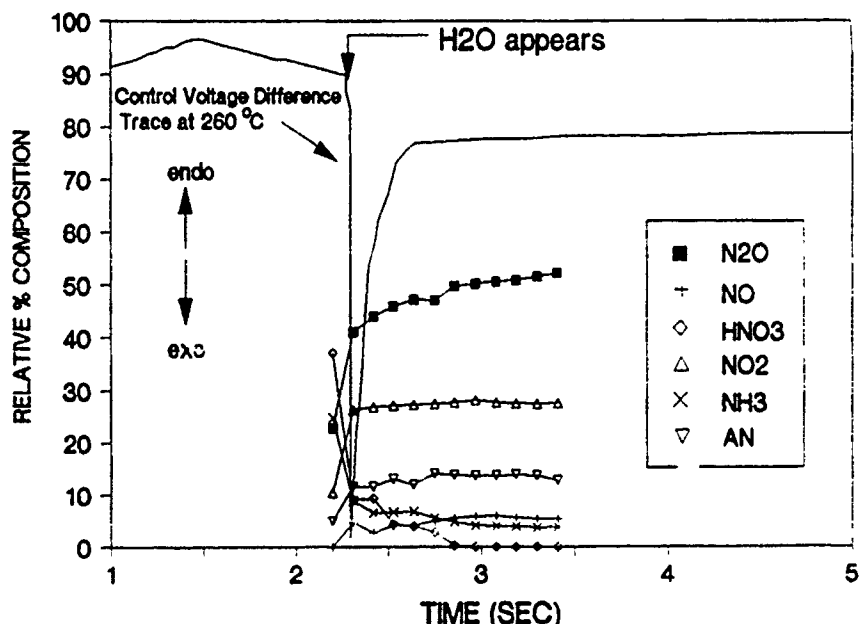


Fig. 5. Gas Products and the Heat Change of  $\text{NH}_4\text{N}(\text{NO}_2)_2$  (ADN) at  $260^\circ\text{C}$  under 1 atm Ar.

**SCHEME II: PROPOSED REACTIONS RESPONSIBLE FOR THE GASES RELEASED BY ADN DURING HIGH RATE PYROLYSIS**

<u>Branch A<sup>1</sup></u>		<u>Approx. ΔH, kcal</u>
	3[ADN → NH <sub>3</sub> + HNO <sub>3</sub> + N <sub>2</sub> O]	3(+11.5)
<u>Branch B</u>		
a	9[ADN → NH <sub>3</sub> + HN(NO <sub>2</sub> ) <sub>2</sub> ]	
b	9[HN(NO <sub>2</sub> ) <sub>2</sub> → NO <sub>2</sub> + HNNO <sub>2</sub> ]	
c	6[HNNO <sub>2</sub> → N <sub>2</sub> O + OH]	
d	2[HNNO <sub>2</sub> + OH → 2NO + H <sub>2</sub> O]	
e	HNNO <sub>2</sub> + NO → NO <sub>2</sub> + HNNO	
f	HNNO + OH → N <sub>2</sub> O + H <sub>2</sub> O	
g	3[NH <sub>3</sub> + OH → H <sub>2</sub> O + NH <sub>2</sub> ]	
h	3[NH <sub>2</sub> + NO → N <sub>2</sub> + H <sub>2</sub> O]	
i <sup>2</sup>	9ADN → 6NH <sub>3</sub> + 7N <sub>2</sub> O + 10NO <sub>2</sub> + 9H <sub>2</sub> O + 3N <sub>2</sub>	-49
j <sup>3</sup>	12ADN → 9NH <sub>3</sub> + 10N <sub>2</sub> O + 10NO <sub>2</sub> + 9H <sub>2</sub> O + 3N <sub>2</sub> + 3HNO <sub>3</sub>	-14
k	4NH <sub>3</sub> + 4NO <sub>2</sub> → 3N <sub>2</sub> + 2NO + 6H <sub>2</sub> O	-309
l <sup>4</sup>	12ADN → 5NH <sub>3</sub> + 10N <sub>2</sub> O + 6NO <sub>2</sub> + 15H <sub>2</sub> O + 2NO + 6N <sub>2</sub> + 3HNO <sub>3</sub>	-323
m <sup>5</sup>	2NH <sub>3</sub> + 2HNO <sub>3</sub> → 2NH <sub>4</sub> NO <sub>3</sub> (aerosol)	
n <sup>6</sup>	12ADN → 3NH <sub>3</sub> + 10N <sub>2</sub> O + 6NO <sub>2</sub> + 15H <sub>2</sub> O + 2NO + 6N <sub>2</sub> + HNO <sub>3</sub> + 2NH <sub>4</sub> NO <sub>3</sub>	-323

<sup>1</sup> Assumes  $\Delta H_f$  (ADN) = -35 kcal/mol, and  $\Delta H$  [ $\text{HNO}_3(\text{g})$ ] is -33 kcal/mol.

<sup>2</sup> Sum of a-h.

<sup>3</sup> Sum of Branches A & B.

<sup>4</sup> Sum of reactions j+k.

<sup>5</sup> Occurs in gas phase away from surface so reaction m is not included in  $\Delta H$ .

<sup>6</sup> Sum of l and m gives the approximate gas phase stoichiometry at the end of the exotherm (Fig. 5).

ADN of about 300 °C [27], which is surprisingly similar to that of AN. At the onset of decomposition, gas products and, in contrast to AN, sharp exothermicity occur instantly. The first detected products are mostly  $\text{HNO}_3$ ,  $\text{NH}_3$  and  $\text{N}_2\text{O}$  in roughly similar amounts. Minor quantities of  $\text{NO}_2$ , AN and  $\text{H}_2\text{O}$  are also present in the initial spectrum.

The formation of  $\text{HNO}_3$ ,  $\text{NH}_3$  and  $\text{N}_2\text{O}$  in comparable amounts at the beginning suggests the presence of Branch A in Scheme II. This mildly endothermic reaction may have a role during slow decomposition at lower temperatures. It appears to be a minor branch during rapid heating, especially because it does not account for the major heat release that is experimentally observed.

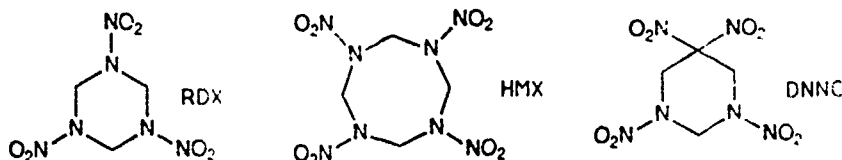
Branch B of Scheme II is proposed to dominate under rapid thermolysis conditions. Reaction *a* of Branch B is dissociation of ADN to produce  $\text{NH}_3$  and  $\text{HN}(\text{NO}_2)_2$ .  $\text{HN}(\text{NO}_2)_2$  is not detected and probably homolyzes in the condensed phase at high temperature by reaction *b* to  $\text{NO}_2$  and  $\text{HNNO}_2$ . Reactions *a* and *b* are endothermic. Because relatively large quantities of  $\text{NH}_3$  and  $\text{NO}_2$  occur early in Branch B, much heat can be generated by reaction *k* in the gas phase near the surface or even as part of the heterogeneous gas-liquid zone at the surface. The high exothermicity is evident in the large control voltage deflection at 2.3 s, and provides the energy to complete the decomposition process very rapidly. Some of the  $\text{NH}_3$  and  $\text{NO}_2$  remains unreacted because it escapes to the cooler region of the atmosphere. Reactions *c-h* are plausible subsequent steps for decomposition of  $\text{HNNO}_2$ , but they are not determined by T-jump/FTIR spectroscopy. They are simply proposed as reasonable sources of stable products in the quantities detected. The net reaction *j* of Branch B is mildly exothermic. Combining Branches A and B yields the exothermic reaction *j*. Adding some gas phase recombination of  $\text{NH}_3$  and  $\text{HNO}_3$  (reaction *m*) to account for the observed AN solid aerosol yields reaction *n*, whose stoichiometry approximates the experimentally observed gas product ratios observed at 2.5 s in Fig. 5. Reaction *n* is strongly exothermic largely because of reaction *k*, which is the reaction of  $\text{NH}_3$  with  $\text{NO}_2$ .

For both AN and ADN, the exothermic  $\text{NH}_3 + \text{NO}_2$  reaction appears to dominate the heat release stage. In the case of AN the exotherm occurs only under a large applied pressure is accompanied by a drop in the amount of  $\text{NH}_3$  and  $\text{NO}_2$  that appear in the gas phase. Although the reaction of  $\text{NH}_3$  and  $\text{NO}_2$  appears to be responsible for this exotherm, the amount of  $\text{NH}_3$  and  $\text{NO}_2$  is smaller for AN than for ADN and, therefore much less heat is generated.

The rapid decomposition process of ADN is strongly exothermic early in the reaction scheme. This behavior is consistent with the ease of formation of a large amount of  $\text{NH}_3$  and  $\text{NO}_2$  in the early decomposition steps. Because the reaction of  $\text{NH}_3$  and  $\text{NO}_2$  can dominate early and produces a large amount of heat, the overall decomposition and gasification process is driven at a much high rate for ADN than AN. Therefore, for both AN and ADN the reaction of  $\text{NH}_3$  with  $\text{NO}_2$  is implicated as the main source of heat when the pure material is decomposed at high temperature. For AN this reaction only becomes important under confinement, such as by the application of pressure.

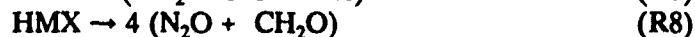
## THE $\text{CH}_2\text{O}-\text{NO}_2$ REACTION OF NITRAMINES

Nitramines, such as HMX and RDX, are especially important as minimum smoke, high energy explosive and propellant ingredients. DNNC is an alternative oxidizer to HMX and RDX. The rapid decomposition mechanism of HMX, RDX and DNNC is



interesting to compare. The decomposition of HMX [28] and RDX [29] is similar and so only HMX will be described. DNNC behaves somewhat differently [15] and will be discussed later. Despite the different decomposition mechanisms, the dominant initial exothermic reaction appears to be the same for all three compounds.

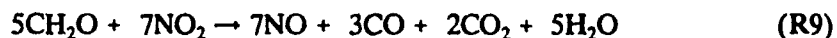
Figure 6 shows T-jump/FTIR data for a thin film of HMX heated at 2000 °C/s to 298 °C and then held isothermally while IR spectra of the near-surface gas products are recorded. The global decomposition branches (R7) and (R8) occur for bulk RDX and HMX. (R7) and (R8) imply that  $\text{N}_2\text{O}$  and  $\text{NO}_2$  should form simultaneously with  $\text{CH}_2\text{O}$  and  $\text{HCN}$ . This is not found at any temperature studied. Rather,  $\text{N}_2\text{O}$  and  $\text{NO}_2$  appear



before  $\text{CH}_2\text{O}$  and  $\text{HCN}$ , which form from the residue left by elimination of  $\text{N}_2\text{O}$  and  $\text{NO}_2$ . This residue is a mixture of products like hydroxymethylformamide and acetamide [30-33], which decompose and delay the release of  $\text{CH}_2\text{O}$ ,  $\text{HCN}$  and  $\text{HNCO}$  [33,34].

The total IR absorbance of the products accelerates between 4.0 and 5.5 s despite the constant heat flow from the filament, which implies that autocatalysis occurs in this stage of decomposition of HMX and RDX. Moreover, the control voltage trace in Fig. 6 reveals only mild exothermicity between 4 and 5.5 s when (R7) and (R8) dominate. Thus, these reactions release little energy in the condensed phase.

A runaway exotherm develops at 5.5 s. The secondary reaction (R9) appears to be responsible because  $\text{CH}_2\text{O}$  and  $\text{NO}_2$  are consumed as  $\text{NO}$ ,  $\text{CO}$ , and  $\text{H}_2\text{O}$  appear. Figure



6 shows that more  $\text{NO}$  than  $\text{CO}$  forms in accordance with (R9). (R9) is highly exothermic as written ( $\Delta H = -320$  kcal) and, by the large exotherm in Fig. 6, it is the main source of heat in the heterogeneous condensed phase. These conclusions also apply at 392 °C (Fig. 6) except that the time-scale is compressed. Hence, this description of the decomposition of HMX at 298 °C applies as well at the surface reaction zone temperature (350 - 400 °C) during combustion. However, the branching ratio of (R7) and (R8) depends on temperature and favors (R7) at higher temperature [28].

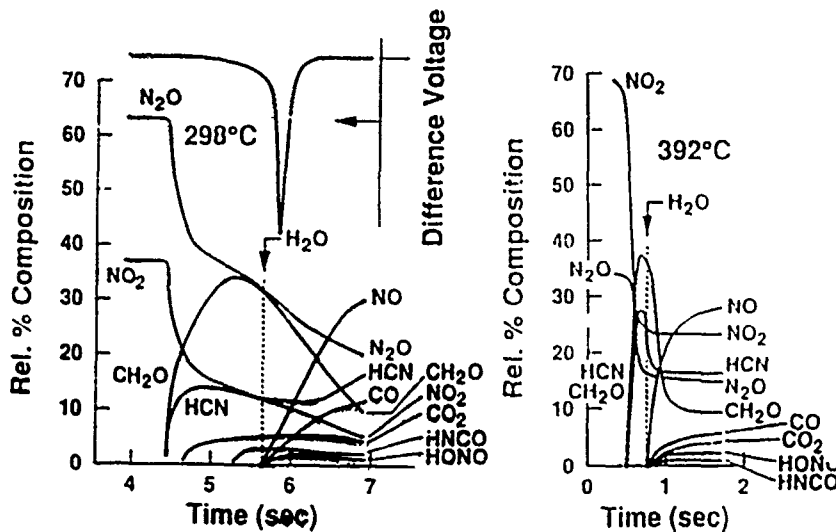


Fig. 6. The Gas Products and Heat Change of HMX at 298 °C and 392 °C under 2.5 atm Ar.

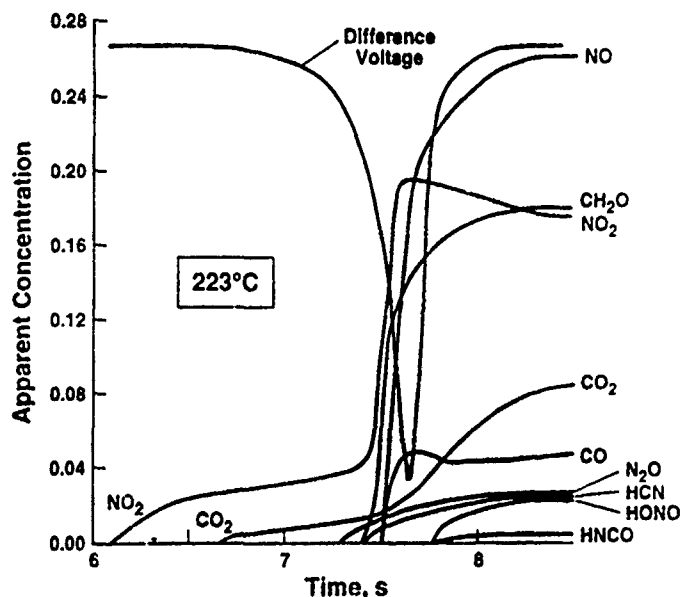


Fig. 7. The Gas Products and Heat Change of DNNC at 223°C under 2.5 atm Ar.

As is the case for RDX and HMX, the decomposition process of DNNC (Fig. 7) becomes strongly exothermic at the time that NO and CO become major products [15]. This suggests that the highly exothermic R9 is occurring. However, the fact that much more NO than CO is liberated by DNNC implies that sources of NO exist other than R9. It is also noteworthy that, in contrast to RDX and HMX, CH<sub>2</sub>O and NO<sub>2</sub> continue to be generated in the exotherm and remain in high concentration in the cool Ar atmosphere after the decomposition is complete. This observation has implications for the flame structure of DNNC. The primary flame of DNNC is expected to be dominated by R9, which releases a large amount of heat close to the surface and influences the surface regression rate. The primary flame zone of RDX and HMX also appears to be dominated by the heat of R9. Therefore, it is not surprising that the burn rates of RDX and DNNC are quite similar [15].

#### FINAL COMMENTS

Our original papers from which the reactions discussed above are abstracted contain many more details about processes that occur in the surface reaction zone of a burning energetic material. As this work develops, numerous connections are apparent with actual propellant combustion studies of Korobeinichev in Novosibirsk, Litzinger at Penn State, and Brewster at Illinois. Connections with theoretical and computational models of propellant combustion by Melius at Sandia National Laboratory Livermore, and Williams at UCSD are quite evident. Consequently, there appears to be great promise in using T-jump/FTIR to validate theoretical work and develop more detailed chemical pathways at the surface than is possible by direct combustion measurements.

#### ACKNOWLEDGMENTS

I am grateful to the Air Force Office of Scientific Research, Aerospace Sciences, for support of this work. Graduate students and postdoctoral students Peter Brush, Jankang Chen, and Dilip Patil, who are coauthors in the reference section, contributed vitally to this program.

## REFERENCES

1. O. K. Rice and R. Ginell, *J. Phys. Chem.*, **54**, 885 (1950).
2. C. Guirao and F. A. Williams, *AIAA J.*, **9**, 1345 (1971).
3. T. Mitani and F. A. Williams, *Proc. 21st Symp. (Int.) Combustion*, 1986, p. 1965.
4. M. Ben-Reuven and L. H. Caveny, *AIAA J.*, **19**, 1276 (1979).
5. N. S. Cohen, G. A. Lo and J. C. Crowley, *AIAA J.*, **23**, 276 (1985).
6. N. Kubota and S. Sakamoto, *Prop. Explos. Pyrotech.*, **14**, 6 (1989).
7. M. Chi, B. Gleeson, J. Hill and R. Willer, US Patent 5071495, Dec. 1991.
8. C. E. Stoner, Jr. and T. B. Brill, *Combust. Flame*, **83**, 302 (1991).
9. T. B. Brill, P. J. Brush, K. J. James, J. E. Shepherd and K. J. Pfeiffer, *Appl. Spectrosc.*, **46**, 900 (1992).
10. T. B. Brill, *Prog. Energy Combust. Sci.*, **18**, 91 (1992).
11. M. D. Timken, J. K. Chen and T. B. Brill, *Appl. Spectrosc.*, **44**, 701 (1990).
12. J. K. Chen and T. B. Brill, *Combust. Flame*, **85**, 479 (1991).
13. J. K. Chen and T. B. Brill, *Combust. Flame*, **87**, 157 (1991).
14. J. K. Chen and T. B. Brill, *Combust. Flame*, **87**, 217 (1991).
15. T. B. Brill, D. G. Patil, J. P. Duterque and G. Lengelle, *Combust. Flame*, submitted.
16. T. B. Brill, P. J. Brush and D. G. Patil, *Combust. Flame*, submitted.
17. N. E. Ermolin, O. P. Korobeinichev, A. G. Tereshenko and V. M. Fomin, *Comb. Explos. Shock Waves*, **18**, 180 (1992).
18. O. P. Korobeinichev and A. G. Tereshenko, in *Tenth Mat. Res. Symp. Charact. High Temp. Vapors and Gases*, NBS publ. 561, Gaithersburg, MD, 1978, p. 479.
19. E. E. Hackman, H. H. Hesser and H. C. Beachell, *J. Phys. Chem.*, **76**, 3545 (1972).
20. T. B. Brill, P. J. Brush and D. G. Patil, *Combust. Flame*, in press.
21. M. Swett, NWC, personal communication (1992).
22. A. G. Whittaker and D. C. Barham, *J. Phys. Chem.*, **68**, 196 (1964).
23. B. T. Federoff, *Encyclopedia of Explosives and Related Items*, Vol. I, Picatinny Arsenal, Dover, NJ, 1960, A3111.
24. R. Kaiser, *Angew. Chem.*, **48**, 149 (1935).
25. W. A. Rosser and H. Wise, *J. Chem. Phys.*, **25**, 1078 (1956).
26. G. Bedford and J. H. Thomas, *J. Chem. Soc. Farad. Trans. I*, 2163 (1972).
27. B. L. Fetherolf and T. A. Litzinger, Penn State Univ., personal communication (1992).
28. T. B. Brill and P. J. Brush, *Phil. Trans. Royal Soc. (Lond.) A*, **339**, 377 (1992).
29. T. B. Brill, P. J. Brush, D. G. Patil and J. K. Chen, *Proc. 28th Symp. (Int.) Combustion*, Sydney, Australia, July, 1992.
30. J. D. Cosgrove and A. J. Owen, *Combust. Flame*, **22**, 13 (1974).
31. J. Kimura and N. Kubota, *Prop. Explos.*, **5**, 1 (1980).
32. R. J. Karpowicz and T. B. Brill, *Combust. Flame*, **56**, 317 (1984).
33. R. Behrens, *J. Phys. Chem.*, **94**, 6706 (1990).
34. S. F. Palopoli and T. B. Brill, *Combust. Flame*, **87**, 45 (1991).

## QUANTUM DYNAMICAL STUDIES OF THE DECOMPOSITION OF ENERGETIC MATERIALS

HERSCHEL RABITZ and EDUARDO VILALLONGA \*

\*Department of Chemistry, Princeton University, Princeton, New Jersey 08544.

### ABSTRACT

We present a theoretical approach aimed at elucidating the microscopic dynamics of energetic materials fragmentation. Two interdependent components are combined to bridge the atomic and bulk realms. A hierarchy of quantal multiple-scattering expansions is first introduced to decompose the complex reaction dynamics into coupled sequences of few-atom interactions, each of which is more amenable to calculation. This microscopic component is complemented by a continuum-mechanical process to account for energy flow into the as yet unreacted bulk material. Such a dual approach allows for quantum-mechanical treatment of coupled atomic-bulk dynamics in a self-consistent way that incorporates large thermal gradients. The analysis, in terms of coupled few-atom interactions, also yields additional insight into the various pathways for reactivity and energy transfer.

### INTRODUCTION

A variety of atomic- and molecular-scale events occur in the decomposition of energetic solids, and perhaps one of the most vexing matters is the lack of detailed understanding of the physical and chemical events occurring at the reactive front [1]. The role of quantum dynamical phenomena at these atomic scales remains to be fully assessed. A fundamental treatment of the basic physics underlying decomposition calls for the introduction of a proper quantum dynamical description. The complexity of the problem also brings into question the utility of the conventional fully-continuum approaches [2]. The power of continuum models resides in their ability to handle macroscopic phenomena, including shock structure, on laboratory scale dimensions. However, continuum models are limited by their lack of detail at the atomic and molecular level where the basic physical and chemical processes are initiated. This has motivated molecular-dynamics simulations in which the classical equations of motion are solved for a large ensemble of atoms or molecules representing a physically meaningful segment of the material [1,3]. The latter approach is clearly more suitable to molecular-scale events, but it neglects quantum effects and becomes impractical for describing a macroscopic piece of material. Nevertheless, the degree of success demonstrated by massive classical simulations and by continuum theory suggests that a judicious combination of discrete (atomic-scale) dynamics and continuum mechanics could prove to be more physically accurate. Therefore, we are developing two new treatments, which exploit the best aspects of the molecular-dynamics and continuum pictures.

The first aspect of the research is concerned with a fully quantal theory of energetic materials fragmentation. Drawing on analogous procedures from nuclear-fragmentation physics [4], this new multiple-fragmentation (MF) theory aims to re-express the many-atom dynamics into a rigorous hierarchy of fewer-atom interactions, each of which is computationally manageable. Such a discrete, i.e. atomic-scale, treatment is essential for describing high frequency, short wavelength motion of molecules undergoing dissociation. On the other hand, collective molecular motion, can be accurately determined from continuum mechanics for the unreacted region [5,6]. Therefore, the second aspect of the research takes

a discrete-continuum hybrid (DCH) approach whereby the region undergoing decomposition is treated at the atomic level while coupled to a continuous medium representing the collective bulk dynamics, as is schematically illustrated in Fig. 1. Due to its dual atomistic-continuum nature, the overall approach can bridge the disparate length scales of molecular and bulk regimes in a self-consistent fashion. Thus far, the research has developed (a) the multiple fragmentation theory without coupling to the underlying bulk, and (b) the discrete-continuum theory of energy transfer into the bulk without reactivity. A summary of this work is given below. Future work will combine these two avenues of study.

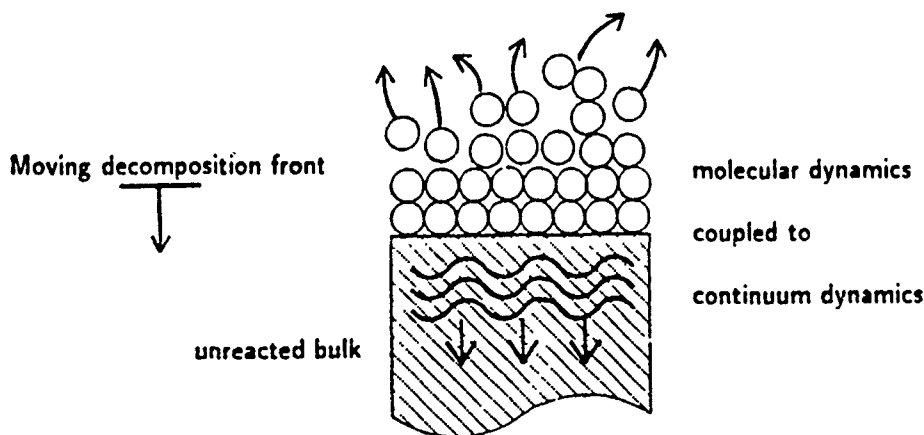


Figure 1: Conceptual essence of the discrete-continuum approach to energetic solid decomposition. Working in the moving reference defined by the decomposition front, molecular dissociation is treated at the atomic level while coupled to a continuum-mechanical process to account for energy propagation (wavy lines) into the yet unreacted bulk material.

## DETAILED METHODOLOGY

### The Multiple-Fragmentation Theory for Energetic Solid Decomposition

The first component of the research is operative at the leading edge of the decomposition front, and it specifically addresses the quantum mechanics of molecular dissociation. A conventional quantum treatment of these reactive processes, based on eigenfunction expansions, would be prohibitively costly. Therefore, we are pursuing a fully-quantal multiple-fragmentation (MF) treatment which bypasses eigenstate expansions, and instead, decomposes the many-atom solid dynamics into sets of partially coupled few-body problems that are more amenable to calculations [4]. The essence of the MF theory can be visualized from the diagram

$$\boxed{\text{Decomposing solid}} \Rightarrow \boxed{\sum \text{fewer-body events}} \Rightarrow \boxed{\sum \text{two-atom events}} \quad (1)$$

Thus, the complex decomposition dynamics is first re-expressed in terms of fewer-body interactions, e.g. between pairs of fragments each of which is composed of several atoms. The fragment-fragment dynamics are then described in terms of more elementary atom-pair events, which can be calculated by standard quantum-mechanical methods.

In accord with these concepts, we work with operators  $T^{(f)}$  that describe the transition between initial ( $i$ ) and final ( $f$ ) fragmentation channels. We illustrate the MF treatment with a prototypical three-body system. Let  $I$ ,  $S$  and  $F$  respectively denote an impacting



body, the solid and one ejected fragment;  $I$  and/or  $F$  may be composed of several atoms,  $F$  is initially included in  $S$ , and either or all of  $I$ ,  $F$  and  $S$  may initially be in a highly energetic internal state. The  $ISF$  interaction can be described by the potential  $V = V_{IS} + V_{FS} + V_{IF} + V'$ , where the  $V_{jk}$  represent the forces between pairs of bodies and  $V'$  contains all three and higher body forces. Typically,  $|V'| \ll |V_{jk}|$ , and the dynamical role of  $V'$  can be minimized further for high-energy fragmentation by making judicious choices of the  $V_{jk}$ . Accordingly, we take  $V \approx V_{IS} + V_{FS} + V_{IF}$ , which naturally leads to a few-body decomposition of the  $T^{(J)}$  by methods analogous to those originated in the physics of nuclear fragmentation [4]. Using the process  $I + FS \rightarrow I + F + S$  as an example, the first step of Diagram (1) decomposes the  $T^{(J)}$  in terms of the operators  $T_{jk}$  that describe interactions between pairs of bodies:

$$T^{(J)} = T_{IS} + T_{IF} + T_{FS}G_0T_{IS} + T_{FS}G_0T_{IF} + T_{IS}G_0T_{IF} + T_{IF}G_0T_{IS} + \dots, \quad (2)$$

where  $T_{jk} = V_{jk} + V_{jk}G_0T_{jk}$  and  $G_0$  corresponds to non-interacting propagation; the remaining terms in the sum include three and more successive pair interactions. Expansions similar to Eq. (2) are straightforwardly formulated for other rearrangements [4]. As a result, the MF theory yields energy-angular probability distributions for all possible fragments. For example, Fig. 2a shows the angular distribution of fragments  $F$  ejected from a prototypical solid upon impact; an alternative process  $I + FS \rightarrow IF + S$  leading to formation of the composite fragment  $IF$  is illustrated in Fig. 2b.

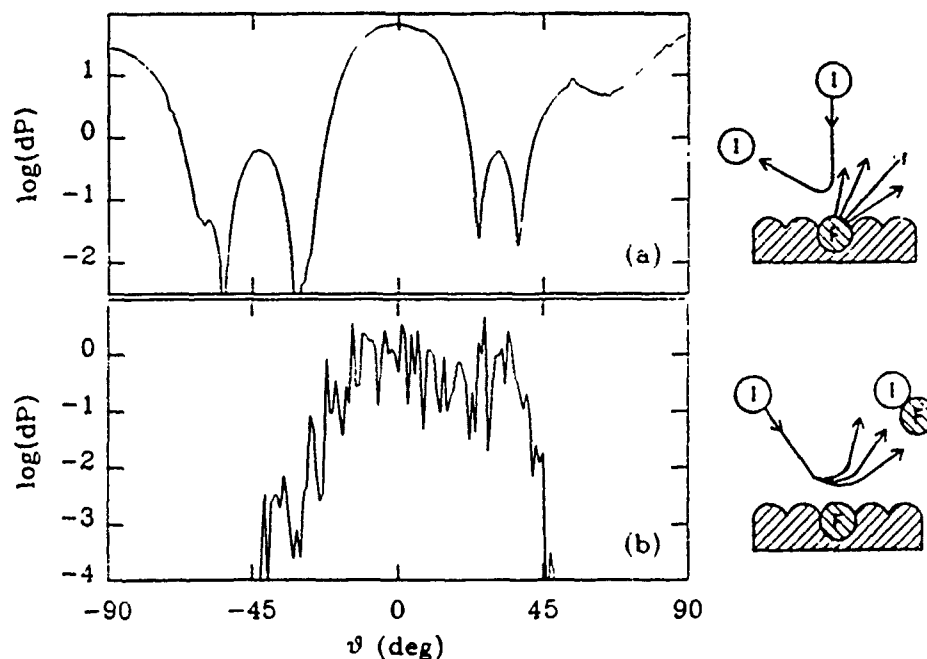


Figure 2: Angular distribution (dP) of fragments ejected in two fragmentation processes:  $I + FS \rightarrow I + F + S$  (a) and  $\rightarrow IF + S$  (b), where local excitation is generated by impacts of  $I$  with high kinetic energy (0.5 eV) onto the surface of the solid. In (a),  $I$  leaves to the left of the surface normal and  $F$  is ejected mostly in the opposite direction, but there is significant probability for  $F$  to be ejected non-classically, i.e. along  $|\theta| \leq 30^\circ$  and  $\theta \leq -60^\circ$ . In (b), the distribution for the composite fragment  $IF$  is calculated with a different  $V_{IF}$  potential favoring formation of the  $I - F$  bond.

An especially important aspect of the MF theory is the straightforward physical picture given by each term of the few-body expansions. For example, the fifth term of Eq. (2),

$T_{FS}G_0T_{IF}$  corresponds to a direct interaction in the fragmentation region ( $T_{IF}$ ), followed by free evolution for a brief time ( $G_0$ ), after which the fragment is ejected from the solid ( $T_{FS}$ ). An alternate mechanism is indicated by the fourth term of Eq. (2),  $T_{FS}G_0T_{IS}$ , whereby momentum and energy are first exchanged with the bulk solid ( $T_{IS}$ ). Quantal MF theory is thus capable of analyzing the relative importance of the various pathways leading to fragmentation, and to relate them to basic physical concepts such as kinematic and geometrical effects, and to the strength of intra- and intermolecular forces.

At this point, the basic foundations of the MF theory have been developed and its feasibility shown for prototypical three-fragment systems. Additional work is underway to extend the treatment to more complex processes by further decomposing the two-fragment interactions into elementary events, each of which involves only two atoms. A deeper level of MF theory, i.e. the second step of Diagram 1 above, is being implemented by expressing each  $V_{jk}$  in terms of interatomic potentials  $v_{\alpha\beta}$ , such that  $V_{jk} \approx \sum_{\alpha} \sum_{\beta} v_{\alpha\beta}$ , where atoms  $\alpha$  and  $\beta$  belong to bodies  $j$  and  $k$ , respectively. Consequently, each of the two-fragment  $T_{jk}$  may be expanded in a series analogous to Eq. (2) but presently involving two-atom operators  $t_{\alpha\beta} = v_{\alpha\beta} + v_{\alpha\beta}g_0t_{\alpha\beta}$  where  $g_0$  describes free-atom propagation. Thus, multi-particle effects can be handled and the overall fragmentation dynamics may be systematically analyzed at the atomic level. For example, Fig. 3 displays preliminary results for the multi-fragmentation process  $I + FS \rightarrow I + f_1 + f_2 + f_3 + f_4 + S$ , where the composite fragment  $F$  further decomposes into four atomic fragments  $f_{\alpha}$ .

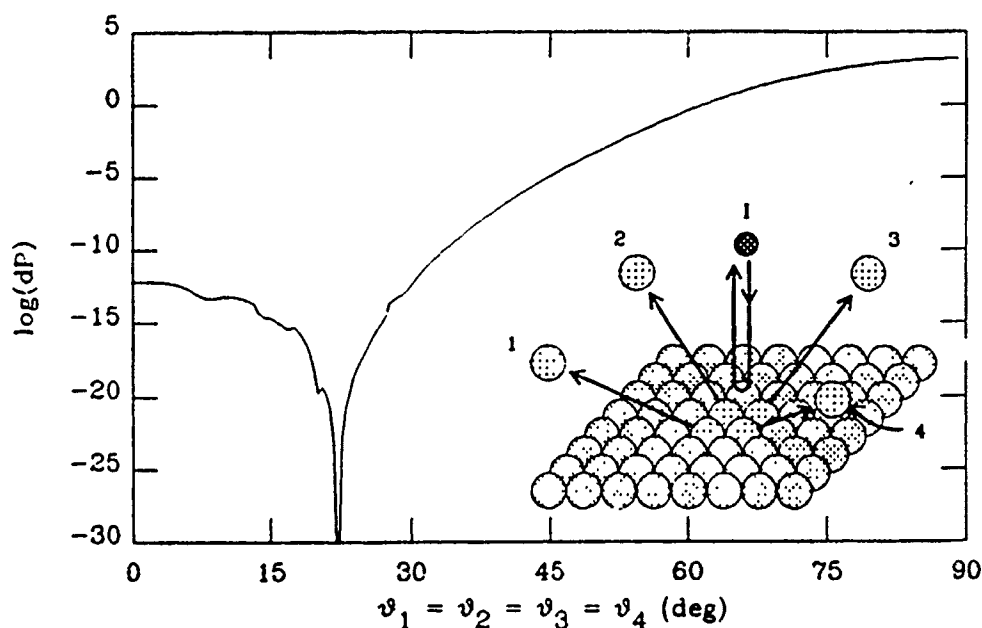


Figure 3: Angular distribution (dP) of fragments ejected in the multi-fragmentation process  $I + FS \rightarrow I + f_1 + f_2 + f_3 + f_4 + S$  where the composite fragment  $F$  further decomposes into four atoms  $f_{\alpha}$ .

#### Discrete-Continuum Hybrid Theory of Molecular-Bulk Dynamics

The second component of the research is aimed at bridging the region of molecular decomposition together with the dynamics of the yet unreacted bulk material. For this purpose, we are developing a discrete-continuum hybrid (DCH) theory, whereby the discrete, i.e. atomic dynamics, of the decomposing region is coupled to a continuous medium accounting for energy exchange with the bulk [5,6]. The mathematical tools needed for the extreme continuum picture are well-known. The key aspect of the DCH approach is the

joining together of the two schemes into a self-consistent hybrid framework. This requires satisfying matching conditions that are rigorously prescribed by the continuity of the vibrational displacements and of their derivatives at the interface between the continuous and the discrete regions. We have carried out this basic theoretical formulation and applied it to several models of polyatomic systems, e.g. chains, rings, lattice inclusions and solid surfaces [5-7]. Present research is carrying this work further along the following lines.

The DCH theory is being used to investigate the cases of energy transfer and propagation alone, in order to more fully understand the role of these processes as precursors to decomposition. Since the simplest form of the continuum is that of an elastic medium, this is the natural first approach. Reactivity, especially involving dissociation, may then be incorporated via the above MF treatment aiming towards a comprehensive theory of energetic materials decomposition. Our previous research on the DCH picture has mostly involved classical mechanics in either its discrete or continuum forms. However, we have found that quantum effects can be important under certain circumstances, due to the atomic nature of the discrete component. Therefore, we have recently enhanced the DCH treatment by extending it into the quantal regime [5].

The DCH approach enables a further analysis of the dynamics in terms of the energies going into the various vibrational modes of the bulk, e.g. Rayleigh-type waves, which convey energy along directions parallel to the front, as well as pressure and shear waves that penetrate into the bulk. The particular dispersal of the bulk energy is expected to have important consequences for the rate of propagation of the decomposition front. As an example of bulk mode dispersals, Fig. 4 compares the probabilities for transferring energy between an impinging hot gas atom and the various bulk modes. The rich structure of the results would not be possible to predict from intuition, since it arises from multi-quantum excitations of high order, and it would have been missed by classical mechanics. We are employing this unique capability of the quantized DCH treatment for investigating the role of mode-specific excitation as a precursor to reactive molecular decomposition.

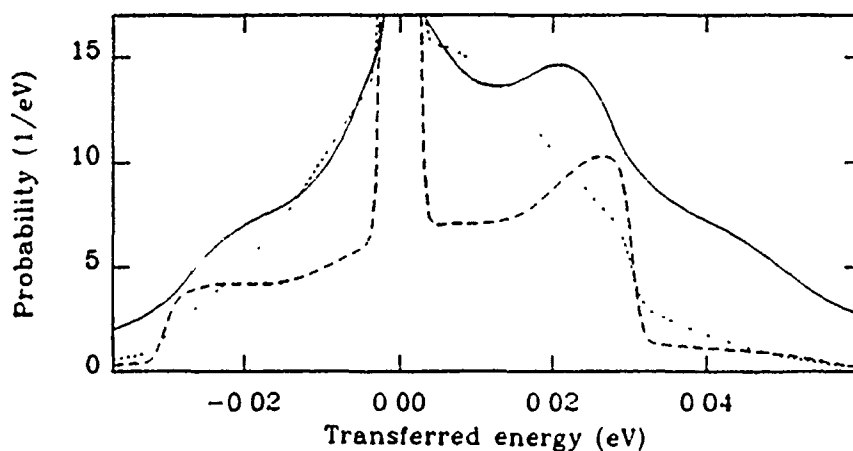


Figure 4: Quantal discrete-continuum hybrid calculation. The energy exchanged between an impinging hot gas atom ( $T_G = 6000\text{K}$ ) and a colder solid material ( $T_S = 300\text{K}$ ) is analyzed in terms of the energies going into/out of the various continuum modes: Rayleigh-type waves which propagate along the surface of the solid (—), and shear-pressure waves that penetrate into the bulk. The latter are further decomposed into: shear displacements parallel to the surface (-----), and pressure plus perpendicular shear (.....), which are coupled at the surface. Positive and negative energies correspond to transfers into and out of the solid, respectively; both processes can be readily treated by the DCH theory.

## CONCLUSION

In summary, this research is concerned with elucidating the various physical/chemical mechanisms that determine the decomposition dynamics of energetic solid materials. A balanced combination of theoretical tools is being employed to span molecular-scale through bulk dynamical phenomena. The fully quantal MF treatment of molecular decomposition can provide much needed insight into the fundamental chemical processes responsible for solid decomposition. This microscopic approach is being complemented by the DCH treatment, in order to bridge the disparate length scales of molecular reactivity and bulk physics. A most significant ultimate development will be the merging of the MF theory with the quantized version of the DCH treatment thus yielding a comprehensive quantum theory of energetic materials decomposition. It is worth noting that these developments are expected to have applications in a variety of materials problems besides that of energetic materials dynamics.

## REFERENCES

1. A. Karo in *ONR Workshop on Energetic Material Initiation Fundamentals*, Chemical Propulsion Information Agency Publication 406, 1984.
2. Y. B. Zel'dovich and Y. P. Raiser, *Physics of Shockwaves and High Temperature Hydrodynamics Phenomena* (Academic Press, New York, 1966).
3. M. L. Elert, D. M. Deaven, D. W. Brenner and C. T. White, *Phys. Rev. B* **39**, 1453 (1989); S. G. Lambrakos, M. Peyrard, E. S. Oran and J. P. Boris, *ibid.* **39**, 993 (1989).
4. H. Cheng, E. Vilallonga and H. Rabitz, to be published; W. Glöckle, *The Quantum-Mechanical Few-Body Problem* (Springer-Verlag, Berlin, 1983).
5. E. Vilallonga and H. Rabitz, *J. Chem. Phys.* **97**, 1576 (1992); **92**, 3957 (1990).
6. A. Askar and H. A. Rabitz, *Surf. Sci.* **245**, 411 and 425 (1991).
7. T. Thacher, H. A. Rabitz and A. Askar, *J. Chem. Phys.* **93**, 4673, (1990); T. Thacher, S. Ganesan, A. Askar, and H. Rabitz, *ibid.* **85**, 3655, (1986).

## CORRELATION TIME FOR POLYMER CHAIN MOTION NEAR THE GLASS TRANSITION IN NITROCELLULOSE.

J. R. P. JAYAKODY<sup>1</sup>, S. BULUSU<sup>2</sup> and R. A. MARINO<sup>1</sup>

<sup>(1)</sup> Dept of Physics, Hunter College and the Graduate Center of CUNY, New York, NY 10021

<sup>(2)</sup> US Army ARDEC, Picatinny Arsenal, NJ 07806

### ABSTRACT

The NMR chemical shift anisotropy (CSA) has a temperature dependence as a result of thermal motions of the NMR site. For slow motions of a polymer chain at or near the glass transition,  $T_g$ , the CSA begins to decrease, with the characteristic powder pattern features, shoulders and divergence, approaching one another. This motional narrowing can be interpreted to yield the correlation time of the thermal motions. If  $\Delta$  is the rigid-lattice shoulder to shoulder chemical shift anisotropy and  $\tau$  is the correlation time of the slow-motion of the polymer chains, the total fractional shift,  $\delta/\Delta$ , for the general asymmetric case is found to be

$$\delta/\Delta = (1/10)[65^{1/4} + 200^{1/4}] (\tau\Delta)^{-1/2}$$

derived using Lee's theory. In this work, Nitrocellulose isotopically highly enriched with <sup>15</sup>N was studied at four temperatures between 27° and 120° Celsius. To circumvent signal-to-noise problems in obtaining CSA data from a polycrystalline/amorphous sample, we used the Magic Angle Spinning (MAS) technique of Herzfeld and Berger. The principal values of the chemical shift tensor were then obtained from the relative intensities of the spinning sidebands in the MAS NMR spectrum. Correlation times were found to be of the order of 400 ms at 70°C, and 17 ms at 120°C.

### INTRODUCTION

This paper describes a nuclear magnetic resonance (NMR) technique with several novel features, which can be used as a general method to obtain the correlation time  $\tau$  of the random thermal motions of polymers at temperatures near the glass-to-rubber transition. The correlation time is interesting since it is the parameter that describes the time scale of the motion. Measurements of  $\tau$  in nitrocellulose (NC) were undertaken as part of a project to understand the mechanical properties of this material at the microscopic level.

The method begins with Sook Lee's analytical theory<sup>1,2,3</sup> of anisotropic paramagnetic centers undergoing slow orientational diffusion. The NMR chemical shift anisotropy (CSA) has the required orientational dependence with respect to the externally applied magnetic field, and the theory can readily be expressed in terms of the CSA's natural variables from Lee's examples of dipole-dipole and quadrupole interactions. For this work, the choice of CSA interaction was dictated by the fact that it could be measured with considerably higher precision in nitrocellulose and other polymers than for either dipole-dipole or quadrupole parameters.

### THEORY

Anisotropic nuclear magnetic resonance centers, such as those involving nuclear quadrupole, dipole-dipole or the chemical shift interaction, undergo random tumbling motion due to thermal orientational diffusion processes in many polycrystalline-amorphous substances (e.g., polymers and glasses) over the temperature ranges of greatest interest. as a result of the tumbling motion nuclear-spin energy levels are modulated in such a way that the resulting NMR lines become broadened or narrowed, and their NMR frequencies shift

from the rigid-limit values.

A few years ago a comprehensive analytical-theoretical treatment<sup>1, 2, 3</sup> was performed for the dynamic behavior of anisotropic nuclear or electron paramagnetic centers for slow-orientational motion in polycrystalline-amorphous condensed matter. Simple analytical expressions were derived for slow-motional line broadening and spectral line shifts for the important orientations of the NMR symmetry axes with respect to the external magnetic field  $H_0$ . The theory develops expressions which can be used to obtain the correlation time from experimental values of NMR frequency shifts.

In this work, the specific NMR fine-structure investigated is the first-order chemical shift anisotropy in nitrocellulose polymers. The first-order NMR CSA Hamiltonian in a coordinate system with the  $z$  axis parallel to the external field  $H_0$  is given<sup>4</sup> by

$$\mathcal{H} = -\gamma\hbar H_0 I_z (1 - \sigma_{zz})$$

where  $\sigma_{zz}$  is the component of the CSA shift tensor along the direction of  $H_0$ . It can be expressed in terms of the diagonal components  $\sigma_1$ ,  $\sigma_2$ , and  $\sigma_3$  of the shift tensor in its principal axis system. The unshifted NMR frequency for a nucleus of gyromagnetic ratio  $\gamma$  is  $\omega_0 = \gamma H_0$ . Then the first-order NMR chemical shifted frequency can be written as

$$\begin{aligned}\omega(\theta, \phi) &= \omega_0 - \omega_0 [\sigma_{zz}(3\cos^2\theta - 1) + \sigma_{\text{anis}} \sin^2\theta \cos 2\phi + \sigma_{\text{iso}}] \\ &= \omega_0 - \omega_0 \sigma_{\text{iso}} - \omega_0 \sigma_{zz} [(3\cos^2\theta - 1) + \rho \sin^2\theta \cos 2\phi]\end{aligned}$$

$$\text{where, } \sigma_{\text{iso}} = (1/3)(\sigma_1 + \sigma_2 + \sigma_3)$$

$$\sigma_{zz} = (1/6)(2\sigma_3 - \sigma_1 - \sigma_2)$$

$$\sigma_{\text{anis}} = (1/2)(\sigma_1 - \sigma_2)$$

$$\rho = 3(\sigma_1 - \sigma_2)/(2\sigma_3 - \sigma_1 - \sigma_2).$$

$\theta$  and  $\phi$  are the spherical angles between the external magnetic field  $H_0$  and the principal axes of the CSA tensor. The dynamic first-order chemical shifted NMR frequency under orientational diffusion motion can then be written as<sup>1</sup>,

$$\omega(\theta, \phi, \tau) = \omega(\theta, \phi) [\tau/T_2][1 - \exp(-T_2/\tau)]$$

where  $\tau$  is the orientational correlation time and  $T_2$  is the spin-spin relaxation time. At the slow tumbling limit,  $T_2/\tau \ll 1$ , valid for temperatures not too far above the glass-to-rubber transition, the above equation reduces to

$$\omega(\theta, \phi, \tau) = \omega(\theta, \phi)[1 - T_2/2\tau].$$

Therefore, the slow motional NMR CSA frequency shift is

$$\Delta\omega(\theta, \phi) = -\omega(\theta, \phi)[T_2/2\tau].$$

The expression for the NMR spin-spin relaxation time  $T_2$  along the three principal directions after inclusion of the tumbling motion can also be readily obtained. They are found to be

$$1/T_2(x, \tau) = 72^{-1/2}(109)^{1/4} \Delta^{1/2} \tau^{-1/2}$$

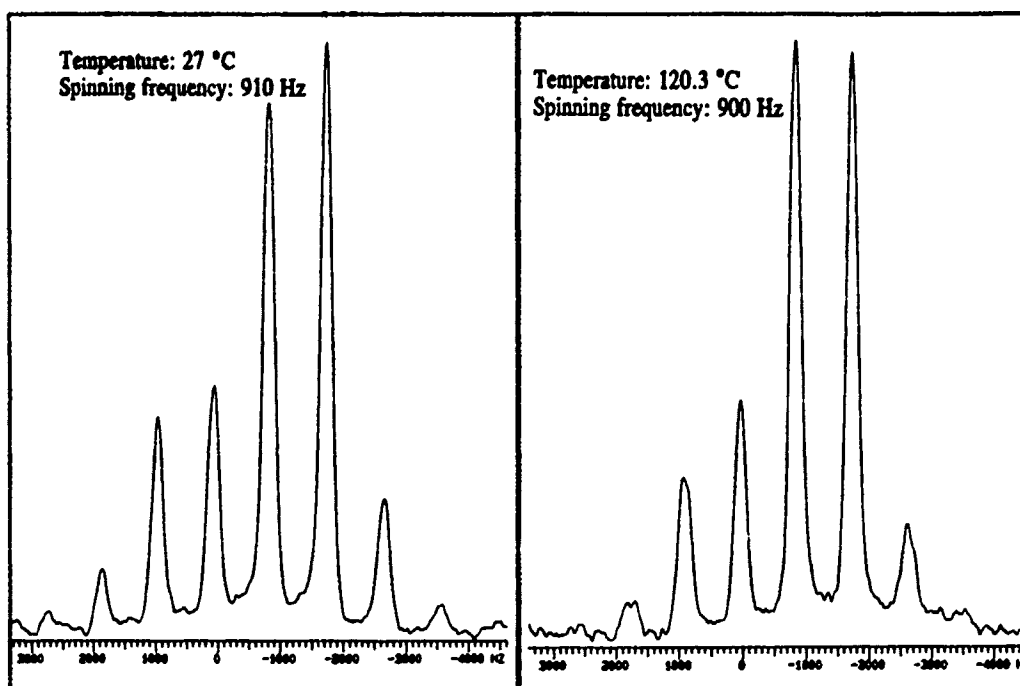


**Figure 1.**  $^{15}\text{N}$  MAS/NMR spectrum of solid nitrocellulose at two different temperatures. Note the spinning sidebands, whose equal spacing is given by the spinning frequency, and whose relative intensities carry the chemical shift anisotropy (CSA) information.

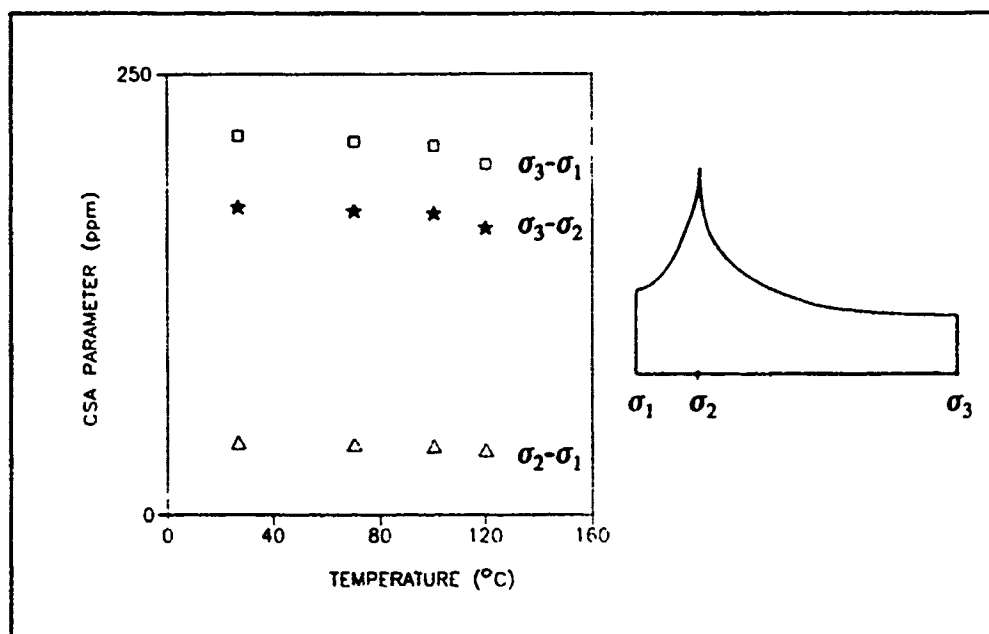


**Figure 2.** Experimental Chemical Shift Anisotropy (CSA) parameters vs. temperature in nitrocellulose. At right is shown a schematic of the broadband NMR line shape for polycrystalline/amorphous samples with asymmetric CSA. Note the definition of the frequency positions  $\sigma_1$ ,  $\sigma_2$ , and  $\sigma_3$ , the principal values of the shielding tensor.

$$1/T_2(y,\tau) = 72^{-1/2}(62.5)^{1/4} \Delta^{1/2} \tau^{-1/2}$$

$$1/T_2(z,\tau) = 72^{-1/2}(201)^{1/4} \Delta^{1/2} \tau^{-1/2}$$

where  $\Delta$  is the rigid-lattice chemical shift anisotropy.

Then, the frequency shifts of the principal features of the CSA spectrum obtained from the above equations, are,

$$\Delta\omega(1,\tau) = 0.284 (\Delta\tau)^{-1/2} \Delta \quad (1a)$$

$$\Delta\omega(2,\tau) = 0.176 (\Delta\tau)^{-1/2} \Delta \quad (1b)$$

$$\Delta\omega(3,\tau) = -0.376 (\Delta\tau)^{-1/2} \Delta \quad (1c)$$

where the indices 1, 2 and 3 denote, respectively, the principal directions x, y, and z.

### EXPERIMENTAL DETAILS

The experimental design was determined by the necessity to obtain spectra of sufficient signal-to-noise ratio at all temperatures before appreciable sample decomposition. For nitrocellulose, this forced timescales of minutes rather than hours or days. Nitrocellulose samples were prepared with 100% Nitrogen-15 isotopic enrichment by nitration of high quality cellulose fibers. At room temperature, Nitrogen-15 broadband NMR spectra of 0.5 gram samples yielded typical CSA powder patterns, with discernible shoulders and divergences. At higher temperatures, sufficient signal-to-noise could only be obtained in a timely fashion by using Magic Angle Spinning (MAS) techniques<sup>5</sup>. At first this may appear contradictory since MAS NMR techniques were developed, in part, to average out CSA broadening. However, by spinning at relatively slow speeds, spectra could be obtained, as shown in Figure 1, which were of sufficient signal-to-noise and with sufficiently intact CSA details. The CSA information is contained in the intensity of the spinning sidebands, and was extracted by the numerical methods of Herzfeld and Berger<sup>6</sup>. The final values of the CSA parameters at each temperature were refined by matching simulated and experimental spectra. The results are shown in Figure 2.

**Table 1.** Temperature dependence of the  $^{15}\text{N}$  chemical shift anisotropy  $\Delta_{31}$ ,  $\Delta_{32}$ , frequency shift  $\delta_{31}$ ,  $\delta_{32}$ , and the values of orientational correlation time  $\tau_{31}$ ,  $\tau_{32}$ , for NC.

T (°C)	$\Delta_{31}(\text{ppm})$	$\Delta_{32}(\text{ppm})$	$\delta_{31}(\text{kHz})$	$\delta_{32}(\text{kHz})$	$\tau_{31}(\text{ms})$	$\tau_{32}(\text{ms})$	$\tau_{av}(\text{ms})$
27.0	215.3	174.2					
70.3	211.4	171.8	0.079	0.049	305	450	$377 \pm 19\%$
100.6	209.5	170.5	0.118	0.075	138	189	$163 \pm 16\%$
120.3	199.0	162.2	0.330	0.243	17	18	$17.5 \pm 3\%$



## RESULTS AND DISCUSSION

At each temperature, three independent CSA parameters could be extracted from the experimental data, as shown in Fig. 2. Since the absolute chemical shifts were not measured, only two independent parameters are available for analysis, namely  $(\sigma_3 - \sigma_1)$  and  $(\sigma_3 - \sigma_2)$ . The discarded parameter,  $(\sigma_2 - \sigma_1)$ , also has the highest percent experimental uncertainty. The NMR results obtained at 27°C are taken to be the "rigid lattice" values, since the glass-to-rubber transition is reported<sup>7</sup> to be above 40°C. The data at the three higher temperatures were then used, with the aid of Eqs. (1), to calculate the corresponding correlation times, denoted  $\tau_{31}$  and  $\tau_{32}$ , respectively for the shoulder-to-shoulder parameter  $(\sigma_3 - \sigma_1)$ , and the divergence-to-shoulder parameter  $(\sigma_3 - \sigma_2)$ . The results are collected in Table 1. The last column in the Table lists the arithmetic average of  $\tau_{31}$  and  $\tau_{32}$ , and their percent difference shown as the uncertainty. Note that as the CSA shifts become larger, as the temperature increases, the agreement between the two independently calculated values,  $\tau_{31}$  and  $\tau_{32}$ , becomes substantially better. It is then presumed that their lack of complete agreement at the lower temperatures is a measure of our experimental uncertainty.

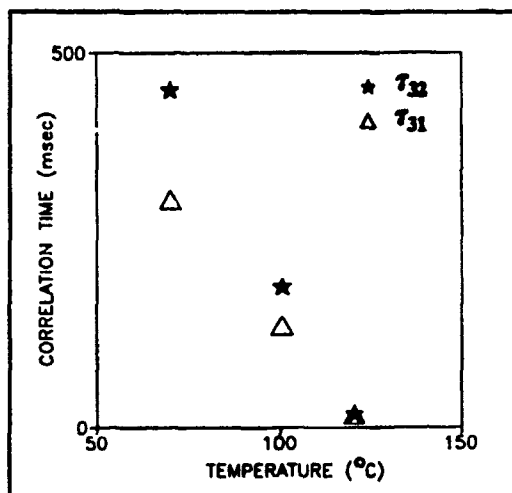


Figure 3. Correlation times for nitrocellulose polymer chain motion vs. temperature.

The final results obtained by this NMR technique are listed in the last column of Table 1. They show that even at 100°C the correlation time for thermal orientational diffusion in nitrocellulose is an appreciable fraction of a second. These results are consistent with the inelastic behavior of stretched 200  $\mu\text{m}$  nitrocellulose films conducted in our laboratory (JRPJ and RAM). It is interesting to compare the results of Table 1 with the results obtained by Owens<sup>7</sup> using ESR techniques in the same temperature region. Owens reports correlation times two orders of magnitude smaller, but they reflect the motion of small paramagnetic ions dissolved in nitrocellulose, not chemically bonded to the polymer chains. It is not surprising that the smallest ions are considerably more mobile.

The experimental method described in this paper differs substantially from traditional NMR methods relying on measurements of relaxation times vs. temperature, which for fixed-frequency NMR spectrometers are often inconclusive. It can easily be extended to other nuclei, like Carbon-13 or Fluorine-19. However, it is limited to slow motion, i.e., to temperatures below those where appreciable motional narrowing occurs.

**Acknowledgements** This work was supported, in part, by the U.S. ARDEC under the auspices of the U.S. Army Research Office Scientific Services Program.

## References

1. S. Lee, Phys. Rev. B30, 2353 (1984)
2. S. Lee and S.Z. Tang, Phys. Rev. B31, 1308 and B32, 2761 (1985)
3. S. Lee and A. Shetty, Phys. Rev. B35, 1 (1987)
4. R. R. Ernst, G. Bodenhausen and A. Wokaun, Principles of Nuclear Magnetic Resonance in One and Two Dimensions, Clarendon Press, Oxford (1987)
5. E.R. Andrew, Prog. NMR Spec. 8, 1 (1971)
6. J. Herzfeld and A.E. Berger, J. Chem. Phys. 73, 6021 (1980)
7. F. J. Owens, J. Macromol. Sci. -Phys., B23, 527 (1984)

## HOT SPOT HISTORIES IN ENERGETIC MATERIALS

A.M. MELLOR\*<sup>1</sup> and <sup>2</sup>, D.A. WIEGAND\*\*<sup>2</sup> AND K.B. ISOM\*\*\*

\*Mechanical Engineering Department, Vanderbilt University, Nashville, TN

\*\*Energetic and Warheads Division, Army RD&E Center, Picatinny Arsenal, NJ

\*\*\*Hercules Aerospace Company, Magna, UT

### ABSTRACT

Interest in the mechanisms by which hot spots either grow to sustained reaction or are quenched results from the observation that the energy required to ignite a propellant or explosive can be significantly less than that needed to bulk heat a test specimen uniformly to its ignition temperature. This result is independent of the original form of non-thermal energy and has been used to interpret data for shock, impact, friction and electrostatic discharge (ESD) stimuli. We present new flowcharts which include 1) events resulting in hot spot formation and 2) subsequent pathways which lead to sustained reaction or quenching. The mechanism appears capable of categorizing and demonstrating the similarities and differences between hot spot growth or quenching, for impact and ESD stimuli. Sample confinement and temperature and stimulus duration are the independent variables whose roles are particularly clarified in the mechanism.

### INTRODUCTION

Current understanding of the events leading to hot spot formation was the focus of a recent Army-supported Workshop. Discussion also included factors contributing to growth and coalescence or quenching of such reactive centers. As the proceedings [1] and a summary of the Workshop [2] are available, here we focus on a mechanism suggested by study of papers given and comments made at the Workshop that clarifies phenomena common to low-velocity impact and electrostatic discharge ignition of energetic materials. Effects of duration of the input energy, sample temperature, and sample confinement are given particular attention. By confinement we mean not only the presence of a case surrounding the energetic material, but also the inertial effects of large specimen volume and/or high ambient gas pressure. In other words, confinement by definition inhibits the release of high pressure, gaseous products of combustion formed by chemically reacting hot spots within an energetic material specimen.

### ESD INITIATION

At the Workshop, Baker et al. [3] reviewed ESD ignition mechanisms proposed in the literature, and here we focus on work at Hercules, where a detailed sequential pathway is proposed from initial stimulus to combustion or quench, based on tests with both bulk and thin, two-dimensional, encased sandwich propellant specimens [4]. Continuous path dielectric breakdown through the composite propellant sample in formulations containing Al particles results in some chemical decomposition of the binder. If the oxidizer, for example, ammonium perchlorate (AP), is sufficiently close to the source(s) of these decomposition products, then chemical reactions between the oxidizer and binder can occur. The path from this point depends on whether cracks are present or form near the chemically reacting hot spot so that the high pressure products of reaction can escape and

<sup>1</sup>Support was provided by the Army Research Office and Army Missile Command under Grants No. DAAL03-91-G-0135 and DAAL03-92-G-0386, Contract No. DAAL03-89-K-0061, and MIPR No. W31P4Q-1-7R-3-125. AMM expresses appreciation to D.M. Mann of the Army Research Office and D.R. Dreitzler of the Army Missile Command for their technical assistance.

<sup>2</sup>The views, opinions and/or findings contained in this paper are those of the authors and should not be construed as an official Department of the Army position, policy, or decision, unless so designated by other documentation.

quench the reaction. Although some small cracks may have formed during the original electrical discharge, Isom and Speed [4, 5] attribute cracks capable of providing venting to the pressure buildup due to reaction. Gibson's [6] results in tests with inert propellants also support this conclusion, and Covino and Hudson [7] note that fracture or decomposition of propellant is observed only upon occasion after breakdown. Finally, if venting from the hot spot is inadequate, then ignition and combustion of the entire specimen are more likely through either flame spreading from the original hot spot or coalescence of multiple hot spots formed in the initial arc, followed by flame spreading.

Earlier work by Larson and Beale [8] and Isom [5] suggested microarcs between Al particles within the propellant rather than continuous path breakdown as precursors of local chemical reaction; continuous path breakdown refers to a visibly evident path. One difficulty with the microarc postulate is that energy deposition is very small compared to that in a continuous breakdown (see, e.g., J. Smith's comments in [2]). However, as will be discussed below, large confinement will suppress mechanical fracture of the propellant; if continuous path breakdown and any cracks which result are affected similarly by confinement, then the microarc route may become more important as sample size or ambient pressure is increased.

Thus, in the flowchart shown in Fig. 1, the main effect of high confinement (the right in

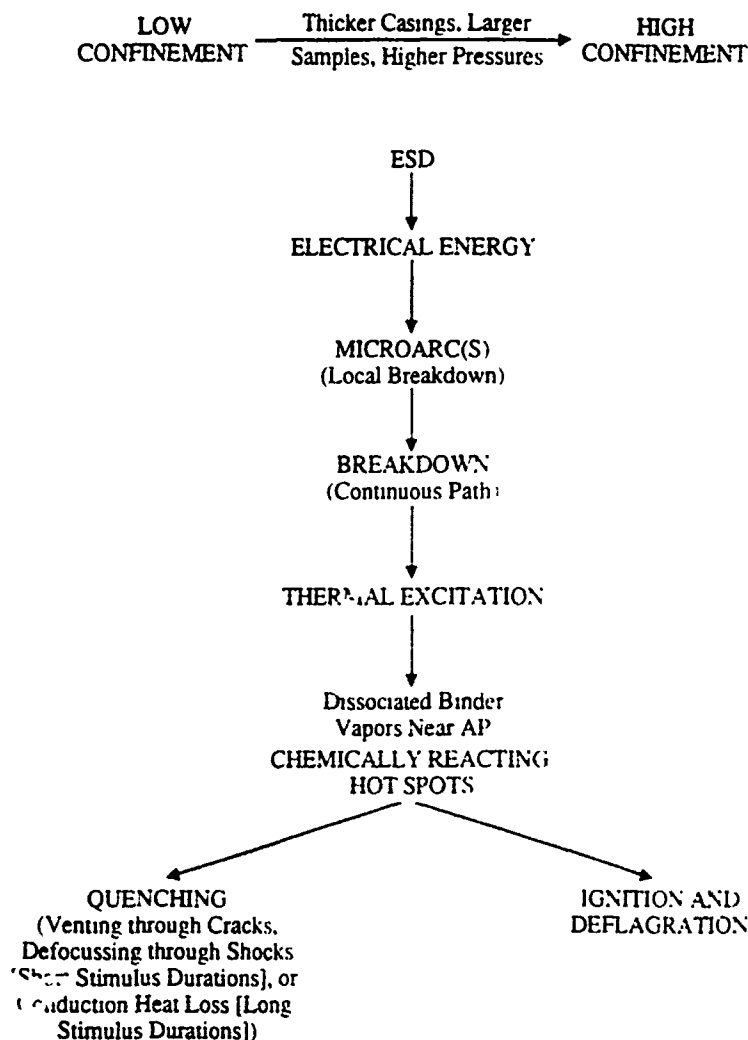


Figure 1. Pathways for absorption of electrostatic-discharge electrical energy by a solid energetic material. Probability of ignition depends on degree of confinement; if chemical reaction extinguishes, then quenching mechanism depends on duration of stimulus (see text).

the figure) is less likelihood of quenching, due to the difficulty of forming large cracks as shown at the bottom of Fig. 1. Following Baker et al. [3], two quenching mechanisms in addition to venting through cracks are listed. In tests at Hercules propellant ignition delay times are long, on the order of ms. Thus the fracture-hot spot venting quench mechanism also occurs at time scales of this order, and other modes of energy loss from the spark channel must be responsible for dissipating spark and any chemical energy release at shorter times. If spark duration is short, as in the breakdown or fast arc regime (Maly and Vogel [9] suggest durations here of  $0.1 \mu\text{s}$  and less for gases), then the initial high rate of the discharge will create a blast wave (Bradley and Lung [10] and Kono et al. [11] show blast wave and flame kernel computations for spark discharges in gaseous media). The shock travels away and removes energy from the arc channel. Heat loss by conduction can also quench the hot spot. Ko et al. [12] estimate for gaseous mixtures the blast wave mechanism dominates for approximately 5 to  $10 \mu\text{s}$ , at which point conduction becomes more important.

The confinement-dependent portion of the mechanism shown at the bottom of Fig. 1 is consistent with some observations reported by Speed and Berger [13]. These workers varied specimen thickness between electrodes in dielectric breakdown studies at atmospheric pressure. Larger samples suffered more damage during the breakdown process and exhibited higher probability of ignition. Also, for premixed combustible gases it is well known that energy required for spark ignition decreases with increasing pressure [14]. Hodges et al. [15] have demonstrated that at constant electrode spacing spark ignition energy also decreases significantly as ambient pressure is increased, and Magann [16] observed similar trends in an experiment designed to simulate the core-pulling process during motor manufacture.

To summarize, the postulated ESD mechanism shown in Fig. 1 differs from that of Isom and Speed [4] primarily in terms of possible quench mechanisms, following the suggestions of Baker et al. [3]. Also, the role of confinement in inhibiting damage, fracture, and cracking from gaseous products of combustion at high pressure is identified. Mechanical failure mechanisms, the subject of the following section, can strongly depend on confinement.

## IMPACT INITIATION

Wiegand [17] notes that for brittle materials low confinement favors fracture of the energetic material, while high confinement generally leads to yield and plastic flow. Here, fracture implies one picks up pieces of the specimen after the test. Either fracture or plastic flow creates localized thermal energy, as shown in Fig. 2, through friction in cracks in compression [18], the generation of reactive species on freshly exposed surfaces [19], or in tensile cracks at the propagating crack tip in the case of fracture (which Wiegand [17] considers unlikely). Viscoplastic heating is the mechanism at high confinement, where ignition is more likely given a particular level of stimulus.

Following Isom and Speed's mechanism for ESD reviewed in the previous section, transformation of the thermal hot spot into a chemically reacting hot spot in composite energetic materials requires that both fuel and oxidizer be available or nearby. For rocket propellants, for example, if the more brittle oxidizer (AP) particles are the preferred location for mechanical stress concentration, then heating by fracture or plastic flow in these crystals initiates chemical decomposition. If binder is available in the vicinity, then hot spot growth and ignition can result.

As suggested by Wiegand [17], combustion is favored by larger samples or at higher ambient pressures, whereas quenching is more likely at low confinement. Unlike the case of ESD initiation, at low confinement cracks pre-exist so that pressure relief of chemically reacting hot spots occurs at lower hot spot pressures in mechanical initiation. The shock dissipation mechanism for quenching is omitted from the impact initiation pathway in Fig. 2 because high rate, localized subsurface mechanical energy input is difficult to envision.

Wiegand and associates [20, 21, 17] have also observed brittle behavior in ductile materials, such as gun propellants at low temperatures. Under such conditions these materials exhibit glassy mechanical behavior and will also follow the pathways shown in Fig. 2. So too may solid rocket propellants at high impact rates, which are of particular relevance in incidents involving bullet, fragment, or shaped charge jet impact [22]. Although Ho and Fong [23, 24] report modified Hopkinson bar impact results on a number of composite rocket propellants and attribute failure to fracture with some ductile

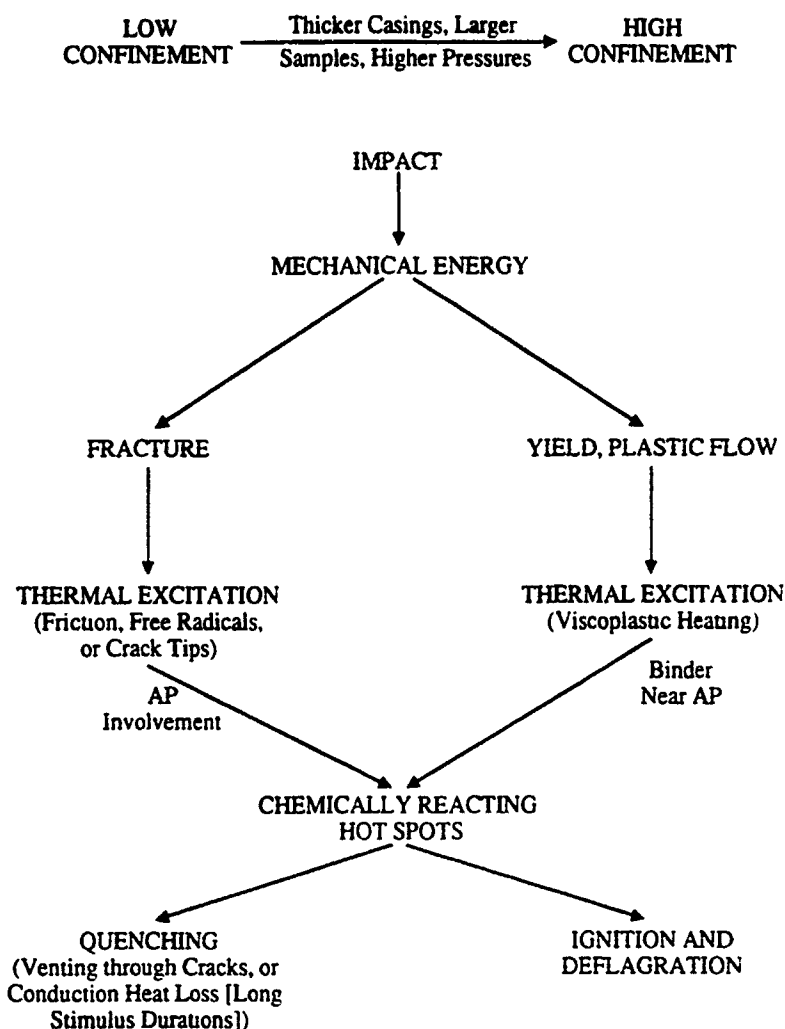


Figure 2. Pathways for absorption of low-velocity-impact mechanical energy by a solid energetic material. Failure mechanism and probability of ignition depend on degree of confinement (see text).

behavior, in later work including microflash photography Ho [25] indicates that HTPB (hydroxyl-terminated polybutadiene)/AP propellants ignite via ductile and/or shear failure. Coffey et al. [26, 27], and Baker et al. [28] use propellant or propellant-like energetic material in instrumented drop weight tests in a similar impact velocity range and also conclude initiation results from viscoplastic heating, specifically in oxidizer crystals. Thus in the strain rate ranges associated with these two test methods, ignition follows the high confinement (and high temperature) path.

The mechanism for initiation presented in Fig. 2 is based largely on Wiegand [17] except that in composite energetic materials the need for both fuel and oxidizer to participate in the formation of chemically reacting hot spots is explicitly stated, following Isom and Speed [4] in their ESD mechanism. In addition, potential quenching processes are identified, in accordance with the work of Baker et al. [3]. Wiegand [17] notes that, in incidents involving initially heavily confined propellants or explosives, the confinement may fail due to penetration of the projectile through the casing before ignition occurs, thus allowing the hot spots to quench. In terms of Fig. 2, this suggestion corresponds to describing an incident which follows the right portion of the mechanism, but terminates at the lower left when the confinement is released. In other words, if times characteristic of the various processes in the mechanism could be estimated, as well as a time associated with failure of the casing in an incident, then the response severity for that incident could be assessed.

## CONCLUSIONS

Literature mechanisms for ESD and low-velocity impact initiation of energetic materials have been reviewed and combined into the flowcharts of Fig. 1 and 2, respectively, which summarize the requirements for and constraints on formation of thermal and chemically reacting hot spots after the stimulus has occurred. Macroscopic damage and quenching of the hot spot are more likely as confinement and temperature are reduced.

Input energy is focused locally and creates a region of thermal excitation that starts binder or oxidizer decomposition and gasification. Energy is dissipated from the hot spot by conduction heat transfer and for ESD by blast waves associated with the breakdown portion of the microarcs. If the hot decomposition products encounter the other reactant in the vicinity of the hot spot, then chemical reactions will initiate, providing further heat generation and pressurization as combustion products form in the gas phase. For situations where confinement and temperature are low, the material is more likely to fracture and release these high pressure gases, probably quenching the hot spot.

Characteristic times for the processes identified in Fig. 1 and 2 when compared with stimulus duration would allow identification of the appropriate response pathway for a given incident. Confinement must be quantified in terms of the appropriate energetic material dynamic mechanical/electrical properties before quantitative use of the mechanisms can be made. Nondimensionalization of the stimulus energy level is also required, perhaps in terms of an overall activation energy for the pre-ignition reaction.

## REFERENCES

1. Workshop on Propellant Ignition Micromechanics Proceedings, Army Research Office (1991).
2. Mellor, A.M., Dreitzler, D.R., Lieb, R.J. and Mann, D.M., Workshop on Propellant Ignition Micromechanics Proceedings (Army Research Office, 1991) pp. iii-xix; see also JANNAF Propulsion Systems Hazards Subcommittee Meeting Proceedings (CPIA Publ. 582, I, 1992), pp. 41-55.
3. Baker, P.J., Mellor, A.M. and Isom, K.B., Workshop on Propellant Ignition Micromechanics Proceedings (Army Research Office, 1991) pp. 1-15.
4. Isom, K.B. and Speed, T.C., Workshop on Propellant Ignition Micromechanics Proceedings (Army Research Office, 1991) pp. 215-233.
5. Isom, K.B., Discussion cited in Mellor, A.M., Dreitzler, D.R., Larson, R.W. and Mann, D.M., Workshop on ESD Ignition of Composite Solid Propellants Proceedings (Army Research Office, 1989) pp. ii-xvi; also JANNAF Propulsion Systems Hazards Subcommittee Meeting Proceedings (CPIA Publ. 538, I, 1990) pp. 219-228.
6. Gibson, P.W. (private communication).
7. Covino, J. and Hudson, F.E. III, J. Propuls. Power 7, 894-903 (1991).
8. Larson, R.W. and Beale, P.D., Workshop on ESD Ignition of Composite Solid Propellants Proceedings (Army Research Office, 1989) pp. 1-11.
9. Maly, R.R. and Vogel, M., Seventeenth Symposium (International) on Combustion (The Combustion Institute, Pittsburgh, 1978) pp. 821-831.
10. Bradley, D. and Lung, F.K.-K., Combust. Flame 69, 71-93 (1987).
11. Kono, M., Niu, K., Tsukamoto, T. and Ujije, Y., Twenty-Second Symposium (International) on Combustion (The Combustion Institute, Pittsburgh, 1988) pp. 1643-1649.

12. Ko, Y., Arpaci, V.S. and Anderson, R.W., *Combust. Flame* **83**, 88-105 (1991).
13. Speed, T.C. and Berger, M.A., *Workshop on Propellant Ignition Micromechanics Proceedings* (Army Research Office, 1991) pp. 199-213.
14. Lewis, B. and von Elbe, G., Combustion, Flames and Explosions of Gases, 2nd ed. (Academic Press, New York, 1961) p. 323.
15. Hodges, R.V., McCoy, L.E. and Raun, R.L., *Workshop on Propellant Ignition Micromechanics* (Army Research Office, 1991) pp. 113-122.
16. Magann, T.F., *Workshop on ESD Ignition of Composite Solid Propellants* (Army Research Office, 1989) pp. 107-118.
17. Wiegand, D.A., *Workshop on Propellant Ignition Micromechanics Proceedings* (Army Research Office, 1991) pp. 149-159.
18. Dienes, J.K., *Workshop on Propellant Ignition Micromechanics Proceedings* (Army Research Office, 1991) pp. 89-99.
19. Dickinson, J.T., *Annual Technical Report, Contract N00014-80-C-0213, Office of Naval Research*, 1985.
20. Nicolaides, S., Wiegand, D.A. and Pinto, J., *Picatinny Arsenal Technical Report ARLCD-TR-82010*, 1982.
21. Pinto, J., Georgevich, D., Nicolaides, S. and Wiegand, D.A., *Picatinny Arsenal Technical Report ARLCD-TR-84006*, 1984.
22. Duffy, K.P. and Mellor, A.M., *AIAA Paper No. 92-3630*, 1992; see also JANNAF Structures and Mechanical Behavior Subcommittee Meeting Proceedings, to appear (1992).
23. Ho, S.Y. and Fong, C.W., *Polymer* **28**, 739-744 (1987).
24. Ho, S.Y. and Fong, C.W., *Combust. Flame* **75**, 139-151 (1989).
25. Ho, S.Y., *Combust. Flame* **91**, 131-142 (1992).
26. Coffey, C.S., DeVost, V.F. and Woody, D.L., Ninth Symposium (International) on Detonation (II, OCNR 113291-7, 1989) pp. 1243-1252.
27. Coffey, C.S., Ninth Symposium (International) on Detonation (I, OCNR 113291-7, 1989) pp. 58-65.
28. Baker, P.J., Mellor, A.M. and Coffey, C.S., *JANNAF Propulsion Systems Hazards Subcommittee Meeting Proceedings* (CPIA Publ. 538, I, 1990) pp. 95-104; see also *J. Propuls. Power* **8**, 578-585 (1992).

## EXPERIMENTAL STUDY AND MODEL CALCULATIONS OF METAL COMBUSTION IN Al/AP UNDERWATER EXPLOSIVES

Philip J. Miller and Raafat H. Guirguis  
Detonation Physics Branch, NAVSWC, White Oak Laboratory,  
Silver Spring, Maryland 20903-5000

### ABSTRACT

A small-scale laboratory experiment in which the detonation products are confined was designed such as to yield for small charges (as little as 1/2 gram) gas expansion rates comparable to those due to the underwater detonation of large-scale charges. The resulting slow expansion allows the aluminum and the other non-ideal components typically used in underwater explosives to react to completion within the time frame of the experiment. Both ideal and non-ideal aluminized explosives were tested. The traditional Jones-Wilkins-Lee (JWL) equation of state reproduced the measurements in the case of the ideal explosives. An extended JWL equation of state in which the time-dependent late energy release is introduced was adjusted until it reproduced the measurements of the non-ideal explosive tested. This derived time-dependent equation of state also reproduced the data of large-scale cylinder tests and underwater detonations using the same non-ideal explosive.

### INTRODUCTION

Composite explosives containing significant amounts of aluminum (Al) and ammonium perchlorate (AP) often release a substantial amount of their energy late in the explosion process<sup>1</sup>. The detonation velocity and pressure are substantially lower than in ideal explosives. But delaying the energy release enhances the damage in underwater applications. Energy release persists in the Taylor rarefaction region, and sometimes even after the bubble has expanded a few times the initial charge size. This late energy release introduces a time-dependency into the problem of determining the equation of state (EOS)<sup>2-4</sup>. As a result, the EOS appears to depend on the size of the charge and the degree of confinement, making it difficult to characterize these explosives using traditional small-scale experiments, such as the cylinder test, the wedge test, etc. In this paper, a small-scale laboratory experiment, called the Moby-Dick test, that can be used to characterize these types of explosives easily and inexpensively, is described. An extended JWL EOS, containing an energy release rate term, was introduced in the DYNA2D hydrocode<sup>5</sup>, and calibrated by fitting the experimental data of the Moby-Dick test. The resulting EOS reproduced the experimental data of large-scale cylinder tests and underwater explosions.

### EXPERIMENT

The Moby-Dick test was designed such that small amounts of explosives, as small as 1/2 gram, could yield expansion rates comparable to those of large-scale underwater explosions involving tens of kgms. of explosives. This was done in order to insure that the measurements reflect most, if not all, of the late energy released due to the reaction of the non-ideal components in typical underwater explosives. In the test (see Figure 1), the explosive sample is confined in a block of steel, except in one direction, where the detonation products are allowed to expand by pushing water along a thick lexan transparent tube of a small diameter attached to the confining steel base. Motion of the interface between the gas and the water was



tracked using an electronic framing and streak camera. Observations in the combined range  $V=2-20$   $t=10-500 \mu s$ , are possible in this arrangement.  $V$  is the relative volume of the products and  $t$  is the time after the Chapman-Jouguet conditions.

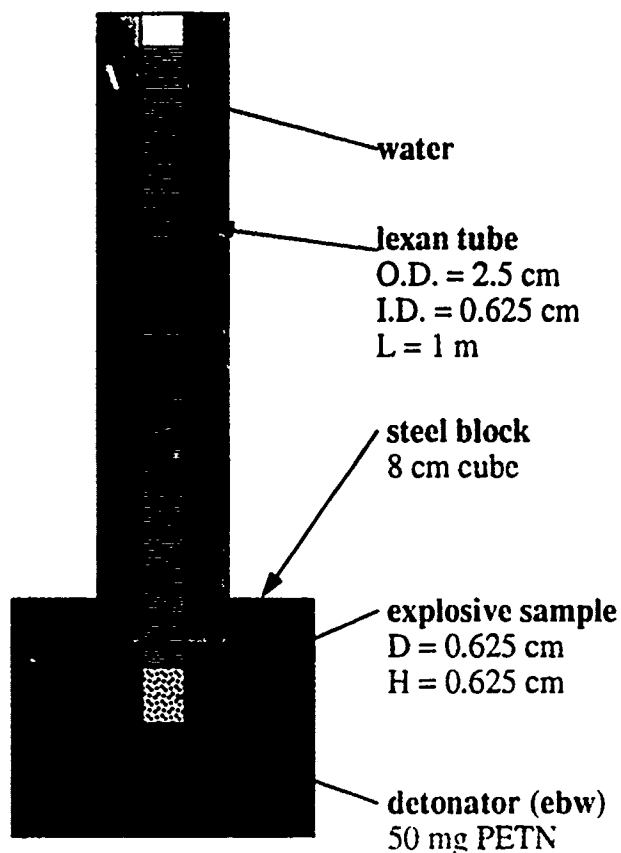


Fig. 1 Moby-Dick test setup.

## RESULTS

Results of these tests, using three different explosives, are presented in this paper. These include Pentolite (50%RDX,50%TNT), PETN and a typical Al/AP underwater explosive containing significant amounts of Al and AP, in addition to other components. The first two are ideal explosives and were used in order to define a base line to which we can compare the behavior of the non-ideal third explosive. In Figure 2, the experimental measurements are compared to the results of the numerical simulations using DYNA2D code with the appropriate EOS. In the case of the two explosives Pentolite and PETN, known JWL EOS (Table I), determined by traditional 1" and 2" cylinder tests<sup>1</sup>, successfully reproduced the experimental data. For the non-ideal Al/AP explosive, the time-dependency (discussed in the next section) had to be introduced in the JWL EOS in order to simultaneously fit both early and late time regimes and yield unique values for the adjustable parameters in the EOS. As explained later, the derived time-dependent EOS also reproduced the data of both large-scale cylinder tests and underwater explosions.

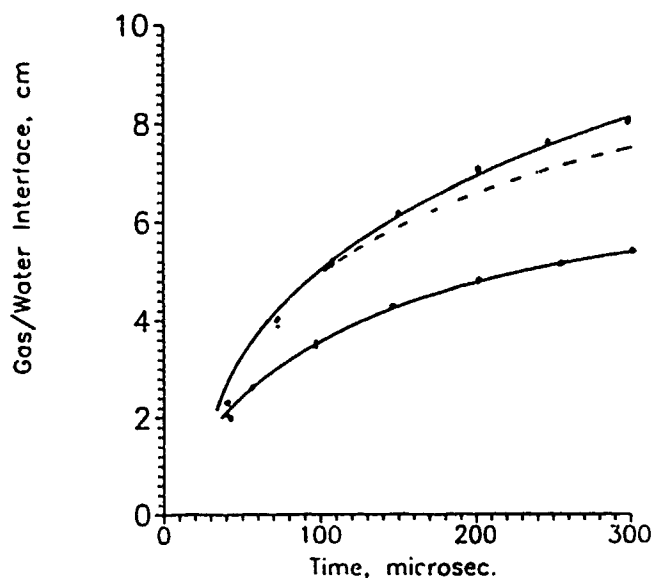


Fig.2 Results from the Moby-Dick test. The upper curve is the Al/AP explosive where the solid line are results from the time-dependent JWL Equation (1) and the dashed line the traditional JWL EOS. The lower curve is for Pentolite with the traditional JWL EOS calculated solid curve.

## MODEL

Previous experiments of aluminum combustion were usually conducted at atmospheric pressure<sup>6</sup>. Some observed aluminum particles burning in a flame. Others measured the oxidation rate of thin sheets of aluminum in an oxidizer gas. Both types of studies have shown that the aluminum reaction is diffusion limited. As the thickness of the  $\text{Al}_2\text{O}_3$  layer formed on the surface gets thicker, the rate of diffusion of the oxidizer gas through the barrier layer decreases, causing a decrease in the reaction rate. During the oxidation of the metal sheet, the surface area is constant. As a result, the oxidation is described by the simple kinetic law,  $\lambda = (kt)^{1/2}$ , where  $\lambda$  is the mass fraction of  $\text{Al}_2\text{O}_3$ , and  $k$  is a constant that depends on the temperature and the pressure of the oxidizer gas. In the combustion of aluminum particles, burning progresses from the surface towards the center, leaving an increasingly thicker layer of  $\text{Al}_2\text{O}_3$ . In addition to the reduction in the rate of diffusion, the area of the interface at which the reaction occurs gets smaller, yielding  $[1 - (1 - \lambda)^{1/3}]^2 = kt/r^2$ , where  $r$  denotes the particle radius. A number of these expressions exist for various reaction conditions and geometric configurations, but the correct one, that is obeyed when an irregularly shaped aluminum particle burns in the high-pressure and temperature environment of the detonation products, is unknown. Here, the rate expression  $d\lambda/dt = a(1 - \lambda)^{1/2}p^{1/6}$  was chosen, where the constant  $a$  includes the dependency on the particle size,  $(1 - \lambda)^{1/2}$  is for the geometrically decreasing reaction surface area, and the pressure dependence  $p^{1/6}$  is based on both theoretical analysis and experimental measurements<sup>7</sup>. The temperature dependence, usually in the form  $e^{-\Delta H/RT}$ , is assumed included in the constant  $a$ , because the aluminum combustion in the detonation products environment occurs within a narrow range of relatively high flame temperatures.

In a previous study<sup>3</sup> involving the development of an EOS for underwater explosives, the pressure traces due to a large-scale underwater explosion were used to derive an extended yet time-independent JWL EOS. An equilibrium JWL EOS for reacting products of similar

Table I. JWL Equation of State Parameters

Parameter	Pentolite	PETN	Al/AP Explosive	
A Mbar	5.3177	6.17	18.83	6.9513 <sup>+</sup>
B Mbar	0.0893	0.169	1.375	0.0313
R <sub>1</sub>	4.6	4.4	8.0	5.4
R <sub>2</sub>	1.05	1.2	4.0	1.4
$\omega$	0.33	0.25	0.40	0.40
E <sub>0</sub> Mbar cc/cc	0.08	0.101	0.095	0.070
a	-	-	-	0.0065
Q Mbar cc/cc	-	-	-	0.110
P <sub>ej</sub> Mbar	0.235	0.335	0.150	0.150
D <sub>ej</sub> mm/ $\mu$ s	7.36	8.30	5.9	5.9
$\rho_0$ g/cc	1.65	1.77	1.88	1.88

<sup>+</sup>time-dependent JWL parameters.

explosives was proposed in reference [4]. In this paper, the JWL EOS was modified to the form

$$P = A(1-\omega/R_1V)\exp(-R_1V) + B(1-\omega/R_2V)\exp(-R_2V) + \omega(E+\lambda Q)/V, \quad (1)$$

where  $d\lambda/dt = a(1-\lambda)^{1/2}p^{1/6}$ .

The late energy release term  $\lambda Q$  was added to the traditional JWL EOS, yielding  $\omega(E+\lambda Q)/V$ . The new parameters  $a$  and  $Q$  were added to the list of adjustable parameters  $A, B, R_1, R_2, \omega$ , and  $E_0$  in the traditional JWL EOS. These are usually determined by fitting the results of hydrocodes to the cylinder test data, and to measured detonation pressures and velocities. Here,  $E_0$  is the energy content of the explosive that sustains the detonation CJ conditions.  $Q$  is the additional energy release after the CJ plane. The adjustable parameters are first evaluated using the TIGER chemical equilibrium code<sup>8</sup>, then fine tuned by fitting the early and late time regimes of the Moby-Dick test. The resulting time-dependent EOS reproduced as well the experimental data of large-scale cylinder tests (Figure 3), the pressure-time history of the pulse induced in water due to the underwater explosion of large explosive charges (Figure 4).

## CONCLUSIONS

In summary, both the small-scale Moby-Dick test and the time-dependent JWL EOS were validated. The EOS of new non-ideal underwater explosives in which late energy release occurs can be now easily and inexpensively derived.

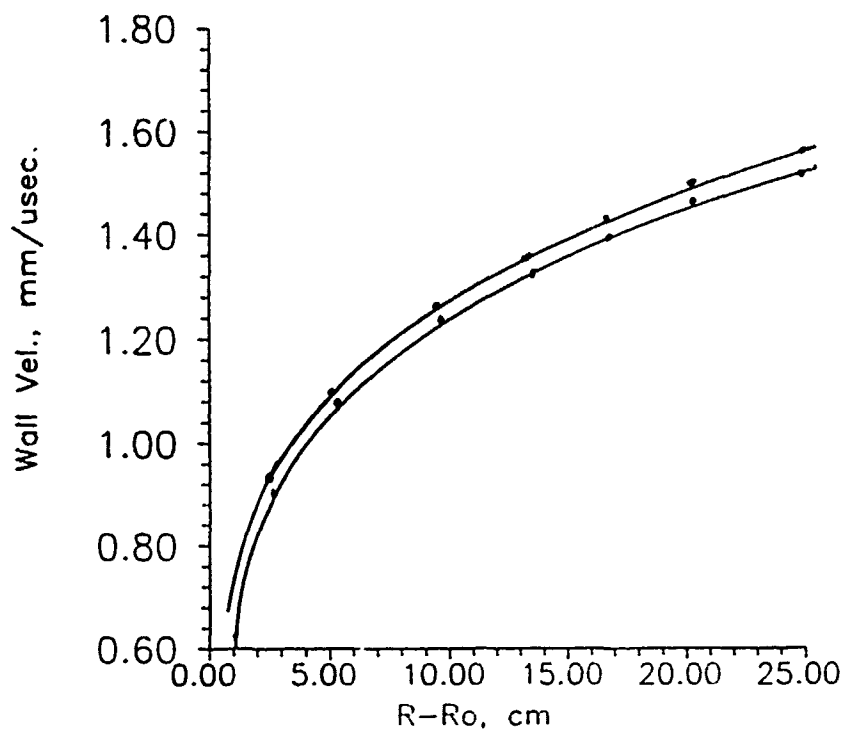


Fig. 3 The data points (from LLNL) are averaged from 4" (lower curve) and 8" (upper curve) cylinder test data for the Al/AP explosive. The solid lines represent calculations based upon equation (1).

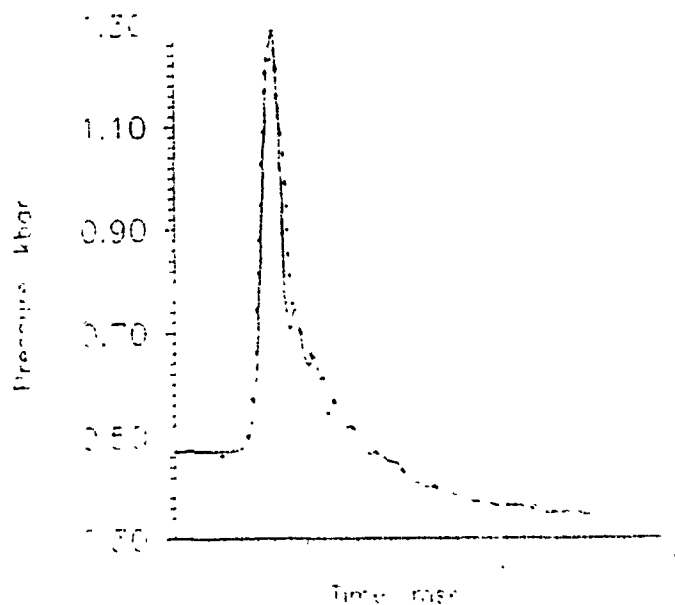


Fig. 4 Results from a 11 lb. large scale test on the Al/AP explosive. The data points are from pressure gauges placed 3 feet from the charge. The solid line is calculated from equation (1).

**REFERENCES**

1. J.W. Kury, H.C. Hornig, E.L. Lee, J.L. McDonnel, D.L. Ornellas, M. Finger, F.M. Strange, and M.L. Wilkins, "Metal Acceleration of Chemical Explosives," Fourth (International) Symposium on Detonation, ACR-126(1965).
2. C.L. Mader, Numerical Modeling of Detonations, University of California Press (1979).
3. H.M. Sternburg and L. Hudson, "Equations of States for Underwater Explosives", Proceedings of the 1987 International Symposium on Pyrotechnics and Explosives, Beijing, China, China Academic Press.
4. R.H. Guirguis, "Modeling of Late Reactions in Aluminized Underwater Explosives," Proceedings of the 1992 JANNAF PSHS, NAVSWC, Silver Spring, MD, CPIA.
5. J.O. Hallquist, "An Explicit Two-Dimensional Hydrodynamic Finite Element Code with Interactive Rezoning and Graphical Display", Rev.3, UCID-18756 1987.
6. W.E. Brown, D. Dollimore, and A.K. Galwey, in Comprehensive Chemical Kinetics, edited by C.H. Bamford and C.F.H. Tipper (Elsevier Scientific Publishers), New York, 1980), p.68.
7. T.B. Grimley, in Chemistry of the Solid State, edited by W.E. Garner (Butterworths Scientific Publications, London, 1955), p.336.
8. M. Cowperthwaite and W.H. Zwisler, Users Guide of the TIGER Computer Program, Stanford Research Institute, Menlo Park, California, (1984).

## DETONATION STUDIES IN DISPERSED SOLID PARTICULATE EXPLOSIVES USING HIGH SPEED TIME-RESOLVED HOLOGRAPHY

Michael J. Ehrlich\*, James W. Wagner\*, Jacob Friedman\*, Heinrich Egghart\*\*

\*The Johns Hopkins University, Center for Nondestructive Evaluation, Department of Materials Science and Engineering, Baltimore, MD 21218

\*\*US Army Belvoir Research, Development and Engineering Center, Fort Belvoir, VA

### Introduction

Clouds of dispersed explosive or combustible solid particles are detonable and such systems may exhibit self-sustained detonation [1-8]. However, the method by which individual particles in the explosive cloud interact to sustain detonation is not well understood. The similar case of liquid fuel/air explosives was investigated in detail during the 1960's and 1970's. For these systems, it was established that incident shock waves serve to shatter large liquid droplets into a mist of micro-droplets. These microdroplets are almost instantaneously accelerated to the convective flow velocity behind the shock wave. The energy released upon ignition of the micromist supports the shock wave and self-sustained detonation results [9-11].

Dispersed solid particles, investigated more recently, are not fragmented by the shock wave and are therefore not accelerated as rapidly as the micromist mentioned above [2,12]. For instance, dense 100 $\mu$ m diameter particles were found to be accelerated by a shock wave to speeds of only 150-250 m/s [13]. In addition, large particles exhibit relatively slow heating and reaction rates. For these reasons, the detonation of solid fuels such as aluminum requires particles of very small size [2]. In the detonation of dispersed explosive particles such as PETN or RDX, which are self-sufficient with regard to oxygen, particle size does not appear to be a critical factor governing detonability, but somewhat longer induction times have been observed for powders consisting of relatively large particles [1].

Most detonation studies of dispersed systems have made use of detonation tubes which permit the determination of detonation velocities, pressures, and the arrival times of shock and reaction fronts [1,2,8]. Such studies provide insight into the macroscopic detonation characteristics of dispersed powder systems. The goal of the work discussed in this paper is to study these systems on a microscopic scale - to study the detonation of individual particles, as well as the interaction between neighboring particles which sustains detonation. Toward this end, the detonation of single 125 $\mu$ m diameter lead azide particles was investigated with a novel high speed time-resolved holographic system [14]. The system is capable of recording a series of nine holographic exposures in rapid succession; the time interval between exposures is discretely variable from 28ns to 170ns. With this system it was possible to record nine sequential images of a detonation event, clearly showing the shock front and reaction volume extents. The majority of the experiments were performed with single particles, the aim being to characterize shock front propagation arising from single particle detonation. In addition, preliminary results for two-particle interaction studies will be presented.

### Time-resolved Holography Experiments

The time-resolved holography system, described in detail elsewhere [14], utilizes a phase-front preserving optical delay line coupled with a specially graded beamsplitter to generate ten sequential, spatially separated output light pulses. A schematic of the system is given in Figure 1. The holographic system was developed to overcome the problems associated with conventional single or double pulse holographic techniques, namely that of obtaining only one or two data points per event. If the event of interest is not exactly

reproducible, it becomes difficult to correlate data obtained from separate experiments. For the case of the single particle detonation experiments reported here, two main factors made quantitative correlations of different experiments difficult. First, particle size and density variations affect the total energy released during detonation. Although the lead azide was sieved to yield nominally 125 $\mu$ m diameter particles, the particles were generally oblong in shape and non-uniform in volume. The second factor was an observed variation in the initiation time exhibited by individual particles following deposition of the laser energy. Detonation of the lead azide particles was initiated by focusing a low energy Nd:YAG laser pulse on the particle. Once the laser energy had been deposited there appeared to be a 400ns window of uncertainty during which detonation would begin. Accordingly, the data for the single particle experiments reported here suffered from a  $\pm 200$ ns timing uncertainty.

Each sequence of holograms recorded was reconstructed using an argon ion continuous wave laser. Each hologram was imaged using a long working distance microscope to provide a field of view approximately 5mm wide. Each holographic image was digitized to an 8-bit 512x480 pixel format, yielding resolution on the order of 10 $\mu$ m per pixel.

## Results and Discussion

Measurements of the shock front extent were made by moving a crosshair cursor over each digitized image. The crosshair was 2 pixels wide, limiting spatial resolution to  $\pm 20 \mu$ m. Figure 2a shows an ensemble of the data collected from all experiments. Two of the data sets have been given triangular symbols on this plot to differentiate them from the other data. It can be seen that these two data sets lie relatively far away from all others. It is believed that the single particles used for these two experiments were of vastly different volume than the majority.

To obtain a working relationship between shock front extent and time, a curve was fit to all data shown in Figure 2a, excluding the two data sets denoted by triangle symbols. The form of the curve used to fit the data included two terms as shown in Eq.(1) below. The first term took the form of the classical point-source solution for a strong shock designed to model the shock early in its lifetime. The second term was linear with time, where the slope coefficient was equal to acoustic velocity in air. Clearly, at very long times the shock will have decayed to an ordinary acoustic wave, and as such will propagate at acoustic velocity. The total form for the curve is given by

$$R = a(t-T)^b + 0.343(t-T). \quad (1)$$

In the preceding equation,  $R$  is the shock radius in micrometers,  $t$  is the time in nanoseconds,  $a$  is a factor incorporating the energy and density dependence for the strong shock relation,  $b$  is the exponent describing the early behavior of the shock front, and  $T$  is a time offset which allows all data to shift as one unit along the abscissa to compensate for uncertainty in the initiation time.

Using a least squared error criterion, the parameters calculated to yield the best fit to the experimental data for the expression given above were  $a=51.45$ ,  $b=0.387$ ,  $T=25.5$  ns. The best fit curve corresponding to the values above is plotted as a solid line in Figure 2a. The fit of the curve to the data seems good, and excluding the triangle data sets, gives an RMS error of 100.0 $\mu$ m.

As stated previously, the actual time origin for each data set is uncertain, however it is believed to exist within a 400ns period for all particles. Taking this into account, the dotted lines in Figure 2a represent the best-fit curve shifted in time by  $\pm 200$ ns. Assuming uniform particle size, all data should fall within these limits.

Having obtained the experimental relationship between shock front extent and time, it is possible to shift individually each data set, along the time axis, until it best coincides with the fit curve. This approximates what the data should resemble provided the time origin of each data set could be determined. The allowed shift for any single data set was limited to  $\pm 200$  ns. Figure 2b shows the time-shifted data, and the best-fit curve obtained earlier. The magnitude of the average shift was 63 ns. The calculated RMS error for all data, including the triangle sets, was  $52 \mu\text{m}$ .

The analytical solution for shock radius as a function of time and explosion energy using a strong shock approximation takes the form [15]

$$R = \xi_0 \left( \frac{E}{\rho_0} \right)^{\frac{1}{3}} t^{\frac{2}{3}}. \quad (2)$$

In this expression,  $E$  is the energy of the explosion,  $\rho_0$  is the ambient atmospheric density ( $\rho_0 = 1.25 \times 10^{-3} \text{ g/cm}^3$  for normal air), and  $\xi_0$  is a proportionality constant incorporating the ratio of specific heats of the gas in which the shock propagates. For normal air  $\xi_0 = 1.014$ .

The analytical solution for shock extent as a function of time given in Eq.(2) shows that the radius should increase as  $t^{0.4}$ . The curve obtained experimentally shows the shock radius increasing as  $t^{0.387}$ , in excellent agreement with the analytical solution.

To determine how close the experimental value of  $a = 51.45$  comes to the predicted value of

$$a = \xi_0 \left( \frac{E}{\rho_0} \right)^{\frac{1}{3}} \quad (3)$$

actual values can be substituted into Eq.(3). For normal air,  $\rho_0 = 1.25 \times 10^{-3} \text{ gm/cm}^3$  and  $\xi_0 = 1.014$ . A handbook value for the explosive strength of lead azide ( $1.9 \times 10^{10} \text{ ergs/gm}$ ) was obtained [16] and used to calculate the explosion energy for a  $125 \mu\text{m}$  diameter particle as  $9.2 \times 10^{10} \text{ ergs}$ . Using this value for  $E$

$$\xi_0 \left( \frac{E}{\rho_0} \right)^{\frac{1}{3}} = 1.014 \left( \frac{9.2 \times 10^{10}}{1.25 \times 10^{-3}} \right)^{\frac{1}{3}} = 37.98. \quad (4)$$

It is seen that the anticipated value calculated above differs from the experimentally determined value  $a = 51.45$  by approximately 35%. If the calculation is reversed, and the explosion energy  $E$  is calculated on the basis of the experimentally determined value of  $a = 51.45$ , it is found that

$$E = \rho_0 \left( \frac{a}{\xi_0} \right)^3 = 4 \times 10^5 \text{ ergs}, \quad (5)$$

a value 4 times larger than that given by the explosive strength. Since particle energy goes as the cube of the radius, a four-fold increase in energy would correspond to a 58% radius increase. This corresponds to a particle diameter of  $200 \mu\text{m}$ . Although the particles were sieved to be  $125 \mu\text{m}$ , the particles were generally not spherical, but rather oblong in shape. Considering this, it is plausible that the average particle volume was in fact greater than  $125 \mu\text{m}$  diameter sphere. Accordingly, the above results appear to be in reasonable agreement with the predicted values.

### Multiple Particle Experiments

A final experiment was performed to demonstrate feasibility for using the time-resolved holographic system to investigate multiple particle interactions. Two single  $\text{PbN}_6$



particles were suspended from individual electronic probe needles. These were manipulated to bring the particles within  $300\mu\text{m}$  of each other. Detonation of one particle was initiated using an infrared laser pulse. A series of holographic exposures were recorded at intervals of  $113.2\text{ns}$ . Figure 3 is a composite photograph of the nine recorded images. Starting with image (a), it can be seen that detonation has not yet been initiated in either particle. Image (b) shows a faint hint of detonation, and  $113.2\text{ns}$  later (c), the left particle has clearly detonated. The reaction volume is readily apparent, as is the shock front. Images (d) through (f) detail the propagation of the shock front and growth of the reaction volume. By the time image (g) was exposed, approximately  $566\text{ns}$  after initiation, the first particle reaction volume had vanished. Initial stages of detonation for the second particle were recorded in image (h), and image (i) shows the second particle in a stage of detonation nearly identical to that exhibited by the first particle nearly  $680\text{ns}$  earlier in image (c). In fact, the last image shows a second shock front contained within the first, generated by detonation of the second particle.

### Conclusions

A novel time-resolved holographic system was used to image transient shock waves as a first step toward investigating the interaction mechanisms in dispersed solid particulate explosives. For the investigation, single energetic particles of lead azide nominally  $125\mu\text{m}$  in diameter were detonated to generate the shock wave. Measurements of shock front extent as a function of time were made, and used to calculate parameters which characterize the shock front propagation. Experimentally determined values that describe the rate of decay for the shock front and the explosive energy released during detonation were found to be in agreement with theoretically predicted values.

Successful application of the time-resolved holographic system for the study of multiple-particle interactions has been demonstrated. The high speed imaging capabilities permit critical stages in the interaction process to be recorded and studied. With proper event timing, it should be possible to determine the critical spacing between particles and the critical particle size necessary to sustain detonation in dispersed particle explosives.

### Figures

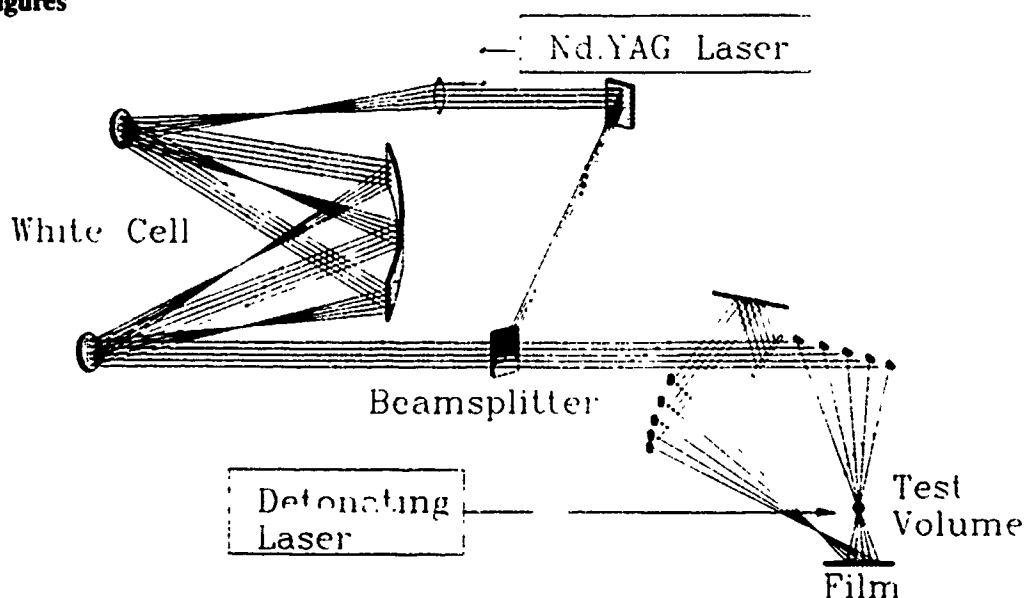


Figure 1. Setup for time-resolved holography

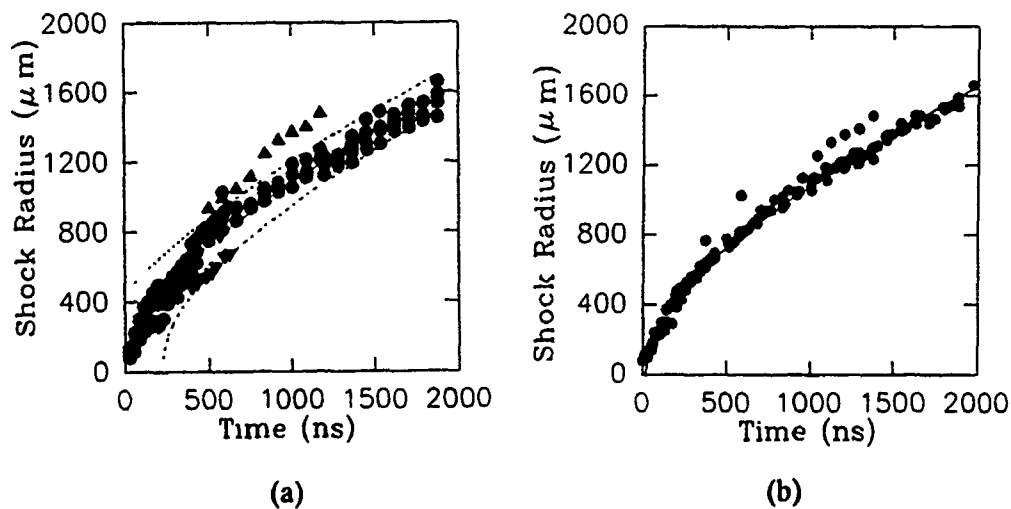


Figure 2. Plot of shock radius data plotted with a best fit curve (solid). In (a) the dotted curves represent the best-fit line time shifted by  $\pm 200$  ns. In (b) the data is shifted within the 200 ns window. Note the equation of the best fit line is as follows: Shock Radius =  $51.45(t-25)^{0.388} + 0.3433(t-25)$ .

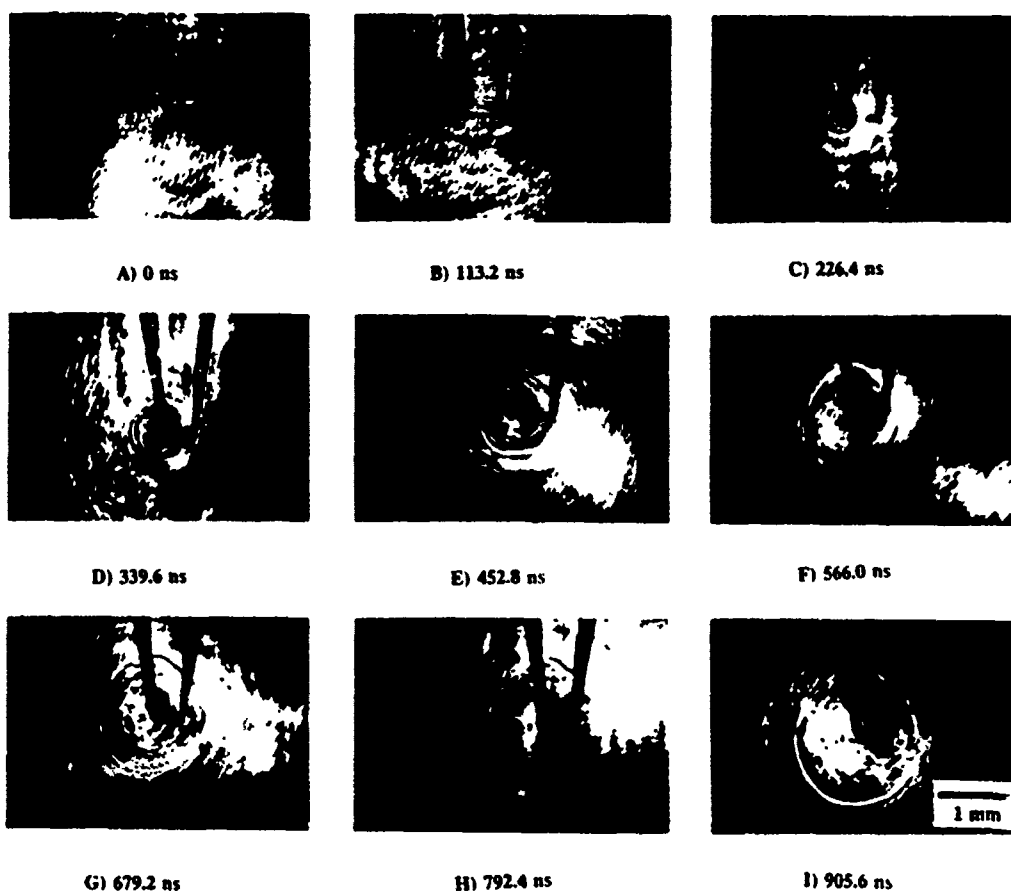


Figure 3. Composite photograph of two-particle interaction study.

## References

1. Tuls, A.J., J.L. Austing, D.C. Heberlein, *Proceedings of the 14th International Symposium on Shock Tubes and Shock Waves*, University of Sydney, Australia, p.447 (1983).
2. Tuls, A.J. and J.R. Selman, *Proceedings of the 19th Symposium on Combustion / The Combustion Institute*, p.625 (1982).
3. Strauss, W.A., *AIAA Journal*, 6(9) 1968.
4. Nettleton, M.A. and Stirling, *Combustion and Flame*, 21 p.307 (1973).
5. C.W. Kauffman, P. Wolanski, A. Arisoy, P.R. Adams, B.N. Maker, J.A. Nicholls, *AIAA Journal*, 94 p.221 (1984).
6. A.J. Tuls, *Proceedings of the First International Colloquium on Explosibility of Industrial Dusts*, p.178 (1984).
7. A.J. Tuls and J.R. Selman, *AIAA Journal*, 94 p.277 (1984).
8. H.C. Egghart, D.C. Heberlein, A.J. Tuls, W.K. Sumida, *Proceedings of the 18th International Pyrotechnics Seminar*, Breckenridge, Colorado, p.1083 (1992).
9. E.K. Dabora, *Acta Astronautica*, 6 p.269 (1979).
10. E.K. Dabora, K.W. Ragland, J.A. Nicholls, *Proceedings of the 12th Symposium on Combustion / The Combustion Institute*, p.19 (1969).
11. A.A. Ranger and J.A. Nicholls, *AIAA Journal*, 7 p.285 (1969).
12. N. Gerber and J.M. Bartos, *AIAA Journal*, 12 p.120 (1974).
13. T.P. Gavrilenko, V.V. Grigoriev, S.A. Zhdan, Y.A. Nikolaev, V.M. Boiko, A.N. Papyrin, *Combustion and Flame*, 66 p.121 (1986).
14. M.J. Ehrlich, J.S. Steckenrider, J.W. Wagner, *Applied Optics*, 31(28) p.5947 (1992).
15. Y.B. Zel'dovich and Y.P. Raizer, *Elements of Gas Dynamics and the Classical Theory of Shock Waves*, New York: Academic Press (1968).
16. G.F. Kinney, *Explosive Shocks in Air*, New York: The Macmillan Company (1962).

## REACTION KINETICS OF METALLIZED EXPLOSIVES

HERMENZO D. JONES AND FRANK J. ZERILLI

Naval Surface Warfare Center, White Oak, Silver Spring, MD 20903-5000.

## ABSTRACT

Time dependence of the energy release of metallized explosives has been observed and must be accounted for in predicting their performance. However, there is no complete theoretical description of this phenomenon. A preliminary investigation of the combustion of aluminum indicates that it probably takes place behind the reaction zone. A flexible time dependent model for the reaction of Al in explosive mixtures has been implemented in EPIC2, a Lagrangian material dynamics computer program. Exploratory calculations for nitromethane/PMMA/Al mixtures indicate that close in pressure measurements could reveal the presence of Al reaction behind the detonation front.

## INTRODUCTION

The chemistry of metallized explosives is not well understood. Metal oxidation is an important factor in the partition of energy between the shock wave and the bubble in under water applications. Chemical equilibrium calculations are used to predict the performance of new explosive compounds and to explain the behavior of existing explosives in under water applications.

For computer calculations of the hydrodynamics of shock wave phenomena, the Jones-Wilkins-Lee (JWL)<sup>1</sup> equation of state,

$$p = Ae^{-R_1 V} + Be^{-R_2 V} + \omega E/V, \quad (1)$$

with parameters determined by observing the expansion of copper cylinders produced by the explosive, is the most widely used description of the reaction products of explosives. In Eq. (1),  $p$  is pressure,  $E$  is internal energy, and  $V$  is the relative volume, while  $A$ ,  $B$ ,  $R_1$ ,  $R_2$ , and  $\omega$  are constants. However, the JWL equation of state is an empirical formulation which combines a solid-like Gruneisen part and a gas-like contribution. In this approach, it is usually assumed that the Gruneisen parameter is a constant, but calculations for  $N_2$  at pressures and temperatures characteristic of the release isentrope for the reaction products shows this to be erroneous. The resulting isentropic exponent,  $-(\partial \ln p / \partial \ln v)_S$ , exhibits a double hump which cannot be explained on physical grounds.

The lack of scaling between small and large scale test results has caused much confusion. However, if the time-dependence of the energy release is accounted for correctly, small scale test results can be used to predict results of large scale tests.

## EQUATION OF STATE

In this work, an equation of state for the reaction products is formulated from basic physics. The formalism of Weeks, Chandler, and Anderson<sup>2</sup> is employed to describe fluids whose molecules interact via a spherically symmetric, modified Buckingham potential. A chemical equilibrium computer program was written to calculate the thermodynamic

properties of a multiphase system as a function of pressure and temperature by minimizing the Gibbs potential. This equation of state for a mixture of nitromethane (NM), polymethylmethacrylate (PMMA), and aluminum (Al) is described in more detail in previous work<sup>3</sup>. From the calculations presented in the previous work, comparing calculated detonation state temperatures with reported brightness temperatures, it was concluded that the reaction of Al is delayed. Figure 1 illustrates the isentropes passing through the Chapman-Jouguet (CJ) detonation state for the NM/PMMA and NM/PMMA/Al mixtures as calculated with this equation of state.

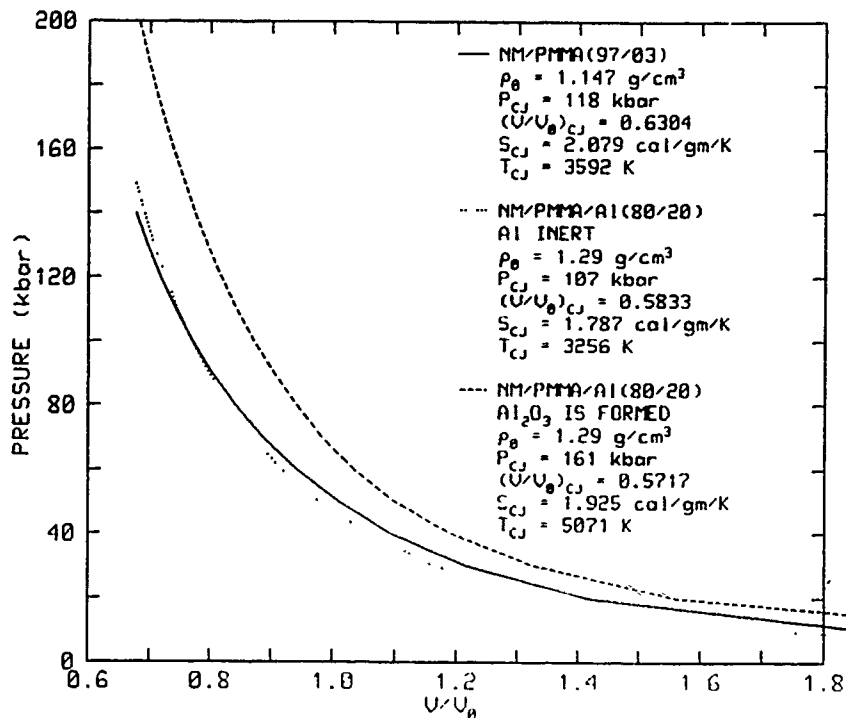


Figure 1. Pressure vs. volume isentropes passing through the CJ detonation state for NM/PMMA/Al mixtures.

The equation was fit to a polynomial representation,

$$p = \sum A_m E^m V^n, \quad (2)$$

and incorporated into the EPIC material dynamics computer program<sup>4</sup>. The time dependence of the aluminum reaction was accounted for with a time dependent pressure given by

$$p(t) = [1 - \lambda(t)] p_1(E, V) + \lambda(t) p_2(E, V) \quad (3)$$

where

$$\lambda(t) = a \frac{1 + \tanh\left(\frac{t - t_d}{b}\right)}{2} \quad (4)$$

and where  $p_1$  is the equilibrium pressure for the case in which the aluminum is unreacted and  $p_2$  is the pressure for the case in which the aluminum has totally reacted to form  $\text{Al}_2\text{O}_3$ . The parameters  $t_d$  (delay time of reaction),

b (rise time of reaction), and a (extent of reaction) are temperature, pressure, and particle size dependent. In principle, the temperature and pressure dependence can be obtained by varying the aluminum concentration.

#### COMPUTER SIMULATION

In order to determine whether the effect of delayed aluminum reaction is experimentally observable, a one dimensional simulation of the detonation of a 6.0 mm length of NM/PMMA/Al next to an 8.0 mm length of water was performed with the modified EPIC code using several reasonable values of time delay and rise time. From the time evolution of measured brightness temperatures reported by Teychenne de Blazi, Malaval, and Lombard<sup>5</sup> it can be inferred that the delay times are of the order of 0.5  $\mu$ s.

The pressure vs. time profiles for several delay and rise times are shown for 3.0 mm into the NM/PMMA/Al mixture in Fig. 2 and for 4.0 mm into the water in Fig. 3. The effects shown in Fig. 3 indicate that close-in pressure vs. time measurements could allow the determination of delay and rise times for the aluminum reaction. The solid curve is the calculated pressure-time profile for the case in which the aluminum is not allowed to react. The dash-dotted curve is the profile when the aluminum is allowed to react with a delay time of 0.2  $\mu$ s and a rise time of 0.04  $\mu$ s. Although a separate peak is distinguishable in the detonation wave pressure profile (Fig. 2), the pressure profile in the water is indistinguishable from one in which the aluminum reacts immediately. With a delay time of 0.5  $\mu$ s (dotted curve), a distinguishable secondary peak is observable in the water. A distinguishable secondary peak is observed also for a delay time of 0.2  $\mu$ s when the rise time is increased to 0.1  $\mu$ s (dashed curve).

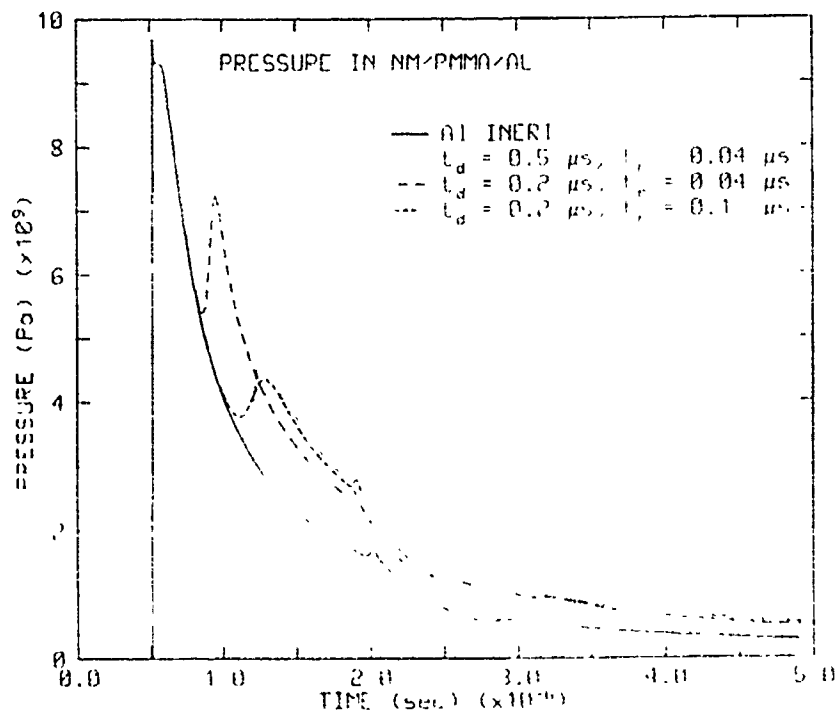


Figure 2. Pressure vs. time at 3.0 mm into detonating NM/PMMA/Al. Profiles for two values of delay time and rise time for the Al reaction are shown.

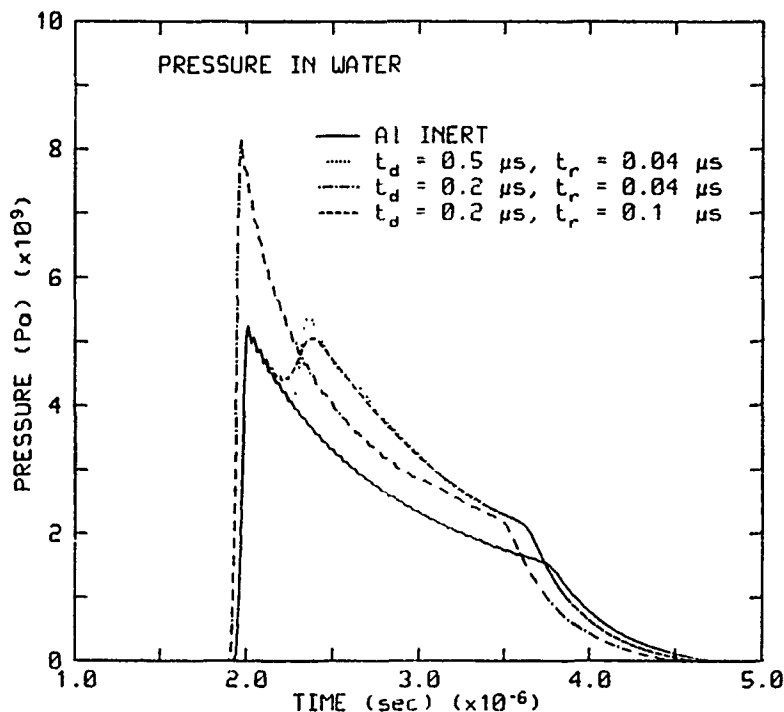


Figure 3. Pressure vs. time at 4.0 mm into water due to shock wave produced by detonating NM/PMMA/Al.

#### SUMMARY

The EOS for the reaction products of aluminized nitromethane has been calculated using liquid state perturbation theory for the fluid constituents and several semi-empirical descriptions for the solid constituents including the aluminized products. A technique has been developed to fit the theoretical  $p(V,E)$  surface for the reaction products of explosives to an analytical form to replace the JWL EOS for use in hydrocodes.

A preliminary investigation of the delayed reaction of Al in nitromethane/PMMA/Al mixtures was undertaken. The  $p(V,E)$  surfaces were constructed for two extreme cases: the first in which the Al was assumed to be inert, the second in which the Al was allowed to react completely. The time dependence of the Al reaction was introduced by joining these two surfaces with a simple time dependent function including a delay time and rise time.

#### CONCLUSION

Previous work indicates that the reaction of aluminum in aluminized nitromethane is delayed. Exploratory calculations of shock propagation in water from a detonation NM/PMMA/Al (80/20) mixture indicate that measurements of close by pressure vs. time profiles in water would enable the measurement of the delay time. However, the authors are unaware of the existence of such measurements at the present time.

#### ACKNOWLEDGEMENTS

This work was supported by NSWC Independent Research Funds. The authors would like to thank J. Forbes of NSWC for many useful discussions.

## REFERENCES

1. E. L. Lee, H. C. Horning, and J. W. Kury, Lawrence Livermore Laboratory, Report UCRL-50422 (1968).
2. J. D. Weeks, D. Chandler, and H. C. Anderson, J. Chem. Phys. 54, 5237 (1971).
3. H. D. Jones and F. J. Zerilli, J. Appl. Phys. 69, 3893 (1991).
4. G. R. Johnson and W. H. Cook, in Proceedings of the Seventh International Symposium on Ballistics, The Hague, The Netherlands, 1983, p. 541.
5. P. Teychenne de Blazi, C. Malaval, and J. M. Lombard, "Etude spectroscopique de la Temperature de Detonation d'un Explosif contenant de l'Aluminum", Report final S75-01, Centre d'Etudes de Gramat, 1975.



---

## PART VI

---

### **Processes, Performance, and Propellants**

## COMBUSTION SYNTHESIS OF COMPOSITE MATERIALS

J.J. MOORE

Department of Metallurgical and Materials Engineering, Colorado School of Mines,  
Golden, CO 80401

### ABSTRACT

This paper discusses the application of combustion synthesis of ceramic and ceramic-metal composites. Several model exothermic combustion synthesis reactions are being used to investigate the effect of reaction parameters, eg. stoichiometry, green density, combustion environment and mode, particle size, physical properties of reactants and products, on the stability and control of the synthesis reaction, product morphology and properties and performance.

### INTRODUCTION

Combustion synthesis or self-propagating high temperature synthesis (SHS)<sup>1</sup> is effected by heating an exothermic reactant mixture, normally in the form of a compressed pellet, to above the ignition temperature ( $T_{ig}$ ). The ignition of the combustion reaction can be performed in two modes: the propagating mode involves heating the pellet locally, initiating the exothermic reaction which then propagates as a combustion wave through the pellet. The simultaneous combustion mode occurs when the whole pellet is allowed to reach  $T_{ig}$  at which point the exothermic reaction is initiated throughout the pellet. A major limitation of combustion synthesis is that relatively high levels of porosity, eg. 50%, remain in the product. Simultaneous or near simultaneous hot pressing, HIPing, and the application of shock waves and explosive compaction<sup>2</sup> have been used to improve the density of the products.

Figure 1 provides a schematic representation of the exothermic combustion reaction which is initiated at  $T_{ig}$  and reaches a maximum combustion temperature,  $T_{ad}$ . If no heat is lost to the surroundings,  $T_{ad}$  will be the adiabatic temperature.  $T_{ad} - T_{ig}$  can be calculated using the Kirchhoff equation in which  $C_p$  is the heat capacity of the product,  $T_{ad}$  the initial temperature of the pellet,  $T_t$  is the transformation point of a reactant [ $-\Delta H(T_t)$ ] or a product [ $+\Delta H(T_t)$ ] and  $\Delta H(T_t)$  is the corresponding heat of transformation

$$T_{ad} - \Delta H(T_{ad}) = \Delta H(T_{ig}) + \int_{T_{ig}}^{T_{ad}} C_{p,d} dT + \Delta H(T_t) + \int_{T_t}^{T_{ad}} C_{p,r} dT \quad (1)$$

$T_{ad}$  can also be determined graphically [Figure 2(a)] from an enthalpy (H)-temperature (T) plot of the corresponding reactant and product Cp.dT curves

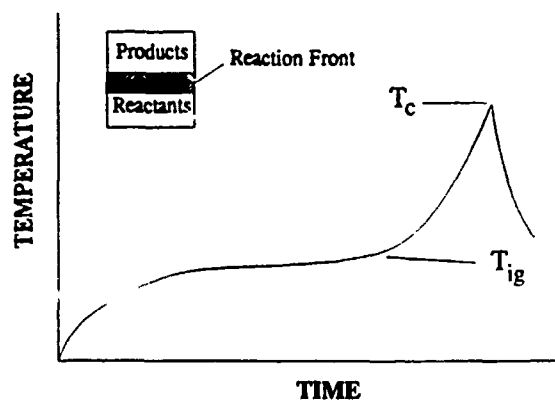
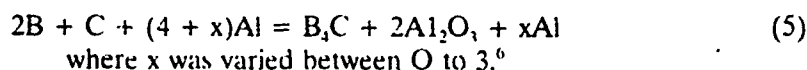
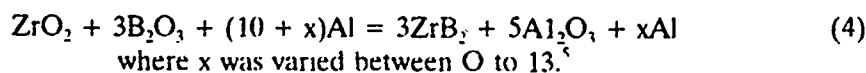
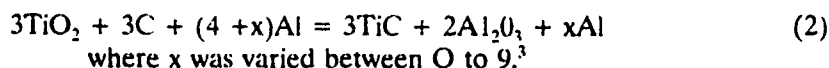


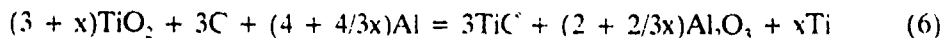
Figure 1. Schematic representation of the combustion process.

### EXPERIMENTAL REACTION SYSTEMS

Several ceramic-metal composite reaction systems are being investigated in which an excess amount of Al is used as a reductant in the SHS reaction and also to generate an excess amount of metal which provides the metal component of the ceramic-metal composite.<sup>3-6</sup> These reaction systems are given below:



A variation of reaction (2) is given in reaction (6) in which Al is used to reduce  $\text{TiO}_2$  and also generate an excess of Ti.

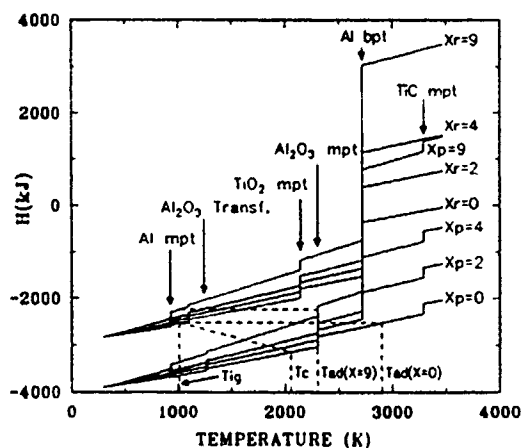


The excess amount of liquid Al or Ti infiltrates the porous ceramic composite, eg.  $3\text{TiC} + 2\text{Al}_2\text{O}_3$  in reaction (2), thereby increasing the relative density. Incorporating a ductile metal into a brittle ceramic matrix has potential for substantial improvements in fracture toughness. H-T plots for these five reaction systems are given in Figure 2 in which  $X_r$  (reactant) and  $X_p$  (product) refer to the corresponding excess moles of Al or Ti. Increasing  $X$  decreases  $T_{ad}$ . Conducting these combustion synthesis reactions under adiabatic conditions will exceed the melting and boiling points of several reactants and products as indicated in Figure 2 and Table I. Such phase changes have been shown to affect the stability of the combustion front.<sup>7</sup> Since heat is lost from the reaction front, SHS reactions are conducted under non-adiabatic conditions, and  $T_f$  is usually less than  $T_{ad}$  as indicated in Figure 2.

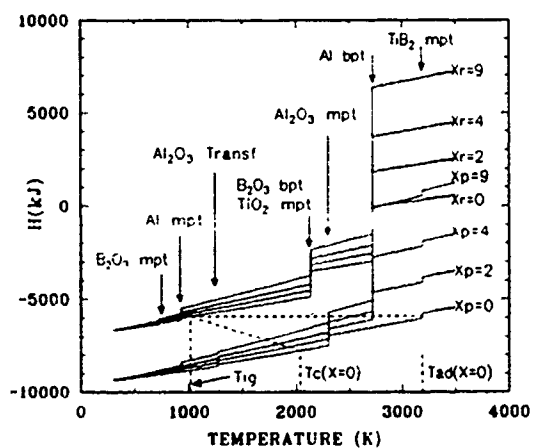
Increasing the excess Al in reactions (2) to (5) does not affect the overall heat of reaction [Figure 3(a)]. However, the generation of a liquid or gaseous phase at the reaction front will temporarily remove heat from the system and result in wave front instabilities. On the other hand, increasing  $x\text{Ti}$  in reaction (6) increases its exothermicity [Figure 3(b)].

The generation of gaseous species at the combustion reaction front can be used to provide a vapor transport medium and hence improved reaction kinetics. The effect of a reactive gas on the combustion synthesis reaction is currently being investigated.

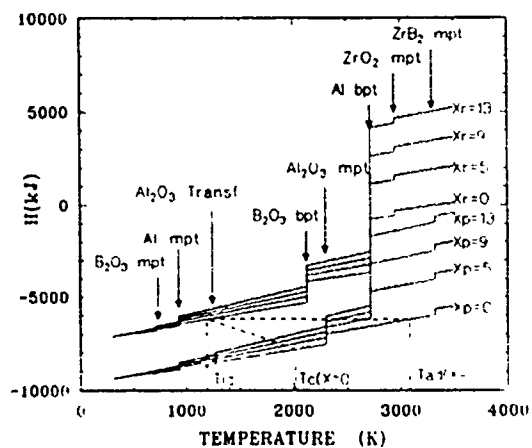
Reaction (2)



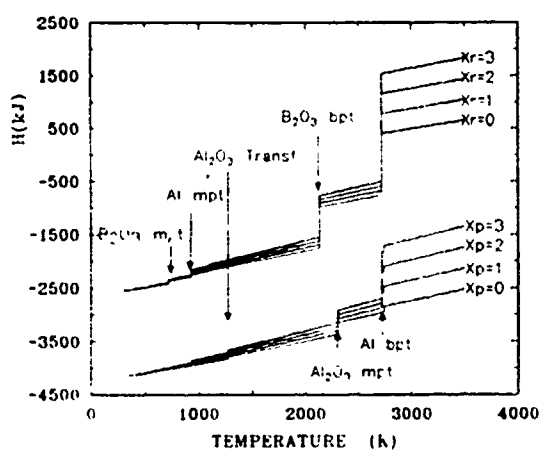
Reaction (3)



Reaction (4)



Reaction (5)



Reaction (6)

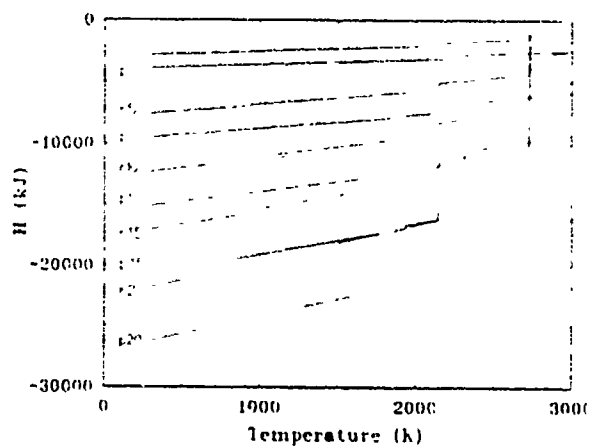


Figure 2 Enthalpy-temperature plots for reactants ( $X_r$ ) and products ( $X_p$ ) for various amounts of excess Al for reactions (2), (3), (4), (5) and (6).

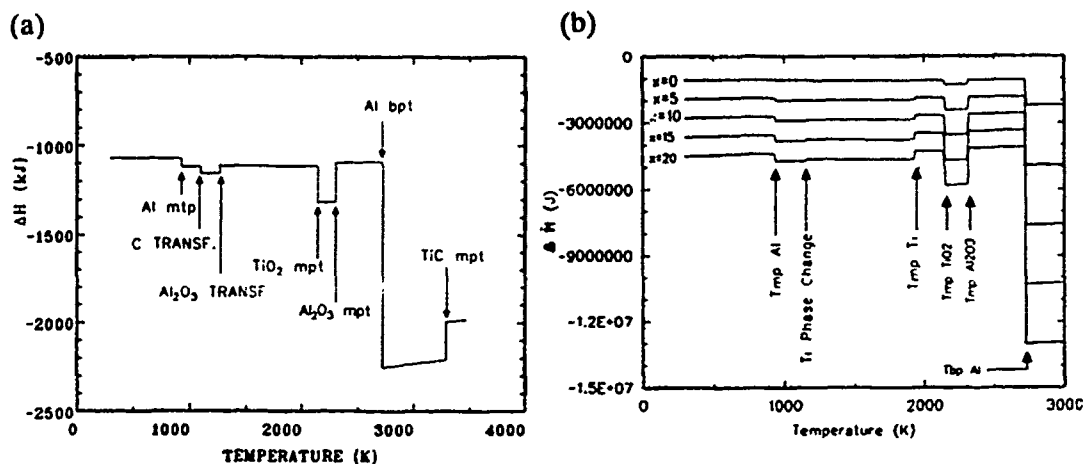


Figure 3. The effect of temperature and excess Al or Ti (x) on the heat of reaction for (a) Reaction (2) and (b) Reaction (6).

using two approaches. The first is presented in reactions (3)-(5) in which reactive gases eg.  $B_2O_3$ , Al, are generated from within the SHS reaction itself. The second approach deliberately engineers the production of volatile intermediate chlorides by conducting the SHS reactions in a reactive HCl gas environment.<sup>8-9</sup> The gaseous chloride intermediates subsequently dissociate to produce the required product(s) and regenerate the reactive gas as indicated in reaction systems (7) and (8), with their corresponding H-T plots given in Figure 4 and Figure 2(b) ( $X_i = 0$ ,  $X_p = 0$ ) respectively.



A thermodynamic analysis of gaseous species expected to be present in reactions (7) and (8) was conducted using free energy minimization criteria using the SOLGASMIX PV algorithms package.<sup>10</sup> These data are presented in Figure 5. Previous analysis<sup>11</sup> of this topic has indicated that gaseous transport becomes significant when the vapor transport species are present to approximately  $10^{-3}$  atmosphere, which is readily achieved.

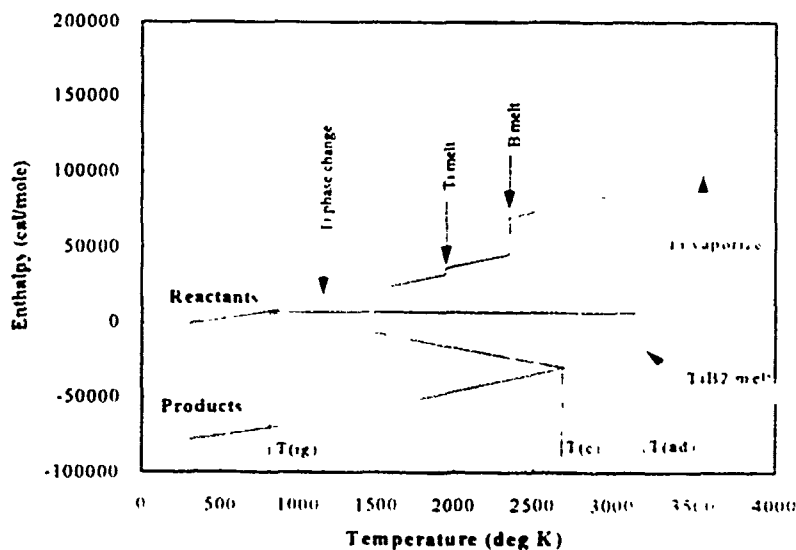


Figure 4. Enthalpy-Temperature Plot for  $Ti + 2B \xrightarrow{\text{(in HCl gas)}} TiB_2$ .

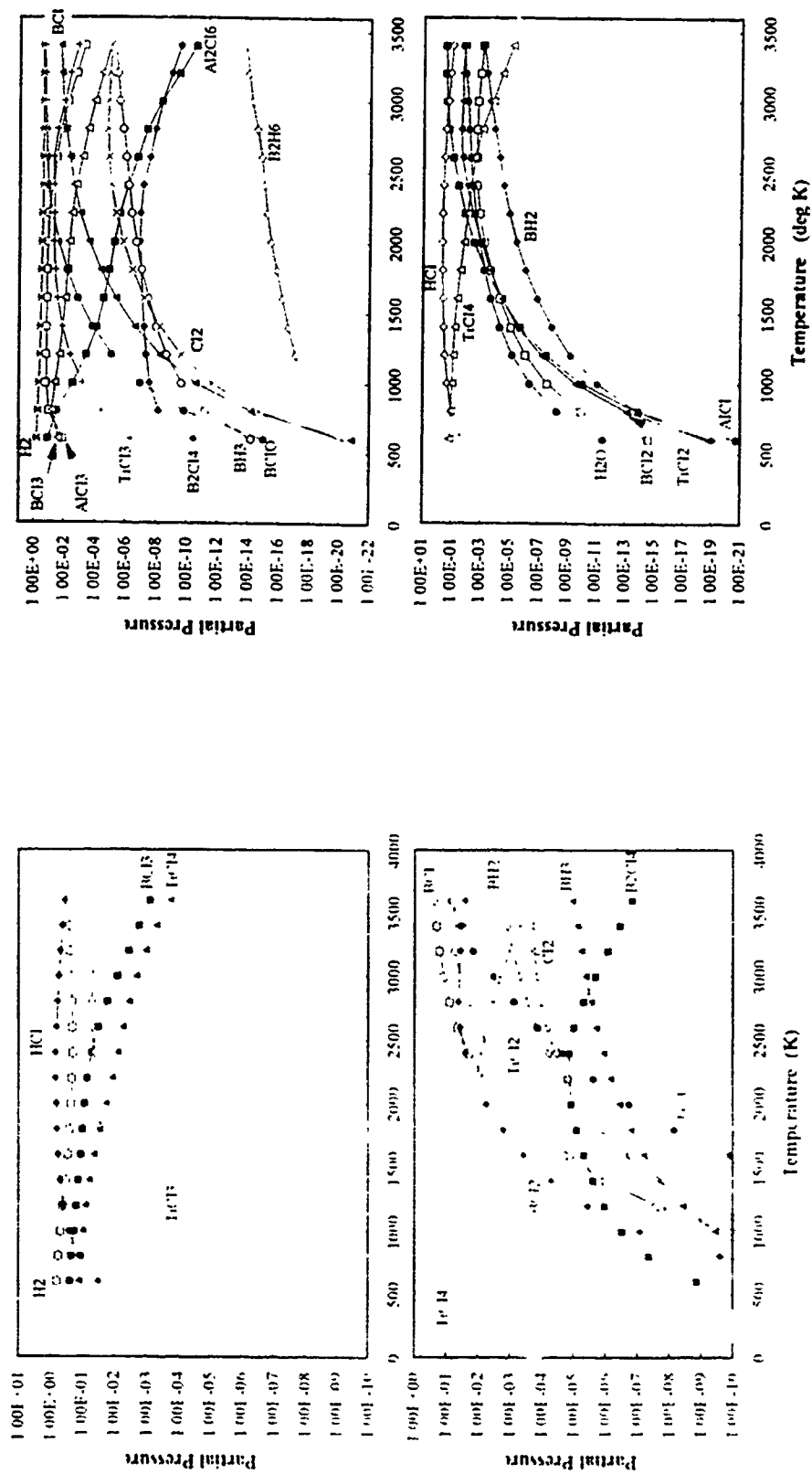


Figure 5(a). Predicted partial pressures of gaseous transport species in the Ti-B system (solid phase is  $\text{TiB}_2$ ).

Figure 5(b). Predicted partial pressures of gaseous transport species in the  $\text{TiO}_2\text{-B}_2\text{O}_3\text{-Al}$  System (solid phases are  $\text{TiB}_2$  and  $\text{Al}_2\text{O}_3$ ).

## EXPERIMENTAL PROCEDURE

The reactant powders (Table I) were thoroughly mixed using porcelain ball milling and pressed to various green densities, with varying values of  $X$ , into cylindrical pellets of 0.5 inches (12.7mm) in diameter and 1 inch (25.4mm) in length, dried for 1 hour at 120°C, and ignited in the propagating mode using a heated tungsten wire in an argon atmosphere (Figure 6).  $T_{ig}$  and  $T_c$  were determined using a Pt-Pt/10%Rh thermocouple and an Ircon Mirage Two Wavelength Infrared Pyrometer respectively. A video camera was used to record the propagation rate and stability of the combustion front along the length of the pellet.

The pellets reacted in a HCl gas environment were prepared in a similar manner to that discussed for reactions (2)-(6) and compared with a controlled experiment conducted in argon. However, these pellets were ignited using the simultaneous combustion mode in that they were placed in a tube furnace containing HCl gas (0.2 atmospheres) controlled at a temperature above  $T_{ig}$  (Figure 7). The ceramic-metal composites produced from both modes of combustion were examined using optical and scanning electron microscopy (SEM) interfaced with an energy dispersive spectroscopy (EDS) facility and also by x-ray diffraction (XRD). The density of the products was determined using an immersion in water technique.

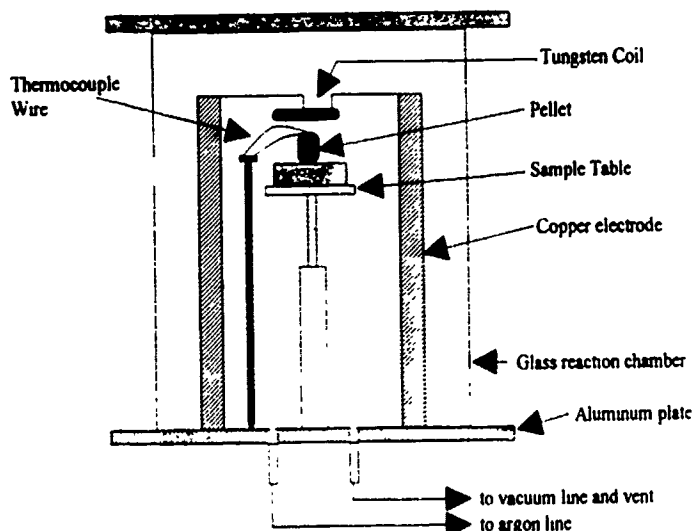


Figure 6. Schematic representation of reaction chamber.

## RESULTS AND DISCUSSION

The effects of green density and excess Al on the stability of the combustion front for reactions (2)-(6) were evaluated using the video recordings of the propagation of the reaction front. A steady state rate of propagation was defined as "stable combustion": a "semi-stable combustion front" was defined as one in which the front slowed down, almost extinguished and subsequently increased and slowed down again. An "unstable combustion front" was defined as that which quenched out at some position along the length of the pellet. Using these definitions, a SHS reaction stability diagram [Figures 8 (a), (b), (c) and (d)] was constructed for each of the reactions. A stable combustion front was observed for each level of excess Al used in reaction (5), i.e.  $x = 0, 1, 2$  and

Table I. Physical Properties of Reactants and Products in Reactions (2) - (8)

Cmd	Mpt °C	Bpt °C	Spec. Gravity	Size (mm)
TiO <sub>2</sub>	1830	3000	4.26	-44
C			2.25	-44
Al	660	2467	2.70	-44
TiC	3140	4820	4.93	
Al <sub>2</sub> O <sub>3</sub>	2050	2980	3.97	
B <sub>2</sub> O <sub>3</sub>	450	1860	2.46	-75
TiB <sub>2</sub>	2900		4.50	
ZrO <sub>2</sub>	2715	5000	5.60	-44
ZrB <sub>2</sub>	3000			6.09
B <sub>4</sub> C	2450	3500	2.52	
Ti	1660	3287	4.54	
B	2300	3930	2.35	44

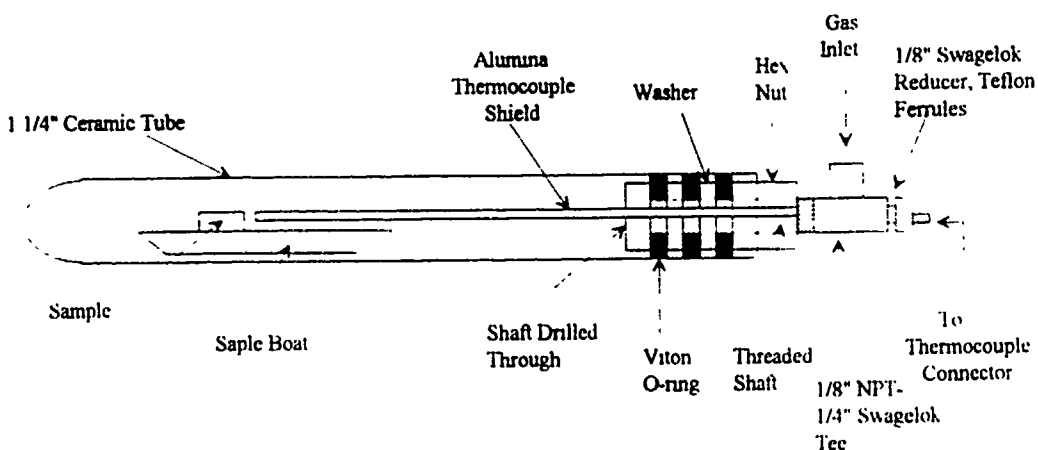


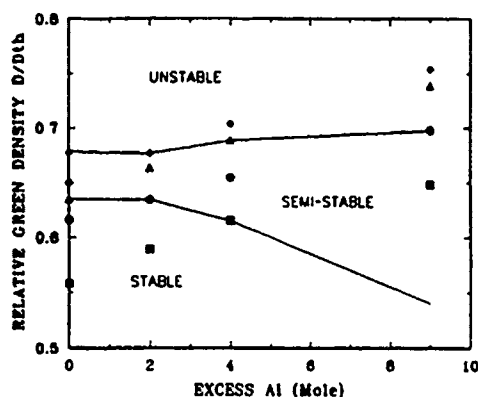
Figure 7. Schematic representation of reaction tube for simultaneous combustion of reactions (7) and (8).

3. In general, increasing excess Al and green density in reactions (2) to (5) eventually resulted in decreased stability of the combustion front and possible quenching out. This is almost certainly the result of increased heat losses from the SHS reaction on account of increased thermal conductivity (increased green density) and latent heat of fusion (increased excess Al). Both reaction systems (2) and (6) produced considerable increases in product density with increased excess Al, eg. from 45% ( $x = 0$ ) to 75% ( $x = 9$ ) relative densities. The effect of density-driven fluid flow of liquid Al was evident in composites produced from reaction (2), ie. the bottom was much denser than the top (Figure 1). For reaction systems (3) and (4), increased composite product densities were achieved using low to moderate green densities, eg.  $\leq 60\%$ , while an expansion of 300 to 400% was produced in pellets from reaction (5). These differences in product density can be explained in the different volumes of gaseous species generated on the corresponding reaction fronts.

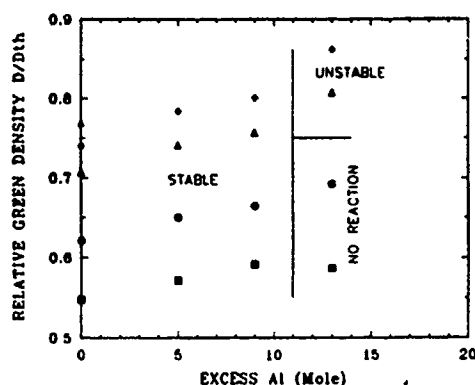


The calculated vapor pressures of the reactant and product species in reactions (2) to (6) are presented in Figure 10 together with their corresponding combustion temperatures. The combustion temperatures produced in reaction (4) produced considerable vapor pressures of both  $B_2O_3$  and Al gases which resulted in  $Al_2O_3$  whiskers produced from a vapor-liquid-solid (V-L-S) mode of synthesis (Figure 11). At the lower combustion temperatures produced in reaction (5) gaseous  $B_2O_3$  was present to a large extent with only a small amount of Al vapor. This largely single, high volume gaseous specie resulted in pushing or expanding the materials ahead of the combustion front in the vertical direction only, with minimum gas phase reactions, thereby producing an expanded, eg. 400% or foamed ceramic-metal composite which exhibited  $\geq 65\%$  porosity (Figure 12).

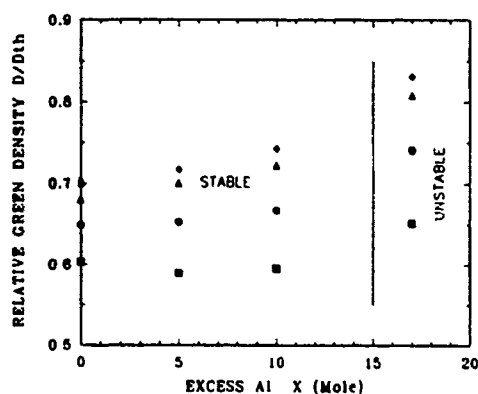
(a) Reaction (2)



(b) Reaction (3)



(c) Reaction (4)



(d) Reaction (6)

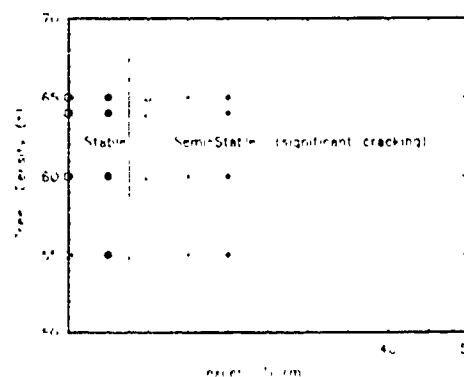


Figure 8. Effect of excess Al and relative green density on the stability of the propagating combustion wave: (a) reaction (2); (b) reaction (3); (c) reaction (4); (d) reaction (6)

The  $\text{TiB}_2$  produced in the  $\text{HCl}$  gas was formed as hollow shells, whereas, that produced in argon was in the form of angular solid particles. Ball milling the  $\text{TiB}_2$  synthesized in these different atmospheres gave strikingly different products. (Figure 13) The smaller particle size and the hollow shells of  $\text{TiB}_2$  formed in the  $\text{HCl}$  gas suggest that both titanium and boron are being transported in the vapor phase, and react at the outer surface of the  $\text{Ti}$  and  $\text{B}$  reactant particles. The result is a small particle size, porous  $\text{TiB}_2$  layer through which one of the gas species diffuses allowing further reaction. The size of these crystals of  $\text{TiB}_2$  can be controlled by heating rate.<sup>8</sup>

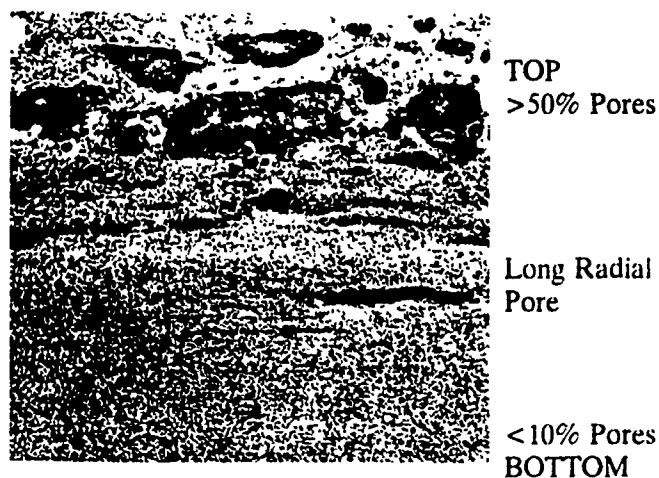


Figure 9. Optical photomicrograph of  $\text{TiC-Al}_2\text{O}_3\text{-9Al}$  composite.

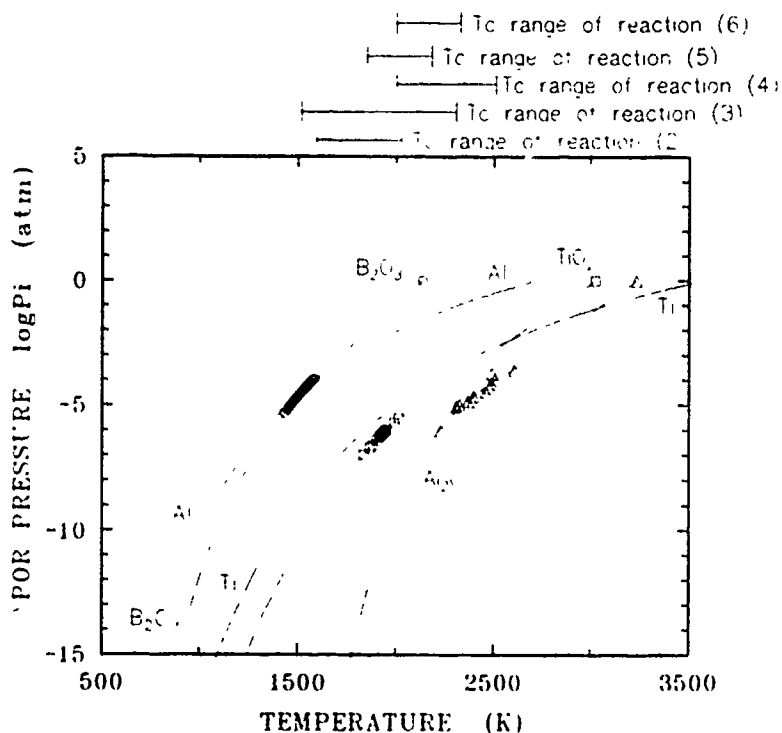


Figure 10. The effect of temperature on the calculated vapor pressures of species present in reactions (1) to (4).

Simultaneous combustion of reaction (8) in HCl gas produced a large volume of  $\text{Al}_2\text{O}_3$  blade-like whiskers (Figure 14), indicating a vapor-solid (V-S) mechanism of formation. This in-situ synthesis of  $\text{Al}_2\text{O}_3$  reinforcing whiskers in a fine  $\text{TiB}_2$  particle matrix, avoids the hazardous materials handling problem associated with whiskers. Conducting these SHS reactions in HCl gas resulted in a lower  $T_{\text{ig}}$  and a higher  $T_{\text{c}}$  in each case compared with argon.



Figure 11.  $\text{Al}_2\text{O}_3$  whisker phase produced during reaction (3).

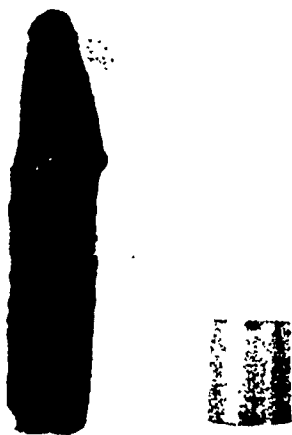


Figure 12. Expanded or foamed ceramic ( $\text{B}_4\text{C}-2\text{Al}_2\text{O}_3$ ) composite produced by reaction (4).

## CONCLUSIONS

Although reaction systems (2) to (6) use the same concept of synthesizing ceramic-metal composites, the different physical properties of the reactants, eg melting and boiling points, thermal conductivity, result in different product formations, morphologies and microstructures. The presence and number of liquid and gaseous species appears to have a significant influence over these product microstructures. The effect of gravity on density-driven fluid flow and vapor transport is therefore likely to be significant in producing tough, dense ceramic-metal composites with uniform microstructures and properties.

This research has demonstrated that, there are some interesting synergistic effects that can be developed by coupling combustion synthesis (SHS) and vapor transport. The lowering of  $T_{\text{m}}$  and raising of  $T_{\text{c}}$ ; the formation of hollow products ( $\text{TiB}_2$ ) which can be milled to submicron particle sizes, the synthesis of  $\text{Al}_2\text{O}_3$  whiskers and the production of highly porous, expanded, foamed ceramics are examples.

(a)



(b)



Figure 13. Ball milled  $\text{TiB}_2$  produced by SHS in (a) argon and (b)  $\text{HCl}$  gas.



Figure 14.  $\text{Al}_2\text{O}_3$  whiskers produced by reaction (8).

#### ACKNOWLEDGEMENTS

The author is grateful for partial support of this work from NASA, Microgravity Sciences, Code SN and to graduate students, H.J. Feng, K.J. Hunter, N.R. Perkins who conducted the experimental work.

## REFERENCES

1. Z. A. Munir, Ceramic Bulletin, 67(2) (1988) 342.
2. J. B. Holt, Material Bulletin, Oct -Nov (1987) 60.
3. H.J. Feng, J.J. Moore, D.G. Wirth, "The Combustion Synthesis of Ceramic-Metal Composites: The  $\text{TiC-Al}_2\text{O}_3\text{-Al}$  System", accepted for publication in Met. Trans.
4. H.J. Feng, J.J. Moore, D.G. Wirth, "Combustion Synthesis of  $\text{TiB}_2\text{-Al}_2\text{O}_3\text{-Al}$  Composite Materials" to be published in proceedings of the Symposium on Developments in Ceramic and Metal Matrix Composites, TMS Annual Meeting, San Diego, March 1-5, 1992. Pub by TMS, pp 219-239.
5. H.J. Feng, J.J. Moore, D.G. Wirth, "Combustion Synthesis of Ceramic Metal Composite Materials: The  $\text{ZrB}_2\text{-Al}_2\text{O}_3\text{-Al}$  System" to be published in proceedings of the International Symposium on Self-Propagating High Temperature Synthesis (SHS), Alma-Ata, USSR, Sept 23-28, 1991; pub by Soviet Academy of Sciences.
6. H.J. Feng, J.J. Moore, D.G. Wirth, "The Combustion Synthesis of  $\text{B}_4\text{C-Al}_2\text{O}_3\text{-Al}$  Composite Materials" to be published in proceedings of the Symposium on Synthesis and Processing of Ceramics: Scientific Issues MRS Fall Meeting, Boston Dec 2-6 1991; pub by MRS.
7. A. K. Filonenko V. 1. Vershinnikov, Combustion Explosion Shock Waves, 11 (1975) 301.
8. N. Perkins, D.W. Readey, J.J. Moore, Synergistic Effects of Coupled Combustion Synthesis and Vapor Phase Transport in the Synthesis of Advanced Materials", ASM Conference, San Francisco, CA, 1992.
9. N. Perkins, D.W. Readey, J.J. Moore, presentation at the Annual Meeting of American Ceramic Society, Minneapolis, April 12-16, 1992.
10. Gunner Eriksson, "Thermodynamic Studies of High Temperature Equilibria, III. SOLGAS, A computer Program for Calculating the Composition and Heat Condition of an Equilibrium Mixture", Acta Chemica Scandinavia, 25 (1971), pp. 2651-2658.
11. D.W. Readey, J. Lee, and T. Quadir, 1984. Vapor Transport and Sintering of Ceramics, Sintering and Homogeneous Catalysis. Ed. by G.C. Kuczynski, Albert E. Miller, and Gordon A. Sargent, New York: Plenum.

## INTERRELATIONSHIP BETWEEN SOLID PROPELLANT COMBUSTION AND MATERIALS BEHAVIOR

KENNETH K. KUO, THOMAS A. LITZINGER AND WEN H. HSIEH

Department of Mechanical Engineering, The Pennsylvania State University, University Park,  
Pennsylvania 16802, USA

### ABSTRACT

Thermochemical and physical processes which occur in various aspects of solid-propellant combustion including steady-state burning, ignition, transient burning, cook-off and crack propagation are presented in this paper. For each case, the various thermochemical and physical properties involved are summarized. In addition, the current direction of solid-propellant research is highlighted. The intent of this paper is to stimulate the interest of materials scientists and engineers in the field of solid propellants so that they will contribute their unique expertise to the advancement of current research. It is also the hope of the authors that the paper will serve as a useful summary of important relationships and parameters for scientists and engineers currently involved in solid-propellant research.

### INTRODUCTION

A solid propellant is a substance in the solid state which contains both oxidizer and fuel ingredients; it can burn in the absence of air or other oxidizers. When burned, solid propellants produce high-temperature combustion products which can be used for propulsion or other applications. Solid propellants can be burned to produce propulsive thrusts for a broad range of applications including rockets, guns and air-breathing propulsion systems. In addition to their use in propulsion systems, solid propellants are used in air bags where a high rate of gas generation is critical and in the joining of heavy duty electrical cables. They also are found in the ejection systems of military aircrafts. It is evident that solid propellants have significant commercial and military applications.

Based upon differences in physical structure, solid propellants are classified into two general categories: homogeneous and heterogeneous. In homogeneous propellants the physical structure and properties are uniform throughout and the fuel and oxidizer are chemically bonded together. Homogeneous propellants are often referred to as double-base propellants because they are generally composed of two major ingredients, nitrocellulose and nitroglycerin. In heterogeneous propellants the oxidizer is usually crystalline and the fuel polymeric. The fuel and oxidizer must be mixed together to form a propellant with a heterogeneous physical structure. Heterogeneous propellants are often referred to as composite propellants.

Because homogeneous and heterogeneous propellants have very complex compositions, some of their physical and thermochemical properties cannot be characterized easily. One of the major motivations of this paper is to inform material research scientists and engineers of the importance of and need for propellant characterization. The primary ingredients of a homogeneous propellant may include fuel, oxidizer, plasticizer and high-energy additives. Combustion modifying additives may be used to catalyze the burning rate. To modify the product temperature or to suppress combustion instability, coolants and metal powders have been utilized. Other ingredients such as a stabilizer and an opacifier may be added to improve propellant storage duration and prevent sub-surface radiation absorption, respectively. However, not all of these ingredients are necessary in a given homogeneous propellant. In heterogeneous propellants the ingredients may include oxidizer crystals, fuel binders, curing and bonding compounds and plasticizers. In addition, metal powders may

be added to raise the flame temperature, or a catalyst may be used to modify the burning rate. Again, a given heterogeneous propellant need not contain all of these ingredients. Clearly, both types of propellants may have complex compositions and physical structures so that thermochemical and physical characteristics are not readily available. (For additional introductory information on the combustion characteristics of solid propellants, readers are referred to Ref. 1.)

To illustrate the need for improved knowledge of the thermochemical and physical characteristics of solid propellants, this paper summarizes the key thermochemical and physical properties of various aspects of solid-propellant combustion, including steady-state burning, ignition, cook-off, transient burning, and crack propagation. For researchers in the solid-propellant field, the paper can provide a useful summary of the key properties involved in their research. In addition, it highlights current research directions and the related materials research required. The hope of the authors is to stimulate the interest of the materials community in contributing their expertise to the advancement of solid-propellant research and development. Beyond the characterization of the materials thermochemical and physical properties, the materials community may contribute new experimental methods for probing key processes that are not accessible to study through current methods.

## IMPORTANCE OF THERMOCHEMICAL, THERMOPHYSICAL AND MECHANICAL PROPERTIES OF SOLID PROPELLANTS

### Steady-State Burning Aspect

For a solid propellant with a given chemical composition, one of the most important and basic performance parameters is its burning rate as a function of operating condition. The burning rate of a solid propellant is also referred to as the regression rate of the burning surface. In assessing the thrust and operation duration of a solid-propellant rocket motor, the burning-rate behavior and associated gas-generation rate must be known. In general, the burning rate of a solid propellant is affected by, among other parameters, the operating pressure and initial temperature of the propellant. According to Saint Robert's burning-rate law, the burning rate is related to the pressure and initial temperature as shown in the following equation.

$$r_b = a(T_i)P^n \quad (1)$$

where the coefficient  $a(T_i)$  can be written as an exponential function of propellant initial temperature  $T_i$

$$a(T_i) = a_0 \exp [\sigma_p (T_i - T_{i,ref})] \quad (2)$$

where the temperature sensitivity of the propellant  $\sigma_p$ , which describes the percentage of change of burning rate with respect to change of initial temperature of the propellant under constant pressure situations, is defined as

$$\sigma_p = \frac{1}{r_b} \left( \frac{\partial r_b}{\partial T_i} \right)_P \quad (3)$$

In addition to the operation pressure and initial temperature of the propellant, the burning rate can also be written as a function of the average surface temperature of the propellant according to the Arrhenius law.

$$r_b = A \exp \left[ -E_a / R_u T_s \right] \quad (4)$$

where  $A$  is the Arrhenius pre-exponential factor,  $E_a$  the activation energy,  $R_u$  the universal gas constant, and  $T_s$  the average burning surface temperature. The burning surface temperature is affected by the energy balance at the burning surface, i.e.,

$$\rho_p r_b Q_s = \lambda_p \frac{\partial T}{\partial y} \Big|_{y=0} - \lambda_g \frac{\partial T}{\partial y} \Big|_{y=0} \quad (5)$$

where  $\rho_p$  is the density of the solid propellant,  $Q_s$  the net heat release due to chemical reactions on the burning surface,  $\lambda_p$  and  $\lambda_g$  thermal conductivities of the propellant and gas immediately above the burning surface, respectively, and  $y$  the coordinate beginning at the surface of the propellant. Under steady-state burning conditions, the temperature distribution inside the solid-propellant heated layer (thermal wave) can be shown to satisfy the following expression for constant propellant thermal diffusivity  $\alpha_p$ .

$$\frac{T - T_i}{T_s - T_i} = \exp [r_b y / \alpha_p] \quad (6)$$

This equation is based upon the assumption that there is no subsurface chemical reaction.

The operating pressure can also affect the burning surface temperature by enhancing the gas-phase chemical reaction near the burning surface and therefore increasing heat feedback from the gas phase to the burning surface. This pressure dependence of the burning surface temperature can be described by the following equation.

$$(T_s - T_{s,ref}) = b (P - P_{ref})^m \quad (7)$$

where  $T_{s,ref}$  and  $P_{ref}$  are the reference burning surface temperature and pressure, respectively. The values of coefficient  $b$  and  $m$  are exponent dependent on the type of the solid propellant.

During the steady-state burning processes of nitramine crystal or nitramine-based solid propellants, a liquid melt layer (or foam layer) exists above the solid-phase crystal and binder (see Fig. 1). The foam layer may contain gaseous bubbles of various sizes (see Fig. 2). The liquid phase may consist of melted nitramine and binder as well as dissolved species including the thermally decomposed radicals and fragmented molecules from the nitramine particles and fuel binders. Vaporization of the liquid phase could occur at the gas/liquid interface and within the foam layer. Dissolved species in the liquid phase can also desorb either to form gas bubbles or to increase the mass of existing bubbles. The vaporized nitramine and fuel binder may also undergo decomposition processes to form thermally decomposed gaseous radicals and fragmented molecules. These decomposed chemical species may attack the surface of the foam layer or react with each other exothermically to form the first-stage reaction zone.

Depending upon the velocity of the bubble moving through the foam layer, the chemical reactions inside the gas bubble could be very important to the overall heat release in the foam layer. The lower the bubble speed, the higher the probability for chemical reactions within bubbles. Also, more dissolved species can participate in gas-phase reactions in bubbles. The amount of liquid converted to gas at the bubble surface is greater for bubbles with longer transit times. It is quite obvious that bubble dynamics are very important in consideration of the surface reaction region. The liquid-phase parameters which could influence bubble formation and dynamics are density ( $\rho_l$ ), viscosity ( $\mu_l$ ), specific heat ( $C_l$ ),



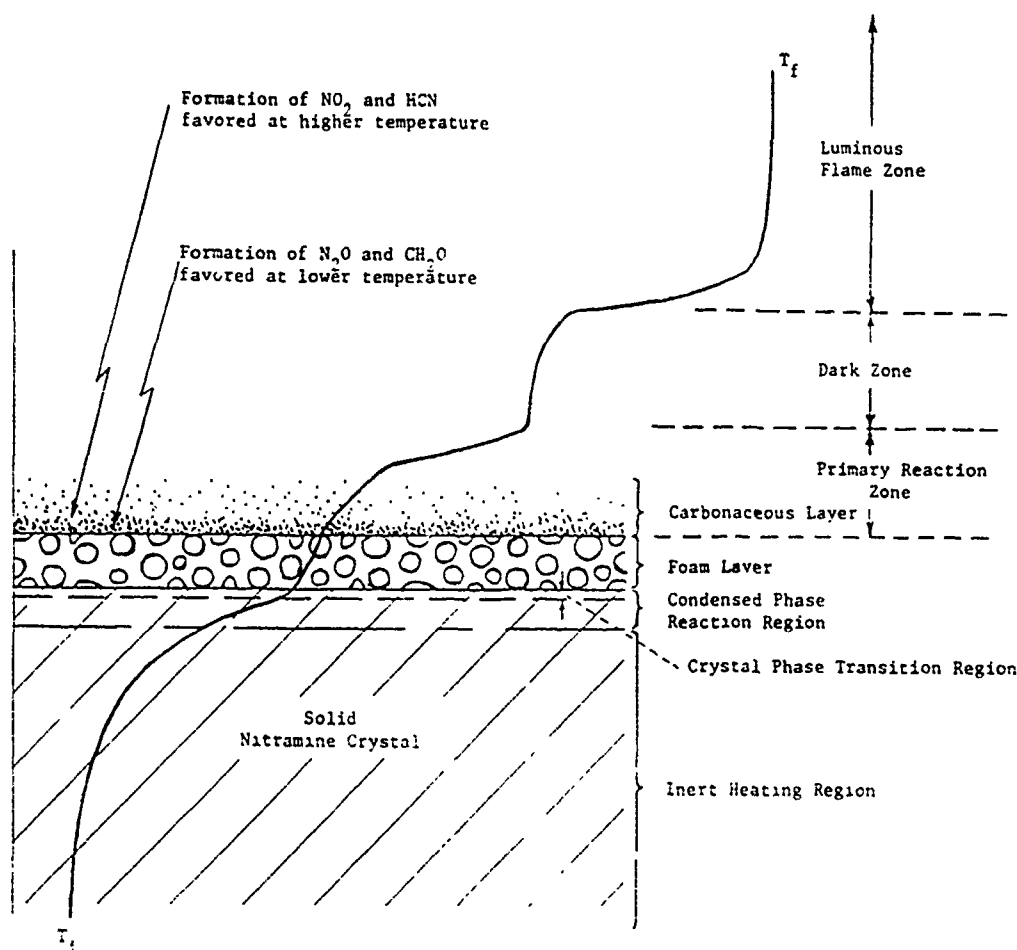


Fig. 1 A Schematic Diagram Showing Various Flame Zones and Condensed Phase Reaction Regions as well as a Typical Temperature Profile

thermal conductivity ( $\lambda_1$ ), surface tension ( $\sigma_{l-g}$ ), and liquefaction temperature or melting temperature ( $T_{melt}$ ). The gas-phase parameters include chemical reaction parameters such as activation energy ( $E_{ak}$ ), frequency factors ( $B_k$ ), temperature exponents of the frequency factor ( $\alpha_k$ ) of the  $k$ th reaction in the gas phase, as well as specific heat  $C_{pi}$ . In addition, the heats of formation all chemical species in the gas and liquid phases should be characterized.

The physical and chemical processes occurring in the melt or foam layer are believed to have significant influence on the burning-rate behavior of the nitramine-based composite propellants. It has been found experimentally that a large fraction of heat feedback to the condensed solid propellant is contributed by the exothermic physicochemical processes in the melt or foam layer and a small fraction of the overall heat feedback that comes from the gas-phase region [2, 3]. In spite of the fact that the gas-phase feedback is less important than that of the surface reaction layer, the gas-phase chemical reaction mechanisms and transport processes are still important in the regression behavior of the solid propellant. Increase in heat feedback from the gas phase can cause the average temperatures in the gas bubble and liquid phase of the foam layer to increase. Slight increases in these temperatures can effectively increase the burning rate of the solid propellant. Therefore, the detailed reaction pathways in the gas-phase region above the foam layer must be investigated.

In order to model the physicochemical processes in the foam layer, each of the gas- and liquid-phase regions in the foam layer must be described by a set of governing equations,

TABLE 1. Important Material Properties Associated with Solid Propellant and Its Burning Rate Law

SYMBOL	DESCRIPTION
$a(T_i)$	Pre-exponential factor of the Saint Robert's burning rate law for propellant at an initial temperature of $T_i$
$n$	Burning rate exponent
$a_0$	Pre-exponential factor of the Saint-Robert's burning rate law for propellant at an initial reference temperature, $T_{i,ref}$
$\sigma_p$	Temperature sensitivity
$A$	Arrhenius pre-exponential factor
$E_a$	Activation energy
$Q_s$	Net heat release from the burning surface reaction
$\lambda_p$	Thermal conductivity of the propellant
$b$	Coefficient defined in Eq. (7)
$m$	Exponent defined in Eq. (7)

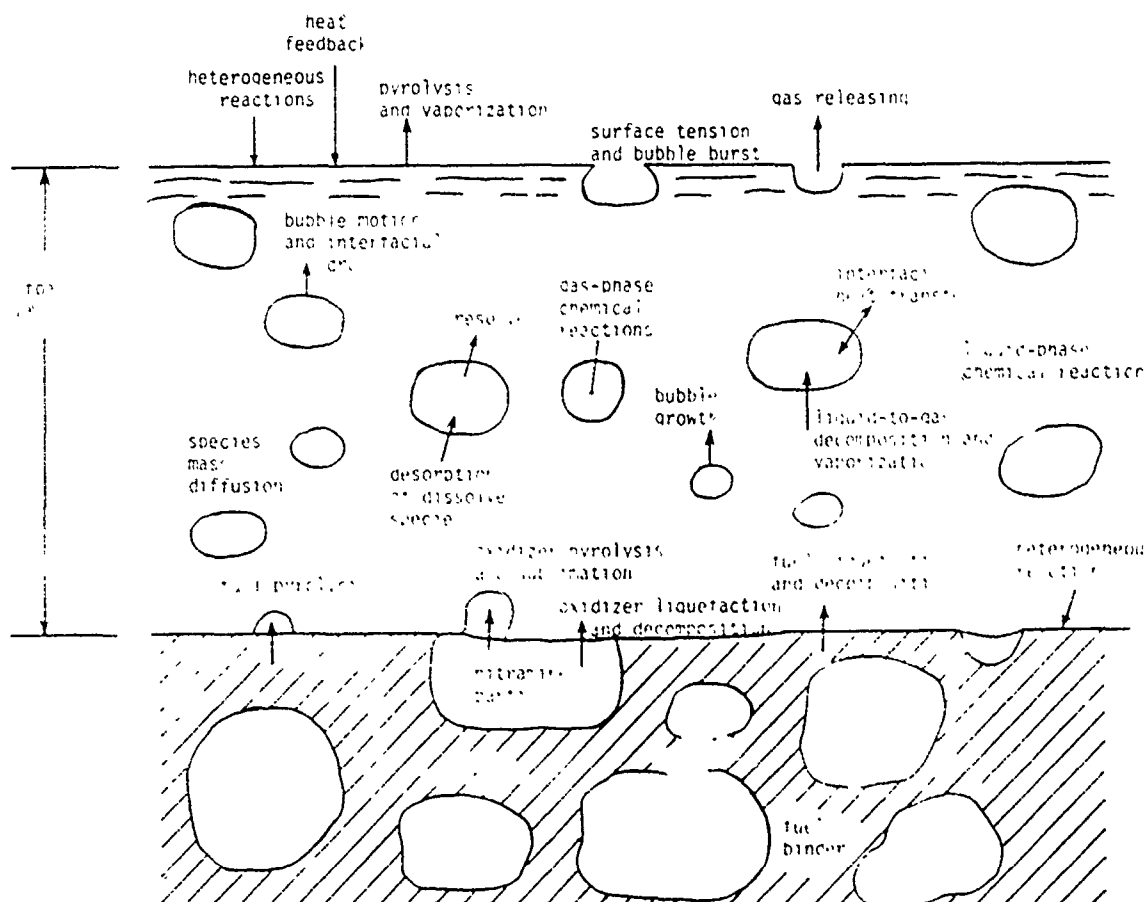


Fig. 2 A Schematic Diagram Showing the Physicochemical Processes in the Foam Layer of a Nitramine-Based Solid Propellant

including conservation equations of mass, momentum species and energy, equation of state, flux balance equations at boundaries, and other necessary boundary conditions, as well as source terms describing rates of chemical species formation, interfacial drag force, interfacial heat-transfer rates, etc. The major unknowns in these governing equations are  $\rho_g$ ,  $\phi$ ,  $Y_{gi}$ ,  $Y_{lj}$ ,  $U_g$ ,  $U_l$ ,  $T_g$ ,  $P$ ,  $\rho_l$ , melt layer thickness, gaseous bubble-size distributions, and rate of conversion from liquid to gas.

TABLE 2. Important Material Properties Related to the Foam Layer of Solid Propellants

Symbol	Description
$\rho_l$	Density of the liquid
$\mu_l$	Viscosity of the liquid
$C_l$	Specific heat of the liquid
$\lambda_l$	Thermal Conductivity of the Liquid
$\sigma_{l-g}$	Surface tension of the liquid
$T_{\text{melt}}$	Liquefaction or melting temperature
$Ea_k$	Activation energy of the kth gas-phase reaction
$B_k$	Frequency factor of the kth gas-phase reaction
$\alpha_k$	Temp. exponent of the frequency factor of the kth gas-phase reaction
$C_{pi}$	Constant-pressure specific heat of the ith gas-phase species

In the gas phase, before reacting in the final flame, the gaseous products from the first-stage reaction zone pass a preparation zone where reaction kinetics are retarded. Existence of the preparation zone depends upon pressure level as well as propellant type. The average velocity of the gaseous products travelling through various flame zones is governed by the regression rate of the propellant, the density gradients in and between the flame zone, and the mass fractions and diffusivities of the gaseous products. The gaseous species concentration distributions and temperature profile depend strongly on chemical reaction processes, diffusion and mixing of chemical species, and flow and heat-transfer behavior in the flame zones.

The final flame temperature and species concentrations significantly affect the performance of the solid propellant and its environmental impact. A performance indicator, the specific impulse (defined as thrust/unit weight flow rate of solid-propellant products) is proportional to the square root of the ratio of flame temperature and the molecular weight of combustion products. Governing equations for the gas-phase region consist of a set of conservation equations for mass, momentum, species and energy, as well as various flux balances at the boundaries. Major unknowns are  $T_g$ ,  $Y_{gi}$ ,  $\rho_g$  and  $U_g$ . The material properties required to complete the theoretical model are listed in Table 3.

In the presence of a crossflow of combustion gases flowing over the propellant surface in part of a rocket motor or any propulsion system, the burning rate of the propellant can differ from that under conditions with no crossflow. Normally, the burning rate of the propellant increases as the crossflow velocity increases. The velocity-dependent contribution to the burning rate of a solid propellant is called "erosive burning." Knowledge about erosive-burning behavior in a solid-propellant rocket motor with a low port-to-throat ratios of prime importance because both thrust level and burning time depend on the erosive-burning rate.

TABLE 3. Important Material Properties Related to the Gas-Phase Flame Region of Solid Propellants

Symbol	Description
$C_{p_i}$ (T)	Specific heat of $i$ th species as a function of temperature
$E_{a,n}$	Activation energy of the $n$ th reaction
$D_{im}$	Mass diffusivity of species $i$ with respect to the mixture
$\lambda_g$ (T)	Thermal conductivity as a function of temperature
$\nu_g$ (T)	Viscosity of gaseous mixture as a function of temperature

Erosive burning of both homogeneous and composite propellants has been studied extensively in the past. [4-6] The erosive-burning mechanism is believed to be caused by the increase in gas-to-solid heat feedback introduced partly by the increase in turbulent transport properties, and partly by the change of flame location due to turbulence-enhanced mixing. For the case of a composite propellant, turbulence-enhanced mixing of the oxidizer- and fuel-rich gases pyrolyzed from the propellant surface can reduce the distance from the propellant surface to the maximum heat release zone. For the case of homogeneous propellants, the same effect can be achieved by turbulence-enhanced mixing of the reacted and un-reacted gases to increase the temperature of the newly pyrolyzed gases from the propellant surface.

To model the erosive-burning behavior, a set of conservation equations for shear flow near the propellant surface must be used with a set of turbulence-transport equations and proper flux-balance boundary conditions. Of the many different erosive-burning expressions developed in the past, [4] one commonly used simple form of erosivity ( $\epsilon_b$ ) is written in terms of pressure and freestream velocity as

$$\epsilon_b \equiv \frac{r_b}{r_b^0} = 1 + K_1 p^{K_2} (U_\infty - U_{th})^{K_3} \quad (8)$$

where  $U_{th}$  is the threshold velocity below which the erosive-burning effect is negligible.  $K_1$ ,  $K_2$  and  $K_3$  can be regarded as erosive-burning rate constants. The threshold velocity and erosive burning rate constants listed in Table 4 can be regarded as part of propellant material properties.

TABLE 4. Important Material Properties Related to the Erosive Burning of Solid Propellants

Symbol	Description
$K_1$	Pre-exponential factor used in erosive-burning rate law
$K_2$	Pressure exponent used in erosive-burning rate law
$K_3$	Velocity exponent used in erosive-burning rate law
$U_{th}$	Threshold velocity

### Conductive Ignition

In determining the vulnerability of propellants in contact with hot metallic spall fragments generated through such weapons as shaped charges and kinetic energy penetrators, the hot fragment conductive ignition (HFCI) test has been adopted as an effective and standard practice. [7] With this method, a hot metallic element of well-defined geometry as the source of energy is brought into contact with the propellant to determine the go/no-go ignition boundary as a function of the initial temperature and mass of the hot metallic element. On the other hand, in actual solid-propellant rocket motors or other propulsion systems using pyrotechnic ignitors for ignition, the pyrotechnic ignitors usually generate significant amounts of metal particles during the ignition time period. These metal particles like the hot metallic element in HFCI tests, are in direct contact with the propellant and thus initiate the conductive ignition processes.

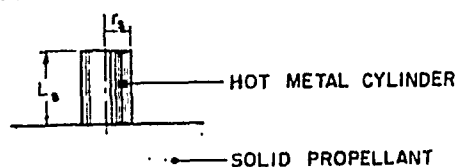
In the early phase of the conductive ignition process (Time Period I), heat is conducted from the hot particle to the propellant without any phase change or pyrolysis (see Fig. 3). As time progresses, the temperature of the propellant increases and that of the particle decreases. Following a period of inert heating, the propellant starts to decompose, melt, and/or gasify (Time Period II). Since the density of the metal particle is much higher than the density of the decomposed propellant, it displaces the decomposed propellant and becomes imbedded in (sinks into) the propellant, as shown in Fig. 3. The amount of imbedding depends on the temperature and size of the hot particle and the composition of the propellant. The decomposed species can further react exothermically in the gas and/or condensed [solid or liquid (foam)] phase to cause ignition. Self-sustained ignition will occur only if the heat generated by the exothermic reactions exceeds the heat losses. The entire process is strongly dependent upon the energy content of the hot particle and the physicochemical properties of the propellant.

In modeling the conductive ignition process, transient heat conduction equations should be used to describe the initial inert heating process of the solid propellant. The major material properties affecting the inert heating process are  $\alpha_p$  and  $\alpha_{\text{hot source}}$ . After the melt layer starts to develop, a set of conservation equations and flux balance boundary conditions, similar to those used to describe the physicochemical processes in the melt (foam) layer during steady-state combustion, are required to simulate the liquefaction, decomposition, and gasification processes, as well as the bubble dynamics in the foam layer. The major unknowns and materials properties are quite similar to those under steady-state combustion conditions, except that HFCI is a transient process. Therefore, all unknowns are functions of time and spatial coordinates.

### Convective Ignition

During convective ignition processes of solid propellants, the propellant is heated by a crossflow of hot combustion products from igniters or solid propellants located upstream of the propellant in question. To determine the convective ignition behavior of solid propellants, the ignition delay time, ignition site, and ignition mechanism have to be characterized as functions of  $T_\infty$ ,  $Y_{O_\infty}$ ,  $P$ ,  $Y_\infty$ , propellant surface roughness, propellant formulation, propellant geometric configuration, and propellant initial temperature. Similar to the case of conductive ignition, the nitramine-based propellant must first go through an inert heating period when it is subjected to convective ignition conditions. Following the inert heating period, the nitramine-based propellant starts to melt, decompose, and/or gasify and form a foam layer on its surface. After a finite delay, the pyrolyzed gases from the foam layer can react actively and release significant amounts of chemical energy to achieve self-sustained combustion. Figure 4 describes the major physical and chemical processes involved in convective ignition of a cylindrical solid-propellant grain. [8]

TIME PERIOD I (BEFORE THE FORMATION OF A MELT LAYER)



TIME PERIOD II (AFTER THE FORMATION OF A MELT LAYER)

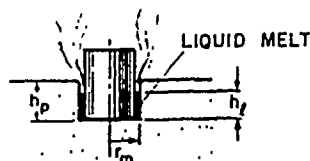


Fig. 3 Physical Event of Hot Fragment Conductive Ignition (HFCI) Processes in Two Different Time Periods

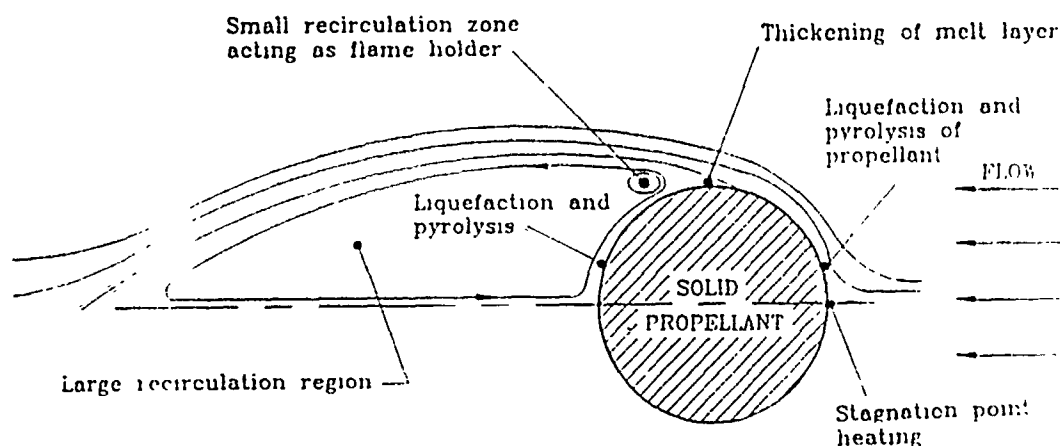


Fig. 4 Major Physical and Chemical Processes Involved in Convective Ignition of a Cylindrical Solid Propellant Grain

In terms of crossflow environment, there is some similarity between the convecting ignition process and the erosive-burning process. In the gas phase, the turbulence nature of the flow must be considered in the theoretical formulation of the process. In addition, the effect of friction force created by the crossflow on the motion of the melt (foam) layer should also be included. The processes of bubble formation, propellant decomposition, and gasification occurring in the melt (or foam) layer are also of significant importance. In general, the time to reach initial light emission ( $t_{LE}$ ) is inversely proportional to a power law of the energy flux to propellant surface ( $\dot{q}''$ ), i.e.,

$$t_{LE} = \frac{C}{[\dot{q}'']^n} \quad (9)$$

where both exponent ( $n$ ), and coefficient ( $C$ ) are functions of ambient gas temperature, propellant initial temperature, ambient oxidizer mass fraction, type of oxidizers, propellant surface roughness ( $\delta_{RH}$ ) flow Reynolds number and Prandtl number, i.e.,

$$n = n(T_{gas,amb}, T_{ini,prop}, Y_{O_2,amb}, \delta_{RH}, Re_D, Pr) \quad (10)$$

$$C = C(T_{gas,amb}, T_{int,prop}, Y_{O_2,amb}, \delta_{RH}, Re_D, Pr) \quad (11)$$

In addition to the above-mentioned material properties related to various aspects of combustion of solid propellants, there are other properties of solid propellants commonly used in the solid propellant community and they are listed in several tables given in later sections.

### Radiative Ignition

Radiative ignition of solid propellants was originally performed to improve understanding of the processes involved in ignition because radiation allowed the incident heat flux to be varied independent of other test parameters. Currently, however, laser ignition is being investigated as a method to ignite propellants of rocket and gun systems as well as gas generators. What was originally a laboratory tool is now rapidly progressing towards actual applications. Current research and development in the area of radiative ignition uses the coherent light from lasers, such as the infrared light from a CO<sub>2</sub> laser or the ultra-violet light from an excimer laser. (e.g., Ref. 9-11) Earlier studies of radiative ignition utilized arc lamps and arc furnaces which delivered a range of wavelengths (e.g., Ref. 12,13). An excellent review of radiative ignition experiments and theories is presented by Hermance. [14] Many physical and chemical processes occur during the radiative ignition of solid propellants, as illustrated in Fig. 5 taken from Ref.15.

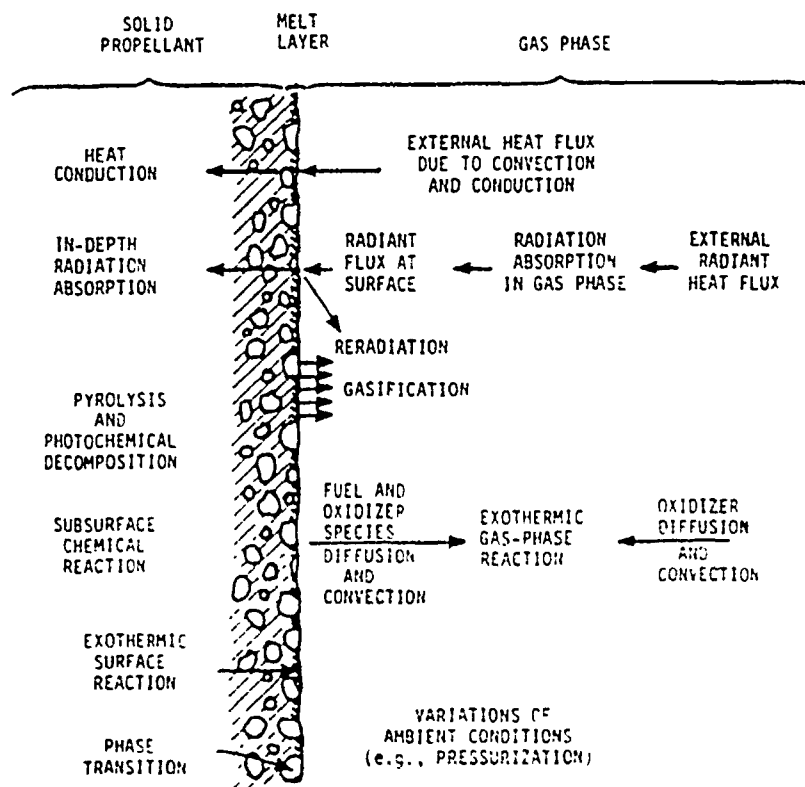


Fig. 5 Physical Processes Involved in Solid-Propellant Ignition.

The experimental study of radiative ignition involves determination of the conditions required for ignition of solid propellants as well as the ignition delay, i.e., the time between onset of radiation and time of ignition. The general relationship of the ignition delay time to heat flux is

$$t_{ID} = c/[q]^n \quad (12)$$

where  $c$  and  $n$  are functions of the composition, surface condition and initial temperature of the propellant as well as ambient gas composition, temperature and pressure. [16] In general, at a given heat flux, a range of heating times exists which result in sustained burning after laser cut-off.

When a radiative source is used for ignition, it is apparent that the radiative properties of the condensed phase and gas phase are important. The radiative properties of the liquid layer and gas-phase species of the solid propellant which must be known as a function of wavelength are listed in Table 5. Many other material properties of importance in the radiative ignition of solid propellants are the same as those important to the steady-state burning discussed above because convective and conductive heat transfer and chemical reactions play dominant roles in both cases. However, differences often exist in the chemical reactions leading to ignition and those important to steady-state combustion. Thus, the chemical reactions leading to ignition must be established along with their rate parameters. In addition, if the laser wavelength is short (as in the case of excimer lasers) such that photolytic decomposition can occur, the chemical species produced and their rates of production must be determined in order to appropriately model the chemistry.

Table 5: Radiative Properties Required for Each Species in Each Physical Region

Physical region	Radiative Properties Needed as Function of Wavelength
Gas phase	absorptivity, transmissivity
Liquid layer	absorptivity, transmissivity, reflectivity, emissivity
Solid phase	absorptivity, transmissivity, reflectivity, emissivity

#### Cook-off Mechanism and thermal Stability of Solid Propellants

In recent years (1960s to 1981), several serious accidents have occurred as a result of propellant cook-off on aircraft carrier decks. To reduce the possibility of hazards associated with solid-propellant cook-off, both experimental and theoretical studies have been carried out recently by numerous researchers. [17] Tests ranging from small-scale laboratory simulation [18] to intermediate (few grams to 5 pounds) and full-scale cook-off tests [19] have been conducted for both fast and slow cook-off experiments. Various cook-off bombs and test rigs have also been developed. The magnitude of heating rates was found to have a definite effect on the reaction violence in subscale cook-off bomb tests. Theoretical modeling and numerical simulation of cook-off phenomena are still far from complete in part because of the lack of thermal kinetic data, specific heat as a function of temperature, thermal diffusivity as a function of temperature, knowledge of products as a function of pressure and temperature as well as failure criteria. Realistic simulation of phase changes, foaming and propellant charge fracture are also essential in the theoretical model formulation. Some of the propellant sensitivity properties and thermal properties which are highly relevant to the cook-off mechanism and the thermal stability of solid propellants are listed in Table 6.

#### Transient Burning, Mechanical Deformation, and Crack Propagation

Since solid propellants are commonly used to generate thrusts in various propulsion systems, the combustion chamber pressure could change drastically with respect to time.



TABLE 6. Physical, Thermal, Optical and Sensitivity Properties of Solid Propellants and Their Ingredients

<b><u>Physical Properties</u></b>	<b><u>Thermal Properties</u></b>
Molecular Weight	Heat of Formation
Melting Point	Heat of Combustion
Boiling Point	Heat of Fusion
Vapor Pressure as a Function of Temperature	Heat of Phase Transition
Solubility in Different Solvents	Heat of Explosion
Volatility as a Function of Temperature	Heat of Vaporization
Hygroscopicity as a Function of Temperature and Relative Humidity	Heat of Detonation
Infrared Spectra	Free Energy of Formation
Hardness	Entropy at a Reference State
	Thermal Stability
	Coeffi. of Thermal Expansion
<b><u>Crystal and Optical Properties</u></b>	<b><u>Sensitivity Properties</u></b>
Crystalline Form (Crystal Structure)	Impact Sensitivity
Unit Cell Dimensions	Brisance (Sand Test)
Space Group	Ballistic Mortar
Lattice Energy	Initiation Sensitivity
Refractive Index	Electrostatic Sensitivity
Molar Refraction	Dielectric Constant as a Function of Temperature
Bi Refringence	Shock Sensitivity
<b><u>Hazards Classification</u></b>	Friction Pendulum Tests
Transportation Classes	Confined "Cook-off" Temperature
Toxicity	Explosion Temperature

This rapid pressure variation can produce two major effects: 1. transient (dynamic) burning effect; and 2. mechanical deformation of the propellant grain with or without crack propagation. The transient burning effect is caused by the finite relaxation times required for the solid phase, surface reaction zone, and gaseous flame zones to adjust their temperature profiles to the changing environment. The instantaneous burning rate under transient conditions may therefore differ significantly from the steady-state value corresponding to the instantaneous pressure. A detailed discussion of transient burning phenomena of solid propellants and a survey of previous work has been conducted by Kuo, Gore and Summerfield. [20] Many material properties influential to the transient burning behavior were listed in the section dealing with steady-state burning. Additional parameters are given in Table 7.

The phenomena of mechanical deformation and crack propagation of solid-propellant grains have been studied extensively by many researchers in recent years. A few representative works are given in Refs. 21 through 27. Usually, mechanical deformations of propellant are closely coupled to flame spreading and combustion processes in damaged zones. This coupling effect is addressed by Kuo and Kooker in Ref. 22. Many mechanical and thermal properties are required for the numerical simulation of the deformation, crack propagation and combustion phenomena. A set of important parameters and solid propellant properties not contained in other tables is given in Table 8.

TABLE 7. Additional Parameters and Solid Propellant Properties Important for Transient Burning Behavior

Symbol	Description
$\lambda_g$	Average thermal conductivity of gaseous product adjacent to the propellant surface
$C_g$	Average constant - pressure specific heat of gaseous product adjacent to the propellant surface
$Q_s$	Net rate of heat release at the surface reaction region
$\phi_{c,p}$	Solid-phase temperature gradient at the propellant surface as a function of chamber pressure and mass burning rate (Zel'dovich map)
$Y_{ox}$	Oxidizer loading fraction in the composite propellant

TABLE 8 Parameters and Solid-Propellant Properties which are Important for Mechanical Deformation and Crack Propagation Processes

Symbol	Description
$a_T$	Time-temperature shift factor
$E_{rel}$	Relaxation modulus of solid propellant under normal stresses
$g_0$	Equilibrium shear modulus, i.e., the asymptotic value of the relaxation modulus for long periods of time
$G$	Relaxation modulus of solid propellant in shear
$V_{cp}$	Crack propagation speed
$K$	Bulk modulus of elasticity
$K_{IC}$	Fracture toughness of solid propellant
$J_{IC}$	Cohesive fracture resistance of solid propellant
$g_1 \dots g_m$	Coefficients of the Prony Series defined in Eq. (21)
$\beta_1 \dots \beta_m$	Inverse relaxation times of the Prony Series defined in Eq. (21)
$\nu$	Poisson's ratio

The crack propagation speed can be expressed in several different forms. Lu [28] found that

$$V_{cp} = (a + b \frac{\partial P}{\partial t}) J^q \quad (13)$$

where  $a$ ,  $b$  and  $q$  are experimentally determined constants. In Eq. (13),  $\partial P/\partial t$  and  $J$  represent the local pressurization rate and J-integral value at the crack tip. Schapery (29) suggested that the crack propagation velocity can be expressed as

$$V_{cp} = \frac{A_1}{a_T} (K_I)^{q_1} \quad (14)$$

where  $A_1$ , and  $q_1$  are material constants.  $K_I$  in Eq. (14) is the opening mode stress intensity factor. Using the pseudo J-integral approach, Schapery [29, 30] also suggested that

$$V_{cp} = A_2 (J_v)^{q_2} \quad (15)$$

where  $J_v$  is the pseudo J-integral deduced from elastic J-integral value through the correspondence principle. Based on the thermodynamic power balance approach, Hufferd and Laheru [31] found the instantaneous crack-propagation speed to be

$$V_{cp} = a_0 C \sinh (C P_{eg}) \frac{dP_{eg}}{dt} \quad (16)$$

where  $a_0$  is the initial crack length and  $C$  a material constant. The crack growth potential ( $P_{eg}$ ) can be determined from

$$P_{eg} = \sqrt{E_{red}/a} \left[ \sqrt{J_I} - \sqrt{J_{IC}} \right] \quad (17)$$

where  $J_{IC}$  is the plane strain cohesive fracture resistance of the solid propellant.

Since solid propellants usually behave as viscoelastic materials in shear, the shear deviator stress tensor can be expressed as

$$S_{ij} = \int_0^\tau G(\tau - \tau') \frac{d}{d\tau'} e_{ij}(\tau') d\tau' \quad (18)$$

where  $G$  is the relaxation modules in shear, and  $\tau$  is a "reduced time" due to a local temperature above a reference state.  $e_{ij}$  represents the strain deviators and  $S_{ij}$  the stress deviators; these two tensors are related to strain tensor ( $\epsilon_{ij}$ ) and stress tensor ( $\sigma_{ij}$ ) by the following relationship:

$$e_{ij} = \epsilon_{ij} - \frac{1}{3} \delta_{ij} \epsilon_{kk} \quad (19)$$

$$S_{ij} = \sigma_{ij} - \frac{1}{3} \delta_{ij} \sigma_{kk} \quad (20)$$

For most viscoelastic materials, it is a common practice to consider a generalized Maxwell model of  $M$  elements formed by a combination of damps and springs. Therefore,  $G$  can be written as

$$G = g_0 + \sum_{m=1}^M g_m e^{-\beta_m \tau} \quad (21)$$

where  $g_0$  is the equilibrium shear modules,  $g_1$  through  $g_m$  the coefficients of the Prony Series, and  $\beta_1$  through  $\beta_m$  the inverse relaxation times of the Prony Series.

The solid propellants behave as elastic in bulk. The bulk behavior can be expressed by

$$\sigma_{kk} = 3K \epsilon_{kk} \quad (22)$$

where  $K$  is the bulk modules. Finally, the overall constitutive equation for a solid propellant can be written as

$$\sigma_{ij} = \int_0^t G(\tau - \tau') \frac{d}{d\tau} \epsilon_{ij}(\tau') d\tau' + \delta_{ij} K \epsilon_{kk} \quad (23)$$

The shear relaxation modules  $[G(\tau)]$  and bulk modules  $[K(\tau)]$  are related to the tensile relaxation modules  $E_{rel}(t)$  and Poisson's ratio ( $\nu$ ) by the following relationships:

$$G(\tau) = \frac{E_{rel}(\tau)}{2(1 + \nu)} \quad \text{and} \quad K(\tau) = \frac{E_{rel}(\tau)}{3(1 - 2\nu)} \quad (24)$$

## CURRENT AND FUTURE RESEARCH DIRECTIONS

Based on observations and predictions of the authors, the major thrust areas for solid propellant combustion include:

- 1) Development of high-energy, high-burning rate propellants for special applications;
- 2) Development of low vulnerability ammunition (LOVA) propellants in order to reduce possibility for hazards;
- 3) Flame structure diagnostics by non-intrusive techniques;
- 4) Theoretical modeling and numerical solution of aerothermochemical processes of propellant flames under various operating conditions;
- 5) Development of solid propellants for commercial use, e.g., for filling air bags in extremely short time intervals, gas generation for operating certain actuation systems;
- 6) Application of fuel-rich solid propellants in air-breathing propulsion systems; and
- 7) Characterization of various properties of solid propellants.

## POSSIBLE CONTRIBUTIONS OF MATERIAL SCIENTISTS AND ENGINEERS

This paper has summarized the key thermochemical and physical properties required to characterize various aspects of solid-propellant combustion in order to make clear the need for contributions by members of the materials community. Such contributions would improve the understanding of the important chemical and physical processes that occur during propellant combustion. A few examples are given below.

A significant contribution could be made through research to characterize the thermochemical and physical properties of the propellants. While some properties of propellants are currently available, like density, specific heat, and heat of explosion, many others are only partially known or entirely unknown. Essentially, all properties of the material in the melt layers and of the solid phase after it has undergone partial decomposition are unknown. Without more complete property characterization, accurate predictions using detailed analysis and modeling of solid-propellant combustion will be difficult to achieve.

In current research on propellant combustion, the study of the chemical reactions that account for both the decomposition of the various ingredients in propellants and the reactions of the decomposition products is an area of active research. Understanding these basic chemical processes is necessary for modeling the various combustion events described in this paper. Even materials that have been used for decades, such as RDX and HMX, are the subject of extensive research to determine their major decomposition pathways. Most current work is limited to observing the gaseous products of decomposition; only now are researchers beginning to probe the decomposition products generated in the liquid phase, foam layer and solid phase. Probing this condensed-phase chemistry stands as a major

challenge to the propellant community as a whole and represents an area where members of the materials community may be able to make important contributions.

Besides the chemical processes, important physical processes that occur during propellant combustion require further investigation. The processes of phase change, melt layer formation and bubble dynamics in the foam layer all need additional study. Most past studies of the surface of reacting propellants were restricted to observation of samples recovered after the combustion event was rapidly quenched. However, direct observation of the surface during pyrolysis or combustion would yield much more information about the actual process. To obtain direct observations, materials researchers collaborating with authors on a propellant combustion project at Penn State are using an environmental scanning electron microscope to observe the surface dynamics of pyrolyzing solid propellant samples. This study can be regarded as an example of the application of materials research techniques to propellant research that has the potential to produce very important results.

## SUMMARY

This paper summarizes various aspects of solid-propellant combustion processes in order for material scientists to gain some basic background in this area. Many basic relationships between material properties and propellant performance are provided to show various interrelationships between solid-propellant combustion and the behavior of materials. To facilitate identification of all important material properties, a set of tables was prepared to indicate the names, physical meanings and mathematical symbols of these properties. This paper emphasizes the importance of potential contributions of material scientists and engineers for advancing the state-of-the-art in the solid-propellant combustion field. Their participation is strongly encouraged.

## ACKNOWLEDGMENT

This work was performed under an ARO-URI Grant DAALO3-92-G-0118 sponsored by the Army Research Office under the management of Dr. Robert W. Shaw. His encouragement and support are highly appreciated.

## REFERENCES

- 1 N. Kubota, "Combustion Characteristics of Rocket Propellants," in Chapter 1 of *Fundamentals of Solid Propellant Combustion*, (Eds. K.K. Kuo and M. Summerfield), AIAA Progress in Astronautics and Aeronautics, Vol. 90, pp. 1-52, 1984.
- 2 N. Kubota, "Combustion Mechanisms of Nitramine Composite Propellants," Eighteenth International Symposium on Combustion, The Combustion Institute, Pittsburgh, PA 1981, p. 187.
- 3 W. H. Hsieh, W. Y. Li, and Y. J. Yim, "Combustion Behavior and Thermochemical Properties of RDX-Based Solid Propellants," AIAA-92-3628, AIAA/SAE/ASME/ASEE 28th Joint Propulsion Conference and Exhibition, July 6-8, 1992, Nashville, TN.
- 4 M. K. Razdan and K. K. Kuo, "Erosive Burning of Solid Propellants," Chapter 10 of *Fundamentals of Solid Propellant Combustion*, (Eds., K. K. Kuo and M. Summerfield), Progress in Astronautics and Aeronautics, Vol. 90, AIAA, New York, NY, 1984.
- 5 W. H. Hsieh and K. K. Kuo, "Erosive and Stagnant Burning of Stick Propellant, Part II: Theoretical Modeling of Erosive-Burning Processes," *Journal of Propulsion and Power*, Vol. 6, No. 4, July-August 1990, pp. 400-406.
- 6 J. C. Godon, J. Duterque, G. Lengelli, "Solid-Propellant Erosive Burning," *Journal of Propulsion and Power*, Vol. 8, No. 4, July-August 1992, pp. 741-747.

- 7 K. K. Kuo, W. H. Hsieh, K. C. Hsieh, and M. S. Miller, "Modeling of Hot Fragment Conductive Ignition of Solid Propellants with Applications to Melting and Evaporation of Solids," *ASME Journal of Heat Transfer*, Vol. 110, August 1988, pp. 670-679.
- 8 S. J. Ritchie, W. H. Hsieh, and K. K. Kuo, "Convective Ignition Phenomena of LOVA Propellants," AIAA 90-2194 AIAA/SAE/ASME/ASEE 26th Joint Propulsion Conference, July 16-18, 1990, Orlando, FL. (Also accepted for publication in the *Journal of Propulsion and Power*.)
- 9 A. Cohen, R.A. Beyer, J.E. Newberry, and S.R. Bilyk, "Laser ignition of Solid Propellants: Comparison of Model Predictions with Pressure and Emission Predictions," 29th JANNAF Combustion Meeting, NASA Langley Research Center, October 1992.
- 10 T. Parr and D. Hanson-Parr, "Species and Temperature Profiles in Ignition and Deflagration of HMX," Paper 87-8 Spring Meeting of the Western States Section of the Combustion Institute, April 1987.
- 11 K.K. Kuo, J-U. Kim, B.L. Fetherolf, and T. Torikai, "Pre-ignition Dynamics of RDX-based Energetic Materials under CO<sub>2</sub> Laser Heating," *Combustion and Flame*, in press.
- 12 L. Deluca, T.J. Ohlemiller, L.H. Caveny, and M. Summerfield, "Radiative Ignition of Double-base Propellants," *AIAA Journal*, Vol 14, No.8, 1976, pp.1111-1117.
- 13 T. J. Ohlemiller, L.H. Caveny, L. Deluca, and M. Summerfield, "Dynamic Effect of Ignitability Limits of Solid Propellants Subjected to Radiative Heating," 14th Symposium (International) on Combustion, The Combustion Institute, 1972.
- 14 C.E. Hermance, "Solid Propellant Ignition Theories and Experiments," in Chapter 5 of *Fundamentals of Solid Propellant Combustion*, (Eds. K.K. Kuo and M. Summerfield), AIAA, Progress in Astronautics and Aeronautics, Vol. 90, 1984, pp. 239-304.
- 15 K.K. Kuo, *Fundamentals of Combustion*, Chapter 10, 1986, pp. 734-791.
- 16 S. J. Ritchie, B. L. Fetherolf, W. H. Hsieh, and K. K. Kuo, "A Comparative Analysis of the Convective and Radiative Ignition Processes of XM-39 Solid Propellant," CPIA Pub. 573, Vol. 1, Oct. 1991, 28th JANNAF Combustion Subcommittee Meeting, pp. 453-461.
- 17 J. Covino and C. T. Hudson, "Cook-off Mechanistic Understanding and Predictive Capabilities," CPIA Publication 586, JANNAF Propulsion Systems Hazards Subcommittee Workshop, HSWC, Silver Spring, MD, April 27-May 1, 1992.
- 18 J. C. Oxley, "Cook-off Small-Scale Thermal Hazard Analysis," CPIA Publication 586, JANNAF Propulsion Systems Hazards Subcommittee Workshop, April 27 - May 1, 1992, pp. 21-43.
- 19 B. Craig and A. G. Butcher, "Intermediate and Full-Scale Cookoff Tests," CPIA Publication 586, JANNAF Propulsion Systems Hazards Subcommittee Workshop, April 27 - May 1, 1992, pp. 5-20.
- 20 K.K. Kuo, J. P. Gore, and M. Summerfield, "Transient Burning of Solid Propellants" Chapter 11 of *Fundamentals of Solid Propellant Combustion*, Eds. by K.K. Kuo and M. Summerfield, Progress in Astronautics and Aeronautics, Vol. 90, pp. 599-659.
- 21 M. Kumar and K. K. Kuo, "Effect of Deformation on Flame Spreading and Combustion in Propellant Cracks," *AIAA Journal*, Vol. 19, No. 12, 1981, pp. 1580-1589.
- 22 K. K. Kuo and D. E. Kooker, "Coupling between Nonsteady Burning and Structural Mechanics of Solid Propellant Grains," Chapter 13, *Nonsteady Burning and Combustion Stability of Solid Propellants*, AIAA Progress Series, Vol. 143, (Eds. L. De Luca, E. Price, and M. Summerfield), pp. 465- 517, 1992.
- 23 J. G. Siefert and K. K. Kuo, "Crack Propagation in Burning Solid Propellants," *Dynamics of Shock Waves, Explosives, and Detonation*, AIAA Progress Series, (Eds. J.R. Bowen, N. Manson, A. K. Oppenheim, and R. J. Soloukhin), Vol. 94, p. 575, 1985.
- 24 S. R. Wu, Y. C. Lu, K. K. Kuo, and V. Yang, "Crack Initiation and Propagation in Burning Metalized Propellants," *Eighteenth International Pyrotechnics Seminar*, The International Pyrotechnics Society, Breckenridge, Colorado, 1992, pp. 985-1003.

- 25 A. F. Belyaev, A. I. Korotkov, A. A. Sulimov, M. K. Sukoyan, and A. V. Obmenin, "Development of Combustion in an Isolated Pore," *Combustion, Explosion, and Shock Waves*, Vol. 5, 1969, pp. 4-9.
- 26 H. R. Jacobs, W. L. Hufferd, and M. L. Williams, "Further Studies of the Critical Nature of Cracks in Solid Propellant Grains," AFRPL-TR-75-14, 1975.
- 27 M. M. Athavale, K. C. Hsieh, W. H. Hsieh, J. M. Char, and K. K. Kuo, "Interaction of Flame Spreading, Combustion, and Fracture of Single-Perforated Stick Propellants Under Dynamic Condition," *Dynamics of Reactive Systems, Part II: Modeling and Heterogeneous Combustion*, AIAA Progress Series, Vol. 105, (Eds. J.R. Bowen, J.-C. Layer, and R. I. Soloukhin), 1986, pp. 267-290.
- 28 Y.C. Lu, "Combustion-Induced Crack Propagation Process in a Solid-Propellant Crack Cavity," Ph.D. Thesis, The Pennsylvania State University, December 1992.
- 29 R. A. Schapery, "A Theory of Crack Initiation and Growth in Viscoelastic Media, I: Theoretical Development," *International Journal of Fracture Mechanics*, Vol. 11, 1975, pp. 141-159.
- 30 R. A. Schapery, "Correspondence Principles and a Generalized J Integral for Large Deformation and Fracture Analysis of Viscoelastic Media," *International Journal of Fracture*, Vol. 25, 1984, pp. 195-223.
- 31 W.L. Hufferd, H. R. Jacobs, and K. L. Laheru, "On the Fracture of Viscoelastic Materials," CPLA 264, 1975, pp. 339-356.

## LABORATORY TESTING AND CONSTITUTIVE MODELING OF COAL INCLUDING ANISOTROPY

Dar-Hao Chen\*, Musharraf M. Zaman\*\*, Anant R. Kukreti\*\*\*

\* Graduate Research Assistant, \*\* Associate Professor, \*\*\* Professor

School of Civil Engineering and Environmental Science, University of Oklahoma, Norman, OK 73019

### ABSTRACT

In this study, the stress-deformation response of coal in the laboratory under three-dimensional (3-D) loading conditions similar to those existing in an actual coal mine is investigated, and a constitutive model, including the effects of anisotropy, is developed. The coal samples were obtained from a mine in LeFlore County, Oklahoma, at a depth of approximately 25-30 ft below the ground surface. A High Capacity Cubical Device with servo-controlled independent loading along three axes of a cubical specimen and a computerized data acquisition and monitoring system were used to conduct the tests. A total of 21 tests under 4 different confining pressures and 5 different stress paths were conducted. The influence of the degree of anisotropy was investigated by comparing the transversely isotropic and isotropic idealizations for different stress paths (Triaxial Compression, Triaxial Extension and Simple Shear) at different confining pressures (1,600, 3,200 and 5,600 psi). The experimental results demonstrated that the coal exhibits inherent anisotropy and that it can be treated approximately as a transversely isotropic material. Also, the Young's moduli were found to be dependent on the confining pressure. The experimental data were used to evaluate the material constants associated with the elasto-plastic constitutive model developed in the study.

### INTRODUCTION

As easily mineable reserves deplete, the coal industry must focus its attention on developing innovative techniques to maximize extraction without detrimental effects, such as instability and ground subsidence. To better understand and develop underground mining techniques, it is imperative to study the deformation characteristics and the failure response of coals under appropriate loading which simulate the field conditions. However, traditionally, material properties are evaluated from either uniaxial or cylindrical triaxial tests under an idealized two-dimensional loading (confining pressure and axial load) that does not reflect the true loading conditions existing in the field. Also, coal being a highly anisotropic material presents additional difficulties to the designer because its response not only varies with location but also with respect to direction or orientation even in the same mining area. Under such a situation, an analysis algorithm, which uses appropriate constitutive relationships and finite element method to discretize the overlying and underlying strata as well as the mined zones, can provide a tool to evaluate the ground control problems related to underground mining [1]. Application of an elastic-plastic constitutive model to analyze a boundary value problem requires input of realistic values of the associated material constants. Thus, 3-D testing and anisotropic modeling of coal are essential to evaluate realistically the material properties that accurately describe the coal behavior in the field. With this in mind, a High Capacity Cubical Device (HCCD) (30,000 psig) was designed and fabricated at the University of Oklahoma. The device has been successfully calibrated and used by Mishra [2] to study the behavior of plain and fiber-reinforced concrete.

A combined experimental and analytical study was undertaken to investigate the deformation behavior of coal specimens under simulated 3-D loading by using the HCCD. The experimental data was used to develop the constitutive model. In this paper, the testing of the cubical coal specimens, determination of associated model parameters, and the formulation of the elasto-plastic constitutive model that describes the stress-strain and volumetric response of the coal, including unloading and reloading sequence, are presented.

### DESCRIPTION OF EQUIPMENT AND PREPARATION OF CUBICAL SPECIMENS

A cubical device is an apparatus that provides independent control for the application of load and measurement of deformation along three mutually perpendicular directions at the same



time. The name cubical device stems from the fact that this apparatus has a cubical space frame, with a central cubical cavity to accommodate the specimen as well as to act as a reaction frame for the loading. The HCCD has five major components : (1) cubical space frame and six side walls; (2) deformation measuring system; (3) hydraulic pressure system; (4) digital data acquisition system; and (5) central monitoring unit. The test set-up and their inter-connections for HCCD are described in detail by Mishra [2].

The device (HCCD) used in this study for 3-D testing requires cubical specimens that are slightly less than 4 in. (approximately 3.94 in.) in size. The coal chunks were first broken into smaller pieces, approximately 7 in. in dimension, using a hand saw and a ruler. These smaller pieces were then used to prepare the desired cubical specimens using a high quality circular saw of 18 in. diameter with clamps to tightly hold the coal sample in place while cutting. The surfaces of coal were rough after cutting. To prevent uneven stress distribution, the irregularities were filled by applying a thin coat of a resin based body filler compound containing polyester styrene monomer, commercially called "Bondo". Then, the surfaces were smoothed by using a sanding machine. These steps not only ascertained uniform distribution of load on the specimen surface, but also helped to prevent moisture from escaping between the time the specimens were prepared and the actual tests were conducted. Before coating the specimen with Bondo, sketches showing the bedding planes, cleat cracks and crack orientations on the specimen surfaces were drawn for all six faces. Those sketches were essential for identification of bedding planes.

## DESCRIPTION OF THE DEVELOPED CONSTITUTIVE MODEL

The most important feature of the constitutive model developed is that it accounts for inherent anisotropy, which is an important property of materials such as coal. Because the nature of deposition and presence of cracks and bedding planes, coals exhibit a high degree of anisotropy. Another attractive feature of the model is that it accounts for anisotropy even in the elastic range. Also, the model is capable of predicting volumetric response in the compressive as well as in the dilative regions.

### Loading Surface

The equation of the loading surface is proposed in the form

$$F = \tilde{r}^2 - \left[ \alpha \tilde{J}_{1A}^n - \frac{\tilde{J}_{1A}^2}{\beta} + \tilde{K}^2 \right] g(\theta, \tilde{J}_1) = 0 \quad (1)$$

where  $\alpha$ ,  $n$  and  $K$  are failure parameters and  $\beta$  is a hardening function. Also,  $\tilde{r}$ ,  $\tilde{J}_1$  and  $\tilde{K}$  are non-dimensional quantities given by :  $\tilde{r} = r/p_a$ ,  $\tilde{J}_1 = J_1/p_a$ , and  $\tilde{K} = K/p_a$ , where  $p_a$  is the atmospheric pressure and  $K$  is the cohesive strength. In these relationships, the stress invariants  $J_1$ ,  $J_{2D}$  and  $J_{3D}$  are given by

$$J_1 = \sigma_{11} = \sigma_{11} + \sigma_{22} + \sigma_{33} ; J_{2D} = \frac{1}{2} S_i S_j ; J_{3D} = \frac{1}{3} S_i S_j S_k \quad (2)$$

in which

$$r = \sqrt{2J_{2D}} , \text{ and } \theta = \frac{1}{3} \cos^{-1} \left[ \frac{3\sqrt{3} J_{3D}}{2(J_{2D})^{3/2}} \right] \quad (3)$$

The variable  $J_{1A}$  in Eq. (1) is given by

$$J_{1A} = (a_{11} \sigma_{11} + a_{22} \sigma_{22} + a_{33} \sigma_{33}) \quad (4)$$

where the coefficients  $a_{11}$ ,  $a_{22}$  and  $a_{33}$  are anisotropic coefficients and are positive quantities that can be determined from the stress-strain response under the hydrostatic compression loading.

Following the work of Faruque and Chang [3] the function  $g(\theta, \tilde{J}_1)$ , which accounts for the shape of the yield surface and the failure surface, is defined as follows :

$$g(\theta, \tilde{J}_1) = \left[ \cos \left( \frac{1}{3} \cos^{-1} (-A \cos 3\theta) \right) \right]^{-2} \quad (5)$$

where

$$A = \exp(-\gamma \tilde{J}_1) \quad (6)$$

The variable  $\gamma$  is another material constant that accounts for the variation of the shape of the yield surface on the octahedral plane.

### Anisotropic Elastic Behavior

Since coals are usually found in nature as a layered material it may be reasonable to treat such materials as transversely isotropic. The linear elastic stress-strain relations for a transversely isotropic material in the elastic range can be written in a matrix form in terms of five elastic constants, as follows :

$$\begin{bmatrix} \epsilon_z \\ \epsilon_x \\ \epsilon_y \\ \gamma_{zx} \\ \gamma_{yz} \\ \gamma_{xy} \end{bmatrix} = \begin{bmatrix} \frac{1}{E'} & -\frac{\nu'}{E'} & -\frac{\nu'}{E'} & 0 & 0 & 0 \\ -\frac{\nu'}{E'} & \frac{1}{E} & -\frac{\nu}{E} & 0 & 0 & 0 \\ -\frac{\nu'}{E'} & -\frac{\nu}{E} & \frac{1}{E} & 0 & 0 & 0 \\ 0 & 0 & 0 & \frac{1}{G'} & 0 & 0 \\ 0 & 0 & 0 & 0 & \frac{1}{G'} & 0 \\ 0 & 0 & 0 & 0 & 0 & \frac{1}{G'} \end{bmatrix} \begin{bmatrix} \sigma_z \\ \sigma_x \\ \sigma_y \\ \tau_{zx} \\ \tau_{yz} \\ \tau_{xy} \end{bmatrix} \quad (7)$$

The physical meaning of  $E$ ,  $E'$ ,  $\nu$ ,  $\nu'$ ,  $G$  and  $G'$  can be found elsewhere [4], and it may be noted that the constant  $G$  is not independent and can be determined from  $G = E / 2(1 + \nu)$ . The material constants  $E$ ,  $E'$ ,  $\nu$  and  $\nu'$  can be determined from a combination of unloading-reloading curves for different loading paths (namely, SS, TE, TC), at the same level of confining pressure. To determine the shear modulus  $G'$ , one needs to have a uniform shear stress state in the cubical specimen on the principal axis of the material. Because this is very difficult to achieve experimentally, Atkinson [5] proposed a procedure in which specimens are prepared by cutting them at an angle of  $45^\circ$  to the bedding plane. Although the procedure appears to be straightforward to prepare a specimen at the  $45^\circ$  angle with the bedding plane, in reality it is not an easy task. Sometimes bedding planes are not clearly visible in coal specimens. Also, cutting coal specimens exactly at  $45^\circ$  angle may be a difficult task. Thus, a direct evaluation of  $G'$  from experimental data is frequently avoided. In this regard, an assumption introduced by Leknitskii [6] was used to relate  $G'$  to  $E$ ,  $E'$  and  $\nu'$  as follows  $G' = [E E'] / [E(1 + 2\nu') + E']$ .

### DETERMINATION OF THE MATERIAL CONSTANTS

The constitutive model outlined in the previous section requires determination of the following fourteen material constants : (1) four elastic constants ( $E$ ,  $E'$ ,  $\nu$  and  $\nu'$ ), (2) two

anisotropic constants associated with the plastic behavior ( $a_{22}$  and  $a_{33}$ ); (3) four constants associated with the transition and the yield surface ( $\alpha$ ,  $n$ ,  $k$  and  $\gamma$ ); and (4) four constants associated with hardening ( $\beta_1$ ,  $\beta_2$ ,  $\eta_1$  and  $\eta_2$ ). These material parameters were determined by conducting tests along various stress paths (namely, Hydrostatic Compression (HC), Conventional Triaxial Compression (CTC), Simple Shear (SS), Triaxial Extension (TE), and Triaxial Compression (TC) [4]) under various confining pressures. It is important that the constitutive law be valid for all the major stress paths that the material (coal) can experience. So the experimental program was designed in such way that the test results can be used directly to determine these material constants or parameters. The different stress paths and values of confining pressures used in the test program are presented in Table 1.

The anisotropic constants ( $a_{22}$  and  $a_{33}$ ) and the hardening parameters ( $\beta_1$ ,  $\beta_2$ ,  $\eta_1$  and  $\eta_2$ ) were determined from the HC tests. Also, the unloading-reloading cycles at the same level of confining pressures for different stress paths were utilized to evaluate the elastic constants ( $E$ ,  $E'$ ,  $\nu$  and  $\nu'$ ). The failure stresses (as given in last column of Table 1) for various shear tests were used to compute the yield and/or failure parameters ( $\alpha$ ,  $n$ ,  $k$  and  $\gamma$ ). The parameters used in this study are presented in Table 2.

## MODEL PREDICTIONS VERSUS EXPERIMENTAL OBSERVATIONS

Although an anisotropic constitutive model may be more appropriate for coals because such materials exhibit some degree of inherent anisotropy, it is desirable to investigate the degree of anisotropy involved in such materials. If the degree of anisotropy is not very significant, then the material can be modeled as isotropic for simplicity. With this objective in mind, an attempt was made to compare the transversely isotropic and isotropic idealizations for the LeFlore coal for TC, TE and SS tests at confining pressures of 1,600, 3,200 and 5,600 psi. The parameters used for isotropic idealization are also presented in Table 2. It can be observed that for isotropic behavior  $E = E'$ ,  $\nu = \nu'$ , and  $a_{22} = a_{33} = 1$ . The comparison between the predicted stress-strain response for both idealizations, transversely isotropic and isotropic, with the experimental data for TC tests at 5,600 psi confining pressure is shown in Fig. 1. An unloading and reloading cycle was conducted in the deviatoric portion of the test. In this case, the unloading-reloading sequence was performed prior to the specimen failure and after the specimen showed a significant amount of non-linearity. The model predictions and the experimental data are found to be in very good agreement for the entire loading history including unloading and reloading. Particularly, for the transversely isotropic idealization the predicted ultimate stress is only slightly different (less than 8%) from the experimental data. Also, it is observed that both the models were able to predict the loading and unloading behaviors quite accurately.

A comparison of the volumetric strain response is presented in Fig. 2. In this figure, the volumetric strain is plotted against the major principal strain ( $\epsilon_z$  for this case). Evidently, the change in the volumetric response from compression to dilation is predicted well by the model. The discontinuity in the experimental data induced by the unloading-reloading operation, as shown in Fig. 2, is possibly caused by the internal cracks; also, it might be partly attributed to the experimental errors. It may be noted that in the experiment, volumetric strains are obtained by adding the normal components of the deviatoric strains along the  $x$ ,  $y$  and  $z$  axes. Similar comparisons with the observed volumetric behavior of SS test at confining pressure of 5,600 psi are compared with the model predictions in Fig. 3. It is observed that the model predicted by the transversely isotropic idealization are in better agreement with the experimental values than those predicted by the isotropic idealization.

A comparison of the predicted stress-strain response with experimental data for SS and TE tests conducted at a confining pressure of 3,200 and 1,600 psi is presented in Figs. 4 and 5. Similar observations, as for the TC stress path test, can be made here. For all the cases tested, it can be seen that the slopes of loading and unloading parts of the stress-strain response are predicted quite accurately, indicating that the representation of the elastic constant ( $E$ ,  $E'$  and  $G'$ ) as a linear function of the initial confining pressure is a good approximation for the range of confining pressure considered.

## CONCLUSIONS

1. Elastic moduli of the LeFlore coal are pressure dependent. For the range of confining pressure ( $\sigma_0$ ) considered, the elastic moduli are linear functions of  $\sigma_0$ .
2. The elasto-plastic transversely isotropic constitutive model is found to satisfactorily represent the stress-strain and the volumetric-axial strain behavior of LeFlore coal under various stress paths and confining pressures.
3. The slopes of unloading-reloading stress-strain response are predicted quite accurately, indicating that the representation of the elastic constants as a linear function of the initial confining pressure is a good approximation.
4. The predictions of stress-strain and volumetric responses using the transversely isotropic model are in better agreement with the experimental data than those predicted by the isotropic model.

## ACKNOWLEDGEMENTS

The financial support for this study was provided by the Oklahoma Mining and Mineral Resources Research Institute (OMMRRRI). Also, technical assistance by Dr. Y.M. Najjar is gratefully acknowledged.

## REFERENCES

1. Z.T. Bieniawski, "Analytical Modeling as a Geomechanics Aid for Mine Design Application in the USA," International Bureau of Rock Mechanics, 7th Plenary Scientific Session, Katowice, 24-26 June, 1981, pp. 7-22. (1981).
2. D. K. Mishra, "A High Capacity Cubical Device : Development and Performance Evaluation," M.S. Thesis, School of Civil Engineering and Environmental Science Univ. of Oklahoma, Norman, Ok. (1991).
3. M.O. Faruque and C.J. Chang, "New Cap Type Model for Failure and Yielding of Pressure Sensitive Materials", J. Eng. Mech. Div., ASCE, Vol. 112, pp. 1041-1053. (1986).
4. W.F. Chen and A.F. Saleeb, Constitutive Equation for Engineering Materials, Vol. 1, Elasticity and Modeling, John Wiley and Sons, New York. (1982).
5. R.H. Atkinson, "Constitutive Relations of An Illinois Coal (Herrin #6 Seam)", Report, Univ. of Colorado, Boulder, 94p. (1974).
6. S.G. Lekhnitskii, Theory of Elasticity of an Anisotropic Body, Mir Publishers, Moscow, pp. 60. (1981).

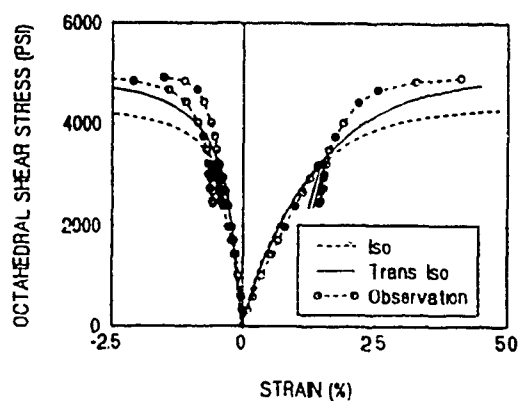


Fig.1 Comparison of Observed and Predicted Stress-Strain Response for Triaxial Compression Tests (TC) at  $\sigma_0 = 5,600$  psi

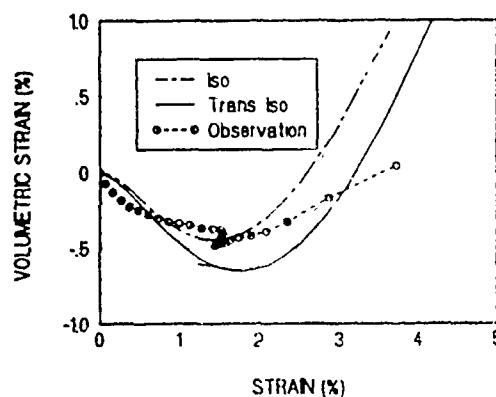


Fig.2 Comparison of Observed and Predicted Volumetric Response for Triaxial Compression Tests at  $\sigma_0 = 5,600$  psi

Table 1 : Test Program and the Effect of Confining Pressures and Stress paths on Failure Shear Strength ( $\tau$ )

Specie. No.	Stress Path	Confining Pressure (psi)	Failure Strength ( $\tau$ ) (psi)
30	TC	800	1837
18	TC	1,200	2572
16	TC	1,600	3307
19	TC	3,200	6001
17	TC	3,200	6001
20	TC	5,600	8328
4	TE	1,600	1837
6	TE	1,600	3555
24	TE	3,200	3674
8	TE	3,200	5634
33	TE	5,600	5756
5	SS	1,200	1556
14	SS	1,600	2121
1	SS	3,200	4101
23	SS	3,600	4384
32	SS	5600	6293
13	CTC	800	6042
21	CTC	800	5716
25	CTC	1,200	6369
26	CTC	1,200	6532
2	HC	14,500	

The failure shear strength ( $\tau$ ) is defined as  $\tau = \sqrt{2J_{2D}}$ . Also, the failure stresses pertaining to experimental data were obtained by extrapolating the stress-strain curve to asymptotes.

Table 2 : Material Constants Used in This Study for Transversely Isotropic and Isotropic idealizations

	Trans. Isotropic	Isotropic
E	a*	c*
E'	b*	c*
v	0.38	0.31
v'	0.22	0.31
a <sub>22</sub> , a <sub>33</sub>	1.29	1
$\alpha$	80.0	80.0
$\gamma$	45.0	45.0
k (psi)	300.0	300.0
n	1.12	1.12
$\beta_1$	1.685	1.685
$\eta_1$	55000.0	55000.0
$\beta_2$	0.91	0.91
$\eta_2$	0.21	0.21

a\* = 190,000 + 93.2 \* confining pressure  
b\* = 230,000 + 95.4 \* confining pressure  
c\* = 220,000 + 100 \* confining pressure

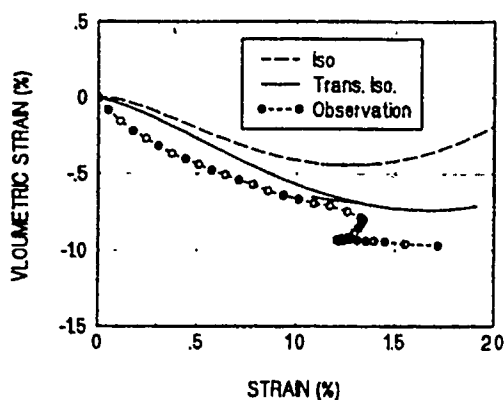


Fig.3 Comparison of Observed and Predicted Volumetric Response for Simple Shear Test (SS) at  $\sigma_0 = 5,600$  psi

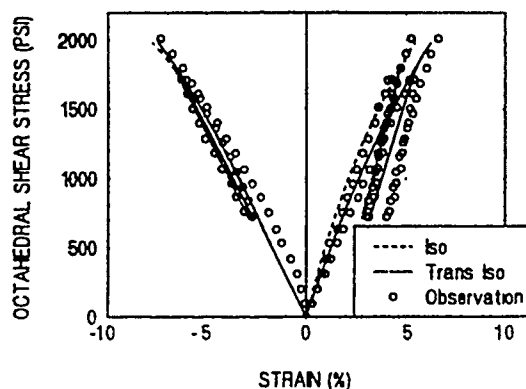


Fig.4 Comparison of Observed and Predicted Stress-Strain Response for Triaxial Extension Tests (TE) at  $\sigma_0 = 3,200$  psi

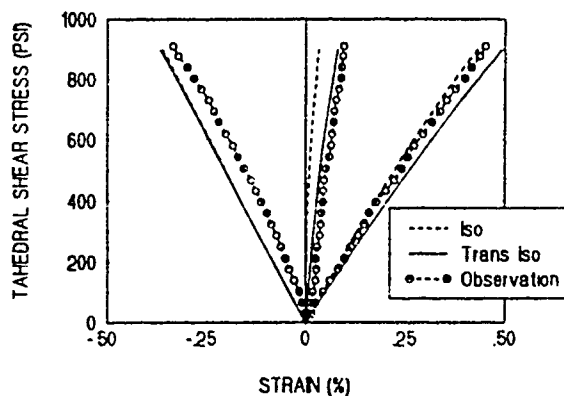


Fig.5 Comparison of Observed and Predicted Stress-Strain Response for Simple Shear Test (SS) at  $\sigma_0 = 1,600$  psi

## TIME LAG DIFFUSION METHOD FOR A SOLID PROPELLANT EMITTING GASES

JAMES K. BAIRD\* AND JENN-SHING CHEN\*\*

\*Department of Chemistry, University of Alabama in Huntsville, Huntsville, AL 35802

\*\*Department of Applied Chemistry, National Chiao Tung University, Hsinchu, Taiwan 30050 Republic of China.

### ABSTRACT

In the ordinary application of the time-lag method to the measurement of the diffusion coefficient of a gas passing through a plane sheet of an inert solid, the gas is pressurized on one side of the sheet and evacuated on the other. After decay of transients, the cumulative amount,  $Q(t)$ , of gas diffused through the sheet in time,  $t$ , assumes the "time-lag" form,  $Q(t) = A(t - L)$ . Measurements of the slope,  $A$ , and the intercept,  $L$ , can be used to determine the diffusion coefficient and the solubility of the gas in the solid. We have rederived this law for the case of a solid which is actively evolving this same gas at an arbitrary rate and have used it to predict the rate of outgassing of the solid upon standing. Practical applications of the theory include radioactive decay of minerals, rejection of plasticizers by plastics, and the decomposition of solid rocket propellants.

### 1. Introduction

The diffusion coefficients of gases passing through inert solids are often measured by the time-lag method.<sup>1-3</sup> In this well-established technique, the gas is pressurized to a concentration,  $c_2$ , on one side of a plane sheet of the solid, while the other side is evacuated. The build-up of gas on the evacuated side is measured as a function of the time,  $t$ . After decay of transients, the amount of gas accumulated,  $Q(t)$ , per unit area of the solid follows the law,

$$Q(t) = A(t - L) \quad (1)$$

where the intercept,  $L$ , on the  $t$ -axis is called the time-lag and gives the method its name.

The theory of  $Q(t)$ , which is based upon solution of Fick's second law, provides expressions for  $L$  and the slope,  $A$ .<sup>1-3</sup> When these are combined with experimental measurements of  $Q(t)$  vs.  $t$ , the diffusion coefficient and other properties of the gas-solid system can be evaluated.

In some cases, the solids are not inert but instead actively evolve various gases. Examples include radioactive decay of minerals to form a gaseous daughter (emanation),<sup>4</sup> rejection of plasticizer from polymer films,<sup>5</sup> and the decomposition of solid rocket propellants in storage. Solid propellants are especially interesting, because as complex mixtures, they are capable of evolving more than one gas.

Below, we develop the time-lag method for the diffusion of a gas through a planar sheet of solid, which is simultaneously evolving the same gas. We also give a formula for the rate of evolution of a gas from the sheet upon passive standing. The latter is useful in assessing the shelf life of the propellant.

### 2. Integration of Fick's Second Law

#### 2.1 Conversion to an Ordinary Differential Equation

Consider a slab of thickness,  $h$ , in the  $x$ -direction. In order to ignore edge effects, the slab will be considered to be infinite in both directions perpendicular to its thickness. The instantaneous concentration of gas at position  $x$  within the slab is  $c(x, t)$ .

In the case of active gas evolution, Fick's second law takes the form

$$\frac{\partial c(x, t)}{\partial t} = D \frac{\partial^2 c(x, t)}{\partial x^2} + f(t), \quad 0 \leq x \leq h \quad (2)$$

where  $D$  is the coefficient of gas diffusion through the solid and  $f(t)$  is the volume rate of internal gas production, which is assumed to be spatially uniform.

The gas just outside the face at  $x = 0$  has the concentration,  $c_1$ . The gas concentration associated with the solid just inside this face is  $kc_1$ , where  $k$  is the thermodynamic distribution coefficient. On the face at  $x = h$ , the analogous concentrations are  $c_2$  and  $kc_2$ , respectively. At  $t = 0$ , the bulk solid contains gas at concentration,  $c_0$  which depending upon the immediate past history of the solid, can be equal to or different from the thermodynamic solubility of the gas. These statements are summarized by the equations,

$$c(x, 0) = c_0 \quad (3)$$

$$c(0, t) = kc_1 \quad (4)$$

$$c(h, t) = kc_2 \quad (5)$$

Eqs. (2) - (5) define a boundary value problem for the function,  $c(x, t)$ . The problem may be solved by the method of Laplace Transforms.<sup>2,6</sup> The result is

$$\begin{aligned} c(x, t) = & kc_1 + k(c_2 - c_1) \left( \frac{x}{h} \right) + \frac{2}{\pi} \sum_{n=1}^{\infty} \frac{kc_2(-1)^n - kc_1}{n} \sin \left( \frac{n\pi x}{h} \right) \exp \left( \frac{-n^2 \pi^2 D t}{h^2} \right) \\ & + \frac{4c_0}{\pi} \sum_{m=0}^{\infty} \left( \frac{1}{2m+1} \right) \sin \left[ \frac{(2m+1)\pi x}{h} \right] \exp \left[ \frac{-(2m+1)^2 \pi^2 D t}{h^2} \right] \\ & + \int_0^t dt' f(t') \frac{4}{\pi} \sum_{m=0}^{\infty} \left( \frac{1}{2m+1} \right) \sin \left[ \frac{(2m+1)\pi x}{h} \right] \exp \left[ \frac{-(2m+1)^2 \pi^2 D (t-t')}{h^2} \right] \end{aligned} \quad (6)$$

### 3. Rate of Outgassing

The flux of gas molecules in the  $x$ -direction at any point within the slab is given by Fick's first law,

$$J(x, t) = -D \frac{\partial c(x, t)}{\partial x} \quad (7)$$

The sum of the fluxes exiting both sides of the slab is

$$J_{\text{tot}}(t) = -J(0, t) + J(h, t) \quad (8)$$

where the minus sign accounts for the fact that the positive  $x$ -axis runs from  $x = 0$  to  $x = h$ .

In the case of a slab of solid propellant under shelf storage conditions, it is likely that the steady state concentrations of gas on either face will be zero or close to it. The concentration of gas anywhere within the slab is then given by setting  $c_1 = c_2 = 0$  in Eq.(6). By combining Eqs.(6) - (8), one obtains

$$J_{\text{tot}}(t) = \frac{8D}{h} \left\{ c_0 \sum_{m=0}^{\infty} \exp \left[ \frac{-(2m+1)^2 \pi^2 D t}{h^2} \right] + \int_0^t dt' f(t') \sum_{m=0}^{\infty} \exp \left[ \frac{-(2m+1)^2 \pi^2 D (t-t')}{h^2} \right] \right\} \quad (9)$$

For times  $t \gg h^2 / \pi^2 D$ , the terms proportional to  $c_0$  in Eq.(9) will be small, and  $J_{\text{tot}}$  takes on the asymptotic form

$$J_{\text{tot}}(t) = \frac{8D}{h} \int_0^t dt' \sum_{m=0}^{\infty} \exp \left[ \frac{-(2m+1)^2 \pi^2 D (t-t')}{h^2} \right] \quad (10)$$

#### 4. Time-Lag Method

##### 4.1 Cumulative Mass Transported

If the gas concentration on the high pressure side at  $x=h$  is  $c_2$ , while on the low pressure side at  $x=0$  it is  $c_1$ , then the cumulative amount of gas passed through the slab after a time,  $t$ , is

$$Q(t) = - \int_0^t dt' J(0, t') \quad (11)$$

After substituting Eq.(6) into Eq.(7) and the resulting equation into Eq.(11), we obtain after performing the integral,

$$\begin{aligned} Q(t) = & \frac{Dk(c_2 - c_1)t}{h} + \frac{2h}{\pi^2} \sum_{n=1}^{\infty} \frac{k((-1)^n c_2 - c_1)}{n^2} [1 - \exp(-n^2 \pi^2 D t / h^2)] \\ & + \frac{4c_0 h}{\pi^2} \sum_{m=0}^{\infty} \frac{1}{(2m+1)^2} [1 - \exp(-(2m+1)^2 \pi^2 D t / h^2)] \\ & + \frac{4h}{\pi^2} \sum_{m=0}^{\infty} \frac{1}{(2m+1)^2} \int_0^t d\theta f(\theta) [1 - \exp(-(2m+1)^2 \pi^2 D (t-\theta) / h^2)] \end{aligned} \quad (12)$$

The exponentials in Eq.(12) are the transient parts of  $Q(t)$  associated with the relaxation of the diffusive flow towards a steady state. In the limit,  $t \gg h^2/\pi^2 D$ , the exponentials in the first two lines of Eq.(12) can be dropped. Use of the sums<sup>1</sup>

$$\sum_{n=1}^{\infty} \frac{1}{n^2} = \frac{\pi^2}{6} \quad (13)$$

$$\sum_{n=1}^{\infty} \frac{(-1)^n}{n^2} = -\frac{\pi^2}{12} \quad (14)$$

$$\sum_{n=0}^{\infty} \frac{1}{(2n+1)^2} = \frac{\pi^2}{8} \quad (15)$$

then allows us to compute the limiting form for the mass transported:

$$\begin{aligned} Q(t) \approx & \frac{Dk(c_2 - c_1)}{h} \left[ t - \frac{h^2}{6Dk(c_2 - c_1)} (k(c_2 + 2c_1) - 3c_0) \right] \\ & + \frac{4h}{\pi^2} \sum_{m=0}^{\infty} \frac{1}{(2m+1)^2} \int_0^t d\theta f(\theta) [1 - \exp(-(2m+1)^2 \pi^2 D (t-\theta) / h^2)] \end{aligned} \quad (16)$$



The first term in Eq.(16) has the standard form of the time-lag law expressed by Eq.(1). The sum of integrals involving  $f(\theta)$ , however is more complex. Depending upon the form of  $f(\theta)$ , this sum may contribute to either or both of the coefficients in Eq.(1); it may in addition introduce terms which are neither constant nor linear in  $t$ , so that Eq. (1) fails to apply at all.

#### 4.2 Constant Rate of Gas Evolution

In the special case that the rate of gas evolution is independent of time,

$$f(t) = R \quad (17)$$

where  $R$  is a constant. Substitution of Eq.(17) into Eq.(16) followed by use of the condition  $t \gg h^2/\pi^2 D$  and the sum<sup>7</sup>

$$\sum_{m=0}^{\infty} \frac{1}{(2m+1)^4} = \frac{\pi^4}{96} \quad (18)$$

yields,

$$Q(t) \equiv \left( \frac{Dkc_2}{h} + \frac{hR}{2} \right) t - \frac{1}{6} \left( h(kc_2 - 3c_0) + \frac{h^3 R}{4D} \right) \quad (19)$$

where we have also set  $c_1 = 0$  as is customary in the case of time-lag experiments.

Eq.(19) has the general time-lag form given by Eq.(1). By comparison of these two equations, one may write

$$hA = Dkc_2 + \frac{1}{2} h^2 R \quad (20)$$

$$\frac{AL}{h} = \frac{kc_2}{6} + \frac{h^2 R}{24D} - \frac{c_0}{2} \quad (21)$$

## 5. Discussion

### 5.1 Analysis of Experimental Data

Eqs.(20) and (21) have been left in forms convenient for the analysis of experimental data so as to obtain values for  $D$ ,  $k$ ,  $R$  and  $c_0$ . The  $Q(t)$  data should be fitted to Eq. (1) by treating  $A$  and  $AL$  as least squares adjustable parameters. If it is assumed that  $h$  is directly measurable, then a plot of  $hA$  vs.  $c_2$  according to Eq. (20) should form a straight line with slope,  $Dk$ , and intercept,  $h^2 R/2$ . From the value of  $h$  and the intercept,  $R$  can be obtained. By comparison, a plot of  $AL/h$  vs  $c_2$  according to Eq. (21) should form a straight line with slope  $k/6$  and intercept  $(h^2 R/24D - c_0/2)$ . The slope of this line determines  $k$  directly, and when combined with the value of  $Dk$ , the value of  $D$  can be computed. Once  $D$  and  $R$  are determined, the value of  $c_0$  can be obtained from the value of  $(h^2 R/24D - c_0/2)$ .

The theory we have presented above ignores the details of the chemical kinetics associated with the solid and the dissolved gas by representing them by the general function  $f(t)$ . This would seem to be appropriate in the case of rocket propellants, for example, where the mechanism of gas evolution is not yet understood.

### 5.2 Summary

Eqs. (10), (12), (16) and (19) have been written with the case of a single diffusing gas in mind. If more than one species is being considered, then subscripts, "i", running over the number of species need to be appended to the symbols  $D$ ,  $k$ ,  $c_1$ ,  $c_2$ ,  $c_0$ ,  $f(t)$ ,  $J_{tot}(t)$ , and  $Q(t)$ . When it is then required to compute the total gas evolution by including the effects of all species involved, the appropriate equation selected from Eqs. (10), (12), (16), and (19) need only be summed over "i" to get the desired result.

Eqs. (6) and (12) have appeared previously for the special case  $f(t) = 0$ .<sup>3</sup> The present work generalizes these equations to an outgasing solid ( $f(t) \neq 0$ ). The specific new results are summarized by Eqs.(6), (9), (10), (12), (16), and (19). Once  $D$  has been determined in a time-lag experiment as described above, Eqs.(9) and (10) (as applicable) can be used to predict the rate of gas evolution per unit area of an active solid. These formulae should have special utility in predicting the shelf-life of solid rocket propellants.

#### Acknowledgments

This research was sponsored by the Morton Thiokol Corporation and by the National Aeronautics and Space Administration through contract NAGW-812 with the Consortium for Materials Development in Space at the University of Alabama in Huntsville.

#### References

1. W. Jost, Diffusion in Solids, Liquids, and Gases, (Academic Press, New York, 1960), p.44.
2. J. Crank, The Mathematics of Diffusion, (Oxford University Press, London, 1957), p. 48.
3. H. Daynes, Proc. Roy. Soc. A **97**, 286 (1920).
4. Ref.1, pp 314-319.
5. I. R. Bellobono, B. Marcandalli, E. Sellhi, and A. Polissi, J. Appl. Polym. Sci. **29**, 3185 (1984).
6. G. Arfken, Mathematical Methods for Physicists, (Academic Press, New York, 1985), pp. 824-859.
7. I.S. Gradshteyn and I.M. Ryzhik, Table of Integrals, Series, and Products, (Academic Press, New York, 1980), p.7. Formula 0.234.5.

## ENERGETIC MATERIALS IN CERAMICS SYNTHESIS

J. J. KINGSLEY AND L. R. PEDERSON

Pacific Northwest Laboratory\*, Richland, WA 99352

### ABSTRACT

Combustion of a proper combination of an oxidizer and a fuel can produce the exothermicity required for the simultaneous synthesis of oxide ceramic powders. Oxidizers include metal nitrates, ammonium nitrate, and ammonium perchlorate, while urea, carbohydrazide, glycine and others have been used successfully as fuels. Combustion methods are particularly well-suited to producing multicomponent metal oxides, yielding compositionally homogeneous, fine particles with low impurity content. Organic fuels, particularly those containing nitrogen, also serve as a complexant in the precursor, which inhibits inhomogeneous precipitation from occurring prior to combustion. The exothermic redox decomposition of these oxidizer-fuel mixtures is initiated at low temperatures, usually  $<250^{\circ}\text{C}$ . Properties of the products are influenced by the nature of the fuel and the oxidizer/fuel ratio. Many technologically important oxide ceramics have been produced by these methods.

### INTRODUCTION

Combustion methods to prepare ceramic oxide powders offer an attractive alternative to traditional solid state reaction approaches. Combustion synthesized powders typically are more homogeneous, contain fewer impurities, have higher surface areas and smaller particle sizes, and are less labor-intensive than powders prepared by traditional methods.

Ceramic oxides that require high temperatures for their formation can be produced by combustion of a proper combination of an oxidizer and a fuel [1-13]. Metals are often incorporated into precursor mixtures as nitrates and serve as the oxidizer. Fuels, usually organic compounds containing nitrogen such as amines, amides, and hydrazides, also serve to complex metal ions, thereby maintaining a high degree of homogeneity in the precursor [11,12]. In addition to complexation, desirable fuel characteristics include a relatively low ignition temperature, controlled (non-violent) combustion or deflagration with a moderate gas volume, and complete conversion to non-toxic gases such as nitrogen, water, and carbon dioxide. The basic principles underlying the formulation of propellants and other high-energy materials, such as oxidizer/fuel ratio and extra-oxidizer have been used to advantage in this novel ceramics synthesis technique. In this paper, the synthesis and properties of a number of technologically important oxides using these high-energy principles is demonstrated.

An important parameter used to describe propellant oxidizer/fuel mixtures is the elemental stoichiometric coefficient,  $\Phi_c$ , which represents the ratio of the oxidizing to reducing (fuel) components of the mixture [14]. Oxidizer-fuel mixtures with  $\Phi_c$  equal to 1 are termed stoichiometric and are known to release maximum energy in condensed oxidizer-fuel systems such as propellants.

\* Operated by Battelle Memorial Institute for the U. S. Department of Energy under contract DE-AC06-76RLO 1830

The concept of total oxidizing and reducing valences immensely helps to simplify the procedure to calculate the stoichiometric compositions of oxidizer-fuel mixtures [15]. Presently, the compositions of the oxidizer-fuel mixtures used for the combustion synthesis of oxide ceramics are calculated using this procedure. For example, the total oxidizing valency of  $\text{Al}(\text{NO}_3)_3$  using the individual components is 15 ( $\text{Al}:1 \times -3$ ;  $\text{N}:1 \times 0$  and  $\text{O}:9 \times 2$ ) and the total reducing valency of urea ( $\text{CH}_4\text{N}_2\text{O}$ ) using the individual components is -6 ( $\text{C}:1 \times -4$ ;  $\text{H}:4 \times -1$ ;  $\text{N}:2 \times 0$  and  $\text{O}:1 \times 2$ ). Therefore, a stoichiometric ( $\Phi_c = 1$ ) mixture of aluminum nitrate and urea would contain one mole of aluminum nitrate to 2.5 moles of urea.

## EXPERIMENTAL

Stoichiometric amounts of corresponding metal nitrates (oxidizers) and fuels were mixed either into a slurry or an aqueous solution. Fuels used are urea, urea-nitrate, carbonylhydrazide (CH), oxalic dihydrazide (ODH), tetraformal trisazine (TFTA), maleic hydrazide (MH), glycine, guanidine nitrate, glucose and sucrose. Slurry mixtures, usually used when urea was the fuel, were decomposed at  $500^\circ\text{C}$  in a furnace (necessary because gases escape when slowly heated, and combustion does not take place). Aqueous precursors containing other fuels such as glycine, CH and others ignited following heating in the range  $140$ – $250^\circ\text{C}$ . Precursor mixtures underwent dehydration and partial decomposition, followed by rapid, exothermic and self-sustaining combustion. This incandescent combustion generates in situ temperatures exceeding  $1000^\circ\text{C}$  as measured using an optical pyrometer. This results in simultaneous production of fine and voluminous ceramic oxide powders. The ceramic oxides were characterized by x-ray diffraction (XRD) and by transmission electron microscopy (TEM). Particle size distributions and BET surface areas were additionally determined.

## RESULTS AND DISCUSSION

A large number of technologically important oxide ceramics have been prepared by this novel combustion method and a partial list of the various oxides produced and their particulate properties is given in Table I (where M = transition or alkaline earth metals; Ln = rare earths).

Table I. Combustion Synthesized Oxide Ceramics

Oxide Ceramics	Fuel	Surface Area ( $\text{m}^2/\text{g}$ )	Agglomerate/ Particle Size	Ref
$\alpha\text{-Al}_2\text{O}_3$ $\text{t-ZrO}_2/\text{Al}_2\text{O}_3$	Urea	8	4 $\mu\text{m}$	1,4
$\text{MAlO}_4$	Urea, CH	1-85	1-6 $\mu\text{m}$	5
$\text{MCr}_2\text{O}_4$	TFTA, MH Urea	8-72	0.5-1.3 $\mu\text{m}$	6-8
$\text{MFe}_2\text{O}_4$	TFTA, ODH	10-120	1-10 $\mu\text{m}$	9
$\text{LnAlO}_3$ $\text{LnFeO}_3$ $\text{LnCrO}_3$	Urea, CH TFTA, ODH, MH	3-45	0.8-9 $\mu\text{m}$	9 10
$\text{La}_2\text{M}_2\text{CrO}_7$ $\text{La}_2\text{M}_2\text{MnO}_7$	Glycine	15-45	< 100 nm	11-13

Combustion synthesis of ceramic oxides and their properties are influenced by the nature of fuel, nature of metal precursor, oxidizer-fuel ratio and use of extra-oxidizer. These factors are discussed with illustrative examples in this section.

Oxidizer-fuel mixtures containing urea undergo foaming during their decomposition and result in combustion with a steady flame. The ceramic powders produced by this high energy combustion (up to 1800°C) are partly sintered agglomerates with typical particle sizes of 1-10  $\mu\text{m}$ . This can be seen in the TEM micrograph of combustion synthesized  $\alpha\text{-Al}_2\text{O}_3$  given in Fig. 1a. Mixtures with other fuels such as carbohydrazide and glycine undergo a smooth deflagration with a propagating exothermic front. They produce fine and weakly agglomerated ceramic powders. This can be seen in the TEM micrograph of  $\text{LaCrO}_3$  produced using glycine-metal nitrates mixture shown in Fig. 1b. In this case, particles are in the 10-100 nm size range.



Figure 1. TEM micrographs of a)  $\alpha\text{-Al}_2\text{O}_3$  (from urea-nitrate) and b)  $\text{LaCrO}_3$  (from glycine-nitrate)

The temperature at which the precursor spontaneously ignited was affected by the identity of the metal ions present as well as by the fuel to oxidant ratio. Metal ions such as copper, iron, manganese, and chromium that form strong complexes with organic nitrogen tended to decompose and combust at a lower temperature than ions that do not form strong complexes such as strontium and calcium.

A comparison of the dehydration and combustion behavior of the two types of precursors is given in Fig. 2. Precursors containing either copper nitrate or strontium nitrate, plus ammonium dichromate, glycine and water were used to produce  $\text{CuCr}_2\text{O}_4$  or  $\text{SrCr}_2\text{O}_4$ . Both of these precursors were stoichiometric mixtures. Ignition of the precursor containing copper nitrate occurred at 143°C, whereas the mixture containing strontium nitrate ignited at 234°C. The formation of charge transfer complexes between transition metal cations and fuel molecules containing organic nitrogen will result in waters of hydration being displaced [16]. In complexant molecules, metal cations and nitrate will thus be present in close proximity and can easily react. This could also lead to different decomposition paths for the precursor complex and the mixture. For alkaline earth cations such as strontium or calcium where charge transfer complexes were not formed, hydration waters were retained to much higher temperatures and therefore their decomposition and ignition occurs at a higher temperature.

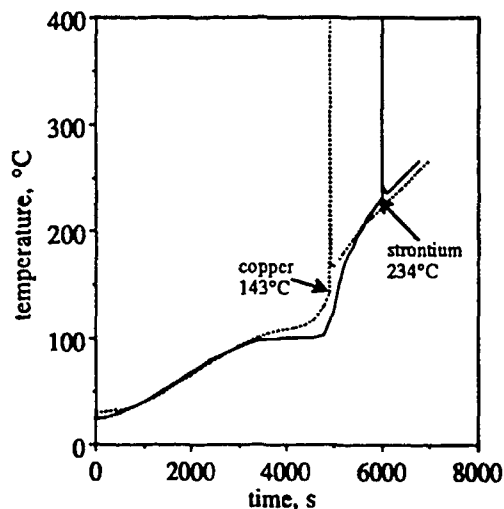


Figure 2. Effect of metal precursors on ignition temperatures

Temperatures of the flame produced during the exothermic combustion of the precursors were influenced by the oxidizer-fuel ratio. Flame temperatures are given as a function of the glycine/nitrate molar ratio in Fig. 3 for aqueous precursors containing glycine, lanthanum nitrate and either chromium nitrate or ammonium dichromate.

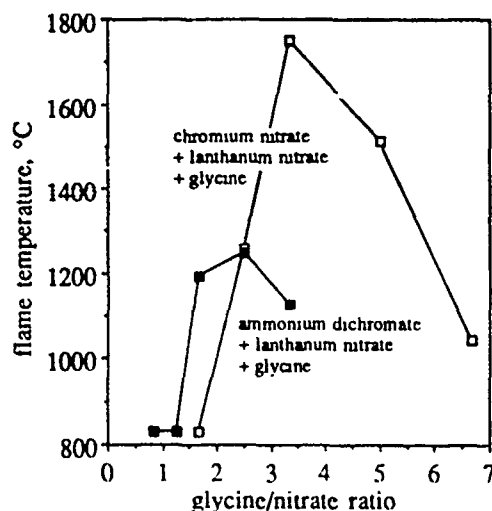


Figure 3. Effect of oxidizer/fuel ratio on flame temperatures

Flame temperatures were consistently highest for stoichiometric oxidizer/fuel mixtures, as expected. In glycine-nitrate mixtures, fuel-rich compositions required additional oxygen from air for complete combustion, while fuel-lean compositions resulted in either incomplete nitrate decomposition or the formation of amorphous ceramic oxides. Ammonium dichromate-containing mixtures, needed less glycine due to the self-redox nature of dichromate during combustion. This results in lower yet sufficiently high flame temperatures to produce crystalline ceramic oxides. Such lowering of flame temperature assists in producing high surface area ceramics (e.g., chromites) for catalytic applications. In contrast, production of certain highly refractory materials such as mullite require higher flame temperatures due to their slower and high-temperature crystallization. For this, the

flame temperatures could be increased by adding ammonium nitrate or ammonium perchlorate, as an extra-oxidizer, and corresponding quantities of fuel to the precursor mixture. Flame temperatures of such mixtures are given in Table II.

Table II. Effect of Extra-Oxidizer in Ceramics Synthesis

Oxidizer-Fuel Mixture	Ceramic Oxide	Flame Temp. (°C)	Surface Area (m <sup>2</sup> /g)	Particle Size (μm)	Ref.
Al nitrate-Urea (1 : 2.5)	$\alpha$ -Al <sub>2</sub> O <sub>3</sub>	1350	8.3	4	1
Al nitrate-Urea-NH <sub>4</sub> NO <sub>3</sub> (1 : 3.5 : 3)	$\alpha$ -Al <sub>2</sub> O <sub>3</sub>	1520	3.2	5	2
Al nitrate-Urea-NH <sub>4</sub> NO <sub>3</sub> (1 : 4.5 : 6)	$\alpha$ -Al <sub>2</sub> O <sub>3</sub>	1800	2.5	6	2
Al nitrate-SiO <sub>2</sub> -Urea (6 : 2 : 15)	Mullite	1275	45.0	2.5	3
Al nitrate-SiO <sub>2</sub> -Urea-NH <sub>4</sub> ClO <sub>4</sub> (6 : 2 : 9.6 : 23)	Mullite	> 1400	12.6	8	3

As flame temperatures increased with extra-oxidizer addition, the product ceramic oxide had decreased surface area and increased particle size. This is due to sintering assisted by the flames produced in these extra-oxidizer containing mixtures, which persist for longer durations (up to few minutes).

Ceramic composites can also be prepared by combustion methods. Second phase crystallites were smaller and more evenly distributed in composites prepared by combustion methods than by conventional techniques. This can be seen in the TEM micrograph of the combustion synthesized 40 wt. % t-ZrO<sub>2</sub>/Al<sub>2</sub>O<sub>3</sub> composite particle given in Fig. 4.

## SUMMARY

A large number of technologically important ceramics have been produced by the use of oxidizer-fuel composition formulated using principles of high energy materials. The oxidizer-fuel ratio, choice of fuel, and inclusion of extra-oxidizers govern both the combustion and powder characteristics. Many propellant compositions with low thrust and fast burning characteristics could be used in future.



Figure 4. TEM micrograph of t-ZrO<sub>2</sub>/Al<sub>2</sub>O<sub>3</sub> composite. Al<sub>2</sub>O<sub>3</sub> (light background) and t-ZrO<sub>2</sub> (dark spots)

## REFERENCES

1. J. J. Kingsley and K. C. Patil, *Materials Letters*, 6(11,12), 427-432 (1988).
2. J. J. Kingsley, Ph. D (Thesis), Indian Institute of Science, 1989.
3. R. Gopi Chandran and K. C. Patil, *Materials Letters*, 10(6), 291-295 (1990).
4. J. J. Kingsley and K. C. Patil, *Ceramic Transactions*, Vol.12, Ceramic Powder Science-III, Ed. G. L. Messing, S. Hirano and H. Hausner (The American Ceramic Society, 1990) pp.217-223.
5. J. J. Kingsley, K. Suresh and K. C. Patil, *J. Mater. Sci.*, 25, 1305-1312 (1990).
6. S. Sundar Manoharan, N. R. S. Kumar, and K. C. Patil, *Mat. Res. Bull.*, 25, 731-738 (1990).
7. R. Gopi Chandran and K. C. Patil, *Materials Letters*, 12, 437-441, (1992).
8. S. Sundar Manoharan and K. C. Patil, *J. Am. Ceram. Soc.*, 75(4), 1012-1015 (1992).
9. K. Suresh, N. R. S. Kumar, and K. C. Patil, *Adv. Mater.*, 3(3), 148-150 (1991).
10. J. J. Kingsley, K. Suresh and K. C. Patil, *J. Solid State Chem.*, 87, 435-442 (1990).
11. L. A. Chick, J. L. Bates, L. R. Pederson and H. E. Kissinger, in: *Proc. 1st. Intern. Symp. on solid Oxide Fuel Cells*, ed. S. C. Singhal (Electrochemical Society, Pennington, NJ, 1989) pp. 170-179.
12. L. A. Chick, L. R. Pederson, G. D. Maupin, J. L. Bates, L. E. Thomas and G. J. Exarhos, *Materials Letters*, 10(1,2), 6-12 (1990).
13. J. Lambert Bates, L. A. Chick and W. J. Weber, *Solid State Ionics*, 52, 235-242 (1992).
14. Bakhman, N. N., *Combust. Explosion. Shock Waves*, 4, 9 (1968).
15. S. R. Jain and K. C. Adiga, *Combustion and Flame*, 40, 71-79 (1981).
16. F. A. Cotton and G. Wilkinson, *Advanced Inorganic Chemistry*, 4th ed., Wiley-Interscience, New York, 1980, p.689.



## INFRARED FIBER OPTIC DIAGNOSTIC FOR SOLID PROPELLANT COMBUSTION

J. WORMHOUDT AND P. L. KEBABIAN

Aerodyne Research, Inc., 45 Manning Road, Billerica, MA 01821

### ABSTRACT

We report on a program to develop and demonstrate a diagnostic technique using infrared fiber optics to probe the decomposition processes in burning gun propellant strands. The present experimental configuration involves measuring the absorption through a small gap between two embedded fibers. The gap can be filled with propellant, or left open to fill with gaseous decomposition products. Spectroscopic detection is presently achieved using pairs of bandpass filters. The absorption record can be correlated with readings from an embedded thermocouple and with a high resolution video recording of the burn. We also report on preliminary experiments in which an electrically heated filament is used to melt the infrared fiber as its transmission and physical appearance are monitored.

The goal of this program is to develop a fast-response probe of solid phase processes which can support the development of a predictive modeling capability for gun propellant combustion. We present examples of data for the atmospheric pressure burning now under investigation. A full assessment of the usefulness of this technique will require further observations and analysis.

### INTRODUCTION

Recently, a study group sponsored by the Army Research Office developed and published an overall basic research plan to guide advanced research on key nitramine propellant ignition and combustion issues which must be addressed to allow the systematic exploitation of this exciting class of energetic materials.<sup>1</sup> Subsequent workshops organized by the Office of Naval Research and the JANNAF Combustion Subcommittee on Nitramine Propellants have further refined the outstanding issues. Our program is a response to a need identified by all these groups, the development of new diagnostic techniques to monitor the progress of decomposition and ignition kinetics in the condensed phase.

There have been very few direct measurements of condensed phase decomposition in burning gun propellants. A technique motivated by recent advances in electro-optical materials which has not been attempted until the present program is the use of embedded optical fibers. We are beginning by investigating the use of infrared fibers in a direct absorption experiment, in which a small gap between a pair of embedded fibers may allow spectroscopic detection of decomposition products within a strand of solid propellant. The components of the experimental apparatus include a chopper-modulated thermal radiation source, a strand burner capable of high pressure operation, a beamsplitter, pairs of bandpass filters, lenses, and infrared detectors, a data acquisition computer, and a synchronized video camera and recorder.

Although ours is the first spectroscopic investigation of the solid phase of burning propellants, it has benefited from a number of related research programs. Infrared absorption has been used to study the decomposition of propellant ingredients, including the nitramines HMX and RDX<sup>2-4</sup> as well as other materials.<sup>5-7</sup> These studies all used Fourier transform infrared spectrometers to measure the changing absorption of thin films of the materials as they underwent rapid heating<sup>2-3</sup> or photolysis by an ultraviolet lamp.<sup>4</sup> In particular, the spectra reported in Reference 2, in which the absorption bands of N<sub>2</sub>O and CO<sub>2</sub> can be seen as these gases accumulate in bubbles forming in confined thin films of HMX and RDX, did much to encourage us in our approach. Other programs providing useful information have included the work by Miller and co-workers on embedding fine-wire thermocouples in burning propellant strands,<sup>8</sup> that by Brewster and co-workers in measuring radiative emission in strand burning using silica optical fibers and near-infrared diode detectors,<sup>9</sup> and the ongoing work at Sandia National Laboratories involving infrared spectra of heated RDX films.<sup>10</sup> This last work deserves particular mention, as we have used their spectra of a 5 micron thick RDX film, aged for 18 hours at 170° C, as a guide to which spectral regions might show larger increases in absorption upon thermal decomposition.

## EXPERIMENTAL TECHNIQUES

The basic approach of the experiment as presently constituted is illustrated by the optical layout shown in Figure 1. The chopping wheel modulates the source and so the transmitted signal at approximately 2000 Hz. The data acquisition computer reads a signal point from each infrared detector at each on and off point of the chopper. Computer data acquisition for each chopper cycle is triggered by the synchronization signal from the commercial chopper controller. The signals from the infrared detectors and pre-amplifiers are passed through buffer amplifiers to minimize the effects of the analog to digital conversion. This also allows optimization of the time response of the signal, so the single data point the computer reads is representative of the entire half-cycle of the chopper. The beginning of data collection is accompanied by a computer signal to the video recorder which starts its time clock.

The strand burner shown in Figure 2 is a copy of a device in use at the U. S. Army Research Laboratory, Aberdeen Proving Ground, with some modifications to accommodate fiber optic feedthroughs. At atmospheric pressure, we find that the strand has a roughly flat burning surface and does not burn down the side with a gas flow through the central inlet composed of 235 STP  $\text{cm}^3/\text{s}$  air and 40 STP  $\text{cm}^3/\text{s}$   $\text{N}_2$ , for a gas velocity around the strand of roughly 3.5 cm/s (the propellant regression rate above the fiber gap is around 180  $\mu\text{m}/\text{s}$ ). The only propellant observed to date has been M39, composed of 75% RDX and 25% binder.

The video system serves two purposes: it records each burn, and (with a different lens) is used as a microscope during fiber insertion. The fiber insertion procedure we have developed involves pressing a groove in one propellant piece using a warmed, stretched wire fixture, positioning the fibers in the groove, inserting a thin slice of propellant in the gap between the fibers if desired, pressing the fibers into the groove using the top propellant piece, and securing the strand with glue across the edges. Figure 3 illustrates the technique.

## EXPERIMENTAL OBSERVATIONS

### Pulsed Fiber Heating Tests

To help us understand our observations of infrared transmission through fibers embedded in burning propellant strands, we set up a test apparatus which allowed us to measure infrared fiber transmission during rapid controlled pulsed heating. This apparatus included the same modulated source, pair of fibers, and filters and infrared detectors used in the propellant studies, and a small section of nichrome ribbon filament connected to a capacitor bank. Data collection began (as in strand burning) with a command to the computer to start reading outputs from the infrared detectors, synchronized with the start of the video clock. The third channel of the computer records the emission of the heating filament as observed by a short-wavelength infrared detector, thus providing a synchronous record of the heat output of the filament.

The major conclusions we have made from these tests to date is that the fibers will transmit well even above their melting point, and that we do not expect heating or melting to affect the relative transmission in different bandpasses. There may be even less effect on the absolute transmission when the fiber is confined, as the strand-embedded fibers are. We expect to continue these tests, including further checking for any effects on the spectral transmission of the fibers due only to heating and melting processes.

### Initial Strand Burning Observations

Figure 4 illustrates the pair of filter bandpasses used in most of the observations to date, superimposed on an absorption spectrum of the bulk M39 propellant. The absorption spectrum was obtained using a 20  $\mu\text{m}$  slice from a strand, and a Fourier transform infrared spectrometer with a resolution of 4  $\text{cm}^{-1}$ . As mentioned above, the choice of filters shown here was based on the observations by the Sandia group of changes in infrared absorption of RDX during slow, low-temperature heating.<sup>10</sup> The 4.6  $\mu\text{m}$  bandpass filter corresponds to a spectral region in which the transmission of their film decreased least (a change of about 0.11 absorbance units for their 5  $\mu\text{m}$  thickness film). The 4.0  $\mu\text{m}$  filter lies in the center of a broad peak in the spectrum of their aged film, which they speculate may be due to nitrile decomposition products. Here, the change in absorbance is 0.15 for the same film, meaning that for a 20  $\mu\text{m}$  slice of RDX the ratio of the two bands would change by 0.85 for the same amount of decomposition.

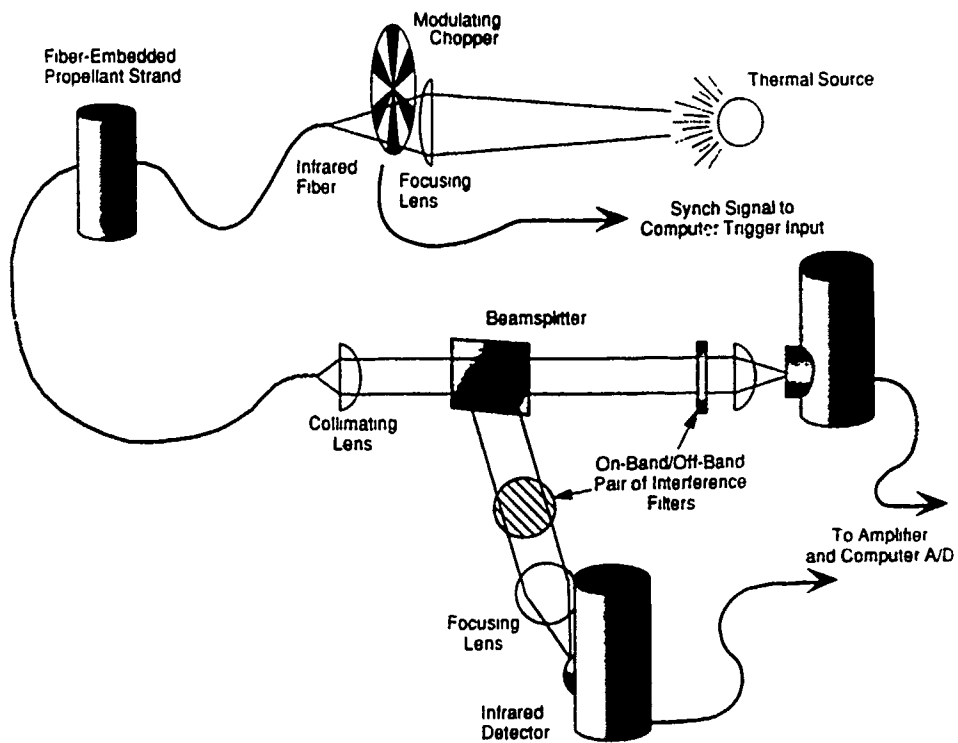


Figure 1. Optical Layout of Infrared Fiber Optic Absorption Experiment

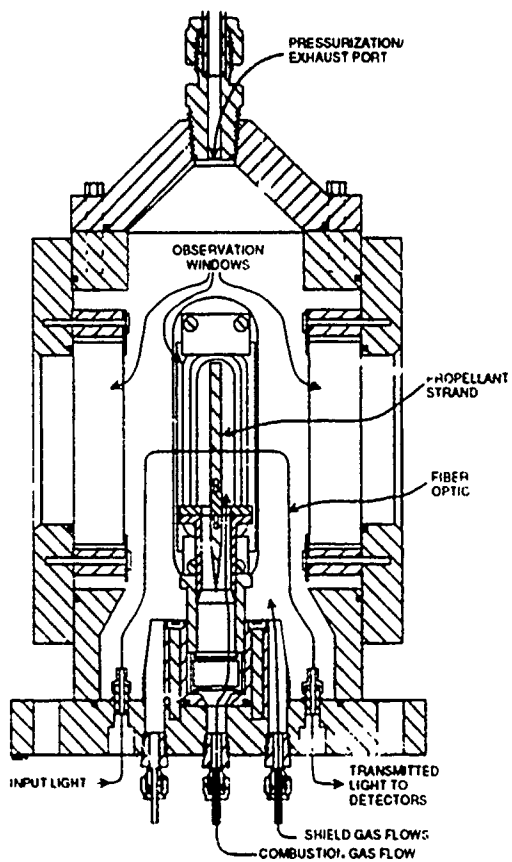


Figure 2. Cross-Section of Strand Burner.

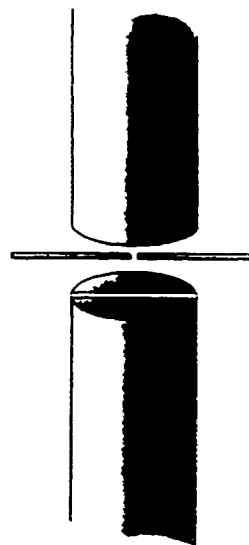


Figure 3. Sketch of Fiber Insertion Procedure

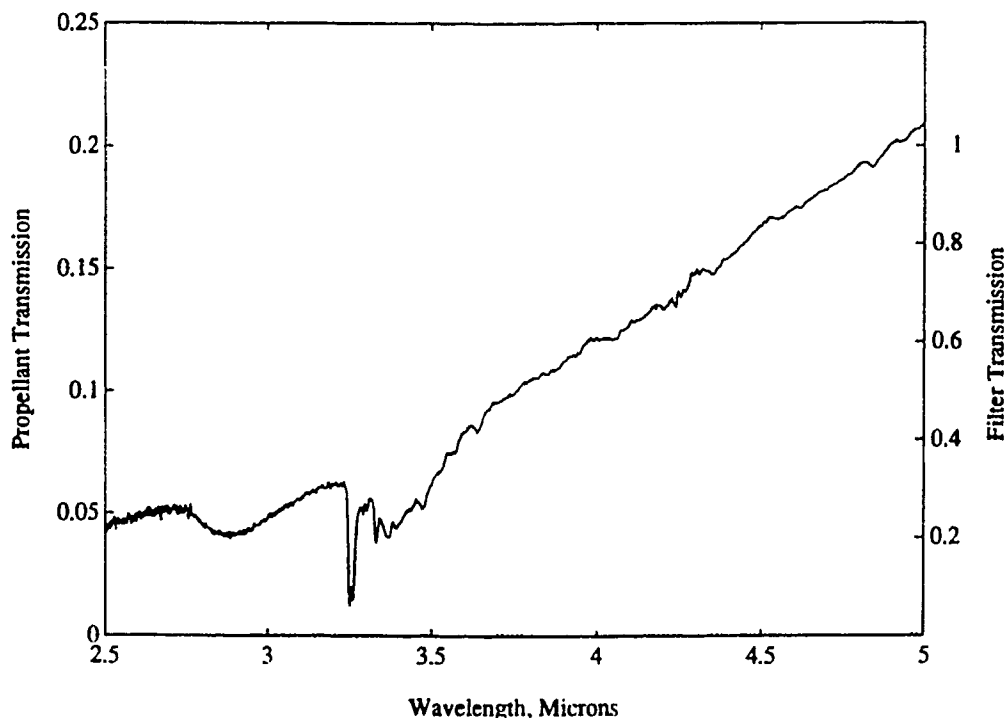


Figure 4. Transmission Spectra of 20  $\mu\text{m}$  Slice of M39 Propellant (Solid Line) and Pair of Bandpass Filters Used in Solid Phase Decomposition Experiments (Dashed Lines).

Figure 5 presents an example of the observations for a burn of a segment of an M39 strand with a slice of propellant approximately 20  $\mu\text{m}$  thick occupying the gap between the fibers. The two filters used are those shown in Figure 4, and Figure 5 presents not only their ratio but the transmitted intensity from one detector and the temperature measured by the embedded thermocouple. Data recording was started when the flame was approximately 1 cm from the fibers.

Up to almost the 25 second point, the temperature increases slowly, the transmitted intensity also increases slowly, and the ratio of the two bandpass intensities remains essentially constant. We interpret this to mean that the physical alignment of the two segments of optical fiber is improving, as the slow heating of the propellant softens it and allows the fibers to move. When the ratio and the transmitted intensity make a simultaneous sharp increase, we infer that at least some of the slice of propellant which was inserted in the gap between the fibers has been removed from the infrared beam, either because of relative motion between the fibers and the solid slice of propellant, or because of melting or dissolution of the slice. As can be seen from Figure 4, a fiber gap containing only air will have a higher 4.1  $\mu\text{m}$  to 4.6  $\mu\text{m}$  ratio than will a gap with inserted propellant. The sudden plunge in intensity, even as the ratio remains in the higher, less-propellant-in-the-gap range, can again be taken as simple physical misalignment of the fibers.

However, the next development, a return of transmitted intensity coupled with a remarkably constant value of a lower ratio, is surprising, and less easy to interpret. Two possibilities suggest themselves: more propellant has found its way into the gap (perhaps by melting), but at the same time the physical alignment has improved so that the transmitted intensity rises; or, roughly the same amount of propellant has in fact suffered the effects of thermal decomposition and changed its spectral characteristics. As noted above, an extrapolation from the Sandia RDX observation would suggest a roughly 15 per cent change in ratio, coupled with a factor of two drop in absolute transmission. Finally, after another loss in intensity, some transmission returns for a last time, with a ratio which is noisier but in the less-propellant-in-the-gap range.

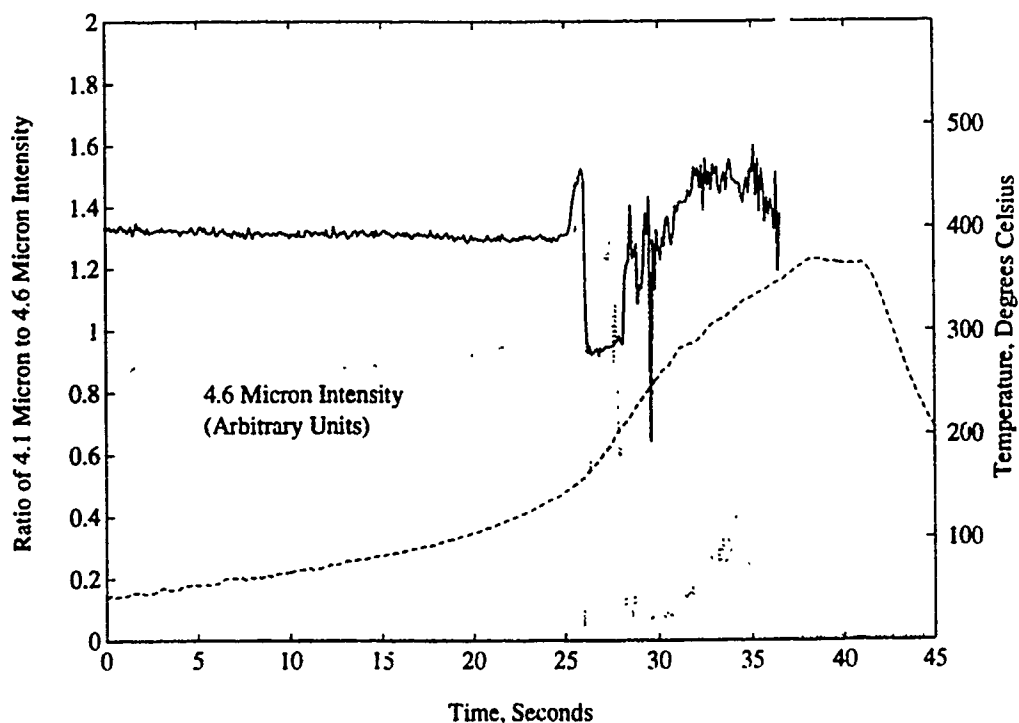


Figure 5. Record of Infrared Transmission in Burning M39 Strand. Solid line is ratio of intensity in  $4.1\ \mu\text{m}$  band to intensity in  $4.6\ \mu\text{m}$  band, dotted line is absolute intensity in  $4.6\ \mu\text{m}$  band, and dashed line is temperature reading of embedded thermocouple.

## CONCLUSIONS

The steps in developing a new diagnostic technology include assembling and operating the apparatus, verifying that the data obtained have an adequate signal to noise ratio and are otherwise free from artifacts, and interpreting the observations in terms of the basic physics and chemistry of the materials studied. We are well into the second of the three steps. To date, we need more observations before we can show that infrared fiber optic measurements can contribute to the understanding of solid phase decomposition processes in burning propellants.

Among the directions we expect to pursue in further work in the near future are strand burning observations using other filter bandpasses, comparison to simulations using electrical heating at a variety of rates, and extensions to other propellants and higher pressures.

## ACKNOWLEDGMENT

This work was sponsored by the U. S. Army Research Office under Contract DAAL03-91-C-0008.

## REFERENCES

1. M. H. Alexander, P. J. Dagdigian, M. E. Jacox, C. E. Kolb, C. F. Mehus, H. Rabitz, M. D. Smooke, and W. Tsang, *Prog. Energy Combust. Sci.* **17**, 263 (1991).
2. R. J. Karpowicz and T. B. Brill, *Comb. Flame* **56**, 317 (1984).
3. P. J. Miller, S. Block and G. J. Piermarini, *Comb. Flame* **83**, 174 (1991).

4. J. P. Toscano and M. McBride, Yale University, private communication, 1989.
5. Y. Oyumi and T. B. Brill, J. Phys. Chem. 91, 3657 (1987), and references therein.
6. G. J. Piermarini, S. Block and P. J. Miller, J. Phys. Chem. 91, 3872 (1987).
7. T. B. Brill, Prog. Energy and Comb. Sci. 18, 91 (1992).
8. M. Miller, U. S. Army Research Laboratory, Aberdeen Proving Ground, private communication, 1991.
9. A. Ishihara, M. Q. Brewster, T. A. Sheridan and H. Krier, Comb. Flame 84, 141 (1991).
10. K. L. Erickson, W. M. Trott, and A. M. Renlund, "Use of Thin-Film Samples to Study Thermal Decomposition of Explosives", paper presented at 18th International Pyrotechnics Seminar, Breckenridge, CO, 13-17 July, 1992.

## LASER-BASED SENSITIVE DETECTION OF ENERGETIC MATERIALS

G.W. LEMIRE<sup>\*</sup>, J.B. SIMEONSSON<sup>\*</sup>, and R.C. SAUSA<sup>\*\*</sup>

*US Army Research Laboratory, AMSRL-WT-PC, Aberdeen Proving Ground, MD 21005*

<sup>\*</sup>NRC/ARL Postdoctoral Research Associate

<sup>\*\*</sup>To whom correspondence should be addressed

### ABSTRACT

The development of a novel technique for sensing trace vapors of  $-NO_2$  containing compounds is reported. This technique is based on the use of one laser operating at 226 nm to both photofragment the target molecule and detect the characteristic NO fragment, formed from a rapid predissociation of  $NO_2$ , by resonance-enhanced multiphoton ionization (REMPI) via its  $A^2\Sigma^+ - X^2\Pi$  (0,0) band origin. The analytical utility of this technique is demonstrated on a number of compounds, including dimethylnitramine, nitromethane, nitrobenzene, TNT, and RDX, employing molecular beam sampling with time-of-flight mass spectrometric analysis of the jet cooled analyte seeded in an atmosphere of buffer gas. For RDX and TNT, a detection limit of 8 and 24 ppb, respectively, is demonstrated using a laser energy of 100 microjoules/pulse.

### INTRODUCTION

The development of laser-based, analytical sensors for the rapid detection and monitoring of trace atmospheric vapors in real-time has been of great interest in recent years.<sup>1-3</sup> Environmental issues pertaining to pollution prevention and compliance have been important driving forces behind this development. Another important related issue deals with the detection of trace atmospheric vapors of energetic materials such as explosives and propellants. This is not surprising given the potential civilian and military applications for these developing technologies in aviation security, and anti-terrorist and demilitarization actions.

Ultraviolet-visible (UV) spectroscopic techniques can at times provide very specific and sensitive methods of detection. However, large molecules are in general more difficult to detect spectroscopically due to the lack of distinguishing structure in their absorption or emission spectra. In addition, large fragile molecules tend to predissociate when irradiated with UV radiation as is the case for most energetic materials. An alternate approach to detecting large fragile molecules is based on the use of UV laser radiation to photodissociate the parent molecules into characteristic fragments for detection.

Characteristic of many energetic materials is the presence of one or more  $-NO_2$  functional groups bonded to either a carbon or nitrogen atom. This functional group is weakly bound to the main skeletal portion of the molecule by approximately 40–50 kcal/mole, depending on the molecule, and is responsible for the weak and structureless absorption feature observed in the UV near 230 nm.<sup>4,5</sup> A perusal of the literature reveals that the UV laser photodissociation of energetic molecules, such as 1,3,5-trinitrohexahydro 1,3,5-triazine (RDX),<sup>6</sup> and model compounds,<sup>7,8,9</sup> under collision-free conditions, results in the production of  $NO_2$  in the initial step in the photolysis. Two common laser-based spectroscopic methods of detecting  $NO_2$  are by LIF and from its prompt emission.<sup>6,7,9</sup> However, both of these methods are very inefficient since the absorbed radiation is radiated over a large spectral region, visible to near infrared. The radiative lifetime for these transitions is also very large, typically ~ 50–120  $\mu$ sec,<sup>10</sup> and is indicative of a weak oscillator strength. Moreover, predissociation to  $NO + O$  predominates over fluorescence at wavelengths less than 400 nm. The NO fragment is better suited for detection since it is readily formed from the predissociation<sup>11,12</sup> of  $NO_2$  and its radiative

lifetime<sup>13</sup> (~ 200 nsec) is significantly shorter than the NO<sub>2</sub> states excited in the visible region. The NO fragment can be detected with a high degree of sensitivity and selectivity by (1+1) REMPI and/or LIF via its A<sup>2</sup>Σ<sup>+</sup> - X<sup>2</sup>Π transition near 226 nm. Thus, one laser can be used for both parent photofragmentation through its structureless UV absorption feature and NO detection.

In this paper, we report on a novel laser photodissociation/NO fragment detection technique to monitor various nitrocompounds. This technique is coupled with pulsed molecular beam (MB) sampling and time-of-flight (TOF) mass spectrometric analysis for increased sensitivity and selectivity. Limits of detection of the nitrocompounds studied are reported and discussed.

## EXPERIMENTAL

The experimental apparatus employed in these studies consists of a MB/TOF apparatus constructed with two main chambers. The first chamber consists of an eight inch Tee pumped out through the bottom of the Tee by a 1000 liter per second turbo molecular pump (Leybold-Heraeus, TurboVac 1000). At the rear of the Tee is a pulsed supersonic valve (R.M. Jordan Co., PSV). At the front of the Tee is mounted an eight inch 4-way cross serving as the second chamber. These two chambers are differentially pumped and are separated by a skimmer with a 3 mm orifice (Beam Dynamics, Inc., Model 2). Mounted on the top of the cross chamber is a commercial time-of-flight mass spectrometer (R.M. Jordan Co.) with a one meter reflectron.

The TOF mass spectrometer distinguishes ions of different masses by their different arrival times to the detector located at the end of the flight tube. Although the time of arrival of the ions depends on the sum of the transit times through various regions of the mass spectrometer, it is proportional to the square root of the mass-to-charge ratio of each ion<sup>14,15</sup>. Therefore, the time of arrival,  $t_1$ , of mass  $m_1$ , is related to the time of arrival,  $t_2$ , of mass,  $m_2$ , by,

$$m_1/m_2 = t_1^2/t_2^2. \quad (1)$$

The determination of any mass,  $m_2$ , may be made with an accurate measurement of  $t_1$  for a known mass,  $m_1$ . In this study NO was used for the calibration of the mass spectra. For a typical set of operating conditions, an acceleration voltage of approximately 2000V (1eV =  $1.60 \times 10^{-12}$  g·cm<sup>2</sup>/sec<sup>2</sup>) and a flight length of two meters, a complete mass spectrum up to a mass of 500 AMU (1amu =  $1.67 \times 10^{-24}$  g) could be recorded in approximately 72 μsec.

Samples of nitromethane (Aldrich), nitrobenzene and TNT (Eastman-Kodak), and DMNA and RDX (ARDEC) were selected for this study. For safety precautions, samples of trinitrotoluene (TNT) and RDX were handled in aliquots of less than 10 mg in a static and shock free environment. All the samples were used without further purification and were introduced into the analysis chamber in a pulsed molecular beam. The vapors of the analytes were seeded in an atmospheric pressure of air (Potomac), nitrogen (Matheson), or argon (BRL) gas, and the mixture expanded into the analysis chamber using a pulsed valve (10 Hz) with a 0.5 mm diameter nozzle. Although the valve has the capability of being heated to temperatures as high as 1000 °C, it was operated at room temperature for all the samples studied, except RDX and TNT. In the case of RDX and TNT, the samples were heated to approximately 100 °C during analysis. A temperature difference of ± 10 °C results in an uncertainty in the vapor pressure determination which would effect the sensitivity measurements by a factor of two. Standard mixtures used to determine the sensitivity were prepared by serial dilution of 0.1% NO/Ar (Matheson), 570 ppm Cl<sub>2</sub>NO<sub>2</sub>/Ar, and 131 ppm



DMNA/Ar. The  $\text{NO}_2$  sensitivity was determined using a 6.2 ppm  $\text{NO}_2$ /air (Scott-Marrin). Sensitivity measurements for nitrobenzene at room temperature, as well as TNT and RDX at 100 °C, were obtained by using Ar mixtures containing the analytes at their respective vapor pressures.<sup>16,17</sup>

The samples were photolyzed and the NO fragment subsequently ionized using focused ( $f=250$  mm or 500 mm lenses) UV radiation near 226 nm. An excimer pumped dye laser (Lumonics Hyper EX-400 and Hyper DYE-300) with second harmonic generator (Lumonics TRAK-1000) operated at 10 Hz was used to generate the tunable UV radiation. Pulsed energies of the order of 10–150  $\mu\text{J}$  with duration of 15–20 nsec were employed for detection. The linewidth of the tunable UV radiation is approximately 0.16  $\text{cm}^{-1}$  (fwhm). Ion signals were directed into a gated integrator (Stanford Research Systems) and were displayed and monitored in real-time on a 125 MHz digital oscilloscope (LeCroy 9400). A PC-AT computer was employed for data acquisition and analysis.

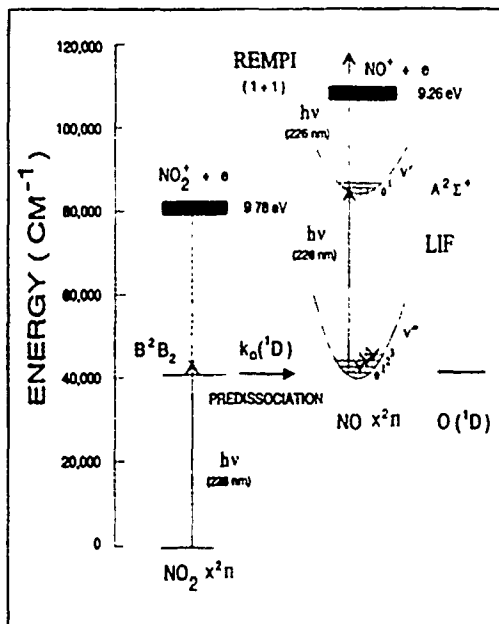
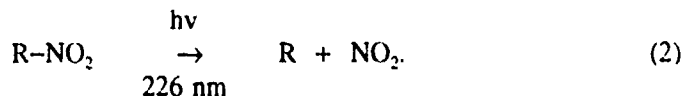


Figure 1. Potential energy diagram of  $\text{NO}_2$  and NO showing the multiphoton scheme

## RESULTS/DISCUSSION

A cursory inspection of most energetic materials reveals that these compounds contain one or more weakly bound  $-\text{NO}_2$  functional groups. The physical processes underlying our approach to the detection of nitrocompounds may be understood by referring to Figure 1 which shows potential level diagrams of  $\text{NO}_2$  and NO. The target molecule ( $\text{R}-\text{NO}_2$ ) is first photolyzed to  $\text{NO}_2$ , along with its corresponding companion radical (R), via the process



The  $\text{NO}_2$  fragment is then detected by monitoring its predissociative product NO using (1+1) REMPI employing its  $\text{A}^2\Sigma^+ - \text{X}^2\Pi$  (0.0) band at 226 nm. This mechanism is similar to that described by Moss and coworkers<sup>8</sup> in a recent paper on the photodissociation dynamics of nitromethane using a two laser pump-and-probe technique. However, in the present results the photolysis wavelength was chosen to coincide with the maximum signal associated with the A-X (0.0) transition in NO, and is generalized to all  $-\text{NO}_2$  containing compounds.

Presented in Figure 2 is a typical mass spectrum obtained when photolyzing DMNA seeded in argon. DMNA was studied since it is a simple analogue of cyclic nitramines such as RDX. This spectrum is characteristic of all the compounds studied. It reveals a prominent peak whose arrival time to the detector is measured as 23.2  $\mu\text{sec}$ . This time corresponds to a mass-to-charge ratio ( $m/z$ ) of 30 and is attributed to the  $\text{NO}^+$  ion. Similar results were obtained when using air or nitrogen as the carrier gas. No such peak was observed, however, when the laser was tuned to an off-resonance transition. The observed peak is void of any interference and is clearly a result of a REMPI process.

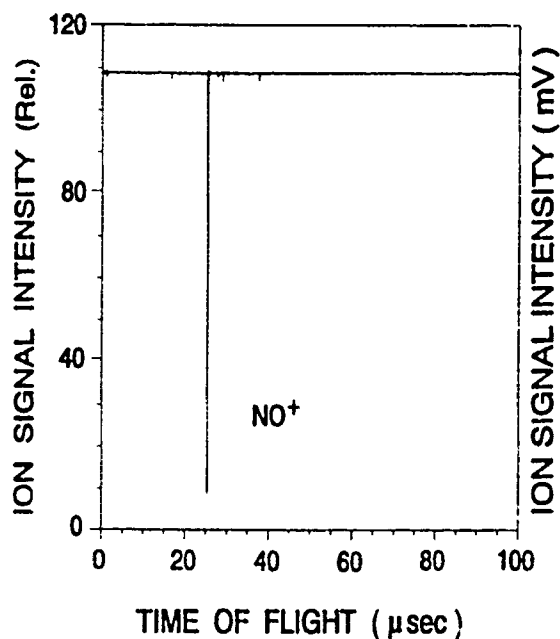


Figure 2 Time-of-flight REMPI mass spectrum of  $\text{NO}^+$  generated from DMNA

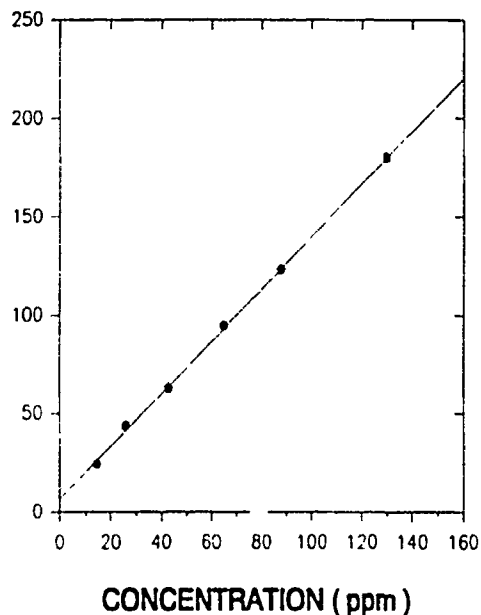


Figure 3. Concentration dependence of the REMPI  $\text{NO}^+$  ion signal obtained from a molecular beam of DMNA. The solid line is a least squares fit of the data (o) with 95% confidence (...)

A plot of the NO REMPI signal intensity as a function of concentration of the precursor molecule, DMNA, is shown in Figure 3. The plot is linear and has a slope of  $1.34 \pm 0.04$  mV/ppm (2SD). A limit of detection of 450 ppb is obtained when using a background noise value of 200  $\mu\text{V}$ . Detection limits are defined in this study as the concentration,  $C_L$  (ppb), that produces a signal, (mV), equal to three times the standard deviation,  $\sigma$  (mV), of the background divided by the sensitivity,  $S$  (mV/ppb), of the method to the compound. The linearity of the plot implies that the NO is formed in a collision-free environment, as expected in a molecular beam, and that this technique is suitable for quantification purposes. The dynamic range of measurements in these studies is limited to about two orders of magnitude due to the limited accuracy of the flow meters used for dilution at low concentration and low vapor pressures of the compounds at high concentrations. However, it is reasonable to anticipate that the method is linear in its response all the way to the detection limit. Indeed, similar studies of NO by REMPI methods have shown the capacity for single ion detection in combination with a large dynamic range of sensitivities.<sup>1b</sup>

Presented in Table I are limits of detection for the compounds studied employing the fragmentation/REMPI technique using 226 nm radiation. The limits of detection refer to the gas concentration of the analyte prior to introduction into the analysis chamber. Vapor pressures of the compounds were obtained from references 16 and 17 and used to estimate the initial concentrations. For one atmosphere of backing pressure, the calculated gas volume throughput of the supersonic nozzle (per pulse) is 6.8 torr-cm<sup>3</sup>. This corresponds to absolute detection limits of 1 and 3 pg for PDX and TNT, respectively and compares favorably with absolute detection limits reported for TNT which are on the order of 200 pg.<sup>19</sup> For nitroethane, Schendel and coworkers<sup>20</sup> reported a concentration detection limit of  $4.2 \times 10^9$  per cc by monitoring the prompt emission resulting from approximately 30 mJ/pulse of ArF laser excitation. A detection limit of 1 ppm in this study corresponds to a concentration of approximately  $6 \times 10^9$  per cc in the probe region of the laser.

The limits of detection for the precursors depend on a number of factors such as the efficiency of sample introduction, the laser pulse energy, the efficiency in the photo-dissociative pathways leading to the formation of NO in its  $X^2\Pi$  ( $v''=0$ ) vibronic state, and the voltage settings of the ion optics and detector. Although the experimental system used for these studies was optimized with respect to these factors in order to obtain the maximum sensitivity possible, the current design of the experimental system could be improved for performing trace analysis. Significant improvements in the sensitivity can be expected with higher laser energies and with a supersonic valve/sampling device whose design increases the sample throughput into the photolysis region. The ability to operate the valve at a higher repetition rate ( $> 50$  Hz) and at elevated temperatures, in order to eliminate condensation of the precursor, would also be desirable.

In the present studies, the experimental conditions were identical for all of the compounds. Thus, any differences shown in

Table I are indicative of different absorption cross sections that the target molecules have at 226 nm and the photodissociation efficiency. It is clear from Table I, that RDX, TNT, and  $\text{NO}_2$  are particularly efficient in generating REMPI signals. In the case of  $\text{NO}_2$ , this was not too surprising since Morrison and coworkers<sup>11,12</sup> observed that by far the most prominent ion fragment generated by the multiphoton excitation of  $\text{NO}_2$  at wavelengths in the region from 425 to 455 nm was the  $\text{NO}^+$ . Their data suggest that the course of excitation in this system is dominated by predissociation into  $\text{NO}(^2\Pi) + \text{O}(^1\text{D})$  at the level of the second photon within the B ( $^2\text{B}_2$ ) state. They contend that this high energy dissociation pathway becomes important soon after this channel becomes energetically accessible. With 226 nm excitation, this pathway is in fact available by a single photon absorption.

As noted earlier, the measured REMPI signals depend on several factors. One compound, DMNA, was chosen to investigate the dependence of the signal on the laser pulse energy. The dependence of ion signal intensity on laser energy was determined using the equation,

$$S = C(I_{226})^n \quad (3)$$

where  $S$  is the ion signal intensity,  $I_{226}$  is the laser beam fluence,  $C$  is a system-dependent constant, and  $n$  the number of photons required to produce the  $\text{NO}^+$  signal. The value of  $n$  was determined from the slope of a log-log plot. *A priori*, one might expect the value of  $n$  to be as high as four, two photons required to generate NO in its  $X^2\Pi$  state and two photons to ionize it. However, the slope of the plot yielded a value of  $n = 1.62 \pm .01$  (2SD) indicating that the formation of the ion requires at least two photons. This near quadratic dependence suggests that one or more of the intermediate photochemical steps necessary to generate  $\text{NO}^+$  from  $\text{R-NO}_2$  is saturated. It also suggests that a significant enhancement in the signal can be

Table I. Limits of detection for compounds studied.

Compound	Limit of Detection (ppb)
NO	8
$\text{NO}_2$	240
$\text{CH}_3\text{NO}_2$	1000
DMNA	450 (2000) <sup>a</sup>
RDX	8
TNT	24
Nitrobenzene	2400
<sup>a</sup> Limit of detection obtained by laser-induced fluorescence of NO via its $A^2\Sigma^+ - X^2\Pi$ (0,0) transition.	

achieved at higher laser intensities.

## SUMMARY/CONCLUSION

A novel technique for the detection of trace  $\text{-NO}_2$  containing compounds has been developed for the purpose of detecting energetic materials such as propellants and explosives. It employs one laser operating at 226 nm and is based on the photofragmentation of the target molecule with subsequent detection of NO by REMPI via its  $A^2\Sigma^+ - X^2\Pi$  (0,0) band origin. The analytical utility has been demonstrated on a number of compounds, including  $\text{NO}_2$ , DMNA, TNT, and RDX using a molecular beam, time-of-flight apparatus. Detection limits in the ppb were shown for RDX and TNT with extremely low laser energies,  $\sim 100 \mu\text{J/pulse}$ . Lower limits of detection are, however, projected by employing an improved system design and higher laser energies.

## ACKNOWLEDGEMENTS

We thank Drs. S Balusu (ARDEC) and Pesce-Rodriguez (WTD) for providing us with some of the sample compounds and Dr. Miziolek for review of the manuscript. Support from the BRL/NRC Postdoctoral Research Program (GWL & JBS), the ARL Combustion Research Mission Program (RCS), and the PIF/OSD Capital Investment Program (RCS) is gratefully acknowledged.

## REFERENCES

1. J. Zhu, D. Lustig, I.S. Sofer, and D.M. Lubman, *Anal. Chem.* **62**, 2225 (1990).
2. A. Feinberg, *Science*, **255**, 1531 (1992).
3. J.A. Syage, J.E. Pollard, and R.B. Cohen, Technical Report-SD-TR-88-13, Space Division Air Force Systems Command (February 1988).
4. M.J. McQuaid and R.C. Sausa, *Appl. Spectrosc.* **45**, 916 (1991).
5. K.J. Smit, *J. Energ. Mater.* **9**, 81 (1991).
6. C. Capellos, P. Papagiannakopoulos, and Y. Liang, *Chem. Phys. Lett.* **164**, 533 (1989).
7. M.J. McQuaid, A.W. Miziolek, R.C. Sausa, and C.N. Merrow, *J. Phys. Chem.* **95**, 2713 (1991).
8. D.B. Moss, K.A. Trentelman, and P.L. Houston, *J. Chem. Phys.* **96**, 237, (1992) and references therein.
9. J.C. Mialocq and J.C. Stephenson, *Chem. Phys. Lett.* **123**, 390 (1986).
10. V.M. Donnelly and F. Kaufman, *J. Chem. Phys.* **69**, 1456 (1978).
11. R.J.S. Morrison and E.R. Grant, *J. Chem. Phys.* **77**, 5994 (1982).
12. R.J.S. Morrison, B.H. Rockney, and E.R. Grant, *J. Chem. Phys.* **75**, 2643 (1981).
13. G.B. McKendrick, C. Fotakis, and R.J. Donovan, *J. Photochemistry*, **20**, 175 (1982).
14. W.C. Wiley and I.H. McLaren, *Rev. Sci. Instrum.* **26**, 1150 (1955).
15. V.I. Karataev, B.A. Mamyrin, and D.V. Shmikk, *Sov. Phys. Tech. Phys.* **16**, 1177 (1972).
16. *Handbook of Chemistry and Physics*, 66th ed. (CRC Pres, Inc., Boca Raton, Florida, 1986) pp. D196-D212.
17. *Lawrence Livermore National Laboratory Explosives Handbook: Properties of Chemical Explosives and Explosives Simulants*, edited by B.M. Dobratz, LLNL Report UCRL 52997, (March 1981).
18. J.C. Miller, *Anal. Chem.* **58**, 1702 (1986).
19. S.D. Huang, L. Kolaitis, and D.M. Lubman, *Appl. Spectrosc.* **41**, 1371 (1987).
20. J. Schendel, R. Hohmann, and E.L. Wehry, *Appl. Spectrosc.* **41**, 640 (1987).

## SHOCKED ENERGETIC MOLECULAR MATERIALS: CHEMICAL REACTION INITIATION AND HOT SPOT FORMATION

M. D. Fayer\*, Andrei Tokmakoff\*, and Dana D. Dlott\*\*

\*Department of Chemistry, Stanford University, Stanford, CA 94305

\*\*School of Chemical Sciences, University of Illinois at Urbana-Champaign, Urbana, IL 61801

### ABSTRACT

A theoretical model is developed to describe multiphonon up-pumping of internal vibrations. The dominant mechanism for up-pumping is anharmonic coupling of excited phonon modes with low frequency molecular vibrations, termed doorway modes. Quantitative calculations were performed which show the extent and rate of multiphonon up-pumping caused by shock excitation. The time dependence of chemical reactivity behind the front is calculated using reaction rate laws for the decomposition of nitramine explosives. A mechanism for hot spot formation, based on defect induced local increases in anharmonic coupling, is discussed.

Shock-initiated molecular reactions require transfer of substantial amounts of mechanical energy from the shock front to the internal vibrational states of the molecules.<sup>1-6</sup> This process is termed multiphonon up-pumping. The energy from the shock deposited in the external phonon modes is transferred to the internal vibrational degrees of freedom of a molecule, heating them to a temperature at which a chemical bond can be broken. The dynamics in this type of system involve the complex interplay of phenomena operating on a variety of time and distance scales.

During the 1980's, several authors recognized the importance of multiphonon up-pumping in energetic materials, and attempts were made to calculate the rate of vibrational up-pumping in nitromethane and in nitramines such as RDX.<sup>1,3,8</sup> The time scales calculated by these authors for the excitation of molecular vibrations by shock induced up-pumping were surprisingly long, ranging from a few tens of ns<sup>3</sup> to hundreds of ns.<sup>8</sup> The inefficiency of up-pumping was attributed to the large gap between the highest phonon frequency and the frequency of molecular vibrations. This gap necessitated a high order multiphonon pump mechanism. These treatments gave rise to much speculation about the relationship between proposed "vibration-starved" molecules behind the front and various experimental observations, such as the rather slow reaction rate constant for the overall formation of the detonation products,<sup>1,9</sup> and the induction period which precedes detonation.<sup>8</sup>

In contrast, recent experimental studies of the flow of vibrational energy into or out of large organic molecular solids showed that these processes were far more efficient than predicted previously. In fact, they occur on the 10 to 100 ps time scale.<sup>5,10-12</sup> Studies on molecular crystals have revealed the existence of a mechanism for up-pumping<sup>5</sup> which is much more efficient than the high order processes considered previously. It was shown that the relatively low frequency, large amplitude vibrations in large molecules can be excited readily via a low order anharmonic coupling process, typically two-phonon absorption. Once these vibrations, termed *doorway modes*, become excited, a variety of efficient intramolecular vibrational redistribution (IVR) processes come into play, redistributing energy from the excited doorway modes to the other internal vibrations. A fundamental conclusion of these studies is that multiphonon up-pumping occurs on a tens of picosecond time-scale, approximately at the rate of doorway mode excitation. Due to efficient IVR processes,

the internal vibrational states of up pumped molecules are unlikely to deviate much from a thermal (Boltzmann) population distribution<sup>5,10,12</sup>

The shock front has a finite rise time, in which the mechanical energy of the shock is transferred to and equilibrates among the phonon modes. Typically, the rise of the front extends over a few nm, corresponding to a rise time of  $\sim 1$  ps<sup>1,4</sup>. In this phonon-rich zone the molecular vibrations have yet to be excited. Behind the shock front, in the up-pumping zone, the energy in the phonon modes is transferred to the vibrations by multiphonon up-pumping processes, and the two baths equilibrate within  $\sim 10^{-10}$  s ( $10^{-7}$  m). As the vibrational modes are excited, reactivity is enhanced and bond breaking due to thermal decomposition occurs in the molecules. This is the ignition zone and extends to  $\sim 10^{-9}$  s ( $10^{-6}$  m) behind the shock front. In energetic materials, endothermic bond breaking reactions are the precursors to detonation, a series of exothermic chain reactions occurring in a reaction zone  $10^{-8}$ - $10^{-6}$  s ( $10^{-5}$ - $10^{-3}$  m) behind the front.<sup>7,13</sup>

The model<sup>5</sup> describes the dynamics of the processes behind the shock front in terms of quasitemperatures  $\theta$ . A quasitemperature is used to characterize the state of a particular collection of degrees of freedom in a situation in which the entire system is not in thermal equilibrium. Initially, the phonon and vibrational quasitemperatures are equilibrated at the ambient temperature,  $\theta_{ph} = \theta_{vib} = T_0$ . At  $t = 0$  the shock is applied and the mechanical energy is quickly deposited exclusively in the external modes. This corresponds to an initial condition where the phonon quasitemperature  $\theta_{ph}(0) \gg T_0$ , but the vibrational quasitemperature  $\theta_{vib}(0) = T_0$ . In the up-pumping zone,  $\theta_{vib}$  increases while  $\theta_{ph}$  decreases, leading to an eventual equilibration of internal and external degrees of freedom at  $\theta_{ph} = \theta_{vib} = T_1$ .

Because of the rapid increase in  $\theta_{vib}$  in the up-pumping zone, the chemical reactivity of the shocked solid increases dramatically. Initial reactions will involve endothermic, unimolecular bond cleavage to form a variety of reactive species. Significant release of chemical energy demands a large local concentration of fuel molecules. With weak shocks, the probability of a chemical reaction occurring in the bulk material is small, and reacted molecules are isolated from each other. Under these circumstances, ignition cannot occur.

It has been suggested by many workers that sub-threshold ignition of energetic materials involves the generation of hot spots.<sup>1,14,15</sup> Although the actual mechanism of hot spot formation has not been experimentally determined, a variety of mechanisms have been proposed for the formation of hot spots, including adiabatic compression of trapped gas in voids, friction involving sliding or impacting surfaces, shear band formation caused by mechanical failure, sparks, triboluminescence, and heating at crack tips<sup>21,16-18</sup>.

The presence of conditions far from equilibrium in the up-pumping zone suggests a fundamentally new mechanism for the formation of hot spots that does not require material failure or plastic deformation. The presence of defects in the up-pumping zone can lead to a local increase in the anharmonic coupling between the hot phonon bath and the molecular doorway modes.<sup>5</sup> The increased anharmonic coupling enhances the effects of up-pumping in a defect-perturbed domain (DPD), which may be larger than the defect itself.<sup>19,20</sup> This leads to the formation of a transient hot spot behind the front, by causing the DPD vibrational quasitemperature,  $\theta_d$ , to momentarily over shoot the final temperature,  $T_1$ . Since the likelihood of a bond-breaking reaction is highly sensitive to the vibrational quasitemperature, a concentrated cluster of reacting and reacted molecules can be formed near the defect. The local high concentration of initial reactions and reaction products provides ideal conditions for the onset of exothermic reactions. Whether the reaction spreads or dies out depends on the peak temperature and size of the hot spot.<sup>18,21,22</sup> The DPDs, which have elevated vibrational quasitemperatures, a high concentration of reacted molecules, and a volume

greater than the defect itself, can form hot spots which lead to ignition. Individual molecules outside a DPD may react; however, under relatively weak shock conditions, the presence of these scattered reaction sites does not favor exothermic reactions, and they are too small to ignite the surroundings

We have performed quantitative calculations based on a model of the processes described briefly above. The full description of these calculations is beyond the scope of this paper. They will be described in detail elsewhere.<sup>5a</sup> The results lead to straightforward predictions regarding the structure of the nonequilibrium layers behind the front and the conditions required for ignition. The multiphonon up-pumping rate is calculated, and its pressure dependence is obtained. The time dependent molecular vibrational temperature is used to calculate the time dependence of the chemical reaction probability and its pressure dependence. The mechanism for anharmonic defect hot spot formation is introduced, the time dependence of up-pumping at DPDs is calculated, and the influence of hot spot formation on chemical reactivity is demonstrated.

The results of calculations for shock compression of naphthalene are shown in Figure 1. Naphthalene is used as an example since the necessary parameters involving both phonons and internal molecular vibrations are known for naphthalene. The compression ratio is  $V_1/V_0 = 0.80$ , corresponding to a shock pressure of 4.7 GPa. In Figure 1, the phonons cool down from an initial state  $\theta_{ph}(0) \approx 2500\text{K}$  to a final state  $\theta_{ph} = T_1 \approx 760\text{K}$ . The vibrations heat up from an initial state  $\theta_{vib}(0) = T_0 = 300\text{K}$  to a final state  $\theta_{vib} = T_1 \approx 760\text{K}$ . One of the important features of this model is the significant disparity in cooling rates. The rate constant for phonon cooling,  $\kappa/C_{ph}$ , is much larger than the rate constant for vibrational heating,  $\kappa/C_{vib}$ , because  $C_{vib} > C_{ph}$ , where  $C_{vib}$  and  $C_{ph}$  are the vibrational and phonon heat capacities respectively. The figure shows that the time scale for multiphonon up-pumping is a few tens of ps. Most of the rapid rise in vibrational quasitemperature is complete by 30 ps, and the system has reached the thermal equilibrium temperature,  $T_1$ ,

by approximately 70 ps. A smaller compression ratio (stronger shock) results in a higher initial phonon quasitemperature and a higher final vibrational temperature. However, independent of the strength of the shock, most of the rise of the vibrational quasitemperature occurs in 30 ps, and thermal equilibrium is reached in approximately twice this time. The details of the time dependencies calculated here depend on the naphthalene parameters used in the calculations. However, for molecular solids as large or larger than naphthalene, such

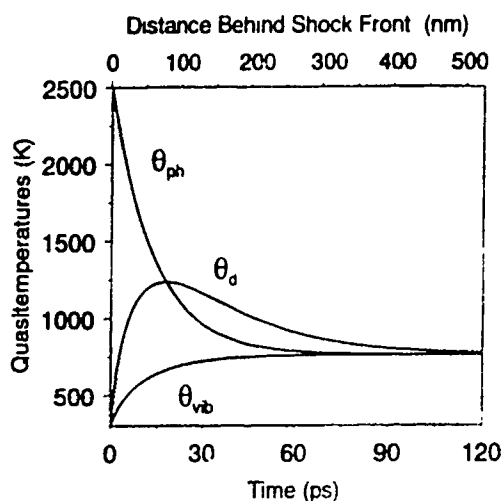


**Figure 1** Time dependence of the phonon quasitemperature,  $q_{ph}$ , the bulk vibrational quasitemperature,  $q_{vib}$ , and the defect perturbed domain vibrational quasitemperature,  $q_d$ , for a shock compression ratio  $V_1/V_0 = 0.80$  ( $p = 4.7$  GPa) and a DPD anharmonic enhancement  $\xi = 2$ . The greater anharmonic coupling in the DPD causes its vibrations to come into equilibrium with the hot phonons faster than the bulk vibrations, producing a temporary temperature overshoot and a transient hot spot.

as HMX, the results should not vary by more than a factor of two from those presented in Figures 1.5a

In a DPD the vibrations are pumped by the phonons faster than the bulk vibrations, so the DPD vibrational quasitemperature,  $\theta_d$ , will overshoot the bulk vibrational quasitemperature  $\theta_{vib}$ . The rapid phonon equilibration will maintain the DPD phonon quasitemperature at the bulk value although  $\theta_d$  exceeds  $\theta_{vib}$ .

Two factors determine the peak DPD vibrational quasitemperature: the shock compression ratio  $V_1/V_0$ , and the defect enhancement factor  $\xi$ .  $\xi$  is the ratio of the DPD anharmonic coupling to the bulk anharmonic coupling of phonons to the doorway modes. A typical calculation of the three quasitemperatures is shown in Figure 1 for  $V_1/V_0 = 0.8$  ( $p = 4.7$  GPa), and  $\xi = 2.0$ .  $\theta_d$  rises faster and peaks at a much higher temperature than  $\theta_{vib}$ . Therefore, a transient hot spot is created in the DPD due to enhanced anharmonic coupling. Because DPD vibrations equilibrate with the phonons so rapidly, hot spots are formed right behind the shock front, typically within 50 nm of the front. Phonons and bulk vibrations equilibrate in about 70 ps, while the hot spot, which heats up and cools down, equilibrates with the bulk in about 120 ps. If the hot spot reacts, it will generate additional heat and will not cool down as shown in Figure 1. Just after the shock front passes, the molecules in the DPD absorb phonons faster than the bulk. If the  $\chi_d$  is small, which is the case being considered here, it does not deplete the phonon bath, and therefore has little effect on the up-pumping of the bulk material. But if  $\chi_d$  is large, as when the DPD is present in a small isolated grain of material, there will not be enough excited phonons in the grain to produce the large temperature overshoot needed for ignition. This suggests a size effect in hot spot initiated shock chemistry.<sup>5</sup> The prediction, that small grains should be less reactive than large grains, has been observed in some experiments.<sup>23,24</sup> It is important to distinguish the size effect on reactivity predicted by our model from the size effect observed in detonation studies. Detonation properties are not a simple function of grain size since grain size changes the reaction probability as well as the porosity, which has a significant effect on the likelihood of detonation.<sup>24</sup>

Using pressure dependent reaction rates for HMX, for a given set of vibrational quasitemperature profiles, as in Figure 1, the reaction probability  $N(p,t)$  can be calculated

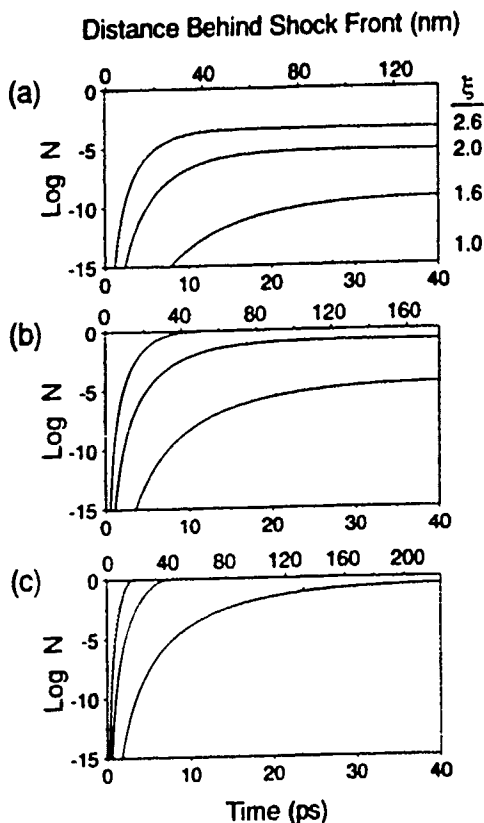


Figure 2 Computed time dependent chemical reaction probabilities for defect perturbed domains and bulk material for shock compression values of (a) 0.85, (b) 0.80, and (c) 0.75. In each panel, solid lines refer to anharmonic enhancements  $\xi$  of 2.6, 2.0, and 1.6, from top to bottom. The bulk reaction probability ( $\xi = 1$ ), given by the dashed curves, remains small until the compression  $V_1/V_0 \leq 0.70$ .



5a for bulk molecules or DPD molecules, using  $\theta_{\text{vib}}(t)$  or  $\theta_d(t)$ , respectively. Figure 2 shows results for the bulk material ( $\xi = 1$ ) and for DPDs with anharmonic enhancement ( $\xi > 1$ ). The different panels are for various compression ratios. It is evident from Figure 2 that a small increase of  $\xi$  above unity enhances the defect reaction probability by many orders of magnitude relative to the bulk. For example, at  $V_1/V_0 = 0.80$  (Figure 2a) and  $\xi = 2$ , the probability of a reaction in the DPD exceeds that in the bulk by about  $10^8$ . For  $V_1/V_0 = 0.85$  (Figure 2b) at 40 ps, the bulk reaction probability is  $\sim 10^{-9}$  while for  $\xi = 2$ , the DPD reaction probability is  $\sim 10^{-1}$ . The reaction probability for the bulk begins to approach unity for  $V_1/V_0 = 0.75$ , so that a shock of about 10 GPa should be sufficient to reproducibly initiate ideal, defect-free, crystalline HMX. At high compressions, the enhancement of DPD reactivity is unimportant since both the bulk and the DPD react completely. The DPD reaches a reaction probability of unity faster than the bulk and closer to the shock front, but since the bulk also obtains a reaction probability, the few tens of ps difference in time will be insignificant. The net result is that the anharmonic enhancement of DPD reactivity takes on the greatest significance for relatively weak shocks.

### Acknowledgments

This research was supported by the US Army Research Office grant DAALO-90-G-0030 to D. D. D., and by the Office of Naval Research, Physics Division grant N00014-89-J-1119 to M. D. F. We gratefully acknowledge many discussions with Prof. Y. Gupta of Washington State University who showed us how to calculate the final temperature after irreversible compression, and several helpful conversations with Dr. Craig Tarver of Lawrence Livermore National Laboratory and Dr. Caryle Storm of Los Alamos National Laboratory.

### References

- (1) Coffey, C. S., Toton, E. T. *J. Chem. Phys.* **1982**, *76*, 949.
- (2) Trevino, S. F., Tsai, D. H. *J. Chem. Phys.* **1984**, *81*, 348.
- (3) Zerilli, F. J., Toton, E. T. *Phys. Rev. B* **1984**, *29*, 5891.
- (4) Walker, F. E. *J. Appl. Phys.* **1988**, *63*, 5548.
- (5) a) Andrei Tomakoff, M. D. Fayer, and D. D. Dlott, *J. Phys. Chem.* accepted 1993.  
b) Dlott, D. D., Fayer, M. D. *J. Chem. Phys.* **1990**, *92*, 3798.
- (6) Wei, T. G., Wyatt, R. E. *Phys. Condens. Matter* **1990**, *2*, 9787.
- (7) Tarver, C. M. *Combustion and Flame* **1982**, *46*, 157.
- (8) Bardo, R. D. *Int. J. Quantum Chem. S* **1986**, *20*, 455.
- (9) Eyring, H., Powell, R. E., Duffrey, G. H.; Darlin, R. B. *Chem. Rev.* **1949**, *45*, 69.  
Eyring, H. *Science* **1978**, *199*, 740.
- (10) Chen, S., Lee, I.-Y. S., Tolbert, W. A., Wen, X., Dlott, D. D. *J. Phys. Chem.* **1992**, in press.
- (11) Dlott, D. D. In *Shock Compression in Condensed Matter 1991*, S. C. Schmidt, R. D.
- (12) Wen, X., Tolbert, W. A., Dlott, D. D. *Chem. Phys. Lett.* **1992**, *192*, 315.
- (13) Mader, C. L. *Numerical Modeling of Detonations*, University of California Press, Berkeley, CA, 1979.
- (14) Johnson, J. N., Tang, P. K., Forest, C. A. *J. Appl. Phys.* **1985**, *57*, 4323.  
Johnson, J. N. *Proc. Roy. Soc. London A* **1987**, *413*, 329. Johnson, J. N. In *Shock Waves in Condensed Matter, 1988*, S. C. Schmidt and N. C. Holmes, Ed., North-Holland, Amsterdam, 1988, p. 527. Karo, A. M., Hardy, J. R. *J. Phys. (Paris) C*

- 1987, 9, 235.
- (15) Bowden, F. P.; Yoffe, A. D. *Fast Reactions in Solids*, Academic Press. New York, 1958.
  - (16) Campbell, A. W.; Davis, W. C.; Travis, J. R. *Phys. Fluids* 1961, 4, 498. Mader, C. L. *Phys. Fluids* 1963, 6, 375.
  - (17) Armstrong, R. W.; Coffey, C. S.; Elban, W. L. *Acta Metall.* 1982, 30, 2111.  
Armstrong, R. W.; Elban, W. L. "Microstructural origins of hot spots in RDX crystals," Chemical Propulsion Information Agency Publication #475, 1987.  
Elban, W. L.; Hoffsommer, J. C.; Armstrong, R. W. *J. Mat. Sci.* 1984, 19, 552.
  - (18) McGuire, R. R. *Working Group Meeting on the Sensitivity of Explosives*, Center for Technology and Research, New Mexico Institute of Technology, 1987; p 624.
  - (19) Wilson, W. L.; Wackerle, G.; Fayer, M. D. *J. Chem. Phys.* 1987, 87, 2498.
  - (20) Tsai, D. H. *J. Chem. Phys.* 1991, 95, 7497.
  - (21) Tang, P. K.; Johnson, J. N.; Forest, C. A. In *Proceedings of the Eighth International Symposium on Detonation Processes*, Office of Naval Research. Silver Spring, MD, 1985; p 52.
  - (22) Kassoy, D. R.; Kapila, A.; Stewart, D. S. *Combust. Sci. Tech.* 1989, 63, 33.
  - (23) Taylor, B. C.; Ervin, L. W. In *Proceedings of the Seventh International Symposium on Detonation Processes*, Office of Naval Research: Silver Spring, MD, 1982; p 3.
  - (24) Neilson, A. T. In *Working Group Meeting on the Sensitivity of Explosives*, Center for Technology and Research, New Mexico Institute of Technology, 1987; p 56.

## Author Index

- Ammon, H.L., 227  
 Armstrong, R.W., 93, 227
- Baird, James K., 355  
 Baker, P.J., 107  
 Bardo, Richard D., 167  
 Beard, B.C., 93, 189, 257  
 Behrens, Jr., Richard, 13  
 Block, S., 199  
 Boris, Jay P., 161  
 Botcher, Tod R., 47  
 Brenner, D.W., 123, 183  
 Brill, Thomas B., 269  
 Bulusu, Suryanarayana, 13, 287
- Cady, Howard H., 243  
 Chen, Dar-Hao, 349  
 Chen, Jenn-Shing, 355  
 Coffey, C.S., 63  
 Covino, J., 173
- De Lozanne, Alex, 221  
 Dick, Jerry J., 75  
 Dlott, Dana D., 379  
 Du, Z.Y., 227
- Egghart, Heinrich, 305  
 Ehrlich, Michael J., 305  
 Elban, W.L., 93, 227  
 Elert, M.L., 123
- Fayer, M.D., 379  
 Finnegan, S.A., 173  
 Fried, Laurence E., 35  
 Friedman, Jacob, 305
- Gallagher, Hugh G., 215  
 Gao, Guang, 149  
 Gilardi, Richard, 233, 237  
 Glancy, B.C., 93  
 Guirguis, Raafat H., 799
- Heimdahl, O.E.R., 173  
 Herley, Patrick J., 87  
 Hsieh, Wen H., 331
- Isom, K.B., 293
- Jayakody, J.R.P., 287  
 Jones, Hermenzo D., 311  
 Jones, William, 87
- Kebahian, P.L., 357  
 Kugler, J.J., 361  
 Kukreti, Anant R., 349  
 Kunz, A. Barry, 149  
 Kuo, Kenneth K., 331
- Lanzerotti, M. Yvonne D., 81  
 Lee, Kien-yin, 237
- Lemire, G.W., 373  
 Lindfors, A.J., 173  
 Litzinger, Thomas A., 331
- Marino, R.A., 287  
 Mellor, A.M., 107, 293  
 Miller, Philip J., 199, 299  
 Mintmire, J.W., 123  
 Moore, J.J., 319
- Nelson, Keith A., 129
- Oran, Elaine S., 161
- Pace, M.D., 53  
 Pandey, Ravindra, 149  
 Pederson, L.R., 361  
 Phillips, Lee, 155, 161  
 Piermarini, G.J., 199  
 Pinto, James J., 41, 81  
 Prieve, Dennis, 141  
 Pringle, J.K., 173
- Rabitz, Herschel, 281  
 Ritchie, James P., 99  
 Robertson, D.H., 123, 183  
 Ruggiero, Anthony J., 35  
 Russell, T.P., 199
- Sandusky, H.W., 93  
 Sausa, R.C., 373  
 Sharma, J., 189, 257  
 Sherwood, John N., 215  
 Simeonsson, J.B., 373  
 Sinkovits, Robert S., 161  
 Stine, James R., 3  
 Storm, Carlyle B., 25
- Tokmakoff, Andrei, 379  
 Travis, James R., 25  
 Tsai, D.H., 113
- Vilallonga, Eduardo, 281
- Wagner, James W., 305  
 Wang, Weining, 129  
 Wefers, Marc M., 129  
 White, C.T., 123, 183  
 Wiegand, D.A., 293  
 Wight, Charles A., 47  
 Wolfe, Allan, 81  
 Wormhoudt, J., 367
- Yoo, Minsun, 221  
 Yoon, Seokwon, 221
- Zaman, Musharraf M., 349  
 Zener, Clarence, 141  
 Zerilli, Frank J., 311  
 Zhang, X.J., 227

## Subject Index

- acoustic modes, 167
- adhesion at propellant-liner interface, 257
- ADN - see ammonium dinitramide
- Al/AP, 299
- Al<sub>2</sub>O<sub>3</sub>, 319
- alpha-NTO, 237
- amalgamated vibrations calculated, 35
- AMBER, computer program, 99
- aminonitrofurazans, 25
- ammonium
  - dichromate, 361
  - dinitramide (ADN), 53, 199, 269
  - nitrate (AN), 269, 361
  - perchlorate (AP), 53, 93, 221, 257, 269, 361
  - picrate, 25
- amorphous film, 47
- anharmonic coupling, 379
- anisotropy, 349
  - of plasticity, 99
- AP - see ammonium perchlorate
- Arrhenius
  - function, 269
  - rate, 25
- atom-atom closest contact, 99
  - interactions, 75
- atomic
  - composition, 3
  - force microscopy (AFM), 221
- atomization of metal products, 87
- Auger electron spectroscopy (AES), 257
- benzotrifuroxan, 25
- beta-NTO, 237
- binding energy, 41
- BN boron nitride, 167
- buckled lattice, 113
- ceramic(s)
  - oxides, 361
  - synthesis, 361
- chemical
  - analyses, 93
  - equilibrium calculations, 311
  - reaction dynamics, 129
- chemically reactive solids, 129
- CH<sub>3</sub>NO<sub>2</sub>, 373
- C-J (Chapman-Jouget)
  - pressure, 25, 299
  - velocity, 25, 299
- CO<sub>2</sub> laser, 47
- coal, 349
- combustion, 269
  - synthesis, 319, 361
- composition
  - B(59%RDX/40%TNT,1%wax), 81
  - tetrahedron, 25
- computer
  - codes, AMBER, 99
  - DYNA2D, 299
  - EPIC, 311
  - MOPAC/PM#, 35
  - generation of multiple excitation pulses, 129
- computing, parallel, 155
- conical face defects, 243
- Connection Machine, 155
- constituent volumes, 3
- constitutive model, 349
- cook-off mechanism, 331
- correlation time, 287
- critical temperature rise, 107
- crystal, 75
  - structure, 233, 237
- crystalline solid, 113
- crystallization, 215
- cubanes, energetic, 233
- DATJ, 189
- debris bubble impact, 173
- decomposition, 13, 355
  - of solids, 281
  - process, 367
  - thermal, 47
  - times, 41
- defect-perturbed domain, 379
- defects, 155, 161
  - impurities, 113
  - propagation of, 113
- density, 25, 299
  - prediction, 3
- detection, 373
- detonation, 123, 155
  - front, 183
  - velocity, 25, 305
- diagnostic technique, 367
- 1,3-diamino-2,4,6-trinitobenzene, 25
- diamond anvil high pressure cell (DAC), 199
- differential scanning calorimetry (DSC), 41
- diffusion coefficient, 355
- DINGU (1,4-dinitroglycoluril), 41
- discrete-continuum theory, 281
- dislocations, 93, 215, 227
  - energy, 63
  - motion, 63
- dispersed solid particles, 305
- DMD (1,4-dimethyl-2,5-dinitroglycoluril), 41
- DMNA, 373
- DNNA (1,3,3,5-tetranitrohexahydro-1,3,5-triazine), 269
- doorway modes, 379
- drop test, 25
- droplet impact, 141
- DYNA2D, computer program, 299
- dynamic deformation, 173

- EDXD spectra, 199
- elastic constants, 349
- electron(-)
  - beam, 87
  - induced decomposition, 87
  - paramagnetic resonance (EPR), 53
  - spin
    - concentration, 53
    - relaxation, 53
- electronic
  - excitations, 189
  - structure, 149
- electrostatic discharge (ESD), 293
- embedded cluster simulation, 149
- energetic
  - layered materials, 167
  - materials, 25, 81, 129, 173, 257, 269, 273, 361
- energy
  - dispersive x-ray diffraction (EDXD), 199
  - localization, 63
  - transfer, 281
    - rates, 35
- enthalpy change, 319
- EPIC, computer program, 311
- EPR spectra, 53
- equation of state, 299, 311
- equilibrium, 113
- explosion, droplet, 141
- explosive(s), 13, 233
  - crystals, 63, 243
- femtosecond spectroscopy, 129
- Fick's
  - first law, 355
  - second law, 355
- fizz zone, 269, 331
- foam
  - layer, 331
  - zone, 269
- fracture, 293
  - mechanics, 227
  - surface topography, 81
- fragment impact modelling, 173
- FTIR spectra, 199
  - spectroscopy, 47, 269
- furoxans, 25
- GAP, 269
- gas, 355
  - evolution rate, 355
  - products, 269
- graphite intercalation, 167
- growing crystals, 243
- Hamiltonian, 35
- hardness, 227
  - testing, 93
- HCl gas, 319
- heat of formation, 3, 25
- hexanitrobenzene, 25
- hexanitrobenzyl, 25
- hexanitrobenzylidiamine, 25
- high(-)
  - acceleration, 81
  - explosives, 25
  - pressure deformation, 349
  - resolution transmission electron microscope (HRTEM), 87
  - speed photography, 93
- HMX, 13, 25, 35, 41, 53, 81, 227, 243, 269, 379
- HNIW (hexanitro-hexaazaisowurtzitane), 41, 53, 199
- holography, time resolved, 305
- homogeneous initiation, 183
- hot
  - fragment conductive ignition, 331
  - spots, 107, 155, 227
    - anelastic/plastic compression, 113
    - elastic compression, 113
    - formation, 293, 379
    - heating, 113
    - quenching, 293
- HTPB(hydroxyl-terminated polybutadiene)/AP, 107, 173, 293
- ignition, 107
  - and combustion behavior of solid propellants, 331
  - temperature, 293
  - threshold, 63
- impact
  - initiation, 293
  - sensitivity, 25, 35, 107, 173
- impurities, 113
- impurity defects, 113
- infrared
  - fiber optics, 367
  - laser pyrolysis, 47
- initiation, 63, 107, 155, 183
- insensitive
  - high explosive, 237
  - materials, 167
- insulator, 221
- intercalated materials, 167
- intermediate products, 13
- IR transmission spectra, 367
- isentropes, NM/PMMA/Al, 311
- Jones-Wilkins-Lee (JWL), 299
  - modified, 299
- Kamlet (oxygen balance), 25
- kinetic energy distribution, 113
- laser-based, 373
- lattices, 161
- lead
  - azide, 305
  - styphnate, 35
- liquid(-)
  - phase decomposition, 13
  - state perturbation theory, 311
- local melting, 113

- M39(RDX75%, binder25%), 367  
 magic angle spinning, 287  
 mass  
   spectrometry, 13  
   transport, cumulative, 355  
 Maxwellian distribution, 113  
 MD, molecular dynamics, 183  
 mechanical  
   behavior, 81  
   twins, 243  
 mechanisms of heating, 113  
 metal  
   azides, 87  
   nitrates, 361  
   oxides, 361  
   particles, 87  
 metallized explosives, 311  
 microindentation, 93  
 microstructure, 93  
 Moby-Dick test, 299  
 model energetic molecular solid, 183  
 molecular(-)  
   bond reorganization, 123  
   bulk dynamics, 281  
   dynamics (MD), 113, 123, 155, 161, 183  
   level theory, 167  
   structure, 3, 41  
 3-D molecular dynamics, 155  
 monotonic Lagrangian grid, 161  
 MOPAC/PM#, computer program, 35  
 Morse potential, 113  
 mullite, 361  
 multi-crystalline explosives, 63  
 multiphonon up pumping, 189, 379  
 multiple  
   fragmentation theory, 281  
   probe femtosecond spectroscopy, 129  
 munitions hazards assessments, 173  
  
 naphthalene, 379  
 NC(13%N), 269  
 nitramine-based solid propellants (RDX), 47, 331  
 nitramines, 13  
 nitrocellulose, 287  
 nitroguanidine, 3  
 nitromethane, 75, 155  
 nitromethane/PMMA/Al, 311  
 nitroso compounds, 227  
 nitroxide free-radical, 53  
 NMR  
   chemical shift anisotropy, 287  
   magic angle spinning (MAS), 287  
 N-N bond distance, 41  
 NO, 373  
 NO<sub>2</sub>, 53, 373  
 N<sub>2</sub>O<sub>4</sub>, 47  
 non-ideal explosive, 299  
 non-wetting surface, 141  
 NTO(5-Nitro-2,4-dihydro-3H-1,2,4-triazol-3-one), 237  
   identification, 237  
  
 octaazacubane, 25  
 Octol(70%HMX/30%TNT), 81  
 optic modes, 167  
 optical  
   absorption, 189  
   polarizing light microscopy, 199  
 outgassing rate, 355  
 oxygen balance, 25  
  
 parallel computing, 155  
 Pb styphnate, 35  
 pentanitroaniline, 25  
 pentolite(50%RDX,50%TNT), 299  
 PETN(pentaerythritol tetranitrate), 3, 75, 99, 167, 243, 299  
 phase transition, 123  
 phonons, 35  
 photofragment, 373  
 picramide, 25, 189  
 picric acid, 25  
 plastic deformation rate, 63  
   flow, 293  
   strain rate, 63  
 PNA p-nitroaniline, 199  
 polarized light strain, 199, 243  
 polycrystalline film, 47  
 polycyclic compounds, 233  
 polymer, 287  
 polymorphs, 237  
 potential energy, 227  
 potentials  
   modified Tersoff, 123  
   Morse, 113  
 power spectral statistical techniques, 81  
 pressure dependence of acoustic, optic modes, 167  
 prompt detonation, 173  
 propellants, 13, 25, 107, 233  
   activation energy, 331  
   combustion, 269  
   radiative properties, 331  
   thermal conductivity, 331  
 pulse shaping, 129  
 pyrolysis, 13  
   by infrared laser, 47  
  
 quantum dynamics, 281  
  
 reaction of Al in explosive mixture, 311  
 radiation damage, 257  
 rapid compression, 113  
 rarefaction shocks, 123  
 RDX cyclotrimethylenetrinitramine, 93  
 RDX (1,3,5-trinitrohexahydro-1,3,5-triazine), 3, 13, 41, 47, 53, 93, 199, 227, 243, 257, 269, 367, 373  
   crystal, 149  
 reaction  
   chamber, 319  
   driven shock simulation, 123  
   front, 305  
   interface, 319  
   onset, 63  
   pathway, 13

relaxation, 113  
 resonance-enhanced multiphoton ionization, 373  
 rigid slip, 99

Saint Roberts burning rate, 331  
 scanning electron microscope (SEM), 237, 243, 257

secondary  
   ion mass spectrometry (SIMS), 257  
   neutral mass spectrometry (SNMS), 257

sensitivity, 25, 161, 189, 257  
   control, 25  
   impact, 173  
   of energetic materials, 331  
   test, 25

shake-up transitions, 189

shear, 75  
   banding, 107  
   bands, 113

shock(s), 155, 173  
   compression, 113  
   front, 305  
   propagation, 305  
   initiated molecular reactions, 379  
   initiation, 25  
   loading, 93

  high amplitude, 63  
   radius, 305  
   reactivity, 93  
   response, 173  
   sensitivity, 75  
   with defects, 161

simulation, 123, 183  
   embedded cluster, 149

simultaneous thermogravimetric modulated  
   beam mass spectroscopy, 13

single bond rotations, 99  
 slip, 99, 227

  planes, 113  
   systems, 113

SOLGASMIXPV computer program, 319

solid propellants, 355

  combustion, 367  
   properties, 331

spatial power spectra (fracture surface  
   profiles), 81

split shock waves, 123  
 stability, 41

  relative, 13

stacking fault, 215

stereographic projection, 227

steric hindrance, 75

strain, 349

  energy, 113

strand burning, 367

stress, 349

  reduction, 99

structure, electronic, 149

supercritical shear, 75

surface analysis by laser ionization (SALI),  
 257

  burning heat release, 331  
   chemistry, 269

mass spectrometry, 257  
 modification, 221  
 synchrotron x-radiation, 215

TATB - see triamino-trinitrobenzene

TEM, 361

temperature-pressure phase diagrams, 199

3-D testing, 349

1,2,4,5-tetranitrobenzene, 25

tetrayl, 3

thermal

  decomposition, 13, 47, 269

  excitation, 293

  gradient analysis (TGA), 41

thermochemical and mechanical properties,  
 331

thin films, 47

TiB<sub>2</sub>, 319

time(-)

  dependent energy release, 311

    by Al reaction, 311

  equation of state, 299

  lag method, 355

  resolved holography, 305

  to-ignition, 167

TNB - see trinitrobenzene

TNT - see trinitrotoluene

transversely isotropic, 349

triamino-trinitrobenzene (TATB), 25, 35, 167,  
 189, 243, 257

1,3,5-triamino-2,4,6-trinitrobenzene, 25

triaxial compression, 349

trinitrobenzene (TNB), 25, 189

trinitrotoluene (TNT), 3, 25, 81, 215, 373

twinning, 215, 227

two particle interaction, 305

TZX (diaminotetrazinedianoxide), 25

ultracentrifuge, 81

ultra-high vacuum, 221

underwater explosives, 299

unit cells, 227

uniaxial strain, 75

urea, 361

uv dissociation, 373

  photolysis, 53

vacancies, 113

vapor deposition, 47

vibron frequencies, 35

Vickers hardness, 93

video imaging burn front, 319

weapon design, 173

wedge test, 173

worm hole defects in TATB, 243

XPS - see photoelectron spectroscopy

x-ray photoelectron spectroscopy, 189

  diffraction (XRD), 361

  irradiation, 41

  photoelectron spectroscopy (XPS), 41, 93,  
 257